Universidad Autónoma de Madrid

Reactividad y alteración en la superficie de contacto entre una bentonita y morteros de cemento: aplicación al comportamiento de barreras de ingeniería en el almacenamiento geológico de residuos radiactivos

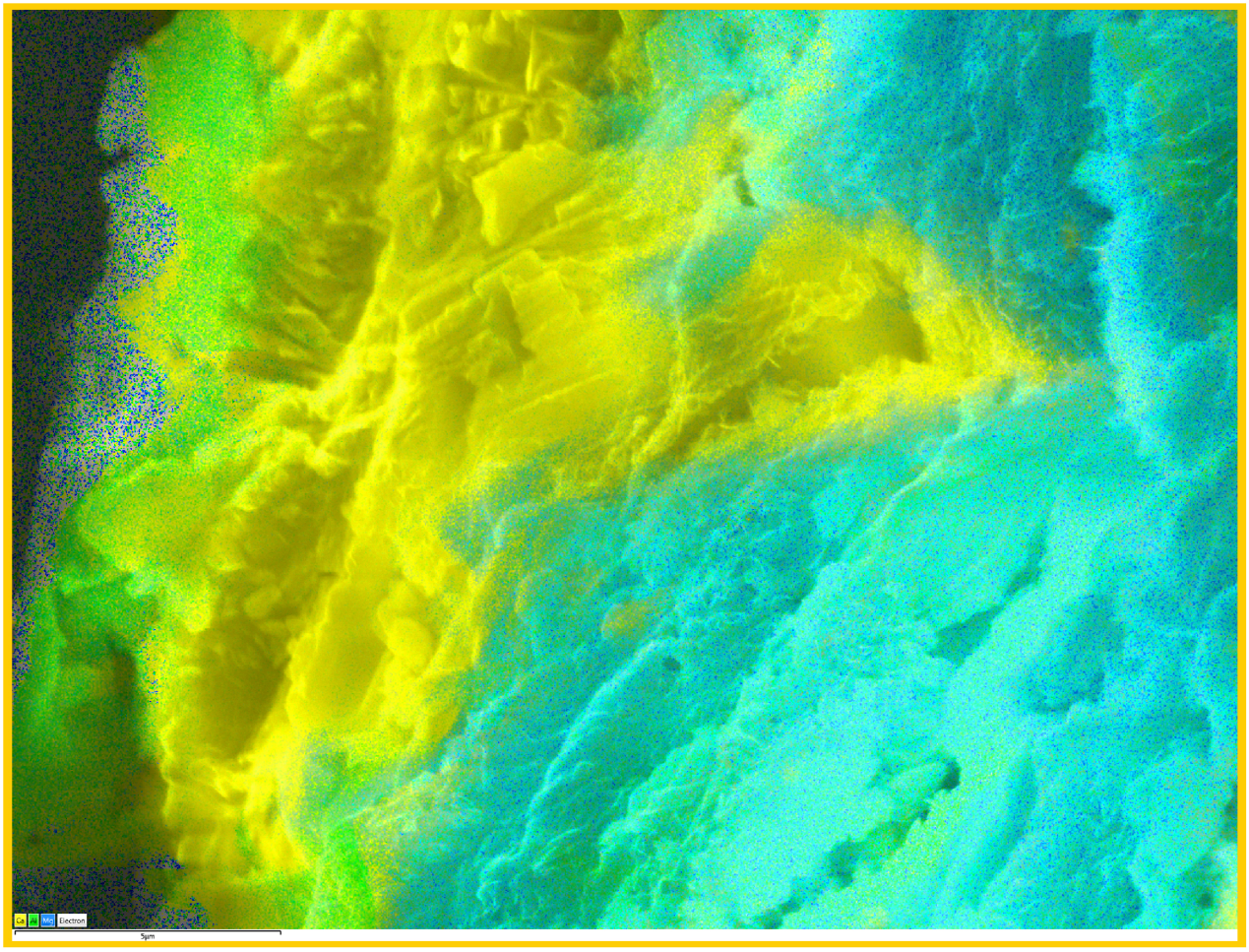

Tesis Doctoral
Daniel González Santamaría
Madrid, 2020

FACULTAD DE CIENCIAS
UNIVERSIDAD AUTÓNOMA DE MADRID

FPI-UAM

Campus Internacional excelencia UAM CSIC

Facultad de Ciencias
Departamento de Geología y Geoquímica

TESIS DOCTORAL

Reactividad y alteración en la superficie de contacto entre una bentonita y morteros de cemento: aplicación al comportamiento de barreras de ingeniería en el almacenamiento geológico de residuos radiactivos

Reactivity and alteration in the contact surface between a bentonite and cement mortars: application to the behaviour of engineering barriers in the geological repository of radioactive waste

DANIEL GONZÁLEZ SANTAMARÍA

MADRID, 2020

Director:
Dr. Jaime Cuevas Rodríguez
Dpto. de Geología y Geoquímica, Facultad de Ciencias, Universidad Autónoma de Madrid

Facultad de Ciencias

Departamento de Geología y Geoquímica

Dr. Jaime Cuevas Rodríguez, Profesor titular del Departamento de Geología y Geoquímica de la Facultad de Ciencias de la Universidad Autónoma de Madrid

CERTIFICA:

que **Daniel González Santamaría** ha realizado bajo mi supervisión, en el Departamento de Geología y Geoquímica de la Facultad de Ciencias de la Universidad Autónoma de Madrid, la Tesis Doctoral con el título:

Reactividad y alteración en la superficie de contacto entre una bentonita y morteros de cemento: aplicación al comportamiento de barreras de ingeniería en el almacenamiento geológico de residuos radiactivos

Reactivity and alteration in the contact surface between a bentonite and cement mortars: application to the behaviour of engineering barriers in the geological repository of radioactive waste

Y para que conste, firmo el presente certificado en Madrid, en julio de 2020

El Director,

Dr. Jaime Cuevas Rodríguez

El Doctorando,

Daniel González Santamaría

Facultad de Ciencias
Departamento de Geología y Geoquímica

Esta Tesis Doctoral se ha realizado en el Departamento de Geología y Geoquímica de la Facultad de Ciencias de la Universidad Autónoma de Madrid, y ha sido realizada gracias al programa de ayudas de Formación de Personal Investigador *FPI-UAM* (SFPI/2017-00163) y el programa Horizonte 2020 de la Unión Europea EUROATOM (H2020 NFRP 014/2015) bajo el acuerdo de subvención nº 662147 (CEBAMA).

Memoria presentada por **Daniel González Santamaría** para optar al Grado de Doctor en Química Aplicada por la Universidad Autónoma de Madrid

Madrid, julio de 2020

El Doctorando, Vº Bº del Director,

Daniel González Santamaría **Dr. Jaime Cuevas Rodríguez**

AGRADECIMIENTOS

Quiero agradecer al Dr. Jaime Cuevas el haber sido mi director y tutor de tesis, Jaime me ha enseñado a investigar desde las etapas como estudiante de grado, posgrado y predoctoral dedicando una generosa cantidad de tiempo y esfuerzo.

En el mismo sentido, quisiera expresar mis agradecimientos al Dr. Raul Fernández que desde el primer momento se ha implicado en la tesis y mi formación empleando su tiempo y paciencia. También quisiera mostrar mi agradecimiento al resto de miembros del grupo de investigación *Arcillas y Control Medioambiental*, especialmente a Ana Isabel y Almudena.

Al Dr. Juan Diego Rodriguez Blanco, tutor durante las estancias en el Trinity College de Dublín, por facilitarme los medios y ayuda necesaria para completar la presente tesis. También a Conor Costello y Lourdes Santamaría por su acogida en Irlanda, sin olvidarme de Sinead, Enya y Brendan que hicieron que mi paso por Dublín fuera excepcional.

A Maria Jesús por su acogimiento durante la estancia en el CIEMAT y Mari Cruz y Jose Luis del IETcc por su asesoramiento en el campo de los materiales de cemento.

A Ana J. y Juan Z, compañeros del Módulo 8 de la facultad, por ayudarme y acompañarme a dar los primeros pasos en este mundo de la investigación.

A Quique, Gabi, Noemí y Ramón del SIdI por su amabilidad y trabajo.

Al personal del departamento de Geología y Geoquímica y especialmente a Amalia Álvarez.

A mis amigos “de siempre” Miki, Gonzalo, Javi, Ángel y Alberto que pese a que les quité numerosos momentos juntos han seguido estando presentes.

A mi familia: Blanca, Rodrigo, Patricia y Patricio pues siempre me han apoyado y ayudado incondicionalmente para que pudiera finalizar esta larga etapa. Quisiera recordar a mi padre Chema pues fue quién sembró en mi la semilla de la curiosidad por el conocimiento.

ÍNDICE

ACRÓNIMOS

AFm	Monosulfate Aluminate Hydrate / Monosulfo Aluminato Hidratado
AFM	Microscopia de Fuerza Atómica
AFt	Trisulfate Aluminate Hydrate, ettringite / Trisulfo Aluminato Hidratado, etringita
AGP	Almacenamiento Geológico Profundo
ATC	Almacenamientos Temporales Centralizado
ATI	Almacenamientos Temporales Individualizados
BET	Brunauer Emmett–Teller method / método Brunauer–Emmett–Teller
C_2S	Silicato dicálcico, belita
C_3A	Aluminato tricálcico
C_3S	Silicato tricálcico, alita
C_4AF	Alumino Ferrit tretracalcium / Ferro Aluminato tetracálcico, ferrita
C-A-S-H / CASH	Calcium Aluminium Silicate Hydrates / Silicatos de Aluminio y Calcio Hidratados
CB / C-B	Cement mortar-Bentonite
CEC	Cation Exchange Capacity / Capacidad de intercambio catiónico
CH	Portlandita
CM	Coloidal Model / Módelo coloidal

CIEMAT	Centro de Investigaciones Energéticas, Medioambientales y Tecnológicas
CmSAH	Calcium monoSulfate-Aluminate Hydrate
C-S-H / CSH	Calcium Silicate Hydrates / Silicatos de Calcio Hidratado
CSIC-IETcc	Eduardo Torroja Institute for Construction Science
CW / C-W	Cement mortar-Water
DDL	Diffuse Double Layer / Doble capa difusa
DGR	Deep Geological Repository
EBS	Engineering Barrier System / Sistema de Barreras de ingeniería
EDL	Electrical Double Layer / Doble capa eléctrica
FEBEX	Full-scale Engineered Barrier EXperiment
GI-XRD	Grazing Incidence X-Ray Diffraction / Difracción de rayos-X en incidencia rasante
GTS	Grimsel Test Site
HLRW	High-Level Radioactive Waste
HpH	High-pH / alto pH
HRTEM	High Resolution Transmission Electron Microscopy / Microscopía de transmisión electrónica de alta resolución
IC-CD	Chromatography Equipment Coupled to a Conductivity Detector
IETcc	Instituto Eduardo Torroja de Ciencias de la Construcción

JCR	Journal Citations Reports
LpH	Low-pH / bajo pH
LpHC	low-pH cement mortar
M-(C)-S-H	Magnesium (Calcium) Silicate Hidrates / Silicatos de Magnesio (Calcio) Hidratados
Mnt	Montmorillonite / Montmorillonita
Mt	Montmorillonite / Montmorillonita
MOX	combustibles mixtos de óxidos de uranio y plutonio
M-S-H / MSH	Magnesium Silicate Hidrates / Silicatos de Magnesio Hidratados
OPA	Opalinus clay rock
OPC	Ordinary Portland cement / Cemento Ordinario Pórtland
PTFE	Polytetrafluoroethylene / politetrafluoroetileno
PZC	Punto cero de carga
RE	Residuos especiales
RAA	Residuos de Alta Actividad
RBMA	Residuos de Baja y Media Actividad
SEM-EDX	Scanning Electron Miscroscopy coupled to Energy Dispersive X-Ray / Microscopía Electrónica de Barrido con Energía Dispersiva de Rayos X
SF	Silica Fume / Humo de Sílice

SSA	Specific Surface Area / superficie específica
TEM	Transmission Electron Microscopy / Microscopía Electronica de Transmisión
URL/s	Underground Research Laboratories / Laboratorios de Investigación Subterráneos
XRD	X-Ray Diffraction / Difracción de Rayos X

RESUMEN

El destino final de los residuos radiactivos procedentes de las centrales nucleares constituye un problema de primer orden a escala mundial. La comunidad científica se inclina por su almacenamiento en medios geológicos situados a profundidades de hasta 1000 m. Este emplazamiento requiere de un sistema de barreras de ingeniería (Engineering Barrier System, EBS) superpuestas capaz de aislar los residuos durante cientos de miles de años, momento en el cual la emisión de radiación de alta actividad específica habría finalizado. Para poder garantizar la estabilidad del EBS es necesario el estudio de la evolución de los materiales que lo constituyen, entre éstos destacan los materiales basados en cemento y arcillas. Una de las vías de estudio consiste en el desarrollo de experimentos de laboratorio capaces de reproducir la reactividad geoquímica que se genera por el contacto entre los distintos materiales de las barreras teniendo en cuenta factores como el entorno geológico y las características de las aguas subterráneas. Esto es factible de reproducir en experimentos de laboratorio instalados en excavaciones subterráneas (Underground Research Laboratories, URL), es decir, realizados *in-situ* en la propia matriz geológica. Partiendo de la base de que los URL son la piedra angular para el estudio del comportamiento del EBS a medio y largo plazo, estos emplazamientos están condicionados por la necesidad de una importante infraestructura, tiempo de experimentación (decenas de años) y sujetos a un número muy limitado de muestras por razones económicas. De modo que los experimentos de laboratorio a pequeña escala podrían cubrir estos aspectos y complementar los resultados de los URL desde las etapas iniciales.

En el presente trabajo se ha desarrollado un modelo experimental basado en celdas de transporte que confinan un mortero de cemento en contacto con una arcilla

bentonítica. Además, se ha simulado la hidratación de tapones de hormigón que actúan de sello de contención de la bentonita compactada infiltrando agua subterránea procedente de un entorno granítico, atravesando primero el mortero y después la bentonita, donde el agua de interacción fue recogida y analizada periódicamente. De esta forma, se ha pretendido reproducir las condiciones previstas de una parte del sistema multibarrera concebido para un almacenamiento geológico profundo (AGP) en granito. Tras una primera etapa de puesta a punto y optimización de los materiales del modelo experimental y la metodología, se procedió a evaluar las perturbaciones geoquímicas generadas por tres tipos de morteros de cemento: *i*) un mortero caracterizado por generar un "bajo pH" en su porosidad intersticial (denominado como LpH), para lo cual se utilizó cemento Pórtland CEM-I y adición de microsílice; *ii*) un mortero con alto pH (HpH) elaborado con cemento Pórtland CEM-I sin adiciones minerales (denominado como CEM-I); y un tercer tipo de mortero, también de alto pH (denominado como CEM-II), elaborado con cemento Pórtland CEM-II con adición caliza. Todos fueron puestos en contacto con el mismo tipo de arcilla, la bentonita-FEBEX (Full-scale Engineered Barrier EXperiment) y agua granítica. El estudio se realizó en intervalos de tiempo de 6 y 18 meses, donde cada tipo de experimento fue duplicado en cada uno de los dos periodos de tiempo estando el modelo experimental constituido por un total de 12 celdas de transporte. Una vez completados los experimentos, los materiales fueron caracterizados en cuanto a: i) su mineralogía mediante técnicas de difracción de rayos X (XRD); ii) su morfología y composición química a escala nano-milimétrica mediante Microscopía Electrónica de Barrido con Energía Dispersiva de Rayos X (Scanning Electron Miscroscopy coupled to Energy Dispersive X-Ray, SEM-EDX), *iii*) y su superficie específica (Specific Surface Area, SSA) por el método Brunauer–

Emmett–Teller con N_2 (g) (BET-N_2). En lo que respecta al agua infiltrada y recogida durante el transcurso de los experimentos, se determinaron: los iones mayoritarios mediante cromatografía iónica y detector de conductividad eléctrica (IC-DC), pH y carbonatos por valoración potenciométrica, y sílice en disolución acuosa por espectrofotometría visible (λ = 800 nm). Complementariamente se calculó la conductividad hidráulica presentada por cada una de las celdas de transporte.

En el estudio piloto de <3 meses de duración se observó una reactividad muy limitada en términos de extensión e intensidad, tanto en el mortero como en la bentonita-FEBEX. Si bien, estas alteraciones mostraban similitudes con aquellas recogidas en la bibliografía científica, de modo que permitían validar una metodología de base para proceder con mayor garantía al estudio simultáneo y sistemático del conjunto de las 12 celdas a lo largo de los 6 y 18 meses. En los experimentos, se observó una diferente evolución de la reactividad en función del tipo de experimento planteado y el tiempo:

- El mortero de LpH presentó formación de brucita en la superficie enfrentada con la bentonita. Ésta posteriormente daría paso a la formación de fases de silicatos de magnesio y calcio hidratados (M-S-H y C-S-H) tras 18 meses de interacción. Además, la composición química del mortero mostró una ligera carbonatación (acumulación de Ca por precipitación de calcita) en las proximidades del contacto (zona denominada también como interfase). Con respecto a la bentonita-FEBEX, se observaron contenidos máximos de Mg a una distancia de decenas de micras del contacto con el mortero. Ambos materiales sufrieron una pérdida de SSA presumiblemente ligada a un proceso de oclusión de la meso-microporosidad.

- En los experimentos de HpH, es decir con CEM-I y CEM-II, los morteros mostraron mayor grado de carbonatación y contrariamente a lo observado en los morteros LpH, no se produjo la precipitación de minerales exclusivamente de Mg como la brucita. En cuanto al estudio de las superficies e interfases de la bentonita-FEBEX, éstas presentaban una mayor alteración por acumulación de Mg en las proximidades del contacto ocasionada por la presencia de fases de silicato de Mg, fundamentalmente constituidas por brucita intercalada entre las láminas de montmorillonita (Mnt) presente en la bentonita-FEBEX, sin que se pueda excluir la neoformación de fases silicatos de Mg hidratados con un alto grado de desorden estructural. También se detectó la presencia minoritaria de calcita en las superficies de la bentonita enfrentadas al mortero y proximidades de la interfase. Por último, sólo los experimentos con CEM-II mostraron una pequeña tendencia a aumentar su SSA con el tiempo.

Otros procesos observados comunes a los 3 tipos de experimentos fueron: *i*) la migración de Al desde la bentonita hacia los morteros, favoreciendo así la precipitación sulfoaluminatos cálcicos (principalmente etringita) además de silicatos de calcio hidratados con baja sustitución de silicio por aluminio (C-(A)-S-H) y estructura similar a la de la tobermorita.

Paralelamente, los parámetros estudiados del efluente mostraron independientemente del tipo de experimento valores de pH y sílice característicos de la bentonita, predominando las especies acuosas de carbonato al final del experimento (18 meses) quedando por tanto condicionados por el equilibrio establecido con ésta.

Los resultados se han obtenido a partir de un modelo experimental no planteado con anterioridad. Es versátil puesto que permite estudiar la reactividad y rendimiento de distintos materiales en periodos de tiempo relativamente cortos y bajo las mismas condiciones experimentales y de repetitividad, lo que en última instancia aporta una mayor robustez a los resultados obtenidos.

Además, la tesis ha permitido evaluar la reactividad que tiene lugar inicialmente en los materiales del EBS que junto con las perturbaciones observadas en los URL realizados *in-situ*, en escalas de tiempo de decenas de años y en tamaños reales, permiten hacer una primera extrapolación o escalado "*up-scaling*" de la evolución de tales perturbaciones.

Por último, aportan datos de gran utilidad para la elaboración de modelos geoquímicos que finalmente sí podrían estimar en un marco razonablemente seguro la perturbación que sufrirían los materiales de base cemento y la barrera de arcilla hasta que decayera la radiactividad a los valores naturales de fondo ($>10^4$ años).

PALABRAS CLAVE

Aislamiento de los residuos radiactivos, Almacenamiento Geológico Profundo, Sistema de Barreras de Ingeniería, bajo pH, alto pH, bentonita-FEBEX, morteros cemento, reactividad geoquímica.

ABSTRACT

The final destination of radioactive waste from nuclear power plants is an on-course problem to be tackled in many countries around the world. The scientific community favours its storage in geological media located at depths of up to 1000 m. This site requires a system of overlapping engineering barriers (Engineering Barrier System (EBS)) capable of isolating such waste for hundreds of thousands of years, at which point the emission of highly specific activity radiation would have been minimized. In order to guarantee the stability of the EBS, it is necessary to study the evolution of its constituent materials. Among these materials, the ones based on cement and clays are the most preeminent. One of the paths of study consists of the development of laboratory experiments capable of reproducing the geochemical reactivity that is generated by the contact between the different materials of the barriers, taking into account factors such as the geological environment and the characteristics of groundwater. This is feasible to reproduce in laboratory experiments installed in underground excavations (Underground Research Laboratories, URL), that is, carried out in-situ in the geological matrix itself. Based on the fact that URLs are the cornerstone for the study of EBS behaviour in the medium- and long-term , these sites are conditioned by the need for important infrastructure, experimentation time (tens of years) and subject to a number very limited samples for economic reasons. Thus, small-scale laboratory experiments could cover these aspects and complement the results of URLs from the initial stages.

In the present work, an experimental model based on transport cells that confine a cement mortar in contact with a bentonite clay has been developed. In addition, the hydration of concrete plugs that act as a containment seal of the compacted

bentonite has been simulated by infiltrating groundwater from a granite environment, first passing through the mortar and then the bentonite, where the interaction water was collected and analysed periodically. The reasoning behind this process is to reproduce the expected conditions of a part of the multi-barrier system designed for deep geological storage (AGP) in granite. After the first stage of set-up and optimization of the experimental model materials and methodology, the geochemical disturbances generated by three types of cement mortars were evaluated: i) a mortar characterized by generating a low pH in its interstitial porosity (called LpH), for which Portland cement CEM-I and addition of microsilica were used; ii) a high pH (HpH) mortar made with Portland cement CEM-I without mineral additions (called CEM-I); and a third type of mortar, also of high pH (called CEM-II), made with Portland cement CEM-II with limestone addition. All were put in contact with the same type of clay, FEBEX-bentonite (Full-scale Engineered Barrier EXperiment) and granitic water. The study was carried out at time intervals of 6 and 18 months, where each type of experiment was duplicated in each of the two time periods, with the experimental model consisting of a total of 12 transport cells. Once the experiments were completed, the materials were characterized in terms of i) their mineralogy using X-ray diffraction techniques (XRD); ii) its morphology and chemical composition on a nano-millimetre scale using Scanning Electron Microscopy coupled to Energy Dispersive X-Ray (SEM-EDX), iii) and its specific surface area (SSA) by the Brunauer–Emmett–Teller method with N_2 (g) (BET-N_2). Regarding the water infiltrated and collected during the course of the experiments, the main ions were determined by means of ion chromatography and an electrical conductivity detector (IC-DC), pH and carbonates by potentiometric titration, and silica in aqueous solution by spectrophotometric measurements (λ = 800 nm).

In addition, the hydraulic conductivity presented by each of the transport cells was calculated. In the pilot study of <3 months duration, a very limited reactivity in terms of extension and intensity was observed in both the mortar and the FEBEX-bentonite. However, these alterations showed similarities with those found in the scientific literature, making it possible to validate a basic methodology to proceed with further confidence to the simultaneous and systematic study of all 12 cells over the 6 and 18 months. The research revealed a different evolution of reactivity depending on the type of experiment proposed and the time:

- The LpH mortar presented brucite formation on the surface facing the bentonite. This would later lead to the formation of hydrated magnesium and calcium silicate phases (M-S-H and C-S-H) after 18 months of interaction. Also, the chemical composition of the mortar exhibited a slight carbonation (accumulation of Ca by calcite precipitation) in the vicinity of the contact (zone also known as the interface). Concerning FEBEX-Bentonite, maximum Mg contents were detected at a distance of tens of microns from the mortar contact. Both materials suffered a loss of SSA presumably linked to a process of meso-microporosity occlusion.

- In the HpH experiments, i.e. with CEM-I and CEM-II, the mortars displayed a higher degree of carbonation and, contrary to what was discovered in the LpH mortars, there was no precipitation of exclusively Mg minerals such as crude oil. As regards the study of the surfaces and interfaces of FEBEX-bentonite, these featured a greater alteration due to the accumulation of Mg in the interface caused by the presence of Mg silicate phases, fundamentally made up of brucite interspersed between the montmorillonite (Mnt) sheets present in FEBEX-bentonite, without it being possible to exclude the neoformation of hydrated Mg silicate phases with a high degree of structural disorder. The minor presence of

calcite was also detected on the surfaces of the bentonite facing the mortar and in the proximity of the interface. Finally, only the CEM-II experiments showed a small tendency to increase their SSA over time.

Other observed processes common to the 3 types of experiments were: i) the migration of Al from the bentonite to the mortars, thus favouring the precipitation of calcium sulfoaluminates (mainly ettringite and minority monosulfoaluminates or AFM phases) in addition to calcium silicate hydrates (with a low replacement of silicon by aluminium) (C-(A)-S-H) and similar structure to that of tobermorite.

Additionally, the studied parameters of the effluent revealed , regardless of the type of experiment, characteristic pH and silica values of bentonite, with aqueous carbonate species prevailing at the end of the experiment (18 months), therefore being conditioned by the equilibrium established with it.

The results have been obtained from an experimental model not previously proposed. It is a versatile tool since it allows to study the reactivity and performance of different materials in relatively short periods of time and under the same experimental and repeatability conditions, which ultimately provides greater robustness to the results obtained.

Furthermore, the thesis has allowed the evaluation of the reactivity that takes place initially in the EBS materials which, together with the disturbances observed in the URLs carried out in-situ, on time scales of tens of years and in real sizes, allow a first extrapolation or "up-scaling" of the evolution of such disturbances.

Finally, they provide valuable data for the development of geochemical models that could finally assess, within a reasonably safe framework, the disturbance that

the cement-based materials and the clay barrier would suffer until the radioactivity decays to the natural background values (>104 years).

KEYWORDS

Radioactive waste isolation, Deep Geological Repository, Engineered Barrier System, low pH, high pH, FEBEX-Bentonite, cement mortar, geochemical reactivity.

CAPÍTULO 1. INTRODUCCIÓN

1.1. Antecedentes

1.2. El Almacenamiento Geológico Profundo

1.3. El Concepto Multibarrera y el Sistema de Barreras de Ingeniería

1.4. Planteamiento del problema y objetivos

1.5. Referencias

1.1 ANTECEDENTES

Desde mediados del siglo XX la obtención de energía procedente de las centrales nucleares supone alrededor del 11% del total de energía generada en el mundo, lo que es especialmente relevante ante el incremento mundial de la demanda energética impulsada por el desarrollo de los países emergentes como China e India. Además, su generación no implica la liberación de gases de efecto invernadero, lo que supone un aspecto a considerar ante el calentamiento global y la contaminación derivada de la obtención de la quema de combustibles fósiles (Goh and Ang, 2018; Saidi and Omri, 2020).

Sin embargo, este tipo de energía produce millones de barras de combustible gastado y toneladas de residuos radiactivos cada año. Un material se define como *residuo radiactivo* en la medida en la que posee radioisótopos en concentraciones y niveles de actividad superiores a los establecidos legalmente (2001). Su liberación en el medio causa graves consecuencias en los seres humanos y el medioambiente cuyos efectos negativos permanecen latentes durante cientos e incluso millones de años. Dos ejemplos de las consecuencias causadas por una liberación no controlada son los últimos accidentes ocurridos en centrales nucleares de Chernóbil y Fukushima (Steinhauser et al., 2014). Los principales elementos responsables de esta radiotoxicidad se generan a raíz de los procesos de fisión nuclear y captura neutrónica que tienen lugar en el reactor nuclear y que originan los actínidos U, Pu, Am Cm y sus descendientes, así como el 90-Sr y 137-Cs. Estos elementos emiten partículas y radiaciones ionizantes: α, β y rayos γ, capaces de generar radicales libres que reaccionan con tejidos, enzimas y

moléculas del ADN donde la exposición a la radiación de alta energía tiene un efecto mutagénico al alterar el material genético (Ward, 1988; Chang, 2016).

Independientemente del futuro de la energía nuclear en las próximas décadas, el volumen de residuos nucleares generado necesita una solución definitiva. En España, los residuos radiactivos se clasifican, por un lado, en residuos de baja actividad (RBBA) y residuos de baja y media actividad (RBMA) donde ambos son almacenados definitivamente en las instalaciones del El Cabril. Por otro lado, junto a éstos se clasifican también los residuos especiales (RE) y residuos de alta actividad (RAA), principalmente constituidos por el combustible nuclear gastado, sin embargo, su disposición final está previsto sea un Almacenamiento Geológico Profundo (AGP) (MITECO, 2020).

Los RBMA contienen radionucleidos emisores de partículas y radiaciones β y γ, con periodos de semidesintegración inferiores a 30 años. Este grupo incluye a los RBBA, que de forma general presentan actividades específicas entre 1 y 100 bequerelios por gramo.

Los RAA emiten partículas α, con periodos de semidesintegración superiores a 30 años. Éstos se caracterizan por su alta actividad específica generando calor por efecto de la desintegración radiactiva.

Por último, los RE hacen referencia a los materiales que han estado en contacto directo con combustible nuclear, las fuentes neutrónicas, la instrumentación intranuclear usada o los componentes sustituidos provenientes del sistema de la vasija del reactor, así como los componentes internos del reactor. Debido a sus características radiológicas, larga vida y actividad significativa, su gestión temporal y definitiva sigue el mismo protocolo que la de los RAA.

Para los RMBA existen tecnologías e infraestructuras que permiten su aislamiento en condiciones de seguridad durante 300 años, 10 veces su período de semidesintegración. Sin embargo, el desafío reside en los RAA, cuya radiotoxicidad se estima en al menos 10^4 años, momento en el cual se alcanzarían valores similares a los del fondo geoquímico natural. Por lo tanto, garantizar el aislamiento de los RAA en dichos periodos de tiempo plantea un reto tecnológico y científico (Ewing et al., 1999; Ewing, 2015; Ewing et al., 2016).

Actualmente los RAA se almacenan dentro de las centrales nucleares en piscinas de agua que absorben la radiactividad y amortiguan el calor generado por el material radiactivo. El problema reside en la limitación que supone el espacio disponible, por ello los materiales radiactivos se trasladan a Almacenamientos Temporales Individualizados (ATI) próximos a la central nuclear de origen. Los ATI están ubicados a nivel superficial y consisten en contenedores metálicos o de hormigón que evitan la liberación de la radiactividad (Fig. 1.1). Posteriormente, los contenedores se trasladan a los Almacenamientos Temporales Centralizados (ATC) o a las plantas de reprocesado para rehabilitar parcialmente el combustible irradiado. Sin embargo, para los RAA y RE, estos emplazamientos no garantizan la seguridad a largo plazo (>300 años) y por tanto necesitan un destino definitivo para su aislamiento (Astudillo, 2001; García Calvo, 2012; Espina, 2020).

Fig.1.1. Fotografía de los contenedores de residuos radiactivos de alta actividad (RAA) presentes en el Almacenamiento Temporal Intermedio (ATI) localizado en las proximidades de la central nuclear de Zorita (Guadalajara, España; diciembre 2019).

Varias opciones han sido propuestas para esta disposición final. Tal es el caso de su confinamiento en casquetes polares, zonas de subducción de la corteza terrestre, inyección en sondeos profundos e incluso su envío al espacio exterior (Astudillo, 2001; Ewing et al., 2016). Sin embargo, estas soluciones no cumplen las condiciones de seguridad y viabilidad necesarias (IAEA, 2011). Por otro lado, también existen líneas de investigación que buscan lograr la transmutación de los radionúclidos iniciales en otros con menor radiotoxicidad y periodos de semidesintegración más cortos (Rodriguez et al., 2003), pero su eliminación total es actualmente imposible dejando un RAA que necesita una ubicación segura en el medio y largo plazo. En otro sentido, sí se ha conseguido reducir el volumen de gran cantidad de material radiactivo mediante la recuperación de los compuestos todavía fisibles en las plantas de reprocesado de forma que pueden volver a entrar en el ciclo de producción de energía nuclear. Estos compuestos con capacidad de producir energía en un segundo proceso se denominan combustibles mixtos de óxidos de uranio y plutonio (MOX). La Figura 1.2 presenta de forma esquemática del ciclo de los residuos radiactivos.

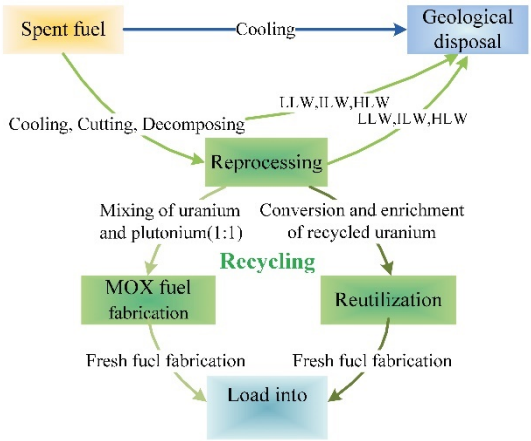

Fig. 1.2 Esquema simplificado los procesos que sigue el combustible nuclear gastado, Mixing oxides of U and Pu (MOX), High level wastes (HLW), intermediate level wastes (ILW) and low level wastes (LLW), Modificado de Shu et al. (2016).

1.2 EL ALMACENAMIENTO GEOLÓGICO PROFUNDO

Ante la necesidad de un emplazamiento seguro a largo plazo se propuso desde hace ya varias décadas el AGP como mejor opción para la disposición final del combustible gastado *e.j.* (DOE, 2014; Alexander et al., 2015; Ewing et al., 2016; Tosoni et al., 2018). El AGP sería construido en el interior de formaciones rocosas a profundidades de entre 300 y 1000 m. Esta opción se fundamenta en la estabilidad observada de estas formaciones pues al seguir el ciclo litológico permanecerían aislados de la superficie durante millones de años, momento en el cual los niveles de radiactividad se habrían reducido hasta niveles aceptables para la vida.

A pesar de que en los últimos 50 años ha habido un gran esfuerzo internacional en el desarrollo de un AGP, en muchos casos éstos no han recibido una aceptación social generalizada, lo que ha obstaculizado la concesión de licencias para su puesta en funcionamiento.

Actualmente el único referente en funcionamiento está ubicado en Nuevo Méjico (EE. UU.). Consiste en una planta piloto para el aislamiento de residuos radiactivos. Sin embargo, está diseñado para la acumulación de elementos radioactivos no emisores de calor procedentes del material armamentístico desmantelado (se trata de los transuránicos 241-Am, 239-Pu, 240-Pu), no siendo válido para el almacenamiento de los residuos procedentes de las plantas nucleares de producción civil. Los transuránicos no emiten el calor de los RAA procedentes de las centrales nucleares y este aspecto es crítico en el diseño del repositorio.

No obstante, EE. UU. tiene construido un repositorio para uso civil en Yucca Mountain en el desierto de Nevada, pero su puesta en funcionamiento aún no ha tenido lugar. Además de EE. UU., más de 30 países poseen investigaciones para el desarrollo de un AGP, algunos de los cuales presentan programas de gestión avanzados en la construcción del repositorio. A nivel internacional destacan países como Canadá, Rusia y China, mientras que en el ámbito europeo Finlandia, Suecia y Francia esperan aprobar la localización definitiva del repositorio antes del año 2030. En el Reino Unido, Alemania o los Países Bajos están todavía en una etapa en la que los conceptos genéricos del depósito están siendo todavía evaluados (Duro et al., 2020). Si bien, cada país está valorando su propio concepto de AGP variando en la disposición de los materiales de relleno (materiales de base cemento, arcillas compactadas o depósitos de sal triturada) y el tipo roca almacén (granitos, arcillas, sales y tobas volcánicas).

1.3 EL CONCEPTO MULTIBARRERA Y EL SISTEMA DE BARRERAS DE INGENIERÍA

El AGP se basa en el *concepto multibarrera,* éste consiste en la superposición de barreras artificiales y naturales (biosfera y geosfera) capaces de impedir o retrasar convenientemente el movimiento de los radionúclidos. De forma genérica el sistema de barreras de ingeniería (Engineered Barrier System, EBS) está constituido en primer lugar por la *i*) *forma química del propio residuo*, ii) el *encapsulado metálico del combustible (canister)* y *iii*) un *recubrimiento de material arcilloso* compactado que sostiene el contenedor metálico y rellena las galerías en donde se van a alojar los residuos radiactivos. Dependiendo del diseño requiere el uso de refuerzos, tapones y diversos materiales de base cemento para facilitar la construcción y sujeción de túneles y galerías, la Figura 1.3. resume el sistema previsto para un EBS confinado en una roca granítica, dicho sistema se ha tomado como referencia para el diseño de los experimentos del presente trabajo.

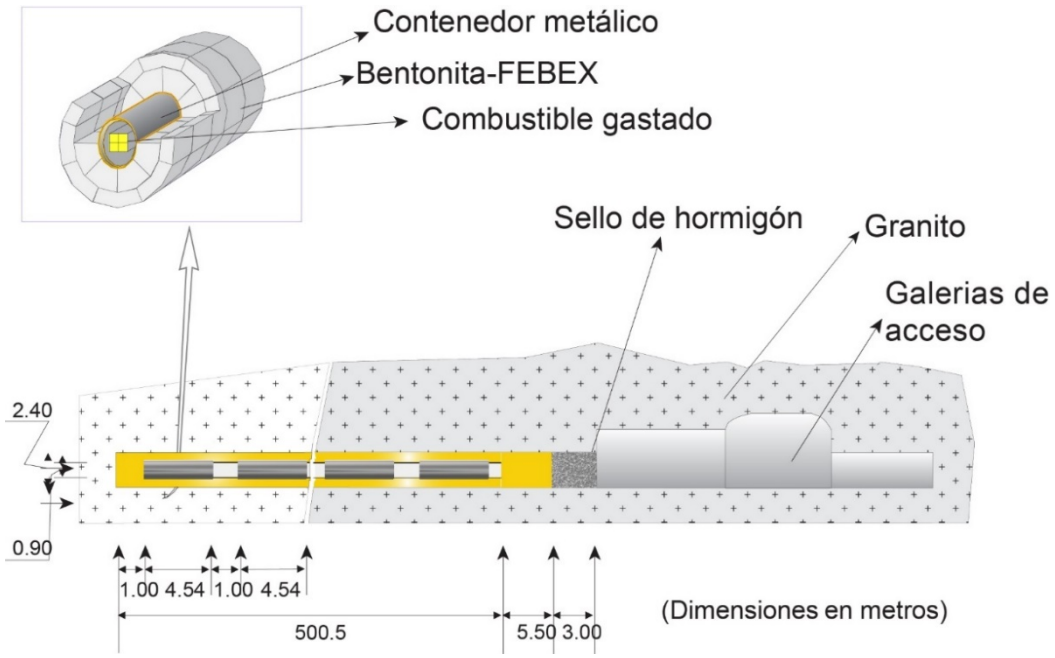

Fig. 1.3. Representación del sistema de barreras de ingeniería (EBS) en una roca granítica. Se muestran los contenedores metálicos que alojan los residuos radiactivos rodeados de bentonita compactada (bentonita-FEBEX). Modificado de ENRESA (2006).

1.4 PLANTEAMIENTO DEL PROBLEMA Y OBJETIVOS

Los materiales base cemento suponen una fuente potencial de disoluciones alcalinas alojadas en su porosidad. Por un lado, éstas podrían favorecer la precipitación de los radionúclidos retardando su transporte una vez superasen las distintas barreras, pero también pueden comprometer las propiedades del material adyacente: barrera de bentonita y roca almacén, debido al gradiente químico existente entre los diferentes materiales. La interacción entre estos materiales y en contacto con agua subterránea genera un sistema químico complejo en constante evolución cuyas reacciones conducen a la alteración de su composición mineral y propiedades *e.j.* (Altmaier et al., 2017). El correcto funcionamiento del EBS va a depender de la extensión e intensidad de estas perturbaciones, por lo que es

necesario estudiar la reactividad de los materiales barrera desde sus primeras etapas.

La evolución geoquímica de este sistema está controlada por:

- El tipo de material base cemento, atendiendo a las condiciones de alto pH, bajo pH y composición mineralógica y/o adiciones entre otros.

- La bentonita, en cuanto a su reactividad superficial, cationes de cambio dominantes, mineralogía y características del agua intersticial presente.

- El contacto con las aguas subterráneas cuya composición va a influir en la alteración de las barreras y dependerá principalmente del entorno geológico.

Existe cierta incertidumbre sobre los cambios geoquímicos a escala nano y microestructural generados a corto, medio y largo plazo en el sistema, que en el peor de los escenarios comprometerían el comportamiento y seguridad global del EBS (Savage, 2014). Han sido revisados diversos aspectos sobre la perturbación química en la interfase hormigón/arcilla destacando la existencia de numerosos estudios que abordan el comportamiento químico de la arcilla cuando se expone a un fluido altamente alcalino (pH >13). Sin embargo, las investigaciones realizadas han señalado que el material basado en cemento no puede ser simulado únicamente por un fluido de pH >13, como ha sido ensayado en múltiples ocasiones (Bildstein and Claret, 2015). En este sentido, los experimentos llevados a cabo en la presente tesis se han basado en el comportamiento de materiales basados en cemento Pórtland, en lugar de disoluciones alcalinas, en contacto con bentonita, reflejando de modo más realista la reactividad generada en las condiciones previstas en el EBS.

Ante las condiciones extremas de alcalinidad, una forma de reducir el pH y sus efectos es utilizar materiales puzolánicos, como humo de sílice (SF; variedad de microsílice), mezclado con cemento Pórtland ordinario (también referido como OPC). Se ha sugerido que este tipo de materiales tienen repercusiones insignificantes en la estructura de los minerales de la arcilla (Bäckblom, 2004; Berner et al., 2013; Cuevas et al., 2016) y muestran una buena resistencia a la agresión de las aguas subterráneas graníticas (García Calvo et al., 2010). Sin embargo, la cuestión acerca de qué tipo de cemento es el más adecuado es todavía un aspecto en discusión. En otros contextos, cementos de bajo pH sometidos a la influencia de aguas subterráneas carbonatadas han mostrado mayores perturbaciones geoquímicas respecto a los cementos de alto pH (Dauzères et al., 2014). Los productos de hidratación presentes en la pasta del cemento son más resistentes por encima de valores de pH de 12-13, pero por debajo, estas fases no permanecen estables durante mucho tiempo y se disuelven (Trotignon et al., 2007). Otros aspectos que motivaron el presente trabajo fueron el menor número de estudios sobre el comportamiento de los materiales de bajo pH en comparación con el mayor grado de conocimiento de las prestaciones y rendimiento del alto pH, en gran parte avalado por la vasta experiencia extraída de la ingeniería civil (Koťátková et al., 2017). Los materiales base cemento de alto pH desarrollan una capa de carbonato cálcico que actúa como barrera de protección y es capaz de reducir los procesos de descalcificación que debilitan el material de cemento. En los casos en que el hormigón requiera de refuerzos de acero, los materiales de cemento de bajo pH cuando están en contacto con el acero no ofrecen una pasivación tan efectiva como los de alto pH que los proteja (Walling and Provis, 2016). Por otro lado, la menor proporción de OPC presente en los cementos de bajo pH dificulta su trabajabilidad, lo que se refleja en un aumento de la viscosidad y por tanto menor maleabilidad, si se pretende proyectar el hormigón. Una forma

de solventar este inconveniente es recurrir al uso de superplastificantes y aceleradores como aditivos orgánicos aniónicos pero esta implementación añadiría aún más incertidumbre en el estudio de la evolución del material de cemento a largo plazo (Mäder et al., 2017).

Debido a que las condiciones de alto pH y bajo pH muestran diferente reactividad, y que algunas fases de nueva formación, características de los contactos hormigón-bentonita, aún no han sido claramente establecidas y estructuralmente dilucidadas, es necesario conseguir más evidencias llevando a cabo nuevos experimentos. En concreto, en relación a la naturaleza de los silicatos de calcio hidratados (C-S-H; pues controlan las propiedades cohesivas del material), silicatos de magnesio hidratado (M-S-H) o silicatos de calcio y aluminio hidratados (C-A-S-H) (Lothenbach et al., 2015), y su relación con la alteración de esta interfase, se hace relevante investigar cuáles son los materiales de base cemento óptimos para moderar la reactividad, así como la evolución de las fases que lo componen y su repercusión en la estabilidad del EBS.

Otro agente relevante, que influye en la estabilidad del sistema son las aguas subterráneas del entorno geológico. El agua es el agente más agresivo que actúa sobre la estructura de hormigón y constituye el principal mecanismo de transporte de iones. Aunque en el caso del hormigón, éste es estable en condiciones de humedad ambiental, el contacto directo con un flujo de agua produce efectos de difusión y alteraciones de las fases sólidas provocando fenómenos de disolución y precipitación de los minerales que lo constituyen. Además, las especies de carbonatos disueltas en el agua son capaces de generar reacciones de carbonatación y disolver parte de la matriz del hormigón liberando compuestos agresivos que terminan debilitando las diferentes barreras. Aunque estos procesos

son lentos, su estudio es importante en el contexto de un AGP, donde se requiere asegurar una durabilidad de cientos de miles de años.

Para la evaluación a corto, medio y largo plazo de las interacciones entre las distintas barreras de ingeniería se suelen llevar a cabo tres aproximaciones complementarias entre sí: (i) experimentos de laboratorio, (ii) estudios de análogos naturales y (iii) modelos geoquímicos (Gaucher and Blanc, 2006).

Dentro de los estudios de laboratorio se puede distinguir entre experimentos de laboratorio a pequeña escala espacio temporal y los estudios llevados a cabo in situ en laboratorios subterráneos (Underground Research Laboratories, URL), siendo éstos uno de los pilares para evaluar la seguridad y viabilidad del repositorio. Los URL reproducen las condiciones reales pues se llevan cabo en la matriz geológica prevista para albergar el EBS presentando dimensiones similares e incluso calentadores que simulan el calor que se produciría por la desintegración de los isótopos radiactivos. Hasta el momento se han cubierto periodos de entre 2 y 20 años, lo que ya va aportando una perspectiva relevante a la magnitud del problema. Desde el punto de vista experimental, para salvar el salto de tiempo de decenas de años a cientos de miles años se ha recurrido al estudio de los análogos naturales. Estos constituyen aspectos parciales que reproducen la evolución del sistema en escalas de tiempo geológico, permitiendo adelantar las alteraciones que sufrirían los materiales del EBS. Las investigaciones de estos análogos naturales permiten la comparación con las perturbaciones observadas a menor escala, y con los resultados derivados de la modelización geoquímica. No obstante, un análogo natural de forma individual no recoge todas las condiciones presentes en el AGP, por lo que éstas solo se pueden estudiar a través de diferentes sistemas naturales (Pelayo, 2014). Por otro lado, tampoco muestran las condiciones iniciales que

dieron lugar a las transformaciones observadas, de ahí la necesidad de complementar estos estudios con los experimentos de laboratorio, en los que sí se conocen las condiciones iniciales y reflejan los cambios producidos desde el estado inicial.

El experimento de laboratorio que se ha desarrollado en esta tesis ha hecho posible la realización de un número considerable de experimentos bajo las mismas condiciones de modo que ha permitido llevar a cabo una comparación directa entre los diferentes tipos de materiales discutidos. Esta posibilidad supone un valor añadido en cuanto a su versatilidad y repetitividad no viables en los URL, debido al alto coste y compleja logística que requiere el proceso de montaje y posterior desmantelamiento para el estudio de las muestras.

En conclusión, si los aspectos físicos y químicos son cuidadosamente caracterizados mediante el estudio de los distintos experimentos de laboratorio y análogos naturales se podría llegar a describir un modelo conceptual como base para predecir de forma razonable la evolución del sistema en las diferentes escalas de tiempo (Fernández, 2011).

Es por tanto que el presente trabajo plantea la simulación a pequeña escala de las interfases generadas a partir de tres tipos de materiales base cemento: uno de bajo pH y dos de alto pH todos ellos contacto con la bentonita utilizada en los experimentos del proyecto FEBEX (Full-scale Engineered Barrier EXperiment). Las características del experimento fueron diseñadas acorde con las condiciones de los experimentos in situ de FEBEX llevados a cabo en el Grimsel Test Site (GTS) (Alexander et al., 2005).

El primer objetivo de esta tesis es desarrollar un modelo experimental, así como una metodología que permitiera estudiar la reactividad generada entre aguas subterráneas y un mortero de cemento en contacto con una bentonita compactada.

El segundo y principal objetivo es describir las perturbaciones geoquímicas observadas en las etapas iniciales entre distintos tipos de morteros de cemento en contacto con bentonita-FEBEX bajo la influencia de un flujo de agua

De este modo se pretende contrastar la reactividad geoquímica y por tanto el rendimiento de tres tipos de materiales de cemento bajo discusión. Concretamente se han utilizado un mortero de bajo pH (LpH: basado en CEM I + SF) y dos morteros representativos de condiciones de alto pH (HpH: basados en CEM-I y CEM-II). Complementariamente, se buscó aproximar un escalado desde las perturbaciones observadas en las etapas iniciales hasta de la reactividad geoquímica observada con los experimentos in situ. Como objetivo a largo plazo y fuera del alcance de esta tesis, siempre ha estado presente la recopilación de datos (fenómenos observados en las condiciones experimentales fijadas) para su posterior modelización geoquímica.

1.5 REFERENCIAS

- Alexander, W., Kickmaier, W., Vomvoris, S., Kaku, K., McKinley, I., 2005. Nagra's Grimsel URL: From underground testing to the demonstration of disposal systems, in, *Proc. ICEM*, ed.

- Alexander, W.R., Reijonen, H.M., McKinley, I.G., 2015. Natural analogues: studies of geological processes relevant to radioactive waste disposal in deep geological repositories. *Swiss Journal of Geosciences*, 108, pp. 75-100, https://link.springer.com/article/10.1007%2Fs00015-015-0187-y#Abs1.

- Altmaier, M., Montoya, V., Duro, L., Valls, A., 2017. *Proceedings of the First Annual Workshop of the HORIZON 2020 CEBAMA Project (KIT Scientific Reports; 7734)*, ed. KIT Scientific Publishing.

- Astudillo, J., 2001. *El almacenamiento geológico profundo de los residuos radiactivos de alta actividad: principios básicos y tecnología*, ed. ENRESA.

- Bäckblom, G., 2004. R&D on low-pH cement for a geological repository, in, *Proc., 2nd Low-pH workshop*, ed.

- Berner, U., Kulik, D.A., Kosakowski, G., 2013. Geochemical impact of a low-pH cement liner on the near field of a repository for spent fuel and high-level radioactive waste. *Physics and Chemistry of the Earth, Parts A/B/C*, 64, pp. 46-56, https://doi.org/10.1016/j.pce.2013.03.007.

- Bildstein, O., Claret, F., 2015. *Chapter 5 - Stability of Clay Barriers Under Chemical Perturbations*, in: Tournassat, C., Steefel, C.I., Bourg, I.C., Bergaya, F., Developments in Clay Science, ed. Elsevier.

- Chang, R., 2016. *QUIMICA*, 12 ed. ed. McGraw-Hill, Mexico.

- Cuevas, J., Ruiz, A.I., Fernández, R., Torres, E., Escribano, A., Regadío, M., Turrero, M.J., 2016. Lime mortar-compacted bentonite–magnetite interfaces: An experimental study focused on the understanding of the EBS long-term performance for high-level nuclear waste isolation DGR concept. 124-125, pp. 79-93, https://doi.org/10.1016/j.clay.2016.01.043.

- Dauzères, A., Le Bescop, P., Cau-Dit-Coumes, C., Brunet, F., Bourbon, X., Timonen, J., Voutilainen, M., Chomat, L., Sardini, P., 2014. On the physico-chemical evolution of low-pH and CEM I cement pastes interacting with Callovo-Oxfordian pore water under its in situ CO2 partial pressure. 58, pp. 76-88, https://doi.org/10.1016/j.cemconres.2014.01.010.

- DOE, 2014. *Assessment of Disposal Options for DOE-Managed High-Level Radioactive Waste and Spent Nuclear Fuel*, ed. United States. Department of, Energy.

- Duro, L., Altmaier, M., Holt, E., Mäder, U., Claret, F., Grambow, B., Idiart, A., Valls, A., Montoya, V., 2020. Contribution of the results of the CEBAMA project to decrease uncertainties in the Safety Case and Performance Assessment of radioactive waste repositories. *Applied Geochemistry*, 112, pp. 104479, https://doi.org/10.1016/j.apgeochem.2019.104479.

- ENRESA, 2006. FEBEX Project Final report Post-Mortem Bentonite Analysis. Publicación Técnica 05-1/2006, Madrid. Spain, p. 183.

- Espina, R.G. 2020. *Modificaciones microestructurales, mineralógicas y geoquímicas en bentonitas sometidas a cambios térmicos e hidráulicos*, Tesis Doctoral. Universidad Complutense de Madrid, p. 258, https://eprints.ucm.es/59992/.

- Ewing, R.C., 2015. Long-term storage of spent nuclear fuel. *Nature Materials*, 14, pp. 252-257, 10.1038/nmat4226.

- Ewing, R.C., Tierney, M.S., Konikow, L.F., Rechard, R.P., 1999. Performance Assessments of Nuclear Waste Repositories: A Dialogue on Their Value and Limitations. 19, pp. 933-958, https://doi.org/10.1111/j.1539-6924.1999.tb00452.x.

- Ewing, R.C., Whittleston, R.A., Yardley, B.W.J.E., 2016. Geological disposal of nuclear waste: a primer. *Elements*, 12, pp. 233-237, https://doi.org/10.2113/gselements.12.4.233.

- Fernández, R., 2011. Engineered barriers for radioactive waste confinement. 61, pp. 485-492, https://10.3989/mc.2011.55909.

- García Calvo, J.L. 2012. *Desarrollo de materiales de construcción con cemento de bajo pH, compatibles con la barrera de ingeniería de un almacenamiento geológico profundo de residuos radiactivos de alta actividad*, Tesis Doctoral. Universidad Autónoma de Madrid, p. 298, http://hdl.handle.net/10486/12309.

- García Calvo, J.L., Hidalgo, A., Alonso, C., Fernández Luco, L., 2010. Development of low-pH cementitious materials for HLRW repositories. *Cement and Concrete Research*, 40, pp. 1290-1297, https://10.1016/j.cemconres.2009.11.008.

- Gaucher, E.C., Blanc, P., 2006. Cement/clay interactions–a review: experiments, natural analogues, and modeling. *Waste Management*, 26, pp. 776-788, https://doi.org/10.1016/j.wasman.2006.01.027.

- Goh, T., Ang, B.W., 2018. Quantifying CO2 emission reductions from renewables and nuclear energy – Some paradoxes. *Energy Policy*, 113, pp. 651-662, https://doi.org/10.1016/j.enpol.2017.11.019.

- IAEA, 2011. *Geological Disposal Facilities for Radioactive Waste*, ed. INTERNATIONAL ATOMIC ENERGY AGENCY, Vienna.

- Koťátková, J., Zatloukal, J., Reiterman, P., Kolář, K., 2017. Concrete and cement composites used for radioactive waste deposition. *Journal of Environmental Radioactivity*, 178-179, pp. 147-155, https://doi.org/10.1016/j.jenvrad.2017.08.012.

- Lothenbach, B., Nied, D., L'Hôpital, E., Achiedo, G., Dauzères, A., 2015. Magnesium and calcium silicate hydrates. *Cement and Concrete Research*, 77, pp. 60-68, https://doi.org/10.1016/j.cemconres.2015.06.007.

- Mäder, U., Jenni, A., Lerouge, C., Gaboreau, S., Miyoshi, S., Kimura, Y., Cloet, V., Fukaya, M., Claret, F., Otake, T., Shibata, M., Lothenbach, B., 2017. 5-year chemico-physical evolution of concrete–claystone interfaces, Mont Terri rock laboratory (Switzerland). *Swiss Journal of Geosciences*, 110, pp. 307-327, https://10.1007/s00015-016-0240-5.

MITECO (2020), Ministerio para la Transición ecológica y el Reto Demográfico. 7º PLAN GENERAL DE RESIDOUS RADIACTIVOS, https://energia.gob.es/es-es/Novedades/Paginas/primer-borrador-del-7-plan-general-de-residuos-radiactivos.aspx.

- Pelayo, M. 2014. *Estudio del yacimiento de bentonita de Morrón de Mateo (Cabo de Gata, Almería) como análogo natural del comportamiento de la barrera de arcilla de un almacenamiento de residuos radiactivos*, Tesis Doctoral. Universidad Complutense de Madrid, p. 241, https://eprints.ucm.es/25430/.

- Real Decreto 783/2001, de 6 de julio, por el que se aprueba el Reglamento sobre protección sanitaria contra radiaciones ionizantes. Presidencia, M.d.l. «BOE» núm. 178, de 26 de julio de 2001. Referencia: BOE-A-2001-14555. https://www.boe.es/eli/es/rd/2001/07/06/783/con.

- Rodriguez, C., Baxter, A., McEachern, D., Fikani, M., Venneri, F., 2003. Deep-Burn: making nuclear waste transmutation practical. *Nuclear Engineering and Design*, 222, pp. 299-317, https://10.1016/s0029-5493(03)00034-7.

- Saidi, K., Omri, A., 2020. Reducing CO2 emissions in OECD countries: Do renewable and nuclear energy matter? *Progress in Nuclear Energy*, 126, pp. 103425, https://doi.org/10.1016/j.pnucene.2020.103425.

- Savage, D., 2014. *An assessment of the impact of the long term evolution of engineered structures on the safety-relevant functions of the bentonite buffer in a HLW repository*, ed. National Cooperative for the Disposal of Radioactive Waste.

- Shu, Y., Liu, Z.-M., Lin, X.-J., Wang, R.-Z., 2016. A Review of the Development of Nuclear Waste Treatment for China's Nuclear Power Industry, in, *2nd 2016 International Conference on Sustainable Development (ICSD 2016)*, ed. Atlantis Press.

- Steinhauser, G., Brandl, A., Johnson, T.E., 2014. Comparison of the Chernobyl and Fukushima nuclear accidents: A review of the environmental impacts. *Science of The*

Total Environment, 470-471, pp. 800-817, https://doi.org/10.1016/j.scitotenv.2013.10.029.

- Tosoni, E., Salo, A., Zio, E., 2018. Scenario Analysis for the Safety Assessment of Nuclear Waste Repositories: A Critical Review. *Risk Analysis*, 38, pp. 755-776, https://doi.org/10.1111/risa.12889.

- Trotignon, L., Devallois, V., Peycelon, H., Tiffreau, C., Bourbon, X., 2007. Predicting the long term durability of concrete engineered barriers in a geological repository for radioactive waste. *Physics and Chemistry of the Earth, Parts A/B/C*, 32, pp. 259-274, https://10.1016/j.pce.2006.02.049.

- Walling, S.A., Provis, J.L., 2016. Magnesia-Based Cements: A Journey of 150 Years, and Cements for the Future? *Chemical Reviews*, 116, pp. 4170-4204, https://doi.org/10.1021/acs.chemrev.5b00463.

- Ward, J.F., 1988. *DNA Damage Produced by Ionizing Radiation in Mammalian Cells: Identities, Mechanisms of Formation, and Reparability*, in: Cohn, W.E., Moldave, K., Progress in Nucleic Acid Research and Molecular Biology, ed. Academic Press.

CAPÍTULO 2. LA BENTONITA

2.1 INTRODUCCIÓN

La bentonita es un tipo de roca arcillosa originada por alteración diagenética o hidrotermal de vidrio volcánico y por neoformación autigénica de materiales ricos en esmectitas (Galán, 2006; Christidis and Huff, 2009). Los estudios de análogos naturales han mostrado que es capaz de conservar sus propiedades durante largos periodos de tiempo (>10^4 años) *e.j.* (Pelayo, 2014). Además, cabe subrayar que se trata de un material natural de fácil acceso y disponible en numerosos yacimientos naturales: *e.j.* EE. UU. (Wyoming, Montana, Arizona), Italia (Ponza, Sardinia), Argelia (Orán), Grecia (Milos), Japón (Yamagata, Kitambuza). En España destacan los yacimientos del Cabo de Gata (Almería) (Galán, 2006).

Durante más de 30 años la bentonita ha sido elegida como material de sellado y amortiguador físico químico para el aislamiento de residuos radiactivos en varios países (*e.j.* Canadá, Alemania, Suecia, Suiza y Francia), donde ocuparía el espacio anular entre la cápsula metálica y la roca almacén. Dos tipos de bentonitas han sido mayoritariamente seleccionadas como barrera en el EBS: la bentonita MX-80 (bentonita sódica) y bentonita-FEBEX (bentonita cálcica) cuyos contenidos en esmectitas son del 85% y 92% aproximadamente. Por lo tanto, podemos decir que la bentonita es una roca compuesta mayoritariamente por esmectita (normalmente montmorillonita, Mnt) que en última estancia le confiere sus propiedades físico-químicas. Entre estas propiedades destacan: una baja permeabilidad, alta capacidad para la retención de cationes, transporte de solutos muy lento por difusión o amortiguador fisicoquímico (Gómez-Espina and Villar, 2016; Kaufhold

and Dohrmann, 2016; Norris, 2017). Estas propiedades por lo tanto van a favorecer su funcionalidad en el EBS facilitando fenómenos clave como:

- La adsorción de radionúclidos en caso de liberación de las cápsulas metálicas.
- La limitación del flujo de agua subterránea desde la roca almacén hasta el material radioactivo.
- El sellado de las posibles formaciones de fracturas circundantes aislando y protegiendo las cápsulas metálicas
- La protección de la cápsula ante deformaciones del terreno.
- Estabilidad a corto y largo plazo frente al aumento de temperatura, así como a los cambios en la composición química del agua subterránea.

Para una mayor comprensión de las propiedades y funcionalidades de la bentonita es necesario conocer las características estructurales, geoquímicas e hidromecánicas de las esmectitas.

2.2 ESTRUCTURA DE LAS ESMECTITAS

Las esmectitas son filosilicatos tipo 2:1, su estructura obedece a la organización en tres capas: dos de las cuales son tetraédricas (capa T) y la tercera se corresponde con una capa octaédrica (capa O). La capa O se encuentra embebida entre las dos capas T formando una estructura tipo *sándwich*: TOT, que en conjunto forma la *lámina* del mineral de la arcilla (Fig. 2.1a). Esta lámina TOT se dispone paralela al eje cristalográfico *c* a la vez que define el espaciado basal (001). El espesor de estas láminas en la dirección *c* es aproximadamente de 9 Å, si bien cuando estas laminas se apilan, pueden encerrar cationes hidratados en la región interlaminar,

el espesor medio de cada estructura laminar aumenta hasta 12 o 15 Å en función del tipo de catión hidratado.

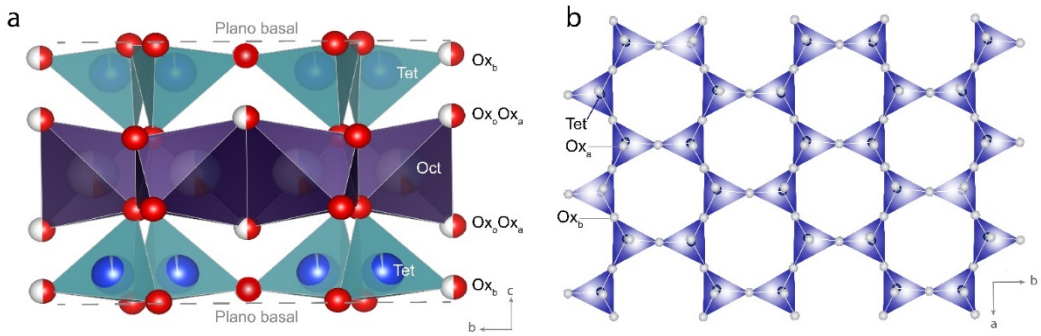

Fig. 2.1. a) Estructura 2:1. Ox_b. átomos de oxígeno basales; Tet. cationes tetraédricos; Oct. cationes octaédricos; Ox_a. átomos de oxígeno apicales; Ox_o. aniones octaédricos (OH^-). b) Capa tetraédrica. Las figuras de las estructuras presentadas a lo largo de este trabajo se han realizado a partir del software VESTA® (Momma and Izumi, 2011).

Las capas T consisten en unidades de tetraedros formados idealmente por un catión de Si^{4+} (si bien puede ser sustituido por un catión trivalente, Al^{3+}, Fe^{3+}) en coordinación con 4 aniones de oxígeno: O_2^{2-}. Estas unidades se unen en el plano basal compartiendo 3 oxígenos (oxígenos basales: O_b) mientras que el cuarto oxígeno (oxígeno apical: O_a) se dispone orientado hacia la capa O. La unión de los oxígenos basales forma una red bidimensional en el plano *a*-*b* (Fig. 2.1b) que define cavidades hexagonales constituidas por 6 tetraedros de SiO_4^{4-}. A su vez, éstos se prolongan longitudinalmente en la dirección de los ejes cristalográficos *a* y *b* a medida que va creciendo el cristal. La capa O está constituida por unidades de octaedros que comparten aristas. Éstos poseen un catión central (principalmente Al^{3+}, Fe^{3+} Mg^{2+}) en coordinación octaédrica con 6 aniones de oxígeno ubicados en los vértices del poliedro: 4 O_2^{2-} y 2 grupos hidroxilo OH^- (Ox_o) quedando una estructura de tipo $MO_4(OH)_2$; dónde *M* representa el catión central.

La capa T y la capa O se unen compartiendo los oxígenos apicales de la capa T que se corresponden con los 4 O_2^{2-} de la capa O, mientras que los dos grupos OH^-

de cada unidad octaédrica quedan ubicados en el mismo plano de los oxígenos apicales, de forma que cada anillo de 6 tetraedros se puede unir a 3 o 2 octaedros dependiendo de la carga del catión central, distinguiéndose así dos grupos de esmectitas (Fig. 2.2):

- a) Trioctaédricas, donde las tres posiciones octaédricas posibles son ocupadas por cationes divalentes (formando una capa de tipo brucítica $Mg_3(OH)_6$).
- b) Dioctaédricas, donde 2/3 de las posiciones octaédricas son ocupadas por cationes trivalentes, quedando una posición vacante (formando una capa octaédrica de tipo gibsítica $Al_2(OH)_6$).

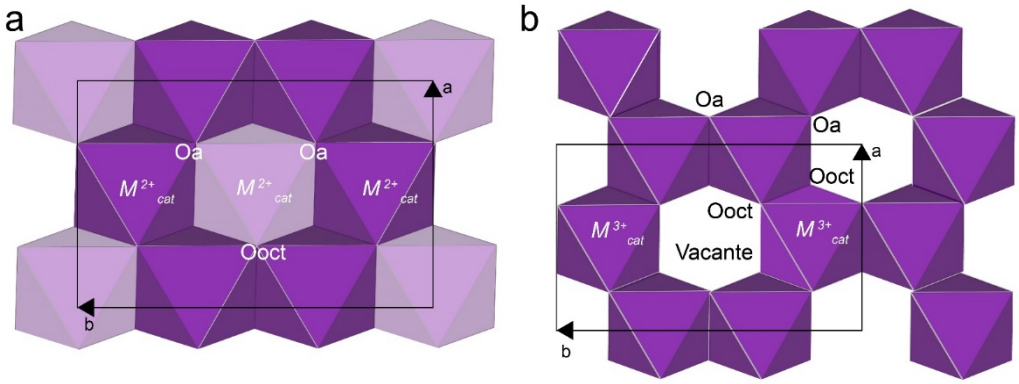

Fig. 2.2. a) capa trioctaédrica; b) capa dioctaédrica, O_a: representa el oxígeno apical compartido con un tetraedro, O_{oct}: representa el lugar aniónico compartido entre octaedros adyacentes. *a* y *b* representan los parámetros celda-unidad.

Las dimensiones en el eje *b* teóricas calculadas para la capa T son 9.27 Å mientras que para para las capas di- y trioctaédricas son 8.19 Å (8.69Å si tenemos en cuenta la elongación de en torno a 0.51 Å del octaedro en la posición vacante) y 8.99 Å, respectivamente. Lo mismo ocurre en el parámetro *a*, pues depende del valor de *b*: $a = \frac{b}{\sqrt{3}}$ (para la Mnt son 8.94-9.00 Å según Deer (1962) y Meunier (2005)). De este modo, para que se puedan unir la capa T a la capa O a través de los oxígenos apicales es necesario que se produzca una serie de deformaciones: los tetraedros

de la capa T sufren una rotación sobre el eje imaginario formado por los oxígenos apicales perpendiculares al plano basal (001). Las capas T pierden su simetría hexagonal y adoptan una simetría ditrigonal, de modo que los anillos toman una forma pseudohexagonal (Fig. 2.3). Las capas di y trioctaédricas se ven alteradas en diferente grado. La presencia de vacantes en las capas dioctaédricas altera la geometría de los octaedros debido a la presencia de vacantes, éste reduce la atracción electrostática entre los aniones y lleva a la elongación de los bordes de esta vacante: de 2.7 a 3.2 Å volviéndose asimétrico. Sin embargo, estas distorsiones son menores en el caso de las capas trioctaédricas. El carácter di y trioctaédrico puede diferenciarse mediante difracción de rayos X atendiendo a la reflexión (06l) ($b = d_{(060)} \times 6$). La longitud en *b* varía con el grado de ocupación de las posiciones octaédricas, siendo mayor en las trioctaédricas que en las dioctaédricas como ya se ha señalado. Para las esmectitas dioctaédricas se sitúa en torno a 1.49-1.51 Å, mientras que para las especies trioctaédricas es de 1.53-1.55 Å (Bouchet et al., 2002).

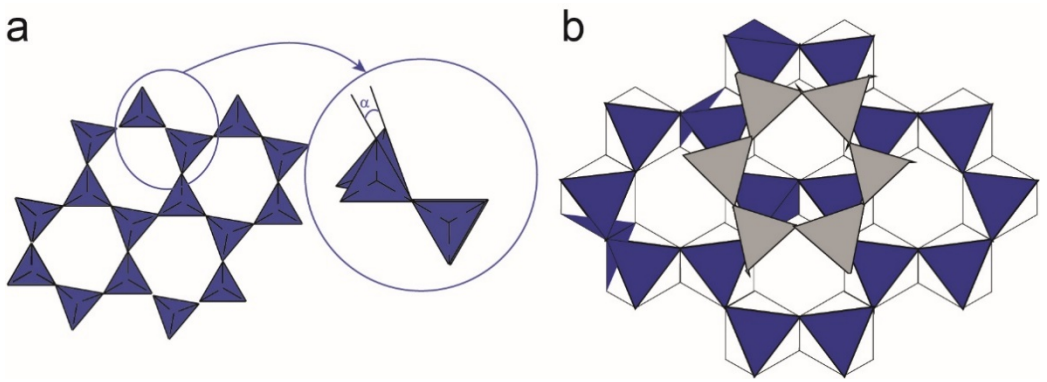

Fig. 2.3. Deformación de la cavidad hexagonal. a) Rotación de los tetraedros. b) Deformación de la simetría hexagonal para transformarse en una simetría ditrigonal en una esmectita dioctaédrica. Modificado de Meunier (2005).

2.3 SUSTITUCIONES ISOMÓRFICAS Y ESPACIO INTERLAMINAR

La cristaloquímica de las capas T y O puede verse modificada por sustituciones isomórficas del catión central: en las capas T la sustitución más común se debe a la entrada de Al^{3+} que desplaza al Si^{4+} ($Si^{4+} \leftrightarrows Al^{3+}$), mientras que en la capa O los cationes, principalmente Al^{3+}, Fe^{3+}, Mg^{2+}, pueden ser sustituidos por otros de menor valencia ($R^{3+} \leftrightarrows R^{2+}$; $R^{2+} \leftrightarrows R^{+}$). Estas sustituciones generan un exceso de carga negativa en la superficie basal de las láminas (carga de capa) de entre 0.20 y 0.65 por fórmula sobre la base de media celdilla unidad, representada por un esqueleto de aniones $O_{10}(OH)_2$ para el caso de las esmectitas.

El exceso de carga negativa es balanceado por la introducción de *cationes interlaminares* (comúnmente Na^+, Ca^{2+}, Mg^{2+} y K^+) entre dos unidades contiguas TOT, conformando así el *espacio interlaminar.* Estos cationes presentan notables entalpías de hidratación: entre -300 y -2000 kJ/mol (Sposito, 2008; Schoonheydt and Johnston, 2013; Johnston, 2018) y se solvatan fácilmente en presencia de moléculas de agua las cuales se disponen formando pseudoláminas que se extienden a lo largo del plano *a*-*b*, mientras que se apilan paralelas al eje cristalográfico *c* (Fig. 2.4). En función del catión interlaminar y de la presión parcial de vapor de agua (P/P_0), el número pseudoláminas de agua apiladas pueden variar entre 0 y 4 para una determinada carga interlaminar (Lagaly and Dékány, 2013; Tournassat et al., 2015). Esta acumulación de moléculas de agua en el espacio interlaminar se produce de forma escalonada y se refleja en un aumento en valores discretos del espaciado basal (001) (en el caso del Na^+ y el Li^+ este patrón no se cumple y el aumento del espaciado basal sigue una tendencia más progresiva respecto a la presión parcial. En un sistema abierto (sin volumen constante), el máximo estado de hidratación de las esmectitas cuando están saturadas en Na^+ o Li^+ es infinito de modo que tienden a dispersarse mientras que

para el Ca^{2+} y el Mg^{2+} se corresponde con tres pseudoláminas de agua. En el caso del K^{+} se podrían llegar a acumular ente 1 y 2 pseudoláminas dependiendo del tipo de esmectita (Meunier, 2005), aunque con elevadas cargas laminares y debido a compatibilidad entre dimensiones del ion K^{+} y la cavidad pseudohexagonal, éste puede unirse directamente a las superficies basales mediante enlaces específicos más estables.

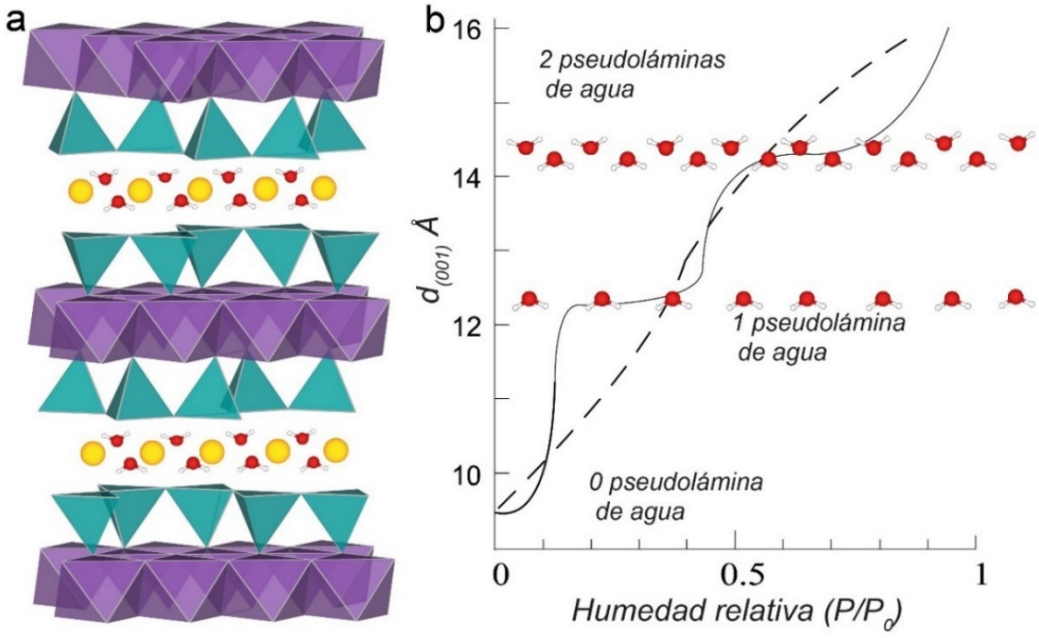

Fig. 2.4. Modelo de organización del agua interlaminar presente en las esmectitas e isoterma de adsorción de agua en una esmectita. a) estructura 2:1 con dos pseudoláminas de moléculas de agua. b) Variación del espaciado basal d(001) y su relación con el número pseudoláminas de agua apiladas en función de la presión relativa (P/P_0).

2.4 NIVELES DE ORGANIZACIÓN

Las *láminas* TOT junto con los cationes y moléculas de agua presentes en el espacio interlaminar se acoplan de forma más o menos coherente a lo largo de la dimensión *c* para formar un nivel superior de organización estructural denominado como *partículas* o *cristalitos* (Fig. 2.5a). Estas partículas se mantienen unidas mediante fuerzas de van der Waals donde la naturaleza del catión interlaminar es determinante en su estructura y por tanto propiedades. Cationes monovalentes como el Na^+ y el Li^+ dan lugar a agrupaciones de partículas de 1-2 láminas de espesor denominadas *tactoides* formando una red poligonal de poros capaz de alojar moléculas de agua (Fig. 2.5b). Por otro lado, las esmectitas con Ca^{2+} y Mg^{2+} en la interlámina tienden a formar agrupaciones de entre 4-7 láminas con 15-150 Å de espesor llamados *cuasicristales*, si bien éstos se pueden hidratar hasta alcanzar espesores de 600 Å conformando una red poligonal con huecos de mayor tamaño. Tomando como referencia el eje cristalográfico *c*, los cuasicristales presentan un mayor grosor y un apilamiento más coherente que los tactoides. Estas partículas se pueden apreciar mediante microscopía electrónica de transmisión (Transmission Electron Microscopy, TEM) (Fig. 2.5c).

Durante el acoplamiento de las láminas TOT se producen movimientos aleatorios de traslación y rotación que dan lugar a un apilamiento irregular denominado turbostrático (Fig. 2.5c) que surge como consecuencia de las sustituciones isomórficas, pues introducen defectos en la estructura al provocar desajustes eléctricos y geométricos (*i. e.* longitud de los enlaces y carga) que se reflejan en esta falta de orden y coherencia (Schoonheydt and Johnston, 2013). Este tipo de apilamiento se caracteriza por identificarse mediante difracción de rayos X (X-Ray Diffraction, XRD) en forma de bandas anchas y asimétricas en los espaciados comprendidos entre 13 y 20 Å.

Cuando las partículas o cristalitos se agrupan mediante fuerzas electrostáticas forman otro nivel de organización estructural conocido como *agregados*, cuyo tamaño oscila entre 1 y decenas de μm. Dentro del grupo de las esmectitas los agregados representan generalmente el máximo nivel de organización.

Esta asociación de *láminas, partículas* y *agregados* forman una compleja red de poros interconectada con diferentes tamaños y formas. La estructura de la red de poros es un factor clave en la dinámica del fluido presente en los minerales de la arcilla. Su conocimiento es necesario para llevar a cabo la modelización precisa de la composición química del agua de poro de las arcillas y los materiales base-cemento en el EBS.

2.5 POROSIDAD E INTERACCIÓN AGUA-ESMECTITA

La suma del volumen de la red de poros normalizados al volumen total del medio poroso es lo que se define como porosidad (ε), de forma que si se conoce la densidad seca o densidad aparente (ρ_s) de la arcilla y la densidad de las partículas (ρ_p) es posible calcular su porosidad: $\varepsilon = 1-(\rho_s)/(\rho_p)$ (Tournassat et al., 2015). En función de su localización se distinguen tres tipos de porosidad: (*i*) *porosidad interlaminar*, originada por la unión de las láminas; (*ii*) *porosidad interpartícula*, originada por la asociación de partículas; (*iii*) *porosidad interagregado*, derivada de los espacios originados entre la asociación de agregados.

Otra forma de clasificación está basada en el tamaño de los poros, de forma que se distingue entre la (*i*) *microporosidad* (<2 nm) la cual se correspondería con la porosidad interlaminar e interpartícula, (*ii*) *mesoporosidad* (>2 e <50 nm)

correspondiente con la porosidad interagregado y (*iii*) *macroporosidad* (>50 nm) (Rouquerol et al., 1994). Esta última en la bentonita compactada es minoritaria de modo que la porosidad presente se corresponde principalmente con la micro y mesoporosidad (Fernández Martín, 2006).

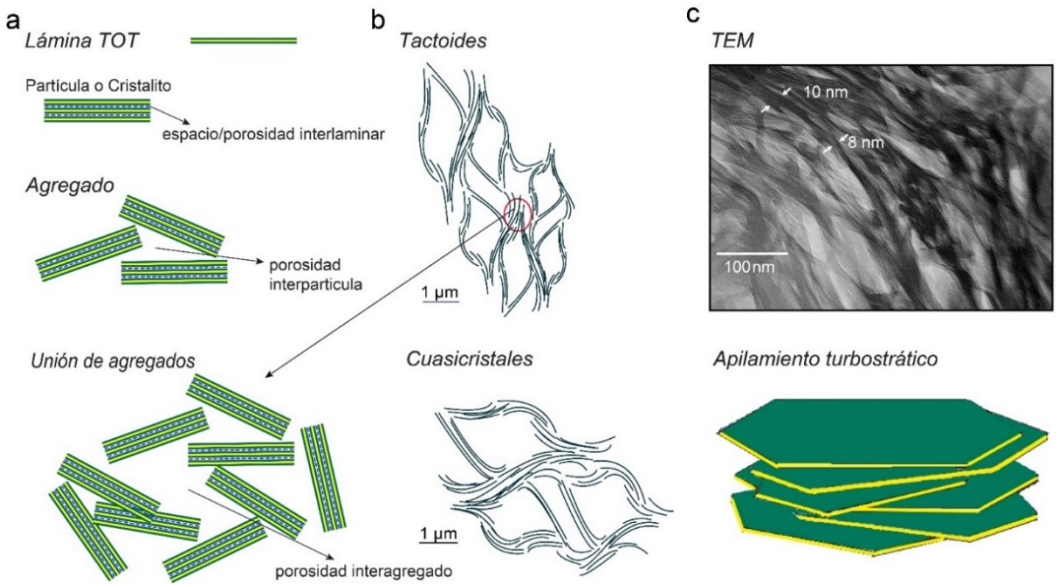

Fig. 2.5. a) Niveles de organización y porosidad presentes en las esmectitas. b) tipos de asociaciones laminares presentes en las esmectitas en función del tipo de catión dominante. c) TEM: imagen tomada por microscopía electrónica de transmisión de una esmectita dioctaédrica y representación del apilamiento turbostrático de las láminas TOT.

Por otro lado, cuando la bentonita es compactada, sometida a un flujo de agua y restringida a un volumen fijo, se produce una resaturación de forma que la porosidad queda totalmente ocupada por agua. En función de su localización y propiedades se pueden diferenciar tres tipos de agua: (*i*) a*gua interlaminar*, (*ii*) *agua de la doble capa difusa* (Diffuse Double Layer, DDL) y (*iii*) *agua libre* (Bradbury and Baeyens, 2002; Bradbury and Baeyens, 2003; Wersin et al., 2004; Appelo, 2013).

- *i*) El *agua interlaminar* se corresponde con las pseudoláminas de moléculas agua localizadas en el espacio interlaminar, entre las unidades TOT. Estas moléculas se caracterizan por formar parte de la estructura cristalográfica de la esmectita y en conjunto también reciben el nombre de *agua interna*, presentando movilidad solo en la dirección del eje *b*. Como ya se ha apuntado, los cationes característicos de la interlámina (Ca^{2+}, Mg^{2+}, Na^{+}, K^{+}) poseen grandes entalpías de hidratación negativas superiores a otros cationes como H^{+}, $Fe^{2+/3+}$, Cs^{+}, Sr^{2+} y se rodean de moléculas de agua al coordinarse con éstas. A su vez, las moléculas de agua hacen de puente entre el catión interlaminar y la superficie de la esmectita formando complejos de esfera externa mediados por fuerzas electrostáticas (Sposito, 2008) que contrarrestan el exceso de carga negativa de los planos basales. La incorporación y apilamiento de las pseudoláminas de agua, la expansión de la esmectita y la limitación a un volumen constante genera un aumento de la presión ejercida sobre la estructura confinante; esta presión recibe el nombre de *presión de hinchamiento*, si la presión se produce por aumento del espaciado interlaminar se denominada *presión de hinchamiento cristalino*.

- *ii*) El agua presente en la porosidad interpartícula constituye la DDL. El concepto de la DDL según el modelo *"Gouy-Chapman-Stern"* considera que la superficie externa de la esmectita se comporta como un condensador plano que acumula cargas negativas uniformemente en la dirección del eje *c*, lo que provoca un campo eléctrico que atrae a los cationes presentes en la porosidad interpartícula. La confrontación de cargas negativas y positivas genera una doble capa eléctrica (electrical double layer, EDL). En un modelo simplificado la DDL está constituida por la *capa rígida de Stern* seguida de una *capa difusa* (Fig. 2.6). En la capa rígida se sitúan primeramente los cationes unidos mediante enlaces de esfera interna (*enlaces específicos* de tipo covalente con aportación iónica que dificultan su

movilidad) seguidos por los cationes unidos mediante complejos de esfera externa (*enlaces inespecíficos* unidos por fuerzas electrostáticas y que por tanto presentan mayor movilidad (McBride, 1998)). En el caso de los cationes interlaminares hidratados de la montmorillonita constituyen exclusivamente complejos de esfera externa. Ambos complejos, de esfera interna y externa. quedarían separados por el *plano interno de Heltmotz* (Grahame, 1947). En la capa difusa los iones influenciados por las cargas negativas del condensador se disponen en forma de gradiente donde el número de cationes disminuye con la distancia a la superficie de la esmectita. Esta distribución seguiría un modelo casi exponencial decreciente hacia el centro de los poros interpartícula. Por el contrario, el número de aniones seguiría el comportamiento inverso produciéndose, al igual que en la interlámina, una exclusión de los aniones derivada de la repulsión del exceso de carga negativa de la superficie externa del mineral de la arcilla.

- *iii*) El *agua libre* o también llamada *agua de poro* se clasifica como *agua externa* y se localiza en la porosidad interagregado pudiendo existir como películas delgadas conectadas entre sí. Las principales propiedades que la caracterizan residen en su neutralidad eléctrica, por lo que no están directamente condicionadas por las fuerzas electrostáticas próximas a la superficie del condensador y su movilidad obedecería a las fuerzas capilares y a la fuerza gravitacional presentes (siempre y cuando no esté sometida a fuerzas externas *e.j.* presión). No obstante, los límites con la capa difusa no son discretos de modo que una pequeña proporción del agua libre es considerada como parte de la capa difusa estando por tanto parcialmente influenciada por ésta.

La diferencia de concentraciones y repulsiones electrostáticas entre ambas capas permite que la DDL actúe como una membrana semipermeable, especialmente si

la bentonita ha sido compactada, lo que permite el paso de agua desde la disolución más diluida (el agua libre) a la más concentrada (el agua en la DDL). Por el contrario, Meunier (2005) expone que además de las moléculas agua, los iones pueden ser intercambiados mediante procesos físicos o químicos entre las láminas, partículas y agregados, por lo tanto, se puede concluir que existe un mínimo intercambio de iones y mayoritario intercambio de agua. En cualquier caso, este proceso también contribuiría a la expansión del material, si bien en menor medida que la expansión producida por la hidratación interlaminar, generando una *presión de hinchamiento*. Cuando ésta es originada en la DDL se conoce como *presión de hinchamiento osmótico*. Por último, también hay que tener en cuenta que las concentraciones de iones disueltos en el agua libre también se verían influenciados por el equilibrio químico establecido con los minerales presentes en la bentonita (*e.j.* cristobalita liberando iones de sílice acuosa ($H_4SiO_4^0$) entre otros). La Figura 2.6 recoge un modelo simplificado de la disposición del agua en la estructura de la bentonita y esmectita.

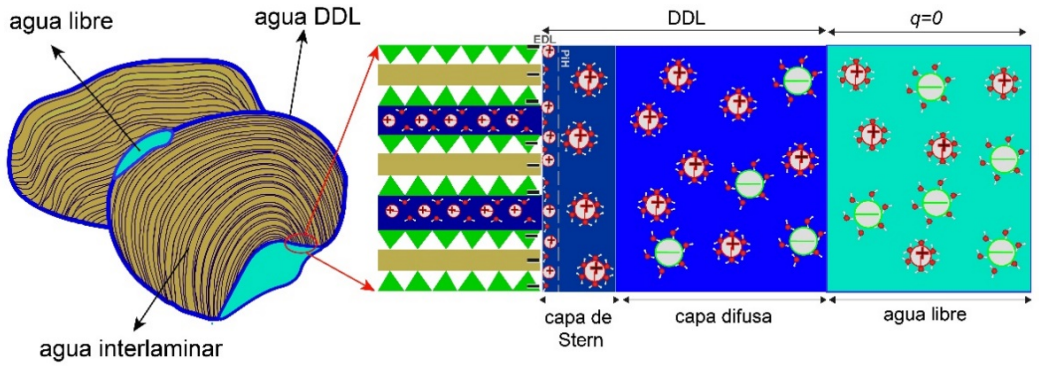

Fig. 2.6. Representación los tipos de agua en la bentonita. La línea de puntos representa el plano de Heltmotz. DDL: agua de la doble capa difusa *q: carga*.

El agua contenida en la porosidad de la bentonita puede ser extraída aumentando la temperatura y/o mediante la aplicación de presión sobre el sólido o sobre el

propio fluido. Debido a que cada tipo de agua posee un estado energético diferente, dependiendo de la intensidad de la presión y/o temperatura aplicada se movilizarían los distintos tipos de agua en función de su estado energético en la secuencia: 1º *agua libre;* 2º*agua DDL;* 3º *agua interlaminar*, siendo por tanto el agua libre o de poro la primera en movilizarse (Madsen and Müller-Vonmoos, 1989). En condiciones de saturación y sometida a un gradiente de presión el agua libre se desplazaría a través de la porosidad interagregado desde las zonas con más presión hacia las zonas con menos presión lo que implica un transporte de solutos por *advección* en el seno de la porosidad interagregado saturada por el agua libre. Por el contrario, el agua interlaminar y de la DDL están condicionados por un transporte difusivo.

2.6 PROPIEDADES HIDROMECÁNICAS

Como se ha expuesto en el capítulo anterior, la interacción con el agua tiene importantes repercusiones en las propiedades mecánicas de las arcillas esmectíticas. El tamaño coloidal de las partículas minerales y su carga eléctrica las hace hidratarse e interactuar, de manera que la bentonita hidratada es un material cohesionado en el que tanto su baja *conductividad hidráulica* como sus propiedades reológicas (*e.j. plasticidad*) son muy favorables para su aplicación como material de barrera en el aislamiento de residuos nucleares.

2.6.1 Conductividad hidráulica

Para conocer la velocidad de un fluido a través de un material la ley de Darcy define el *coeficiente conductividad hidráulica* o *de permeabilidad* (*k*). Se expresa en metros por segundo (m/s) y relaciona el *gradiente de presión o hidráulico* (*i*)

con la *velocidad* (*v*) que experimenta el agua a través de un material tal que: *v=ki*. Varios autores han expresado que no es aplicable a los materiales arcillosos *e.j.* (Gonçalvès et al., 2015), pues fue inicialmente concebida para su uso en arenas y gravas, sin embargo, su uso está generalizado en el ámbito de las arcillas, por lo que resulta de gran utilidad al permitir establecer comparaciones directas entre los distintos trabajos científicos.

Partiendo de la base de que el agua fluye principalmente a través de la porosidad interagregado, es decir obedece al movimiento del agua libre, algunos factores que afectan a la conductividad hidráulica son el grado de saturación de los poros (en arcillas expansivas), la presión de hinchamiento (una disminución aumentaría la permeabilidad) el volumen y conectividad de los poros, y el tamaño y tipo de unión de las partículas o cristalitos (uniones cara-cara o cara-borde). Por lo tanto, en base a estos factores y a las características de las esmectitas, la bentonita posee una conductividad hidráulica baja con valores inferiores a 1×10^{-12} m/s (Pusch, 2006; Wagner, 2013). Para estos valores de conductividad hidráulica los procesos de difusión, esto es, por diferencia de concentraciones entre dos fases toman gran relevancia y se convierte en el mecanismo dominante de transporte de solutos por encima del transporte por advección.

2.6.2 Plasticidad

Las bentonitas presentan una elevada *plasticidad* derivado de su morfología laminar, el pequeño tamaño de partícula y su alta capacidad de hinchamiento. La plasticidad implica la capacidad de deformarse sin fracturarse ante un esfuerzo mecánico conservando la deformación al retirarse la carga. Además, el carácter expansivo facilita el sellado ante la aparición de posibles fracturas favoreciendo

así el aislamiento de la cápsula metálica que confina el material radiactivo. Esta propiedad sería especialmente relevante ante posibles fenómenos geodinámicos como seísmos (Astudillo, 2001; Takahashi et al., 2007).

2.7 PROPIEDADES FÍSICO-QUÍMICAS: SUPERFICIE ESPECÍFICA Y CAPACIDAD DE INTERCAMBIO CATIÓNICO (CIC)

2.7.1 Superficies e interfases de los minerales de arcilla

Las propiedades físicas y mecánicas expuestas surgen a partir de las reacciones químicas e interacciones eléctricas generadas en la superficie de la bentonita en una escala nano y micrométrica. Los mecanismos que controlan estas reacciones físico-químicas dependen de las características intrínsecas de las superficies e interfases del mineral, donde también intervienen las condiciones del medio externo, principalmente el pH y la fuerza iónica. En los minerales de arcilla con estructura 2:1 se distinguen dos tipos de superficies: *i*) las *superficies basales* también llamadas superficies siloxano, que comprenden por un lado las superficies expuestas a la capa interlaminar y por otro lado las superficies expuestas al medio poroso externo y *ii*) las *superficies de borde* ubicadas en al final de las capas T y O donde generalmente presentan grupos OH coordinados con un metal tetra o trivalente M^{n+}–(OH).

i) En las superficies basales se encuentran las *cargas permanentes,* las cuales permanecen estables independientemente del pH externo y son ampliamente mayoritarias respecto a las cargas de borde. Se localizan en las cavidades pseudohexagonales (cavidad ditrigonal) donde se comportan como bases de Lewis (Fig. 2.7a) debido a los electrones aportados por los 6 oxígenos basales

correspondientes a los vértices de los tetraedros de Si^{4+} y/o Al^{3+} en caso de sustituciones isomórficas. Cuando la carga de la capa es neutra (es decir, no han tenido lugar las sustituciones isomórficas), los electrones difícilmente llegan interaccionar con moléculas dipolares y cationes solvatados e incluso llegan a presentar un comportamiento hidrófobo.

En el caso de que se hayan originado sustituciones isomórficas en la capa O se genera el exceso de carga negativa y los electrones se redistribuyen entre los 10 oxígenos correspondientes a los 4 tetraedros unidos a cada octaedro (McBride, 1998; Meunier, 2005; Sposito, 2008) de modo que el carácter básico, y por tanto la capacidad para donar electrones de la cavidad ditrigonal (pseudohexagonal) es suficientemente fuerte para formar complejos de esfera externa (Fig. 2.7b).

Por último, si las sustituciones isomórficas se producen en la capa T, el exceso de carga negativa se distribuye entre los tres oxígenos basales del tetraedro, generando así superficies aún más básicas y reactivas que pueden formar complejos de esfera interna más estables (principalmente con cationes monovalentes de pequeño radio: K^+ o Li^+). Si bien este fenómeno es más común en minerales 1:1 tipo kaolinitas o 2:1 tipo ilitas caracterizado por presentar un catión de K^+ en el espacio interlaminar (Fig. 2.7c).

En el caso de las esmectitas, la carga laminar es más baja, formando complejos de esfera externa, generalmente con cationes divalentes de Ca^{2+} y Mg^{2+}. Entre los parámetros principales que controlan la interacción de los diferentes iones destacan su radio iónico (si la carga proviene de una sustitución octaédrica) y su entalpía de hidratación.

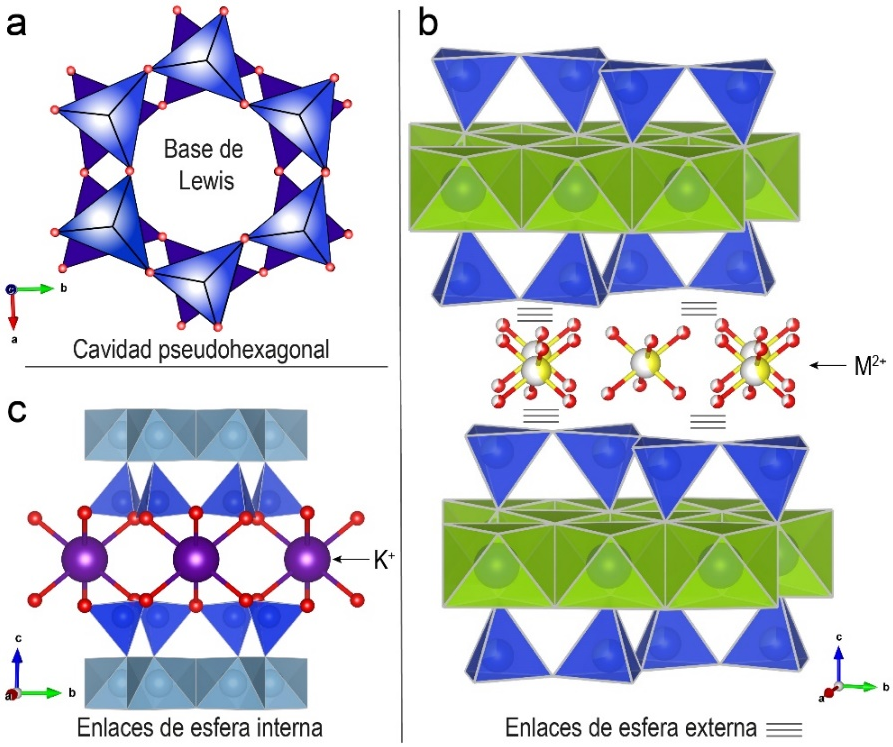

Fig. 2.7. Representación de distintas estructuras presentes en esmectitas. a) Cavidad pseudohexagonal. b) Láminas TOT presentes en las esmectitas unidas por cationes divalentes interlaminares (M^{2+}) formando complejos de esfera externa. c) Ilita donde se representa el enlace específico del K^+.

ii) En las superficies generadas en los bordes de las capas, por rotura o falta de la continuidad de los cristalito o partículas en el plano *a-b* se localizan cargas variables también llamadas "*pH-dependientes*" puesto que varían en función del pH externo. Los tetraedros de los extremos de las capas T poseen un exceso de carga positiva (actuando como ácidos de Lewis) ya que el átomo de oxígeno externo presenta una valencia libre, de modo que se compensa captando un H^+ del medio formando grupos hidroxilo coordinados con el metal tetraédrico de (generalmente Si en el caso de las esmectitas) $Si–O^- + H^+ \leftrightarrows Si–OH$ donde el grupo OH puede sufrir protonación, desprotonación o formar complejos (Borisover and Davis, 2015) en función del pH adquiriendo así un

comportamiento anfótero (*z-witterion*) lo que constituye en sí mismo un sistema amortiguador. En caso de una perturbación ácida o básica del fluido externo los grupos OH se protonarían/desprotonarían respectivamente regulando el pH externo. En las esmectitas esta capacidad se ve incrementada pues se caracterizan por presentar numerosas rupturas y discontinuidades y por tanto mayor número de superficies de borde con grupos Si–OH. Además, otro factor importante que aumenta este efecto tampón es la baja relación líquido/sólido de la bentonita compactada (Fernández et al., 2004).

2.7.2 Capacidad de intercambio catiónico: CEC

La capacidad de intercambio catiónico (Cation Exchange Capacity, CEC) refleja el número de cationes adsorbidos de forma reversible por unidad de peso *e.j.* (McBride, 1998; Sparks, 2003; Bleam, 2017) expresados como centimoles de carga por kg (cmol/kg). Tienen su origen en las sustituciones isomórficas de los cationes tetraédricos y octaédricos que originan las cargas negativas en las superficies basales. Además, a estas cargas permanentes hay que añadir la contribución de aquellas derivadas de las superficies de borde de la capa T (en el caso de minerales 2:1). Por lo que la $CEC_{total} = CEC_{cargas\ permanentes} + CEC_{cargas\ variables}$. Es por tanto que la CEC está relacionada inversamente con el tamaño de las partículas o cristalitos, así cuanto mayor sea la CEC menor será el tamaño de partícula.

Por otro lado, es importante resaltar que un aumento de la carga de capa (carga por media celda unidad (X)) no implica necesariamente una mayor CEC. Esto se debe a que la CEC que no contabiliza los cationes unidos por complejos de esfera interna. Cuando este valor es superior a ~0.75 la atracción electrostática es

suficientemente fuerte para formar enlaces de esfera interna no reversibles, por tanto, los cationes dejan ser intercambiables y el mineral deja de ser una esmectita expansiva (Fig. 2.8a). Un ejemplo es el mostrado con el K^+ en la Figura 2.7c. Este fenómeno tiene especial relevancia en las superficies basales orientadas hacia la interlámina pues pierden su capacidad de hinchamiento al no permitir la entrada de moléculas de agua.

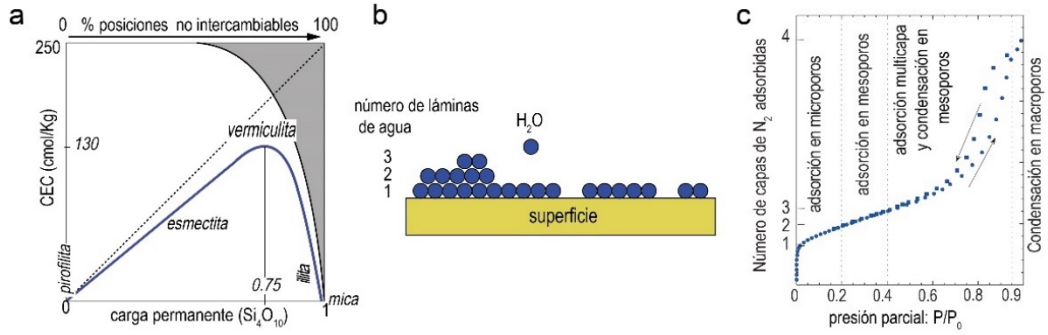

Fig. 2.8. a) Representación no lineal de la capacidad de intercambio catiónico en función de la carga laminar. b) Nucleación de moléculas de agua adsorbidas en la superficie de la arcilla. c) Isoterma de adsorción de N_2 dónde se recoge el número capas de un gas adsorbidas en las distintas porosidades en función de la presión parcial. CEC: capacidad de intercambio catiónico. Figuras modificadas de Meunier (2005) y Michot and Villiéras (2006).

2.7.3 Superficie específica (specific surface area, SSA)

La superficie específica (specific surface area, SSA) es una de las propiedades más importantes que controla los fenómenos superficiales de los minerales de arcilla. El pequeño tamaño de las partículas (<<2 μm) les proporciona una elevada superficie en contacto con el medio externo por unidad de masa (m^2/g). En esta escala nano-micrométrica las fuerzas electrostáticas cobran gran relevancia generando superficies muy reactivas que las permite interactuar con una gran variedad de moléculas tanto orgánicas como inorgánicas en interfases sólido-líquido o sólido-gas (Michot and Villiéras, 2006). Esta propiedad les confiere un especial interés para su aplicación en procesos industriales (Murra, 2006; Bergaya

et al., 2013). En el contexto del aislamiento de residuos radiactivos una elevada SSA favorecería la adsorción de los radionúclidos en el momento de su liberación.

La SSA de un sólido se corresponde a la suma de las superficies de todos los sitios accesibles a la adsorción de un determinado ion o molécula utilizado para su medida, un gas inerte como el N_2 o Ar entre otras moléculas. Una vez completada la adsorción, conociendo la masa (o también, el área de la sección transversal de la molécula o ion en su caso) de las monocapas completas que han recubierto las superficies del sólido, se puede calcular la superficie total accesible (no obstante, esta monocapa antes de completarse puede sufrir nucleación acumulándose una segunda y tercera capa antes de que la primera se haya completado (Fig. 2.8b)).

Las caracterizaciones experimentales de las superficies de los minerales de arcilla frecuentemente se basan en el método BET-N_2 (Brunauer Emmett and Teller) (Brunauer et al., 1938). A partir de N_2 (g) a 77 K se obtienen isotermas de adsorción que describen la cantidad gas adsorbido en función de la presión relativa (P/P_0). En materiales con microporosidad este método describe la combinación de fenómenos como la adsorción en superficies de partículas externas, con fenómenos espaciales como la condensación en micro, meso y macroporos (Michot and Villiéras, 2006).

Dependiendo del tamaño de partícula, el catión interlaminar (en minerales de arcilla expansivos), la organización de los poros y las propiedades energéticas de la superficie se obtienen distintos tipos de isotermas. Dentro de cada isoterma se pueden observar 4 regiones características: *i*) una región de baja presión relativa (P/P_0 = 0-0.2) donde la adsorción del gas se produce en la superficie externa de las partículas y en la superficie de los microporos de diámetros de 0 a 20 Å; *ii*) entre valores de presiones relativas comprendidas entre 0.2 y 0.9 se produce la

adsorción de la segunda y tercera capa, donde las moléculas N_2 (g) se condensan en mesoporos de 40-400 Å de sección. Finalmente, a presiones relativas >0.95, se produce la condensación en los macroporos (>400 Å) (Fig. 2.8c).

Sin embargo, a la hora de interpretar los resultados hay que tener en cuenta las limitaciones de la técnica, principalmente la baja exactitud del método en muestras microporosas y la incapacidad del gas para penetrar en todas las superficies, en el caso de las esmectitas el N_2 (g) no accede al su espacio interlaminar subestimando por tanto su valor de SSA. A pesar de estas consideraciones, el método BET-N_2 permite obtener información de importante utilidad, se trata de una técnica ampliamente extendida de modo que se utiliza comúnmente como referencia entre distintos materiales. Además, atendiendo a las isotermas de adsorción del N_2(g), éstas pueden proporcionar información sobre el tamaño, la estructura, los diferentes tipos porosidades e incluso información de la forma de las partículas y agregados presentes minerales de la arcilla (Tournassat et al., 2015).

2.8 REFERENCIAS

- Appelo, C.A.J., 2013. A review of porosity and diffusion in bentonite. Finland, p. 36, http://inis.iaea.org/search/search.aspx?orig_q=RN:45087776.

- Astudillo, J., 2001. *El almacenamiento geológico profundo de los residuos radiactivos de alta actividad: principios básicos y tecnología*, ed. ENRESA.

- Bergaya, F., Beneke, K., Berry, R.W., Lagaly, G., Tankersley, K.B., 2013. *Chapter 15 - Clay Science: A Young Discipline and a Great Perspective*, in: Bergaya, F., Lagaly, G., Developments in Clay Science, ed. Elsevier.

- Bleam, W., 2017. *Chapter 4 - Ion Exchange*, in: Bleam, W., Soil and Environmental Chemistry (Second Edition), ed. Academic Press.

- Borisover, M., Davis, J.A., 2015. *Chapter 2 - Adsorption of Inorganic and Organic Solutes by Clay Minerals*, in: Tournassat, C., Steefel, C.I., Bourg, I.C., Bergaya, F., Developments in Clay Science, ed. Elsevier.

- Bouchet, A., Meunier, A., Sardini, P., 2002. *Minéraux argileux: structure cristalline, identification par diffraction de rayons X.*, ed., France.

- Bradbury, M.H., Baeyens, B., 2002. Porewater chemistry in compacted re-saturated MX-80 bentonite: Physico-chemical characterisation and geochemical modelling. Switzerland, p. 54, http://inis.iaea.org/search/search.aspx?orig_q=RN:50041726.

- Bradbury, M.H., Baeyens, B., 2003. Porewater chemistry in compacted re-saturated MX-80 bentonite. *Journal of Contaminant Hydrology*, 61, pp. 329-338, https://doi.org/10.1016/S0169-7722(02)00125-0.

- Brunauer, S., Emmett, P.H., Teller, E., 1938. Adsorption of gases in multimolecular layers. *Journal of the American chemical society*, 60, pp. 309-319, https://doi.org/10.1021/ja01269a023.

- Christidis, G.E., Huff, W.D., 2009. Geological aspects and genesis of bentonites. *Elements*, 5, pp. 93-98, https://doi.org/10.2113/gselements.5.2.93.

- Deer, W.A., 1962. *Rock-forming minerals: Sheet silicates*, ed. Longmans.

- Fernández, A.M., Baeyens, B., Bradbury, M., Rivas, P., 2004. Analysis of the porewater chemical composition of a Spanish compacted bentonite used in an engineered barrier. *Physics and Chemistry of the Earth, Parts A/B/C*, 29, pp. 105-118, https://doi.org/10.1016/j.pce.2003.12.001.

- Fernández Martín, R. 2006. *Transporte reactivo de disoluciones alcalinas en la interfase mortero de cemento-bentonita*, Tesis Doctoral. Universidad Autónoma de Madrid, p. 256, http://hdl.handle.net/10486/2549.

- Galán, E., 2006. *Chapter 14 Genesis of Clay Minerals*, in: Bergaya, F., Theng, B.K.G., Lagaly, G., Developments in Clay Science, ed. Elsevier.

- Gómez-Espina, R., Villar, M.V., 2016. Time evolution of MX-80 bentonite geochemistry under thermo-hydraulic gradients. *Clay Minerals*, 51, pp. 145-160, https://doi.org/10.1180/claymin.2016.051.2.03.

- Gonçalvès, J., Adler, P.M., Cosenza, P., Pazdniakou, A., de Marsily, G., 2015. *Chapter 8 - Semipermeable Membrane Properties and Chemomechanical Coupling in Clay*

Barriers, in: Tournassat, C., Steefel, C.I., Bourg, I.C., Bergaya, F., Developments in Clay Science, ed. Elsevier.

- Grahame, D.C., 1947. The Electrical Double Layer and the Theory of Electrocapillarity. *Chemical Reviews*, 41, pp. 441-501, https://doi.org/10.1021/cr60130a002.

- Johnston, C.T., 2018. *4 - Clay mineral–water interactions*, in: Schoonheydt, R., Johnston, C.T., Bergaya, F., Developments in Clay Science, ed. Elsevier.

- Kaufhold, S., Dohrmann, R., 2016. Distinguishing between more and less suitable bentonites for storage of high-level radioactive waste. *Clay Minerals*, 51, pp. 289-302, https://doi.org/10.1180/claymin.2016.051.2.14.

- Lagaly, G., Dékány, I., 2013. *Chapter 8 - Colloid Clay Science*, in: Bergaya, F., Lagaly, G., Developments in Clay Science, ed. Elsevier.

- Madsen, F.T., Müller-Vonmoos, M., 1989. The swelling behaviour of clays. *Applied Clay Science*, 4, pp. 143-156, https://doi.org/10.1016/0169-1317(89)90005-7.

- McBride, M.B., 1998. *Environmental chemistry of soils*, ed. Oxford University Press, New York, N.Y.

- Meunier, A., 2005. *Crystal Structure — Species — Crystallisation*, in, Clays, ed. Springer Berlin Heidelberg, Berlin, Heidelberg.

- Michot, L.J., Villiéras, F., 2006. *Chapter 12.9 Surface Area and Porosity*, in: Bergaya, F., Theng, B.K.G., Lagaly, G., Developments in Clay Science, ed. Elsevier.

- Momma, K., Izumi, F., 2011. VESTA 3 for three-dimensional visualization of crystal, volumetric and morphology data. *Journal of Applied Crystallography*, 44, pp. 1272-1276, https://doi.org/10.1107/S0021889811038970.

- Murra, H.H., 2006. Current Industrial Applications of Clays. *Clay Science*, 12, pp. 106-112, https://10.11362/jcssjclayscience1960.12.Supplement2_106.

- Norris, S., 2017. Radioactive waste confinement: clays in natural and engineered barriers – introduction. *Geological Society, London, Special Publications*, 443, pp. 1-8, https://doi.org/10.1144/SP443.26.

- Pelayo, M. 2014. *Estudio del yacimiento de bentonita de Morrón de Mateo (Cabo de Gata, Almería) como análogo natural del comportamiento de la barrera de arcilla de un*

almacenamiento de residuos radiactivos, Tesis Doctoral. Universidad Complutense de Madrid, p. 241, https://eprints.ucm.es/25430/.

- Pusch, R., 2006. *Chapter 6 Mechanical Properties of Clays and Clay Minerals*, in: Bergaya, F., Theng, B.K.G., Lagaly, G., Developments in Clay Science, ed. Elsevier.

- Rouquerol, J., Avnir, D., Fairbridge, C.W., Everett, D.H., Haynes, J.M., Pernicone, N., Ramsay, J.D.F., Sing, K.S.W., Unger, K.K., 1994. Recommendations for the characterization of porous solids (Technical Report). 66, Berlin, Boston, p. 1739-1758, https://www.degruyter.com/view/journals/pac/66/8/article-p1739.xml.

- Schoonheydt, R.A., Johnston, C.T., 2013. *Chapter 5 - Surface and Interface Chemistry of Clay Minerals*, in: Bergaya, F., Lagaly, G., Developments in Clay Science, ed. Elsevier.

- Sparks, D.L., 2003. *6 - Ion Exchange Processes*, in: Sparks, D.L., Environmental Soil Chemistry (Second Edition), ed. Academic Press, Burlington.

- Sposito, G., 2008. *The chemistry of soils*, ed. Oxford university press.

- Takahashi, M., Mizoguchi, K., Kitamura, K., Masuda, K., 2007. Effects of clay content on the frictional strength and fluid transport property of faults. 112, pp., https://doi.org/10.1029/2006JB004678.

- Tournassat, C., Bourg, I.C., Steefel, C.I., Bergaya, F., 2015. *Chapter 1 - Surface Properties of Clay Minerals*, in: Tournassat, C., Steefel, C.I., Bourg, I.C., Bergaya, F., Developments in Clay Science, ed. Elsevier.

- Wagner, J.F., 2013. *Chapter 9 - Mechanical Properties of Clays and Clay Minerals*, in: Bergaya, F., Lagaly, G., Developments in Clay Science, ed. Elsevier.

- Wersin, P., Curti, E., Appelo, C.A.J., 2004. Modelling bentonite–water interactions at high solid/liquid ratios: swelling and diffuse double layer effects. *Applied Clay Science*, 26, pp. 249-257, https://doi.org/10.1016/j.clay.2003.12.010.

CAPÍTULO 3. MATERIALES DE BASE CEMENTO

3.1 INTRODUCCIÓN

El AGP implica la utilización de importantes volúmenes de materiales de base cemento, en el caso un almacenamiento en granito está estimado el uso de en torno a los 40.000 m^3 (García Calvo, 2012) o 16.000 kg para el tapón de sellado (Vehmas and Holt, 2016). En el EBS su función principal es el sellado y sostenimiento de las gallerías.

Formalmente, el cemento se puede definir como un material adhesivo e inorgánico, no metálico, finamente molido que cuando se mezcla con agua y áridos forma un conglomerado que en pocas horas sufre un espesamiento, es decir, *fragua* y endurece formando un material sólido y resistente denominado hormigón o mortero dependiendo del tamaño de partícula del árido empleado para su elaboración (hormigón si la sección del árido es superior a 4 mm y mortero si es inferior; (Taylor et al., 1978)).

Es importante resaltar que durante estos procesos los áridos se mantienen casi inertes (sí bien la interfase árido/pasta constituye una zona de transición de diferentes características químicas y físicas de las presentes en la matriz o pasta del cemento (Taylor, 1997b), por lo que desde el punto de vista químico la investigación del cemento puede hacerse legítimamente en ausencia del árido grueso siendo conveniente si no se van a realizar determinaciones físicas (*e.j.* resistencia mecánica).

De entre los distintos tipos de cementos, el cemento Pórtland es con diferencia el más importante siendo el material industrial por volumen más utilizado en el mundo. Para su fabricación, se parte de materiales calizos y arcillosos

(denominados *crudos*), los cuales son sometidos a altas temperaturas (~1400-1500ºC) hasta su fusión parcial. Tras su enfriamiento se obtiene el *clínker,* que molido con un pequeño porcentaje de yeso (5%) da lugar al cemento Pórtland donde la función del yeso es la de ralentizar la reactividad del cemento. Por otro lado, el cemento Pórtland puede ser mezclado con adiciones minerales (>5%) con el fin de obtener una determinada funcionalidad de interés, lo que da lugar a distintos tipos de materiales de base cemento. La norma UNE-EN 197-1:2011 establece la nomenclatura y clasificación de los tipos de cementos Pórtland distinguiendo 5 grupos: CEM I, II, III, IV o V. A su vez, en función de su resistencia, tipo y contenido de adiciones minerales se establecen distintos subgrupos.

La composición aproximada del clínker es de: 67% en CaO, 22% en SiO_2, 5% en $A1_2O_3$, 3% de Fe_2O_3 y 3% de otros compuestos minoritarios, entre ellos impurezas tales como el Al, Mg, Na, K, S, etc.

Cada grano de cemento Pórtland es un policristal que contiene varias fases minerales llamadas *anhidros* (Fig. 3.1), las más abundantes son:

i) Silicato tricálcico [Ca_3SiO_5 (alita, C_3S[1])] presente en un 50-70%.

ii) Silicato dicálcico [Ca_2SiO_4 (belita, C_2S[1])] presente en un 15-30%.

iii) Aluminato tricálcico [$Ca_3Al_2O_6$ (C_3A[1])] presente en un 5-10%.

iv) Ferro-aluminato tetracálcico [$Ca_4Al_2Fe_2O_{10}$ (ferrita, C_4AF[1])] presente en un 5-15%.

[1]La fórmula química se ha establecido en base a la nomenclatura empleada en el campo de la química del cemento (Taylor, 1997b), la lista de abreviaturas de uso común es la siguiente:

C = CaO	S = SiO_2	A = $A1_2O_3$	F = Fe_2O_3	H = H_2O
M=MgO	K = K_2O	$\underline{S}$ = SO_3	N = Na_2O	$\underline{C}$ = CO_2

Estas fases presentan sustituciones isomórficas a causa de la migración de las impurezas de forma que su composición ideal se ve modificada.

Además de estos componentes, el clínker presenta compuestos minoritarios como óxido de magnesio (periclasa, MgO), óxido de calcio (cal libre, CaO) y sulfatos de álcalis (*e.j.* Na_2SO, K_2SO_4).

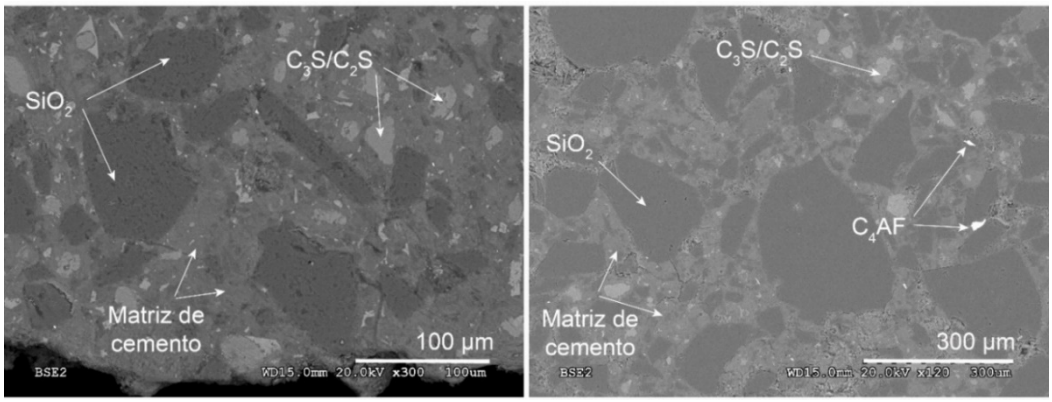

Fig. 3.1. Fases anhidras presentes junto con granos de cuarzo (representados con la fórmula SiO_2) en morteros de cemento hidratados. C_3S/C_2S: silicatos tri y di tetracálcicos. C_4AF: Ferro-aluminatos tetracálcicos. (Imágenes obtenidas durante el estudio de los materiales de la presente tesis).

3.2 HIDRATACIÓN DEL CEMENTO PÓRTLAND

La hidratación del cemento es entendida como la reacción entre el propio cemento no hidratado o alguno de sus componentes con agua, lo cual lleva asociados cambios químicos y físico-mecánicos del sistema, en particular *i*) el fraguado y el endurecimiento *ii*) aumento del volumen, *iii*) desprendimiento de calor y *iv*) formación de nuevas fases sólidas, los hidratos del cemento. (La Figura 3.1

muestra la matriz o pasta de cemento formada durante la hidratación del clínker). Aunque en principio pueden parecer reacciones sencillas, presentan gran complejidad y siguen siendo motivo de investigación *e.j.* (Bullard et al., 2011; Rahimi-Aghdam et al., 2017; Bogner et al., 2020; Zhu et al., 2020). La hidratación de la pasta de cemento Pórtland a temperatura ambiente es comúnmente descrita en varias etapas: *i*) *pre-inducción*, la cual transcurre durante los primeros minutos, *ii*) *período de inducción (durmiente)* que abarca las primeras horas, *iii*) *etapa de aceleración* (3-12 horas tras la mezcla) y *iv*) *periodo de post aceleración* (Taylor, 1997b; Beaudoin and Odler, 2019).

De forma resumida, se puede exponer que en una primera etapa se disuelven iones de calcio, silicatos y aluminatos entre otros en el agua de poro; rápidamente la disolución se satura y en cuestión de horas precipitan nuevos compuestos procedentes de la hidratación de las fases anhidras: silicatos di y tricálcicos, y aluminatos cálcicos.

La hidratación del C_3S y más tarde del C_2S da lugar a silicatos de calcio hidratados (C-S-H: los guiones indican que no está implícita una composición específica) y portlandita (referidos como hidróxidos de calcio: $Ca(OH)_2$, o CH) (Fig. 3.2). Los C-S-H se caracterizan por ser amorfos o presentar un alto grado de desorden estructural y gran variabilidad en su composición durante las diferentes etapas. Esta fase es la más importante del cemento Pórtland y es responsable última su alta cohesión, constituyendo entre un ~50-60% del volumen total de sólidos (ver sección 3.3. C-S-H).

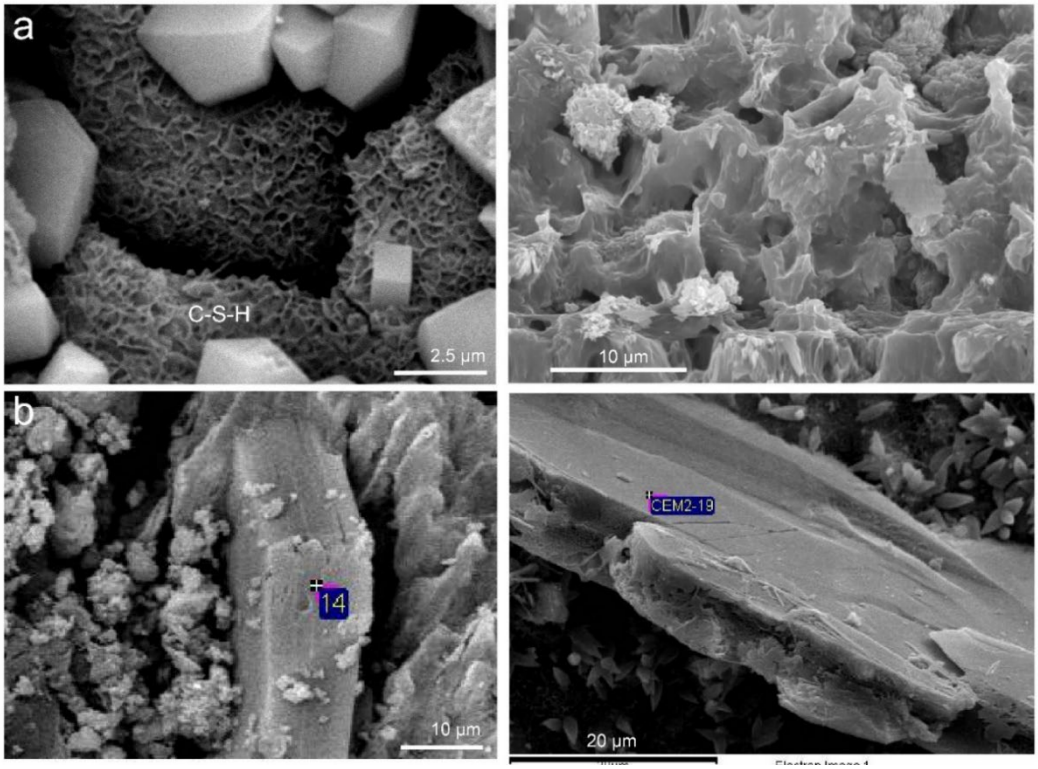

Fig. 3.2. Micrografías tomadas mediante SEM-EDX. a) Se muestran dos tipos de morfologías de C-S-H, una reticular presente entre cristales de carbonato cálcico (izq.) y otra morfología tipo gel (dcha.). b) Portlanditas pseudohexagonales presentes en cemento Pórtland de alto pH. Imágenes obtenidas el estudio de los materiales de la presente tesis.

Tras una primera etapa de formación de C-S-H, tiene lugar la precipitación de portlandita (Fig. 3.3) caracterizados por formar cristales hexagonales que suponen un total del 20-25% de la pasta de cemento. Las ecuaciones químicas (*eq*) 1 y 2 resumen las reacciones de hidratación de estos silicatos cálcicos. Cabe destacar la mayor velocidad de reacción, así como el mayor calor liberado en el caso del C_3S. Además, su hidratación genera mayor cantidad de portlandita (La fórmula $C_3S_2H_4$ es una aproximación, pues como se ha comentado su composición varía notablemente con el tiempo).

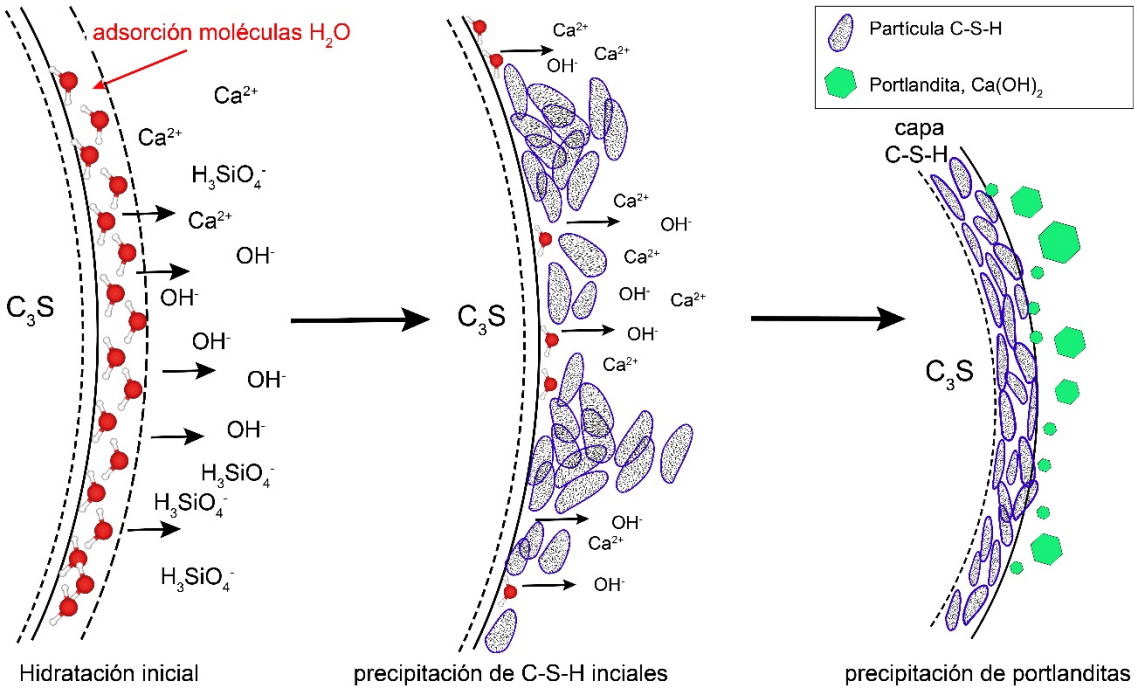

Fig. 3.3. Modelo simplificado de la hidratación de los silicatos cálcicos, concretamente del C_3S. La figura recoge el ataque de iones H^+ proporcionados por el agua y liberación de sílice acuosa, Ca^{2+} y OH^-, lo que facilita la precipitación de geles C-S-H. Una vez consumida la sílice, el exceso de Ca^{2+} y OH^- da paso a la formación de portlandita.

$$2C_3S + 7H^+ \leftrightarrows 2C_3S_2H_4 + 3CH \quad (eq.\ 1)$$

Alita $\leftrightarrows$ *C-S-H + portlandita*

$$C_2S + 5H^+ \leftrightarrows C_3S_2H_4 + CH \quad (eq.\ 2)$$

Belita $\leftrightarrows$ *C-S-H + portlandita*

Entre los anhidros presentes en el cemento Pórtland, el aluminato tricálcico (C_3A) es el más reactivo, los iones de aluminato rápidamente se combinan con iones de calcio y sulfato proporcionados por el yeso ($CaSO_4{\cdot}2H_2O$; simplificado: $C\underline{S}H_2$) añadido en la molienda, lo que permite la formación de aluminatos cálcicos hidratados. Este proceso se realiza en dos etapas fuertemente exotérmicas; en la primera etapa hay suficiente sulfato disponible en el medio poroso y se forma trisulfoaluminato hidratado (AFt o etringita, $C_6A\underline{S}_3H_{32}$) reconocible por presentar

cristales en forma de aguja (Fig. 3.4). En la segunda etapa, cuando la concentración de sulfato en solución disminuye suficientemente, la etringita se vuelve inestable y disuelve, de modo que comienzan a precipitar diferentes especies de monosulfoaluminatos hidratados (AFm, *e.j.* $C_4A\underline{S}H_{12}$) en características finas láminas hexagonales (*eq.* 3-4).

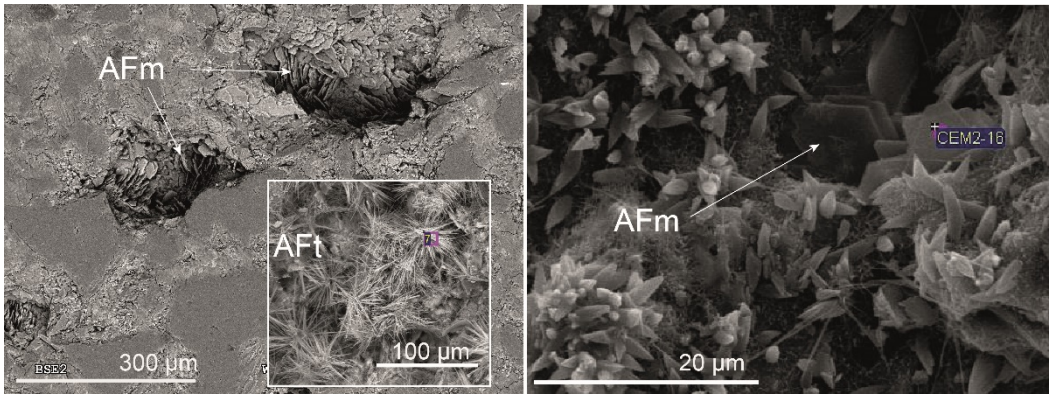

Fig. 3.4. Micrografías de distintas morfologías de fases de trisulfoaluminato hidratado o etringita (AFt) y monosulfoaluminatos hidratados (AFm). Imágenes obtenidas durante el estudio de los materiales de la presente tesis.

$$C_3A + 3C\underline{S}H_2 + 26H_2O \leftrightarrows C_6A\underline{S}_3H_{32} \qquad eq.\ 3$$

Aluminato + yeso ⇆ etringita (AFt)

$$2C_3A + C_6A\underline{S}_3H_{32} + 4H_2O \leftrightarrows 3C_4A\underline{S}H_{12} \qquad eq.\ 4$$

Aluminato + etringita ⇆ (AFm)

A largo plazo la etringita tiende a disolverse por completo para formar distintas variedades de hidratos hexagonales pertenecientes al grupo de los AFm (Fig. 3.5).

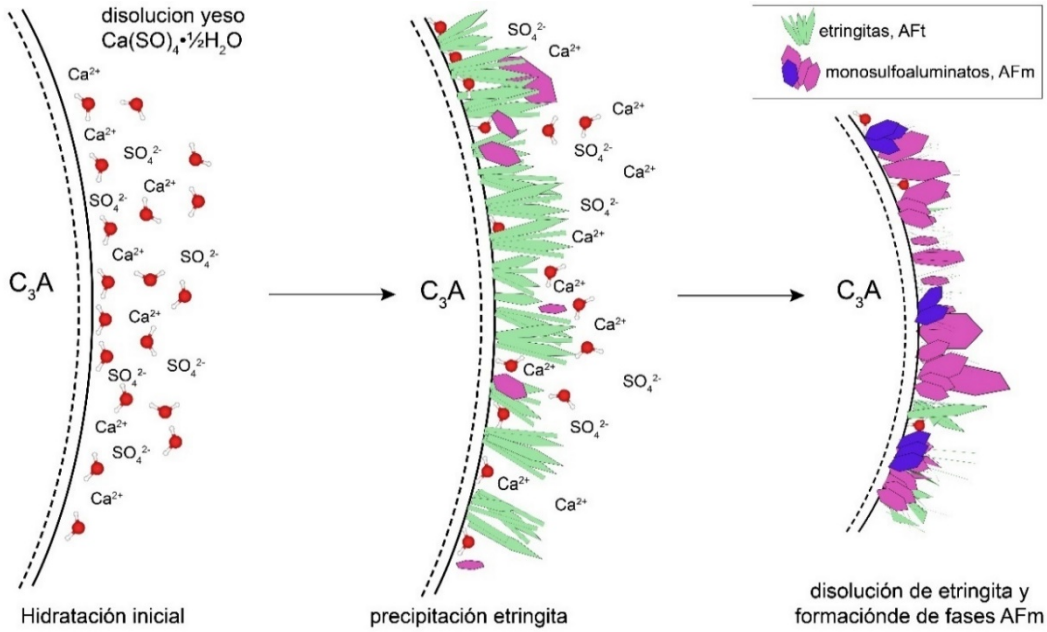

Fig. 3.5. Modelo simplificado de la hidratación del aluminato tricálcico. La figura muestra como el yeso se disuelve en Ca^{2+} y SO_4^{2-} y da lugar a la precipitación de etringita, a medida que se va consumiendo los iones sulfato el equilibrio se desplaza para formar fases de AFm (*eq*. 4).

En cuanto al ferro aluminato tetracálcico también aquí denominado como ferrita: C_4AF, sigue la misma dinámica que los C_3A si bien tiene una cinética mucho más lenta. En la práctica difícilmente se hidratan, y en tal caso llegan formar fases de AFm sin sulfatos (*e.j.* C_4FH_6, fase termodinámicamente más estable).

Una característica importante es la porosidad del material, una vez fragua y endurece el cemento presenta una red poros que influye en su resistencia y durabilidad. Entre los distintos métodos de caracterización de la porosidad destaca la utilización del método BET-N_2 (una revisión más detallada de la porosidad a nivel de C-S-H es descrita en la sección 3.3).

Los productos de hidratación ocupan el espacio disponible dentro de la pasta, que se corresponde con el volumen originalmente ocupado por el agua intersticial.

Debido a que el volumen molar de los hidratos es mucho mayor que el de las fases anhidras, a medida que avanza la hidratación se produce una disminución de la porosidad intergranular inicial pues los productos de reacción tienden a ocupar este espacio. Además, provoca una expansión del cemento si bien, en principio no compromete las propiedades del material.

Se pueden distinguir entre *poros capilares o cavidades* (10-50 nm) que representan el espacio no ocupado por las fases del cemento y *poros de gel* (1-10 nm) formados en los espacios generados entre los agregados de C-S-H (Fig. 3.6) (Powers, 1958). No obstante, durante el amasado pueden quedar burbujas de aire que originan poros de mayor tamaño.

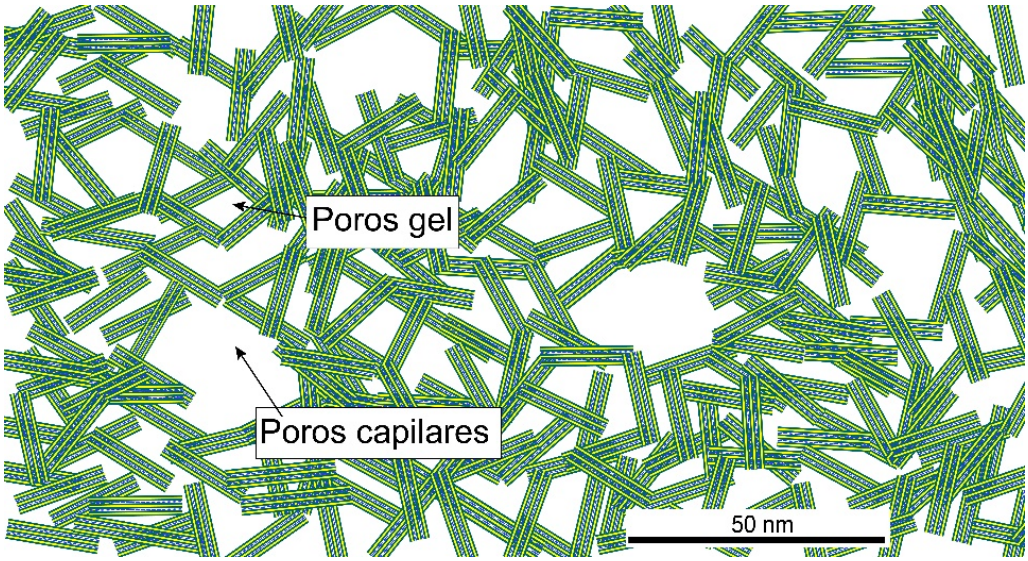

Fig. 3.6. Porosidad propuesta por Powers (1958) en el cemento Pórtland.

Es importante subrayar que no todos los hidratos tienen el mismo crecimiento durante su formación, los C-S-H y la portlandita crecen alrededor de partículas sólidas y detienen su crecimiento en presencia de obstáculos. Por el contrario, la etringita desarrolla una presión de crecimiento sino encuentra poros libres. Este

comportamiento expansivo es de especial relevancia y tiene lugar cuando su formación se produce después del endurecimiento de la pasta pudiendo causar hendiduras y agrietamiento en la matriz del cemento. Este tipo de etringita se denomina *etringita secundaria expansiva* y ha sido objeto de numerosos estudios por sus implicaciones en la durabilidad del material base-cemento (ver sección 3.4. *Durabilidad del cemento Pórtland*).

3.3 SILICATOS DE CALCIO HIDRATADO: C-S-H

Los C-S-H son sin duda las principales fases de unión del cemento (Grangeon et al., 2013; Van Damme et al., 2013) siendo, como ya se ha mencionado, los productos de hidratación mayoritarios y los principales responsables de las propiedades cohesivas del cemento (no obstante, en menor medida también influyen las fases de AFm en la cohesión del material), por lo tanto, el conocimiento de su comportamiento y evolución en el EBS es esencial. Dado que los C-S-H controlan las propiedades mecánicas y químicas del cemento, han sido objeto de estudio durante décadas (Richardson, 2008) sin embargo, su estructura aún no ha sido totalmente resuelta. Se trata de un material altamente complejo y desordenado, de ahí su denominación como gel. La estructura tipo gel considera la presencia de pequeñas partículas individuales unidas por fuerzas superficiales, entendiéndose como una dispersión en la que las interacciones atractivas entre sus elementos son suficientemente fuertes para que todo el sistema desarrolle una estructura de red rígida que bajo pequeñas tensiones se comporta elásticamente (Taylor et al., 1978; Vehmas and Holt, 2016).

Una aproximación relativamente sencilla y asequible que proporciona valiosa información sobre la composición y estructura de los C-S-H es el cálculo de la

relación estructural entre los átomos de calcio y silicio, esto es, la relación Ca/Si (Richardson, 2008; Roosz et al., 2015). Comúnmente se asume que varía de 0.6 a 2.0 de modo que a medida que aumenta esta ratio la estructura va sufriendo modificaciones progresivas en su composición y organización estructural.

Para modelizar la estructura de los C-S-H se ha recurrido a minerales cristalinos de silicato de calcio hidratado cuyo ordenamiento sí es conocido, éste es el caso de la 14Å-tobermorita ($Ca_5Si_6O_{16}(OH)_2 \cdot 4H_2O$) y la jenita ($Ca_9Si_6O_{18}(OH)_6 \cdot 8H_2O$) con relaciones Ca/Si de 0.66 y 1.33. Ambos han probado ser de gran utilidad para aproximar la estructura de los C-S-H, donde a medida que aumenta el contenido en Ca se incrementa la presencia de defectos estructurales.

Las tobermoritas se disponen en capas 2:1 de nanómetros de espesor. La capa interior está formada por un doble plano de iones de Ca^{2+} coordinados con 6 o 7 iones de O_2^{2-} generando octaedros de CaO, a los cuales se acoplan unidades tetraédricas de SiO_4 a ambos lados (Fig. 3.7).

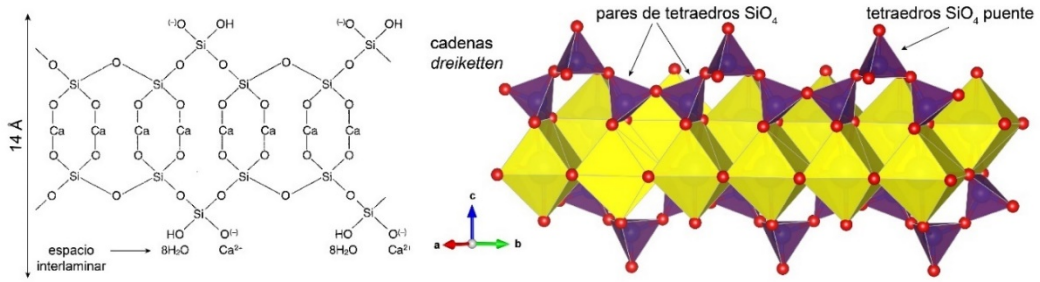

Fig. 3.7. Estructura de un dímero en dos dimensiones de la 14Å-tobermorita y representación tridimensional de las cadenas dreiketten (tetraedros de Si) y octaedros de Ca.

Pese a que numerosas estructuras de C-S-H han sido propuestas, la mayoría se basan en el en el modelo "*dreierkette*" (Richardson, 2004, 2008; Beaudoin and Odler, 2019). Partiendo de la estructura de la tobermorita, las unidades básicas (*bloques de construcción*) consisten en la repetición de pares de tetraedros de Si

unidos a los octaedros de CaO, de forma que éstos comparten dos átomos de oxígeno por tetraedro mediante enlaces iónico-covalentes. A continuación, un tercer tetraedro de Si hace de puente uniendo los pares de tetraedros (unidades dímeras) al disponerse orientados hacia el exterior de la hoja de octaedros de CaO (en el sentido del eje *a*) compartiendo sólo un oxígeno con el CaO quedando uno de los oxígenos libre, de este modo en cada tetraedro puente existe un grupo $Si\text{-}O^-$ que puede protonarse. Por otro lado, también quedan sin enlazar uno de los oxígenos los tetraedros de los bordes de la capa.

Las láminas de los C-S-H se apilan a lo largo de la dirección 001 o eje cristalográfico *c* configurando, al igual que en los minerales de la arcilla, un espacio interlaminar. Para relaciones Ca/Si <0.83 este espacio queda ocupado por una o dos láminas de agua en el caso de la 11Å-tobermorita y 14Å-tobermorita. A partir de ratios Ca/Si >0.83 en el espacio interlaminar se produce un reemplazo de los protones de los tetraedros puente por iones de Ca^{2+}. Esta primera evolución estructural es progresiva y aumenta en función del pH y por tanto la actividad de Ca^{2+} presentes en la porosidad intersticial (Taylor, 1986).

Cuando la relación Ca/Si alcanza el valor de 1, las cadenas de silicatos (*cadenas dreierketten*) comienzan a perder los tetraedros puente, de modo que por cada tetraedro puente ausente se forma un grupo adicional de Si-OH y Ca-OH. Igualmente, si la concentración de Ca^{2+} sigue aumentando el número de tetraedros puente perdidos también aumenta, lo que se traduce en un menor grado de polimerización de las cadenas hasta formar en el caso más extremo las unidades dímeras, además cabe destacar que se establece una relación lineal negativa entre la ratio Ca/Si y la longitud de la cadena. En este rango Ca/Si de 1, el C-S-H puede

considerarse como una solución sólida de tobermorita-jenita (Taylor, 1993; Van Damme and Gmira, 2006).

Cuando la relación Ca/Si alcanza valores próximos a 1.33, el modelo propuesto para para definir la estructura de los C-S-H se ajusta mejor a la configuración de la jenita. Mientras que en la tobermorita todos los átomos de oxígeno presentes en la capa de los poliedros de CaO están compartidos con los tetraedros de Si o los poliedros de CaO adyacentes, en la jenita solo la mitad de los oxígenos son compartidos mientras que la otra mitad forman grupos Ca-OH (Fig. 3.8) (Taylor, 1986; Bonaccorsi et al., 2004).

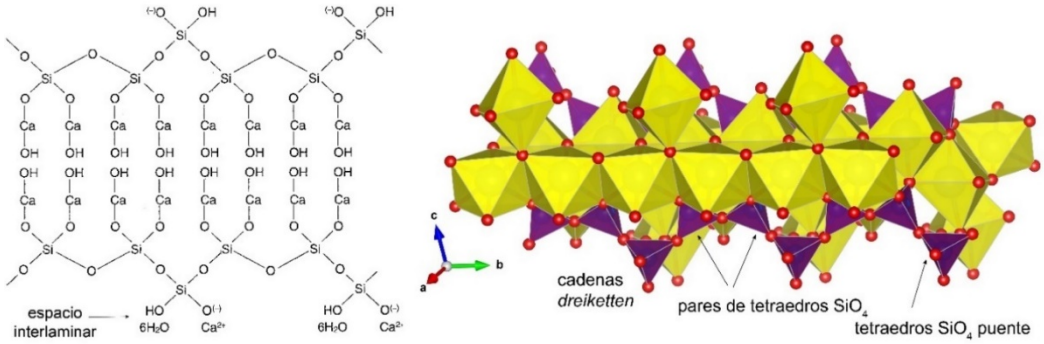

Fig. 3.8. Estructura dimérica en dos dimensiones y representación tridimensional de la jenita.

En cuanto a las propiedades superficiales, los C-S-H contienen grupos ≡Si-OH que evolucionan a medida que aumenta el pH (y por tanto también la concentración de Ca^{2+}) para desprotonarse y formar grupos ≡Si-O cuando se sobrepasa el punto cero de carga (PZC), de este modo se forman partículas coloidales cargadas negativamente. Sin embargo, la alta afinidad del Ca^{2+} por los grupos ≡Si-O^- lleva a la formación de nuevos grupos superficiales en la secuencia SiOH, SiO^- (cuando la ratio Ca/Si <0.83) y $SiOCa^+$, SiOCaOH (cuando la ratio Ca/Si >1.2-1.3) donde parte de la carga superficial se torna positiva.

Un aspecto importante en los C-S-H es que pueden incorporar otros iones entre los que destacan el Al, éste forma silicatos de calcio y aluminio hidratados (C-A-S-H) (Richardson and Groves, 1993; Taylor, 1997b; L'Hôpital et al., 2015) y su incorporación se puede producir en diferentes posiciones de los C-S-H: en la superficie, en la interlámina y sustituyendo al Si^{4+} presente en los tetraedros puente de las cadenas dreierketten, donde la carga negativa en exceso resultante de la sustitución isomórfica podría ser compensada por un catión monovalente.

Por otro lado, iones de K^{+} podrían quedar adsorbidos en la superficie o en la interlámina sustituyendo al Ca^{2+} lo que finalmente incrementaría la caga negativa de las superficies más externas.

En cuanto a los niveles de organización de los C-S-H, los denominados modelos dreierketten (Richardson, 2008) abordan las propiedades nanoestructurares a escala atómica y molecular. Sin embargo, para explicar la organización en niveles superiores se ha recurrido al uso de modelos coloidales. El estudio de la organización micro y mesoestructural de los C-S-H es aún más compleja y sigue siendo una cuestión en revisión, investigaciones con microscopía de transmisión electrónica de alta resolución (HRTEM) han señalado la falta de coherencia de los C-S-H a nivel local (Viehland et al., 1996; Gatty et al., 2001). Por otro lado, estudios mediante microscopia de fuerza atómica (AFM) (Nonat, 2004) (Fig. 3.9) muestran la formación de coloides globulares de dimensiones nanométricas donde cada uno de estos agregados consistiría en el apilamiento de unas pocas láminas de C-S-H. Sin embargo, estos estudios no se han realizado sobre matrices de cemento reales y para ser abordados directamente sobre el material real en cuestión, los modelos coloidales han recurrido al uso de determinaciones indirectas como la porosidad, densidad y SSA.

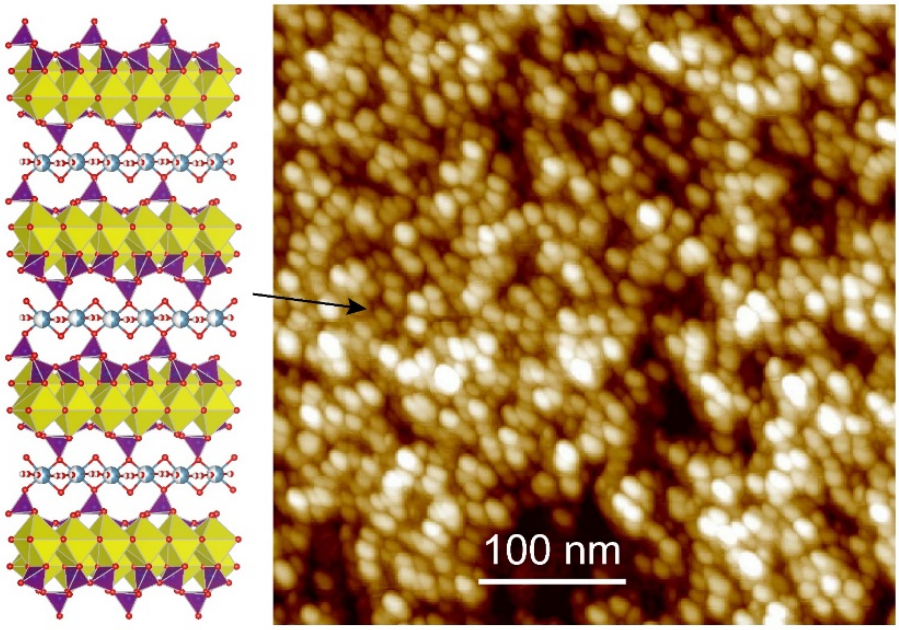

Fig. 3.9. Estructura e imagen tomada mediante microscopia de fuerza atómica (AFM), dónde se muestran láminas de C-S-H con apariencia pseudoesférica. Figura modificada de Nonat (2004).

Entre los distintos modelos propuestos destaca el modelo coloidal-capa Feldman-Sereda (Feldman and Sereda, 1970). Este modelo, resumido en la Figura 3.10a, muestra los tipos de agua interlaminar adsorbida en la micro y mesoestructura de los C-S-H, donde se puede observar su característico desorden.

Posteriormente, el modelo de Feldman-Sereda se ha ido complementando con otros modelos entre los que destacan los *modelos coloidales I* y *II* (*coloidal models I* y *II*, CM-I y CM-II) o también conocidos como *modelos de Jennings.*

El CM-I incorpora la existencia de agregados de C-S-H de baja densidad con poros de 4 a 20 nm de sección, que evolucionan a agregados de alta densidad donde los poros disminuyen a diámetros de 1-4 nm (Fig. 3.10b). Este modelo presenta unidades básicas globulares de 5 nm correspondientes a geles C-S-H con una

estructura mixta entre tobermorita y jenita (Jennings, 2000; Thomas and Jennings, 2006).

Mientras que el CM-I estuvo basado en el estudio a partir de isotermas de absorción con N_2, más tarde este fue refinado por Jennings (2008) mediante el estudio de las isotermas de adsorción de agua, proponiendo el CM-II, modelo más avanzado hasta la fecha (Beaudoin and Odler, 2019). El CM-II define la localización de las moléculas de agua y su unión con la estructura, éste sigue considerando la existencia de C-S-H de baja y alta densidad, pero muestra diferencias en la organización, de modo que capas pseudoparalelas de C-S-H se distribuyen en una red partículas prismáticas de ~5 nm agrupadas en agregados. En un nivel estructural superior, éstos conforman flóculos globulares de 30-60 nm (Fig. 3.10c). Cada asociación de capas de C-S-H (que correspondería al nivel de partícula explicado en la sección niveles de organización en las esmectitas) contiene una monocapa de agua externa y capas de aguas en su interior. Además, el modelo define tres porosidades: intrapartícula, IGP (<1 nm); interpartícula, SGP (1-3 nm) e interagregado LPG (3-12 nm).

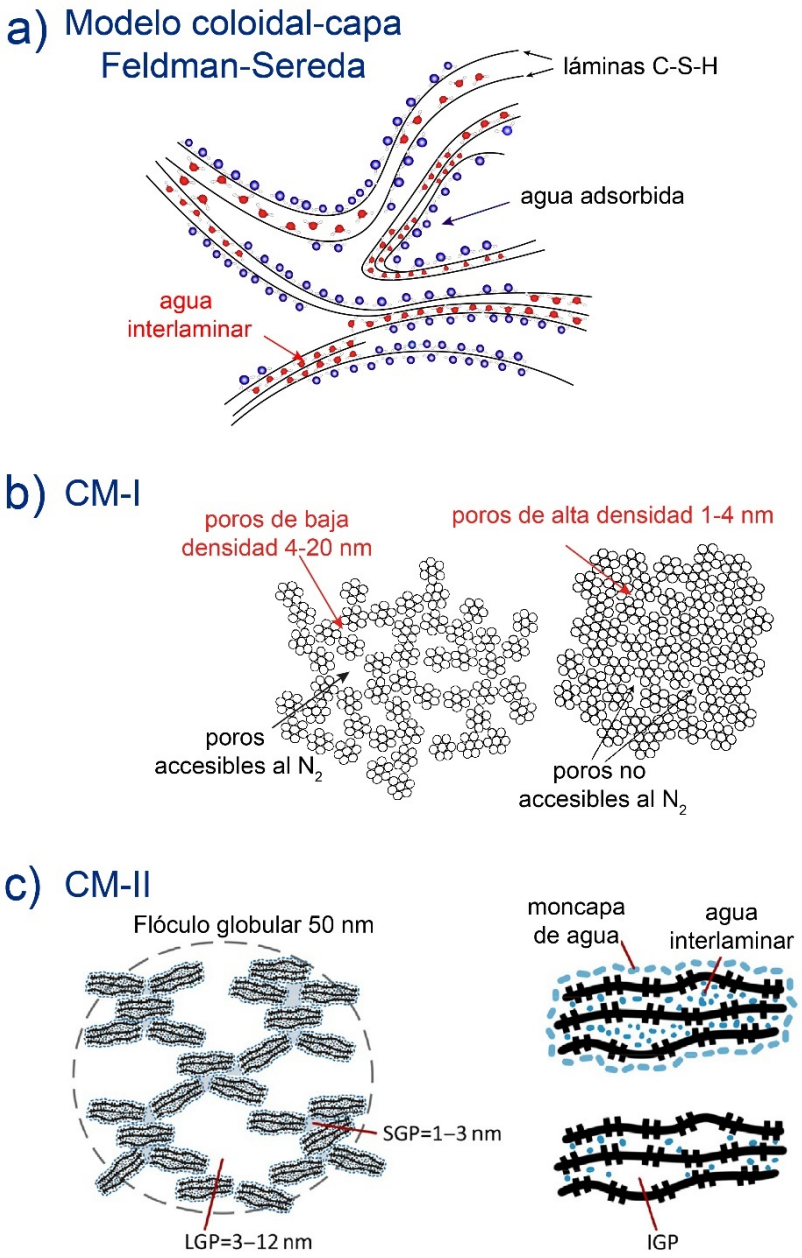

Fig. 3.10. Modelos coloidales propuestos para el estudio de la micro y mesoestructura de los geles C-S-H. a) Representación del modelo propuesto por Feldman-Sereda. b) Modelo coloidal I (CM-I) (imagen modificada de (Jennings, 2000)). c) Modelo coloidal II (CM-II) (imagen modificada de Jennings (2008)). SGP: poros interglobulares, LGP: poros interagregado, IGP: poros intraglobulares.

3.4 DURABILIDAD DEL CEMENTO PÓRTLAND

Los materiales base cemento son extremadamente resistentes incluso bajo condiciones adversas, un ejemplo son los bloques de hormigón levantados en tiempos del imperio romano, donde las construcciones han quedado sumergidas bajo aguas marinas durante 2000 años manteniendo sus propiedades (Jackson et al., 2013). Sin embargo, si la formulación del material de cemento no es la adecuada al entorno dónde va a ser emplazado éste corre el riesgo de deteriorarse y perder su funcionalidad.

Aunque la velocidad de degradación del cemento es muy baja, dentro del EBS es necesario mantener sus propiedades durante largos periodos de tiempo por lo que seleccionar cuidadosamente la formulación del material de base cemento es esencial. Su diseño para una vida mínima especificada requiere del conocimiento de los procesos que causan su deterioro. Para un AGP construido en granito, las principales zonas de degradación del cemento serán las superficies expuestas a las aguas subterráneas, así como aquellas zonas en contacto con la bentonita. Esta degradación del cemento tiene su origen en la movilización de las especies solubles presentes en el agua de poro en equilibrio con las fases sólidas del cemento. Entre la composición de las aguas subterráneas y el agua de poro característica de la bentonita existe un gradiente químico que ocasiona un transporte por difusión de las especies iónicas, de modo que la composición del agua intersticial del cemento se ve modificada y, por tanto, la superficie sólida del cemento también se altera al reequilibrarse con la composición química del agua de poro. A continuación, se destacan los principales procesos que tienen la capacidad de deteriorar el cemento Pórtland en el sistema planteado: aguas subterráneas-hormigón-bentonita *e.j*. (Rozière et al., 2009; Alonso et al., 2017).

3.4.1 Lixiviación

Como ya se ha introducido, las fases sólidas del cemento Pórtland se equilibran con la fase acuosa determinando su composición química. En un estado inicial el agua de poro está parcialmente saturada por álcalis (Na^+, K^+), Ca^{2+}, y OH^-, responsables de los altos valores de pH (~13) (Fig. 3.11a). Sin embargo, si el cemento entra en contacto con un flujo de agua externo de diferente composición química y pH, el agua intersticial presente en su porosidad se verá alterada de modo que esta última cambiará en busca de equilibrarse con la disolución exterior y del mismo modo los minerales de la fase sólida se reequilibrarán con la solución porosa. Así, durante la interacción y el equilibrio con las aguas circundantes, los cambios creados en la composición química de la solución de los poros darían lugar la modificación de la pasta del cemento, como se ha indicado en el apartado anterior, llegando en último término a su desintegración (Kari and Puttonen, 2014).

En una descripción detallada del proceso, podemos distinguir cuatro etapas:

i) la pérdida por difusión de los iones Na^+, K^+, Ca^{2+} y OH^- hacia el agua subterránea y la bentonita, disminuyendo así el pH y favoreciendo la continuidad de la disolución de los hidróxidos alcalinos en la fase sólida. *ii*) En la segunda etapa, el pH queda controlado por la portlandita que comienza a disolverse (junto con los C-S-H de elevada relación Ca/Si) liberando Ca^{2+} y grupos OH^-. Una vez consumida la portlandita, entre 12.6 y 10.0, el pH pasa a ser regulado por los C-S-H, los cuales sufren descalcificación parcial liberando Ca^{2+} que degeneran en geles C-S-H de menor relación Ca/Si. Esta etapa también va acompañada por la disolución de las fases de AFm liberando Ca^{2+}, Al^{3+} y SO_4^{2-}. *iii*) Por debajo de valores de pH~10 comienzan a disolverse los aluminatos cálcicos de Al y Fe (Fig.

3.11b) (Berner, 1992; García Calvo, 2012). *iv*) Finalmente, una vez desintegrados la totalidad de los hidratos del cemento, el agua de poro quedaría en equilibrio con la sílice amorfa.

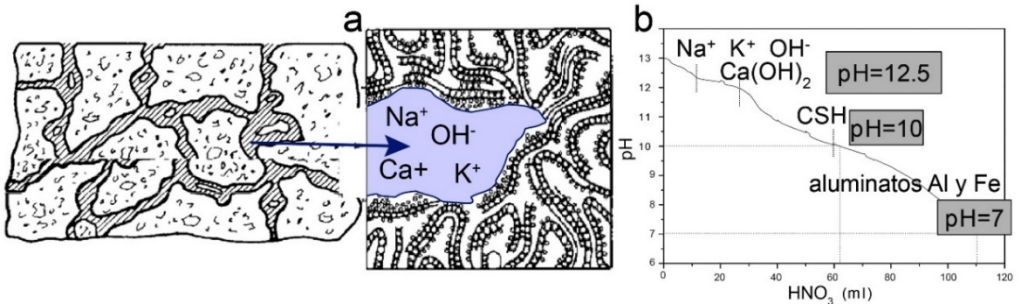

Fig. 3.11. a) Solución porosa presente en el cemento Pórtland. b) Sucesión de las fases minerales a medida que disminuye el pH. Imagen modificada de García Calvo (2012).

En conclusión, en el proceso de lixiviación se produce una pérdida principalmente de Ca conocida como descalcificación, la cual va acompañado de un incremento de la porosidad y permeabilidad que aceleran la degradación del cemento y producen una pérdida de su resistencia mecánica.

3.4.2 Carbonatación

El carbono disuelto presente en las aguas subterráneas y en el agua de poro de la bentonita, generalmente se presenta como aniones bicarbonato (HCO_3^-) en condiciones cercanas a la neutralidad (pH 8-9) y carbonato (CO_3^{2-}) en condiciones alcalinas (pH >10.5). Cuando entra en contacto con el cemento el HCO_3^- se difunde en su porosidad desprotonándose debido a las condiciones alcalinas presentes (pH >10) liberando carbonatos (CO_3^{2-}) y protones H^+. Éstos últimos reaccionan con la portlandita y los C-S-H de elevada relación Ca/Si, liberando Ca^{2+} al medio poroso donde en presencia de grupos OH^- y CO_3^{2-} promueven la precipitación de $CaCO_3$ (Fig. 3.12), mientras que los C-S-H sufren un proceso de

disolución incongruente que contribuye a la formación de los geles C-S-H de menor relación Ca/Si (*eq.* 5-8).

$$HCO_3^- + H^+ \leftrightarrows 2H^+ + CO_3^{2-} \quad \text{eq. 5}$$

$$Ca(OH)_2 + 2H^+ \leftrightarrows Ca^{2+} + 2OH^- \quad \text{eq. 6}$$

$$CO_3^{2-} + Ca^{2+} \leftrightarrows CaCO_3 \quad \text{eq. 7}$$

$$*C\text{-}S\text{-}H + CO_3^{2-} \leftrightarrows **C\text{-}S\text{-}H + CaCO_3 + 2H^+ \quad \text{eq. 8}$$

*(*relación Ca/Si ~1.6. ** relación Ca/Si ~1.2-0.7)*

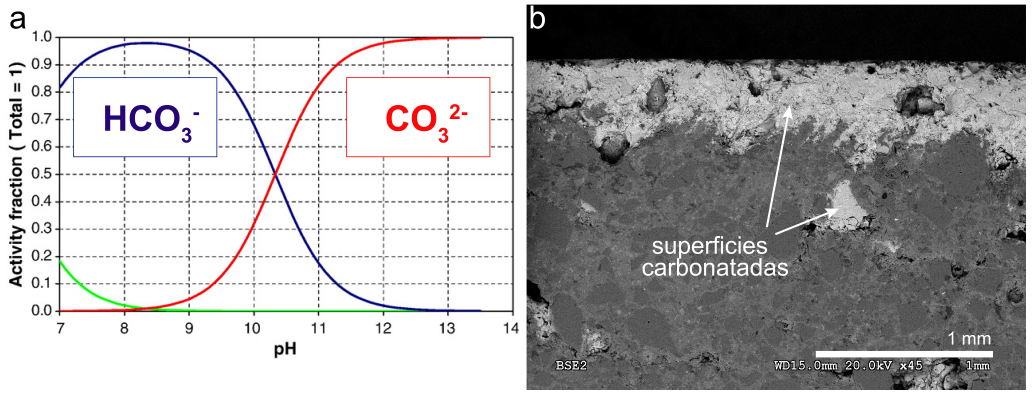

Fig. 3.12. a) Especiación del carbono en función del pH. b) Imagen SEM de un mortero carbonatado obtenida durante el estudio de los materiales de la presente tesis.

Por otro lado, la carbonatación tiene efectos positivos desde el punto de vista de la durabilidad del material base cemento. La precipitación del $CaCO_3$ resulta en una reducción de la porosidad del material y favorece la formación de una capa protectora en la superficie del material *e.j.* (Taylor, 1997b; Glasser et al., 2008; Jenni et al., 2014) evitando la entrada de iones reactivos tales como SO_4^{2-}, Cl^-, Mg^{2+}, H^+ procedentes del medio externo.

3.4.3 Degradación por sulfatos

Los sulfatos están presentes en el agua de poro de las arcillas, así como en aguas subterráneas. Además, el propio material de cemento puede contener una fuente extra de SO_4^{2-} si se han utilizado durante su elaboración áridos contaminados con azufre. Los iones SO_4^{2-} reaccionan con las especies iónicas de la solución porosa (*e.j.* Na^+, Ca^{2+}, Mg^{2+}, Cl^-) precipitando como yeso y *etringita secundaria expansiva*. Si la reacción se produce a bajas temperaturas (<15ºC) puede precipitar taumasita ($Ca_3[Si(OH)_6\text{-}12H_2O]\text{-}(CO_3)\text{-}SO_4$) (Glasser et al., 2008). La formación de estas fases induce un aumento de volumen ejerciendo una presión extra en el material base cemento. A 25°C, la etringita presenta un amplio intervalo de estabilidad (Damidot and Glasser, 1993), de modo que durante un ataque por sulfatos es uno de los minerales que mayormente precipitan. Se denomina etringita secundaria para diferenciarla de la *etringita primaria* formada durante la primera fase de hidratación del cemento Pórtland y que no genera un aumento de volumen que pudiera comprometer las prestaciones del cemento (sección 3.2). El mecanismo principal de formación de esta etringita secundaria comienza con la reacción entre la portlandita y el SO_4^{2-}, formando yeso secundario (también con cierto comportamiento expansivo). A partir de éste, en una zona próxima a donde se está descalcificando la portlandita y por tanto con alto contenido en Ca^{2+}, se forma etringita secundaria (*eq.* 9-10) caracterizada por precipitar súbitamente, lo que origina cristales de pequeño tamaño y aspecto masivo con volúmenes molares de entre 3 y 8 veces superiores a los iniciales. Como consecuencia de esta expansión se producen las grandes presiones de cristalización ya mencionadas que desarrollan tensiones elevadas y la consecuente formación de agrietamientos y pérdida de propiedades del cemento Pórtland (Duval and Hornain, 1992; Irassar et al., 2003). No obstante, cabe destacar que no siempre la formación de etringita

secundaria conlleva el fenómeno de expansión, debido a que parte de esta precipita rellenando el espacio poroso presente, este es el caso de la etringita secundaria no expansiva. La Figura 3.13 muestra la morfología de una etringita secundaria expansiva y una etringita secundaria no expansiva.

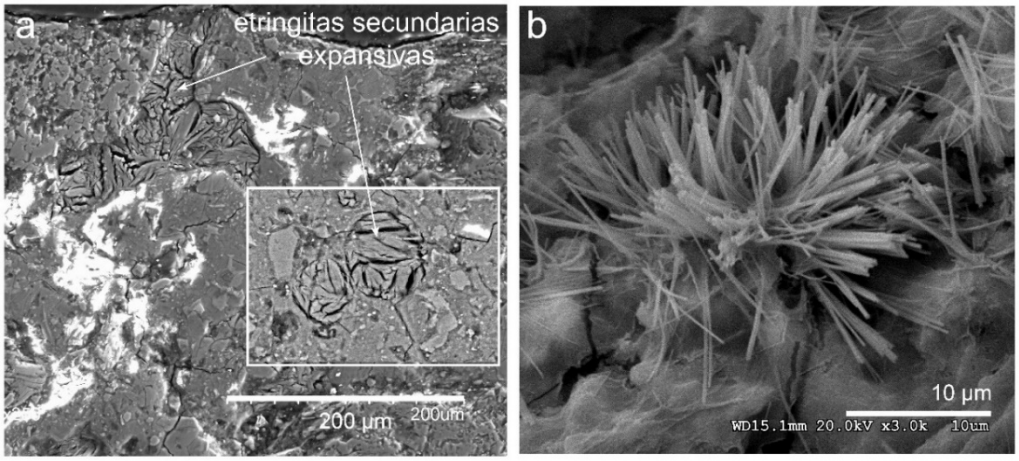

Fig. 3.13. Micrografía SEM de distintos tipos de etringitas. a) Etringita secundaria expansiva (imagen modificada de Alonso et al. (2017). b) Etringita secundaria no expansiva (imagen obtenida durante los análisis de los materiales de la presente tesis).

$$Ca(OH)_2 + Na_2SO_4 + 2H_2O \leftrightarrows CaSO_4 \cdot 2H_2O + NaOH \quad \text{eq. 9}$$

(disolución de portlandita por reacción con sulfato sódico)

$$C_4A\underline{S}H_{12} + 2Ca^{2+} + 2SO_4^{2-} + 20H_2O \leftrightarrows C_6A\underline{S}_3H_{32} \quad \text{eq. 10}$$

(formación de etringita a partir de una fase del grupo de los AFm. Los iones SO_4^{2-} son proporcionados por la solución externa, mientras que el Ca^{2+} proviene de la portlandita).

3.4.4 Degradación por iones de Magnesio

El Mg puede aparecer formando sales de cloruro de magnesio o sulfato de magnesio ($MgCl_2$, $MgSO_4$). Concentraciones <3 mol/L de $MgCl_2$ han mostrado afectar al cemento Pórtland produciendo una expansión y un aumento de la salinidad (Taylor, 1997b; Bernard, 2017b, a). El Mg^{2+} reacciona con la portlandita

y provoca la precipitación de brucita y geles M-S-H en un tiempo del orden de meses (Dauzères et al., 2016; Bernard et al., 2018).

En el estudio de cementos Pórtland sumergidos en soluciones de $MgSO_4$ se ha observado la formación de una capa superficial de brucita: $Mg(OH)_2$ y yeso (*eq.* 11-12) (Bonen and Cohen, 1992a, b). El equilibrio de solubilidad de la brucita implica una disminución del pH (<10.5) (Pokrovsky and Schott, 2004) favoreciendo así la pérdida de Ca de los geles C-S-H, la presencia de Ca^{2+} en la solución porosa junto con suficiente concentración de sílice acuosa y Mg^{2+} conduciría a la precipitación de Mg para formar geles M-(C)-S-H, si bien la cantidad de calcio que incorporan es mínima (<10 %). También existe la posibilidad de la unión de iones de Mg^{2+} a los C-S-H (Bonen, 1992), aunque esta incorporación sería minoritaria según las observaciones experimentales de Bernard et al. (2018).

$$Ca(OH)_2 + MgSO_4 \leftrightarrows CaSO_4 + Mg(OH)_2 \qquad eq.\ 10$$

$$C\text{-}S\text{-}H + MgSO_4 \leftrightarrows CaSO_4 \cdot 2H_2O + M\text{-}(C)\text{-}S\text{-}H \qquad eq.\ 11$$

Por último, hay que señalar que estas fases de Mg y Si presentan una estructura de baja cristalinidad similar a las de las arcillas magnésicas del grupo de la serpentina y talco (Gollop and Taylor, 1992; Roosz et al., 2015; Walling and Provis, 2016; Bernard et al., 2017).

3.4.5 Degradación por Cloruros

Uno de los principales mecanismos que causan el deterioro del hormigón es la corrosión causada por el Cl^-. Éste se caracteriza por presentar una rápida difusión a través de la matriz del cemento llegando a alcanzar los refuerzos de acero

presentes en hormigón armado. En contacto con el acero, pese al pasivado protector que se forma por las condiciones de alto pH, se produce su oxidación, lo que conlleva una expansión y agrietamiento del material circundante.

Por otro lado, el Cl^- en contacto con la pasta del cemento conduce a la disolución de la portlandita y los C-S-H (Dauzères et al., 2016). Adicionalmente, cuando interacciona con etringitas o fases de AFm da lugar a la formación principalmente de sal de Friedel ($3CaO \cdot Al_2O_3 \cdot CaCl_2 \cdot 10H_2O$) la cual es estable para un amplio rango de concentraciones de Cl^-, si bien puede formar fases similares donde el Cl^- se une la interlámina de estructuras afines a los AFm $[Ca^{2+}Al(OH^-)2H_2O]^+$ por adsorción (Suryavanshi et al., 1996).

Otros mecanismos de reacción propuestos consisten en el intercambio de iones Cl^- por OH^-, o SO_4^{2-} en el caso de interaccionar con monosulfatos en las posiciones de cambio (*eq*. 13-14; *X*: representa las posiciones de cambio) (Glasser et al., 2008).

$$X\text{-}OH^- + Cl^- \leftrightarrows X\text{-}Cl^- + OH^- \qquad eq.\ 13$$

$$X\text{-}SO_4^{2-} + Cl^- \leftrightarrows X\text{-}Cl^- + SO_4^{2-} \qquad eq.\ 14$$

Por otro lado, los Cl^- presentes en la solución porosa también, aunque en menor medida, pueden unirse a los geles C-S-H por adsorción específica, así como presentarse en una doble capa difusa (Henocq et al., 2006).

3.5 CEMENTOS COMPUESTOS: ADICIONES MINERALES

Cómo se ha introducido, además de los tres componentes esenciales de los materiales base cemento (cemento, agua y áridos), se pueden añadir aditivos y/o

adiciones minerales que mejoran o modifican alguna de sus propiedades, lo que les confiere nuevas prestaciones y funcionalidades, principalmente trabajabilidad, durabilidad y resistencia *e.j.* (García Calvo, 2012; Pérez, 2016). Entre las más utilizadas se encuentran las cenizas volantes, escorias de alto horno, puzolanas naturales, microsílice o SF y caliza. Éstas pueden ser molidas junto al clínker de cemento y el yeso o bien pueden ser añadidas al cemento Pórtland antes de proceder a su mezcla con agua (Taylor, 1997b).

En el contexto del aislamiento de los residuos nucleares, se ha mostrado especial interés por el uso de adiciones minerales de caliza, escorias de alto horno y SF, estos dos últimos con el fin reducir el elevado pH del cemento Pórtland. A continuación se destacan las adiciones de caliza y SF utilizados en los materiales de cemento del presente trabajo.

3.5.1 Humo de sílice

El SF es un subproducto generado durante el proceso de obtención de sílice o aleaciones ferrosilícicas a partir de cuarzo de elevada pureza y carbón. Para ello se reduce el cuarzo en hornos eléctricos a elevadas temperaturas (2000ºC); en esta etapa se liberan moléculas de SiO que se oxidan al entrar en contacto con el aire y precipitan como nano-micropartículas esféricas de sílice amorfa. Esta nano-microsílice posee un diámetro de ~100 nm y alcanza valores de SSA de ~14-25 m^2/g, lo que le confiere una considerable reactividad (también llamada reactividad puzolánica). La incorporación de SF en los materiales base cemento tiene varios efectos; además de la aceleración de la hidratación de las fases del clínker; la sílice se disuelve por el elevado pH e interacciona con la portlandita disminuyendo su contenido en favor de la precipitación de geles C-S-H de baja relación: Ca/Si ~0.9

e.j. (Taylor, 1997b; Mehta and Ashish, 2020), mientras que el pH de la solución porosa disminuye notablemente. Asimismo, la nano-microsílice cambia las propiedades texturales puesto que rellena los espacios vacíos localizados en la en la interfase árido/pasta aumentando la resistencia y reduciendo la permeabilidad del material. Por el contrario, disminuye su trabajabilidad y aumenta considerablemente las necesidades de agua, por lo que en ocasiones es necesario recurrir al uso de aditivos orgánicos (superplastificantes) que aumentan su viscosidad. Por otro lado, también se ha expuesto que el SF podría favorecer la formación de etringita disminuyendo la precipitación de fases AFm (Atkins et al., 1993).

3.5.2 Caliza

La caliza además de $CaCO_3$ presenta de impurezas de SiO_2, Al o Mg. Ésta se añade en forma de nano-micro partículas tras ser finamente triturada (~700 nm de diámetro medio) y por lo general es previamente mezclada y molida con el clínker originando cemento Pórtland tipo CEM-II A-L (Addition Limestone; ver norma UNE-EN 197-1:2011). El pequeño tamaño de partícula le permite actuar como material de relleno entre los granos del clínker de modo que uno de los efectos que produce es la reducción de la porosidad y un aumento de la resistencia a la compresión, pero a diferencia del SF, no disminuye su trabajabilidad. Desde el punto de vista químico el $CaCO_3$ acelera notablemente la hidratación del C_3S y C_3A y lleva a una mayor formación inicial de portlandita y geles C-S-H, todo ello generando unas reacciones notablemente más exotérmicas. Forma monocarboaluminnatos ($CA\underline{C}H_{11}$) que estabilizan las etringitas en detrimento de la formación de fases AFm, lo que se traduce en un incremento mayor del volumen

y disminución de la porosidad (Matschei et al., 2007; Lothenbach et al., 2008), lo cual sería favorable para su aplicación en el AGP.

3.6 REFERENCIAS

- Alonso, M.C., García Calvo, J.L., Cuevas, J., Turrero, M.J., Fernández, R., Torres, E., Ruiz, A.I., 2017. Interaction processes at the concrete-bentonite interface after 13 years of FEBEX-Plug operation. Part I: Concrete alteration. *Physics and Chemistry of the Earth, Parts A/B/C*, 99, pp. 38-48, https://doi.org/10.1016/j.pce.2017.03.008.

- Atkins, M., Lachowski, E.E., Glasser, F.P., 1993. Investigation of solid and aqueous chemistry of lO-year-old Portland cement pastes; with and without silica modifier. 5, pp. 97-102, https://doi.org/10.1680/adcr.1993.5.19.97.

- Beaudoin, J., Odler, I., 2019. *5 - Hydration, Setting and Hardening of Portland Cement*, in: Hewlett, P.C., Liska, M., Lea's Chemistry of Cement and Concrete (Fifth Edition), ed. Butterworth-Heinemann.

- Bernard, E. 2017a. *Magnesium silicate hydrate (MSH) characterization: temperature, calcium, aluminium and alkali*, Doctoral Thesis. Bourgogne Franche-Comté, p. 248, https://www.theses.fr/2017UBFCK025.

- Bernard, E. 2017b. *Magnesium silicate hydrate (MSH) characterization: temperature, calcium, aluminium and alkali* Doctoral Thesis. Bourgogne Franche-Comté, p. 248, https://www.theses.fr/2017UBFCK025.

- Bernard, E., Dauzères, A., Lothenbach, B., 2018. Magnesium and calcium silicate hydrates, Part II: Mg-exchange at the interface “low-pH” cement and magnesium environment studied in a C-S-H and M-S-H model system. *Applied Geochemistry*, 89, pp. 210-218, https://doi.org/10.1016/j.apgeochem.2017.12.006.

- Bernard, E., Lothenbach, B., Rentsch, D., Pochard, I., Dauzères, A., 2017. Formation of magnesium silicate hydrates (M-S-H). *Physics and Chemistry of the Earth, Parts A/B/C*, 99, pp. 142-157, https://doi.org/10.1016/j.pce.2017.02.005.

- Berner, U.R., 1992. Evolution of pore water chemistry during degradation of cement in a radioactive waste repository environment. *Waste Management*, 12, pp. 201-219, https://doi.org/10.1016/0956-053X(92)90049-O.

- Bogner, A., Link, J., Baum, M., Mahlbacher, M., Gil-Diaz, T., Lützenkirchen, J., Sowoidnich, T., Heberling, F., Schäfer, T., Ludwig, H.M., Dehn, F., Müller, H.S., Haist, M., 2020. Early hydration and microstructure formation of Portland cement paste studied by oscillation rheology, isothermal calorimetry, 1H NMR relaxometry, conductance and SAXS. *Cement and Concrete Research*, 130, pp. 105977, https://doi.org/10.1016/j.cemconres.2020.105977.

- Bonaccorsi, E., Merlino, S., Taylor, H.F.W., 2004. The crystal structure of jennite, Ca9Si6O18(OH)6·8H2O. *Cement and Concrete Research*, 34, pp. 1481-1488, https://doi.org/10.1016/j.cemconres.2003.12.033.

- Bonen, D., 1992. Composition and Appearance of Magnesium Silicate Hydrate and Its Relation to Deterioration of Cement-Based Materials. 75, pp. 2904-2906, https://doi.org/10.1111/j.1151-2916.1992.tb05530.x.

- Bonen, D., Cohen, M.D., 1992a. Magnesium sulfate attack on portland cement paste-I. Microstructural analysis. *Cement and Concrete Research*, 22, pp. 169-180, https://doi.org/10.1016/0008-8846(92)90147-N.

- Bonen, D., Cohen, M.D., 1992b. Magnesium sulfate attack on portland cement paste — II. Chemical and mineralogical analyses. *Cement and Concrete Research*, 22, pp. 707-718, https://doi.org/10.1016/0008-8846(92)90023-O.

- Bullard, J.W., Jennings, H.M., Livingston, R.A., Nonat, A., Scherer, G.W., Schweitzer, J.S., Scrivener, K.L., Thomas, J.J., 2011. Mechanisms of cement hydration. *Cement and Concrete Research*, 41, pp. 1208-1223, https://doi.org/10.1016/j.cemconres.2010.09.011.

- Damidot, D., Glasser, F.P., 1993. Thermodynamic investigation of the CaO-Al2O3-CaSO4-H2O system at 25°C and the influence of Na2O. *Cement and Concrete Research*, 23, pp. 221-238, https://doi.org/10.1016/0008-8846(93)90153-Z.

- Dauzères, A., Achiedo, G., Nied, D., Bernard, E., Alahrache, S., Lothenbach, B., 2016. Magnesium perturbation in low-pH concretes placed in clayey environment—solid characterizations and modeling. *Cement and Concrete Research*, 79, pp. 137-150, https://doi.org/10.1016/j.cemconres.2015.09.002.

- Duval, R., Hornain, H., 1992. *Chapitre 9: La durabilité du béton vis-à-vis des eaux agressives*, in, La durabilité des bétons, ed.

- Feldman, R., Sereda, P., 1970. A NEW MODEL FOR HYDRATED PORTLAND CEMENT AND ITS PRACTICAL IMPLICATIONS. *Engineering Journal*, pp., http://web.mit.edu/parmstr/Public/NRCan/rp454.pdf.

- García Calvo, J.L. 2012. *Desarrollo de materiales de construcción con cemento de bajo pH, compatibles con la barrera de ingeniería de un almacenamiento geológico profundo de residuos radiactivos de alta actividad*, Tesis Doctoral. Universidad Autónoma de Madrid, p. 298, http://hdl.handle.net/10486/12309.

- Gatty, L., Bonnamy, S., Feylessoufi, A., Clinard, C., Richard, P., Van Damme, H., 2001. A transmission electron microscopy study of interfaces and matrix homogeneity in ultra-high-performance cement-based materials. *Journal of Materials Science*, 36, pp. 4013-4026, https://doi.org/10.1023/A:1017938725748.

- Glasser, F.P., Marchand, J., Samson, E., 2008. Durability of concrete — Degradation phenomena involving detrimental chemical reactions. *Cement and Concrete Research*, 38, pp. 226-246, https://doi.org/10.1016/j.cemconres.2007.09.015.

- Gollop, R.S., Taylor, H.F.W., 1992. Microstructural and microanalytical studies of sulfate attack. I. Ordinary portland cement paste. *Cement and Concrete Research*, 22, pp. 1027-1038, https://doi.org/10.1016/0008-8846(92)90033-R.

- Grangeon, S., Claret, F., Linard, Y., Chiaberge, C., 2013. X-ray diffraction: a powerful tool to probe and understand the structure of nanocrystalline calcium silicate hydrates. *Acta crystallographica Section B, Structural science, crystal engineering and materials*, 69, pp. 465-473, https://doi.org/10.1107/S2052519213021155.

- Henocq, P., Marchand, J., Samson, E., Lavoie, J.-A., 2006. Modeling of ionic interactions at the C–S–H surface—Application to CsCl and LiCl solutions in comparison with NaCl solutions, in, *2nd Int. Symp. On Advances in Concrete through Science and Engineering, RILEM Proceedings*, ed. RILEM Publications France.

- Irassar, E.F., Bonavetti, V.L., González, M., 2003. Microstructural study of sulfate attack on ordinary and limestone Portland cements at ambient temperature. *Cement and Concrete Research*, 33, pp. 31-41, https://doi.org/10.1016/S0008-8846(02)00914-6.

- Jackson, M.D., Chae, S.R., Mulcahy, S.R., Meral, C., Taylor, R., Li, P., Emwas, A.-H., Moon, J., Yoon, S., Vola, G., Wenk, H.-R., Monteiro, P.J.M., 2013. Unlocking the secrets of Al-tobermorite in Roman seawater concrete†. *American Mineralogist*, 98, pp. 1669-1687, https://10.2138/am.2013.4484

- Jenni, A., Mäder, U., Lerouge, C., Gaboreau, S., Schwyn, B., 2014. In situ interaction between different concretes and Opalinus Clay. *Physics and Chemistry of the Earth, Parts A/B/C*, 70-71, pp. 71-83, https://doi.org/10.1016/j.pce.2013.11.004.

- Jennings, H.M., 2000. A model for the microstructure of calcium silicate hydrate in cement paste. *Cement and Concrete Research*, 30, pp. 101-116, https://doi.org/10.1016/S0008-8846(99)00209-4.

- Jennings, H.M., 2008. Refinements to colloid model of C-S-H in cement: CM-II. *Cement and Concrete Research*, 38, pp. 275-289, https://doi.org/10.1016/j.cemconres.2007.10.006.

- Kari, O.P., Puttonen, J., 2014. Simulation of concrete deterioration in Finnish rock cavern conditions for final disposal of nuclear waste. *Annals of Nuclear Energy*, 72, pp. 20-30, https://doi.org/10.1016/j.anucene.2014.04.035.

- L'Hôpital, E., Lothenbach, B., Le Saout, G., Kulik, D., Scrivener, K., 2015. Incorporation of aluminium in calcium-silicate-hydrates. *Cement and Concrete Research*, 75, pp. 91-103, https://doi.org/10.1016/j.cemconres.2015.04.007.

- Lothenbach, B., Le Saout, G., Gallucci, E., Scrivener, K., 2008. Influence of limestone on the hydration of Portland cements. *Cement and Concrete Research*, 38, pp. 848-860, https://doi.org/10.1016/j.cemconres.2008.01.002.

- Matschei, T., Lothenbach, B., Glasser, F.P., 2007. The role of calcium carbonate in cement hydration. *Cement and Concrete Research*, 37, pp. 551-558, https://doi.org/10.1016/j.cemconres.2006.10.013.

- Mehta, A., Ashish, D.K., 2020. Silica fume and waste glass in cement concrete production: A review. *Journal of Building Engineering*, 29, pp. 100888, https://doi.org/10.1016/j.jobe.2019.100888.

- Nonat, A., 2004. The structure and stoichiometry of C-S-H. *Cement and Concrete Research*, 34, pp. 1521-1528, https://doi.org/10.1016/j.cemconres.2004.04.035.

- Pérez, Á.F. 2016. *Mezclas ternarias en el desarrollo de materiales base cemento con un bajo impacto ambiental*, Tesis Doctoral. Universidad Autónoma de Madrid, p. 237, https://repositorio.uam.es/handle/10486/677071.

- Pokrovsky, O.S., Schott, J., 2004. Experimental study of brucite dissolution and precipitation in aqueous solutions: surface speciation and chemical affinity control.

Geochimica et Cosmochimica Acta, 68, pp. 31-45, https://doi.org/10.1016/S0016-7037(03)00238-2.

- Powers, T.C., 1958. Structure and Physical Properties of Hardened Portland Cement Paste. 41, pp. 1-6, https://doi.org/10.1111/j.1151-2916.1958.tb13494.x.

- Rahimi-Aghdam, S., Bažant, Z.P., Abdolhosseini Qomi, M.J., 2017. Cement hydration from hours to centuries controlled by diffusion through barrier shells of C-S-H. *Journal of the Mechanics and Physics of Solids*, 99, pp. 211-224, https://doi.org/10.1016/j.jmps.2016.10.010.

- Richardson, I.G., 2004. Tobermorite/jennite- and tobermorite/calcium hydroxide-based models for the structure of C-S-H: applicability to hardened pastes of tricalcium silicate, β-dicalcium silicate, Portland cement, and blends of Portland cement with blast-furnace slag, metakaolin, or silica fume. *Cement and Concrete Research*, 34, pp. 1733-1777, https://doi.org/10.1016/j.cemconres.2004.05.034.

- Richardson, I.G., 2008. The calcium silicate hydrates. *Cement and Concrete Research*, 38, pp. 137-158, https://doi.org/10.1016/j.cemconres.2007.11.005.

- Richardson, I.G., Groves, G.W., 1993. The incorporation of minor and trace elements into calcium silicate hydrate (C-S-H) gel in hardened cement pastes. *Cement and Concrete Research*, 23, pp. 131-138, https://doi.org/10.1016/0008-8846(93)90143-W.

- Roosz, C., Grangeon, S., Blanc, P., Montouillout, V., Lothenbach, B., Henocq, P., Giffaut, E., Vieillard, P., Gaboreau, S., 2015. Crystal structure of magnesium silicate hydrates (M-S-H): The relation with 2:1 Mg–Si phyllosilicates. *Cement and Concrete Research*, 73, pp. 228-237, https://doi.org/10.1016/j.cemconres.2015.03.014.

- Rozière, E., Loukili, A., El Hachem, R., Grondin, F., 2009. Durability of concrete exposed to leaching and external sulphate attacks. *Cement and Concrete Research*, 39, pp. 1188-1198, https://doi.org/10.1016/j.cemconres.2009.07.021.

- Suryavanshi, A.K., Scantlebury, J.D., Lyon, S.B., 1996. Mechanism of Friedel's salt formation in cements rich in tri-calcium aluminate. *Cement and Concrete Research*, 26, pp. 717-727, https://doi.org/10.1016/S0008-8846(96)85009-5.

- Taylor, H.F., 1997a. *Cement chemistry*, ed. Thomas Telford.

- Taylor, H.F., Rossi, F.R., Fernández, J., Montemayor, M., 1978. *La química de los cementos*, ed. Urmo.

- Taylor, H.F.W., 1986. Proposed Structure for Calcium Silicate Hydrate Gel. 69, pp. 464-467, https://10.1111/j.1151-2916.1986.tb07446.x.

- Taylor, H.F.W., 1993. A discussion of the papers "Models for the composition and structure of calcium silicate hydrate (C-S-H) gel in hardened tricalcium silicate pastes" and "The incorporation of minor and trace elements into calcium silicate hydrate (C-S-H) gel in hardened cement pastes". *Cement and Concrete Research*, 23, pp. 995-998, https://doi.org/10.1016/0008-8846(93)90056-F.

- Taylor, H.F.W., 1997b. *Cement chemistry*, 2nd edition ed. Thomas Telford London.

- Thomas, J.J., Jennings, H.M., 2006. A colloidal interpretation of chemical aging of the C-S-H gel and its effects on the properties of cement paste. *Cement and Concrete Research*, 36, pp. 30-38, https://doi.org/10.1016/j.cemconres.2004.10.022.

- Van Damme, H., Gmira, A., 2006. *Chapter 13.3 Cement Hydrates*, in: Bergaya, F., Theng, B.K.G., Lagaly, G., Developments in Clay Science, ed. Elsevier.

- Van Damme, H., Pellenq, R.J.M., Ulm, F.J., 2013. *Chapter 14.3 - Cement Hydrates*, in: Bergaya, F., Lagaly, G., Developments in Clay Science, ed. Elsevier.

- Vehmas, T., Holt, E., 2016. Cebama project deliverable D 1.03, WP1 Experimental studies -State of the art literature review. p., https://www.cebama.eu/Content/PublicArea/WP1/D1.03_Draft_PP.pdf.

- Viehland, D., Li, J.-F., Yuan, L.-J., Xu, Z., 1996. Mesostructure of Calcium Silicate Hydrate (C-S-H) Gels in Portland Cement Paste: Short-Range Ordering, Nanocrystallinity, and Local Compositional Order. 79, pp. 1731-1744, https://doi.org/10.1111/j.1151-2916.1996.tb07990.x.

- Walling, S.A., Provis, J.L., 2016. Magnesia-Based Cements: A Journey of 150 Years, and Cements for the Future? *Chemical Reviews*, 116, pp. 4170-4204, https://doi.org/10.1021/acs.chemrev.5b00463.

- Zhu, Z., Xu, W., Chen, H., Tan, Z., 2020. Evolution of microstructures of cement paste via continuous-based hydration model of non-spherical cement particles. *Composites Part B: Engineering*, 185, pp. 107795, https://doi.org/10.1016/j.compositesb.2020.107795.

CAPITULO 4. MATERIALES Y MÉTODOS

4.1. Diseño experimental

4.2. Técnicas analíticas

4.3. Procedimiento de muestreo

4.4. Agua infiltrada

4.5. Bentonita FEBEX

4.6. Tipos de morteros de cemento

4.7. Referencias

El presente capítulo recoge una descripción de la metodología y características de los materiales utilizados complementariamente a los descritos en el capítulo 5 correspondiente a las contribuciones publicadas, no obstante, algunos métodos de la publicación 5.1 fueron mejorados y pueden diferir ligeramente respecto a lo expuesto en este capítulo, ya que se adaptaron estas mejoras en las posteriores publicaciones. En un primer apartado se describe el diseño de los experimentos: materiales utilizados y montaje experimental; a continuación se recogen las técnicas analíticas utilizadas y metodología seguida; y finalmente se presenta la descripción y caracterización inicial del agua subterránea infiltrada, la bentonita FEBEX y los de tipos de morteros de cemento utilizados en el experimento.

4.1 DISEÑO EXPERIMENTAL

Los experimentos fueron diseñados a partir de pequeñas celdas de transporte a las que les era inyectada agua del entorno granítico de Grimsel (Suiza), obtenido en el Sondeo BOADUS operado por científicos del Centro de Investigaciones Energéticas, Medioambientales y Tecnológicas (CIEMAT) en el laboratorio subterráneo del GTS (Grimsel Test Site) (Torres et al., 2019) donde cada celda estaba rellena por una capa de mortero de cemento en contacto con otra capa de bentonita FEBEX compactada. El agua efluente se recogía por el extremo de la bentonita en una jeringuilla y era posteriormente analizada (Fig. 4.1). Se realizaron tres tipos de experimentos que se diferenciaban en el tipo de mortero utilizado, si bien todos incluían la misma variedad de bentonita. Cada uno de estos tipos de experimento fue duplicado y a su vez testado en dos periodos de tiempo: 6 y 18 meses, de modo que el número total de celdas de transporte preparadas fue de 12 (3 tipos experimentales ×2 dúplicas por cada tipo de experimento ×2 intervalos de tiempo) (Fig. 4.1).

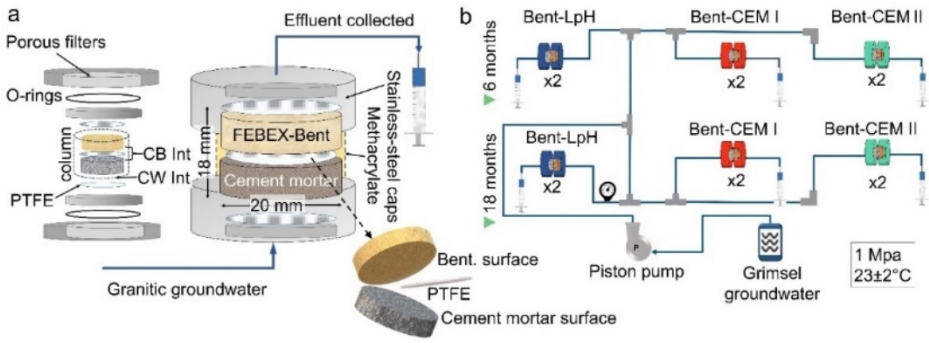

Fig. 4.1. Diseño experimental. (a) Celda de transporte (b) y esquema del montaje experimental. PTFE: politetrafluoroetileno, CB int: interfase mortero/bentonita, CW int: interfase mortero/agua infiltrada. Bent: bentonita.

Los morteros y la bentonita-FEBEX fueron confinados en un cilindro de metacrilato cubierto y sellado por dos piezas de acero inoxidable. La sección interna de las celdas ocupada por el mortero y la bentonita tiene un diámetro de 20 mm mientras que la altura alcanza los 18 mm (9 mm de altura para los morteros y 9 mm para la bentonita-FEBEX). Para conseguir un modelo de celda compacto capaz de resistir la presión de hinchamiento generada por la bentonita-FEBEX a una temperatura de 23ºC, se recurrió al uso de juntas y filtros porosos permitiendo así el paso de agua. Esta era inyectada a una presión de 1 MPa mediante una bomba de pistón (modelo Gilson 307) y conducida a través de tubos fabricados en PEAK. Las interfases generadas entre el mortero y la bentonita, denominadas como CB (cement mortar-bentonite interface) y entre el mortero expuesto al agua infiltrada, denominadas como CW (cement mortar-water interface) fueron separados por membranas de politetrafluoroetileno (PTFE). También fue colocada una membrana sobre la superficie superior de la bentonita-FEBEX. De este modo se facilitaba la posterior separación y diferenciación de los materiales para su análisis, además de evitar el transporte de coloides producidos potencialmente por la dispersión de la bentonita en este extremo.

4.2 TÉCNICAS ANALÍTICAS

- La caracterización del agua recogida a la salida por la cara superior de la bentonita-FEBEX se realizó mediante *i*) el análisis de HCO_3^- y pH por valoración potenciométrica mediante un equipo Metrohm 888™; *ii*) se determinó la sílice disuelta mediante espectrofotometría visible fijando una longitud de onda de 825 nm para la detección del complejo azulado de molibdato amónico utilizando un equipo Milton Roy Spectronic® 1200; *iii*) por último, se midieron las concentraciones del resto de los iones mayoritarios

mediante cromatografía iónica acoplada a un detector de conductividad con un equipo Metrohm 802 compact IC plus. Adicionalmente, la toma de muestras periódica permitió estudiar la evolución de estos parámetros con el tiempo además de la conductividad hidráulica en cada una de las celdas de transporte.

- La caracterización de las fases sólidas implicó las siguientes técnicas analíticas:

i) experimentos de XRD en polvo policristalino para la determinación de la composición mineralógica de los materiales. Complementariamente, para el estudio de la mineralogía superficial presente en las caras enfrentadas separadas por la membrana de PTFE (Fig. 4.1), se realizaron barridos θ-2θ y experimentos de difracción de rayos-X en incidencia rasante (GI-XRD), si bien, estos fueron realizados directamente sobre las muestras sólidas y planas. El estudio de las muestras de polvo de los morteros y la bentonita-FEBEX se realizó en un equipo X'Pert PANalytical con geometría θ-2θ y detector X'Celerator. Los patrones de XRD fueron tomados en el rango angular comprendido entre 3-70° 2θ y en pasos angulares de 0,016° cada 100 segundos. El voltaje e intensidad utilizados por el tubo de rayos X con anticátodo de Cu fue de 45 kV y 40 mA. Los análisis de GI-XRD y barridos θ-2θ fueron realizados con un equipo de incidencia rasante en un ángulo fijo de 0.5º y en la configuración θ-2θ respectivamente, con un paso angular de 0.04º y 2 segundos de registro por paso.

ii) También se llevaron a cabo análisis por SEM-EDX, el propósito de estos análisis fue de obtener un perfil químico desde la interfase CB, analizar zonas puntuales de la pasta de cemento (matriz) comprendida entre los granos de cuarzo, y la composición de los agregados y fases localizadas, si bien, teniendo en cuenta las limitaciones de la técnica. El equipo utilizado

fue un microscopio electrónico de barrido modelo Hitachi S-3000N acoplado a un analizador de energía dispersiva de rayos X INCAx-sight Oxford Instruments™. La composición química por EDX se estableció a partir de patrones estándar internos semicuantitativos.

iii) Por último, se realizaron medidas de SSA por el método BET-N_2 para la medida de las superficies externas accesibles al N_2 (g). Para su determinación se utilizó un porosímetro modelo Gemini V de Micromeritics®.

Los datos obtenidos fueron sometidos a test ANOVA y KrusKal-Wallis para comprobar si estadísticamente hubo diferencias significativas entre los tipos de experimentos y los resultados obtenidos por cada grupo de experimentos, estableciendo un p-valor inferior a 0.05.

4.3 PROCEDIMIENTO DE MUESTREO

Una vez los periodos de 6 y 18 meses concluyeron, se procedió a la apertura de las celdas de transporte y muestreo del mortero y bentonita para su caracterización. Esta división se llevó a cabo mediante un equipo diseñado para el corte de muestras blandas y plásticas marca Well®2000 con hilo de diamante. La columna fue primeramente cortada en dos mitades (Fig. 4.2a, d); una de ellas fue a su vez cortada en dos cuartos (Fig. 4.2d) para realizar los análisis de XRD de muestras en polvo, medida de la SSA y exploración de las superficies (Fig. 4.2b). No obstante, esta mitad fue previamente dividida en 3 submuestras paralelas a la interfase CB situadas entre los 0-3, 3-6 y a 6-9 mm de distancia a ésta, lo que permitió evaluar la evolución de la mineralogía y SSA en función de la distancia. Adicionalmente, las superficies en contacto con las membranas de PTFE

(submuestras B1, C1 y C3) fueron examinadas mediante SEM-EDX para la identificación de agregados minerales.

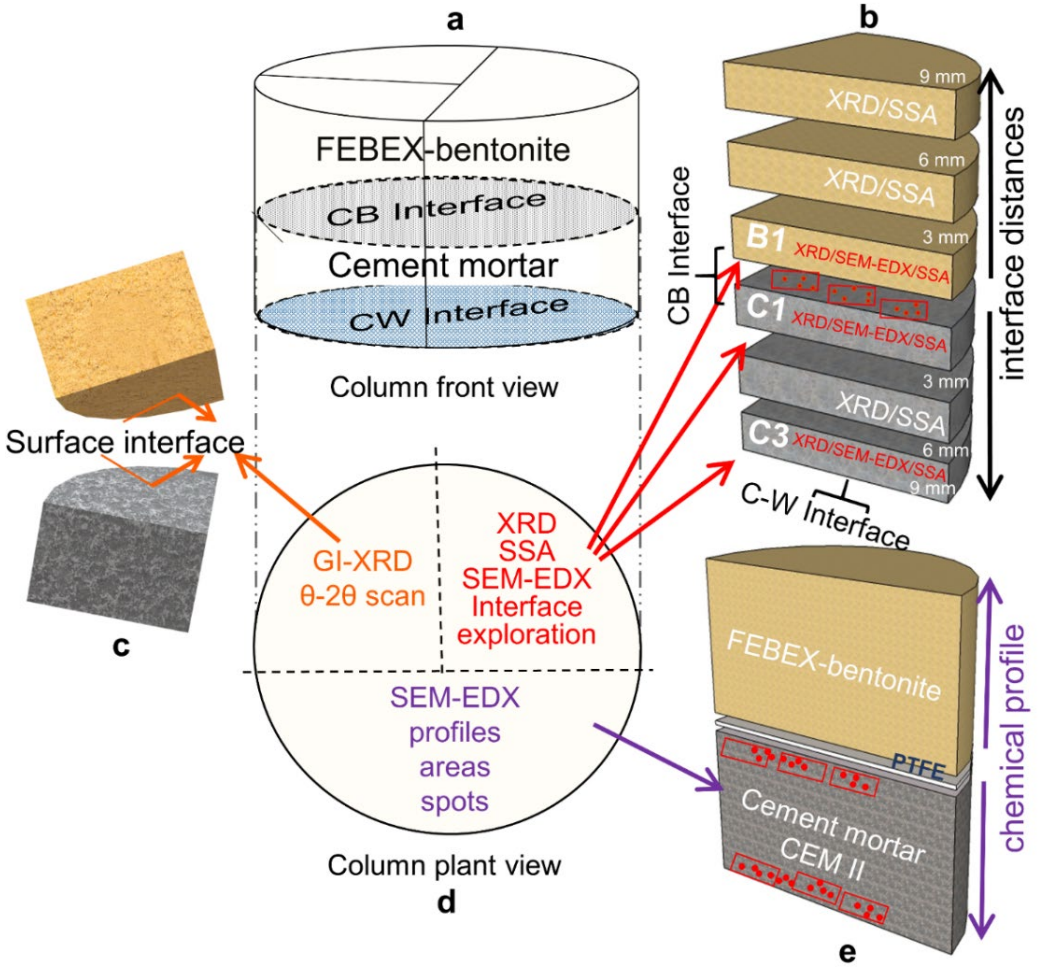

Fig. 4.2. Representación del procedimiento de corte y muestreo. a) vista frontal donde se indican las interfases mortero de cemento/bentonita (CB) en gris y mortero de cemento/agua infiltrada (CW) en azul. b) segmentación de muestras para realizar los análisis de XRD, SSA y la exploración de las superficies enfrentadas en las submuestras B1, C1 y C3. c) cuartos de muestras reservadas para los barridos θ-2θ y de GI-XRD. d) Visión en planta de la columna con los respectivos cortes trazados. e) Mitad de columna cortada para la elaboración mediante SEM-EDX del perfil químico del mortero y bentonita, así como la realización de análisis en las matrices del mortero de cemento próximas a la interfase.

En el otro cuarto (Fig. 4.2c) se realizaron los análisis mineralógicos de las superficies planas en la interfase CB mediante los barridos θ-2θ y de GI-XRD. La mitad inicialmente dividida (Fig. 4.2e), muestra la sección cortada a lo largo del diámetro de la columna que contiene el trayecto desde el mortero a la bentonita, incluyendo la zona de interfase. Este corte se preparó para ser pulido y utilizado para la elaboración mediante SEM-EDX del perfil químico del mortero y la bentonita, así como la realización de análisis en las matrices de cemento próximas a la interfase. Antes de analizarla por SEM-EDX, se realizó una preparación de la muestra; fue sumergida en nitrógeno líquido y secada en condiciones de vacío 10^{-4} Pa, induciendo una liofilización a temperatura ambiente con el fin de evitar la alteración de su estructura. Una vez secadas, fueron embebidas en epoxy-resina (EpoThin®) para conservar aislada la muestra. Finalmente y previamente a su análisis, la superficie fue secuencialmente pulida mediante lijas P200, P400, P600, P800, P1200, P2500 y P4000 de la casa BUEHLER®.

4.4 AGUA INFILTRADA

En los experimentos se utilizó agua subterránea del entorno granítico del GTS. Este agua se caracteriza por presentar un pH de 8.1, valores bajos de conductividad:~104 μS, e iones solubles con la siguiente concentración en mg/L: Cl^- (3.5), SO_4^{2-} (9.6), HCO_3^- (42.7), Na^+ (11.5), K^+ (<0.1), Ca^{2+} (12.0), y Mg^{2+} (<0.1) (Torres et al., 2019).

4.5 BENTONITA-FEBEX

La bentonita utilizada procede del yacimiento del Cortijo de Archidona en el sureste de la Serrata de Níjar, localizada en la región volcánica del Cabo de Gata

(Almería. España) (Fig. 4.3). El origen de esta variedad de bentonita es el resultado de la exposición de las rocas volcánicas a aguas marinas y meteóricas durante los procesos de regresión-transgresión y la alteración del vidrio volcánico por fluidos hidrotermales (Caballero et al., 2005).

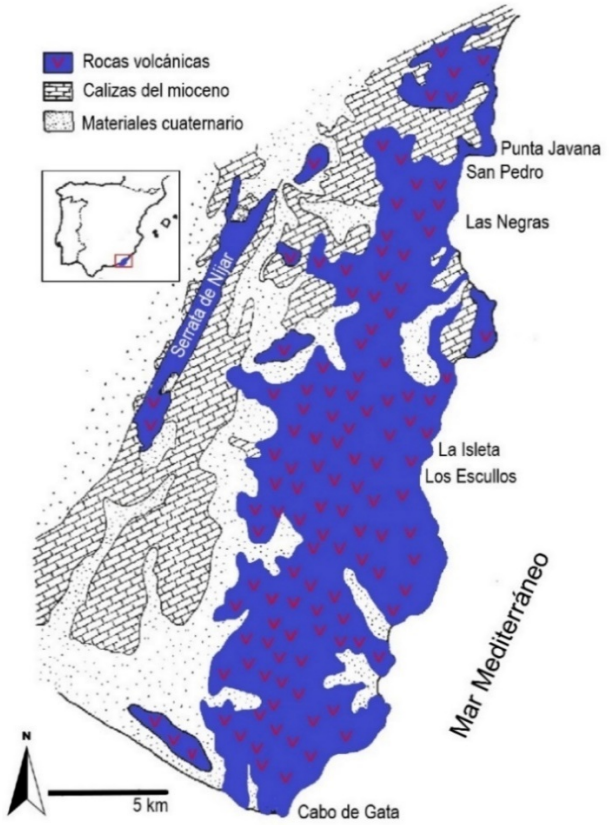

Fig. 4.3. Mapa: modificado de Caballero et al. (1985).

El acrónimo FEBEX (como ya se ha indicado, Full Scale Engineered Barrier EXperiment) fue añadido por ser la bentonita elegida para los experimentos de laboratorio *in-situ* realizados dentro del proyecto FEBEX. De entre los distintos yacimientos de bentonita evaluados se eligió la bentonita del Cabo de Gata puesto que reúne propiedades óptimas tales como el alto contenido en esmectitas y un buen comportamiento frente a la compactación.

La bentonita utilizada en el laboratorio es originalmente extraída de la cantera y posteriormente disgregada por machaqueo, homogenizada y cribada hasta tamaños de partícula inferiores a 5 mm, donde el 85% de los granos poseen un tamaño menor de 75 µm. Desde el punto de vista mineralógico el contenido en esmectitas es superior al 92% siendo de tipo dioctaédrico, principalmente Mnt (ENRESA, 2006). Entre los minerales presentes en la bentonita-FEBEX destacan: cuarzo (2±1%), plagioclasa (3±1%), feldespato potásico (<1%), calcita (<1%) y cristobalita (2±1%). Durante su caracterización mediante SEM-EDX se observó un aspecto homogéneo si bien se detectó la presencia de otros minerales traza, como apatito, biotita, augita, hornblenda o rutilo entre otros, aunque en conjunto éstos suponen menos de un 1% en peso total (Fig. 4.4).

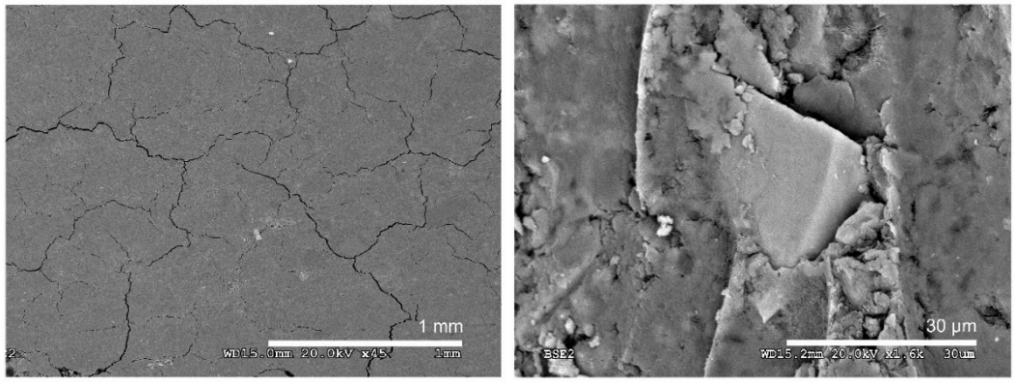

Fig. 4.4. Imágenes de SEM-EDX de la bentonita-FEBEX. De izquierda a derecha, vista general de la bentonita, y mineral traza presente en la matriz de ésta.

La CEC total es de 98-106 meq/100 g y entre los cationes de cambio destacan el Ca^{2+}(35-42 meq/100 g) y el Mg^{2+} (31-32 meq/100 g), y en menor concentración también Na^{+} (24-27 meq/100 g) y K^{+} (2-3 mg/100 g).

La composición química determinada por Villar (2001) se muestra en la Tabla 4.1 mientras que la fórmula estructural determinada para la Mnt presente en la bentonita es: $X_{0.90}[(Al_{2.95}Fe_{0.33}Mg_{0.74}]^{VI}[(Si_{7.78}Al_{0.22}]^{IV}O_{20}(OH)_4$ siendo *X* los

cationes presentes en la interlámina en sus respectivas proporciones (Ca^{2+}, Mg^{2+}, Na^{+} y K^{+}) (Fernández, 2004).

Tabla 4.1. Composición química de la muestra total (en % en peso) (Villar, 2001)

SiO_2	Al_2O_3	Fe_2O_3 tot	MgO	MnO	CaO	Na_2O	K_2O
58.7±1.9	18.0±0.7	3.1±0.1	4.2±0.1	0.04±0.00	1.8±0.1	1.3±0.1	1.1±0.1
TiO_2	P_2O_5	H_2O^-	H_2O^+	CO_2 org	CO_2 inor	SO_2 total	F^-
0.2±0.0	0.02±0.00	6.6±2.5	6.4±0.3	0.4±0.0	0.3±0.1	0.2±0.1	0.2±0.0

Las sales solubles presentes en el agua de poro de la bentonita-FEBEX se muestran en la Tabla 4.2. El pH determinado es de 8.73, la conductividad eléctrica de la disolución obtenida es de ~1135 μS/cm y su fuerza iónica se sitúa en torno a 0.01M.

Tabla 4.2. Sales solubles en el agua de poro, extraída por *squeezing* de la bentonita FEBEX en mg/L (Fernández, 2004).

Cl^-	SO_4^{2-}	HCO_3^-	Na^+	K^+
150	201	154	246	6.1
Mg^{2+}	Ca^{2+}	Sr^{2+}	Fe^{3+}	SiO_2
2.9	4.3	0.1	0.2	19

El resultado obtenido para la SSA externa mediante el método BET-N_2 es de 61±2 m^2/g (Martín Barca, 2002). La densidad aparente (ρ_a) determinada por intrusión de mercurio en muestras compactadas es de 1.60 g/cm3, con poros de tamaños promedio de 0.006 μm que representan el 73-78% del volumen de porosidad total. Por último, la conductividad hidráulica (k) en base a la ecuación $log\ k = -2.96\rho_a - 8.57$ establecida en Espina (2020) para determinar la conductividad hidráulica de una arcilla estaría dentro del orden de 1×10^{-13} m/s para un valor de 1.60 g/cm^3 de densidad aparente.

4.6 TIPOS DE MORTEROS DE CEMENTO

4.6.1 Mortero de cemento de bajo pH

Los morteros de bajo pH (referido en los trabajos publicados como LpH) se prepararon con OPC tipo CEM I 42.5 R SR mezclado con SF (OPC [60 wt.%.] + SF [40 wt.%], siendo wt% el porcentaje en peso) donde ambos materiales fueron suministrados por el Instituto Eduardo Torroja de Ciencias de la Construcción (IETcc). A continuación, a la mezcla se le añadió agua destilada en una relación 0.7 agua:OPC+SF. Finalmente, se añadieron tres partes de arena (99% de cuarzo y tamaño de grano <1 mm) por mezcla OPC+SF+agua.

La composición química del LpH tras un periodo de 90 días hidratación se muestra en la Tabla 4.3.

Tabla 4.3. Composición del mortero de referencia LpH.

% óxidos	media	desviación estándar
Al_2O_3	0.95	0.13
SiO_2	83.23	1.06
SO_3	0.43	0.42
K_2O	0.34	0.13
CaO	14.12	0.99
FeO_{tot}	1.00	0.37

Su composición mineralógica (Fig. 4.5) muestra la ausencia de portlandita, característica de los materiales de cemento de elevado pH, y probable presencia de C-(A)-S-H junto con las fases anhidras características del clínker.

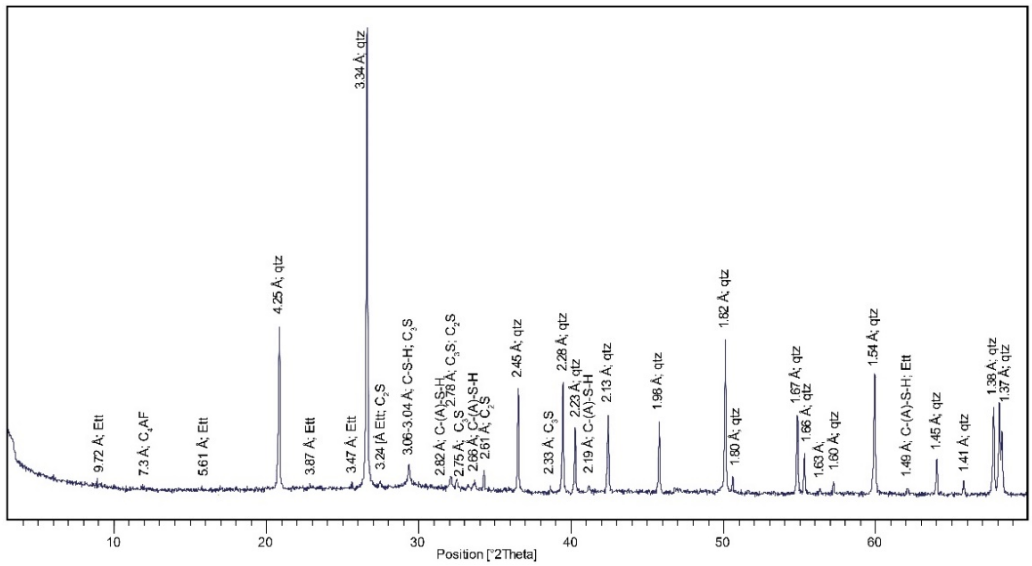

Fig. 4.5. Análisis de difracción de rayos X (XRD) del mortero de cemento de bajo pH (LpH). Ett: etringita. C_4AF: ferro-aluminato tetracálcico. qtz: cuarzo. C_2S: silicato dicálcico. C-S-H: silicato de calcio hidratado. C_3S: silicato tricálcico. C-(A)-S-H: silicato de calcio-(aluminio) hidratado. Los espaciados se muestran en angstroms (Å).

Las relaciones Ca/Si obtenidas mediante SEM-EDX sobre la matriz o pasta del cemento presentaron relaciones Ca/Si de 0.9±0.2 (Fig. 4.6). Además, destacó la presencia etringita entre los poros del material.

En cuanto a la SSA, el LpH presentó un valor de 9.3±0.0 m^2/g. Por último, el pH obtenido, siguiendo el método de lixiviación *ex situ* propuesto por García Calvo (2012) fue de 11.0±0.1.

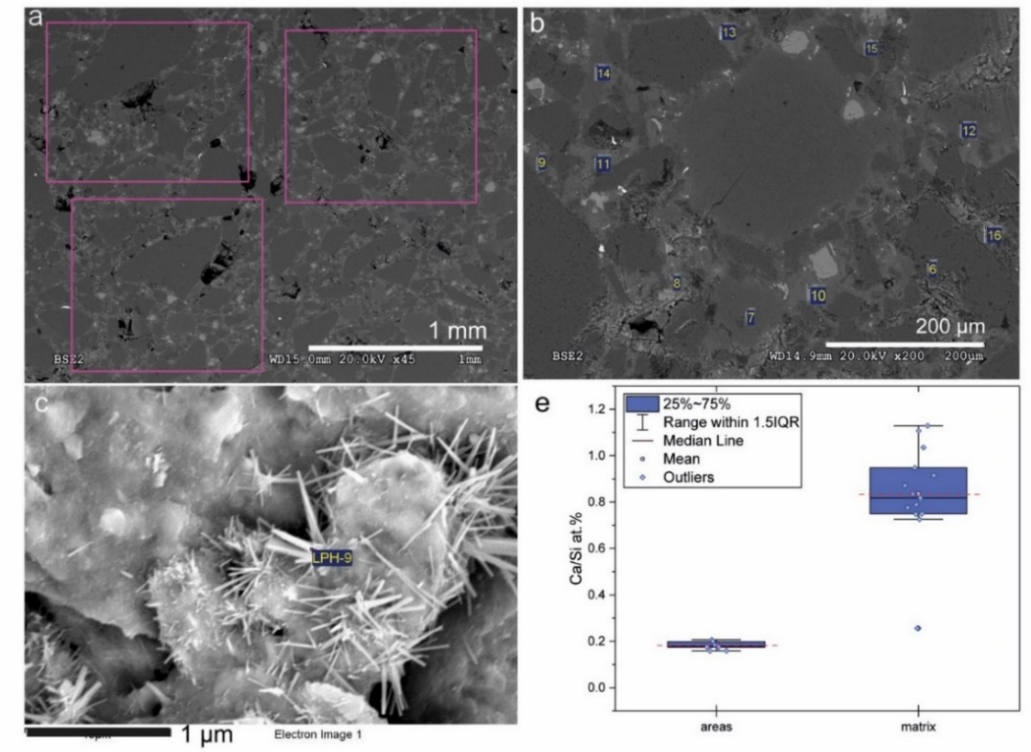

Fig. 4.6. Caracterización inicial del mortero de LpH. (a) Análisis de áreas realizados a 45 aumentos (x45). (b) Micrografía de SEM donde se señalan los análisis de la matriz del cemento realizados a 200 aumentos (x200). (c) Micrografía de una etringita primaria. (e) *Box-plots* elaborados con a partir de los análisis realizados en las áreas (aumentos x45) y matrices del LpH). Los números corresponden a las zonas analizadas.

4.6.2 Mortero de cemento de alto pH: CEM-I

Este tipo de morteros (denominados como CEM-I) fueron elaborados del mismo modo que los morteros de LpH, si bien, no fue añadido SF y se utilizó una relación agua destilada:OPC de 0.42 en lugar de 0.7 debido al mayor requerimiento de agua de los materiales de LpH.

La composición química inicial del CEM-I una vez hidratado se muestra en la Tabla 4.4.

Tabla 4.4. Composición del mortero de referencia CEM-I

% óxidos	media	desviación estándar
MgO	0.1	0.2
Al_2O_3	1.2	0.1
SiO_2	75.8	1.3
SO_3	1.2	0.0
K_2O	0.3	0.1
CaO	20.1	1.6
FeO tot	1.3	0.1

La composición mineralógica muestra la presencia de etringita, portlandita, C-(A)-S-H, y las fases anhidras C_2S, C_3S y C_4AF, sin descartar la presencia de C-S-H desordenados o amorfos (Fig. 4.7).

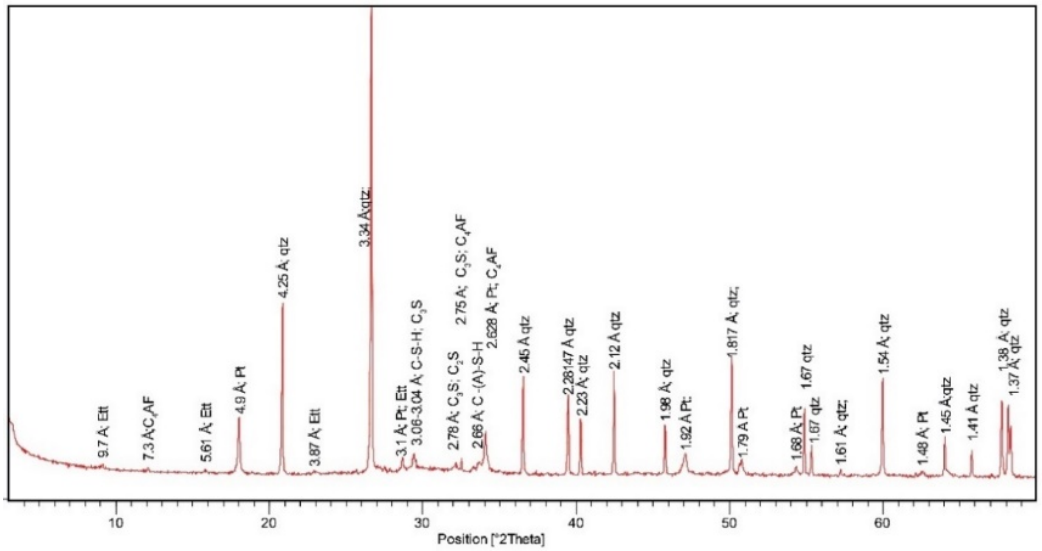

Fig. 4.7. Análisis de difracción de rayos X (XRD) del mortero de cemento de alto pH (CEM-I). C_4AF: ferro-aluminato tetracálcico. Ett: etringita. Pt: portlandita. qtz: cuarzo. C_2S: silicato dicálcico. C-S-H: silicato de calcio hidratado. C_3S: silicato tricálcico. C-(A)-S-H: silicato de calcio-(aluminio) hidratado.

Las relaciones Ca/Si a 200 aumentos correspondientes a la matriz fueron de 1.7±0.2 (Fig. 4.8). Además, se observaron productos de hidratación como etringita y portlandita.

La SSA externa medida fue de 7.8±0.0 m^2/g, mientras que el pH extraído por lixiviación *ex situ* fue de 11.5±0.0.

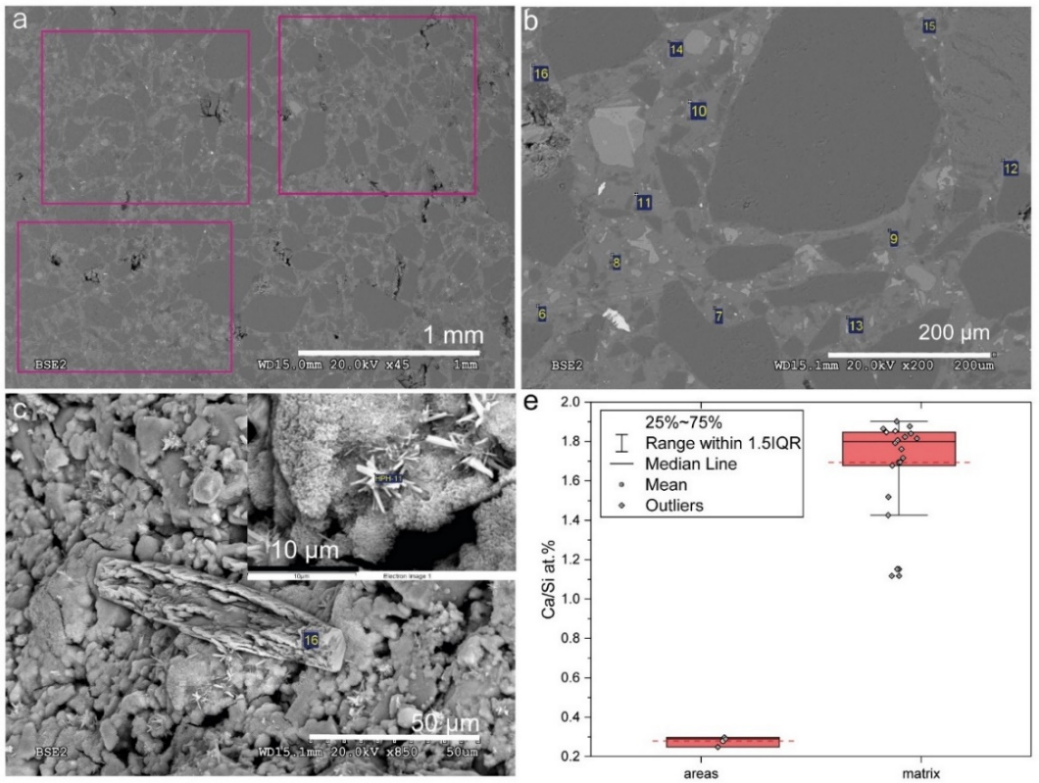

Fig. 4.8. Caracterización inicial del mortero tipo CEM-I. a) Análisis de áreas realizados a 45 aumentos (x45). (b) Micrografía de SEM donde se señalan los análisis de la matriz del cemento realizados a 200 aumentos (x200). (c) Micrografía de etringita primaria (parte superior derecha) y portlandita. (e) *Box-plots* elaborados a partir de los análisis realizados en las áreas y matrices del mortero.

4.6.3 Mortero de cemento de alto pH: CEM-II

Este último tipo de mortero también de elevado pH y aquí denominado como CEM-II se preparó de la misma forma que los morteros CEM-I anteriores, con la diferencia de que se utilizó un OPC tipo CEM II/A-L 42.5 R S proporcionado por la compañía Cementos Portland Valderrivas. Este tipo de cemento Pórtland se caracteriza por presentar adición de caliza, diferenciándose del OPC convencional CEM-I.

La composición química inicial del CEM-II tras los 90 días de hidratación se muestra en la Tabla 4.5.

Tabla 4.5. Composición del mortero de referencia CEM-I

% óxidos	media	desviación estándar
MgO	0,1	0,2
Al_2O_3	1,9	0,3
SiO_2	76,0	1,5
SO_3	1,3	0,6
K_2O	0,5	0,2
CaO	19,7	0,9
FeO_{tot}	0,8	0,1

La composición mineralógica muestra la presencia de calcita, yeso, cuarzo, así como portlandita, etringita y los anhidros heredados del clínker: C_4AF, C_2S y C_3S (Fig. 4.9).

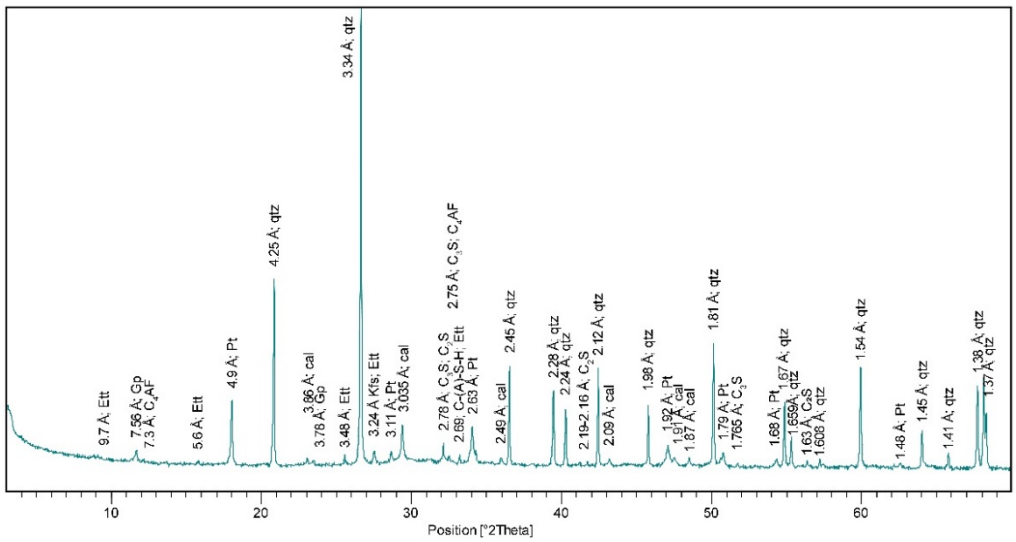

Fig. 4.9. Análisis de difracción de rayos X (XRD) del mortero de cemento basado en CEM-II. Ett: etringita, Gp: yeso, C_4AF: ferro-aluminato tetracálcico, Pt: portlandita, qtz: cuarzo, cal: calcita, Kfs: feldespato potásico, C-(A)-S-H: silicato de calcio-(aluminio) hidratado. C_3S: silicato tricálcico, C_2S: silicato dicálcico. Los espaciados se muestran en angstroms (Å).

Las relaciones Ca/Si a 200 aumentos representando la matriz del mortero fueron de 2.1±0.2 (Fig. 4.10). Como fases características este tipo de mortero destacó por presentar principalmente etringita y AFm.

La SSA obtenida fue de 9.3±0.1 m^2/g, mientras que el pH obtenido por lixiviación *ex situ* fue de12.3±0.1.

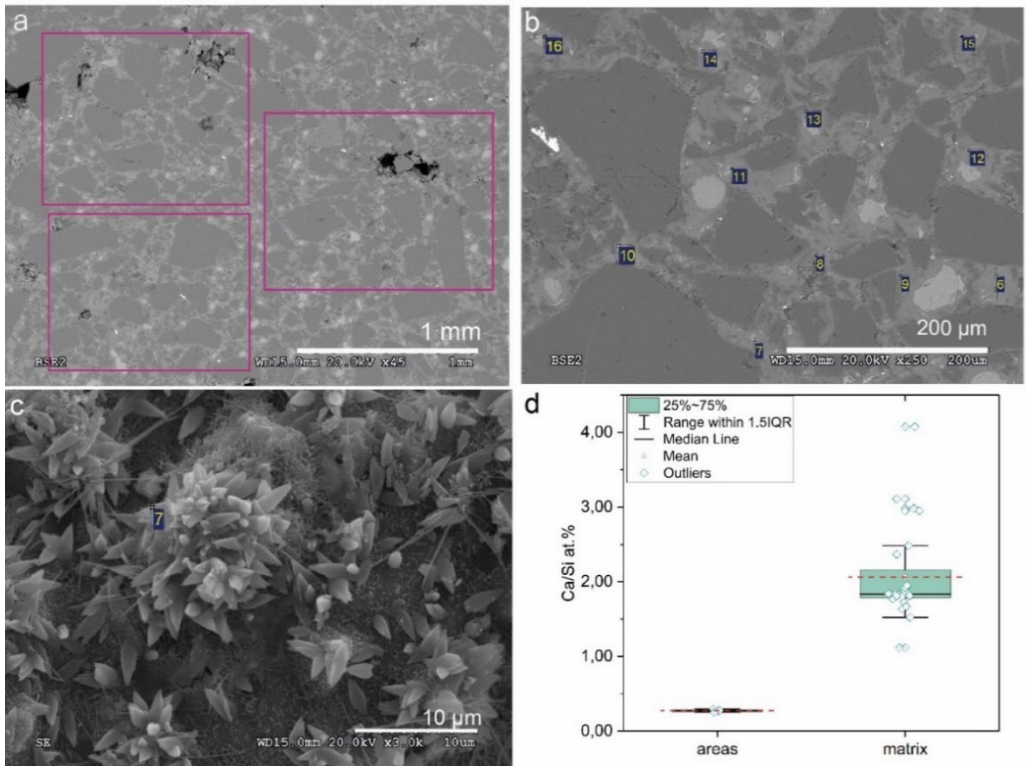

Fig. 4.10. Caracterización inicial del mortero CEM-II a) Análisis de áreas realizados a 45 aumentos. (b) Micrografía de SEM donde se señalan los análisis de la matriz del cemento realizados a 200 aumentos. (c) Micrografía de etringita primaria (parte superior derecha) y portlandita. (d) *Box-plots* elaborados a partir de los análisis realizados en las áreas y matriz.

4.7 REFERENCIAS

- Caballero, E., Jiménez de Cisneros, C., Huertas, F.J., Huertas, F., Pozzuoli, A., Linares, J., 2005. Bentonites from Cabo de Gata, Almería, Spain: a mineralogical and geochemical overview. *Clay Minerals*, 40, pp. 463-480, https://doi.org/10.1180/0009855054040184.

- Caballero, E., Reyes, E., Yusta, A., Puerta, F.J.H., González, J.L., 1985. Las bentonitas de la zona sur de Cabo de Gata (Almería). Geoquímica y Mineralogía. *Acta geológica hispánica*, pp. 267-287.

- ENRESA, 2006. FEBEX Project Final report Post-Mortem Bentonite Analysis. Publicación Técnica 05-1/2006, Madrid. Spain, p. 183.

- Espina, R.G. 2020. *Modificaciones microestructurales, mineralógicas y geoquímicas en bentonitas sometidas a cambios térmicos e hidráulicos*, Tesis Doctoral. Universidad Complutense de Madrid, p. 258, https://eprints.ucm.es/59992/.

- Fernández, A.M. 2004. *Caracterización y modelización del agua intersticial de materiales arcillosos: estudio de la bentonita de Cortijo de Archidona*, Tesis Doctoral. Universidad Autónoma de Madrid, p., http://hdl.handle.net/10486/665484.

- García Calvo, J.L. 2012. *Desarrollo de materiales de construcción con cemento de bajo pH, compatibles con la barrera de ingeniería de un almacenamiento geológico profundo de residuos radiactivos de alta actividad*, Tesis Doctoral. Universidad Autónoma de Madrid, p. 298, http://hdl.handle.net/10486/12309.

- Martín Barca, M. 2002. *Procesos geoquímicos y modificaciones texturales en bentonita FEBEX compactada sometida a un gradiente termohidráulico*, Tesis Doctoral. Universidad Autónoma de Madrid, p. 258, http://hdl.handle.net/10486/672582.

- Torres, E., Turrero, M.J., Garralón, A., Cuevas, J., Fernández, R., Ortega, A., Ruíz, A.I., 2019. Stable isotopes applied to the study of the concrete/bentonite interaction in the FEBEX in situ test. *Applied Geochemistry*, 100, pp. 432-443, https://doi.org/10.1016/j.apgeochem.2018.12.017.

- Villar, M. 2001. *Caracterización termo-hidro-mecánica de una bentonita de Cabo de Gata*, Tesis Doctoral. Universidad Complutense de Madird, p. 336, https://eprints.ucm.es/7289/.

CAPÍTULO 5. PUBLICACIONES

5.1. Low-pH cement mortar-bentonite perturbations in a small-scale pilot laboratory experiment

5.2. Bentonite/CEM-II cement mortar interface experiments: a proxy to in situ deep geological repository engineered barrier system surface reactivity

5.3. High-pH/Low-pH ordinary Portland cement mortars impacts on compacted bentonite surfaces: application to clay barriers performance

Durante la elaboración de la presente tesis doctoral se publicaron secuencialmente 3 artículos de investigación en revistas indexadas en *Journal Citations Reports* (JCR) y clasificadas en los cuartiles Q3, Q2 y Q1 respectivamente.

El presente capítulo incorpora los documentos que fueron aceptados en el formato original en que se enviaron a la revista (*docx*). Complementariamente, en el ANEXO II se pueden consultar las publicaciones aceptadas en su formato original.

El autor de la presente tesis ha llevado a cabo el montaje de los experimentos, caracterización y análisis, elaboración de resultados y figuras, contribución a la discusión y extracto de conclusiones, figurando por ello como primer autor.

Adicionalmente, son referenciadas las publicaciones en las que la tesis ha contribuido directamente, todas ellas en el contexto del proyecto europeo CEBAMA financiador de los experimentos:

- Cuevas, J., Ruiz, A.I., Fernández, R., González-Santamaría, D., Angulo, M., Ortega, A., Torres, E., Turrero, M.J., 2018. Authigenic Clay Minerals from Interface Reactions of Concrete-Clay Engineered Barriers: A New Perspective on Mg-Clays Formation in Alkaline Environments. *Minerals*, 8(9), pp. 386, https://doi.org/10.3390/min8090362.

- Fernández, R., González-Santamaría, D., Angulo, M., Torres, E., Ruiz, A.I., Turrero, M.J., Cuevas, J., 2018. Geochemical conditions for the formation of Mg silicates phases in bentonite and implications for radioactive waste disposal. *Applied Geochemistry*, 93, pp. 1-9, https://doi.org/10.1016/j.apgeochem.2018.03.012.

Low-pH cement mortar-bentonite perturbations in a small-scale pilot laboratory experiment (sección 5.1).

En este artículo se sientan las bases de los materiales y métodos utilizados durante la tesis doctoral. Concretamente en este experimento piloto se analizó la reactividad generada entre la bentonita FEBEX en contacto con un mortero de cemento de bajo pH elaborado mediante la adición SF, confiriendo así el característico bajo pH del agua de poro del material de cemento. Ambos materiales, bentonita y LpH, fueron expuestos a un flujo de agua destilada durante 75 días, momento tras el cual fueron analizados. Los resultados indicaron la presencia de alteraciones, aunque con un desarrollo muy limitado.

La principal aportación de esta publicación reside en que establece una metodología robusta que permite aproximar la reactividad generada en el EBS, utilizando para ello materiales reales en una escala espacio temporal relativamente corta, siendo ésta una aproximación que no se había realizado hasta la fecha.

Referencia:

González-Santamaría, D., Angulo, M., Ruiz, A., Fernández, R., Ortega, A., Cuevas, J., 2018. Low-pH cement mortar-bentonite perturbations in a small-scale pilot laboratory experiment. *Clay Minerals* 53, pp. 237-254, https://doi.org/10.1180/clm.2018.16.

Bentonite/CEM-II cement mortar INTERFACE EXPERIMENTS: A proxy to in situ deep geological repository engineered barrier system surface reactivity (sección 5.2).

Una vez finalizados los experimentos, análisis y estudio de los datos, se publicaron los resultados observados en los morteros basados en cemento Pórtland tipo CEM-II en contacto con la bentonita-FEBEX. La importancia e interés de esta publicación se debe a que los materiales y su disposición se corresponden con los utilizados en el laboratorio subterráneo *in-situ* FEBEX de Grimsel (Suiza), lugar donde se ubica uno de los experimentos de referencia a gran escala asociados al proyecto bajo el cual se enmarca esta investigación. El hecho de que este experimento-*in situ* reproduzca las dimensiones reales previstas para un EBS en intervalos de tiempo de 13 años supuso un punto de referencia que permitió extrapolar (*"up-scaling"*) la reactividad observada desde los primeros meses en el presente trabajo.

Referencia:

González-Santamaría, D.E., Fernández, R., Ruiz, A.I., Ortega, A., Cuevas, J., 2020. Bentonite/CEM-II cement mortar INTERFACE EXPERIMENTS: A proxy to in situ deep geological repository engineered barrier system surface reactivity. *Applied Geochemistry* 117, pp. 104599, https://doi.org/10.1016/j.apgeochem.2020.104599.

High-pH/low-pH ordinary Portland cement mortars impacts on compacted bentonite surfaces: Application to clay barriers performance (sección 5.3).

Por último, el tercer artículo engloba los resultados obtenidos durante el proyecto de doctorado. Incorpora las perturbaciones generadas por los tres modelos de experimentos planteados: LpH, CEM-I y CEM-II en contacto con la bentonita FEBEX. Este enfoque permitió evaluar y comparar la reactividad desarrollada por lo distintos materiales, todo ello en las mismas condiciones mediante experimentos duplicados, lo cual no se había realizado hasta ahora, representando por tanto un hecho novedoso en el presente campo de investigación.

Referencia:

González-Santamaría, D.E., Fernández, R., Ruiz, A.I., Ortega, A., Cuevas, J., 2020. High-pH/low pH ordinary Portland cement mortars impacts on compacted bentonite surfaces: Application to clay barriers performance. *Applied Clay Science* 193, pp. 105672, https://doi.org/10.1016/j.clay.2020.105672

5.1 LOW-PH CEMENT MORTAR-BENTONITE PERTURBATIONS IN A SMALL-SCALE PILOT LABORATORY EXPERIMENT

Daniel E. González-Santamaría[1*], María Angulo[1], Raúl Fernández[1], Ana. I. Ruiz[1], Almudena Ortega[1], Jaime Cuevas[1]

[1]Department of Geology and Geochemistry, Faculty of Sciences, Autonomous University of Madrid, Cantoblanco, 28049, Madrid, Spain

Keywords: Radioactive waste confinement, alkaline alteration, low-pH cements, bentonite, laboratory experiments.

Abstract

A novel method to perform small-scale laboratory experiments that reproduce concrete–bentonite and concrete–groundwater interactions has been developed. Such interfaces will prevail in engineered barrier systems used for isolation of nuclear waste. With the goal of optimizing the experimental method, this work has analysed the geochemical interaction of distilled water, low-pH cement mortar and FEBEX-bentonite for 75 days. Limited but evident reactivity between the materials was observed, mainly decalcification in cement mortar, carbonation at the interface with bentonite and Mg enrichment in bentonite. These results are consistent with the state-of-the-art literature and were used to validate this small-scale pilot laboratory experiment to establish the basis for further studies comparing the behaviour of different buffer and cement materials.

Introduction

The present and future management of high-level radioactive waste (HLRW) is a major environmental issue, especially considering its long radiotoxicity (10^4–10^6 years). Currently, the deep geological repository (DGR) is the most accepted management option for HLRW long-term isolation (NEA-OECD, 2003; U.S. DOE, 2014). Within the European Union, Finland, Sweden and France are expected to approve a final DGR location before 2020 (Gibney, 2015; Ewing *et al.*, 2016). The DGR concept is based on a multi-barrier system (engineered barrier system, EBS) to avoid/delay the release of radionuclides into the biosphere. A generic EBS constructed in a granitic host-rock formation consists of the following parts: (1) a metallic canister as a first barrier in contact with the radioactive waste; (2) a clay barrier surrounding the canister; and (3) concrete to seal and close the galleries. The clay barrier acts as both a hydraulic seal and a physical-chemical buffer. Bentonite is a swelling clay material that has been selected by most of the waste-management organizations (IAEA-TECDOC-1718, 2013; NEA-OECD, 2003) as an optimal material for the backfilling and sealing of HLRW repositories due to its low permeability, low diffusivity, high retention of cations and swelling capacity (Meunier *et al.*, 1998; Kaufhold *et al.*, 2013; Gómez-Espina & Villar, 2016; Kaufhold & Dohrmann, 2018). Concrete and bentonite will be in close contact, and they will interact within each other. In addition, the EBS system will be in contact with flowing groundwater in the host rock, which will affect the long-term safety in case that degradation processes develop. In the long term, the interaction between water, concrete and clay will generate an indeterminately complex chemical system that might compromise the storage security (Savage, 2014). Furthermore, its evolution will vary depending on the type of cement and clay used as a barrier (Dauzères *et al.*, 2010; Jenni *et al.*, 2014). Thus, understanding the degradation pathways due to barriers and groundwater

interactions and clarifying the critical parameters involved herein are of fundamental interest to advance the DGR design. Conventional Portland type cementitious materials generate alkaline fluids (pH > 13) by the dissolution of alkali hydroxides and $Ca(OH)_2$ (portlandite) in the porewater of the cement matrix, which may attack smectite crystal lattice in neighbouring clay seals (Liu *et al*., 2014). Therefore, the hyperalkaline front might modify the smectite mineralogy and its properties. Previous investigations have analysed the behaviour of different clays in contact with the hyperalkaline front. However, the concrete should not be simulated by means of a high pH solution in equilibrium with $Ca(OH)_2$ (pH = 12) or alkali hydroxides (Bildstein & Claret 2015) alone, *i*.e. omitting the chemical and mineralogical evolution of the concrete itself. Previous works have outlined the relative absence of representative experiments in real clay/concrete interfaces (Gaboreau *et al*., 2011, 2012; Bartier *et al*., 2013; Mäder *et al*., 2017) and the difficulty of taking into account the effects of real volumes and the composition of solutions migrating through connected porosities (Cuevas *et al*., 2016). Moreover, few works have put low-pH cementitious materials in contact with clays (Jenni *et al*., 2014; Dauzères *et al*., 2016; Lerouge *et al*., 2017). To avoid extreme alkalinity, experiments have been carried out with low-pH cement mortars (pH < 12). Several studies suggest that low-pH cement-based materials have insignificant effects on clay structures (Bäckblom, 2005; Berner *et al*., 2013; Cuevas *et al*., 2016), while simultaneously they have demonstrated a resistance to granitic groundwater exposure (García Calvo *et al*., 2010). However, low-pH cements have shown a lower resistance than high-pH cements to the influence of carbonated waters (Dauzères *et al*., 2014) as some of the cement paste hydration products, such as ettringite, are more unstable (Trotignon *et al*., 2007) and precipitate calcite and gypsum. Low-pH cement based materials may display carbonation, but the high-pH cementitious materials may develop a larger

protective calcium carbonate film that increases the retardation of the decalcification process, at least temporarily (Jenni *et al*., 2014). In addition to these uncertainties, the complex structure and chemistry of the mineral phases formed during the alkaline perturbation at these interfaces were unclear until a few years ago (Bildstein & Claret, 2015), but recent experiments have examined and provided new characterizations of their structure and chemistry (Roosz *et al*., 2015; Nied *et al*., 2016; Lerouge *et al*., 2017). This might be the case for mineral phases such as magnesium silicate hydrates (M-S-H) or calcium aluminium silicate hydrates (C-A-S-H; Lothenbach *et al*., 2015). The composition of concrete includes a wide range of mineral phases such as calcium silicate hydrates (C-S-H) with different Ca/Si ratios and aluminate-, calcium- and sulfate-bearing phases such as ettringite and calcium monosulfate-aluminate hydrate (CmSAH; Van Damme & Pellenq, 2013). Experimental research on C-S-H in low-pH concretes is sparse, and their parameters of formation and stabilization are not yet known sufficiently to allow for a feasibility assessment. In this context, small-scale laboratory experiments might be significant because they approach real conditions through a simplified system, facilitating the control of different parameters and allowing the assessment of the different possible conditions expected in a DGR. These experiments may provide reaction pathways on a short time scale, making them useful tools as sources of data for geochemical modelling. In addition, they can complement other types of experiments, such as batch experiments or large in situ underground laboratory experiments. Consequently, the aim of this study was the development and optimization of a new representative small-scale laboratory experiment able to reproduce the contact between concrete and bentonite that would occur in a DGR and to test procedures and methods for assessing and describing the geochemical perturbations under different conditions.

Materials and methods

Experimental setup and characterization techniques

The pilot experiment was performed using distilled water, simulating diluted granitic groundwater, low-pH cement mortar and FEBEX-bentonite as the reference Spanish bentonite for the DGR. The experiment was run for 75 days under isothermal conditions (25 ± 5°C), based on the range of temperatures expected at the concrete–bentonite interface according to the data provided by Villar *et al*. (2012) for a FEBEX in situ experiment after 13 years for a sealing concrete plug in a granitic DGR. The low-pH cement mortar and the compacted FEBEX-bentonite clay were placed in a 4 mm-thick methacrylate sleeve confined by two stainless steel cylindrical caps (Fig. 1). The cell dimensions were 20 mm in internal diameter and 9 mm in height for each material (18 mm in total). The objective of the design of these cells included the minimization of undesirable effects during the dismantling of the cells for further solid characterization, such as the tedious separation of cement mortar and bentonite from the carcase and the creation of fractures or deformations in both materials, avoiding the interaction of the materials with the atmosphere. The design of a compact external stainless-steel case (together with connections and filters) able to resist the high-pressure conditions (1–5 MPa) caused by the hydration of bentonite (Villar & Lloret, 2004) was required. The setup of columns also involved two porous steel filters that allowed pressurized water infiltration. The constant hydraulic head of the distilled water was fixed to 1 MPa using an automatic piston pump (Gilson, 307 model) and carried through PEEK tubes. The cement mortar–bentonite interface generated (referred to hereafter as the C–B interface) and the cement mortar–distilled water interface (referred to hereafter as the C–W interface) were separated by a 0.45 μm

polytetrafluoroethylene (PTFE) membrane to facilitate the separation of materials and access to both interfaces.

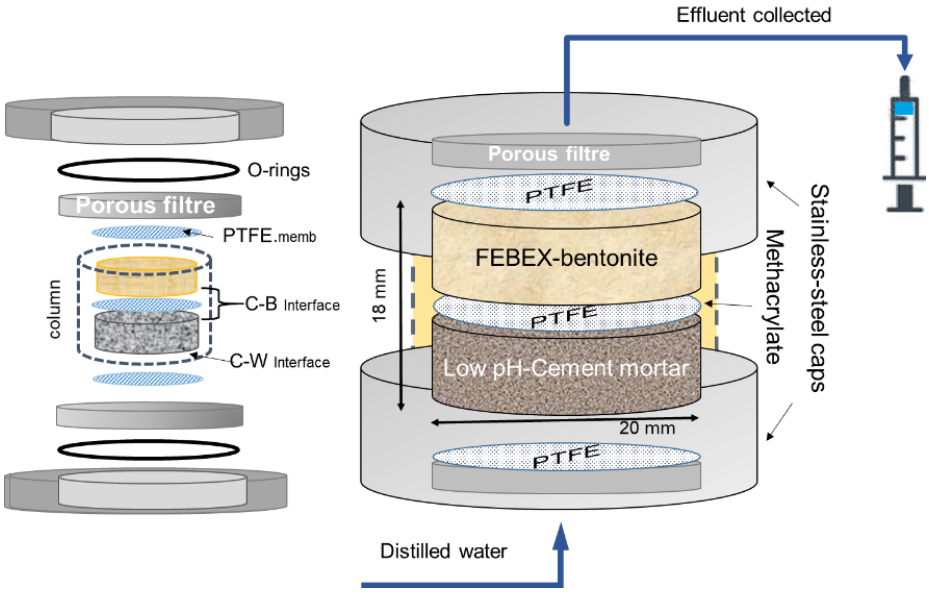

FIG. 1. Compacted column formed from cement mortar and compacted bentonite. Both materials are separated by a PTFE membrane and encased in an open, stainless-steel sleeve. A methacrylate piece seals the column. Two porous filters allow water transport at both column ends. C–B: cement mortar–bentonite interface; C–W: cement–water interface.

The infiltrated water was collected in a syringe for the aqueous-phase survey. This effluent was subjected to the determination of the following (1): alkalinity using a Metrohm 888™ potentiometric titrator; (2) soluble silica in water (as SiO_2) by spectrophotometric determination of molybdate-reactive silica in the effluent using a Milton Roy Spectronic® instrument at a wavelength of 825 nm; and (3) major chemical ions by ion chromatography coupled to a conductivity detector using a Metrohm 802 compact IC plus model. The hydraulic conductivity (k) was calculated by Darcy's law according to equation 1:

$$Q = k/A * \Delta h/\Delta L \quad (1)$$

where Q = the quantity of water leached over time t (m^3/s); k = hydraulic conductivity (m/s); A = cross-sectional area (m^2); Δh = hydraulic head (m); and L = column length.

The solid-phase characterization was performed by X-ray diffraction (XRD), grazing incidence X-ray diffraction (GI-XRD) and by using a scanning electron microscope attached to an energy dispersive X-ray analyser (SEM-EDX). The mineral identification by XRD was performed on bulk, randomly oriented cement mortar and bentonite powders using a θ/2θ X'Pert PANalytical instrument with an X'Celerator detector. The XRD patterns were recorded over the angular range 3–70° 2θ. This method allowed measurements equivalent to 0.016° angular steps for 100 s at each step. The voltage and intensity of the X-ray Cu tube were 45 kV and 40 mA, respectively. To perform the GI-XRD analyses, angles of 1°, 5° and 8°2θ were used with 0.04° 2θ of angular step and 2 s time step increases, respectively. The SEM-EDX equipment consisted of an Hitachi S-3000N SEM coupled with an INCAx-sight Oxford Instruments™ energy dispersive X-ray analyser. The EDX quantification was performed by means of internal standard semi-quantitative analyses.

Semi-quantitative EDX elemental composition analysis was performed for the following reasons: (1) to determine the elemental composition variations along a linear transect through the whole cement-mortar/bentonite composite probe, taken from the hydration mortar face to the porewater outflow at the end of the compacted bentonite; and (2) to perform localized point analyses to describe either the chemistry of the cement mortar matrix for the intergranular zones between the quartz grains or the discrete mineral-phase compositions where singular morphologies (crystals, polycrystalline aggregate-defined morphologies) were

distinguished. To evaluate the quality of these results, EDX spectra of a heterogeneous 300 μm×200 μm area, typical of the analysis performed on the linear transect in the cement mortar, were acquired using various integration times, from 10 s to 80 s, at 5 s intervals. The % deviation was calculated as 100 times the ratio of the standard deviation to the determined % chemical element value. For major elements in the concrete (Al, Si and Ca), instrumental % deviations, obtained by taking their average value in the 30–50 s interval, were <10%, related to their concentration being less for silicon (<1%) and greater for Al (9%) (Table 1). The % deviation from measured values, however, was <6% for the average measurement value. For elements that have contents within 1–5% (K, Fe), the % deviation from the average of the measured values was typically 10–15%. A period of 40 s was considered to be sufficient that the analysis quality would not be compromised and to avoid excessively time-consuming data acquisition. In terms of the point analyses, with a typical 5 μm×5 μm spot, the analysis data for a needle-like ettringite polycrystalline aggregate are shown in Table 1. In general terms, the atomic ratios obtained, considering that some impurities are always present (Si phases and carbonates), are within 10–15% deviation using theoretical values for ettringite.

TABLE 1. Relative error evaluation of SEM-EDX-determined chemical element concentrations.

Element	% element 40s*	% ID 10s-80s**	Average ID % 30s-50s	Average MD % 30s-50s
Al	5.9	17-7.0	9.0	6.0
Si	69.2	6.5-2.3	0.8	3.2
Ca	18.0	9.0-3.2	1.9	4.5
Ettringite $Ca_6Al_2(SO_4)3(OH)_{12}\cdot 26H_2O$			Ca/S Theoretical=2.0	Al/S Theoretical=0.7
Example***				
Al	16.0	5.8	1.8	0.6
Si	6.6	10.5		
S	26.9	4.5		
Ca	48.8	2.9		
Fe, Mg	< 0.2	50-75		

*The selected integration time to determine any SEM-EDX measurement was 40 s. The element % is referenced to the sum of the major analysed elements, excluding C and O (normally, the sum of Mg, Al, Si, K, S, Ca, and Fe).**Deviation data are expressed as a percentage given by the ratio of the standard deviation to the value determined using either the instrumental standard deviation of the integrated signal counts (ID: instrumental deviation) or the average value of several measurements (MD: measurement deviation).***Analyses for ettringite were described by Fernández *et al*. (2017).

FEBEX-bentonite

The experiments were performed using FEBEX-bentonite from the Cortijo de Archidona deposit (Almería, Spain; Caballero *et al*., 2005). The physical-chemical properties of the FEBEX-bentonite, as well as its most relevant thermo-hydro-mechanical and geochemical properties, have been studied extensively and published elsewhere (e.g. ENRESA, 2006). The FEBEX-bentonite was compacted with its hygroscopic water content (13%) at room conditions (23 ± 1°C) and at a nominal dry density of 1.60 g/cm^3. Finally, the bentonite was placed inside the methacrylate sleeve (Fig. 1).

Low-pH cement mortar

The low-pH cement binder was prepared with ordinary Portland cement (OPC) CEM I 42.5 R SR mixed with silica fume (SF) (OPC [60 wt.%] + SF [40 wt.%]). Both materials were provided by the Eduardo Torroja Institute for Construction Science from CSIC (Spanish National Research Council). Subsequently, a 0.42 ratio of distilled water/binder and a 1:3 ratio of binder/silica sand (grain size <1 mm) were added. The fresh, low-pH cement mortar obtained was pressed inside the methacrylate sleeve and covered by the PTFE membrane. After the bentonite was compacted to fill the whole sleeve, the cement mortar was stored in a hydration chamber and exposed to a water-saturated atmosphere for 90 days. The chemical composition of the low-pH cement mortar (Table 2) and the composition of major ions in the pore solution after 90 days of curing time (presumably at equilibrium) were provided by García Calvo (2012; Table 3).

TABLE 2. Chemical composition (wt.%) of ordinary Portland cement (OPC) and silica fume (SF) (García Calvo, 2012).

Weight %	OPC	SF
SiO_2	17.40	92.70
Al_2O_3	4.68	0.60
Fe_2O_3	5.08	5.38
total CaO	60.30	1.31
MgO	1.78	0.93
SO_2	3.17	-
Na_2O	0.18	0.15
K_2O	0.34	0.37
Free CaO	1.85	0.01

TABLE 3. Major ions, alkalinity, aqueous silica and pH in the effluent and chemical composition of a reference low-pH cement mortar (LpHC) pore solution (90 days old) provided by García Calvo (2012).

Ion/aqueous species	Effluent (mg/L)	LpHC (mg/L)
Ca^{2+}	93.2	612
Mg^{2}+	2.2	nd
Na^{+}	211.1	120
K^{+}	2.73	322
NO_3^{-}	3.9	nd
Cl^{-}	187.3	nd
F^{-}	2.2	nd
SO_4^{2-}	176.2	84.4
HCO_3^{-}	237.9	nd
$SiO_{2\ (aq)}$	12.8	nd
pH	8.3	11.1

Nd: not determined.

To obtain an initial reference sample, a slice of the initial low-pH cement mortar was cut, polished and characterized by SEM-EDX. The pH measured in the pore solution of the initial low-pH cement mortar (Table 3) was obtained following the leached *ex situ* method (García Calvo, 2012). The powder XRD patterns and GI-XRD showed the absence of portlandite [$Ca(OH)_2$] and the presence of C-S-H together with characteristic clinker phases that were not yet hydrated (Fig. 2).

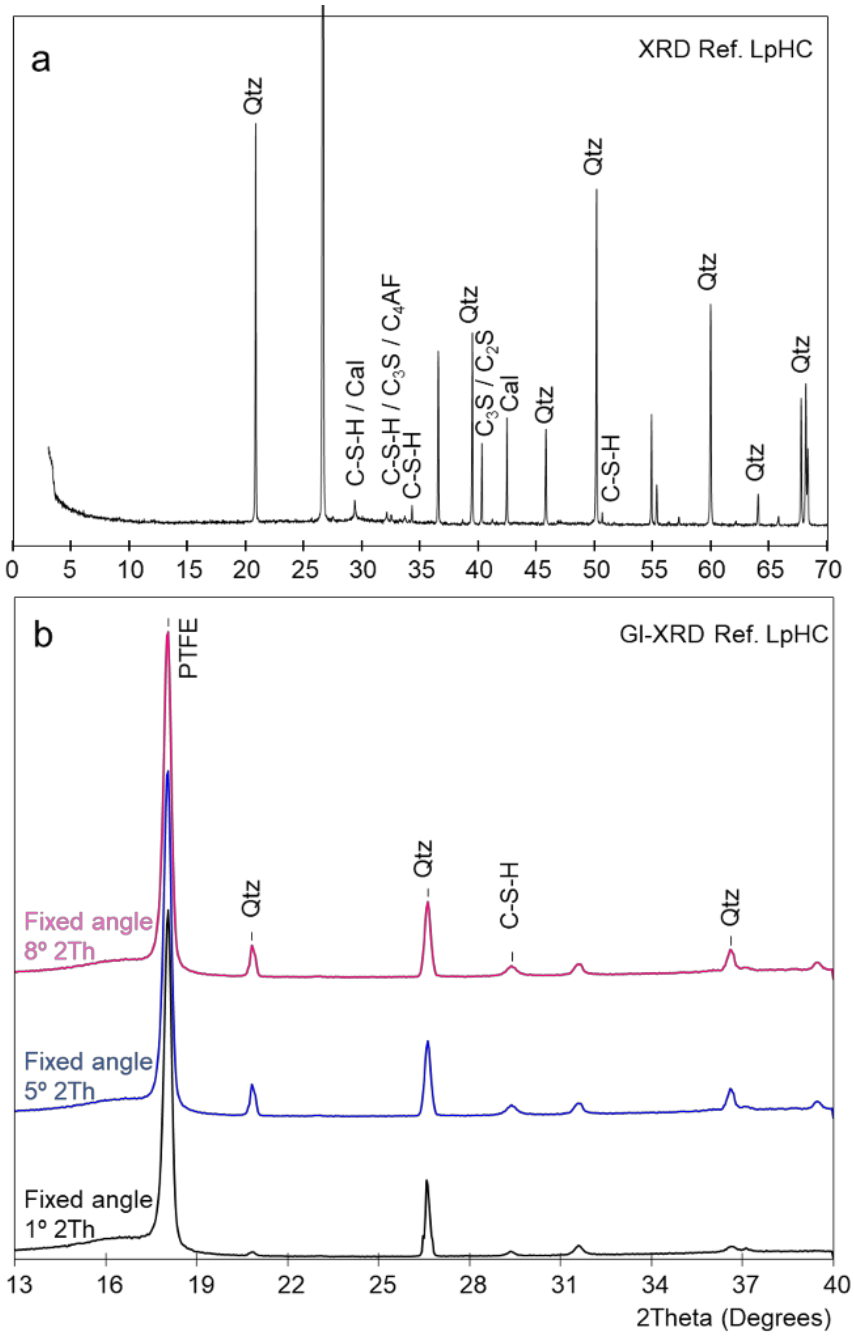

FIG. 2. (a) XRD traces of the reference low-pH cement mortar (ref. Low-pHC); (b) GI-XRD patterns with fixed angles of 8°, 5°, and 1° 2Theta of the initial-reference, low-pH cement mortar. Qtz: quartz. Cal: calcite. C3S: tricalcium silicate. C_4AF: tetracalcium aluminoferrite. C-S-H: calcium silicate hydrates. C2S: dicalcium silicate. PTFE: polytetrafluoroethylene. *d* spacings of reflections are given in Å.

The SEM images showed homogeneously distributed grains of silica sand within the cement matrix (Fig. 3a). In addition, the reference low-pH cement mortar showed the presence of non-reacted silica fume grains, which indicated incomplete dispersion. Nevertheless, the conversion of portlandite to C-S-H was complete. The EDX analyses were conducted considering only the cement matrix and taking a representative number of analyses, where silica grains were avoided intentionally. Under these conditions, a Ca/Si ratio of 0.9 ± 0.1 was obtained, representative of the cement matrix composition (based on 14 analyses; see the detail of the spot size selected in Fig. 3a; a supplementary Table S1 with EDX data has been provided and is available here https://doi.org/10.1180/clm.2018.16. This result can be applied to the C-S-H composition present in the reference low-pH cement mortar as C-S-H are the main and almost unique hydrated phases present in the binder (García Calvo *et al.*, 2012). The Ca/Si ratios determined are in agreement with Stronach & Glasser (1997), who indicated that to obtain a low pH in the cement materials, the Ca/Si ratio must be <1.1. Additionally, the SiO_2 content in these ratios might be overestimated due to the presence of small micro-silica particles (silica fume) (García Calvo *et al.*, 2010). In the point analysis, morphologies typical of ettringite were observed locally (Fig. 3b). The EDX chemical analyses corroborate the identification of such mineral phases (Al/S = 0.8; theoretical Al/S = 0.67), although they cannot be detected and quantified in our XRD patterns.

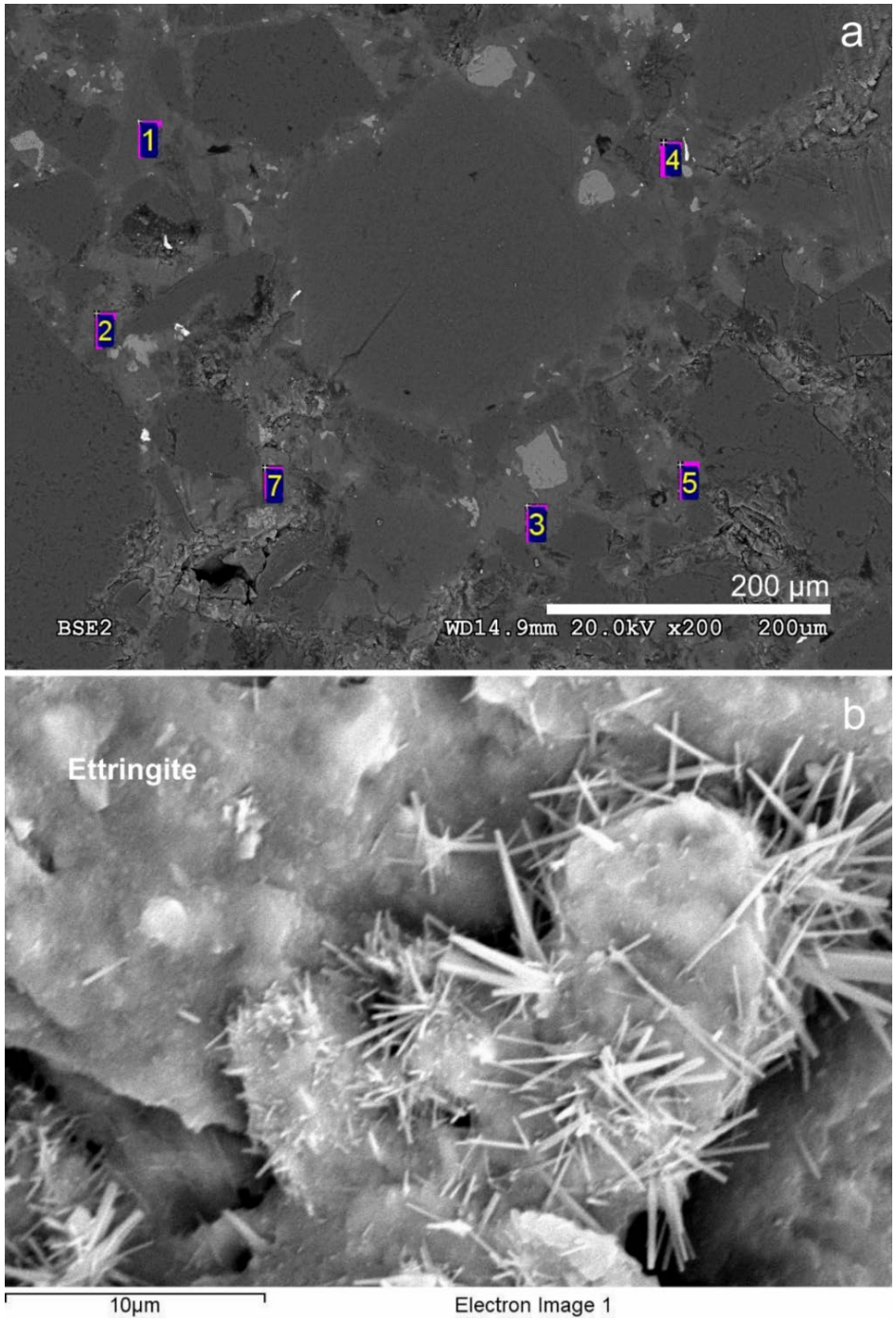

FIG. 3. (a) SEM-EDX spots analysed in the initial-reference, low-pH cement mortar to calculate the Ca/Si ratio in the cement matrix. (b) Presence of ettringite in local regions of the initial-reference, low-pH cement mortar. The numbers correspond to EDX analysis points.

Dismantling, cutting and sampling

After 75 days of reaction, the cement mortar-bentonite column was dismantled and divided into subsamples using a Well®2000 cutting machine model with a diamond wire saw. Various subsamples were sliced from the initial column (Fig. 4). The number of subsamples and their sizes were determined by the quantity needed to carry out the post-mortem analyses.

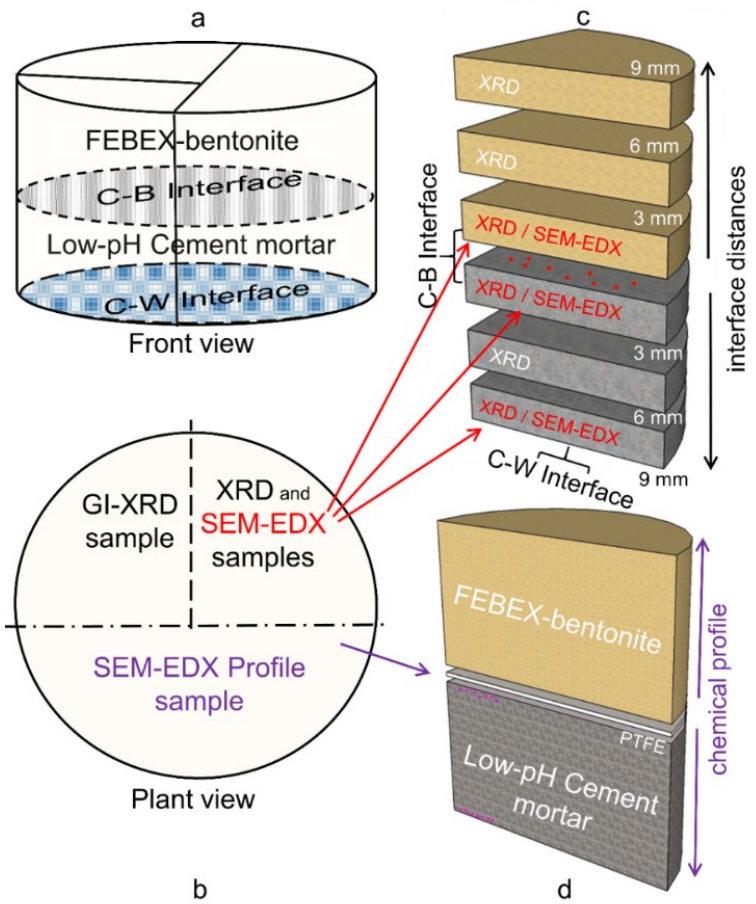

FIG. 4. Cutting and sampling scheme. (a) Front view where the cement mortar-bentonite (C–B) interface and the cement mortar–water (C–W) interface have been drawn. (b) Plan view of the cement mortar–bentonite column. (c) Subsample segmentation for XRD and punctual SEM-EDX analyses performed on the surfaces of the subsamples next to the C–B and C–W interfaces. (d) Sample for SEM-EDX profile analyses and punctual SEM-EDX analyses near the C–B and C–W interfaces.

A half-sample of the cement mortar-bentonite column was divided into two: one quarter was used to perform XRD and SEM-EDX analyses, and the other quarter was used to perform GI-XRD analyses. All analyses were performed to study the influence between both materials and the effects of the water flow. The subsample prepared for XRD and SEM-EDX analyses was sliced into six new subsamples, each 3 mm thick, parallel to the interface (Fig. 4). The segmentation permitted the study of perturbations as a function of distance from the interface (3, 6 and 9 mm) and then the assessment of the spatial progress of the geochemical reactions. Finally, prior to performing the analyses, these subsamples were dried in a vacuum chamber.

The other half-sample was used for optical inspection to analyse a longitudinal chemical profile of the elemental distribution along the column axis measured by SEM-EDX and was used to carry out spot EDX analyses on the cement matrix near the C–W interface and C–B interface. This profile sample was freeze-dried in liquid nitrogen, dried under vacuum in a P_2O_5-dehydrated atmosphere until 10^{-4} Pa and polished up to 2500 grit sheet sandpaper.

The chemical profile was obtained by SEM-EDX analyses in selected areas. Using the C–B interface as a reference, EDX measurements were conducted towards the bentonite end of the column and towards the interface with the infiltrating water solution (C–W interface). Ten analyses with rectangular dimensions of 10 μm in the direction perpendicular to the C–B interface and ~120 μm in the direction parallel to the C–B interface were performed. The next five analyses had dimensions of 100 μm×300 μm in directions perpendicular and parallel to the C–B interface, respectively. Finally, eight analyses towards the bentonite column end and ten analyses towards the C–W interface of 1μm×3 mm were performed. The analysed areas are illustrated in Fig. 5.

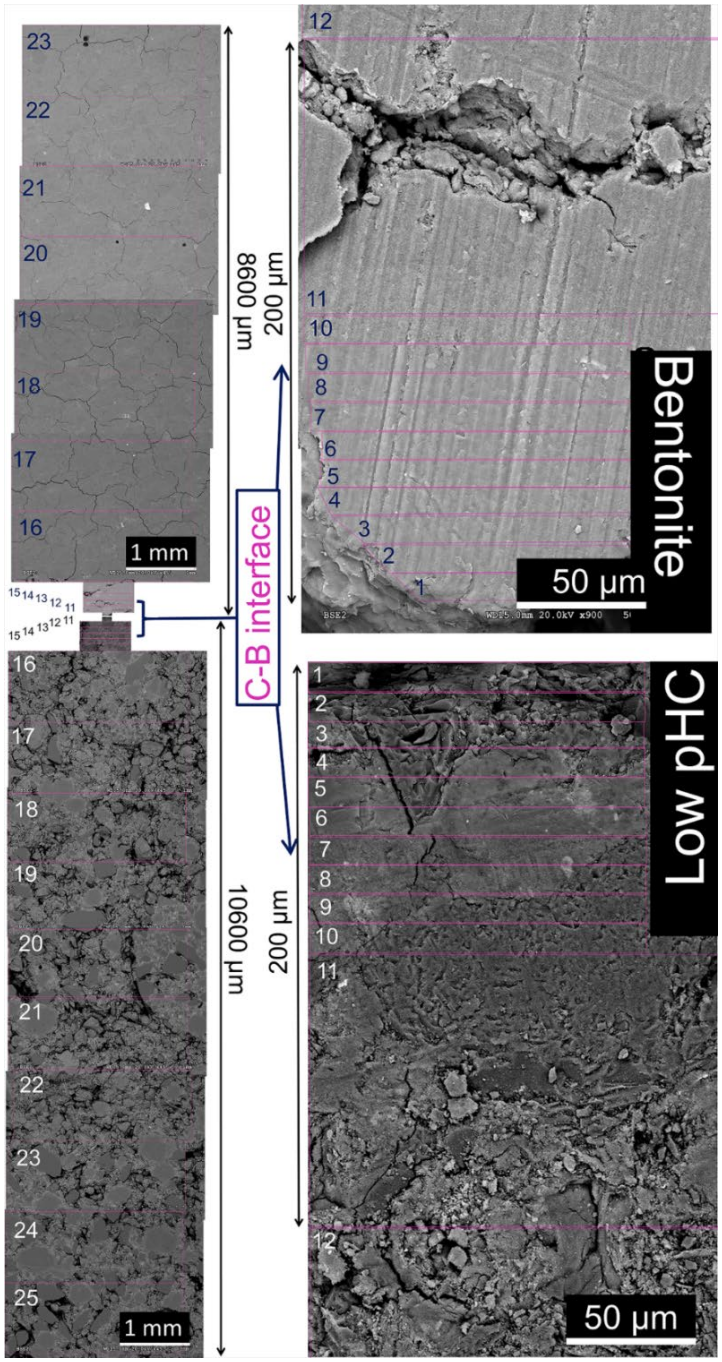

FIG. 5. Backscattered electron (BSE) images showing an overview of the methodology used to create the SEM-EDX profile of the elemental compositions in the cement mortar-bentonite column. Note the increasing magnification at the interface region.

Results

Aqueous phase

The volume of aqueous solution effluent collected after 75 days was 2.03 mL. The concentrations of major ions, aqueous SiO_2, the alkalinity, and the pH are listed in Table 3. The calculated hydraulic conductivity (equation 1) was 1.6×10^{-13} m/s based on a single measurement.

General overview of the small-scale pilot laboratory experiment

The profile sample of the post-mortem low-pH cement mortar-bentonite column is shown in the backscattered electron image (Fig. 5). The freeze-drying process, in preparation for the SEM-EDX analyses, produced a decrease in the bentonite volume and a few macroscopic cracks in the bentonite part. However, the general aspect of the bentonite texture remained homogeneous. The low-pH cement mortar showed an increased presence of air voids (Fig. 5) compared to the reference cement mortar sample (Fig. 3a), suggesting a leaching process of the cement matrix towards bentonite.

The chemical composition profiles obtained by EDX analyses illustrate the elemental distribution along the complete column axis (Fig. 6a). The main chemical perturbations were observed at the C–B interface, although a visible decrease in Ca was also observed in the cement mortar near the C–W interface.

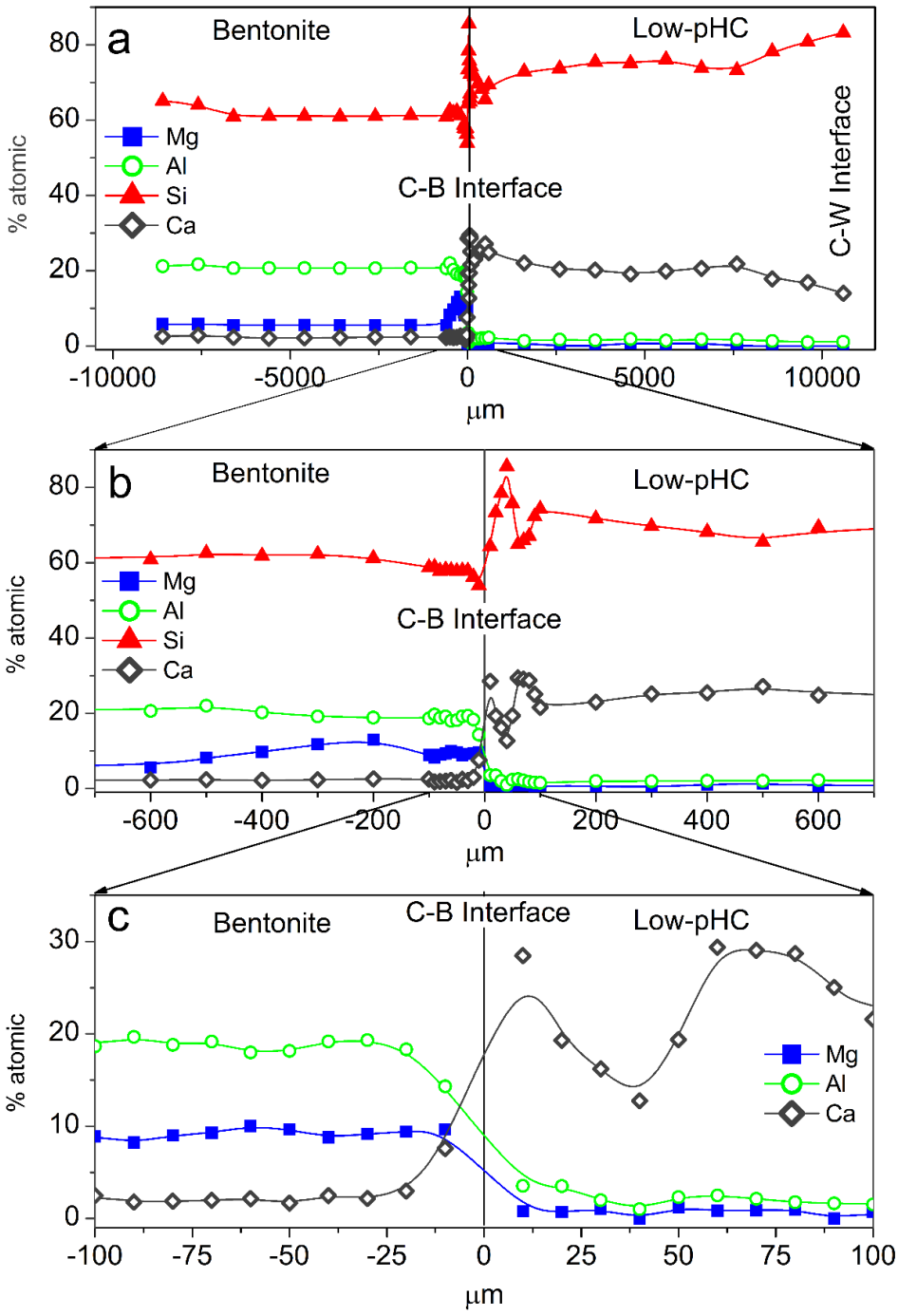

FIG. 6. EDX profile of the column at different scales: (a) 1000 μm, (b) 600 μm, and (c) 100 μm. Bentonite is shown on the left side and low-pH cement mortar (Low-pHC) on the right side of the figure.

Low-pH cement mortar perturbations

The chemical profile showed a slight decrease in the percentage of Ca over the first 3 mm from the C–W interface (Fig. 6a). Conversely, the EDX profile showed an increase in Ca towards the C–B interface, and close to the C–B interface (in the range 0–100 μm); two peaks of Ca were observed with an associated opposite effect on the Si concentration (Fig. 6b-c). A slight increase in Al (2.5–4.0%) was observed in the cement mortar near the C–B interface (25 μm), and although the increase in concentration is low, it is significant within an established 20–25% relative error (Fig. 6c). In addition, spot SEM-EDX analyses performed on the polished cement mortar sample near the C–W interface showed Ca/Si ratios in the range 0.7 ± 0.1 (based on eight analyses performed on selected cement matrix regions; Fig. 7a), while the spot analyses obtained near the C–B interface showed Ca/Si ratios in the range 0.8 ± 0.1 (based on seven analyses also performed on selected cement matrix regions; Fig. 7b). Moreover, the morphologies of C-S-H (with a Ca/Si ratio = 0.6 obtained by EDX) and ettringite-like crystals (Al/S = 0.6) were observed on the surface of low-pH cement in contact with only the bentonite (Fig. 8a–b).

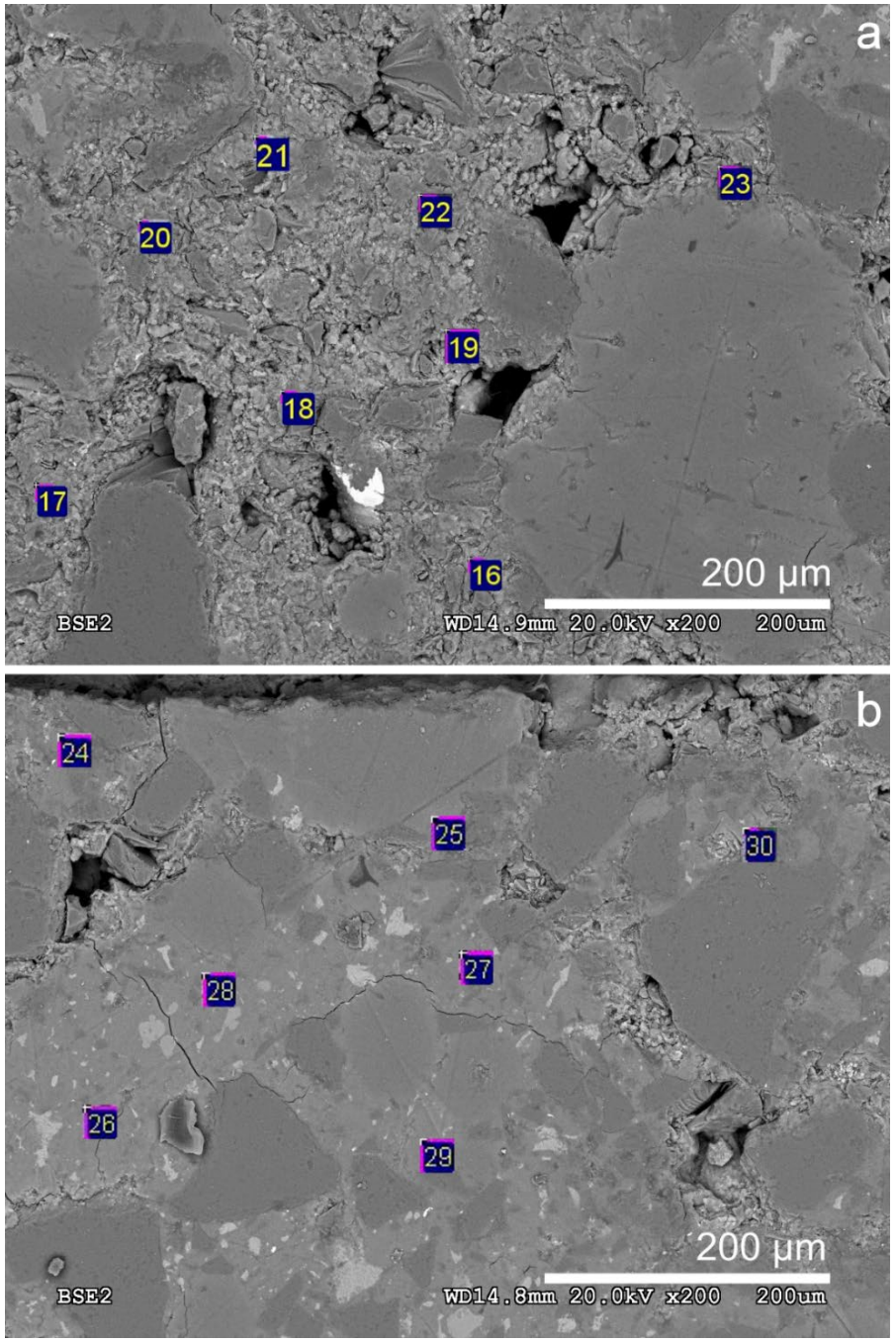

FIG. 7. (a) Locations of the SEM-EDX spots analysed in the cement matrix of the low-pH cement mortar near the C–W interface and (b) spots analysed in the cement matrix of the low-pH cement mortar near the C–B interface.

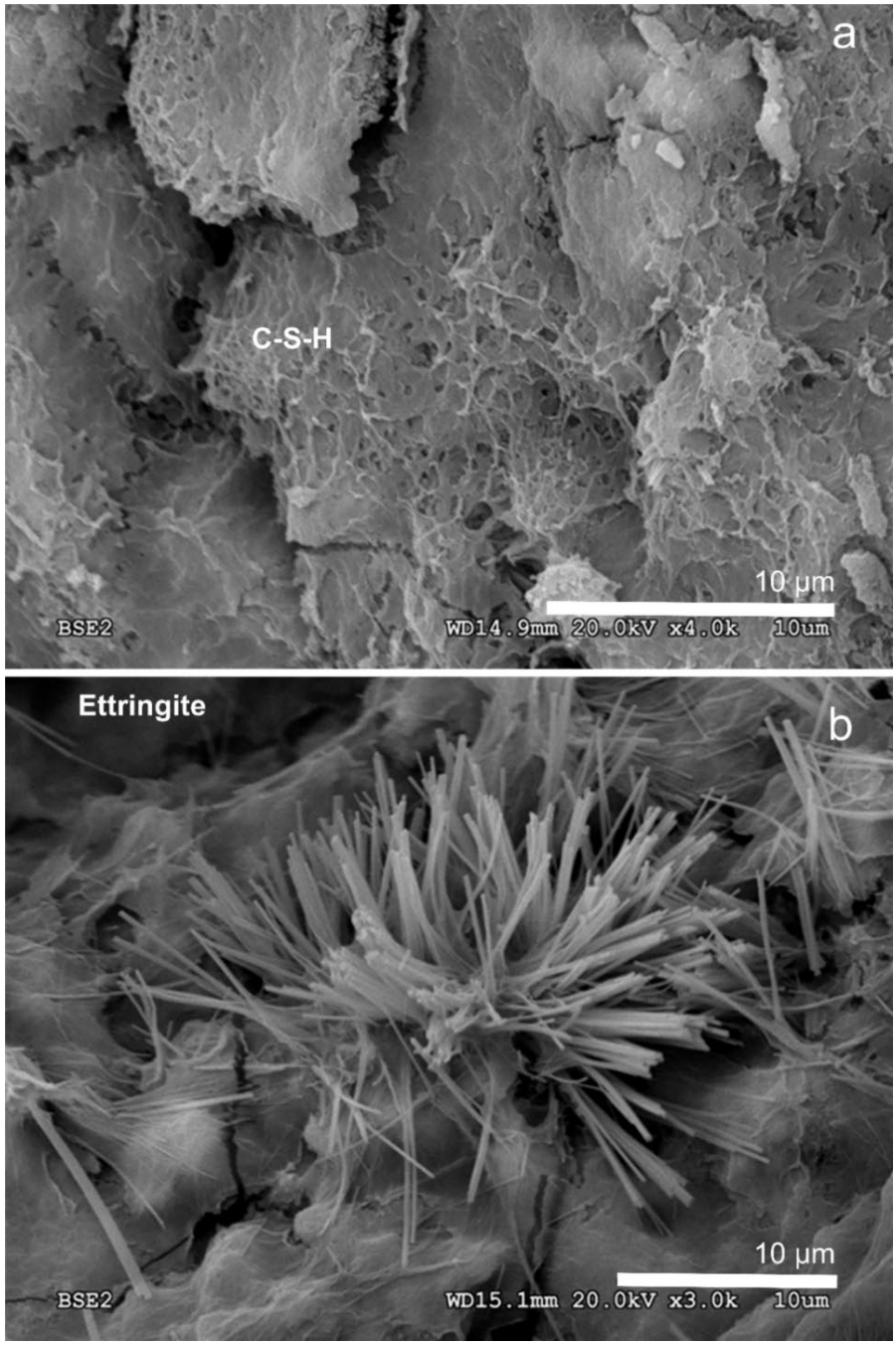

Fig. 8. Backscattered electron (BSE) images: (a) C-S-H present on the low-pH cement mortar side next to bentonite; and (b) ettringite present on the low-pH cement mortar side next to bentonite.

The XRD analyses of the reference low-pH cement mortar sample and the post-mortem subsamples are shown in Fig. 9a–b. The XRD trace shows weak changes at 3.04–3.06 Å among the reference low-pH cement mortar and the low-pH cement mortar subsamples. Regarding the reference low-pH cement mortar, characteristic reflections of C-S-H phases (2.79 Å, 2.75 Å, 2.66 Å and 2.61 Å) were not observed clearly in the post-mortem subsamples. In addition, a reflection at 3.03 Å was observed in the subsample next to the C–B interface; this reflection is characteristic of calcite and sharper than the reflection at 3.04–3.06 Å.

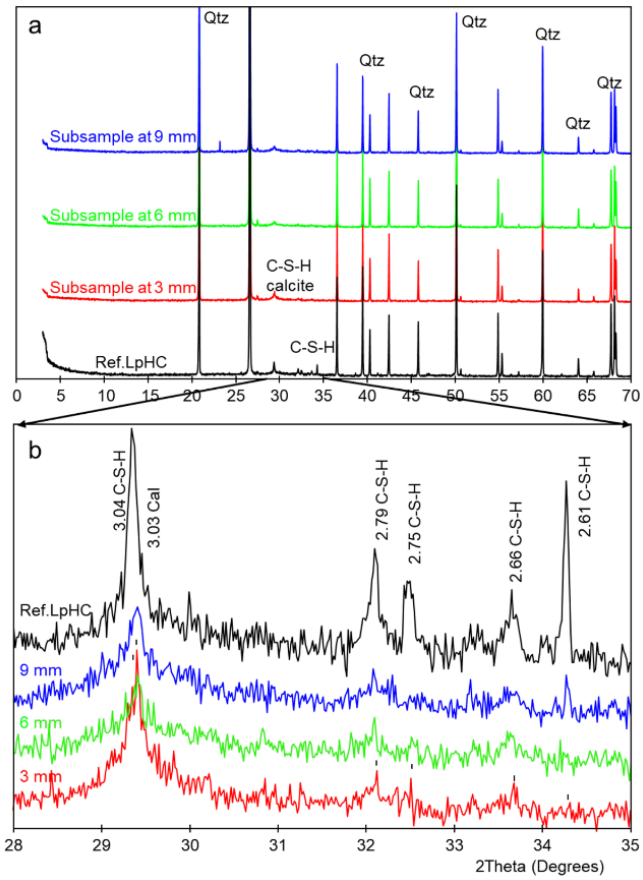

FIG. 9. (a) XRD of the reference low-pH cement mortar (Ref. LpHC) sample and reacted subsamples at 9, 6 and 3 mm from the C–B interface. (b) Magnification of the XRD trace in the range 28–35°2θ. Qtz: quartz, C-S-H: calcium silicate hydrates, and Cal: calcite. d spacings are given in Å.

The GI-XRD patterns of the surface of the low-pH cement mortar (separated by a PTFE membrane from the bentonite) showed little difference from the patterns recorded on the reference material (Fig. 10a). A subtle peak broadening and a shift from 3.05 to 3.03 Å was also detected in the low fixed-angle (1°) pattern, representing a small thickness surficial cement mortar area accessible to the X-rays.

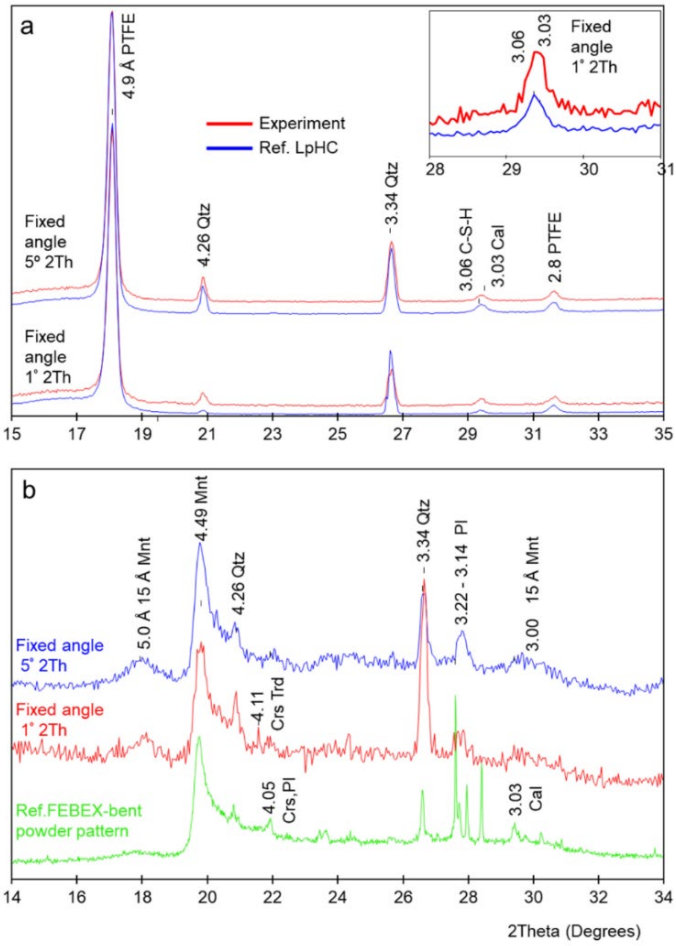

FIG. 10. (a) GI-XRD pattern recorded for the reference low-pH cement mortar (Ref. LpHC) and the surface of the sample exposed to bentonite after the experiment. (b) Conventional random powder XRD pattern recorded for the reference FEBEX-bentonite and GI-XRD for the surface of the sample exposed to low-pH cement mortar after the experiment. PTFE: polytetrafluoroethylene, Mnt: montmorillonite, Qtz: quartz, Crs: cristobalite; Crs-Trd: cristobalite-tridymite; Pl: plagioclase, and Cal: calcite. d spacings are given in Å.

The SEM-EDX images and spot analyses of the same subsample showed typical calcite morphologies composed of Ca and carbon (Fig. 11a).

FEBEX-bentonite perturbations

The chemical perturbations observed in the FEBEX-bentonite have a thickness of ~ 500-600 μm from the C-B interface (Fig. 6b). The EDX compositional profile indicates a Ca increase at 20 μm from the C-B interface, in agreement with an Al depletion in the same region (Fig. 6c). Additionally, the EDX analyses showed a Mg/Si ratio of 0.5 ± 0.1 (based on 8 analyses) on the surface of bentonite (Fig. 11b) in contact with only the low-pH cement mortar and 0.2 ± 0.05 if the Mg/Si ratio is obtained from the first 13 analyses performed from the C-B interface on the EDX profile, representative of a thickness of 400 μm from the C-B interface. The enrichment in Mg near the cement mortar interface contrasts with the Mg/Si ratio of 0.10 ± 0.05 obtained from 9 analyses far from the interface (in the range of 600-8600 μm from the C-B interface) using the same approximation.

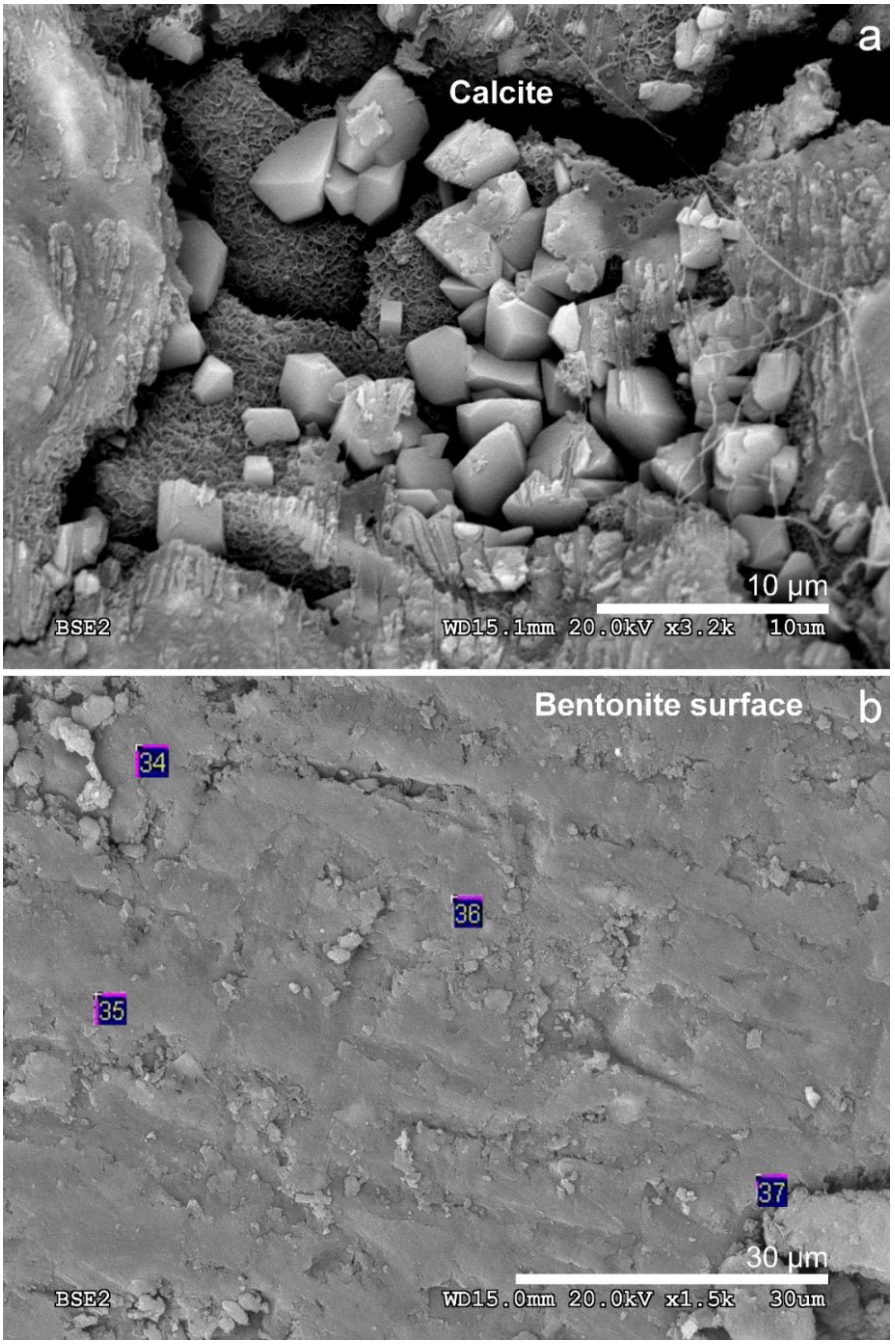

FIG. 11. (a) Backscattered electron (BSE) image of calcite present in the low-pH-cement mortar side near the interface with bentonite. (b) Backscattered electron image of the bentonite surface exposed to cement mortar. The numbers correspond to the EDX analysis points.

The mineralogical data obtained by XRD and GI-XRD (Figs. 10b and 12) showed minimal changes in montmorillonite (Mnt) compared to those in the reference sample of FEBEX-bentonite. These changes are characterized by a weak decrease in the intensity of the Mnt basal reflection at 14.7 Å as the subsamples approach the C-B interface (Fig. 12). This effect was accompanied by an increase in the background towards higher angles using the Mnt basal reflection as the reference (from 7 to 17° for 2θ) in the subsample at 3 mm from the C-B interface.

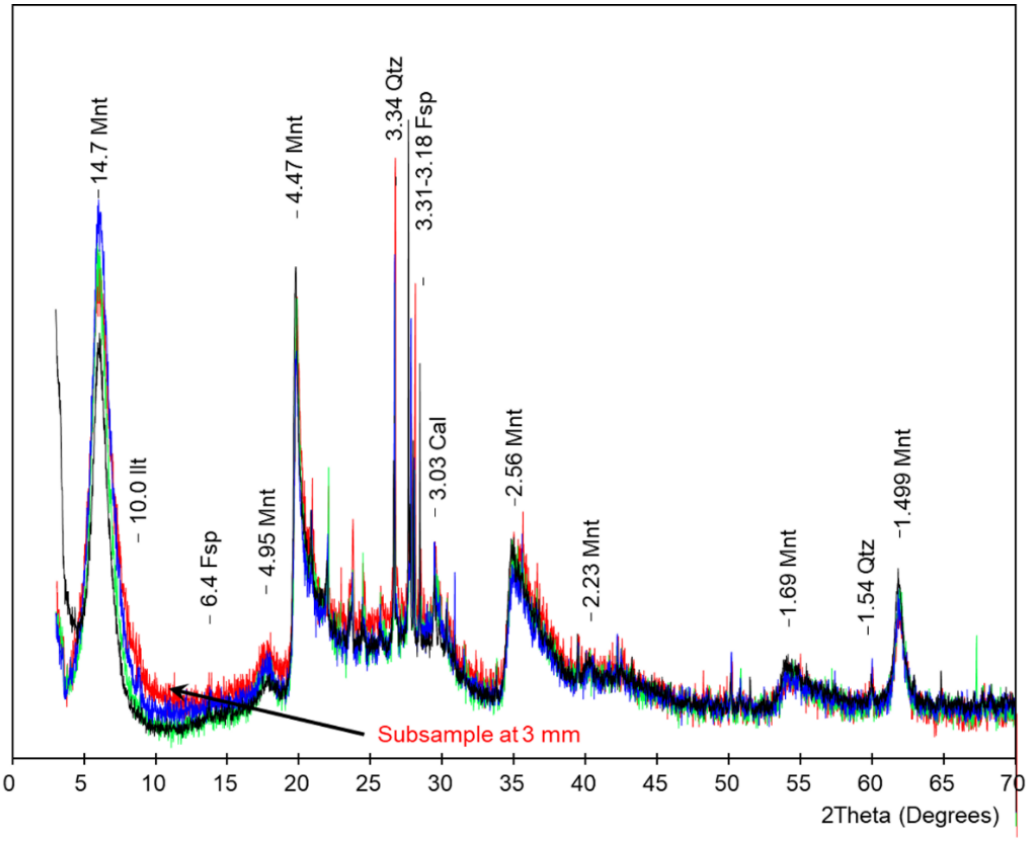

FIG. 12. FEBEX-bentonite XRD pattern. The reference FEBEX-bentonite is shown together with the overlapping subsamples at 9, 6 and 3 mm from the C–B interface. Mnt: montmorillonite, Ilt: illite, Qtz: quartz, Fsp: feldspar, Cal:calcite. d spacings are given in Å.

Discussion

The FEBEX-bentonite buffer capacity is manifested by to the pH 8.3 obtained from the water collected (Table 3), very close to the porewater pH measured in the original bentonite and consistent with the exchange complex and bentonite mineral equilibria (Fernández *et al*., 2004). Aqueous SiO_2 showed concentrations within the solubility equilibrium of quartz and cristobalite (Williams *et al.*, 1985), which are present in bentonite. The dissolution of Mnt in the first microns and the precipitation of secondary phases may also have an important role with regard to the pH decrease, where the OH– consumption at the C–B interface will prevent further alteration of bentonite (Gaucher & Blanc, 2006; Savage *et al*., 2007). In addition to the buffer capacity, bentonite also controls the hydraulic conductivity. The FEBEX-bentonite hydraulic conductivity at room temperature (23 °C) and at a dry density of 1.60 g/cm^3 has been reported previously to be on the order of 10-13 m/s (Villar, 2000; Villar, 2002; Villar et Lloret, 2004), in agreement with the value of hydraulic conductivity calculated in the present study (1.6×10-13 m/s). This could support the pilot experimental setup validity because the advective transport regime was very low and the diffusion was relevant (Muhammad, 2004; Bourg & Tournassat, 2015), as expected in a real repository scenario. Three main chemical disturbances have been observed around the reactive interfaces in the experiment: *i*) decalcification of C-S-H at the C-W and C-B interfaces, *ii*) carbonation at the C-B interface (on the low-pH cement mortar side), and *iii*) Mg-perturbation in bentonite next to the C-B interface.

Decalcification of C-S-H

The Ca leaching process has been mainly identified at the C-W interface. The deterioration of low-pH cement-based materials starts with Na and K dissolution

followed by decalcification of the C-S-H. Although low-pH cement leaching has not been widely studied, aqueous silica is expected to remain saturated with respect to quartz. Then, Ca leaching in such a solution might cause the formation of secondary C-S-H with a lower Ca/Si ratio than the initial C-S-H phases. Compared with the thickness of decalcification at the C-W interface (~3 mm) observed in the present experiment, an alteration thickness of 700 μm was reported in a low-pH concrete composed of Portland cement with additions of silica fume after 14 months and exposure to granitic groundwater flow (García Calvo *et al*., 2010).

At the C-B interface, the decalcification of C-S-H may have occurred according to the lower Ca/Si ratio of the spot EDX analyses from the cement matrix (0.8 ± 0.1) and the C-S-H (Ca/Si = 0.6) found on the surface of the cement mortar in contact with only bentonite. These low Ca/Si ratios are close to the results provided by García Calvo (2012), and they are also consistent with leaching experiments by Baston et al., 2012 with low-pH concrete under similar experimental conditions. Possible evidence for C-S-H alteration of the low-pH cement mortar was determined by means of the XRD patterns (Fig. 9a-b). Moreover, the migration of Al from bentonite next to the C-B interface could lead to the formation of metastable C-A-S-H (Pegado et al., 2014); although C-A-S-H have not been identified, this migration of Al to the low-pH cement mortar due to the exchange of soluble species (Fig. 6c), together with enough sulphate content, may favour the ettringite precipitation, as suggested by the presence of needle morphologies in the EDX and SEM images from the punctual analyses. Low-pH concrete in contact with clayey rocks rich in sulphates was studied by the Cement–Opalinus Clay Interaction project (CI) experiment in Mont Terri (Dauzères et al., 2016) where secondary ettringite precipitates at this interface, with this mineral

being stable in the pH range of 11.0-12.5 (McCarthy et al., 1991), as determined in the low-pH cement mortar in the present study.

Carbonation at the C-B interface

A carbonation process (calcite precipitation) is suggested by the SEM images (e.g., Fig. 11a) and the XRD and GI-XRD analyses (Figs. 9a-b and 10a) at the C-B interface. The dissolved CO_2 species could be provided by the clayey pore solutions (Dauzères *et al*., 2014, Jenni *et al*., 2014) mainly as HCO^{3-}, which is unstable in alkaline environments compared to CO_3^{2-}. Then, these carbonates could react with the available Ca ions in the low-pH cement mortar pore solution to precipitate as $CaCO_3$ on the cement-mortar interface. This is experimentally observed by the increase in Ca observed at the C-B interface (0-100 μm on the cement mortar side), and it is complemented by the images of the abovementioned calcite. Calcite precipitation at the interface has been observed by other authors in much longer time experiments to lead to a decrease in porosity (Cuevas *et al*., 2014).

Mg perturbation at the C-B interface

Mg is present as an exchangeable cation in FEBEX-bentonite so that it can be readily displaced by Ca ions leached from the cement mortar pore water. In fact, the decrease of exchangeable Mg in the FEBEX-bentonite in contact with concrete has been probed in an in situ experiment at the Grimsel-test site (Switzerland) (Villar *et al*., 2018). The pH > 11.0 porewater of the low-pH cement mortar is sufficient to form new mineral Mg-phases, such as brucite (pH 10.5) or Mg-silicate hydrates (M-S-H; e.g., Nied *et al*., 2016). These Mg-rich phases have not been detected by XRD in the present study because of the narrow thickness (<500 μm),

in which a slight Mg enrichment has been detected by EDX at the bentonite side of the C-B interface. Although not measured in the present study, a redistribution of the exchangeable cation population in bentonite is expected. Surface mobility may induce Mg to move from the exchange complex and precipitate in the alkaline medium. Mg perturbation at the bentonite-cement interface has been previously reported by other authors to a greater extent (Fernández *et al*., 2010). However, those previous studies were performed over longer experimental times and under more highly alkaline conditions imposed by OPC concrete. The presence of larger amounts of Mg may expand the number of phases to be considered from brucite to brucite-intercalated Mnt and serpentine-like phases (Fernández *et al*., 2009; Fernández *et al*., 2013).

Conclusions

In this study, a novel and reliable method to perform small-scale laboratory experiments concerning concrete–bentonite reactivity in a granitic DGR has been tested. Only minor reactivity has been observed. However, the following chemical perturbations have been detected in spite of the short experimental time: 1) cement mortar decalcification at the cement mortar-bentonite and cement mortar-water interfaces, 2) slight carbonation in the low-pH cement mortar next to the interface with bentonite, and 3) Mg enrichment in bentonite at the interface with the cement mortar. These results are spatially limited but coherent with those previously observed over the long-term, either at the laboratory-scale or in large underground facilities. Presently, this experimental design is being applied to interactions of bentonite with high-pH cement mortar over longer times and using real groundwater compositions. Additional analytical techniques will be required for an improved interpretation of the results, which should provide valuable

information and contribute to the knowledge of the interaction between geochemical barriers under different scenarios planned for DGR.

Acknowledgements

The research leading to these results has received funding from the European Union's Horizon 2020 Research and Training Programme of the EURATOM (H2020-NFRP-2014/2015) under grant agreement n° 662147 (CEBAMA). We also thank the expertise of Dr. Enrique Rodríguez Cañas in driving the SEM-EDX equipment shared for research in the Interdepartamental Research Service (SIdI) of the Autonomous University of Madrid.

Supplementary material

Supplementary material associated with this article is provided in the ANNEXE I- and is available in https://doi.org/10.1180/clm.2018.16.

References

Bäckblom G. (2005) R&D on low-pH cement for a geological repository in: *SKB and the ESDRED project: 2nd low-pH workshop proceedings*. Enresa, Madrid, Spain.

Bartier D., Techer I., Dauzères A., Boulvais P., Blanc-Valleron M-M. & Cabrera J. (2013) In situ investigations and reactive transport modelling of cement paste/argillite interactions in a saturated context and outside an excavated disturbed zone. *Applied Geochemistry,* **31**, 94-108.

Baston G.M.N., Clacher A.P., Heath T.G., Hunter F.M.I., Smith V. & Swanton S.W. (2012) Calcium silicate hydrate (C-S-H) gel dissolution and pH buffering in a cementitious near field. *Mineralogical Magazine*, **76**(8), 3045–3053.

Berner U., Kulik D. & Kosakowski G. (2013) Geochemical impact of a low-pH cement liner on the near field of a repository for spent fuel and high-level radioactive waste. *Physics and Chemistry of the Earth,* **64**, 46–56.

Bildstein O. & Claret F. (2015) Stability of barriers under chemical perturbations. Pp. 155-188 in: *Natural and Engineered Clay Barriers* (C. Tournassat, C.I. Steefel, I.C. Bourg & F. Bergaya, editors). Elsevier Ltd, Amsterdam.

Bourg I.C. & Tournassat C. (2015) Self-diffusion of water and ions in clay barriers. Pp. 189–226 in: *Natural and Engineered Clay Barriers*. (C. Tournassat, C.I. Steefel, I.C. Bourg & F. Bergaya, editors). Elsevier Ltd, Amsterdam.

Caballero E., de Cisneros C., Huertas F., Huertas F., Pozzuoli A. & Linares J. (2005) Bentonites from Cabo de Gata, Almería, Spain: a mineralogical and geochemical overview. *Clay Minerals*, **40**, 463-480.

Cuevas J., Samper J., Turrero M.J. & Wieczorek K. (2014) Impact of the Geochemical Evolution of Bentonite Barriers on Repository Safety Functions. Pp. 35-42 in: *PEBS Case 4. Proceedings International Conference on the Performance of Engineered Barrier: Physical and Chemical Properties, Behavior and Evolution* (BGR. A. Schäfers & S. Fahland, editors). Hannover, Germany.

Cuevas J., Ruiz A.I., Fernández R., Torres E., Escribano A., Regadío M. & Turrero M.J. (2016) Lime mortar-compacted bentonite–magnetite interfaces: An experimental study focused on the understanding of the EBS long-term performance for high-level nuclear waste isolation DGR concept. *Applied Clay Science*, **124-125**, 79-93.

Dauzères A., Le Bescop P., Sardini P. & Cau Dit Coumes C. (2010) Physico-chemical investigation of clayey/cement-based materials interaction in the context of geological waste disposal: Experimental approach and results. *Cement and Concrete Research*, **40**, 1327-1340.

Dauzères A., Le Bescop P., Cau-Dit-Coumes C., Brunet F., Bourbon X., Timonen J. Voutilainen M., Chomat L. & Sardini P. (2014) On the physico-chemical evolution of low-pH and CEM I cement pastes interacting with Callovo-Oxfordian pore water under its in situ CO_2 partial pressure. *Cement and Concrete Research*, **58**, 76-88.

Dauzères A., Achiedo G., Nied D., Bernard E., Alahrache S. & Lothenbach B. (2016) Magnesium Perturbation in low-pH Concretes Placed in Clayey Environment—Solid Characterizations and Modeling. *Cement and Concrete Research*, **79**, 137-150.

ENRESA. (2006) Post-mortem bentonite analysis. Pp. 183 In: *FEBEX project final report* (M.V. Villar, editor). Publicación técnica 1-5/2006, Madrid, Spain.

Ewing R., Whittleston R. & Yardley B. (2016) Geological Disposal of Nuclear Waste: a Primer. *Elements*, **12**, 233-237.

Fernández AM., Baeyens b., Bradbury M. & Rivas P. (2004) Analysis of the porewater chemical composition of a Spanish compacted bentonite used in an engineered barrier. *Physics and Chemistry of the Earth*, **29**, 105-118.

ernández R., Fernández R., Mäder U., Rastrero M., Vigil de la Villa Mencía R. & Cuevas J. (2009) Alteration of compacted bentonite by diffusion of highly alkaline solutions. *European Journal of Mineralogy*, **21**, 725–735.

Fernández R., Mäder U. & Cuevas J. (2010) Modeling experimental results of diffusion of alkaline solutions through a compacted bentonite barrier. *Cement and Concrete Research*, **40**, 1255-1264.

Fernández R., Vigil de la Villa R., Ruiz A.I., García R. & Cuevas J. (2013) Precipitation of chlorite-like structures during OPC porewater diffusion through compacted bentonite at 90°C. *Applied Clay Science*, **83-84**, 357-367.

Fernández R., Torres E., Ruiz A.I., Cuevas J., Alonso, M.C., García Calvo, J.L., Rodríguez E. & Turrero M.J. (2017) Interaction processes at the concrete-bentonite interface after 13 years of FEBEX-Plug operation. Part II: Bentonite contact. *Physics and Chemistry of the Earth*, Parts A/B/C, **99**, 49–63.

Gaboreau S., Prêt D., Tinseau E., Claret F., Pellegrini D & Stammose D. (2011) 15 years of in situ cement–argillite interaction from Tournemire Characterisation of the multi-scale spatial heterogeneities of pore space evolution. *Applied Geochemistry*, **26**, 2159-2171.

Gaboreau S., Lerouge C., Dewonck S., Linard Y., Bourbon X., Fialips C.I., Mazurier A., Prêt d., Borschneck D., Montouillout V., Gaucher E. C. & Claret F. (2012) In-situ interaction of cement paste and shotcrete with Claystones in a deep disposal context. *American Journal of Science*, **312**, 314-356.

García Calvo J.L., Hidalgo A., Alonso C. & Fernández L. (2010) Development of low-PH Cementitious Materials for HLRW Repositories. *Cement and Concrete Research*, **40**, 1290-1297.

García Calvo J.L. (2012) Desarrollo De Materiales de Construcción con Cemento de Bajo pH, compatibles con la Barrera de Ingeniería de un Almacenamiento Geológico Profundo de Residuos Radiactivos de Alta Actividad. PhD thesis, Instituto Eduardo Torroja de Ciencias de la Construcción, Spain.

Gaucher E. & Blanc P. (2006) Cement/clay interactions – A review: Experiments, natural analogues, and modelling. *Waste Management*, **26**, 776-788.

Gibney E. (2015) Why Finland now leads the world in nuclear waste storage. *Nature.* doi.org/10.1038/nature.2015.18903.

Gómez-Espina R. & Villar M.V. (2016) Time evolution of mx-80 bentonite geochemistry under thermo-hydraulic gradients. *Clay Minerals*, **51**, 145-160.

IAEA-TECDOC-1718. Characterization of Swelling Clays as Components of the Engineered Barrier System for Geological Repositories. Results of an IAEA Coordinated Research Project 2002–2007.

Jenni A*.,* Mäder U., Lerouge C., Gaboreau S. & Schwyn B. (2014) In situ interaction between different concretes and Opalinus Clay. *Physics and Chemistry of the Earth*, **70**–**71**, 71–83.

Kaufhold S., Dohrmann R., Sandén T., Sellin P. & Svensson D. (2013) Mineralogical investigations of the first package of the alternative buffer material test – I. Alteration of bentonites. *Clay Minerals*, **48**, 199-213.

Kaufhold S. & Dohrmann R. (2018) Distinguishing between more and less suitable bentonites for storage of high-level radioactive waste. *Clay Minerals*, **51**, 289-302.

Lerouge C., Gaboreau S., Grangeon S., Claret F., Warmont F., Jenni A., Cloet V. & Mäder U. (2017) In situ interactions between Opalinus Clay and Low Alkali Concrete. *Physics and Chemistry of the Earth*, **99**, 3–21.

Liu S., Jacques D., Govaerts J. & Wang L. (2014) Conceptual model analysis of interaction at a concrete-Boom Clay Interface. *Physics and Chemistry of the Earth*, **70-71**, 150–159.

Lothenbach B., Nied D., L'Hôpital E., Achiedo G. & Dauzères A. (2015) Magnesium and Calcium Silicate Hydrates. *Cement and Concrete Research,* **77**, 60-68.

Mäder U., Jenni A., Lerouge C., Gaboreau S., Miyoshi S., Kimura Y., Cloet V., Fukaya M., Claret F., Otake T., Shibata M. & Lothenbach B. (2017) 5-year chemico-physical evolution of concrete–claystone interfaces, Mont Terri rock laboratory (Switzerland). *Swiss Journal of Geosciences,* **110**, 307-327.

McCarthy G., Hassett D. & Bender J. (1991) Synthesis, Crystal Chemistry and Stability of Ettringite, A Material with Potential Applications in Hazardous Waste Immobilization. *MRS Proceedings*, *245*, 129. doi:10.1557/PROC-245-129.

Meunier A., Velde B. & Griffault L. (1998) The reactivity of bentonites: A review. An application to clay barrier stability for nuclear waste storage. Pp. 187. *Clay Minerals*, **33**, 187-193

Muhammad N. (2004) Hydraulic, Diffusion, and Retention Characteristics of Inorganic Chemicals in Bentonite. PhD thesis, University of South Florida, EEUU.

NEA-OECD. (2003) Engineered Barrier Systems and the Safety of Deep Geological Repositories. State-of-the art Report. OECD Publications, Paris. 70 pp.

Nied D., Enemark-Rasmussen K., L'Hopital E., Skibsted J. & Lothenbach B. (2016) Properties of magnesium silicate hydrates (M-S-H). *Cement and Concrete Research*, **79**, 323-332.

Roosz C., Grangeon S., Blanc P., Montouillout V., Lothenbach B., Henocq P., Giffaut E., Vieillard P. & Gaboreau S. (2015) Crystal structure of magnesium silicate hydrates (M-S-H): The relation with 2:1 Mg–Si phyllosilicates. *Cement and Concrete Research*, **73**, 228-237.

Pegado L., Labbez C. & Churakov S. V. (2014) Supporting Information for: Mechanism of aluminium incorporation into C–S–H from ab initio calculations. *Journal of Materials Chemistry* A, **2**, 3477.

Savage D., Walker C., Arthur R., Rochelle C., Oda C. & Takase H. (2007) Alteration of bentonite by hyperalkaline fluids: a review of the role of secondary minerals. *Physics and Chemistry of the Earth,* **32**, 287-297.

Savage D. (2014) An assessment of the impact of the long-term evolution of engineered structures on the safety-relevant functions of the bentonite buffer in a HLW repository. Pp. 88 in*: National Cooperative for the Disposal of Radioactive Waste. Technical Report 13-02* (Nagra Editor). Wettingen, Switzerland.

Stronach S.A. & Glasser F.P. (1997) Modelling the impact of abundant geochemical components on phase stability and solubility of the CaO-SiO_2-H_2O system at 25 °C: Na+, K+, SO_3^{2-}, CT and CO_2^{3-}. *Advances in Cement Resesarch*, **9**, 167S-181S.

Trotignon L., Devallois V., Peycelon H., Tiffreau H. & Bourbon X. (2007) Predicting the Long Term Durability of Concrete Engineered Barriers in a Geological Repository for Radioactive Waste. *Physics and Chemistry of the Earth*, Parts A/B/C 32 (**1-7**): 259-274.

U.S. DOE. 2014. U.S. Department of Energy. (2014) Evaluation of Options for Permanent Geologic Disposal of Spent Nuclear Fuel and High-Level Radioactive Waste, Volume I. Used Fuel Disposition Campaign. Sandia National.

Van Damme H. & Pellenq R.J.M. (2013) Chapter 14.3-cement hydrates. Pp. 801-817 *In: Developments in Clay Science* (F. Bergaya, G. Lagaly, editors.). Elsevier Ltd, Amsterdam.

Villar M.V. (2000) Caracterización termohidro-mecánica de una bentonita de Cabo de Gata. PhD thesis, Universidad Complutense de Madrid, Spain.

Villar M.V. 2002 Thermo-hydro-mechanical characterisation of a bentonite from Cabo de Gata.Pp 285 in: *A study applied to the use of bentonite as sealing material in high level radioactive waste repositories*. Technical publication. ENRESA 01/2002, Madrid, Spain.

Villar M.V. & Lloret A. (2004) Influence of temperature on the hydro-mechanical behaviour of a compacted bentonite. *Aplied Clay Science,* **26**, 337-350.

Villar M.V., Martín P.L., Bárcena I., García-Siñeriz J.L., Gómez-Espina R. & Lloret A. (2012) Long-term experimental evidences of saturation of compacted bentonite under repository conditions. *Engineering Geology*, **149**–150, 57-69.

Villar M.V., Fernández A.M., Romero E., Dueck A., Cuevas J., Plötze M., Kaulhold S., Dohrman R., Iglesias, R.J., Sakaki T., Zheng L., Kawamoto K., Kober F. (2018) FEBEX-DP Postmortem THM/THC. *Analysis Report.* Pp 142. Nagra NAB 16-017. under review.

Williams L.A., Parks G.A. & Crerar D.A. (1985) Silica Diagenesis, I. Solubility Controls. *SEPM Journal of Sedimentary Research*, **55**, 0301-0311

5.2 BENTONITE/CEM-II CEMENT MORTAR INTERFACE EXPERIMENTS: A PROXY TO IN SITU DEEP GEOLOGICAL REPOSITORY ENGINEERED BARRIER SYSTEM SURFACE REACTIVITY

Daniel E. González-Santamaría[1*], Raúl Fernández[1], Ana. I. Ruiz[1], Almudena Ortega[1], Jaime Cuevas[1]

[1]Department of Geology and Geochemistry, Faculty of Sciences, Autonomous University of Madrid, Cantoblanco, 28049, Madrid, Spain

Abstract

The present study focuses on the interaction between cement mortar (OPC-based CEM-II) and the FEBEX-bentonite; this interaction takes place at a small spatial scale (~1 cm/~1 cm; compacted cement mortar/compacted bentonite thickness) within a timeline of 6 and 18 months. This work was designed to determine the early interaction processes and compare them with large-scale FEBEX *in situ* underground research laboratory experiments. The study aimed at the primary reactions that occurred at the interface in a small spatial scale (nm-µm scale). The experimental device consisted of a composite column containing the cement mortar/bentonite materials. A granitic groundwater solution was injected through the cement mortar/bentonite system and collected out of the column in sequential syringes for analysis of the chemical composition evolution. For the study of the post-mortem samples, an innovative use of grazing incidence X-ray diffraction was performed to determine the phases produced at the interface. Scanning electron microscopy coupled to energy dispersive X-rays and local specific surface area measurements were also applied. The main results showed the initial development of a Mg perturbation in FEBEX-bentonite at the interface related to

the formation of 7 Å precursors of Mg-clay 2:1 sheet silicates as the main neogenic phases expected in the long term. Additionally, a Ca-carbonation skin (calcite) occurred in cement mortar at the interface. The specifications of the reaction products observed at small scales of time and space (μm) are highly promising for the development of reaction concepts and support modelling in the future, which could offer a useful perspective for advancement in the upscaling of concrete/bentonite interface perturbation.

Keywords: deep geological repository, alkaline alteration upscaling, engineered barrier system, cement-bentonite interface, carbonation, Mg silicates hydrates.

Highlights

Cement mortar/bentonite interface reactions occur at short time and small spatial scale

Mg perturbations are visible in bentonite due to the formation of Mg silicates hydrates

Calcite crusts at the interface occur from decalcification in the cement matrix

Al migration from bentonite promotes the formation of ettringite and C-A-S-H into the cement

The specific surface area increases next to the interface

Introduction

In recent decades, concern related to high-level radioactive waste (HLRW) management has been growing. HLRW, mostly spent fuel, is presently safely

hosted within the facilities of nuclear power plants but its storage at long term requires international consensus based on the safest technical and scientific practices due to its long-lived radiotoxicity (10^4-10^5 years). Currently, the deep geological repository (DGR) is considered as the best solution for long-term isolation of HLRW to avoid its release to the biosphere. The DGR is based on a multiple engineered barrier system (EBS), which is placed in a host rock formation (Ewing et al., 2016). Concrete and bentonite are two main components of the EBS when considering granitic bedrock for a DGR. Those materials are exposed to the groundwater from the granite, whose composition depends on the characteristics of each site. Cementitious materials produce alkaline pore fluids with a pH from 10 to 13.5 (Berner, 1992), in contrast with the almost neutral pH of bentonite. This disequilibrium results in geochemical reactions that progress at changing rates during the entire life span of the facility. It is crucial to assure the safety of EBS and to gain full knowledge of the key reaction pathways involved from the initial stages to understand its evolution in the long term. For this reason, efforts are being made to evaluate those disturbances and their evolution at different spatial scale (from small laboratory to real size *in-situ* experiments) and temporal scale (from a few months to over decades). Several approaches are underway, and pertinent knowledge is expected from the study of clay reactions in natural alkaline environments as natural reactivity analogues (Khoury et al., 1985). Long-term concrete/bentonite systems studies at repository scale are available throughout experiments performed in underground research laboratories (URLs). URLs are essential to supplying scientific and technical data from several years to decades of reaction to the real spatial scale of a repository.

The results of cement/clay interaction from large-scale facilities usually offer instant pictures of the resulting reactivity that characterizes interfaces after long

periods of time (e.g. Fernández et al., 2018; Tinseau et al., 2006). However, the interpretation of results is not always straightforward because, due to the large dimensions, the reactivity is heterogeneous. Therefore, knowledge acquired on the reactivity by homogeneous laboratory scale experiments is useful to interpret and predict the reactivity at long-term (Cuevas et al., 2018a).

The state-of-the-art on the alkaline alteration of bentonite has been well described by Dauzères et al. (2010) and reviewed by Gaucher and Blanc (2006) and Savage et al. (2007).

Short-term laboratory-based experiments enable to study different materials in virtually equal controlled conditions in order to compare their behaviour, what is relevant to determine the most suited materials to be implemented, which is currently a discussion issue (González-Santamaría et al., 2018). For example, low-pH cement-base materials (pH<12) were proposed to avoid the extreme alkalinity (Berner et al., 2013) and García-Calvo et al. (2010) demonstrated their resistance to granitic groundwater exposure after 2 years of interaction. In contrast, under the influence of carbonated water, low-pH cements exhibit lower resistance than that of high-pH cements (Dauzères et al., 2016), and hydration products such as ettringite are more unstable (Trotignon et al., 2007). The present short-term experiments might be able to supply complementary data on the early stage of geochemical interactions and evidence for reactions that are implemented in geochemical modelling (Churakov and Prasianakis, 2018). Additionally, this information can aid in the upscaling of processes that take place from months to decades.

This study focuses on the interactions of cement mortar with CEM II (hereafter referred to as cement mortar or CEM II-C) and FEBEX-bentonite. Our objective

is to be able to compare materials interactions similar to those observed after 13 years from the dismantling of the FEBEX *in situ* experiment at the granitic Grimsel Test Site (GTS) URL in Switzerland (Fernández et al., 2017). The FEBEX *in situ* experiment simulated thermo-hydro-mechanical and chemical conditions of a DGR by substituting radioactive waste containers for two metallic heaters. The experiment lasted 18 years but one heater was switched off after 5 years and then extracted. The emptied part of the gallery was sealed with a sprayed concrete plug that remained in contact with the compacted bentonite barrier for the next 13 years until the final dismantling. The methodological approach of the present study is based on the previous procedures developed in a pilot project to study the geochemical reactions on a short-term scale (González-Santamaría et al., 2018).

The experiments performed in this work have been designed to detect early reactions at the interface in a small range extension (nm-µm scale) and have been practised in a composite column containing the cement mortar-bentonite (CB) materials. The innovative use of grazing incidence X-ray diffraction (GI-XRD) and θ-2θ scans on the solid post-mortem samples has been applied to determine the phases produced at the immediate interface of cement mortar and bentonite. The different X-ray diffraction (XRD) techniques applied have been combined with complementary scanning electron microscopy coupled to energy dispersive X-rays (SEM-EDX) and local specific surface area (SSA) measurements. In addition, the effluent displaced out of the column has been determined to study the evolution of the aqueous chemical composition.

Methods

Experimental setup

Cured cement mortar and FEBEX-bentonite (compacted at a dry density of 1.60 g/cm^3) were placed in a methacrylate cylindrical sleeve confined by two stainless steel caps, which constitute a transport cell, and separated by a 0.45 μm polytetrafluoroethylene (PTFE) membrane (Fig. 1). The cell dimensions were 20 mm in internal diameter and 9 mm in height for each material (18 mm in total). The objective of the design was ease of dismantling of the transport cells for further solid characterization, thus allowing the rapid separation of cement mortar and bentonite from the carcase. This design prevented deformation and drying of both materials and also avoided atmospheric interaction. The compact external stainless-steel case (together with connections and filters) was able to resist the high-pressure conditions caused by the hydration of bentonite (Villar and Lloret, 2004). In accordance with the *in situ* conditions at the GTS (Alonso et al., 2017; Fernández et al., 2017), granitic groundwater was injected at a constant 1 MPa hydraulic head through PEEK tubes using an automatic piston pump (Gilson, 307 model). The effluent volume was measured and collected at the bentonite end.

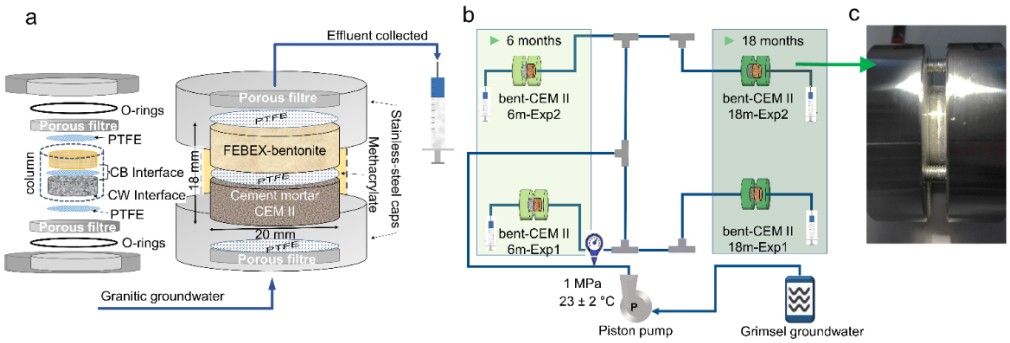

Fig. 1. Design of the transport cells. (a) Transport cells formed by cement mortar/compacted bentonite separated by a PTFE membrane and encased in an open stainless-steel sleeve. A methacrylate cylinder contains the column. Two porous filters allow water transport at both column ends. CB: cement mortar-bentonite interface; CW: cement-water interface. (b) it is represented the experimental scheme of the duplicated cells at two different periods: 6 and 18 months. bent: FEBEX-bentonite, CEM II. Cement mortar with CEM II as ordinary Portland cement (OPC). (c) Photograph of one of the transport cells.

Two duplicated transport cells were run for 6 months, and the other two cells were run for 18 months, under virtually isothermal laboratory conditions (23 ± 2 °C). In fact, this condition is similar to the temperatures expected at the concrete bentonite interface, according to the data obtained from the FEBEX in situ experiment (Villar et al., 2012).

Sampling procedures (subsamples sectioning)

After the experiments were run, the cement mortar-bentonite columns were dismantled and divided into several samples using a cutting machine (Well®2000 model) with a diamond wire saw (Fig. 2) that allows to cut in dry conditions without heating the sample. The cut is slow and the sample is covered with parafilm to protect any interaction with the atmospheric air. The aim was to identify the presence of newly formed mineral phases at the CB-interface by studying the surfaces of the C1 and B1 slices, and the CW-interface was also studied in the external surface of the C3 slice (Fig. 2b) via SEM-EDX.

To assess the evolution of the materials in terms of distances, subsamples with 3 mm thickness sliced parallel to the interface were cut (Fig. 2b) for XRD and SSA analyses. After vacuum drying and grinding, cement mortar samples were stored in a hermetic chamber in the presence of NaOH lentils to prevent absorption of CO_2 by the cement-mortar, at a relative humidity (R. H.) <10%. The FEBEX-bentonite slices were also ground and equilibrated in 50% R. H. before XRD analysis to rehydrate the exchangeable cations and stabilize the smectite basal spacing.

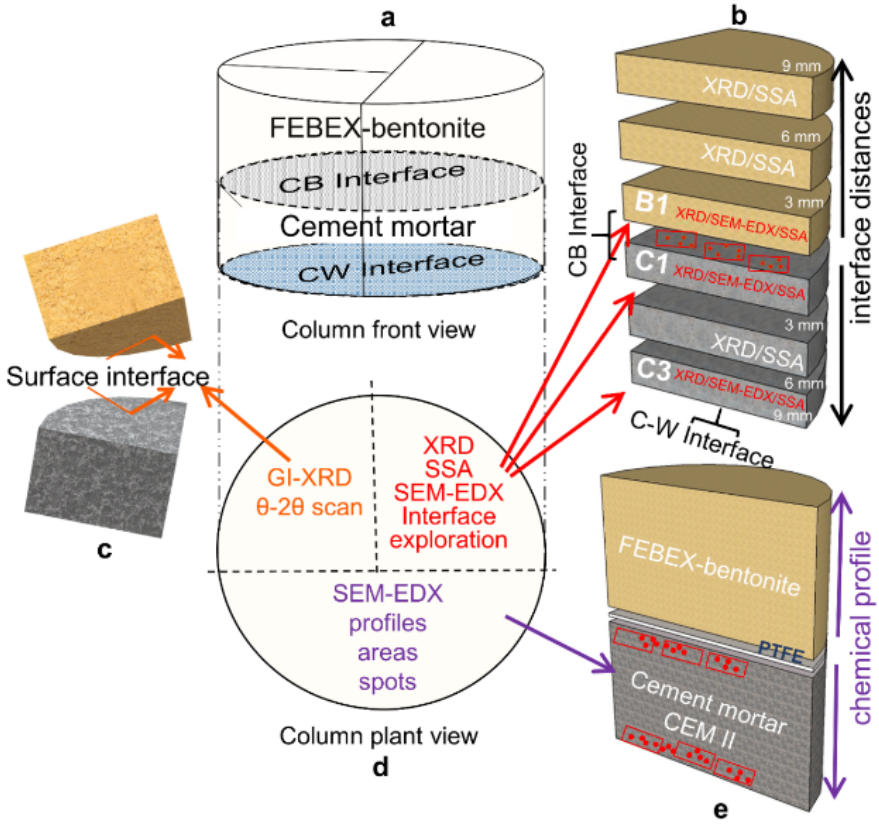

Fig. 2. Cutting and sampling scheme. (a) Front view with CB-interface and the CW-interface drawn (grey and blue ellipses). (b) Sample segmentation for XRD, SSA measurements and previous SEM-EDX exploration of the surface interfaces in slices B1, C1 and C3. (c) Sample quarter for GI-XRD and θ-2θ scans. (d) Plan view of the column. (e) Half column cut to show both the complete profile and also areas and punctual analysis next to the CB and CW-interfaces by SEM-EDX.

GI-XRD and θ-2θ scans of the cement and bentonite interfaces (facing the PTFE membrane) were conducted on one of the cut quarters (Fig. 2c). The remaining flat surface of the half column perpendicular to the interface (Fig. 2e) was polished after freeze-drying treatment and was subsequently embedded in epoxy resin. Epoxy resin does not enter the materials and serves as a protective framework to confine the sample without destroying its integrity during the polishing operation, although the freeze-drying process can destabilize ettringite and other cement hydrates. After polishing, the sample was prepared for elemental chemical profiling via SEM-EDX. The linear transect selected to determine the elemental composition profile of the entire column was obtained using the CB-interface as the origin of distance coordinates. EDX measurements were collected towards the bentonite end of the column and towards the interface with the infiltrating groundwater solution (CW-interface) crossing the cement mortar. These analyses were performed in additional detail next to the CB-interface, with area dimensions of 10 μm height × 100 μm width in the direction perpendicular to the CB-interface. The following 5 analysis were executed with dimensions of ~50 μm × 500 μm, followed by 7 and 16 analysis towards the bentonite column end and 10 analysis towards the CW-interface with dimensions of 100 μm × 1200 μm and 500 μm x 3000 μm, respectively. A similar methodology can be found in (Fernández et al., 2017; González-Santamaría et al., 2018) and Fernández et al. (2017). A schematic sketch of the number of analyses and increasing areas is shown in the latter paper.

In the same half sample (Fig. 2e), the CEM II-C side was analysed as follows. Three rectangular areas of approximately 1 mm^2 were registered for major element quantification near the CB and CW-interfaces (Fig. 3a). Within these areas, punctual (also referred as spot) EDX analyses of the cement matrix were

conducted at 200x magnification, and at least 7 spots were acquired in representative fields for the cement matrix (Fig. 3b).

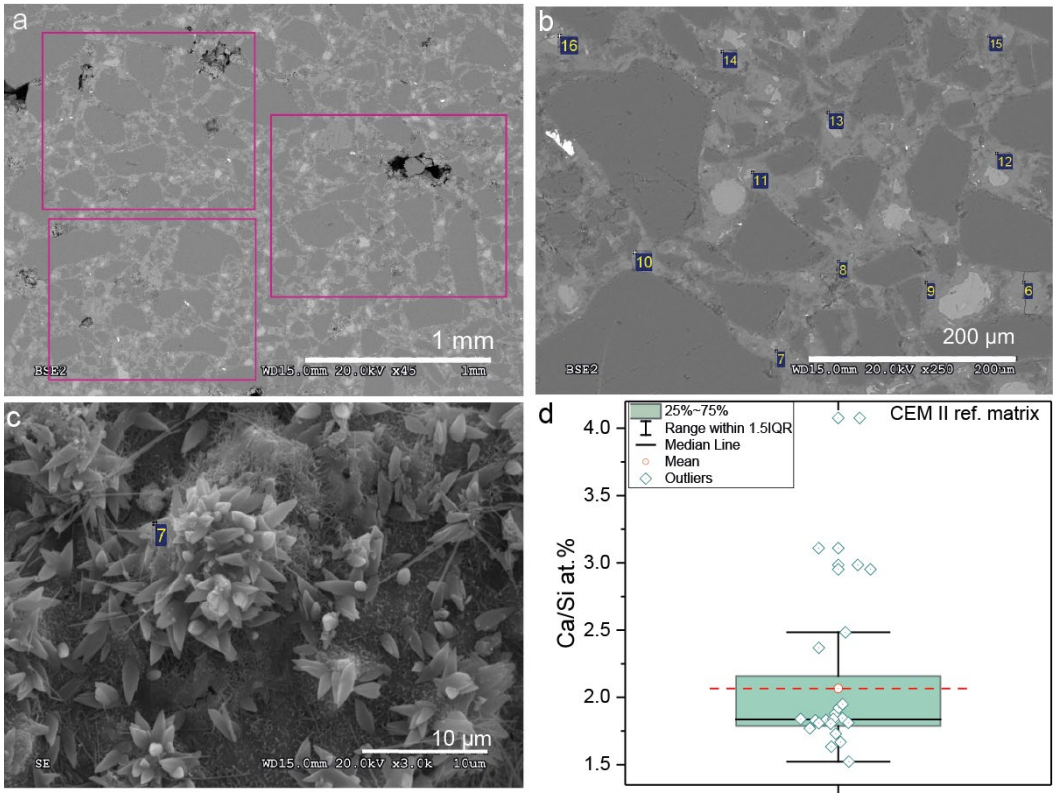

Fig. 3. SEM backscattering images from (a) area analyses conducted at 45x magnification, (b) matrix spot analysis locations conducted at 200x magnification and (c) micrograph in which calcium carbonate (bi-sphenoids) and ettringite needles are supported in the C-S-H cement matrix, and (d) statistical analysis of the Ca/Si atom ratio in the cement matrix.

Analytical techniques

XRD analysis of randomly oriented cement mortar and bentonite powders (samples shown in Fig. 2b) were conducted using a θ-2θ X'Pert PANalytical instrument with an X'Celerator detector. XRD patterns were recorded in an angular range of 3-70° 2θ. The detector allowed measurements equivalent to 0.016° angular steps for 100 s at each step. The voltage and intensity of the

operated X-ray Cu tube were 45 kV and 40 mA, respectively. Complementarily, the GI-XRD analysis and θ-2θ scans were performed at both surfaces of the CB-interface (samples shown in Fig. 2c) to assess the perturbation that occurred in the first microns. The GI-XRD was configured with a fixed incidence angle of 0.5° 2θ. Both measurements were performed using 0.04° and 2 seconds of angular step and time step increases, respectively. Finally, the angular range recorded was 3-70º 2θ.

The SEM-EDX equipment was run on a Hitachi S-3000N scanning electron microscope coupled to an INCAx-sight Oxford Instruments™ energy-dispersive X-ray analyser. EDX semi-quantification of major elements was performed using internal standard semi-quantitative analysis. The statistical quality of elemental concentrations is detailed in (González-Santamaría et al., 2018). In summary, on the cement mortar side and for elements > 20% (Al, Si, Ca), the instrumental % deviations obtained were less than 10% because their concentrations were lower for silicon (<1%), Ca (<5%) and higher for Al (9%). For elements with contents within 1–5% (Mg, Ca, K, Fe), the percentage of deviation from the average of the measured values was typically 10–15%. Punctual analysis acquired in EDX areas or spots acquired for characterizing cement matrix or phase composition were treated with IBM® SPSS® Statistic software. Test one-way ANOVA, multiple comparisons (Post Hoc Test) and test KrusKal-Wallis (p-value<0.05) were done to compare the different groups of experiments.

Specific surface area (SSA) was measured by means Gemini V porosimeter Micromeritics® equipment to relate the external surface and size of particles present in the materials. The technique is based on the method of adsorption of N_2(g) as analysed by the Brunauer, Emmett and Teller (BET) equation (Webb and

Orr, 1997). Bentonite samples were heated at 90 ºC for 24 h in a sample holder and then outgassed in a nitrogen current for 2 h in a degasification station before measurement, as in Cuevas et al. (2016). However, cement mortar samples were only heated for 2 h, instead of 24 h, to prevent dehydration of hydrated cement phases.

The aqueous effluent parameters picked up by the disc in the disposed syringe were analysed using a Metrohm 888™ automated potentiometric titration device for measurement of pH and alkalinity. Silica was determined by visible spectrophotometry using the molybdate blue complex method in a Milton Roy Spectronic® instrument at a wavelength of 825 nm. The major chemical ions were analysed with ion chromatography equipment coupled to a conductivity detector (IC-CD) using a Metrohm 802 compact IC plus model. Additionally, the hydraulic conductivity was also calculated for each transport cell by periodical weighing of the collection syringes to measure the flow rate and applying the Darcy's law.

Materials

Granitic groundwater

The main characteristics of the groundwater obtained from the GTS are its notably diluted composition of Na^+, Ca^{2+}, HCO_3^-, Cl^-, and SO_4^{2-} ions. GTS-groundwater has a value of 104 µS/cm for electrical conductivity, and the main ions concentrations (mg/L) are Cl^- (3.5), SO_4^{2-} (9.6), HCO_3^- (42.7), Na^+ (11.5), K^+ (<0.1), Ca^{2+} (12.0), and Mg^{2+} (<0.1), with a pH of 8.1 (Torres et al., 2019).

FEBEX-bentonite

FEBEX-bentonite was obtained from the Cortijo de Archidona deposits (Caballero et al., 2005) and contains more than 90% montmorillonite (Mnt) and variable quantities of quartz (qtz; (2 ±1), plagioclase (pl; 3 ± 1), K-feldspar (Kfp; (< 1), calcite (Cal; < 1) and cristobalite (Crs; 2 ± 1). The FEBEX-bentonite contains approximately 1/3, 1/3 and 1/4 cmol (+ charge)/kg of Mg^{2+}, Ca^{2+} and Na^{+} exchangeable cations, respectively, for a cation exchange capacity (CEC) of 102 ± 2 cmol(+)/kg. The physical-chemical properties of the FEBEX bentonite and its most relevant thermo-hydro-mechanical and geochemical properties have been studied and are published elsewhere e.g.(ENRESA, 2006).

The bentonite, milled to a grain size < 1 mm, was compacted with its hygroscopic water content (13 wt.%) at room temperature conditions (23 ± 2°C) and at a nominal dry density of 1.60 g/cm^3 inside the methacrylate sleeve, where the cement mortar was previously hardened.

Cement mortar

Cement mortar was prepared with CEM II/A-L 42.5 R cement formulated with powder limestone addition (10%). Subsequently, a 1/2.4 ratio of distilled water/cement and a 1/3 ratio of cement/silica sand (grain size <1 mm; 99% of quartz) were added. The materials used to prepare the CEM II-C were supplied by the Eduardo Torroja Institute for Construction Science (CSIC-IETcc) and were cast inside a methacrylate sleeve, uniaxially pressed at 1-2 kg/cm^2 and covered by pressing of a circular PTFE porous membrane. The cast CEM II-C was cured in a water-saturated chamber (100% R. H.) for 90 days. After the CEM II-C was cured, the compacted FEBEX-bentonite was emplaced.

The SSA of the cement mortar was 9.3 ± 0.1 m^2/g, and the pH value measured in the pore solution following the *ex situ* method of (García Calvo, 2012) was 12.2 ± 0.1.

To obtain an initial reference sample, the CEM II-C was prepared and characterized in manner similar to that of the other experimental samples.

The average elemental composition obtained by EDX analyses of the areas acquired at 45x magnification (approximately 1 mm^2) and the matrix punctual analyses acquired at 200x magnification are shown in Table 1. See that punctual analyses exclude mortar aggregates, mainly quartz grains, and consequently the Si content decreases in the cement matrix, increasing thereby the rest of elements.

Table 1. Chemical composition of CEM II cement mortar (CEM II-C) and average composition of cement matrix. Major elements are recalculated to 100%

	Areas at 45x mag	Matrix at 200x mag
At.%	Mean ± Sx (3-5 areas)	Mean ± Sx (7 spots)
Mg	n.d.	n.d.
Al	2.36 ± 0.30	3.54 ± 2.85
Si	74.70 ± 1.29	30.62 ± 6.75
S	1.24 ± 0.39	2.26 ± 0.76
K	n.d.	n.d.
Ca	20.46 ± 1.01	60.39 ± 7.56
Fe	0.65 ± 0.09	0.85 ± 0.54

Sx: Standard deviation, At.%: atomic percentage, mag: magnification, n.d.: not detected. Areas and matrix analyses are shown in Fig. 3a-b.

The XRD powder patterns showed the presence of calcite, gypsum, quartz, and phases commonly present in the hydrated cement, namely, portlandite, ettringite, ferrite and dicalcium/tricalcium silicate anhydrous phases (see section 4.3). Calcium silicate hydrates (C-S-H) are the major hydration products and binding phases in cements, but they were not detected by XRD because they do not diffract

well (Techer et al., 2012). Instead, C-S-H were observed by SEM-EDX as nano-crystalline phases, mostly identified by their chemical composition because the SEM resolution do not reach the nm scale.

The presence of anhydrous phases determined by XRD is coherent with the analysis conducted at 200x magnifications for the characterization of cement mortar matrix. The median Ca/Si ratio based on 26 analyses ranged from ~1.7 to 2.0 (Fig. 3d). In general, this ratio indicates an excess of Ca, overestimated due to the size of the microanalysis area and the existence of limestone microparticles (Alonso et al., 2017). Several determinations exceed a Ca/Si ratio of 2.3 that clearly indicates that contribution. The SEM-EDX exploration confirmed a combination of phases determined by the presence of ettringite, portlandite, calcium carbonate (identified as calcite by XRD), and C-S-H (Fig. 3).

Results

SEM-EDX

- *SEM-EDX 45x (bulk cement mortar) and 200x (cement mortar matrix) analysis areas*

Only the cement mortar side was analysed at 45x and 200x magnification because the bentonite composition is rather homogenous under area or spot analyses, and its variation is better described by EDX elemental profiles (see section 4.1.2). The area and spot measurements performed on the CEM II-C were acquired to assess the evolution of the entire cement mortar material and the matrix of the cement mortar, respectively. The data from the duplicated cells were grouped into 6 and 18 months, representing averaged values for each experiment.

The bulk cement mortar compositions acquired from area analyses at the CB or CW-interfaces after interaction are compared with the composition of the reference cement mortar in Table 2. The CB-interface shows a significant decrease in Ca and Si after 6 months. Conversely, Ca increases again up to the initial values after 18 months. In the CW-interface, Ca leaching after 6 months is not important and highly variable. Additionally, Mg is detected in the composition after 18 months at both the CB and CW-interfaces. Overall, no statistically significant differences were observed with respect to the area analyses.

Table 2. EDX area analyses performed at different time-scales (0, 6 and 18 months) and interfaces (CB and CW). Averaged values include standard deviations.

	Reference	CB-interface		CW-interface	
Element (At.%)	0 months	6 months	18 months	6 months	18 months
Mg	n.d.	n.d.	0.28 ± 0.16	n.d.	0.24 ± 0.13
Al	2.36±0.30	2.54±0.85	2.48±0.38	1.58±0.43	2.39±0.31
Si	74.70±1.29	80.08±2.87	74.10±2.10	77.31±4.48	72.88±4.07
S	1.24±0.39	0.76±0.39	1.47±0.39	0.86±0.21	1.12±0.37
K	n.d.	n.d.	n.d.	n.d.	n.d.
Ca	20.46±1.01	15.54±2.27	20.90±1.44	19.09±4.77	22.60±3.44
Fe	0.65±0.09	0.76±0.26	0.76±0.14	0.88±0.16	0.73±0.29

At.%: atomic percentage, n.d.: not detected.

At the CB-interface, the cement mortar matrix compositions showed an averaged significant decrease in the Ca/Si ratio from the reference (0 months; ~ 1.8) to 6 months (~1.5). After 6 months, this parameter remained stable until 18 months (Fig. 4a). Independently of the time of reaction, the Ca/Si displays a spread of values from 1.2 to 1.8, showing an uneven degree of hydration and decalcification of C-S-H. The spread of the Ca/Si ratio data is slightly larger after 18 months, with notably high values (>2), presumably due to calcite precipitation. In contrast, values < 1.0-0.6 are more typical of low Ca/Si tobermorite, C-S-H or C-A-S-H.

The presence of C-A-S-H is detected in the CB-interface with Al/Si ratios that are clearly higher than in the reference cement mortar matrix (Fig. 4b).

At the CW-interface, the Ca/Si ratio does not decrease at the same rate as at the CB-interface. The slightly decreasing shift from 0 to 6 months and from 6 to 18 months is consistent with the presence of hydrated and lower Ca/Si C-S-H phases. Both interfaces show more dispersed data for the cement matrix than the reference.

The differences in distribution of Al/Si (Fig. 4b) were significant across categories of interfaces (CB-CW-interface) but not significant across the time scale (6 and 18 months experiments).

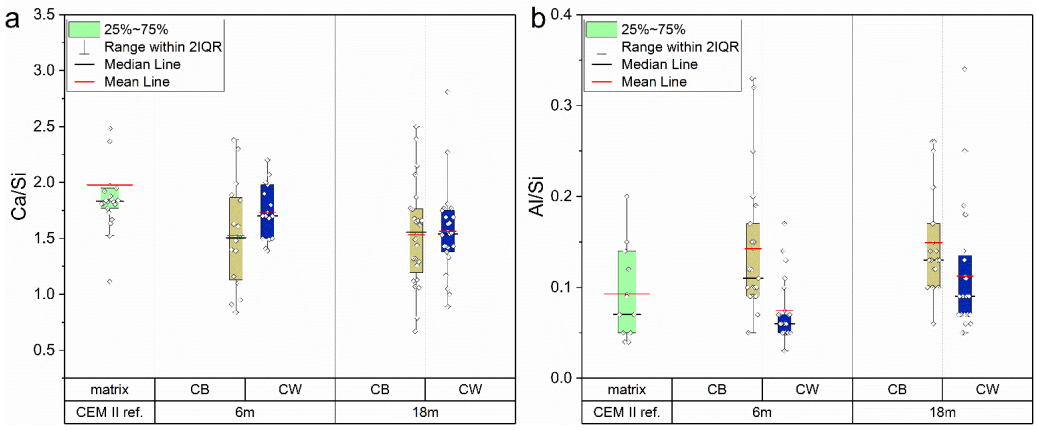

Fig. 4. Box plot of the Ca/Si ratios (a) and Al/Si ratios (b) analysed in the matrix of the cement mortar. Horizontal black lines inside the box charts represent the median value of the data. Colour boxes indicate the values contained within the 25-75% interquartile range (IQR), the range of the vertical bars extent to 2 IQR, median line is shown in black and mean line in red.

- *SEM-EDX profiles of chemical composition in cement mortar and bentonite*

The chemical evolution of Si, Ca, Al and Mg as a function of time (6 and 12 months) in cement mortar and bentonite is presented in Fig. 5a. In general, the Ca content shows a maximum on the cement mortar interface side, and Mg increases

in the bentonite at the CB-interface. These anomalies are accompanied by the decreasing of Si and Al.

At the bentonite side, Mg concentration increased substantially in a length < 1000 μm from the CB-interface (from approximately 5 to >20 at.% within the first 50 μm), but the increase of concentration from 6 to 18 months was short (Fig. 5a).

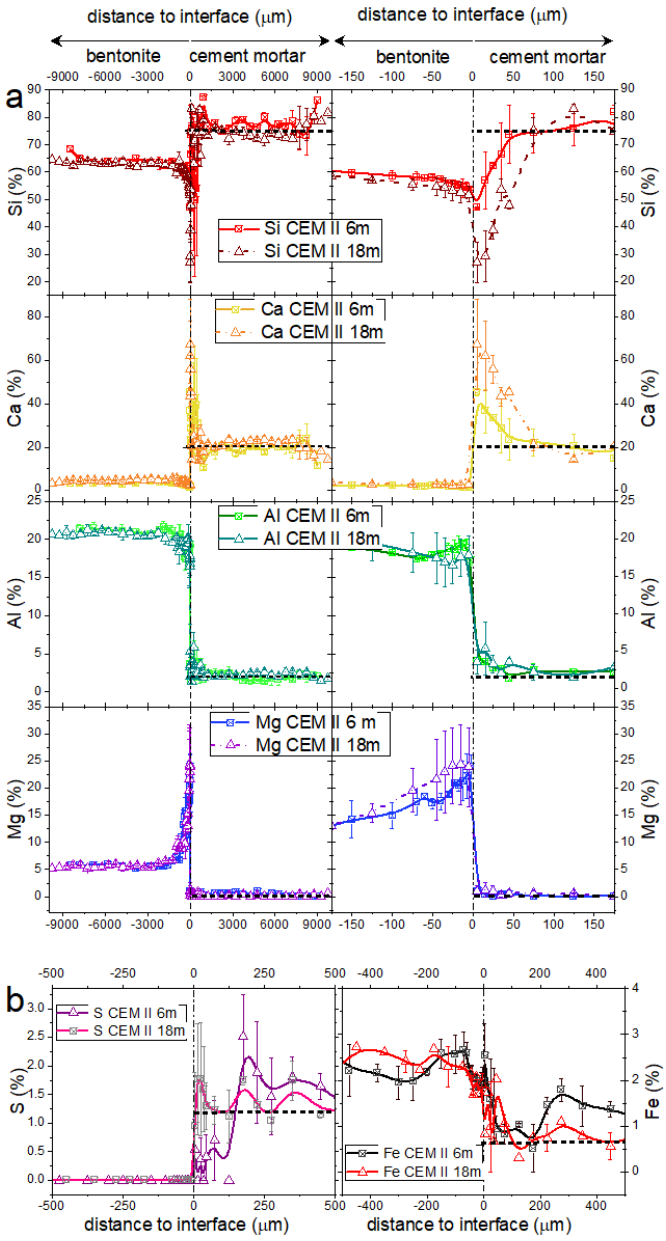

Fig. 5. Chemical profiles of composition in bentonite-CEM II cement mortar experiments after 6 and 18 months. All profiles were obtained based on the average values of the duplicated experiments and include error bars of standard deviation. Each profile is depicted at different ranges: from -9000 to 9000 μm (left column) and from -200 to 200 μm (right column) (a). The CB-interface (placed at 0 μm, black dashed line) was taken as a reference. Additionally, a reference horizontal dotted line of the unaltered cement mortar reference sample is plotted for each element. Separately, the S and Fe profiles nearest to CB-interface (0-500 μm) are plotted at the bottom of figure (b).

Ca increases its relative concentration near the CB interfase, in the cement mortar side. As for Mg, an increment of Ca concentration is observed from 6 to 18 month, but in this case, the increment is significant (20 at.% initially, 40% after 6 months and 60% after 18 months, as maximum averaged values). Therefore, the processes associated to the Ca enrichment does not seem to have reached a stationary state. Such a high increase is followed by a 1-2 mm Ca minimum, which is less pronounced after 18 months. This minimum agrees with the decalcification of C-S-H (lower Ca/Si ratios at the CB interface in Fig. 4a) and a presumably portlandite dissolution zone that causes calcite precipitation at the cement mortar side, as further confirmed by the GI-XRD study (section 4.3.1).

According to the possibility of C-A-S-H formation in the CB-interface, the Al profiles tend to increase with time in the first μm of the cement mortar side (<25 μm). Fig. 5b shows the profile evolution of S and Fe in a narrow -500 to 500 μm band. S is depleted after 6 months but is relatively concentrated in the cement mortar side of the interface after 18 months. However, a certain amount of transfer of Fe from bentonite to cement matrix is evident with rather irregular distribution.

- *SEM-EDX: surface interface crystal aggregate morphologies and composition*

The nature of the Ca or Mg anomalies detected, mainly at the CB-interfaces and occasionally at the CW-interfaces (in the case of Ca), were first approached by exploration of singular crystal aggregates found in the fresh pristine surfaces separated at the end of the experiments. The composition of singular phases determined in the surface interfaces corresponding to B1, C1 and C3 slices and their distribution are indicated in Table 3. The characteristic morphologies and

polycrystalline aggregates identified are illustrated by the SEM micrographs (Fig. 6).

Regarding to the bentonite interface, high Mg/Si platy (flat) and sheet (curled) like morphologies forming sometimes a Mg-rich crust were identified in B1 at any time (Fig. 6a and 6b). As for cement mortar side, the surface of the interface from C1 subsample was plenty of euhedral sphenoidal calcite microcrystals precipitation resulting in the formation of carbonated crusts (Fig. 6c, 6e, 6g). In addition, C-S-H, C-A-S-H, ettringite (6f, 6i and 6d, respectively) and hexagonal platy morphologies of Cl-Aluminium Ferrite monosulfate phases (AFm), presumably Friedel salt-monosulfate AFm phases, (Fig. 6h) were observed. Mainly ettringite was found as the main mineral phase, either in C1 (from the CB-interface) or C3 (from the CW-interface) and was significantly less frequent in the 18 months experiments at the CW-interface, indicating dissolution in this extreme.

Table 3. Summary of the observed phases and morphologies localized in slices B1-C1 (CB-interface surfaces) and C3 (CW-interface surfaces)

Exp	Surface interface	High Mg-Si crust/matrix	Mg-Si rich platelets	*C-A-S-H	Calcite	**Ettringite	***AFm	****C-S-H
	B1	X			X(-)			
18-Exp1	C1			X	X			
	C3					X		
	B1	X	X		X(-)			
18-Exp2	C1		X	X	X	X	X	
	C3			X				
	B1	X			X			
6-Exp1	C1				X(+)	X(+)	X(+)	X(+)
	C3							
	B1	X	X(-)			X		
6-Exp2	C1			X		X	X	
	C3					X(+)	X	

*C-A-S-H: Calcium aluminium silicate hydrate (Al/(Al+Si) = 0.2, and Ca/Si ~ 0.8). **Ettringite (Al/S= 0.7, and Ca/S = 2). ***AFm: Calcium aluminium monosulphate (Al/S > 2; Ca/S > 4). ****C-S-H: Calcium silicate hydrate: Ca/Si = 0.6-2.3). X, (+), (-) indicate “presence”, “high presence”, and “medium-low presence”, respectively. Exp: experiments.

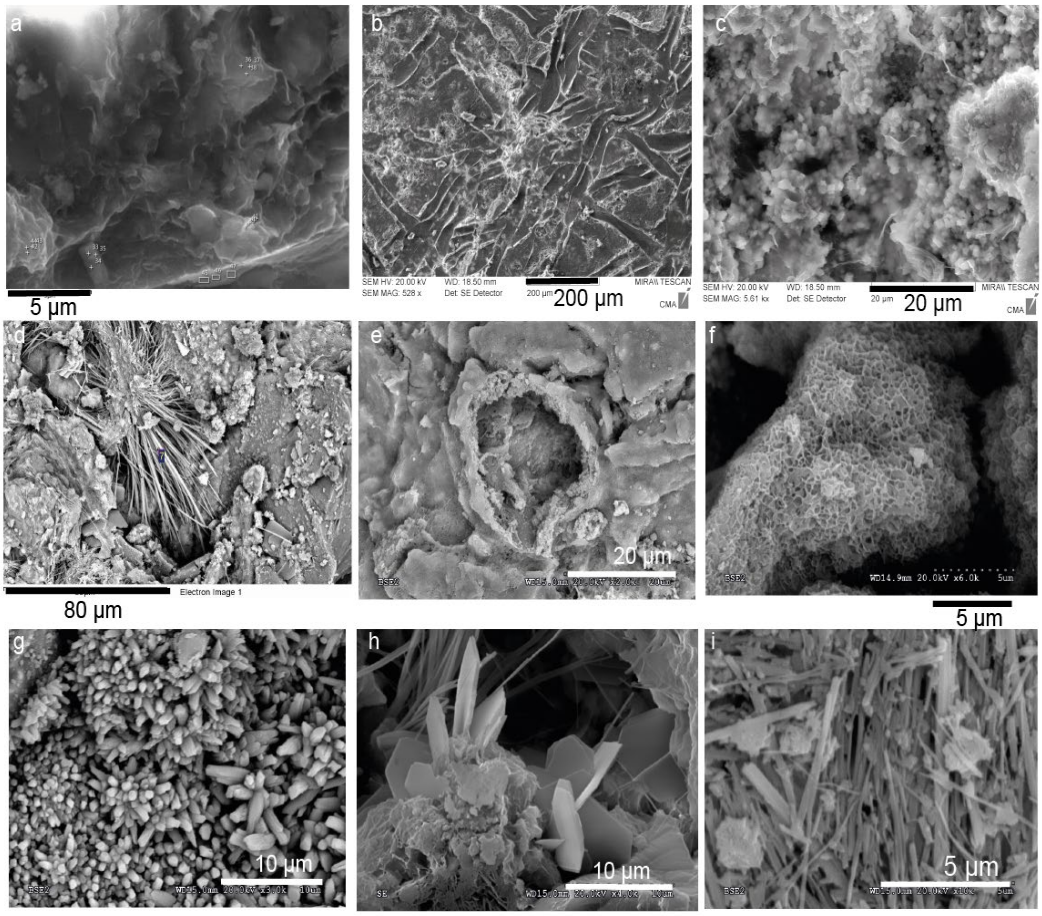

Fig. 6. SEM micrographs of the summary of phases and morphologies found in fresh pristine surface interfaces from B1-C1-C3 slices. (a) Mg-Si-rich platy morphologies. (b) Mg-Si-rich crust shaped by fibres of the PTFE membrane. (c) Calcite crystals growing among C-S-H. (d) Ettringite needles observed after 6 months in C1. (e) Calcite crust. (f) C-S-H. (g) Calcite sphenoidal crystal aggregates observed after 6 months. (h) Ca-Al-(S, Cl) crystals. (I) C-A-S-H needles. (Identification was made according to the chemical formula and the EDX).

X-RAY DIFFRACTION ON BENTONITE

- *GI-XRD 0.5° and θ-2θ scans on bentonite*

The GI-XRD analyses and θ-2θ scans under the GI-XRD configuration facilitated study of the mineralogy in the first 10 μm of the surface interface of bentonite exposed to the influence of the CEM II-C porewater (Fig. 7a). The difference between GI-XRD 0.5 º and θ-2θ used in this description is that the first is more superficial and the second corresponds to the diffracting result of higher sample volume.

The diffractograms at the interface of the reacted surface bentonite samples are characterized by the presence of 7.6-7.4 Å broad reflections not visible in the reference bentonite. These reflections were developed in all the θ-2θ scans, but they are not developed in the GI-XRD analyses performed on samples that reacted for 6 months. At lower angles, a critical intensity declines of the 14-15 Å reflection was observed, more generalized after 6 than after 18 months. In addition, a small shift is detected from 15.0 Å in the bentonite reference towards 14.8-14.5 Å in both sets of experiments (6 and 18 months). This shift is correlated with a small decrease in the position of the second-order basal reflection at 4.9-4.8 Å *d*-spacings, that becomes significantly more intense compared with the reference sample. These effects are better visualized by the θ-2θ scans in all experiments.

Characteristic di-octahedral Mnt reflections at 1.49 Å were found in the reference bentonite, and a broad band centred in 1.54-1.53 Å is always present in the reacted bentonite samples, indicating a tri-octahedral component that can be linked to the Mg/Si increase near the interface with the cement mortar. Quartz is occasionally present, as evidenced by a sharp reflection at 1.55 Å.

With respect to the more superficial GI-XRD 0.5º analysis, a broad reflection at 1.54-1.53 Å, observed after 18 months, is not present after 6 months neither the reference bentonite, which could be an indication of the precipitation of a tri-octahedral phase at long term. The 14-15 Å reflection, characteristic of the basal spacing of smectite is not present, indicating that the neogenic clay mineral presents high stacking disorder at the surface.

It is important to note how the θ-2θ scans demonstrate the presence of the calcite 3.03 Å peak, which is not detectable in the reference sample, thus confirming that the carbonation is not homogeneously distributed at the first microns of the bentonite interfaces.

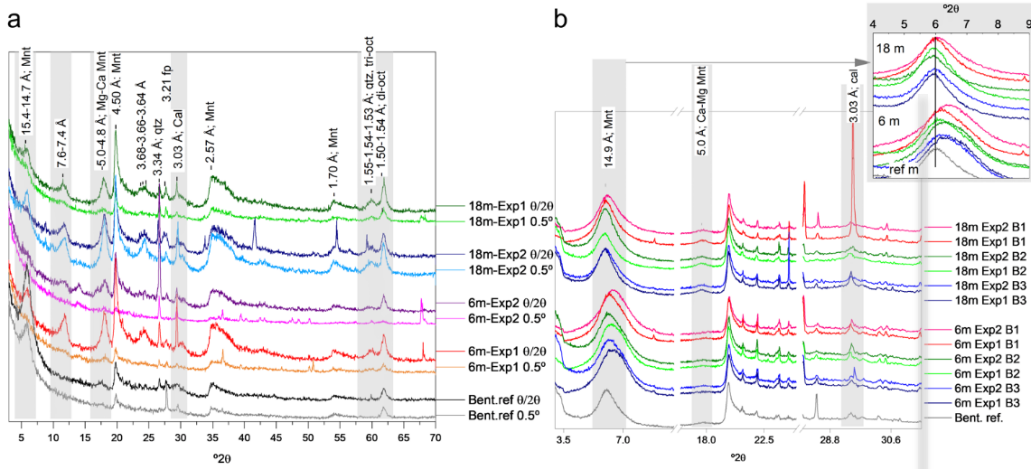

Fig. 7 (a). GI-XRD analyses and θ-2θ scans over flat fresh solid subsamples from the surface of bentonite. Numbers indicate d-values in Å; Mg-Ca Mnt: Mg-Ca montmorillonite, qtz: quartz, fp: feldspars, Cal: calcite, di: di-octahedral sheet, tri: tri-octahedral sheet. (b) XRD on randomly oriented powder bentonite samples at different distances from the interface (0-3 mm at B1; 3-6 mm at B2; 6-9 mm at B3) and different time scales (6 and 18 months). Upper right corner: close-up image of the (001) basal reflection region (4-9° 2θ). Bent. ref: diffractograms of the unaltered reference bentonite.

- *Random powder X-ray diffraction on bentonite*

The XRD analyses on powder samples supply information on the time evolution and spatial alteration of bentonite as a function of distance from the CB interface (Fig. 7b). Subtle variations were found in the (001)-reflection region (5-8° 2θ position). Two shifts can be observed in that region related to the time evolution. First, the reference bentonite diffractogram shows reflections at ~15.0 Å, and the diffractograms obtained after 6 months present these reflections at ~14.5 Å, with a tail towards high angles compared with the 18 months experiments, where the basal reflection increases again to 15 Å and is more symmetrical. This differentiation in the basal space might be related to a change of the cations population in the interlayer. The initial Ca-Mg bentonite becomes slightly richer in monovalent cations (Na^+, K^+) as a result of local precipitation of Ca and Mg phases, however, the rate of transformation decreases with time and the population distribution is further homogenized as a result of the preferential leaching of monovalent cations out of the column (section 4.5).

In contrast to the small perturbations detected in Mnt by XRD on randomly oriented powder samples, the presence of the 3.03 Å reflection, characteristic of calcite, in one of the B1 slices run for 18 months (close to the cement mortar) is significant compared to all the other diffractograms. This observation is in agreement with the presumable calcite precipitation at both sides of the interface.

X-RAY DIFFRACTION ON CEMENT MORTAR

- *GI-XRD 0.5° and θ-2θ scans on cement mortar*

The main geochemical perturbations that can be remarked by XRD on the cement mortar are related to the evolution of ettringite, gypsum, portlandite and calcite mineral phases as they are well crystalline (Fig. 8a).

Distinctive reflections of gypsum and portlandite (7.6 Å and 4.9 Å, respectively) were identified in the reference CEM II-C but are absent after 6 and 18 months.

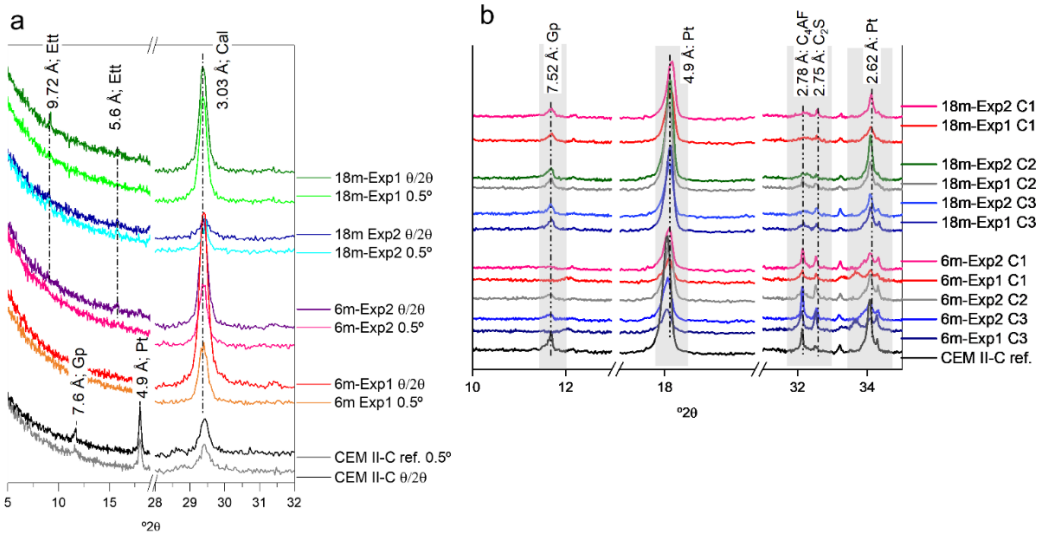

Fig. 8. (a) Close-up view of the θ-2θ scans and GI-XRD analyses performed on the flat surface interface of CEM II-C. (b) Close-up view of the XRD patterns of cement mortar on randomly oriented powder samples at different distances from the interface (0-3 mm at C1; 3-6 mm at C2; 6-9 mm at C3) and at different time scales (6 and 18 months). Numbers indicate d-values in Å. Ett: ettringite, Cal: calcite, Gp: gypsum, Pt: portlandite, C_4AF: calcium aluminoferrite, C_2S: di-calcium silicate.

Characteristic reflections of ettringite (9.8 Å and 5.6 Å) were found after 6 and 18 months, but these reflections did not appear evident in the reference CEM II-C. Most of the ettringite found can be considered as secondary ettringite.

The reflections at 3.03 Å, 3.86 Å, 1.91 Å and 1.87 Å, characteristic of calcite, increase in intensity as time evolve. This is observed comparing the reference cement mortar with the altered cement mortars after 6 and 18 months, however, there is a substantial variation comparing the duplicated experiments. These variations indicate that the uneven distribution in calcite coatings might be better developed in macropores, as shown in Fig. 6g.

- *Random powder X-ray diffraction on cement mortar*

As observed for the bentonite slices, subtle differences were found in cement mortar by XRD on randomly oriented powder samples (Fig. 8b). A detailed study of the range between the 32 and 33 º2θ positions shows an intensity decrease in the characteristic reflections of anhydrous phases, such as calcium aluminoferrite (C_4AF) and di-calcium silicate (C_2S) after 18 months (2.74 Å and 2.78 Å, respectively). These rearrangements occur as a result of progressive hydration of the anhydrous phases and the formation of secondary C-S-H characterized by a disordered structure and broad and weak diffraction maxima (Grangeon et al., 2013), which complicate their identification.

Minor differences were also found in the spatial progress by the study of samples C1, C2 and C3. The 6 and 18 months experiments showed a small decrease in the 7.56 Å reflection, characteristic of gypsum, and the reflections at 4.9 and 2.62 Å, characteristic of portlandite, suggesting their dissolution (Fig. 8b). However, the increase of calcite reflections, previously shown by the θ-2θ scans in the first μm of the surface interfaces, were not found across C1, C2 and C3 and, therefore, the carbonation process could occur only in a close spatial range at the immediate proximity to the interface with bentonite.

SPECIFIC SURFACE AREA

The SSA analyses performed throughout the bentonite and cement mortar slices to assess their spatial and temporal evolution are shown in Fig. 9. At the bentonite side, three main observations can be outlined: (*i*) the lower SSA values compared with the reference bentonite, (*ii*) the decrease in SSA from 6 to 18 months, and (*iii*) the decreasing tend of SSA away from the interface. At the CEM II-C side, C3 slices (facing the water interface) presents a slightly higher SSA than the reference sample. In addition, as time evolves from 6 to 18 months, the C2 and C1 slices increase in SSA.

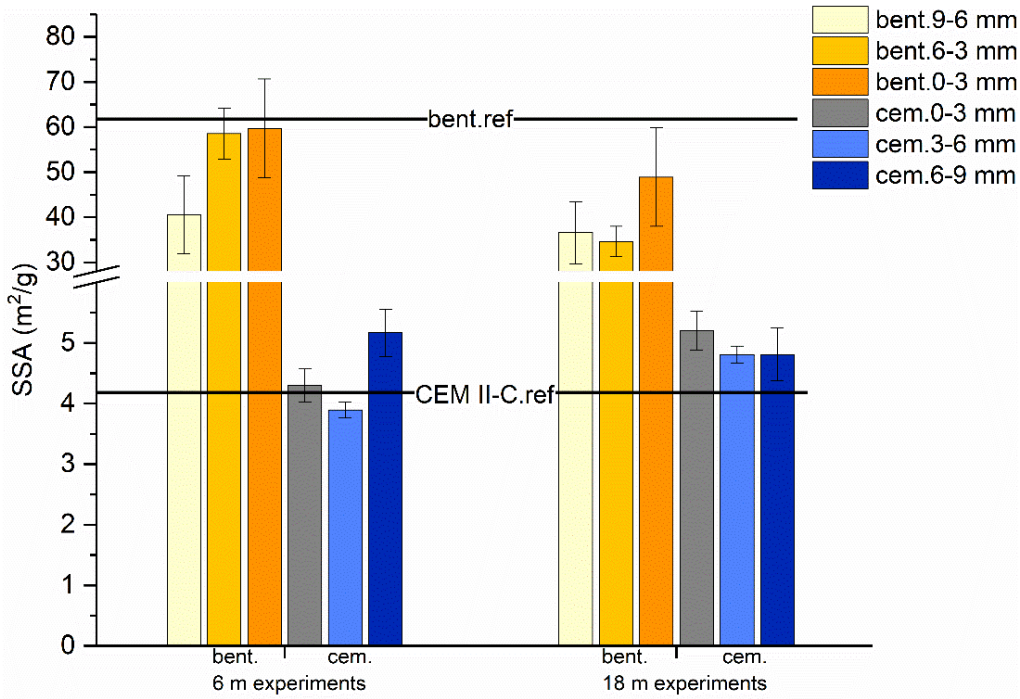

Fig. 9. SSA of bentonite and CEM II-C as a function of distance from the C-B interface. Note that the CB-interface is located between the orange and grey bars, and the CW-interface is located at the end of the dark blue bars.

EFFLUENT PARAMETERS

The hydraulic conductivity (H.C.) was calculated by the outflow data considering that the initial time corresponds to the beginning of the infiltration. The H.C. remains stable in the range 10^{-12}-10^{-13} m/s (Fig. 10a) for the whole experimental time (up to 18 months). In the averaged experiments performed for 6 months the H.C. is higher than in the experiments performed for 18 months, but this should only be attributed to random differences derived from the preparation of the initial materials that are not completely homogeneous. The accumulated volume of effluent collected in one of the experiments run for 6 months was similar to those collected in the experiments run for 18 months, indicating the presence of preferential pathways for fluid circulation in that specific experiment. As the data are presented as averaged values for experiments performed for 6 and for 18 months, the error bars for the 6 months experiments in Fig. 10a are large.

Bentonite is compacted at its characteristic water content (approximately 14 wt.%) in its dried state at the laboratory ambient conditions (30 – 50% R. H.) therefore, the initial conditions are unsaturated. Aqueous SO_4^{2-}, Cl^-, Na^+ and K^+ are leached initially in higher concentrations than all other ions and correspond with the displaced bentonite porewater (Fig. 10b), known to be concentrated in these ions (Cuevas et al., 2002). SO_4^{2-} is almost exhausted after 7-8 pore volumes (one pore volume is calculated as the total porosity of bentonite, ~1.3 cm^3), whereas Cl^- decreases drastically its concentration at the beginning and gets mostly exhausted after 13-14 pore volumes. Na^+ is the dominant cation and achieves a low constant value after 6 – 10 pore volumes, presumably regulated by the cation exchange equilibrium ruled by Mnt, since Na^+ is the less selective cation in the cation exchange equilibrium concerning the FEBEX bentonite (Fernández et al., 2004). The alkalinity represented mainly by HCO_3^- (with certain contribution of CO_3^{2-},

not accounted in the charge balance), becomes the main anion with time (after 6 pore volumes). The Ca^{2+} concentration critically decreases to 21-23 mg/L, and aqueous Mg^{2+} becomes negligible in solution due to fixation related to the Mg increase in the solid phase determined at the bentonite interface with cement mortar (section 4.1.2).

The pH and aqueous silica remained almost constant regardless of time (Table 4). These values are near the characteristics of FEBEX-bentonite porewater: 10 – 30 mg/L SiO_2 (cristobalite dissolution, Williams et al., 1985), pH = 9 – 7, depending on leaching or squeezing method used, respectively (Fernández et al., 2004). In spite of these authors, who used edge site protonation constants to explain the FEBEX bentonite pH buffering, Cuevas et al. (2006) calculated that the characteristic pH is obtained by taking into account the coupled reaction of cation exchange and calcite dissolution present in bentonite: $CaCO_3 + H^+ + 2\ NaX \rightleftharpoons HCO_3^- + CaX_2 + 2\ Na^+$.

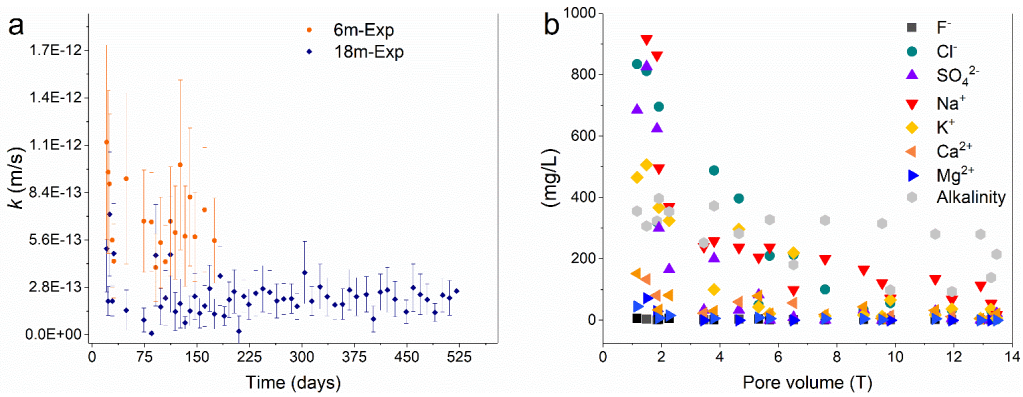

Fig. 10. (a) Averaged hydraulic conductivity calculated as a function of time for experiments performed for 6 (orange) and 18 months (blue). (b) Concentrations of major ions collected at the end of the bentonite side; data for experiments conducted for 6 and 18 months are represented in the same plot.

Table 4. pH and aqueous silica results after 6 and 18 months.

Experiment	pH	$SiO_{2(aq)}$ (mg/L)
6m-Exp	8.2 ± 0.1	12.8 ± 0.1
18m-Exp	8.3 ± 0.1	17.3 ± 0.2

6m-Exp: experiments conducted for 6 months, 18m-Exp: experiments conducted for 18 months.

Discussion

Mg perturbation

The results of small-scale laboratory experiments reveal the development of Mg perturbation in the cement mortar/FEBEX-bentonite interface at a notably shorter time compared with the FEBEX *in situ* experiment performed at large scale. Indeed, limited development of this perturbation is observed in the laboratory experiments from 6 to 18 months. Large accumulation of Mg was identified in the FEBEX *in situ* experiment after 13 years of concrete-bentonite interaction in highly similar conditions but at much larger spatial scale (Fernández et al., 2017). 10 m^3 of concrete in contact with 40 m^3 of FEBEX-bentonite were placed in the *in situ* experiment, while 0.57 cm^3 of cement mortar and 0.57 cm^3 of FEBEX-bentonite were placed in the laboratory experiment. The Mg perturbation reached an extension of 2-3 mm from the CB-interface in the FEBEX *in situ* experiment, whereas a length < 1 mm was observed in this work. The magnitude of the Mg perturbation in the FEBEX *in situ* experiments, that reached up to 20-45 wt.% in bentonite at the interface (Fernández et al., 2017) cannot be directly compared with the results obtained in the present study (~25 at.%) because of the different units of measurement. However, a simple estimation reveals similar degree of Mg enrichment in the accumulation zone near the interface.

The Mg increase has not only been observed in cement or concrete/bentonite interfaces. Stiff clay rocks under the influence of high-pH concrete pore water (pH

>12) showed a characteristic Mg perturbation e.g. (Moyce et al., 2014; Mäder et al., 2017). In concrete/clay systems, this perturbation is also evidenced at the concrete side and it is remarkable when low-pH cementitious materials have been tested (Dauzères et al., 2016).

Mg-silicates can precipitate as a result of the alkaline influence supplied by the cement. The nature of the Mg-silicates formed in large scale experiments, such as the FEBEX *in situ* experiment, is complex considering the variety of compositions that have been identified as a result of the bentonite alkaline alteration. In a similar way as Al may be accommodated in C-S-H phases to form C-A-S-H, exchangeable Mg can also be incorporated in silicates to form saponite-like smectites, as predicted by Roosz et al. (2015) or used to form a variety of Mg-silicates, including M-S-H phases (e.g. Fernández et al., 2018).

The variety of Mg-silicates identified in literature as a result of cement/clay interaction are compatible with the presence of tri-octahedral phyllosilicates 1:1 or 2:1 sheet silicate (Shimbashi et al., 2018). The complex chemical compositions of the zone with anomalous high Mg concentrations have been found to be compatible with a mixture of brucite and Mnt, as the Al content maintained constant, and the di-octahedral character of the Mnt remained, as observed by the XRD-diffraction patterns (Fernández et al., 2017; Cuevas et al., 2018). In fact, Lerouge et al. (2017) identified grain compositions related to Mg perturbation that were highly rich in Mg and compatible with these types of mixtures. In the present experiments, structural characterization of the bentonite interface surface reveals a broad peak at 7.5 Å, that can be related to mixture such as an intercalated $Mg(OH)_2$-Mnt complex. This mixture was considered as one of the main reaction components of the early stage hyperalkaline alteration of Mg-Mnt in presence of

KOH 0.5 M solutions (Fernández et al., 2013). The generalized presence of this type of phase in these early surface experiments can point to these types of phases as a precursor of more common mineral phases formed in Mg-rich natural alkaline environments as saponite or stevensitic minerals (Eberl et al., 1982). These Mg neogenic phases reveal structural properties similar to those of 2:1 and 1:1 sheet silicates and generally form a poorly crystalline but precise structure that is still under investigation (Walling and Provis, 2016). As in this work, M-S-H has been described as a homogeneous gel-like structure with a sheet-like morphology and Mg/Si ratios greater than 0.8 (Lothenbach et al., 2015; Bernard et al., 2017), but their formation has been primarily reported in the concrete side. The presence of any Mg-silicate hydrated phase in bentonite is highly difficult to ascertain because of mixing with other complex clay mineral phases with significant Al quantities.

Ca perturbation

At the cement mortar side, the formation of a calcite skin (~50 μm from the CB-interface) was identified after 6 months and more pronounced after 18 months. This Ca increase, associated with the precipitation of soluble inorganic carbon species, occurs coupled to the decalcification of the C-S-H, identified by SEM-EDX analyses on the cement and by the profiles of chemical composition. HCO_3^-, that becomes the dominant aqueous anion species after 6 months, may act as a source of carbonates precipitation at high pH, which indeed, is supported by the dissolution of portlandite.

The formation of calcite at the concrete-bentonite interface was also reported in the FEBEX *in situ* experiment as a result of interaction of HCO_3^- from the clay porewater and Ca^{2+} from concrete (Fernández et al., 2017), resulting in calcite precipitation that forms a protective crust of low porosity, that increases its

resistance against groundwater and porewater penetration (Jenni et al., 2014). Therefore, the localized development of Ca increase, in the order of μm in cement mortar observed in the present study, evolves to the mm scale (~1 mm) after 13 years of ageing in the FEBEX *in situ* experiment.

At the bentonite side, the Ca increase observed by the SEM-EDX profiles of chemical composition was not as significant as in the cement mortar side, although higher amounts of calcite than those naturally present in the reference bentonite were detected by XRD. The Ca increase can be estimated as 1-5 at.% in the bentonite side, which is far from the Ca increase of 29-80 at.% detected at the cement mortar interface. It has been observed a certain amount of calcite dissolution affecting several cm to the concrete interface in certain locations in the FEBEX *in situ* experiments. Precipitation of calcite at the interface was also found in both, the bentonite and concrete sides, an effect that was clearly separated in the Mg-silicate precipitation. (Turrero and Cloet, 2017).

Al-S phase dynamics

Ettringite was almost always present in the studied cement mortar interface. SEM-EDX and XRD data suggest its formation as a secondary phase within the interface. Ettringite was not detected by XRD in the reference cement mortar sample or was less often observed, presenting different morphologies. The presence of ettringite is favoured by the limestone additions, since cement materials with higher quantities of carbonate additions tend to avoid the conversion of ettringite to AFm (Lothenbach et al., 2008). The origin of secondary ettringite comes from the incorporation of (*i*) Al supplied by Mnt dissolution (Gaucher and Blanc, 2006), (*ii*) S released by dissolution of gypsum and supplied by the porewater from bentonite, and (*iii*) Ca delivered by decalcification of C-S-

H and portlandite present in the cement mortar (Cuevas et al., 2016). At long-term, ettringite is not stable at the interface and in the FEBEX *in situ* experiment, ettringite was detected within the concrete matrix but further from the interface and as secondary phase-filling pores (Alonso et al., 2017).

AFm phases seem to have been occasionally stabilized by incorporating Cl^- diffusing as a soluble species in bentonite porewater. Friedel salt is a more stable Cl-AFm phase and has also been described in the FEBEX *in situ* experiment further from the interfase (Alonso et al., 2017). Cl^- monitoring is important because it is a potential corrosion agent of reinforced concrete (Chen and Mahadevan, 2008), but in this context, its role is of little relevance because Cl^- has a high diffusion rate, and Cl^- fixation by the cement AFm phases was not significant, as demonstrated by the Cl^- performance in the present experiment, that was easily leachable.

Al can also follow other reaction pathways, rather than forming Al-S ettringite phases. Ettringite coexists with carbonates, and C-A-S-H forms as a result of the Al supplied by bentonite pore fluids, as suggested by the SEM-EDX profiles of chemical composition (Section 4.1.2). The ability to accommodate cations from the pore fluid is inversely related to the Ca content of C-S-H, and after the observed decalcification process, C-S-H with lower Ca/Si ratios could easily uptake Al to form C-A-S-H phases (Fernández et al., 2016).

Specific surface area

The SSA represents the external surface area exposed to the porous space, considering the edge sites (Fernández et al., 2013) and excluding the surface area

of the internal basal planes. This parameter depends on sample pretreatment, exchangeable cations and microporosity (Kaufhold et al., 2010).

At the bentonite side, the SSA reduction in the samples compared with the reference bentonite could be related with the existence of certain clogging processes, presumably due to calcite or other nanoscale cements. This process promotes the aggregation of clay particles, thus hindering $N_2(g)$ access to occluded pores, and consequently, the SSA decreases. With respect to the spatial evolution studied from the interface to the bentonite end, the increasing trend of the SSA nearest the CB-interface can be attributed to the decrease in the average size of the smectite particles affected by neogenic Mg-clay mineral nanocrystal aggregates. This newly formed phase can occupy larger pores, thus increasing the weight of the microporosity in the original pore distribution. We consider this interpretation to be more reliable than the increment of the microporosity due to a decrease in the major exchangeable cations of Ca^{2+} and Mg^{2+} (Metz et al., 2005) or the dissolution of Mnt and the consequent reduction of the 2:1 layers (Lowell and Shields, 2013). In our case, only a weak reflection displacement towards lower d-spacings in the basal reflection (001) was observed.

At the cement mortar side, the higher SSA found after 6 and 18 months at the CB and CW-interfaces compared with the intermediate sample (3-6 mm) and the reference cement mortar is attributed to the decalcification and formation of low Ca/Si C-S-H of lower crystal size and greater disorder, thus increasing the SSA (Phung et al., 2016).

Evaluation of leachate

If the general SSA decrease observed in bentonite were attributed to precipitation of nanoscale cements and formation of Mg-Clays near the interface, as evidenced after 6 months, it could be related to the lower hydraulic conductivity values (Alonso et al., 2017) stabilized after < 6 months. (section 4.5). However, this observation does not agree with the increase in SSA from 6 to 18 months in the cement mortar side. This difference in behaviour can be explained because the leachate was collected at the end of the bentonite side, which control the fluid flow due to its low effective porosity and hydraulic conductivity. In the same way, the pH and silica results were similar to those characteristics of the reference FEBEX-bentonite. Therefore, the buffer characteristic of bentonite is demonstrated.

The high concentrations of sulphate and chloride found in the first pore volumes and the subsequent absolute decline mostly occur as a result of their depletion from the porewater of bentonite. Na^+ is naturally present as 1/3 of the exchangeable cation complex in FEBEX-bentonite, but a subset of the Na^+ and K^+ might originate from the alkalis of the cement mortar, increasing their concentration at an early leaching stage. Later, the monovalent ions, together with Ca^{2+} and Mg^{2+}, suffer a decrease related to their regulation as exchangeable cations (mainly Ca^{2+}, Na^+) and the precipitation of calcite and Mg-silicates (Mg^{2+}). The decrease in these exchangeable cations has also been described nearest the interface (Mäder et al., 2017) related to the precipitation of Mg-silicates.

Conclusions

This study assesses the geochemical reactions occurring at the early stage (0.5-1.5 years) of the interaction between cement mortar-CEM II and FEBEX-bentonite

with the aim to facilitate a better comprehension of the large-spatial and long-term results observed after 13 years of concrete-bentonite interaction from the dismantling of the FEBEX *in situ* experiment. The expected reaction paths, which are more progressed in long-term experiments, are consistent with the initial evolution of the results summarized in this study:

- Decalcification of C-S-H in an environment in which portlandite dissolution occurs and anhydrous phases are progressive hydrated.

- Development of a Ca-carbonation skin (calcite) in the cement mortar side and dispersed precipitation of calcite in localized zones of bentonite.

- Initial development of a Mg-perturbation at the bentonite side, related to the formation of precursors of Mg-clay 2:1 sheet silicates as the main neogenic phases expected at the long-term.

- Formation of secondary ettringite at the cement mortar interface.

The geochemical reactions observed at small spatial scale (μm) and short-term (up to 18 months) are promising for development of reaction concepts and support modelling in the future, thus offering a useful prospective to advance upscaling of the concrete-bentonite interface perturbations at long-term.

Acknowledgements

This work was supported by funding from the European Union's Horizon 2020 Research and Training programme from EUROATOM [H2020-NFRP 2014, 2015] under grant agreement nº662147; CEBAMA. The authors thank Juan D.

Rodriguez-Blanco Professor in Nanomineralogy from Trinity College Dublin for assistance with analytical support.

Supplementary material

A mathematical fitting of the chemical evolution of the outflow solution as a function of the pore volume is given in Tables S1 and S2 in the ANNEXE I-B.

References

- Alonso, M.C., García Calvo, J.L., Cuevas, J., Turrero, M.J., Fernández, R., Torres, E., Ruiz, A.I., 2017. Interaction processes at the concrete-bentonite interface after 13 years of FEBEX-Plug operation. Part I: Concrete alteration. *Physics and Chemistry of the Earth, Parts A/B/C*, 99, pp. 38-48, https://doi.org/10.1016/j.pce.2017.03.008.

- Bernard, E., Lothenbach, B., Rentsch, D., Pochard, I., Dauzères, A., 2017. Formation of magnesium silicate hydrates (M-S-H). *Physics and Chemistry of the Earth, Parts A/B/C*, 99, pp. 142-157, https://doi.org/10.1016/j.pce.2017.02.005.

- Berner, U., 1992. Evolution of pore water chemistry during degradation of cement in a radioactive waste repository environment. *Waste management*, 12, pp. 201-219, https://doi.org/10.1016/0956-053X(92)90049-O.

- Berner, U., Kulik, D.A., Kosakowski, G., 2013. Geochemical impact of a low-pH cement liner on the near field of a repository for spent fuel and high-level radioactive waste. *Physics and Chemistry of the Earth, Parts A/B/C*, 64, pp. 46-56, https://doi.org/10.1016/j.pce.2013.03.007.

- Caballero, E., Jiménez de Cisneros, C., Huertas, F.J., Huertas, F., Pozzuoli, A., Linares, J., 2005. Bentonites from Cabo de Gata, Almería, Spain: a mineralogical and geochemical overview. *Clay Minerals*, 40, pp. 463-480, https://doi.org/10.1180/0009855054040184.

- Chen, D., Mahadevan, S., 2008. Chloride-induced reinforcement corrosion and concrete cracking simulation. *Cement and Concrete Composites*, 30, pp. 227-238, https://doi.org/10.1016/j.cemconcomp.2006.10.007.

- Churakov, S.V., Prasianakis, N., 2018. Review of the current status and challenges for a holistic process-based description of mass transport and mineral reactivity in porous media. *American Journal of Science*, 318, pp. 921-948, https://doi:10.2475/09.2018.03.

- Cuevas, J., Ruiz, A., Fernández, R., González-Santamaría, D., Angulo, M., Ortega, A., Torres, E., Turrero, M., 2018. Authigenic Clay Minerals from Interface Reactions of Concrete-Clay Engineered Barriers: A New Perspective on Mg-Clays Formation in Alkaline Environments. *Minerals*, 8, pp. 362, https://doi:10.3390/min8090362.

- Cuevas, J., Ruiz, A.I., Fernández, R., Torres, E., Escribano, A., Regadío, M., Turrero, M.J., 2016. Lime mortar-compacted bentonite–magnetite interfaces: An experimental study focused on the understanding of the EBS long-term performance for high-level nuclear waste isolation DGR concept. 124-125, pp. 79-93, https://doi.org/10.1016/j.clay.2016.01.043.

- Dauzères, A., Achiedo, G., Nied, D., Bernard, E., Alahrache, S., Lothenbach, B., 2016. Magnesium perturbation in low-pH concretes placed in clayey environment—solid characterizations and modeling. *Cement and Concrete Research*, 79, pp. 137-150, https://doi.org/10.1016/j.cemconres.2015.09.002.

- Eberl, D.D., Jones, B.F., Khoury, H.N., 1982. Mixed-Layer Kerolite/Stevensite from the Amargosa Desert, Nevada. *Clays and Clay Minerals*, 30, pp. 321-326, https://doi.org/10.1346/CCMN.1982.0300501.

- ENRESA, 2006. FEBEX Post-Mortem Bentonite Analysis. Madrid. Spain, p.

- Ewing, R.C., Whittleston, R.A., Yardley, B.W.J.E., 2016. Geological disposal of nuclear waste: a primer. *Elements*, 12, pp. 233-237, https://doi.org/10.2113/gselements.12.4.233.

- Fernández, R., Ruiz, A.I., Cuevas, J., 2016. Formation of CASH phases from the interaction between concrete or cement and bentonite. *Clay Minerals*, 51, pp. 223-235, https://doi.org/10.1180/claymin.2016.051.2.09.

- Fernández, R., Torres, E., Ruiz, A.I., Cuevas, J., Alonso, M.C., García Calvo, J.L., Rodríguez, E., Turrero, M.J., 2017. Interaction processes at the concrete-bentonite interface after 13 years of FEBEX-Plug operation. Part II: Bentonite contact. *Physics and Chemistry of the Earth, Parts A/B/C*, 99, pp. 49-63, https://doi.org/10.1016/j.pce.2017.01.009.

- Fernández, R., Vigil de la Villa, R., Ruiz, A.I., García, R., Cuevas, J., 2013. Precipitation of chlorite-like structures during OPC porewater diffusion through compacted bentonite at 90°C. *Applied Clay Science*, 83-84, pp. 357-367, https://doi.org/10.1016/j.clay.2013.07.021.

- García Calvo, J.L. 2012. *Desarrollo de materiales de construcción con cemento de bajo pH, compatibles con la barrera de ingeniería de un almacenamiento geológico profundo de residuos radiactivos de alta actividad*, Tesis Doctoral. Universidad Autónoma de Madrid, p. 298, http://hdl.handle.net/10486/12309.

- Gaucher, E.C., Blanc, P., 2006. Cement/clay interactions–a review: experiments, natural analogues, and modeling. *Waste Management*, 26, pp. 776-788, https://doi.org/10.1016/j.wasman.2006.01.027.

- González-Santamaría, D., Angulo, M., Ruiz, A., Fernández, R., Ortega, A., Cuevas, J., 2018. Low-pH cement mortar-bentonite perturbations in a small-scale pilot laboratory experiment. *Clay Minerals*, 53, pp. 237-254, https://doi.org/10.1180/clm.2018.16.

- Grangeon, S., Claret, F., Linard, Y., Chiaberge, C., 2013. X-ray diffraction: a powerful tool to probe and understand the structure of nanocrystalline calcium silicate hydrates. *Acta crystallographica Section B, Structural science, crystal engineering and materials*, 69, pp. 465-473, https://doi.org/10.1107/S2052519213021155.

- Jenni, A., Mäder, U., Lerouge, C., Gaboreau, S., Schwyn, B., 2014. In situ interaction between different concretes and Opalinus Clay. *Physics and Chemistry of the Earth, Parts A/B/C*, 70-71, pp. 71-83, https://doi.org/10.1016/j.pce.2013.11.004.

- Kaufhold, S., Dohrmann, R., Klinkenberg, M., Siegesmund, S., Ufer, K.J., 2010. N2-BET specific surface area of bentonites. *Journal of colloid interface science*, 349, pp. 275-282, https://doi.org/10.1016/j.jcis.2010.05.018.

- Khoury, H.N., Salameh, E., Abdul-Jaber, Q., 1985. Characteristics of an unusual highly alkaline water from the Maqarin area, northern Jordan. *Journal of Hydrology*, 81, pp. 79-91, https://doi.org/10.1016/0022-1694(85)90168-4.

- Lerouge, C., Gaboreau, S., Grangeon, S., Claret, F., Warmont, F., Jenni, A., Cloet, V., Mäder, U., 2017. In situ interactions between Opalinus Clay and Low Alkali Concrete. *Physics and Chemistry of the Earth, Parts A/B/C*, 99, pp. 3-21, https://doi.org/10.1016/j.pce.2017.01.005.

- Lothenbach, B., Le Saout, G., Gallucci, E., Scrivener, K., 2008. Influence of limestone on the hydration of Portland cements. *Cement and Concrete Research*, 38, pp. 848-860, https://doi.org/10.1016/j.cemconres.2008.01.002.

- Lothenbach, B., Nied, D., L'Hôpital, E., Achiedo, G., Dauzères, A., 2015. Magnesium and calcium silicate hydrates. *Cement and Concrete Research*, 77, pp. 60-68, https://doi.org/10.1016/j.cemconres.2015.06.007.

- Lowell, S., Shields, J.E., 2013. *Powder surface area and porosity*, ed. Springer Science & Business Media.

- Mäder, U., Jenni, A., Lerouge, C., Gaboreau, S., Miyoshi, S., Kimura, Y., Cloet, V., Fukaya, M., Claret, F., Otake, T., Shibata, M., Lothenbach, B., 2017. 5-year chemico-physical evolution of concrete–claystone interfaces, Mont Terri rock laboratory (Switzerland). *Swiss Journal of Geosciences*, 110, pp. 307-327, https://10.1007/s00015-016-0240-5.

- Metz, V., Raanan, H., Pieper, H., Bosbach, D., Ganor, J., 2005. Towards the establishment of a reliable proxy for the reactive surface area of smectite. *Geochimica et Cosmochimica Acta*, 69, pp. 2581-2591, https://doi.org/10.1016/j.gca.2004.11.009.

- Moyce, E.B.A., Rochelle, C., Morris, K., Milodowski, A.E., Chen, X., Thornton, S., Small, J.S., Shaw, S., 2014. Rock alteration in alkaline cement waters over 15 years and its relevance to the geological disposal of nuclear waste. *Applied Geochemistry*, 50, pp. 91-105, https://doi.org/10.1016/j.apgeochem.2014.08.003.

- Phung, Q.T., Maes, N., Jacques, D., De Schutter, G., Ye, G., 2016. Investigation of the changes in microstructure and transport properties of leached cement pastes accounting for mix composition. *Cement and Concrete Research*, 79, pp. 217-234, https://doi.org/10.1016/j.cemconres.2015.09.017.

- Roosz, C., Grangeon, S., Blanc, P., Montouillout, V., Lothenbach, B., Henocq, P., Giffaut, E., Vieillard, P., Gaboreau, S., 2015. Crystal structure of magnesium silicate hydrates (M-S-H): The relation with 2:1 Mg–Si phyllosilicates. *Cement and Concrete Research*, 73, pp. 228-237, https://doi.org/10.1016/j.cemconres.2015.03.014.

- Shimbashi, M., Sato, T., Yamakawa, M., Fujii, N., Otake, T., 2018. Formation of Fe- and Mg-Rich Smectite under Hyperalkaline Conditions at Narra in Palawan, the Philippines. *Minerals*, 8, pp. 155, https://doi.org/10.3390/min8040155.

- Techer, I., Bartier, D., Boulvais, P., Tinseau, E., Suchorski, K., Cabrera, J., Dauzères, A., 2012. Tracing interactions between natural argillites and hyper-alkaline fluids from engineered cement paste and concrete: Chemical and isotopic monitoring of a 15-years old deep-disposal analogue. *Applied Geochemistry*, 27, pp. 1384-1402, https://doi.org/10.1016/j.apgeochem.2011.08.013.

- Torres, E., Turrero, M.J., Garralón, A., Cuevas, J., Fernández, R., Ortega, A., Ruíz, A.I., 2019. Stable isotopes applied to the study of the concrete/bentonite interaction in the FEBEX in situ test. *Applied Geochemistry*, 100, pp. 432-443, https://doi.org/10.1016/j.apgeochem.2018.12.017.

- Trotignon, L., Devallois, V., Peycelon, H., Tiffreau, C., Bourbon, X., 2007. Predicting the long term durability of concrete engineered barriers in a geological repository for radioactive waste. *Physics and Chemistry of the Earth, Parts A/B/C*, 32, pp. 259-274, https://10.1016/j.pce.2006.02.049.

- Turrero, M.J., Cloet, V., 2017. FEBEX-DP Concrete ageing, concrete/bentonite and concrete/rock interaction analysis. 5430 Wettingen Switzerland, p. 282.

- Villar, M.V., Lloret, A., 2004. Influence of temperature on the hydro-mechanical behaviour of a compacted bentonite. *Applied Clay Science*, 26, pp. 337-350, https://doi.org/10.1016/j.clay.2003.12.026.

- Villar, M.V., Martín, P.L., Bárcena, I., García-Siñeriz, J.L., Gómez-Espina, R., Lloret, A., 2012. Long-term experimental evidences of saturation of compacted bentonite under repository conditions. *Engineering Geology*, 149-150, pp. 57-69, https://doi.org/10.1016/j.enggeo.2012.08.004.

- Walling, S.A., Provis, J.L., 2016. Magnesia-Based Cements: A Journey of 150 Years, and Cements for the Future? *Chemical Reviews*, 116, pp. 4170-4204, https://doi.org/10.1021/acs.chemrev.5b00463.

- Webb, P.A., Orr, C., 1997. *Analytical methods in fine particle technology*, ed. Micromeritics Instrument Corp.

5.3 HIGH-PH/LOW-PH ORDINARY PORTLAND CEMENT MORTARS IMPACTS ON COMPACTED BENTONITE SURFACES: APPLICATION TO CLAY BARRIERS PERFORMANCE

Daniel E. González-Santamaría[1], Raúl Fernández[1], Ana. I. Ruiz[1], Almudena Ortega[1], Jaime Cuevas[1*]

[1]Department of Geology and Geochemistry, Faculty of Sciences, Autonomous University of Madrid, Cantoblanco, 28049, Madrid, Spain

Abstract

The design of engineered barrier systems for high-level radioactive waste isolation requires the use of cement-based materials. Small-scale surface reactivity interface experiments were designed to perform a reference laboratory study. It simulated granitic groundwater infiltration through cement mortar/bentonite (CB) composite columns. The tests ran duplicated over 6 and 18 months and included low-pH, CEM I and CEM II ordinary Portland cement mortars in contact with bentonite. After the experiments, the materials were analysed using scanning electron microscopy attached to energy dispersive energy X-ray analysis (EDX), surface mineralogy using grazing incidence X-ray diffraction configurations, specific surface area and effluent chemistry. EDX chemical profiles measured from CB interface contact reproduced, in 100 μm to 1 mm thickness, a characteristic geochemical Mg perturbation in the bentonite and calcite precipitation in cement materials. These processes are known to be developed in 10- 15-years within < 5 mm of the interface. The comparison of these long, large scale experiments with the small scale experiments showed that the chemical perturbation thickness development rate will decrease over time. The limestone addition (CEM II) leaves

less room for calcite precipitation, and ettringite became stabilized, which limited the extent of dissolution-precipitation processes. Then, the CEM II mortar had better resistance to perturbation.

Keywords

Engineered barrier system, cement mortar, bentonite, geochemical perturbation, high pH, low pH

Highlights

The reactivity of three OPC mortars in contact with bentonite was studied

Six solid interfaces duplicated experiments offer a unique consistent study

The lab experiments reproduced well the reactivity of long-term large-scale experiments

The CEM II, with additions of 10 wt.% limestone, is less deteriorated

Introduction

In the context of high-level radioactive waste isolation, the engineered barrier system (EBS) is a cornerstone among the different concepts of deep geological repositories (DGR) (e.g., Tournassat et al., 2015). An EBS restrains the radionuclides mobility for as long as required and keeps it isolated from groundwater.

Clays are planned to be implemented either in the role of a repository host rock (Nagra, 2002; ANDRA, 2005) or as part of the repository in the EBS as backfill and/or buffer and sealing material (Keusen et al., 1989). Clays present properties

such as very low permeability, slow diffusive transport mechanisms, high retention capacity for radionuclides, chemical buffer effects, and self-sealing and swelling capacities (Galán et al., 1986; Meunier et al., 1998; Gómez-Espina and Villar, 2016; Kaufhold and Dohrmann, 2016; Norris, 2017). Concrete is used as structural support for galleries and for plugging seals for galleries. In spite of these adequate functional properties, chemical gradients produced when concrete and clays are held in contact, induce their mutual perturbation, causing reaction diffusive fluxes that lead to the formation of new solid phases and the alteration of material properties in the near field (Savage, 2014).

To date, a small spatial progression of the perturbations in concrete/clay rock or concrete/bentonite interfaces has been observed, within a centimetre scale in the laboratory or *in situ* experiments run for a decade (*i.e.* Fernández et al., 2017, Lerouge et al., 2017, Mäder et al., 2017, Duro et al., 2020, and references therein); whereas numerical models, either built with early state-of-the-art knowledge or more detailed recent approaches (ECOCLAY-II, 2005, Idiart et al., 2020 and references therein), predicted several decimetres impact in the long term. However, the nature of the neogenic phases formed at the interface (e.g., calcium aluminium silicate hydrates (CASH) and magnesium silicate hydrates (MSH)), as well as their role in the alteration of porosity/permeability and swelling pressure, remain unclear (Lothenbach et al., 2015; Walling and Provis, 2016).

Geochemical processes observed within the concrete (OPC-based)/clay interface, based on laboratory and *in situ* experiments can be related to decalcification of concrete; dissolution of montmorillonite (Mt); precipitation of calcium silicate hydrates (CSH), calcite and secondary chloride or sulphate Ca-Al phases (ettringite and calcium aluminate monosulfate); cation exchange in Mt; and MSH

formation. All these reactions seem to produce a porosity increase in concrete and pore clogging at the clay interface (Read et al., 2001; Baur et al., 2004; Fernández et al., 2006; Florea and Brouwers, 2012; Dauzères et al., 2014a; Jenni et al., 2014; Cuevas et al., 2016; Fernández et al., 2016; Fernández et al., 2017; Turrero and Cloet, 2017). The extent and location of these perturbations are conditioned by the composition of the cementitious material (Lerouge et al., 2017). In this context, some authors suggested the better performance of high-pH cement materials (pH > 13), e.g., CEM I, by the development of a protective calcium carbonate film, which would reduce the decalcification process (Jenni et al., 2014; Mäder et al., 2017). Conversely, others reported the advantage of using low-pH cements (pH < 11) to reduce the influence of alkaline dissolution of clays and, at the same time, improving the resistance of concrete to granitic groundwater exposure (García Calvo et al., 2010; García Calvo, 2012). However, less resistance to concrete matrix dissolution of low pH cement products was described for these materials under the influence of clay pore waters (Trotignon et al., 2007; Dauzères et al., 2014b).

Underground research laboratories (URL) are long-term *in situ* facilities in which demonstration tests are carried out in support of the development of DGR (Blechschmidt and Vomvoris, 2010; Wang, 2014). These demonstration tests help to determine the future evolution of the materials interfaces in the repository system considering, in this case, groundwater, cementitious materials and clays interactions. Geochemical perturbations have been observed in URL experiments testing reference cement-based materials, mainly ordinary Portland Cement (OPC) based cement: CEM I, CEM II (limestone addition to improve its durability, Hawkins et al., 1996; Vuk et al., 2001) and CEM I mixed with silica fume (SF) as a low-pH material. URL emplacements have different types of clay rocks such as

Opalinus (OPA) in Switzerland or Callovo-Oxfordian argillite in France as host rocks and bentonite as backfill (Ewing et al., 2016). Table S1, also included in the supplementary file (ANNEXE-I-C), summarizes the timescale and spatial extent of geochemical perturbations produced in these URL tests.

Table S1. Geochemical perturbation observed at the cement/clay interfaces studied in reference Underground Research Laboratory (URL) tests.

Interface	years	Cement based material side	Clay side	URL experiment	Reference
CEM I/OPA	2	Perturbations from 0 to 300 µm: Ca depletion, carbonation; presence of Mg hydrates.	Perturbations over 200 µm: Ca enrichment; weak Mg and S enrichment.	Cement–clayey interaction experiment at the Mont Terri Underground Rock Laboratory (Switzerland)	(Jenni et al., 2014; Mäder et al., 2017)
CEM I/OPA	5	Perturbations from 0 to 300-500 µm: Ca depletion, S enrichment; carbonation; presence of Mg hydrates.	No significant alteration.	Cement–clayey interaction experiment at the Mont Terri Underground Laboratory (Switzerland)	(Jenni et al., 2014; Mäder et al., 2017)
Low-pH/OPA	2	Ca depletion (300-450 µm), followed by Ca and Mg enrichment (300-45 µm; calcite is present); followed by Mg depletion (0-45 µm). S enrichment (300-0 µm); S depletion (450-700 µm).	0 to 200 µm: Mg enrichment; weak S enrichment.	Low-pH cement (ESDRED) interaction with clayey at Mont-Terri Rock laboratory (Switzerland)	(Dauzères et al., 2016; Mäder et al., 2017)
Low-pH/OPA	5	Perturbation from 0 to 1.4 mm: Ca and weak S depletion; Mg enrichment coexisting with calcite and Mg-hydrates: 0 to 300 µm.	Perturbations from 0 to 200 µm: Mg enrichment.	Low-pH cement (ESDRED)-interaction with clayey at Mont-Terri rock laboratory (Switzerland)	(Dauzères et al., 2016; Mäder et al., 2017)
Low alkali/OPA	5	Perturbations limited to 1 mm with development of a crust band containing Mg-rich phase, calcite and CSH with low Ca/Si molar ratio.	Small changes of mineralogy: Mg-enriched (300-400 µm thick layer). Changing cation occupancies (Ca, Mg and K increase while Na decrease).	Low alkali cement (LAC) interaction with clayey (Textural, mineralogical and chemical changes study) at Mont Terri Underground Rock Laboratory (Switzerland)	(Lerouge et al., 2017)

CEM II/Bent.	13	S enrichment (1 to 5 mm): newly formed ettringite. Carbonation (< 1 mm), Cl-diffusion and concentration in 5-10 mm coupled to decalcification. Portlandite dissolution 0-5 mm.	Perturbation from 0 to 4-5 mm; large Mg enrichment (< 1 mm). Tri-octahedral Mg-Si clay formation.	Concrete-bentonite interaction experiment at Grimsel Test Site - international Underground Laboratory (Switzerland)	(Fernández et al., 2017)
CEM II/Argillite	15	Perturbations from 0 to 10-15 mm: Portlandite dissolution, CSH decalcification and calcite precipitation.	Perturbations from 0 to18-20 mm: CSH precipitation; calcite dissolution followed by new calcite precipitation in the alkaline front.	Interactions between natural argillites and hyper-alkaline fluids from cement paste and concrete located in the Tournemire Experimental Platform (Aveyron, France)	(Techer et al., 2012)
CEM II/Argillite	18	Perturbations: 0-100 µm decalcification of portlandite and CSH linked to a porosity increase.	Perturbations from 0 to 11-13 mm: specific surface area decrease associated with neoformation of low Ca/Si CSH; calcite precipitation; possible illite precipitation.	Cement paste-argillite interaction at Tournemire Experimental Platform (Aveyron, France)	(Bartier et al., 2013)

OPA: Opalinus clay, Bent: bentonite, CSH: calcium silicate hydrate, CASH: calcium aluminium silicate hydrate, tri-Mg-Si: tri-octahedral Mg-silicate, brc: brucite, srp: serpentine, SSA: specific surface area. CEM I and CEM II correspond to the ordinary Portland cement (OPC) used. ESDRED: type of low-pH cement base material made with 60% of CEM I and 40% of silica fume, LAC: type of low-pH cement that contains 90% of CEM III/B and 10% of nanosilica.

The comparison of *in situ* and laboratory experiments is valuable to obtain a multiscale approach of the material performances. The nature of the reaction products depends on the experimental conditions (Dauzères et al., 2010; Fernández et al., 2016) and reveal a high degree of heterogeneity in their spatial length distribution. Thus, *in situ* experiments are more realistic and may need many sampling locations at the interface to be representative (Gaboreau et al., 2011; Gaboreau et al., 2012; Bartier et al., 2013; Mäder et al., 2017); unfortunately, this is not usually done because of cost reasons. In this context, small-scale, homogeneous, reproducible and controlled experiments concerning

real EBS interfaces are needed as alternative to have an experimental reference in order to disclose what happened *in situ*. The present work compares the behaviour of different types of cement materials, CEM I and CEM II as high-pH cement and CEM I + SF as a low-pH, in a simulated EBS under virtually equal conditions. The geochemical reactions observed at a small scale of time and space (μm) in the present work are envisaged to be used in the development of reaction concepts to model the experiments in the future, thus offering a useful prospective to advance the upscaling of concrete-bentonite interface chemical perturbation.

Materials and methods

MATERIALS

- *Granitic groundwater*

The groundwater used as injecting water in the experiments was obtained from the Grimsel Test Site (GTS) research facility excavated in granite. The GTS groundwater is characterized by a dilute (104 μS/cm), pH = 8.1 composition of Na^+, Ca^{2+}, HCO_3^-, Cl^-, and SO_4^{2-} ions (Garralón et al., 2017; Torres et al., 2019).

- *FEBEX bentonite*

FEBEX bentonite was obtained from the Cortijo de Archidona deposits (Caballero et al., 2005). It contains > 90% montmorillonite, with accessory quartz (qtz; (2 ±1), plagioclase (pl; 3 ± 1), K-feldspar (Kfs; (< 1), calcite (Cal; < 1) and cristobalite (Crs; 2 ± 1). The FEBEX bentonite contains close to 1/3, 1/3 and 1/4

cmol (+)/kg of Mg^{2+}, Ca^{2+} and Na^{+} exchangeable cations respectively for a cation exchange capacity (CEC) of 102 ± 2 cmol(+)/kg (ENRESA, 2006).

The bentonite was compacted (dry density of 1.60 g/cm^3) with its hygroscopic water content (13 wt.%) at room temperature (23 ± 2°C) and inside a methacrylate cylinder sleeve, where the mortar was previously hardened and cured (100% R. H. for 90 days), Fig. 1.

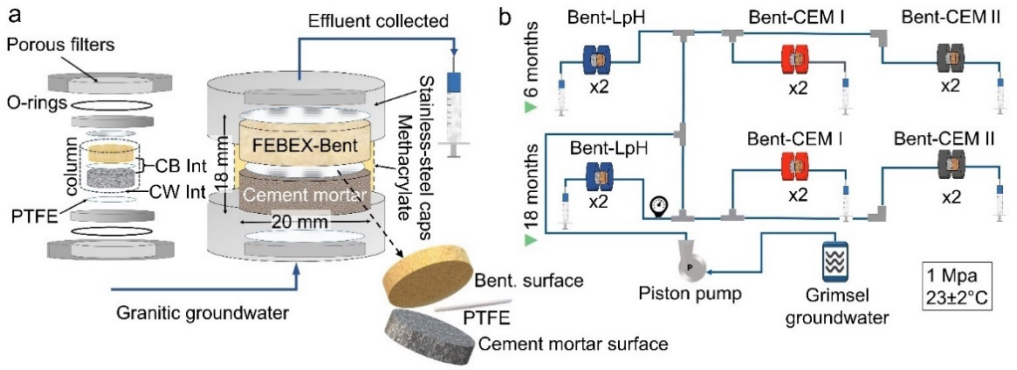

Fig. 1. Scheme of the experiments. (a) Transport cell and (b) representation of the experimental setup. The cell dimensions were 20 mm in internal diameter and 9 mm in height for each material (18 mm in total). PTFE: polytetrafluoroethylene membrane, CB int: cement mortar/bentonite interface, CW int: cement mortar/water interface. Bent: bentonite.

- *Cement mortars*

Three types of mortars were used: one low-pH (LpH) mortar and two high-pH (HpH). The LpH cement mortar was made with 60 wt.% CEM I 42.5 R SR mixed with 40 wt.% SF, similar to the ESRED EU project formulation (Jenni et al., 2014; Dauzères et al., 2016). The HpH mortars were based on CEM I 42.5 R SR (CEM I) and CEM II/A-L 42.5 R formulated with 10 wt.% limestone (CEM-II). The materials were supplied by the Eduardo Torroja Institute for Construction Science (CSIC-IETcc) (CEM I, SF and quartz sand) and Cementos Portland Valderivas group Company (CEM II). Each material was mixed using a 0.42 distilled

water/binder ratio and 1+3 binder/quartz sand. The pH indicative of the pore solution of the initially cured mortars (references) was measured according to the leached or aqueous extract *ex situ* method (García Calvo, 2012), obtaining a pH of 11.0 ± 0.1 for LpH, 11.5 ± 0.1 for CEM I and 12.2 ± 0.1 for CEM II.

METHODS

A detailed explanation for a pilot experiment is available in González-Santamaría et al. (2018) and a short description of the setup of the experiments is provided here. The column arrangement (Fig. 1) allowed separate study of the cement mortar or bentonite surfaces at the interface as they were separated by a PTFE membrane (<0.45 μm pore size, 10 μm thickness), limiting the mineral complexity of the cement mortar/bentonite mixtures (Huertas and Santiago, 1997; Alonso et al., 2017; Fernández et al., 2017). Each experiment was duplicated and run for two periods (p) of time: 6 and 18 months (m). Thus, 12 experiments were studied under virtually equal conditions: 2r×2p×3 cell types: LpH, CEM I and CEM II.

Scanning electron microscopy combined with energy dispersive X-ray detection (SEM-EDX), powder X-ray diffraction methods (XRD), and specific surface area analyses (SSA) were performed to study the mineralogical and physical perturbations of the solid samples. For this task, at the end of the tests, the column was divided into several subsamples according to the different analyses carried out. Regarding the collected aqueous solution effluents, the volume flow rates were measured for hydraulic conductivity calculation. Water was injected through the mortar at a constant hydraulic pressure of 1 MPa. The collected effluent, at the bentonite end, filled syringes, which were periodically weighed to calculate flow rates, and eventually used for aqueous chemical analysis.

- SEM-EDX analyses

The average bulk chemical composition of mortars was assessed by areas (1 mm^2) and spot analyses by means of SEM-EDX. For spot analyses, quartz grains were avoided. These measurements were performed in a 2 mm thickness polished section taken from the CB interface. Bentonite analysis was made by areas.

The variation of the elemental composition of both mortar and bentonite materials in relation to the distance from the CB interface was studied by tracing a line perpendicular to the CB, where detailed EDX area analysis was acquired. Previously the samples were polished after a freeze-drying and embedded in epoxy resin. SEM-EDX analysis was conducted on a Hitachi S-3000N scanning electron microscope coupled to an INCAx-sight Oxford Instruments™ energy-dispersive X-ray analyser. For EDX semi-quantification of major elements, the statistical quality of the measurements is better than 10% determination error for the elements analysed (González-Santamaría et al., 2018).

Finally, the morphology and composition of crystals or crystal aggregates at the surfaces facing to each other were also explored and analysed.

- *XRD and grazing incidence X-ray diffraction (GI-XRD) analysis*

GI-XRD configuration was used at a fixed incidence angle of 0.5° θ, and also to obtain θ/2θ scans. The exploration of the mortar and bentonite fresh surfaces provided information from the first ~100 μm thickness from the PTFE membrane. This configuration allowed to study the interface mineralogy by maximizing the sampling area using a fixed low diffraction angle. XRD experiments were recorded in a 3-70º 2θ angular range using 0.04° angular step (2 s time). The equipment used was an X'Pert PRO PANalytical θ/θ diffractometer with parallel

beam optics, secondary monochromator and Xenon detector. XRD powder patterns of mortar and bentonite were obtained from slices cut at different distances (0-3, 3-6, 6-9 mm) from the CB interface. The equipment used was a θ-2θ X'Pert PANalytical instrument with an X'Celerator detector. XRD patterns were recorded for 0.016° angular steps (100 s time) in an angular range of 3-70° 2θ. The voltage and intensity of the operated X-ray Cu tube were 45 kV and 40 mA.

- *SSA analyses*

SSA analyses determined by the BET equation method (N_2 gas adsorption, Webb and Orr, 1997) were performed in the slices. A 0.2 g subsample was ground in an agate mortar and oven dried to 90ºC prior to SSA analyses using Micromeritcs® GEMINI V equipment. The degassing phase (18 h 90ºC in N_2 gas atmosphere), was carried following standard UNE-EN 1015-11.

- *Aqueous solution analyses*

The characterization of the effluents consisted in pH and alkalinity measurement (Metrohm 888™ titration device); silica analysis (825 nm visible spectrophotometry using the molybdate blue complex method in a Milton Roy Spectronic® 1200 instrument); and major ions (Cl^-, SO_4^{2-}, Na^+, K^+, Ca^{2+} and Mg^{2+}) determination by ion chromatography (Metrohm 802™ compact IC plus).

Results

SEM-EDX analyses

The average chemical compositions of the areas of the mortars are accessible in the supplementary file (Table S2). Whit regards to spot chemical compositions, the Ca/Si ratio was 0.88 ± 0.13 for LpH, whereas the Ca/Si ratio of CEM I and CEM II presented mean ratios of 1.76 ± 0.13 and 1.72 ± 0.33, respectively (Fig. S1). These values are characteristic of a mixture of calcium silicate (CS) anhydrous and CSH hydrated phases in low pH and high pH concrete matrices (Grangeon et al., 2013; Grangeon et al., 2016). The ratios tended to decrease slightly over time although with a high dispersion owing to the redistribution of Ca in a 100 μm scale.

Table S2. EDX area analysis performed at different time-scales (0 months, 6 months and 18 months) and cement mortar/bentonite (CB) interface of LpH-CEM I and CEM II cement mortars.

	Initial-references 0 months			CB-interface 6 months			CB-interface 18 months		
At.%	LpH	CEM I	CEM II	LpH	CEM I	CEM II	LpH	CEM I	CEM II
Mg	n.d.	n.d.	n.d.	n.d.	1.1±0.5	n.d.	0.6±0.5	0.5±0.5	0.3±0.2
Al	1.0±0.1	1.4±0.0	2.4±0.3	1.1±0.2	1.5±0.5	2.5±0.8	1.7±0.1	2.5±0.9	2.5±0.4
Si	83.3±0.5	74.8±1.0	74.7±1.3	88.1±0.3	84.7±1.7	80.1±2.9	84.5±1.1	76.3±1.4	74.1±2.1
S	n.d.	0.9±0.0	1.2±0.4	n.d.	n.d.	0.8±0.4	n.d.	1.2±0.3	1.5±0.4
K	0.4±0.3	0.4±0.1	n.d.	n.d.	n.d.	n.d.	n.d.	n.d.	n.d.
Ca	14.2±0.6	21.2±1.4	20.4±1.0	10.0±0.5	11.5±1.3	15.5±2.3	12.2±0.8	18.1±1.5	20.9±1.4
Fe	0.9±0.3	1.1±0.1	0.7±0.1	n.d.	0.9±0.3	0.8±0.3	0.9±0.2	1.3±0.1	0.8±0.1

At.%: atomic percentage, n.d: not detected. LpH: Low-pH cement mortar. CEM I: High-pH cement mortar made with CEM I as ordinary Portland cement. CEM II: High-pH cement mortar made with CEM II A-L as ordinary Portland cement.

The measured elemental chemical profiles presented significant perturbations at the 0-200 µm scale from the interface towards both sides, cement mortar and bentonite, focusing mainly on Ca, Mg, Al and S variations (Fig. 2). Si was the element with the highest concentration due to quartz sand grains, and its change counteracted the relative variations of the others, so its variation is not interpreted as net precipitation or dissolution of silica. In general, there was less elemental variability beyond 200 µm, affecting both sides in the three tested materials, with high homogeneity on the bentonite side.

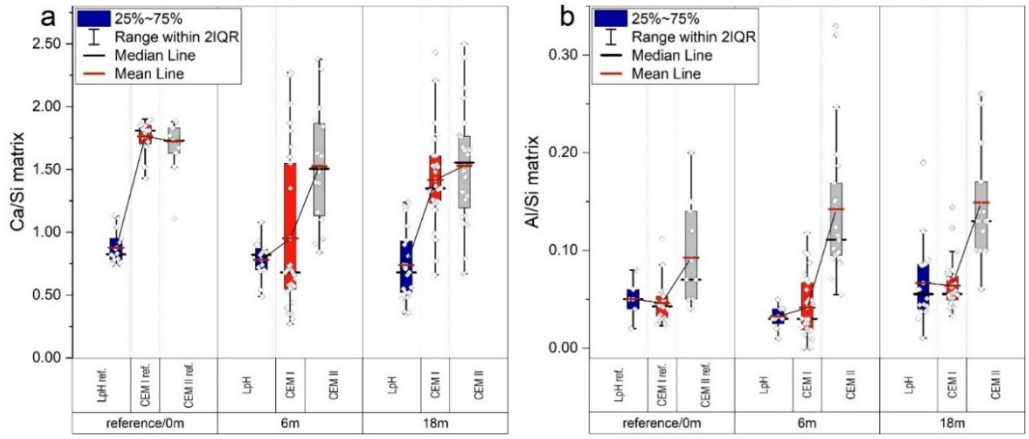

Fig. S1. EDX analysis of the cement mortars near the field of the interface. (a) Ca/Si ratio from 0 months (reference) to 18 months. (b) Al/Si ratio from 0 to 18 months. ref: reference. m: months.

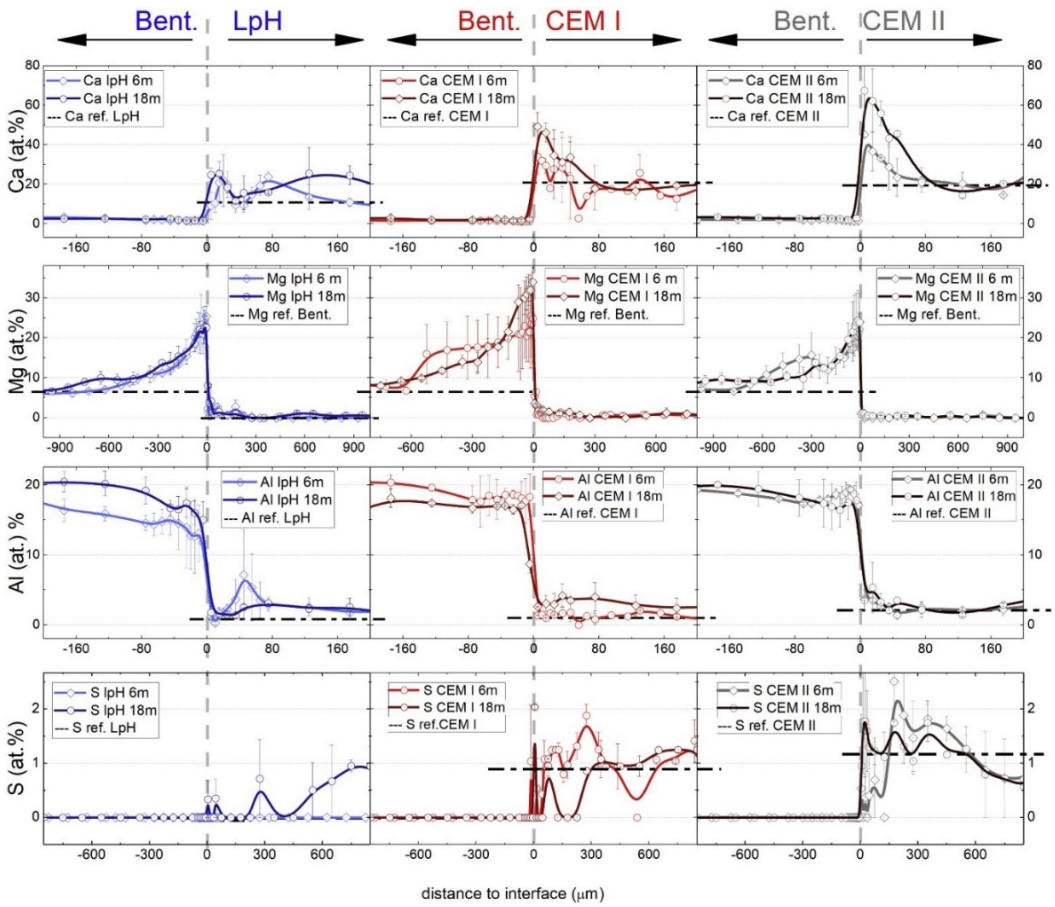

Fig. 2. Ca, Al and S (at.%). chemical profiles of the three types of mortar/bentonite interfaces. All profiles were obtained based on the average values of the duplicated experiments (error bars marked). The interface is represented at 0 μm as a vertical grey dashed line. Reference (ref.) at.% of Ca, Al and S of each type of cement mortar, and basal at.% Mg of FEBEX bentonite have been plotted (horizontal dashed lines). The whole experimental scale profiles at the whole experimental scale can be found in the supplementary file (Fig. S2). m: months.

At the mortar side, Ca at.% presented a significant increase next to the interfaces (< 100 μm thickness). These increases contrast with the general decrease in Ca observed in the averaged data corresponding to the spots matrix analyses within a 2 mm thickness (Table S2). In the LpH cement mortar, Ca at.% grew from 14 to ~20 at.% and reached two maxima at 6 months, approximately 20 and 80 μm from the interface. For CEM I and CEM II, the Ca increase was higher than that in LpH and reached maxima of ~50 and ~60 at.%, respectively. Lower Ca at.% levels in

CEM I are due to differences and heterogeneities in duplicated experiments (wide error bars), and also to the absence in limestone addition in the cement paste. The Ca/Si ratios in these Ca-rich zones were >>2, higher than cement matrix and CSH, which suggests the presence of calcite. CEM I and CEM II Ca at.% profiles also suggested the presence of small decalcification zones between ~60 and ~170 μm. Ca at.% increased from 6 to 18 m for all experiments. FEBEX bentonite is not affected by this Ca perturbation in any of the materials tested.

Mg at.% was increased in the FEBEX bentonite surface facing the PTFE membrane. This pattern is the opposite to that described for Ca at.% in the mortar material behind the CB interfaces. Minor Mg at.% increments were developed near the CB interface in the LpH mortar side (< 50 μm), where relative Mg at.% increases in bentonite reached an extension of approximately 600 μm. The bentonite interface Mg at.% values were higher in the experiments performed with CEM I (~25-35 Mg at.%) than in LpH and CEM II (~ < 25 Mg at.%). Both HpH experiments presented a Mg at.% step at 600-400 μm from the interface, which is smoothed from 6 to 18 months, whereas the Mg at.% is maximum at the CB wall (> 40% in CEM I). Mg at.% reaches the reference line at ≈ 1500 μm.

For Al behaviour, its at.% was above reference lines in CEM I (at 18 months) and CEM II mortars within a few μm (~100 μm) near the CB wall. These increases grew from 6 to 18 months. Different behaviour was observed in LpH; a broad Al peak was detected at ~60 μm for 6 months profiles. The presence of Al sulphates can presumably be inferred as Al at.% and S at.% are in some regions together above the reference lines. However, they are not correlated, presumably due to the error in the determination of the low S content (~ <2 at.%).

At the FEBEX bentonite side, in all experiments, Al at.% showed a smooth continuous decrease up to the CB interface from ~150 μm, being more noticeable in general at 18 months and in the CEM I tests. Both in LpH and in CEM I, a general increase of Al at.% in cement mortar is produced in a ~100 μm region with respect to the CB interface. In CEM II was less pronounced, although also detected.

As regards crystal aggregates and undifferentiated mineral masses, they were presumably produced due to pore fluids interactions. They were found on the fresh surfaces of the facing planes and identified by their singular chemical compositions or morphologies. The distribution of these phases according to the type of experiment and time scale is summarized in Table 1.

Table 1. Distribution of phases in the surface of the facing planes.

time	Surface	Brucite	Mg-Si crust	Mg-Si platelets	Cal	CSH	CH	C-A-S-H	ett(+) / CmSAH (-)
18 months	Bent.		LpH / CEM I / CEM II	L CEM I / CEM II	CEM $I^{(-)}$ / CEM $II^{(-)}$				
	CEM mortar	LpH	LpH		LpH / CEM $I^{(+)}$/ CEM $II^{(+)}$	LpH / CEM I / CEM II			CEM I / CEM II
6 months	Bent.		LpH /CEM I / CEM II	LCEM I / CEM II	CEM$I^{(-)}$ / CEM $II^{(-)}$			CEM $I^{(?)}$	
	CEM mortar	LpH			LpH / CEM I / CEM II	CEM I	CEM I	LpH / CEM I / CEM II	LpH / CEM I / CEM $II^{(+)}$

CH: portlandite, Cal: calcite, CSH: calcium silicate hydrates, CASH, calcium aluminium silicate hydrates, ett: ettringite (hydrated Ca-Al-Fe tri-sulphate), CmSAH (hydrated Ca-Al-Fe monosulphate). LpH: low-pH cement mortar, CEM I: high-pH cement mortar, CEM II: high-pH cement mortar with limestone addition, (+) High frequency; (-) Low frequency; (?) possible, Mg-Si: Mg-silicates. Bent; bentonite.

Concerning cement mortar surfaces, brucite ($Mg(OH)_2$) was identified only at LpH mortar surfaces after 6 months (Fig. 3a, b), filling voids with crystal

aggregates of trigonal prism morphologies (Fernández et al., 2006). Later, at 18 months, similar voids were filled with mixtures, alternatively rich in Mg-Si mixed with Ca signals, these ones coming from precipitates of calcium carbonates scalenohedral calcite crystals and undifferentiated coatings of Ca phases (Fig. 3c). Calcite crystals and coatings were found in the three types of experiments but were mostly found in CEM II experiments (Fig. 3d, e, f), which agrees with the Ca wt.% from EDX profiles as shown in Fig. 2. Euhedral calcite crystals with sizes of 5-10 μm were also found in CEM II voids at the surface of mortars (Fig. 3f).

Hydrated cement products were found mixed in aggregates or needle-tabular morphologies. Examples of CSH (Fig. 3d, on the right side), ettringite (Fig. 3g), and CASH (Fig. 3i) in HpH and LpH were identified. Portlandite was just found at 6 months in CEM I (Fig. 3h). Regarding CEM II, the presence of Al-S phases, as ettringite, is related to the relative high content of Al in the cement mortar (Table S2).

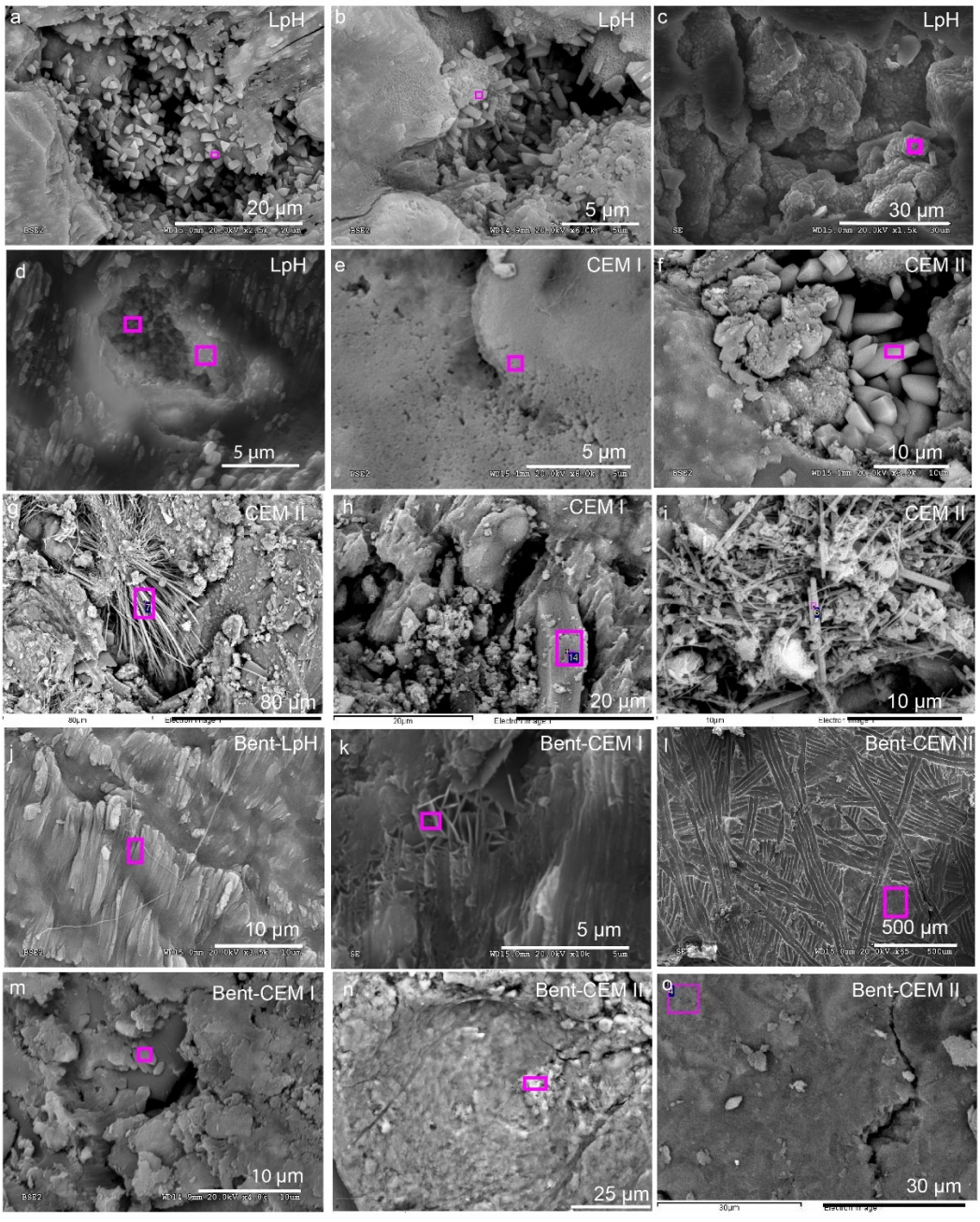
a
LpH
20 µm
b
LpH
5 µm
c
LpH
30 µm
d
LpH
5 µm
e
CEM I
5 µm
f
CEM II
10 µm
g
CEM II
80 µm
h
-CEM I
20 µm
i
CEM II
10 µm
j
Bent-LpH
10 µm
k
Bent-CEM I
5 µm
l
Bent-CEM II
500 µm
m
Bent-CEM I
10 µm
n
Bent-CEM II
25 µm
o
Bent-CEM II
30 µm

Fig. 3. SEM-EDX micrographs in the surface of the facing planes. a) Brucite prismatic trigonal crystal aggregates in LpH cement mortar at 6 m. b) Brucite crystals and honeycomb coatings of Mg, Ca-Si phases in LpH cement mortar at 6 m. c) Mg-Si spheroidal aggregates from LpH at 18 m experiments. d) Crystal aggregates of calcite mixed with Ca-Si coatings growing in between (18 m sample in LpH cement mortar). e) Ca crust (nanosized calcium carbonate) from a CEM I cement mortar in 6 m experiments. f) Scalenohedral calcite crystals from the CEM II experiment run over 6 m. g) Ettringite needles from the CEM II 6 m sample. h) Portlandite from the CEM I 6 m sample. *i*) CASH from CEM II 6 m. j) Mg-Si rich crust from Bent-LpH in 6 m. k) Mg (minor Fe) rich platy morphologies from bentonite in contact with CEM I in 6 m samples. l) Mg(Fe)-Si rich crust characteristic of Bent-CEM II experiments where the marks of the separation PTFE membrane are visible. m) Mixture of silicon and carbonate from the bentonite surface at the CEM I. n and o) Calcite crusts from Bent-CEM II at 18 and 6 m, respectively. Purple rectangles show the area covered by the analysis (the EDX analyses and EDX spectra of crystal aggregates are listed in Table S3a and b). m: months.

On the bentonite side, Mg-(minor Fe)-Si phases were found in the three types of interfaces. These phases were characterized by crusts morphologies, which exhibit moulded shapes of the PTFE membrane (Fig. 3j, l). In some depressions, edge-to-face aggregates of platy crystals are visible on the nm to μm scales (Fig. 3k). Crusts and platelets showed the highest Mg contents (Mg/Si ratios ranged from 0.6 to > 2). Punctually, small and localized Ca enrichment areas with an extension < 10 μm in diameter were found in bentonite surfaces exposed to HpH mortars (Fig. 3m, n, o).

With regard to the EDX analysis conducted in the fresh surfaces arising from the open CB interface, the results exceeded several times the Mg/Si ratios of reference FEBEX bentonite (Table 2). The analyses taken from these surfaces in Mg-Si-Al rich compositional zones, exhibit high standard deviations for silicate structural cations, including areas with high Mg/Si ratios (> 1.5). Conversely, unaltered reference FEBEX bentonite presented a very homogenous chemical composition at the same scale of observation, and Mg/Si ratios remained constant at reference levels (Mg/Si 0.14 ± 0.02). Irrespective of time, the average Mg/Si ratios recorded

were as follows: LpH, Mg/Si 0.53 ± 0.26, CEM I: 0.88 ± 0.18 and CEM II: 0.66 ± 0.15. CEM II exhibits intermediate values not as high as those of CEM I.

Table 2. Mean and standard deviation of Mg/Si ratios from the surface of the facing planes.

Exp.	Bent-LpH	Nº analyses	Bent-CEM I	Nº analyses	Bent-CEM II	Nº analyses	Ref. Bent.	Nºanalyses
Bent. 6 months	0.50 ± 0.22	23	0.85 ± 0.16	8	0.68 ± 0.15	19	0.14 ± 0.02	21
Bent. 18 months	0.55 ± 0.28	33	0.88 ± 0.19	86	0.64 ± 0.16	37		
total mean	0.53 ± 0.26	56	0.88 ± 0.18	94	0.66 ± 0.15	56		

Exp: experiments, Bent: bentonite, Ref: reference.

The crystal-chemical nature of bentonite surface zones at the interface was approached by the use of chemical coordinates ternary plots (Velde, 1985; see the supplementary file, Fig. S3). The presence of di-octahedral and tri-octahedral clay minerals compositions can be determined using the chemical analyses taken from surface zones of bentonite in the CB interface. Most of the CEM I and CEM II experimental spot coordinates were located in a linear combination built considering the intercalation of a complete brucite layer in the Mt interlayer (Mt-F-brc in Fig. S3). However, a small group of analyses tended to saponitic compositions over time in CEM I and LpH. This was less obvious for LpH if the ecxhangeable cation component is taken into account (M+R3-2R3-3R2 diagrams in Fig. S3), in which 18 months data visibly depart from saponite (Fig. S3b). In the case of CEM I at 18 m, the analysed compositions tended to saponitic terms in the representations of Fig.S3.

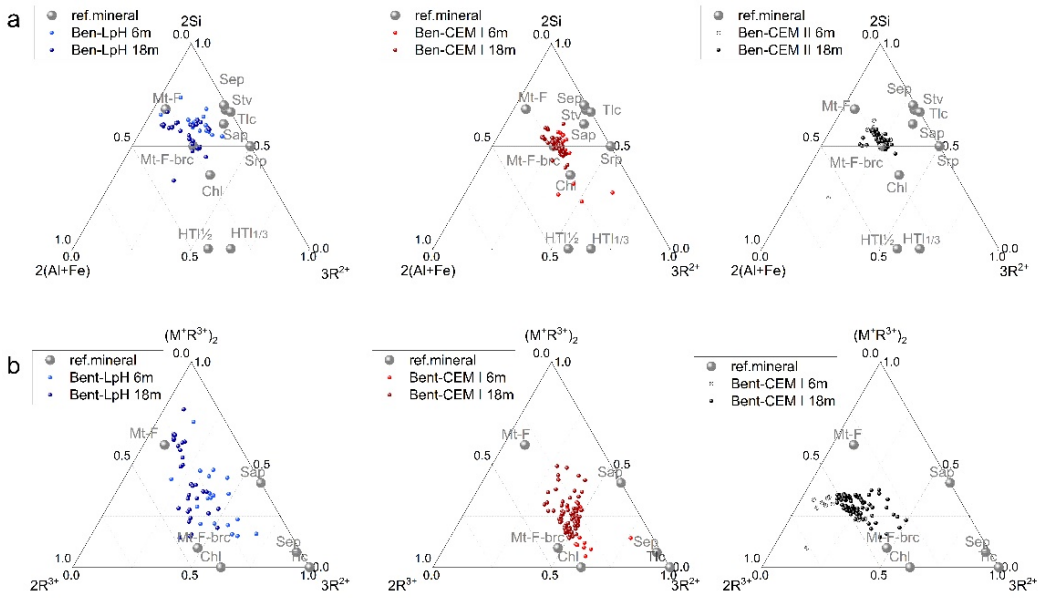

Fig. S3. Chemical projections of EDX surface analyses from bentonite. a) 2Si -- $3R^{2+}$ -- 2(Al+Fe): 2Si: Si/2; $3R^{2+}$: Mg/3; 2(Al+Fe): (Al+Fe)/2; b) $(M+R^{3+})2$ -- $3R^{2+}$ -- $2R^{3+}$: (M^{+}: charge of exchangeable cations: $Na^{+}+K^{+}+2{\cdot}Ca^{2+}$); $3R^{2+}$: Mg/3; $2R^{3+}$: (Al+Fe $-M^{+}$)/2. Mt-F: Montmorillonite FEBEX bentonite reference; Mt-F-bcr: Montmorillonite FEBEX bentonite intercalated with a brucitic layer; Sap: saponite; Srp: serpentine; Stv: stevensite; Tlc: talc; Sep: sepiolite; Chl: Chlorite; HTl ½: hydrotalcite ½ Al/Mg; HTl ⅓: hydrotalcite ⅓ Al/Mg. m: months

Concerning cement matrices and diagrams designed for hydrated cement phases (Gaboreau et al., 2017; Lerouge et al., 2017; Fig. S4 in supplementary file) a large number of spots tended to calcite (Ca pole) due to cement mortar interface surface enrichments. In the case of LpH, the dispersion of dots in the diagrams was especially complex due to the Mg, Al, Ca, Si mixing phases in the mortar. In contrast, regarding CEM II interface mortars compositions that fit Al-tobermorite with structure similar to CASH, were frequent, where the incorporation of Al is favoured in the low Ca/Si CSH. Al-tobermorite has been described in specific environments, such as relict lime clasts in volcanics (Jackson et al., 2013), and in the context of cement-based materials and bentonite interactions (Fernández et al., 2016).

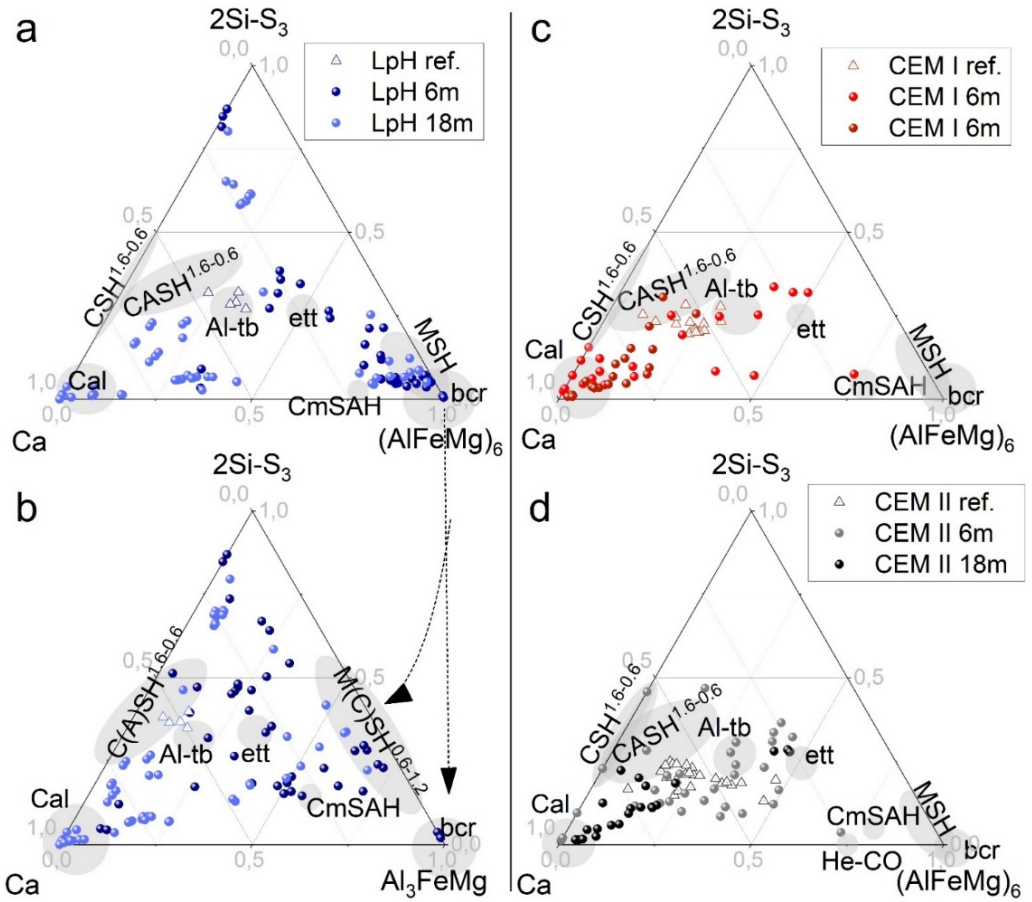

Fig. S4. Chemical projections of EDX surface analyses from cement mortars. $(AlFeMg)_6$: 6(Al+Fe+Mg), Al_3FeMg:3Al+Fe+Mg, $2Si\text{-}S_3$: Si/2 +3·S. CSH 1.6-0.6: calcium silicate hydrates with 1.6 and 0.6 Ca/Si ratios, CASH 1.6-0.6: calcium aluminium silicate hydrates with 1.6 and 0.6 Ca/Si ratios, Cal: calcite, Al-tob: aluminium tobermorite, CmSAH: hydrated Ca-Al-Fe monosulphate, MSH: magnesium silicate hydrate, bcr: brucite, C(A)SH: calcium (aluminium) silicate hydrate, M(C)SH 0.6-1.2: magnesium (calcium) silicate hydrate. m: months.

X-ray diffraction analyses

Results based on the surface θ/2θ scans are presented in Fig.4. Powder patterns of parallel slices exhibited no differences with untreated materials, and GI-XRD 0.5º θ on surfaces showed, with less quality, the same information as surface θ/2θ scans (comparison is shown only in the supplementary file, Fig. S5). The XRD θ/2θ scans registered at the bentonite surface interfaces showed the characteristic d001-

value of Mt at 14.8 Å, followed by a decrease in intensity as a function of time. Position changes are also presented in comparison with the reference bentonite (Fig. 4a). The d001-value disappeared after 18 months in the CEM I and CEM II experiments, and at the same time, a broad 7.6-7.4 Å and 3.66 Å reflections developed at 6 and 18 months. These reflections were only evidenced in bentonite exposed to CEM I after 18 months, whereas in bentonite exposed to CEM II it was well developed already after 6 months. In contrast, bentonite exposed to LpH and reference FEBEX-bentonite did not show any 7.6-7.4 Å d-value. Both 7.5 and 3.66 Å reflections are typical of Mg-tri-octahedral layered minerals such as serpentine or chlorite (Brindley and Brown, 1980; Shimbashi et al., 2018). With regard to the 06l reflection the CEM I experiments developed broad diffraction peaks at 1.53 Å not present in reference bentonite at 1.49-1.50 Å (Fig. 4b). However, the predominant presence of the 1.50 Å reflection indicated the persistence of di-octahedral smectites (Mt). Finally, it is worth noting that there was no evidence for the 3.03 Å calcite reflection in the LpH experiments, whereas CEM I after 18 months, and CEM II after 6 and 18 months contains clear calcite reflections.

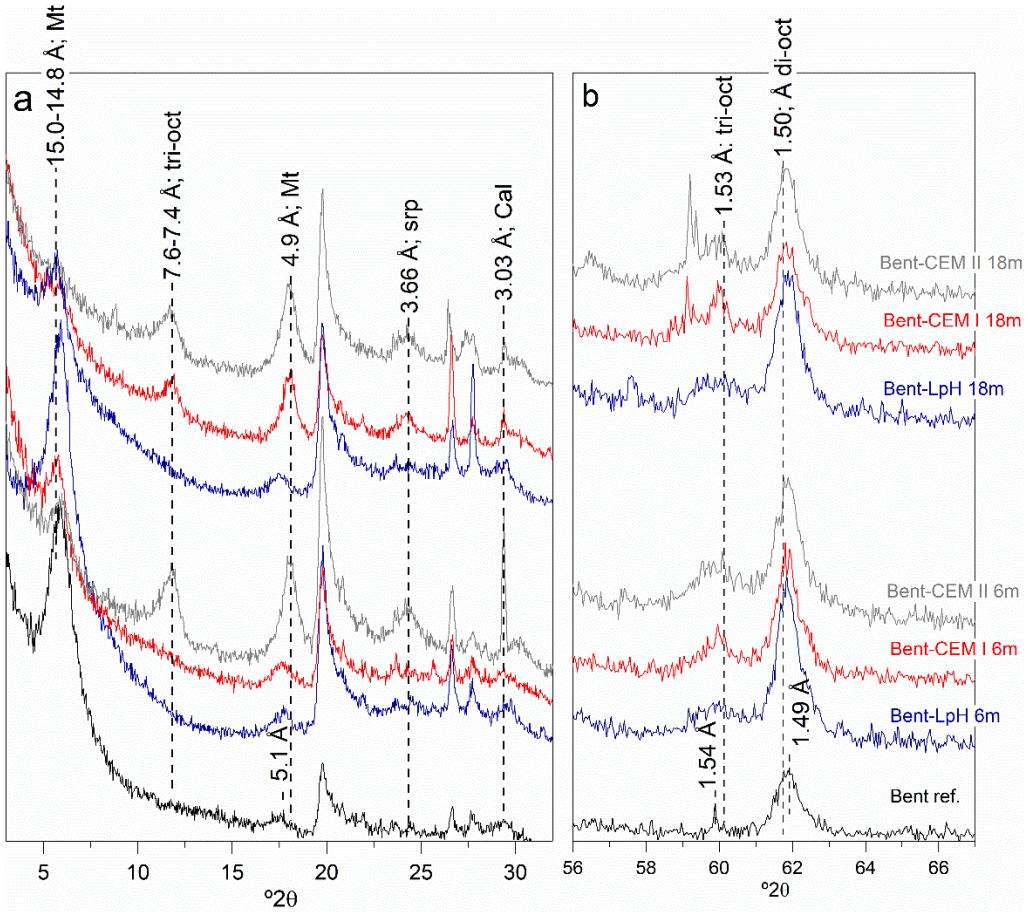

Fig. 4. θ/2θ scans performed on bentonite surface interfaces. a) Region of the diffractograms from the 3 to 31 º2θ position. b) Region from 56 to 67 º2θ position. Numbers indicate d-values in Å. Mt: montmorillonite, tri-oct: tri-octahedral clay mineral, srp: serpentine mineral group, di-oct: di-octahedral clay mineral.

With regards to cement mortars, the X-ray diffraction results showed minor differences regarding reference hydrated mortars (Fig. S6). On the LpH surface, characteristic brucite d-values at 4.77 and 2.36 Å were found after 6 and 18 months (Fig. S6a). Conversely, these reflections were not detected in the HpH surfaces, whereas calcite 3.03 Å d-values were detected in all experiments (Fig.S6b).

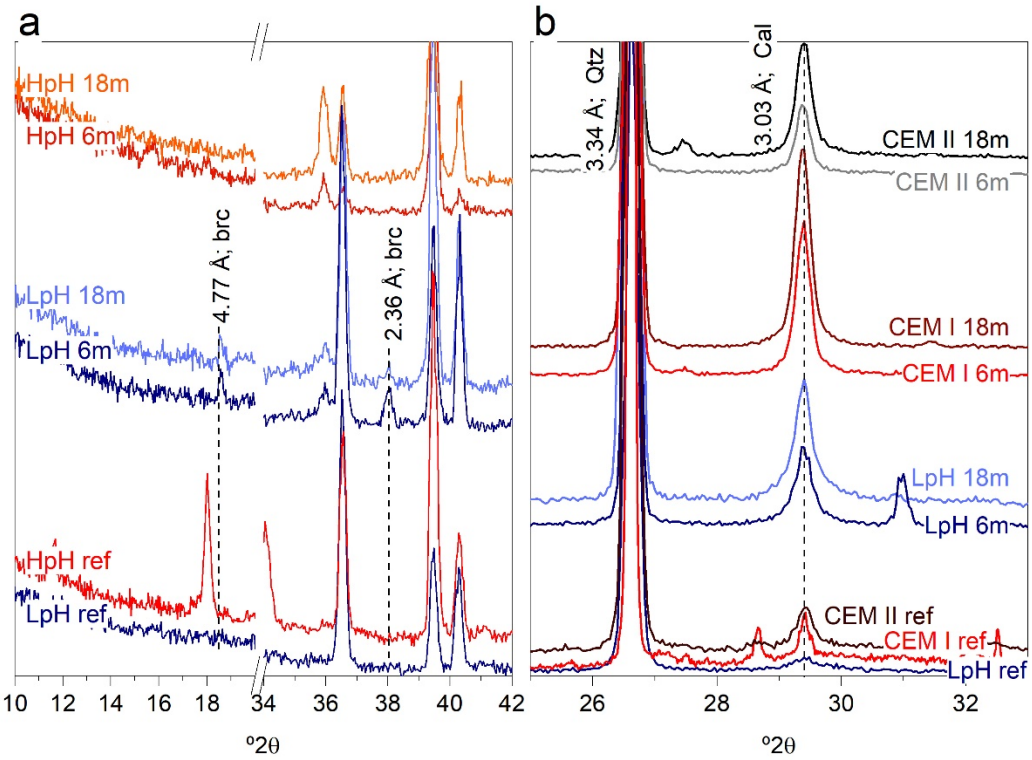

Fig. S6. θ/2θ scans carried out on the surface of cement mortars. a) Diffractograms of LpH and HpH cement mortars. HpH diffractograms represent the CEM I and CEM II experiments. b) Calcite reflection observed in the reference samples and cement mortars tested. m: months

Specific surface area

SSA changes indicate the existence of new phase precipitation processes with small crystal sizes and high external SSA, which led to an increase in global SSA; alternatively, it is possible that the formation of cement made N_2 gas inaccessible to part of the external surface pores with an associated SSA decrease (Lai and Krevor, 2014). Due to the short spatial extension of the perturbations observed in experiments, limited to < 1 mm at the CB interface, only the SSA of the first 3 mm slices sampled in both sides of the CB interface is presented (Fig. 5). Overall, the SSA of all samples next to the CB interface showed a decreasing tendency from 6 to 18 m, in both cement mortar and bentonite samples. After 6 and 18 months,

bentonite in contact with CEM I presented the lowest values, compared to LpH and CEM II.

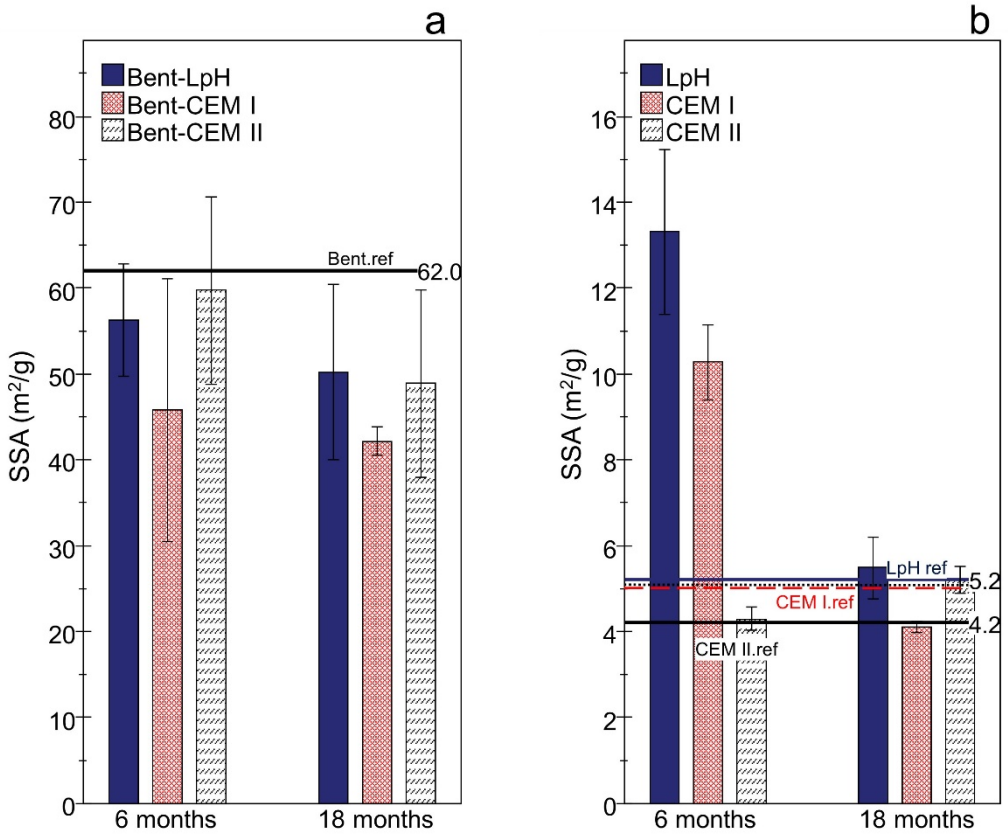

Fig. 5. Specific surface area (SSA; m^2/g) of the experiments performed at 6 and 18 months. a) SSA results of the first 3 mm of bentonite from the CB interface. b) Results of the first 3 mm obtained for cement mortars. SSA: specific surface area.

Compared to bentonite, the cement mortars SSA showed more significant changes. At 6 months, LpH and CEM I presented higher SSA than their references. Later, the LpH and CEM I SSA decreased over time, whereas CEM II remained close to the reference CEM II SSA, increasing from 4.2 m^2/g to 5.2 m^2/g after 18 months.

Aqueous solution

Effluent flow measurements show how the hydraulic conductivity is consistent with the reference FEBEX bentonite, in the order of 10^{-13} m/s (Villar and Lloret, 2004). Concrete and mortars made with similar materials, displayed high variability in hydraulic conductivity (*i.e.* 10^{-11} m/s for FEBEX CEM II concrete plug or 10^{-13} -10^{-14} m/s for CEM I concrete or CEM II mortar with limestone addition; Schneider et al., 2012; Turrero and Cloet, 2017;). It depends on porosity, initial water content, water/cement ratio, etc. Hydraulic conductivity slightly decrease over time (not showed), especially in CEM I experiments that present the lowest value (Table 3).

Table 3. Mean values of the pH, aqueous silica and hydraulic conductivity registered during the 18 months.

Experiment	pH	$SiO_{2(aq)}$ (mg/L)	Hydraulic conductivity (m/s)
Bent-LpH	8.2 ± 0.3	13.0 ± 2.3	$2.1\times10^{-13} \pm 1.3\times10^{-13}$
Bent-CEM I	7.9 ± 0.3	12.7 ± 0.9	$1.7\times10^{-13} \pm 1.1\times10^{-13}$
Bent-CEM II	8.3 ± 0.1	15.1 ± 3.2	$3.2\times10^{-13} \pm 1.9\times10^{-13}$

The evolution of the major chemical ions is presented as a function of the dimensionless number of pore volumes (V_p; V_p =1.3 cm^3; Fig. 6). Fewer data were obtained for experiments conducted with HpH cement mortars, owing to the low hydraulic conductivity of these experiments. The ions solution concentration decreased exponentially with time due to the relatively higher measured initial concentrations than in the long term collected fluids, due to initial soluble salts leaching. Highly soluble salts, chlorides, sulphates and bicarbonates with alkaline counter-ions (*i.e.* Na^+ and K^+), were readily leached, followed by an asymptotic decrease. Most of the ions were at very low concentrations at the end of the experiments, but not in the case of HCO_3^-, which ranged from 400 to 100 mg/L. The experiments with CEM II and LpH maintained higher HCO_3^- concentrations

because of the presence of calcite or the relatively lower pH at the CB interface, respectively. CEM I showed a sharp decrease in Mg and Ca to close to zero, in agreement with the more intense precipitation of hydrated Mg silicates and calcite. Conversely, CEM II leached more Ca because of the influence of the limestone addition. The values of the pH (7.9-8.3) and silica (13.0-15.1 mg/L) were homogenous and their content remained stable and constant regardless of the type of cement mortar and time (Table 3).

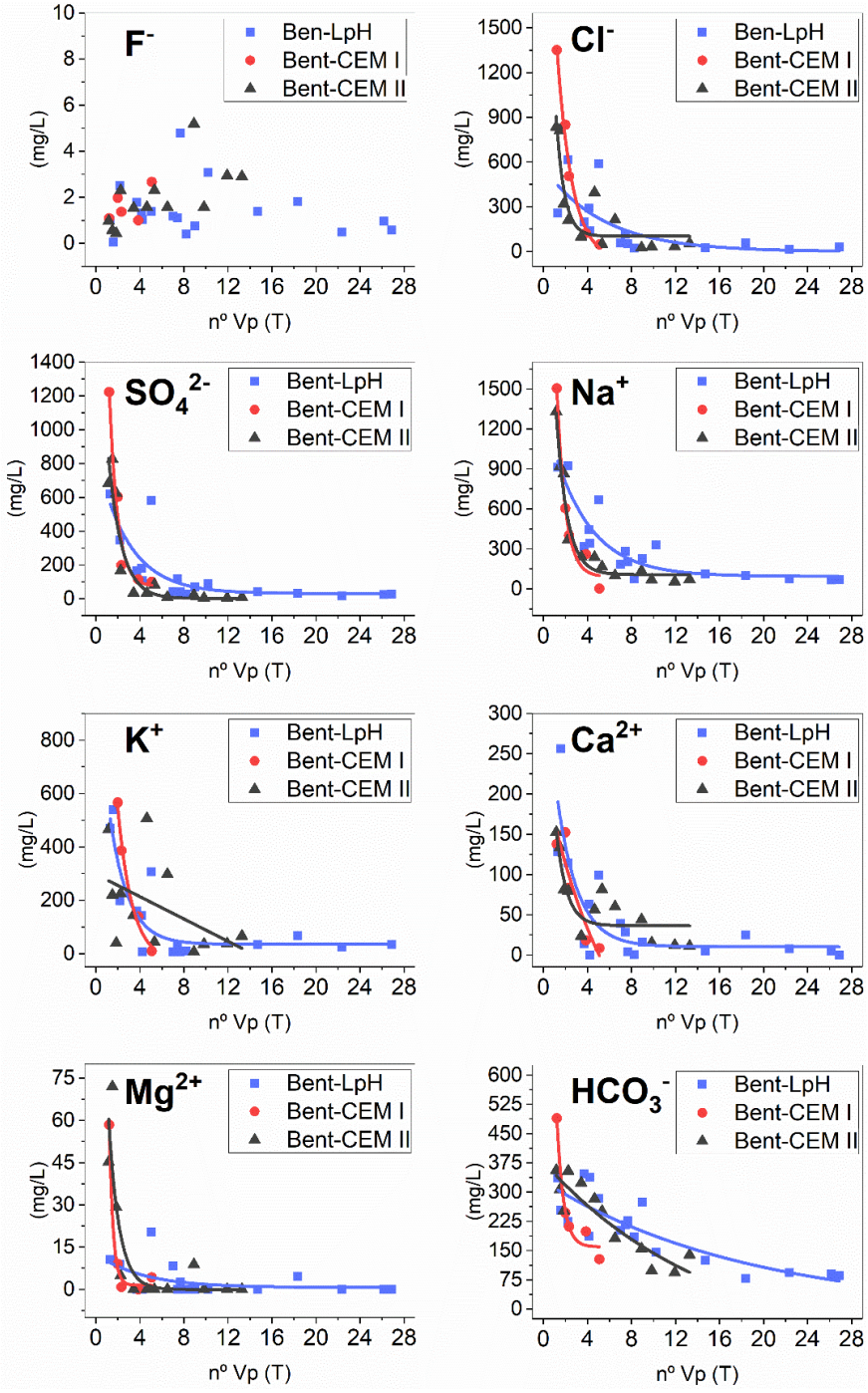

Fig. 6. Major chemical ions of the leachate collected at the end of the bentonite side.

Discussion

The study of the early reaction steps within the experimental simulated concrete/bentonite interfaces revealed perturbations influenced by the use of different types of cement mortars. The redistribution of Ca and Mg at both sides of the interface are indicators of the geochemical reactions involved. The Ca redistribution was mainly due to the decalcification of high Ca/Si CSH (1.7-1.4) to form (1) tobermorite (CSH Ca/Si ~0.8), (2) Al-tobermorite (CASH) if dissolved Al is available; (3) calcite if there exists a source for dissolved carbonate ions, and (4) Ca-Al sulphates, mainly ettringite, incorporating chloride and carbonate ions if there exists a source for sulphate or other anions. These processes were identified with different intensities related to the formation of by-products located on the mortar side of the interface. The precipitation of Mg-containing phases is characteristic of bentonite perturbation, except in LpH mortar in which they were present at both sides of the interface. Due to the mobility of this element (*i.e.* cation exchange from smectites interlayers to be incorporated to porewater solution), they were concentrated as (1) brucite, driven by precipitation at pH > 10.5, as observed by Pokrovsky and Schott, 2004 and (2) hydrated Mg silicate in the form of 2:1 or 1:1 tri-octahedral clay minerals if reactive silica was available and activated by the alkaline conditions at pH > 9 imposed by cement hydrated phase equilibrium. Examples of the combination of the aforementioned processes in concrete/clay interfaces were described for instance by Dauzères et al. (2010), Dauzères et al. (2014a), Jenni et al. (2014), Dauzères et al. (2016), Fernández et al. (2017) and Mader et al. (2017).

- The Ca geochemical perturbation within the CB interface was related to the precipitation of calcite in the mortar pores at the interface wall. HpH cement mortars developed a Ca maximum corresponding to calcite, increasing with time,

as detected by surface θ/2θ scans. On the other hand, EDX profiles revealed a decrease in Ca compared to reference values, with high heterogeneity, produced beyond 80 µm from the CB interface. Portlandite and high Ca/Si CSH dissolution was the calcium source for calcite precipitation, which is produced in the mixing zone where carbonated bentonite porewaters (pH 8-9) react with pH > 11 mortar porewaters (Dauzères et al., 2014a; Alonso et al., 2017). Significant calcite precipitation did not occur in the LpH experiments as far as portlandite was not present in the reference LpH hydrated mortar, and CSH already had a relatively low Ca/Si (0.8).

- Concerning Al and S redistribution, an increase located at the interface was generally observed in all mortars. In the case of CEM II, the limestone addition favoured the formation of ettringite at the expense of CmSAH as stated by Lothenbach et al., 2008. The Al diffusion from bentonite to mortars was due to the partial dissolution of Al-di-octahedral Mt increasing after 18 months. These alterations have been reported at similar studied interfaces in larger scale experiments: clay/LpH, clay/CEM I and clay/CEM II (Jenni et al., 2014; Dauzères et al., 2016; Alonso et al., 2017; Mäder et al., 2017), where Al dissolved from bentonite precipitated as CASH and secondary ettringite.

- Mg perturbations characterized the bentonite material at the CB interface. HpH CEM I, imposing the high pH gradient initially without calcite buffering, produced the highest perturbations compared to HpH CEM II and LpH. The development of a calcite crust may limit transport by diffusion, favouring the high intensity of Mg phase accumulation on this clay side as observed by Lalan et al., 2016. Exchangeable Mg in Mt was transferred to the pore solution, replaced by Ca and precipitated as hydroxide or hydrated silicates as discussed by Gaucher and Blanc

(2006) and observed experimentally by Fernández et al. (2013) and Mäder et al. (2017).

LpH cement mortar induced the precipitation of brucite, which were not identified in the other cement mortar interfaces (CEM I and CEM II). Initially (6 months), there was not sufficient silica in solution to produce hydrated Mg-silicates, further identified at 18 months by SEM-EDX with honeycomb morphologies similar to those described in Cuevas et al., 2018, for the *in situ* 13-year-old concrete-bentonite FEBEX experiment. HpH experiments XRD θ/2θ scans in the bentonite interface (Fig. 4) reveal structures related to the presence of Mg minerals with 7.5 Å spacing (chlorite-like) not identified in the LpH bentonite interface. As far as the characteristic basal spacing of divalent exchanged Mt (~14.8 Å) disappeared with time, the hypothesis of brucite intercalation, introducing disorder in the layer stacking in the interlayer structure of Mt is coherent with the observed linear chemical compositional mixture of brucite and Mt (Fig. S3). This fact was shown in previous studies (Fernández et al., 2013; Cuevas et al., 2018). However, clay mineral tri-octahedral sheet characteristic XRD reflections (06l reflection at 1.53 Å) were also identified in HpH cement mortar experiments, in agreement with time-dependent compositions trending to saponitic chemical coordinates. The nature and proximity of these MSH to clay minerals structures and compositions was already discussed by many authors (Lothenbach et al., 2015; Roosz et al., 2015; Walling and Provis, 2016; Lerouge et al., 2017). The Mg/Si ratios in CB bentonite surfaces (Table 2) matched with those characteristics of 2:1 clay minerals such as talc, saponite (Mg/Si: 0.75) sepiolite (Mg/Si: 0.67) and 1:1 serpentine group minerals (Mg/Si: 1.5), *i.e.* chrysotile. In any case, regardless of the cement type, the bentonite Mg-concentrated zone reaches 10% relative Mg at.% at 600 μm, smoothly reaching a homogeneous content in bentonite at 6.5%

after 1500 μm. Relatively further distances (~4-5 mm) were observed after 13 years ageing of CEM II and FEBEX bentonite in the *in situ* FEBEX experiment (Fernández et al., 2017), where Mg at.% maximum was higher than those observed in Opalinus clay and closer to the Mg content showed in this study for CEM I (Fig. 2). FEBEX bentonite has far more exchangeable Mg than Opalinus clay, and if a high pH is maintained, the potential Mg precipitation under the exchanged Mg displacement process will be more important.

The chemical profiles developed in these small scale experiments reproduced those found in large (*in situ*) to medium-scale (laboratory) long-term interfaces studied previously. Taking into account that the time scale ratio is approximately 10:1 between the two groups of scenarios (long-term: short-term) and that the thickness affected for chemical perturbation in larger experiments was 2-5 mm; it can be estimated that the comparable progression of the Mg or Ca chemical fronts represents in the worst (more rapid) case a 2:1 rate factor. Thus, considering the mineralogical and chemical heterogeneity of real-like interfaces in long-term experiments, this slow time advance is a good sign for EBS safety.

Apart from the mineralogical and chemical evidence for the geochemical perturbation, SSA changes could indicate the existence of new phase precipitation processes with small crystal sizes and high external SSA (Schoonheydt, 1995, Kaufhold et al., 2010) or the formation of cement clogging micropores (Lai and Krevor, 2014). This may be the case, as far as bentonite experienced a decrease in SSA from 6 to 18 months in contact with CEM I, with more intense Mg-phase and calcite precipitation. In fact, these phenomena have been supported by reactive transport modelling that predicts a clogging process at concrete-clay interfaces (De Windt et al., 2008; Marty et al., 2009; Kosakowski et al., 2013).

The resistance of CEM II against the change in SSA was remarkable. The limestone addition left less room for calcite precipitation, and Al-Ca sulphates became stabilized, which limited the extent of dissolution-precipitation processes as was predicted by (Matschei et al, 2007). This agrees with the low sulphate concentration in the CEM II effluents collected at the compacted bentonite end compared with those in the other experiments. In any case, irrespective of the type of cement mortar, pH and dissolved silica were in the range of those characteristic of FEBEX bentonite being regulated by clay mineralogy and accessory constituents in accordance with the buffer capacity of FEBEX bentonite (Fernández et al., 2000; Lloret and Villar, 2007). The presence of cristobalite and the pH buffer built by the presence of accessory calcite dissolution and the cation exchange equilibrium made these variables stable in the effluent collected at the bentonite end of the transport column.

Conclusions

Chemical reactivity at the cement-bentonite interface was assessed using three types of mortars and FEBEX compacted bentonite, infiltrating water from a granite source. The processes at the interface were analysed in terms of the spatial extension of the redistribution of Ca and Mg at both sides of the interface, as perturbation indicators. The high-pH mortars CEM I and CEM II developed a calcite rim (<100 μm) at the CB interface. There, near-neutral bentonite porewater, containing carbonate aqueous species, reacted within the generated pH gradient to precipitate the Ca ions leached from the mortars as $CaCO_3$. The Mg perturbation affected < 1500 μm thickness on the bentonite side and was less developed on the LpH and CEM II interfaces. However, LpH was the only mortar affected by the precipitation of Mg hydroxides and silicates within a 100 μm interface region.

Geochemical reactions observed at small scales of time and space (μm) in the present work are thought to have value to support modelling concepts of the behaviour of different materials that can configure the engineered barrier system. The presence of calcite in CEM II attenuated the reactivity in this HpH cement compared to CEM I and exhibited less reactivity than LpH. Then, the combination of CEM II with bentonite seems to have advantages compared to the other two simulated mortars in EBS.

The geochemical reactions observed at small spatial scale (μm) and short-term (up to 18 months) are promising for the development of reaction concepts and support modelling in the future, thus offering a useful prospective to advance upscaling of the concrete-bentonite interface perturbations at long-term.

Acknowledgements

It is important to us to pay credit to prof. Emilio Galán Huertos, for the motivation we had from him to work in the environmental application of clays during his fruitful life. We want also to acknowledge the comments of two anonymous referees and editor allowing us to improve the paper.

The experimental work was supported by funding from the European Union's Horizon 2020 Research and Training programme from EUROATOM [H2020-NFRP 2014, 2015] under grant agreement nº662147; CEBAMA.

Supplementary material

The complete supplementary material associated with this article is provided in the ANNEXE I-C.

References

Alonso, M.C., García Calvo, J.L., Cuevas, J., Turrero, M.J., Fernández, R., Torres, E., Ruiz, A.I., 2017. Interaction processes at the concrete-bentonite interface after 13 years of FEBEX-Plug operation. Part I: Concrete alteration. *Physics and Chemistry of the Earth*, Parts A/B/C 99, 38-48, https://doi.org/10.1016/j.pce.2017.03.008.

ANDRA, 2005. Dossier 2005 argile, synthesis: Evaluation of the feasibility of a geological repository in an argillaceous formation. Meuse/Haute-Marne site. ANDRA, Agence nationale pour la gestion des de´chets adioactifs., Paris, France.

Bartier, D., Techer, I., Dauzères, A., Boulvais, P., Blanc-Valleron, M.-M., Cabrera, J., 2013. In situ investigations and reactive transport modelling of cement paste/argillite interactions in a saturated context and outside an excavated disturbed zone. *Applied Geochemistry* 31, 94-108, https://doi.org/10.1016/j.apgeochem.2012.12.009.

Baur, I., Keller, P., Mavrocordatos, D., Wehrli, B., Johnson, C.A., 2004. Dissolution-precipitation behaviour of ettringite, monosulfate, and calcium silicate hydrate. 34, 341-348, https://doi.org/10.1016/j.cemconres.2003.08.016.

Blechschmidt, I., Vomvoris, S., 2010. 4 - Underground research facilities and rock laboratories for the development of geological disposal concepts and repository systems, in: Ahn, J., Apted, M.J. (Eds.), Geological Repository Systems for Safe Disposal of Spent Nuclear Fuels and Radioactive Waste. Woodhead Publishing, pp. 82-118.

Brindley, G.W., Brown, G., 1980. Crystal Structures of Clay Minerals and their X-Ray Identification. Mineralogical Society of Great Britain and Ireland.

Caballero, E., Jiménez de Cisneros, C., Huertas, F.J., Huertas, F., Pozzuoli, A., Linares, J., 2005. Bentonites from Cabo de Gata, Almería, Spain: a mineralogical and geochemical overview. Clay Minerals 40, 463-480, https://doi.org/10.1180/0009855054040184.

Cuevas, J., Ruiz, A.I., Fernández, R., Torres, E., Escribano, A., Regadío, M., Turrero, M.J., 2016. Lime mortar-compacted bentonite–magnetite interfaces: An experimental study focused on the understanding of the EBS long-term performance for high-level nuclear waste isolation DGR concept. 124-125, 79-93, https://doi.org/10.1016/j.clay.2016.01.043.

Cuevas, J., Ruiz, A., Fernández, R., González-Santamaría, D., Angulo, M., Ortega, A., Torres, E., Turrero, M., 2018. Authigenic Clay Minerals from Interface Reactions of Concrete-Clay Engineered Barriers: A New Perspective on Mg-Clays Formation in Alkaline Environments. Minerals 8, 362, https://doi:10.3390/min8090362.

Dauzères, A., Le Bescop, P., Sardini, P., Cau Dit Coumes, C., 2010. Physico-chemical investigation of clayey/cement-based materials interaction in the context of geological waste disposal: Experimental approach and results. Cement and Concrete Research 40, 1327-1340, https://doi.org/10.1016/j.cemconres.2010.03.015.

Dauzères, A., Le Bescop, P., Cau-Dit-Coumes, C., Brunet, F., Bourbon, X., Timonen, J., Voutilainen, M., Chomat, L., Sardini, P., 2014a. On the physico-chemical evolution of low-pH and CEM I cement pastes interacting with Callovo-Oxfordian pore water under its in situ CO2 partial pressure. Cement and Concrete Research 58, 76-88, https://doi.org/10.1016/j.cemconres.2014.01.010.

Dauzères, A., Le Bescop, P., Cau-Dit-Coumes, C., Brunet, F., Bourbon, X., Timonen, J., Voutilainen, M., Chomat, L., Sardini, P., 2014b. On the physico-chemical evolution of low-pH and CEM I cement pastes interacting with Callovo-Oxfordian pore water under its in situ CO2 partial pressure. 58, 76-88, https://doi.org/10.1016/j.cemconres.2014.01.010.

Dauzères, A., Achiedo, G., Nied, D., Bernard, E., Alahrache, S., Lothenbach, B., 2016. Magnesium perturbation in low-pH concretes placed in clayey environment—solid characterizations and modeling. Cement and Concrete Research 79, 137-150, https://doi.org/10.1016/j.cemconres.2015.09.002.

De Windt, L., Marsal, F., Tinseau, E., Pellegrini, D., 2008. Reactive transport modeling of geochemical interactions at a concrete/argillite interface, Tournemire site (France). Physics and Chemistry of the Earth, Parts A/B/C 33, S295-S305, https://doi.org/10.1016/j.pce.2008.10.035.

Duro, L., Altmaier, M., Holt, E., Mader, U., Claret, F. Grambow, B., Idiart, A., Valls, A., Montoya, V., 2020. Contribution of the results of the CEBAMA project to decrease uncertainties in the Safety Case and Performance Assessment of radioactive waste repositories. Applied Geochemistry 112, 104479, https://doi.org/10.1016/j.apgeochem.2019.

ECOCLAY-II, 2005. Effects of Cement on Clay Barrier Performance—Phase II, final report (Contract FIKW-CT-2000-00028). European Commission, Nuclear Science and Technology.

ENRESA, 2006. FEBEX Project Final Report. Post-mortem bentonite analysis, Enresa publicación técnica 05-1/2006. Madrid. Spain, p. 183.

Ewing, R.C., Whittleston, R.A., Yardley, B.W.J.E., 2016. Geological disposal of nuclear waste: a primer. Elements 12, 233-237, https://doi.org/10.2113/gselements.12.4.233.

Fernández, A.M., Cuevas, J., Rivas, P., 2000. Pore Water Chemistry of the Febex Bentonite. MRS Proceedings 663, 573, https://doi.org/10.1557/PROC-663-573.

Fernández, R., Cuevas, J., Sánchez, L., De La Villa, R.V., Leguey, S., 2006. Reactivity of the cement–bentonite interface with alkaline solutions using transport cells. Applied Geochemistry 21, 977-992, https://doi.org/10.1016/j.apgeochem.2006.02.016.

Fernández, R., Vigil de la Villa, R., Ruiz, A.I., García, R., Cuevas, J., 2013. Precipitation of chlorite-like structures during OPC porewater diffusion through compacted bentonite at 90°C. Applied Clay Science 83-84, 357-367, https://doi.org/10.1016/j.clay.2013.07.021.

Fernández, R., Ruiz, A.I., Cuevas, J., 2016. Formation of C-A-S-H phases from the interaction between concrete or cement and bentonite. 51, 223-235, https://doi.org/10.1180/claymin.2016.051.2.09.

Fernández, R., Torres, E., Ruiz, A.I., Cuevas, J., Alonso, M.C., García Calvo, J.L., Rodríguez, E., Turrero, M.J., 2017. Interaction processes at the concrete-bentonite interface after 13 years of FEBEX-Plug operation. Part II: Bentonite contact. Physics and Chemistry of the Earth, Parts A/B/C 99, 49-63, https://doi.org/10.1016/j.pce.2017.01.009.

Florea, M.V.A., Brouwers, H.J.H., 2012. Chloride binding related to hydration products. Cement and Concrete Research 42, 282-290, http://dx.doi.org/10.1016/j.cemconres.2011.09.016.

Gaboreau, S., Prêt, D., Tinseau, E., Claret, F., Pellegrini, D., Stammose, D., 2011. 15 years of in situ cement–argillite interaction from Tournemire URL: Characterisation of the multi-scale spatial heterogeneities of pore space evolution. Applied Geochemistry 26, 2159-2171, https://doi.org/10.1016/j.apgeochem.2011.07.013.

Gaboreau, S., Lerouge, C., Dewonck, S., Linard, Y., Bourbon, X., Fialips, C., Mazurier, A., Prêt, D., Borschneck, D., Montouillout, V., 2012. In-situ interaction of cement paste and shotcrete with claystones in a deep disposal context. American journal of science 312, 314-356, https://doi:10.2475/03.2012.03.

Gaboreau, S., Prêt, D., Montouillout, V., Henocq, P., Robinet, J.-C., Tournassat, C., 2017. Quantitative mineralogical mapping of hydrated low pH concrete. Cement and Concrete Composites 83, 360-373, https://10.1016/j.cemconcomp.2017.08.003.

Galán, E., Alvarez, A., Esteban, M.A., 1986. Characterization and technical properties of a Mg-rich bentonite. Applied Clay Science 1, 295-309, https://doi.org/10.1016/0169-1317(86)90006-2.

García Calvo, J.L., Hidalgo, A., Alonso, C., Fernández Luco, L., 2010. Development of low-pH cementitious materials for HLRW repositories. 40, 1290-1297, https://doi.org/10.1016/j.cemconres.2009.11.008.

García Calvo, J.L., 2012. Desarrollo de materiales de construcción con cemento de bajo pH, compatibles con la barrera de ingeniería de un almacenamiento geológico profundo de residuos radiactivos de alta actividad. Universidad Autónoma de Madrid, Madrid, Spain.

Garralón, A., Gómez, P., Peña, J., Buil, B., Turrero, M., Torres, E., Sánchez, L., 2017. Hydrogeochemical Characterization of the Groundwater in the FEBEX Gallery, in: Nagra Arbeitsbericht, N.-. (Ed.). Nagra Arbeitsbericht, NAB.

Gaucher, E.C., Blanc, P., 2006. Cement/clay interactions–a review: experiments, natural analogues, and modeling. Waste Management 26, 776-788, https://doi.org/10.1016/j.wasman.2006.01.027.

Gómez-Espina, R., Villar, M.V., 2016. Time evolution of MX-80 bentonite geochemistry under thermo-hydraulic gradients. Clay Minerals 51, 145-160, https://doi.org/10.1180/claymin.2016.051.2.03.

González-Santamaría, D., Angulo, M., Ruiz, A., Fernández, R., Ortega, A., Cuevas, J., 2018. Low-pH cement mortar-bentonite perturbations in a small-scale pilot laboratory experiment. Clay Minerals 53, 237-254, https://doi.org/10.1180/clm.2018.16.

Grangeon, S., Claret, F., Linard, Y., Chiaberge, C., 2013. X-ray diffraction: a powerful tool to probe and understand the structure of nanocrystalline calcium silicate hydrates. Acta crystallographica Section B, Structural science, crystal engineering and materials 69, 465-473, https://doi.org/10.1107/S2052519213021155.

Grangeon, S., Claret, F., Roosz, C., Sato, T., Gaboreau, S., Linard, Y., 2016. Structure of nanocrystalline calcium silicate hydrates: insights from X-ray diffraction, synchrotron X-ray absorption and nuclear magnetic resonance. Journal of Applied Crystallography 49, 771-783, https://doi:10.1107/S1600576716003885.

Hawkins, P., Tennis, P.D., Detwiler, R.J., 1996. The use of limestone in Portland cement: a state-of-the-art review. Portland Cement Association.

Huertas, F., Santiago, J.L., 1997. The FEBEX Project. General Overview. MRS Proceedings 506, 343, https://doi.org/10.1557/PROC-506-343.

Idiart, A., Laviña, M., Kosakowski, A., Cochepin, B., Meeussen, J.C.L., Javier Samper, J., Mon, A., Montoya, V., Munier, I., Poonoosamy, J., Montenegro, L., Deissmann, G.,

Rohmen, S. Damiani, L.H., Coene, E., Naves, A., 2020. Reactive transport modelling of a low-pH concrete / clay interface. Applied Geochemistry 115, 104562, https://doi.org/10.1016/j.apgeochem.2020.

Jackson, M.D., Chae, S.R., Mulcahy, S.R., Meral, C., Taylor, R., Li, P., Emwas, A.-H., Moon, J., Yoon, S., Vola, G., Wenk, H.-R., Monteiro, P.J.M., 2013. Unlocking the secrets of Al-tobermorite in Roman seawater concrete†. American Mineralogist 98, 1669-1687, https://10.2138/am.2013.4484

Jenni, A., Mäder, U., Lerouge, C., Gaboreau, S., Schwyn, B., 2014. In situ interaction between different concretes and Opalinus Clay. Physics and Chemistry of the Earth, Parts A/B/C 70-71, 71-83, https://doi.org/10.1016/j.pce.2013.11.004.

Kaufhold, S., Dohrmann, R., Klinkenberg, M., Siegesmund, S., Ufer, K., 2010. N_2-BET specific surface area of bentonites. Journal of Colloid and Interface Science 349, 275-282, https://doi.org/10.1016/j.jcis.2010.05.018.

Kaufhold, S., Dohrmann, R., 2016. Distinguishing between more and less suitable bentonites for storage of high-level radioactive waste. Clay Minerals 51, 289-302, https://doi.org/10.1180/claymin.2016.051.2.14.

Keusen, H.R., Ganguin, J., Schuler, P., Buletti, M., 1989. Grimsel test site: geology, Switzerland, p. 167.

Kosakowski, G., Berner, U., 2013. The evolution of clay rock/cement interfaces in a cementitious repository for low- and intermediate level radioactive waste. Physics and Chemistry of the Earth, Parts A/B/C 64, 65-86, https://doi.org/10.1016/j.pce.2013.01.003.

Lai, P., Krevor, S., 2014. Pore scale heterogeneity in the mineral distribution and surface area of Berea sandstone. Energy Procedia 63, 3582-3588, https://doi.org/10.1016/j.chemgeo.2015.07.010.

Lalan, P., Dauzères, A., De Windt, L., Bartier, D., Sammaljärvi, J., Barnichon, J.-D., Techer, I., Detilleux, V., 2016. Impact of a 70°C temperature on an ordinary Portland cement paste/claystone interface: An in situ experiment. Cement and Concrete Research 83, 164-178, https://doi.org/10.1016/j.cemconres.2016.02.001.

Lerouge, C., Gaboreau, S., Grangeon, S., Claret, F., Warmont, F., Jenni, A., Cloet, V., Mäder, U., 2017. In situ interactions between Opalinus Clay and Low Alkali Concrete. Physics and Chemistry of the Earth, Parts A/B/C 99, 3-21, https://doi.org/10.1016/j.pce.2017.01.005.

Lloret, A., Villar, M.V., 2007. Advances on the knowledge of the thermo-hydro-mechanical behaviour of heavily compacted "FEBEX" bentonite. Physics and Chemistry of the Earth, Parts A/B/C 32, 701-715, https://doi.org/10.1016/j.pce.2006.03.002.

Lothenbach, B., Le Saout, G., Gallucci, E., Scrivener, K., 2008. Influence of limestone on the hydration of Portland cements. Cement and Concrete Research 38, 848-860, https://doi.org/10.1016/j.cemconres.2008.01.002.

Lothenbach, B., Nied, D., L'Hôpital, E., Achiedo, G., Dauzères, A., 2015. Magnesium and calcium silicate hydrates. Cement and Concrete Research 77, 60-68, https://doi.org/10.1016/j.cemconres.2015.06.007.

Mäder, U., Jenni, A., Lerouge, C., Gaboreau, S., Miyoshi, S., Kimura, Y., Cloet, V., Fukaya, M., Claret, F., Otake, T., Shibata, M., Lothenbach, B., 2017. 5-year chemico-physical evolution of concrete–claystone interfaces, Mont Terri rock laboratory (Switzerland). Swiss Journal of Geosciences 110, 307-327, https://10.1007/s00015-016-0240-5.

Marty, N.C.M., Tournassat, C., Burnol, A., Giffaut, E., Gaucher, E.C., 2009. Influence of reaction kinetics and mesh refinement on the numerical modelling of concrete/clay interactions. Journal of Hydrology 364, 58-72, https://doi.org/10.1016/j.jhydrol.2008.10.013.

Matschei, T., Lothenbach, B., Glasser, F.P., 2007. The role of calcium carbonate in cement hydration. Cement and Concrete Research 37, 551–558, https://doi.org/10.1016/j.cemconres.2006.10.013

Meunier, A., Velde, B., Griffault, L., 1998. The reactivity of bentonites: a review. An application to clay barrier stability for nuclear waste storage. Clay Minerals 33, 187-196, https://doi.org/10.1180/000985598545462.

Nagra, 2002. Project Opalinus Clay—safety report. Demonstration of disposal feasibility for spent fuel, vitrified high-level waste and long-lived intermediate-level waste, Nagra Technical Report, 02-05. Nagra, Wettingen, Switzerland.

Norris, S., 2017. Radioactive waste confinement: clays in natural and engineered barriers – introduction. Geological Society, London, Special Publications 443, 1-8, https://doi.org/10.1144/SP443.26.

Pokrovsky, O.S., Schott, J., 2004. Experimental study of brucite dissolution and precipitation in aqueous solutions: surface speciation and chemical affinity control. Geochimica et Cosmochimica Acta 68, 31-45, https://doi.org/10.1016/S0016-7037(03)00238-2.

Read, D., Glasser, F.P., Ayora, C., Guardiola, M., Sneyers, A., 2001. Mineralogical and microstructural changes accompanying the interaction of Boom Clay with ordinary Portland cement. Advances in cement research 13, 175-183, https://doi.org/10.1680/adcr.2001.13.4.175.

Roosz, C., Grangeon, S., Blanc, P., Montouillout, V., Lothenbach, B., Henocq, P., Giffaut, E., Vieillard, P., Gaboreau, S., 2015. Crystal structure of magnesium silicate hydrates (M-S-H): The relation with 2:1 Mg–Si phyllosilicates. Cement and Concrete Research 73, 228-237, https://doi.org/10.1016/j.cemconres.2015.03.014.

Savage, D., 2014. An assessment of the impact of the long term evolution of engineered structures on the safety-relevant functions of the bentonite buffer in a HLW repository. National Cooperative for the Disposal of Radioactive Waste.

Schneider, S., Mallants, D., Diederik, J. (2012). Determining hydraulic properties of concrete and mortar by inverse modelling. Mater. Res. Soc. Symp. Proc. Vol. 1475 © 2012 Materials Research Society, https://doi.org/10.1557/opl.2012.601.Schoonheydt, R., 1995. Clay mineral surfaces, from: Mineral Surfaces by DJ Vaughan and RAD Pattrick, The mineralogical society. Chapman & Hall.

Shimbashi, M., Sato, T., Yamakawa, M., Fujii, N., Otake, T., 2018. Formation of Fe- and Mg-Rich Smectite under Hyperalkaline Conditions at Narra in Palawan, the Philippines. Minerals 8, 155, https://doi.org/10.3390/min8040155.

Torres, E., Turrero, M.J., Garralón, A., Cuevas, J., Fernández, R., Ortega, A., Ruíz, A.I., 2019. Stable isotopes applied to the study of the concrete/bentonite interaction in the FEBEX in situ test. Applied Geochemistry 100, 432-443, https://doi.org/10.1016/j.apgeochem.2018.12.017.

Tournassat, C., Steefel, C.I., Bourg, I.C., Bergaya, F., 2015. Natural and Engineered Clay Barriers, in: Tournassat, C., Steefel, C.I., Bourg, I.C., Bergaya, F. (Eds.), Developments in Clay Science. Elsevier, pp. 1-4.

Trotignon, L., Devallois, V., Peycelon, H., Tiffreau, C., Bourbon, X., 2007. Predicting the long term durability of concrete engineered barriers in a geological repository for radioactive waste. Physics and Chemistry of the Earth, Parts A/B/C 32, 259-274, https://doi.org/10.1016/j.pce.2006.02.049.

Turrero, M.J., Cloet, V., 2017. FEBEX-DP Concrete ageing, concrete/bentonite and concrete/rock interaction analysis, in: Nagra (Ed.), NAB 16-18, 5430 Wettingen Switzerland, p. 282.

Velde, B., 1985. Clay minerals. Elsevier Science Pub. Co., Inc., New York, NY, United States.

Villar, M.V., Lloret, A., 2004. Influence of temperature on the hydro-mechanical behaviour of a compacted bentonite. Applied Clay Science 26, 337-350, https://doi.org/10.1016/j.clay.2003.12.026.

Vuk, T., Tinta, V., Gabrovšek, R., Kaučič, V., 2001. The effects of limestone addition, clinker type and fineness on properties of Portland cement. Cement and Concrete Research 31, 135-139, https://doi.org/10.1016/S0008-8846(00)00427-0.

Walling, S.A., Provis, J.L., 2016. Magnesia-Based Cements: A Journey of 150 Years, and Cements for the Future? Chemical Reviews 116, 4170-4204, https://doi.org/10.1021/acs.chemrev.5b00463.

Wang, J., 2014. On area-specific underground research laboratory for geological disposal of high-level radioactive waste in China. 6, 99-104, https://doi.org/10.1016/j.jrmge.2014.01.002.

Webb, P.A., Orr, C., 1997. Analytical methods in fine particle technology. Micromeritics Instrument Corp.

CAPÍTULO 6. RESUMEN de RESULTADOS y DISCUSIÓN

Ante la necesidad de asegurar la estabilidad a largo plazo (>10^4 años) de un sistema de barreras de ingeniería para el aislamiento de residuos nucleares, es necesaria la caracterización completa de la reactividad generada por el contacto entre los materiales que componen las barreras que se interponen como elementos de seguridad, al menos en las etapas iniciales como aproximación a su evolución posterior. Entre estos materiales barrera, destacan los materiales base-cemento y las arcillas por la reactividad generada entre ambos, condicionada por a su vez por el contacto con aguas subterráneas.

En la tesis doctoral se ha desarrollado un modelo experimental, así como una metodología que, mediante el uso de celdas de flujo herméticas que dejan el paso de agua a través de materiales poco permeables, permite estudiar la reactividad generada en materiales de base cemento en contacto con bentonita-FEBEX y con un flujo de agua subterránea granítica característica del almacenamiento. El experimento llevado a cabo constituye una herramienta versátil para aproximarse al estudio de las alteraciones geoquímicas en plazos de tiempo relativamente cortos bajo las mismas condiciones experimentales, lo que en última instancia permite contrastar el comportamiento geoquímico de los distintos materiales hoy considerados por la comunidad científica como barreras para el aislamiento de los residuos nucleares.

En una primera aproximación con el fin de poner a punto una metodología de base para su posterior desarrollo, se llevó a cabo un experimento piloto. Los resultados obtenidos mostraron alteraciones geoquímicas tras 75 días de interacción del

sistema agua–mortero de bajo pH–bentonita, si bien la reactividad observada en este intervalo de tiempo fue muy limitada tanto en la intensidad como en el alcance espacial. No obstante, se detectaron las principales alteraciones, cuyo alcance se estudió con detalle en los experimentos llevados a cabo posteriormente.

Una vez optimizadas las bases metodológicas, se iniciaron un total de 12 experimentos, bajo las mismas condiciones, en las cuales la bentonita FEBEX se puso en contacto con tres tipos de materiales de base cemento considerados para su implementación en el sistema de barreras aislantes. Estos consistieron en un mortero de bajo pH, basado en cemento Pórtland tipo CEM-I con adición de SF y otros dos morteros de alto pH basados en cemento Pórtland tipo CEM-I y CEM-II respectivamente, éste último caracterizado por presentar una adición extra de caliza.

A continuación, se analizaron los resultados de 4 celdas que confinaban los morteros de cemento elaborados con CEM-II en contacto con la bentonita-FEBEX y agua granítica subterránea, en coherencia con las características y materiales empleados en los experimentos *in-situ* de FEBEX. Dos de estas celdas se analizaron tras 6 meses de interacción mientras que los otras dos se analizaron tras 18 meses.

Las principales perturbaciones detectadas estuvieron relacionadas con la movilidad del Mg, Ca, Al y S en las proximidades del contacto mortero de cemento/bentonita-FEBEX.

En cuanto al Mg, se produce un aumento de hasta un 20% en la superficie de la bentonita con un alcance de ~800 μm, inferior a la longitud observada en los experimentos *in situ*-FEBEX del GTS (>1 mm). En su evolución, no se

constataron aumentos significativos de intensidad en la acumulación de Mg entre los periodos de 6 y 18 meses, pero tampoco en comparación con los experimentos *in situ*-FEBEX.

Por otro lado, el Ca se acumuló notablemente en las primeras 50-70 μm del mortero incrementando su intensidad de 6 a 18 meses (~40-60% at.). Este aumento se deriva de la influencia del agua de poro de la bentonita, de carácter neutro (pH ~8) y con alto contenido en HCO_3^-, lo que provoca una la disminución del pH en la porosidad del mortero que se traduce en la liberación de Ca^{2+} procedente principalmente de la descalcificación parcial de los C-S-H y la disolución de la portlandita. Finalmente, el Ca^{2+} en presencia de HCO_3^- reacciona para formar una capa de carbonato cálcico que ocluye el espacio poroso y actúa como una capa aislante. En los experimentos *in situ* esta perturbación evoluciona hasta alcanzar distancias superiores a un 1 mm desde la interfase.

En cuanto al presente estudio, el comportamiento del Ca en la bentonita mostró un discreto incremento de entre el 1-5% de Ca debido a la influencia del fluido de poro de los morteros que favorecerían una precipitación de forma localizada de carbonato cálcico, además de su probable incorporación al espacio interlaminar de la Mnt. Aunque este fenómeno no fue claramente detectado en los perfiles longitudinales de EDX, si fue observado en los estudios de SEM y XRD. Por otro lado, esta precipitación sí ha sido identificada con un mayor alcance en los experimentos *in situ*, presentando igualmente un carácter localizado y disperso en forma pequeñas zonas con carbonato cálcico.

En lo que respecta al Al y el S, los resultados muestran una migración desde la bentonita hacia el mortero de cemento. El Al procede de la Mnt disuelta por el frente alcalino del mortero, de modo que se libera Al^{3+} (como $Al(OH)_4^-$, en medio

básico) de la capa octaédrica al medio poroso donde sufre transporte por difusión hacia el mortero. Una vez en contacto con el agua de poro del mortero, el Al disuelto sigue dos caminos de reacción: *i*) puede entrar a sustituir al Si de la cadenas *dreiketten* en los C-S-H que han sufrido descalcificación, y/o *ii*) *reaccionar* con el S, también difundido desde la bentonita en especies de aniones sulfato o SO_4^{2-} característicos de su agua de poro; ambos, Al y S en presencia del Ca^{2+} precipitan como etringita secundaria observada como *no expansiva* pues se presentó ocupando los poros de la matriz del mortero, presumiblemente poros originados por la descalcificación de los C-S-H y portlandita. En menor medida y de forma puntal también se observó la precipitación de hidratos hexagonales de AFm con trazas de iones Cl^- similares a la sal de Friedel. En este sentido, los experimentos *in situ* de FEBEX han descrito fases de AFm-Cl de manera puntual. En cuanto a la etringita, de forma parcialmente distinta a lo aquí observado, su presencia en los experimentos *in situ*, siendo importante, no se observa en todos los contactos, lo que se justifica por el hecho de que a largo plazo esta tiende a desestabilizarse y perder S y Al, evolucionando hacia fases de la familia de los AFm, o directamente llegando a la formación de yeso.

En lo que respecta a la bentonita, los estudios de SSA mostraron una disminución progresiva desde el inicio hasta el final de los experimentos (0, 6 y 18 meses). Una explicación se fundamenta en la reducción de la microporosidad del material consecuencia de la precipitación de las fases magnésicas formadas por cuasi-cristales de tamaños nanométricos. Esta disminución también sería favorecida por la precipitación de carbonato cálcico, si bien, su contribución hubiera sido mínima en este material.

En cuanto al mortero de cemento, teniendo en cuenta la disminución de su SSA, la precipitación de etringita secundaría rellenando poros y la formación de la capa

protectora de carbonato cálcico se facilitaría la reducción de la porosidad del mortero, sin embargo, ésta se produce sólo en las primeras micras. Hay que añadir que teniendo en cuenta que la superficie especifica analizada abarca secciones de 3 mm de grosor, esta reducción de la porosidad en parte podría ser mayor por la descalcificación de los C-S-H y disolución de la portlandita, de modo que el balance neto resultaría en un ligero aumento de la SSA tras 18 meses en el CEM-II.

En el análisis de los lixiviados recogidos tras atravesar primero el mortero y finalmente la bentonita FEBEX, destaca la disminución de la conductividad hidráulica a lo largo de los primeros meses (<6 meses) para posteriormente estabilizarse. Esta disminución se puede relacionar con la precipitación de las nuevas fases minerales pues al causar cierta oclusión reducirían la conectividad del espacio poroso y por tanto la conductividad hidráulica. Si bien, este parámetro está en última instancia controlado por la bentonita, de modo que el ligero aumento de la SSA observado en los morteros apenas se vería reflejado en la reducción de la conductividad hidráulica. En cualquier caso, ésta se sitúa en valores muy bajos, adecuados para retrasar el movimiento de los radionúclidos en caso de su liberación.

Los iones mayoritarios analizados muestran una disminución a medida que aumenta el número de volúmenes de poro. Este proceso es observado con claridad en el caso del SO_4^{2-}, Cl^-, Na^+ y K^+. Estos iones están naturalmente presentes en el agua de poro de la bentonita-FEBEX. Por ello al comienzo del experimento sufren una lixiviación mostrando concentraciones más altas en las primeras muestras de efluente. Además, su desplazamiento se vería favorecido por la mayor influencia del transporte por advección propiciado a su vez por el estado inicialmente

deshidratado de la bentonita-FEBEX. La arcilla seca induciría un mayor potencial de succión hasta que se saturase en agua donde el transporte por difusión incrementaría su relevancia. En este momento, el notable descenso observado en el SO_4^{2-} y Cl^- estaría también influido por su transporte por difusión hacia el mortero de cemento, no siendo así en el caso el K^+ y el Na^+. La disminución del Mg^{2+} y el Ca^{2+} se debería principalmente a su precipitación como silicatos e hidróxidos de Mg, y calcita sobre la superficie de la bentonita-FEBEX. Por último, tanto el pH como la concentración de sílice acuosa (SiO_2 *aq*) se mantienen virtualmente constantes desde el inicio hasta el final de los experimentos en las muestras de lixiviado recogidas. Estos valores son acordes con aquellos característicos con las aguas de poro en equilibrio con las asociaciones minerales características de la bentonita-FEBEX, por lo que cuando el fluido atraviesa los 9 mm de la capa de bentonita estos parámetros quedan amortiguados a pesar de la influencia alcalina de los morteros.

Finalmente, los datos obtenidos a lo largo de la tesis doctoral se presentaron conjuntamente mostrando así los resultados de las 12 celdas de transporte que incluían los tres tipos de experimentos: LpH, CEM-I y CEM-II, estudiados en dos intervalos de tiempo: 6 y 18 meses. El principal objetivo fue contrastar la reactividad química de la interfase mortero/bentonita-FEBEX desarrollada por cada tipo de experimento.

Los resultados constataron que el tipo de mortero condiciona la reactividad de los materiales desde los primeros meses. Los procesos observados en los tres modelos estudiados difieren en su alcance espacial e intensidad, en ocasiones conduciendo a la formación de distintas fases minerales.

Como se ha señalado anteriormente, la redistribución de los iones de Ca, Mg Al y S explica mayoritariamente la reactividad geoquímica los sistemas planteados.

La fuente de Ca susceptible de movilizarse reside principalmente en la descalcificación de los C-S-H de alto contenido en Ca (>1.4) y portlandita, fases únicamente presentes en los morteros de HpH (CEM-I y CEM-II) por lo que las perturbaciones relacionadas con el Ca fueron más notables en este grupo de experimentos. La evolución del Ca puede seguir varias rutas de reacción para formar distintas fases minerales dependiendo de las especies iónicas presentes y condiciones de pH del medio poroso. Tal es el caso de la precipitación C-S-H tipo tobermorita (Ca/Si ~0.8). Por último, se vuelve a observar en los tres tipos de morteros la precipitación de carbonato cálcico con diferentes tamaños de cristal. En este punto, los morteros de cemento de alto pH (HpH) basados en CEM-I y CEM-II desarrollan la formación de la capa de $CaCO_3$ aislante con mayor intensidad (con una extensión inferior a 100 μm de y más del 30% de aumento de Ca) que los morteros de bajo pH, si bien la extensión es similar. Otro aspecto para resaltar es que esta formación de carbonato cálcico está precedida por una descalcificación previa de la matriz del cemento situada más allá de las 100 μm desde la interfase.

En la bentonita-FEBEX, la precipitación de $CaCO_3$ fue poco significativa, siendo característicos, por el contrario, los incrementos en la concentración de Mg.

Los tres tipos de experimentos presentan alteración (perturbación de Mg) en las proximidades de la interfase (<1500 μm) y de forma especialmente notable en las primeras micras. La alteración por acumulación de Mg es más intensa en los experimentos con CEM-I mientras que los realizados con LpH presentaron el menor incremento. Esta acumulación es debida a que el Mg interlaminar presente

en la Mnt pasa a la solución de poro al ser sustituido por Ca, para precipitar como fases de alto contenido en Mg. La naturaleza de estas fases aún no ha sido claramente identificada. En este contexto, han sido descritas como fases de hidróxidos de Mg (brucita, $Mg(OH)_2$), arcillas magnésicas de estructura 2:1, 1:1 o M-S-H (estructuras desordenadas similares a las arcillas magnésicas conocidas en la naturaleza). En el presente estudio en base a los resultados obtenidos se sugiere la formación de capas de brucita que se intercalarían en el espacio interlaminar de la Mnt, sin bien no se excluye la posibilidad de la precipitación adicional de minerales de arcilla trioctaédricas de estructura 2:1 (*e.j*. saponita) y 1:1 del grupo de la serpentina (*e.j.* crisotilo, si bien éste último más improbable).

En cuanto al comportamiento del Mg en los morteros de cemento, destacan los experimentos con LpH pues a diferencia de los otros dos modelos muestran precipitación de brucita al cabo de 6 meses y en menor medida al cabo de 18 meses tras haber evolucionado para formar presumiblemente estructuras altamente desordenadas de M-S-H. Esta influencia de Mg en los LpH está relacionada con el menor desarrollo de la capa aislante de carbonato cálcico en comparación con el CEM-I y CEM-II que facilitaría una mayor difusión del Mg hacia el LpH al no encontrar una barrera. Además, explicaría la mayor acumulación de Mg observada en la bentonita en los experimentos CEM-I y CEM-II pues impediría su transporte hacia los morteros. Por otro lado, también hay que considerar que la presencia de SF en los morteros de bajo pH influiría en la formación de M-S-H al suponer una fuente de sílice, así como el menor pH existente favorecería su formación.

En el estudio de la redistribución del Al y S, se observa que el Al liberado por la disolución parcial de la Mnt migra hacia el mortero en los tres modelos de experimentos. Como ya se ha señalado los C-S-H incorporan Al para formar geles C-A-S-H de estructura similar a la Aluminio-tobermorita, especialmente si éstos

han sufrido previamente un proceso de descalcificación. En presencia de S también pueden formar sulfatos de Ca y Al como etringitas o fases de AFm las cuales han destacado por su mayor presencia en los morteros de CEM-II. Estas perturbaciones también han sido identificadas en los diferentes URL que reproducen condiciones similares, es decir interfases arcilla en contacto con materiales de base cemento basados en LpH, CEM I y CEM II.

Si las dimensiones de los experimentos y de las perturbaciones observadas se extrapolan o escalan a los URL se puede estimar un coeficiente en cuanto a la escala de volumen de 10:1 entre ambos escenarios, y 2:1 en cuanto al alcance de las perturbaciones de Mg y Ca. Es por tanto que el avance de la reactividad está muy ralentizado y presenta una evolución que no comprometería la seguridad del EBS, lo que sugiere su estabilidad y viabilidad a largo plazo.

La SSA observada en los morteros muestran un notable aumento en los primeros 6 meses debido al proceso de descalcificación, excepto en el caso del CEM-II que se mantiene constante. A continuación, tras 18 meses, los morteros de LpH y CEM-I disminuyen su SSA hasta alcanzar los valores iniciales consecuencia de la precipitación de carbonato cálcico, más pronunciado en el CEM-I, y la precipitación de fases como etringita y M-S-H para el caso de los LpH. Sin embargo, el CEM-II no sigue esta dinámica, además de presentar una mayor resistencia a la descalcificación con el tiempo. Una hipótesis complementaria a la presentada en el 2º artículo podría sustentarse en que la adición de caliza dejaría menos espacio para la precipitación de fases secundarias como el $CaCO_3$ y sulfatos. En cualquier caso, se muestra como material base cemento más estable en cuanto a su SSA y a la lixiviación.

Por último, los resultados de pH y sílice acuosa presentes en el lixiviado demuestran el efecto buffer de la bentonita-FEBEX, ya señalados en los experimentos con CEM-II detallados, si bien en el presente trabajo este comportamiento es también extensible a experimentos con LpH y CEM-I.

CAPÍTULO 7. CONCLUSIONES

La Figura 6.1 engloba de forma esquemática la intensidad y el alcance de las perturbaciones geoquímicas observadas entre los morteros de cemento evaluados y la bentonita-FEBEX.

Se ha implementado un método novedoso y fiable para realizar experimentos de laboratorio a pequeña escala con respecto a la reactividad hormigón-bentonita característica de un AGP en granito. Si bien, se han detectado alteraciones mínimas a muy corto plazo, pudiéndose observar las siguientes perturbaciones geoquímicas: *i*) descalcificación de mortero de cemento en las interfases mortero de cemento-bentonita y mortero de cemento-agua, *ii*) ligera carbonatación en el mortero de cemento de bajo pH en la superficie de contacto con la bentonita, y *iii*) enriquecimiento de Mg en la bentonita. Estos resultados son espacialmente limitados, pero coherentes con los observados previamente a más largo plazo, ya sea a escala de laboratorio o en las instalaciones subterráneas con experimentos de demostración *in-situ*.

El estudio de las reacciones geoquímicas que ocurren en una etapa temprana (0.5-1.5 años) durante la interacción entre el mortero de cemento-CEM II y la bentonita FEBEX se ha llevado a cabo mediante los ensayos en celdas de transporte a pequeña escala que se han puesto a punto previamente. Esto ha permitido facilitar una mejor comprensión de los resultados a largo plazo observados después de 13 años de interacción hormigón-bentonita tras el desmantelamiento del experimento *in situ* de FEBEX. Las rutas de reacción esperadas, que progresan más en los experimentos *in situ* a largo plazo, son consistentes con la evolución inicial de los

resultados obtenidos en este experimento de laboratorio a pequeña escala, siendo relevantes:

-La descalcificación de C-S-H en un entorno en el que se produce la disolución de portlandita e hidratación progresiva de las fases anhidras.

-El desarrollo de una capa de carbonato de calcio (calcita) en el lado del mortero de cemento, además de la precipitación dispersa de calcita en zonas localizadas de la bentonita.

-El desarrollo inicial de una perturbación de Mg en el lado de la bentonita, relacionada con la formación de precursores de silicatos de Mg, con estructura de filosilicatos 2:1, como las principales fases neogénicas esperadas a largo plazo.

-La formación de etringita secundaria en la interfase del mortero de cemento.

Las características de la reactividad y alteración en el entorno del contacto entre los morteros de cemento y la bentonita son diferentes en función del tipo de mortero ensayado en los experimentos.

Los procesos en el contacto mortero-bentonita se analizaron en términos de la extensión espacial en la redistribución de Ca y Mg en ambos lados de la interfase, como indicadores de perturbación. Los morteros de alto pH CEM I y CEM II desarrollaron una costra de alteración por precipitación de calcita (<100 μm) en la interfase de mortero de cemento. En este lugar, el agua de poro de la bentonita casi neutra, que contiene especies acuosas de carbonato, reaccionó en función del gradiente de pH generado para precipitar los iones de Ca lixiviados de los morteros, como $CaCO_3$. La perturbación de Mg afectó <1500 μm de espesor en el lado de la bentonita y se desarrolló menos en las interfases con LpH y CEM II. Sin

embargo, el mortero con LpH fue el único afectado por la precipitación de hidróxidos y silicatos de Mg dentro de una región de 100 μm desde la interfase.

Los perfiles químicos medidos en estos experimentos a pequeña escala reproducen las características de los que se han encontrado en interfases hormigón-bentonita a largo plazo (experimentos *in situ*) a mediana escala (experimentos de laboratorio) estudiados con anterioridad. Teniendo en cuenta que la relación de escala de tiempo es aproximadamente 10:1 entre los dos grupos de escenarios (largo plazo: corto plazo), y que el espesor afectado por la perturbación geoquímica en experimentos a largo plazo fue de 2-5 mm; se puede estimar que la progresión comparada de los frentes químicos de Mg o Ca representan, en el peor de los casos, es decir, en los casos de desarrollo más rápido, un decrecimiento en la progresión de las perturbaciones en una relación 2:1. Por lo tanto, considerando la heterogeneidad mineralógica y química de las interfases reales en los experimentos *in situ* a largo plazo, este avance lento con el tiempo es un buen indicador para la seguridad de EBS.

Teniendo en cuenta la perspectiva ofrecida de los tres morteros de cemento estudiados, podemos afirmar que las reacciones geoquímicas observadas a pequeñas escalas de tiempo y espacio (meses y μm) en el presente trabajo tienen valor para respaldar conceptos de modelado del comportamiento de diferentes materiales que pueden configurar el diseño del sistema de barreras de ingeniería.

La presencia de calcita en CEM II atenuó la reactividad en este cemento de HpH en comparación con el CEM I, además exhibió menos reactividad que el LpH. En consecuencia, la combinación de CEM II con bentonita parece tener ventajas en comparación con los otros dos morteros simulados en el EBS.

Finalmente, las reacciones geoquímicas observadas a pequeña escala espacial (µm) y a corto plazo (hasta 18 meses) son prometedoras para el desarrollo de conceptos de reacción y modelos de apoyo en el futuro, ofreciendo así una perspectiva útil para avanzar en el escalado del impacto de las perturbaciones observadas en la bentonita y el hormigón a largo plazo. Es por tanto que los próximos esfuerzos se concentrarán en el desarrollo de un modelo geoquímico.

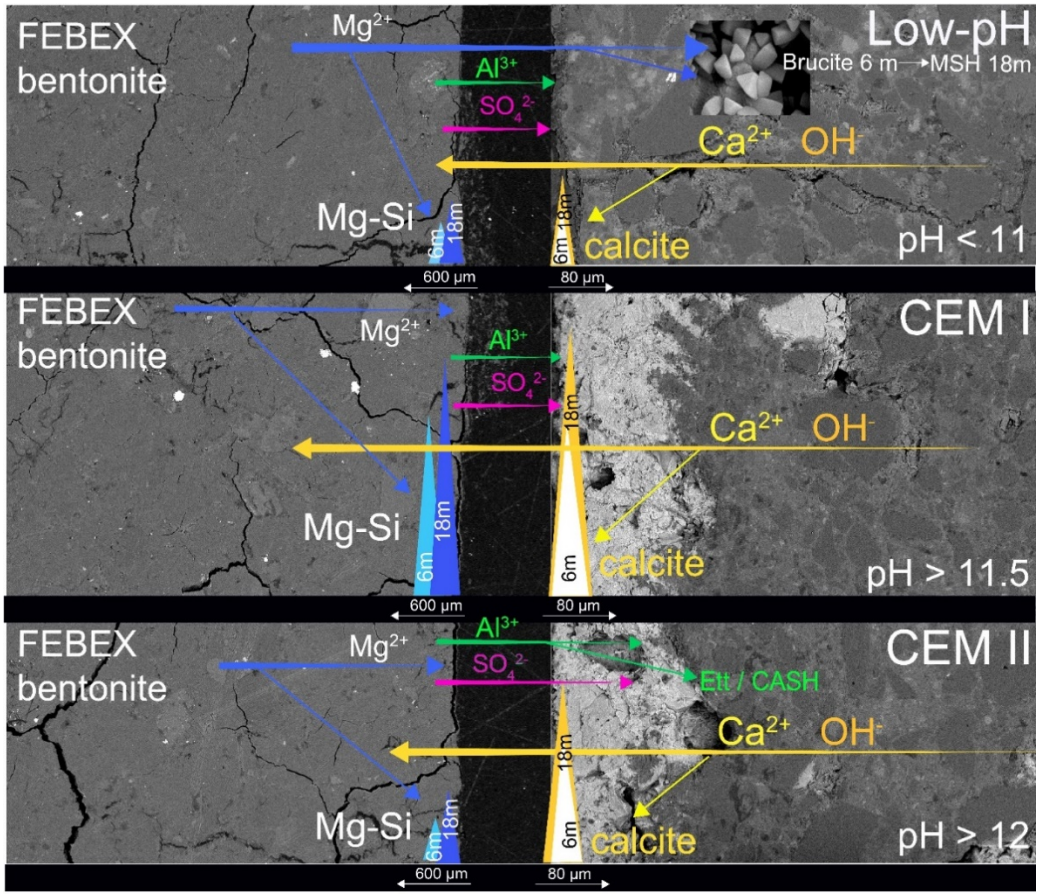

Fig. 6.1. Visión general de las principales alteraciones observados en los tres tipos de morteros de cemento y la bentonita-FEBEX. Puede observarse la dinámica de los iones, así como la intensidad y alcance de dichas perturbaciones.

CAPÍTULO 7. CONCLUSIONS

Figure 6.1 shows a schematic view of the intensity and extent of geochemical disturbances observed between the cement mortars assessed and FEBEX-Bentonite.

A novel and reliable method to perform small-scale laboratory experiments concerning concrete-bentonite reactivity in a granitic DGR has been tested. Only minor alterations have been observed within the very first stages ; however, the following chemical perturbations have been detected : i) cement mortar decalcification at the cement mortar-bentonite and cement mortar-water interfaces, ii) slight carbonation in the low-pH cement mortar next to the interface with bentonite, and iii) Mg enrichment in bentonite at the interface with the cement mortar. These results are spatially limited but coherent with those previously noticed over the long-term, either at the laboratory-scale or in large underground facilities.

The study of the geochemical reactions that occur at an early stage (0.5-1.5 years) during the interaction between the cement mortar-CEM II and the FEBEX bentonite has been carried out by means of the implemented small-scale cell tests. This has facilitated a better understanding of the large-spatial and long-term results observed after 13 years of concrete-bentonite interaction from the dismantling of the in situ FEBEX experiments. The expected reaction paths, which have progressed further in the in situ long-term experiments, are consistent with the initial evolution of the results summarized in this small scale laboratory experiment, being worth highlighting:

-The decalcification of C-S-H in an environment in which portlandite dissolution occurs and anhydrous phases are progressively hydrated

The development of a calcium carbonate layer (calcite) on the cement mortar side and dispersed precipitation of calcite in localized zones of bentonite.

-The initial development of a Mg perturbation at the bentonite side, related to the formation of precursors of 2:1 Mg-clay sheet silicates as the main neogenic phases expected at the long-term.

- The formation of secondary ettringite at the cement mortar interface.

The reactivity and alteration characteristics in the vicinity of the contact between cement mortar and bentonite are different depending on the mortar tested in the experiments.

The processes at the interface were analysed in terms of the spatial extension of the redistribution of Ca and Mg at both sides, as perturbation indicators. The high-pH mortars CEM I and CEM II developed a calcite precipitation layer (< 100 μm) at the CB interface. There, near-neutral bentonite porewater, containing carbonate aqueous species, reacted within the generated pH gradient to precipitate the Ca ions leached from the mortars as CaCO3. The Mg perturbation affected < 1500 μm on the bentonite side and was less developed on the LpH and CEM II interfaces. However, LpH was the only mortar altered by the precipitation of Mg hydroxides and silicates within a 100 μm interface region.

The chemical profiles developed in these small scale experiments reproduced those found in large- (in situ) to medium-scale (laboratory) long-term interfaces

studied previously. Taking into account that the time scale ratio is approximately 10:1 between the two groups of scenarios (long-term: short-term) and that the chemical perturbation in larger-scale experiments involved the first 2-5 mm; it can be estimated that the comparable progression of the Mg or Ca chemical fronts represent, in the worst (more rapid) case, a 2:1 rate factor. Thus, considering the mineralogical and chemical heterogeneity of real-like interfaces in long-term in situ experiments, this slow time advance is a good sign for EBS safety.

Considering the offered perspective of the three cement mortars studied, geochemical reactions observed at small scales of time and space (μm) in the present work are thought to have value to support behaviour modelling concepts of different materials that can configure the engineered barrier system.

The presence of calcite in CEM II attenuated the reactivity in this HpH cement compared to CEM I and exhibited less reactivity than LpH. Hence , the combination of CEM II with bentonite seems to have advantages compared to the other two simulated mortars in EBS.

Finally, the geochemical reactions observed at small spatial scale (μm) and short-term (up to 18 months) are promising for the development of reaction concepts and supporting modelization in the future, thus offering a useful perspective to advance on the upscaling of the concrete-bentonite interface perturbations at long-term. Consequently, further efforts will be focused on the development of a geochemical model.

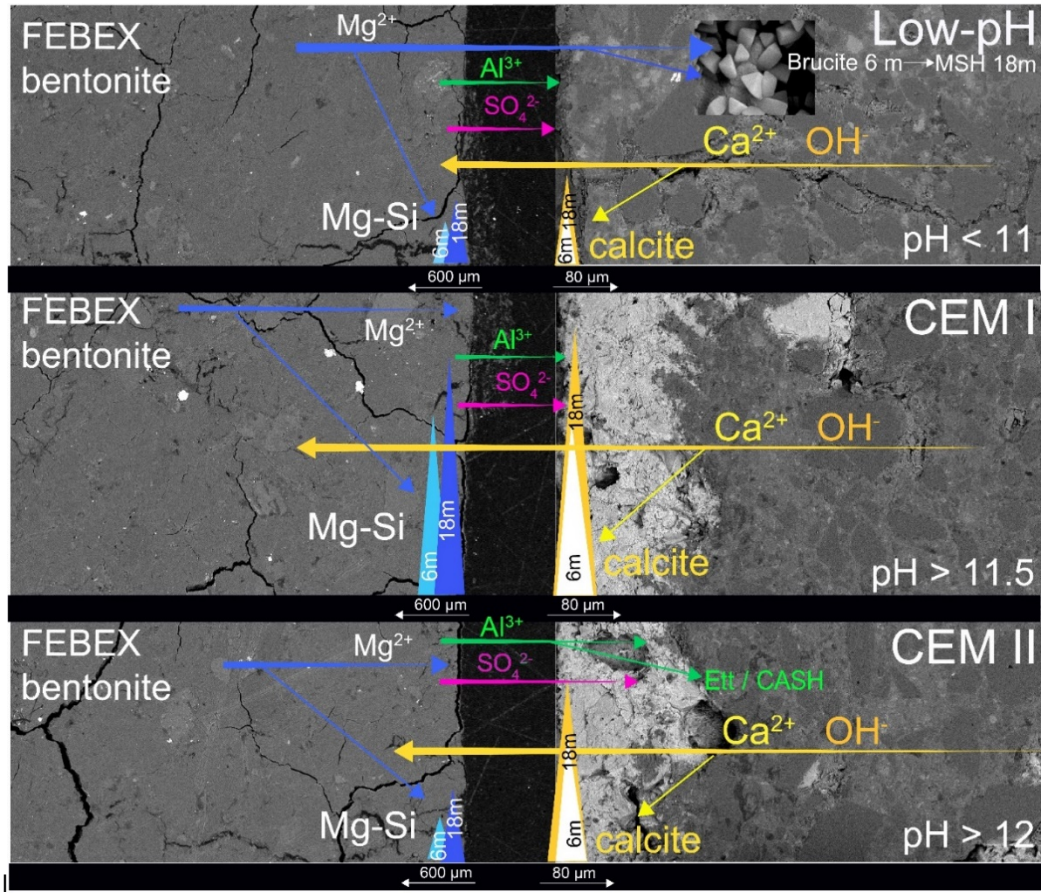

Fig. 6.1. Summary of the main alterations observed in the three types of cement mortars and FEBEX-bentonite. The dynamics of the ions can be observed, as well as the intensity and scope of the mentioned alterations.

ANEXO-I. Supplementary Materials

- *ANNEXE-I-A*
- *ANNEXE-I-B*
- *ANNEXE-I-C*

ANNEXE-I-A

TABLE S1. Analyses performed at different places of the sample (%) atomic.

	Nº	Mg	Al	Si	S	K	Ca	Fe	Ca/Si	Al/S	Mg/Si	Mineral
ref. low-pHC	1	0.0	0.4	40.6	29.5	0.0	29.5	0.0	0.7			cement matrix
	2	2.2	3.2	42.1	1.4	0.0	47.5	3.7	1.1			cement matrix
	3	0.7	0.0	53.3	0.8	0.7	44.5	0.0	0.8			cement matrix
	4	0.7	2.1	50.5	1.5	0.0	44.0	1.3	0.9			cement matrix
	5	3.5	6.7	39.4	2.9	0.0	37.4	10.1	0.9			cement matrix
	6	0.0	0.7	50.2	1.5	0.0	46.0	1.7	0.9			cement matrix
	7	0.0	0.6	54.9	0.0	0.0	44.5	0.0	0.8			cement matrix
	8	0.0	0.0	56.3	0.0	0.0	43.7	0.0	0.8			cement matrix
	9	0.0	2.0	52.0	3.4	0.0	41.1	1.5	0.8			cement matrix
	10	1.0	3.0	51.6	2.4	2.1	38.7	1.2	0.7			cement matrix
	11	1.3	2.5	53.7	0.9	0.0	40.2	1.8	0.7			cement matrix
	12	1.0	3.6	46.5	2.7	0.0	44.1	2.1	0.9			cement matrix
	13	1.2	1.7	43.0	3.7	0.0	47.5	2.9	1.1			cement matrix
	14	0.9	1.3	52.3	1.3	0.0	42.8	1.3	0.8			cement matrix
	*$\bar{y}$±s								0.9±0.1			
C-W Interface	15	1.2	4.4	34.0	5.7	0.0	50.8	3.7	-	0.8		ettringite
	16	3.7	2.3	47.5	1.1	0.0	42.9	2.5	0.9			cement matrix
	17	2.3	2.2	50.5	1.6	0.0	40.8	2.6	0.8			cement matrix
	18	2.3	4.2	49.9	2.0	0.3	36.6	4.7	0.7			cement matrix
	19	1.6	2.7	48.1	2.6	0.0	43.0	2.0	0.9			cement matrix
	20	0.0	1.7	60.9	0.5	0.0	39.1	1.7	0.6			cement matrix
	21	0.0	0.0	62.2	0.0	0.0	37.8	0.0	0.6			cement matrix
	22	1.2	2.5	52.5	2.5	0.0	41.3	0.0	0.8			cement matrix
	23	0.0	0.0	63.1	0.0	0.0	36.9	0.0	0.6			cement matrix
	$\bar{y}$±s								0.7±0.1			
C-B Interface	24	0.8	2.8	56.0	0.0	0.4	38.4	1.5	0.7			cement matrix
	25	2.1	1.4	49.1	0.0	0.0	45.6	1.8	0.9			cement matrix
	26	0.0	1.4	52.7	0.0	0.0	44.1	1.9	0.8			cement matrix
	27	1.2	2.2	49.3	1.0	0.0	44.1	2.1	0.9			cement matrix
	28	0.9	1.8	60.7	2.3	0.0	32.9	1.5	0.5			cement matrix
	29	3.3	3.3	50.4	0.6	0.0	39.1	3.3	0.8			cement matrix
	30	0.6	2.5	54.0	3.0	0.0	38.8	1.1	0.7			cement matrix
	$\bar{y}$±s								0.8±0.1			
Surface Bentonite	31	5.2	1.5	58.4	0.0	0.0	34.2	0.6	0.6			C-S-H
	32	2.8	8.1	25.6	12.7	0.0	43.5	7.3	-	0.6		ettringite
	33	3.3	43.0	0.6	0.0	46.6	3.3	0.0	-			calcite
	34	25.5	15.6	54.1	0.0	1.2	1.1	2.4			0.5	**Mnt-Mg
	35	29.4	10.7	54.9	4.9	0.0	0.0	0.0			0.5	Mnt-Mg
	36	29.7	6.8	60.5	0.0	0.7	0.6	1.6			0.5	Mnt-Mg
	37	37.2	10.1	49.0	0.0	1.0	0.8	1.9			0.8	Mnt-Mg
	38	23.7	16.9	52.5	0.0	1.4	1.6	1.4			0.5	Mnt-Mg
	39	28.1	16.1	52.8	0.0	0.6	0.8	1.5			0.5	Mnt-Mg
	40	32.7	13.6	50.3	0.0	0.8	0.8	1.8			0.7	Mnt-Mg
	41	19.9	18.7	54.8	0.0	1.4	1.1	2.8			0.4	Mnt-Mg
	$\bar{y}$±s										0.5±0.1	

**Mnt-Mg: Montmorillonite rich in magnesium.

$\bar{y}$±s: arithmetic mean ± standard deviation.

ANEXE-I-B

Table S1. Mathematical fitting of concentrations of major ions in effluents collected during 6 months (mg/L) as a function of the pore volume.

Time	Pv	F^-	Cl^-	SO_4^{2-}	Na^+	K^+	Ca^{2+}	Mg^{2+}	Alkalinity	EB (%)		pH	SiO_2(aq)
	1.5	2.9	611.6	853.9	965.8	509.6	133.7	72.0	325.8	36.3		8.2	12.9
	3.0	1.4	454.3	154.5	406.2	395.0	34.0	1.4	276.6	21.6		8.1	12.8
	4.5	1.4	334.0	27.8	195.0	302.5	29.5	<0.1	235.7	10.3		8.5	12.9
6m	6.0	1.4	241.1	4.5	114.3	227.2	29.3	<0.1	201.6	4.5		8.4	12.8
	7.5	1.4	169.3	0.2	83.5	165.9	29.3	<0.1	173.1	3.5		8.1	12.8
	9.0	1.4	113.5	<0.1	71.6	115.7	29.3	<0.1	149.1	6.0		8.1	12.5
	10.5	1.4	70.8	<0.1	67.1	75.1	29.3	<0.1	129.2	10.9		8.0	12.7
	12.0	1.4	37.8	<0.1	65.4	42.1	29.3	<0.1	112.5	17.9		8.3	13.0
	13.0	1.4	20.0	<0.1	64.9	23.5	29.3	<0.1	103.0	23.9		-	-
	RMSE	0.9	166.0	37.9	61.0	20.4	22.6	0.2	36.4				
	Adj. R-Square	*	0.65	0.99	0.97	0.99	0.72	1.00	0.85		$\bar{x}$±SD	8.2±0.2	12.8±0.1

EB (%): percent of error in the electrical balance, calculated as (Cat-An)/(Cat+An)×100

Pv: Pore volume.

$\bar{x}$±SD: mean ± standard deviation.

RMSE: root-mean-square error.

Adj. R-Square: goodness of curve fit (Exponential Decrease).

*: not converged.

.-: not detected.

Table S2. Mathematical fitting of concentrations of major ions in effluents collected for 18 months (mg/L) as a function of the pore volume

Time	Pv	F^-	Cl^-	SO_4^{2-}	Na^+	K^+	Ca^{2+}	Mg^{2+}	Alkalinity	EB (%)		pH	SiO_2(aq)
	1.5	4.9	773.3	466.1	413.1	416.2	95.0	23.6	378.8	-0.6		-	-
	3.0	3.1	460.8	104.4	309.4	187.2	33.6	5.1	362.6	-2.3		-	-
	4.0	2.4	270.6	43.5	237.4	84.6	29.8	4.5	346.4	-2.6		-	-
18m	6.0	1.7	152.9	33.0	186.6	37.9	29.6	4.4	330.2	-2.2		-	-
	7.5	1.4	81.2	31.2	151.2	17.0	29.6	4.4	314.0	-1.3		-	-
	9.0	1.3	36.9	30.9	126.3	7.5	29.6	4.4	297.7	0.0		8.1	16.5
	10.5	1.2	9.7	30.9	108.9	3.2	29.6	4.4	281.5	1.6		8.1	17.2
	12.0	1.2	0.0	30.9	96.8	1.3	29.6	4.4	265.3	1.4		8.4	17.9
	12.9	1.2	0.0	30.9	91.2	0.7	29.6	4.4	255.4	0.4		8.3	17.8
	RMSE	1.5	75.9	55.4	45.9	25.1	26.0	4.1	25.0				
	Adj. R-Square	0.44	0.94	0.92	0.88	0.98	0.62	0.89	0.78		$\bar{x}$±SD	8.2±0.1	17.3±0.6

EB (%): per cent of error in the electrical balance, calculated as (Cat-An)/(Cat+An)×100.
Pv: Pore volume.
$\bar{x}$±SD: mean ± standard deviation.
RMSE: root-mean-square error.
Adj. R-Square: goodness of curve fit (Exponential Decrease).
*: not converged.
.-: not detected.

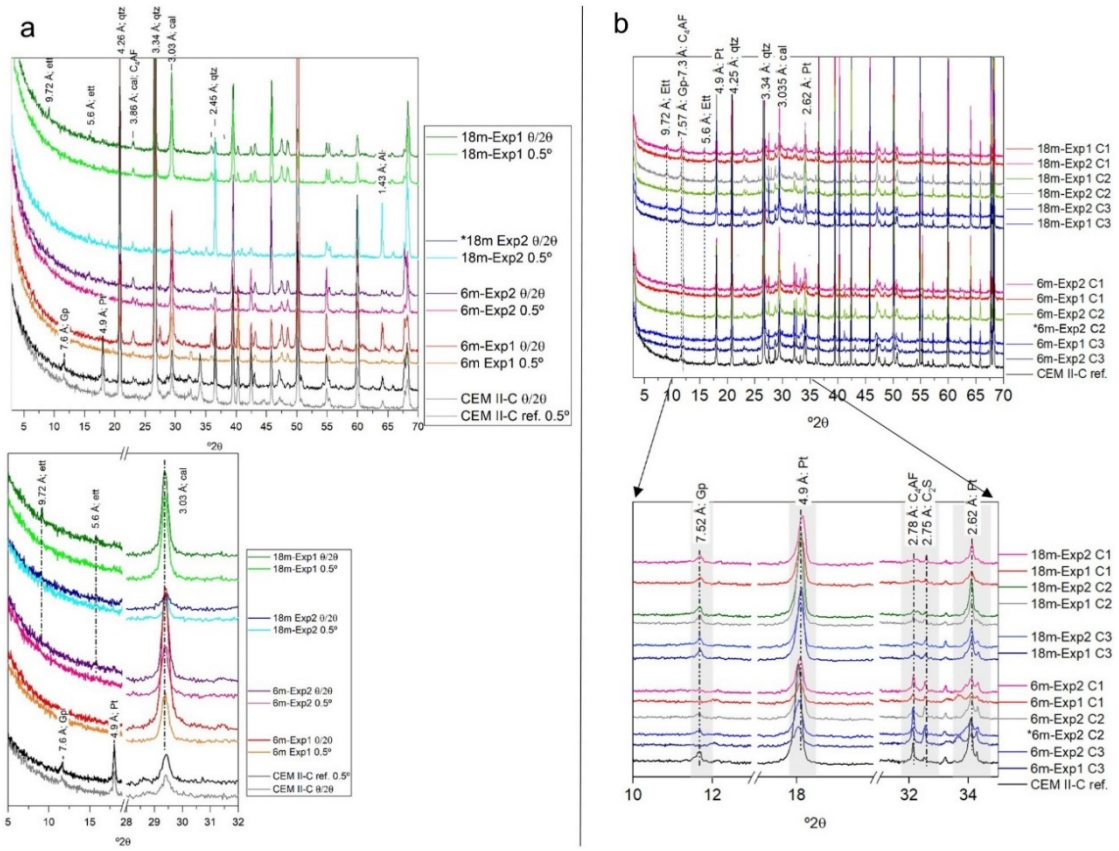

Fig. S1. a) Total patterns and close-up view of the θ-2θ scans and GI-XRD analyses performed on the flat surface interface of CEM II-C. (b) Total patterns and close-up view of the XRD analysis of cement mortar on randomly oriented powder samples at different distances from the interface (0-3 mm at C1; 3-6 mm at C2; 6-9 mm at C3) and at different time scales (6 and 18 months). Numbers indicate d-values in Å. Ett: ettringite, qtz: quartz, C_4AF: calcium alumino ferrite, cal: calcite, Gp: gypsum, Pt: portlandite, C_2S: di-calcium silicate. *The diffractograms of the18m Exp2 θ/2θ and 6m-Exp2 C2 is not shown owing to a failure during the analysis.

ANNEXE-I-C

Corresponding to introduction (section 1):

1. Introduction

Underground research laboratories (URL) are long-term *in situ* facilities in which technical and geochemical tests are carried out in support of the development of DGR (Blechschmidt and Vomvoris, 2010; Wang, 2014). To mimic DGR conditions, URL produce valuable scientific data to understand the physical-chemical interactions and the future evolution of the complex system established among groundwater, cementitious materials and clays. A representative overview of the mineral and geochemical perturbation observed in reference URL (Mont Terry rock laboratory (Switzerland), Tournemire experimental platform (France) and Grimsel Test Site (Switzerland)) after interaction times from 2 to 18 years (Table S1). These URL are testing reference cement-based materials expected to be used in DGR, mainly OPC-based cements: CEM I, CEM II (characterized by limestone addition to improve its durability, strength and workability (Hawkins et al., 1996; Vuk et al., 2001)) and CEM I mixed with SF as a low-pH material. Additionally, different types of clays such as opalinus clay (OPA) in Switzerland or Callovo-Oxfordian argillite in France as host rocks and bentonite as backfill have been tested for different DGR (Ewing et al., 2016).

Table S1. Geochemical perturbation observed at the cement/clay interfaces studied in reference Underground Research Laboratory (URL) tests.

Interface	years	Cement based material side	Clay side	URL experiment	Reference
CEM I/OPA	2	Perturbations from 0 to 300 µm: Ca depletion, carbonation; presence of Mg hydrates.	Perturbations over 200 µm: Ca enrichment; weak Mg and S enrichment.	Cement–clayey interaction experiment at the Mont Terri Underground Rock Laboratory (Switzerland)	(Jenni et al., 2014; Mäder et al., 2017)
CEM I/OPA	5	Perturbations from 0 to 300-500 µm: Ca depletion, S enrichment; carbonation; presence of Mg hydrates.	No significant alteration.	Cement–clayey interaction experiment at the Mont Terri Underground Laboratory (Switzerland)	(Jenni et al., 2014; Mäder et al., 2017)
Low-pH/OPA	2	Ca depletion (300-450 µm), followed by Ca and Mg enrichment (300-45 µm; calcite is present); followed by Mg depletion (0-45 µm). S enrichment (300-0 µm); S depletion (450-700 µm).	0 to 200 µm: Mg enrichment; weak S enrichment.	Low-pH cement (ESDRED) interaction with clayey at Mont-Terri Rock laboratory (Switzerland)	(Dauzères et al., 2016; Mäder et al., 2017)
Low-pH/OPA	5	Perturbation from 0 to 1.4 mm: Ca and weak S depletion; Mg enrichment coexisting with calcite and Mg-hydrates: 0 to 300 µm.	Perturbations from 0 to 200 µm: Mg enrichment.	Low-pH cement (ESDRED)-interaction with clayey at Mont-Terri rock laboratory (Switzerland)	(Dauzères et al., 2016; Mäder et al., 2017)
Low alkali/OPA	5	Perturbations limited to 1 mm with development of a crust band containing Mg-rich phase, calcite and CSH with low Ca/Si molar ratio.	Small changes of mineralogy: Mg-enriched (300-400 µm thick layer). Changing cation occupancies (Ca, Mg and K increase while Na decrease).	Low alkali cement (LAC) interaction with clayey (Textural, mineralogical and chemical changes study) at Mont Terri Underground Rock Laboratory (Switzerland)	(Lerouge et al., 2017)
CEM II/Bent.	13	S enrichment (1 to 5 mm): newly formed ettringite. Carbonation (< 1 mm), Cl-diffusion and concentration in 5-10 mm coupled to	Perturbation from 0 to 4-5 mm; large Mg enrichment (< 1 mm). Tri-octahedral Mg-	Concrete-bentonite interaction experiment at Grimsel Test Site - international	(Fernández et al., 2017)

		decalcification. Portlandite dissolution 0-5 mm.	Si clay formation.	Underground Laboratory (Switzerland)	
CEM II/Argillite	15	Perturbations from 0 to 10-15 mm: Portlandite dissolution, CSH decalcification and calcite precipitation.	Perturbations from 0 to18-20 mm: CSH precipitation; calcite dissolution followed by new calcite precipitation in the alkaline front.	Interactions between natural argillites and hyper-alkaline fluids from cement paste and concrete located in the Tournemire Experimental Platform (Aveyron, France)	(Techer et al., 2012)
CEM II/Argillite	18	Perturbations: 0-100 µm decalcification of portlandite and CSH linked to a porosity increase.	Perturbations from 0 to 11-13 mm: specific surface area decrease associated with neoformation of low Ca/Si CSH; calcite precipitation; possible illite precipitation.	Cement paste-argillite interaction at Tournemire Experimental Platform (Aveyron, France)	(Bartier et al., 2013)

OPA: Opalinus clay, Bent: bentonite, CSH: calcium silicate hydrate, CASH: calcium aluminium silicate hydrate, tri-Mg-Si: tri-octahedral Mg-silicate, brc: brucite, srp: serpentine, SSA: specific surface area. CEM I and CEM II correspond to the ordinary Portland cement (OPC) used. ESDRED: type of low-pH cement base material made with 60% of CEM I and 40% of silica fume, LAC: type of low-pH cement that contains 90% of CEM III/B and 10% of nanosilica.

Corresponding to results (section 3.1):

3.1. SEM-EDX analyses

The EDX study performed on the polished cement mortar areas in cement matrices in a 2 mm thickness section is shown in (Table S2). The results showed more Si content for LpH due to the SF addition and consequently presented relatively less Ca compared to HpH cement mortars.

Table S2. EDX area analysis performed at different time-scales (0 months, 6 months and 18 months) and cement mortar/bentonite (CB) interface of LpH-CEM I and CEM II cement mortars.

	Initial-references 0 months			CB-interface 6 months			CB-interface 18 months		
At.%	LpH	CEM I	CEM II	LpH	CEM I	CEM II	LpH	CEM I	CEM II
Mg	n.d.	n.d.	n.d.	n.d.	1.1±0.5	n.d.	0.6±0.5	0.5±0.5	0.3±0.2
Al	1.0±0.1	1.4±0.0	2.4±0.3	1.1±0.2	1.5±0.5	2.5±0.8	1.7±0.1	2.5±0.9	2.5±0.4
Si	83.3±0.5	74.8±1.0	74.7±1.3	88.1±0.3	84.7±1.7	80.1±2.9	84.5±1.1	76.3±1.4	74.1±2.1
S	n.d.	0.9±0.0	1.2±0.4	n.d.	n.d.	0.8±0.4	n.d.	1.2±0.3	1.5±0.4
K	0.4±0.3	0.4±0.1	n.d.	n.d.	n.d.	n.d.	n.d.	n.d.	n.d.
Ca	14.2±0.6	21.2±1.4	20.4±1.0	10.0±0.5	11.5±1.3	15.5±2.3	12.2±0.8	18.1±1.5	20.9±1.4
Fe	0.9±0.3	1.1±0.1	0.7±0.1	n.d.	0.9±0.3	0.8±0.3	0.9±0.2	1.3±0.1	0.8±0.1

At.%: atomic percentage, n.d.: not detected. LpH: Low-pH cement mortar. CEM I: High-pH cement mortar made with CEM I as ordinary Portland cement. CEM II: High-pH cement mortar made with CEM II A-L as ordinary Portland cement.

Focusing on the CB interface, LpH presented an increase in Si and a decrease in Ca from 0 to 6 months. After 18 months, Si decreased and Ca increased until reaching values near the initial reference. The same behaviour with more intensity was observed for CEM I and CEM II, owing to the dissolution-precipitation time-dependent process and redistribution of the cement mortar components linked to the decalcification of CSH and

portlandite. Regarding the other elements, Al increased with time in LpH and CEM I but remained stable in CEM II. The S and Fe apparently increased slightly after 18 months in CEM I, although the variations are near the standard deviation of the results.

With regards to EDX spot analyses, the time evolution of the cement mortar matrix chemical composition at the CB interface (surrounding quartz grains) was evaluated through the Ca/Si and Al/Si ratios of the different materials (Fig. S1). In general, the results showed wide variation ranges in experimental samples (6 and 18 months) owing to the uneven hydration or dissolution-precipitation reactions affecting mostly Si, Ca and Al redistribution in the analysed zone.

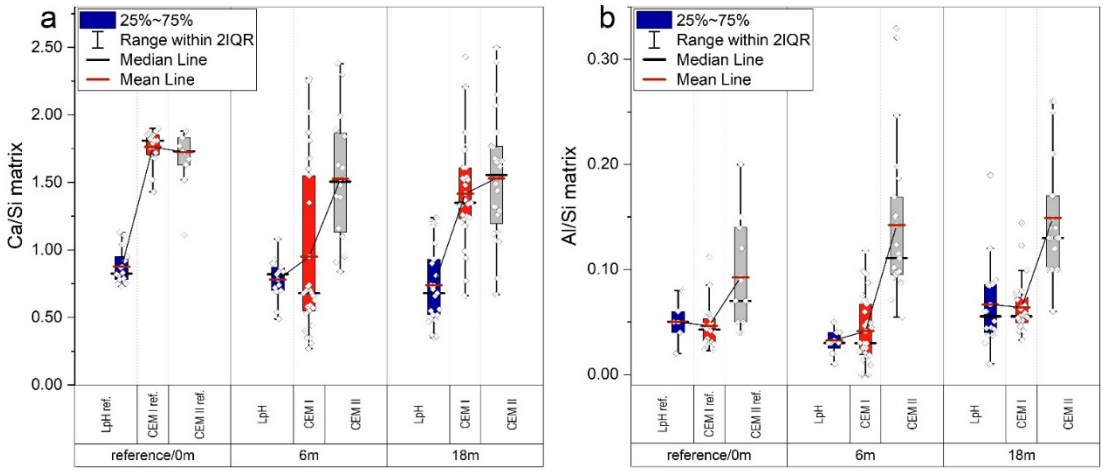

Fig. S1. EDX analysis of the cement mortars near the field of the interface. (a) Ca/Si ratio from 0 months (reference) to 18 months. (b) Al/Si ratio from 0 to 18 months. ref: reference. m: months.

The LpH reference sample presented mean values of Ca/Si = 0.88 ± 0.13, in accordance with the presence of a tobermorite-like structure of CSH, whereas the Ca/Si ratio of CEM I and CEM II presented mean ratios of 1.76 ± 0.13 and 1.72 ± 0.33, respectively, characteristic of a mixture of anhydrous phases and tobermorite-jennite-like structures of CSH (Grangeon et al., 2013; Grangeon et al., 2016). The CB interface concrete matrix analyses based on spots confirm both LpH and HpH decalcification at 6 months followed by a recalcification process after 18 months. CEM I cement mortar exhibited the greatest Ca/Si ratio decrease from 0 to 6 months, in contrast to LpH, which was virtually

unchanged from 0 to 18 months. Despite these variations, after 18 months, all experiments presented an average net loss of Ca for the CB interface and, more importantly, a wide variation of values due to the redistribution of calcium in different by-products, presumably calcite and low Ca/Si CSH, especially in CEM I experiments.

In agreement with the area analyses (Table S2), the Al/Si ratios of the cement matrix in the CEM II reference showed higher values than those of the LpH and CEM I reference samples: 0.09 ± 0.05 for CEM II, 0.05 ± 0.02 for LpH, and 0.05 ± 0.02 for CEM I. The Al/Si mean ratio of CEM II tended to gradually increase with time from 0.09 ± 0.05 to 0.15 ± 0.06. In contrast, LpH and CEM I presented small variations in Al/Si, within standard deviations and presumably due to the relative compensation of Ca and Si variations as far as the sum of analysed (detected) elements were adjusted to sum 100%.

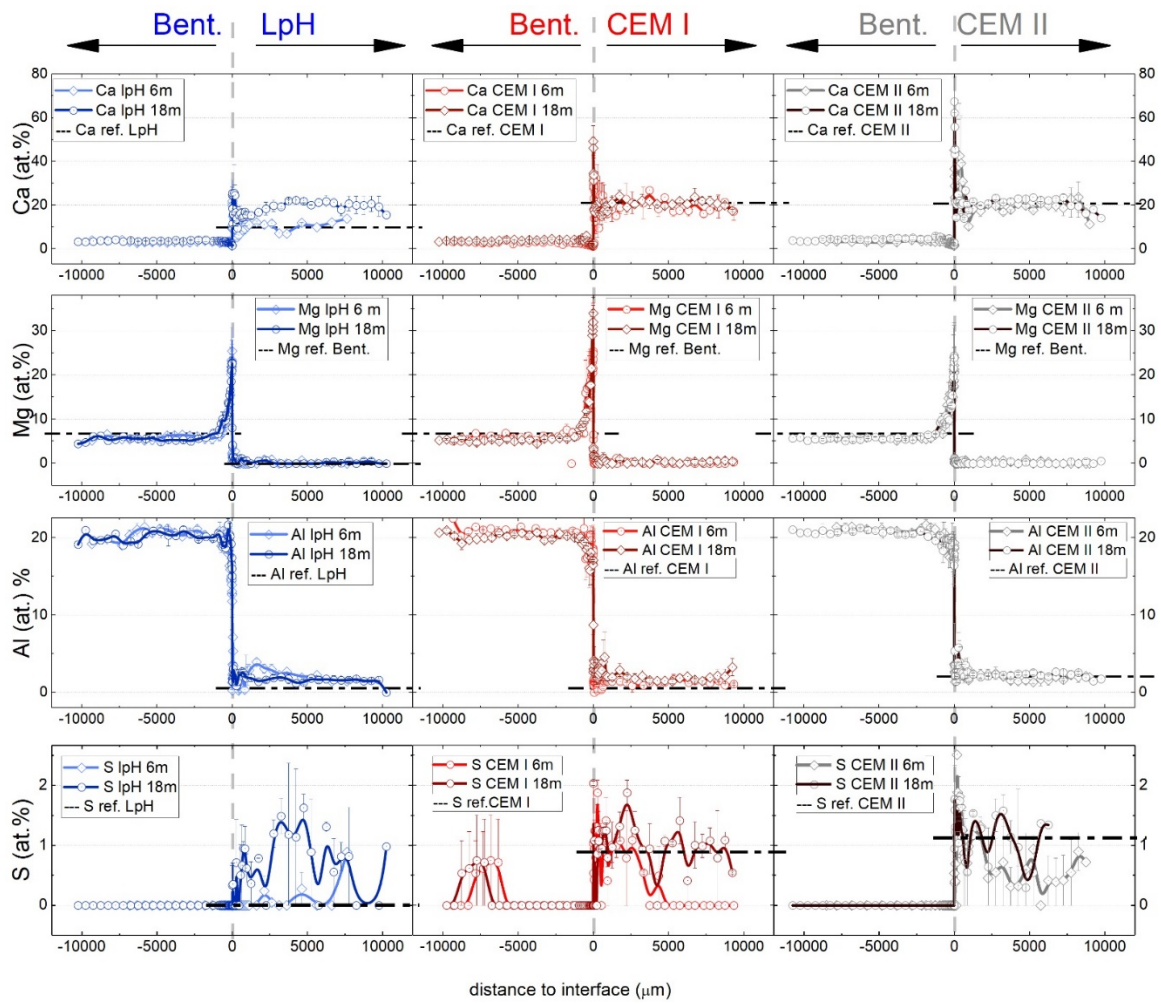

Fig. S2. Complete range of EDX analyses. Ca, Mg, Al, and S (at.%) chemical profiles of the three types of experiments. All profiles were obtained based on the average values of the duplicated experiments (error bars marked). The interface is represented at 0 μm and it is depicted as a vertical grey dashed line. Additionally, it is depicted reference (ref.) at.% of Ca, Al and S of each type of cement mortar, and basal Mg of FEBEX-bentonite has been plotted (horizontal dash lines). m: months.

EDX analyses of crystal aggregates

Table S3a. Complete chemical compositions based on EDX analyses of crystal aggregates and undifferentiated masses.

SEM micrograph	O	Na	Mg	Al	Si	S	K	Ca	Fe	Phase description
Fig. 3a	73.97	nd	15.62	0.15	7.26	nd	nd	3.00	nd	Brucite prismatic trigonal crystal aggregates
Fig. 3b	71.50	nd	10.57	0.52	7.83	nd	nd	8.75	0.84	Brucite crystals and honeycomb coatings of Mg,Ca-Si phases
Fig. 3c	75.80	nd	6.67	3.76	12.78	nd	0.25	0.40	0.34	Mg-Si spheroidal aggregates
Fig. 3d	84.80	nd	0.04	0.04	0.97	nd	0.00	14.10	0.03	scalenoedral crystal aggregates of cacite
Fig. 3d'	62.07	0.40	0.40	1.83	20.70	nd	nd	14.60	0.00	Ca-Si coatings
Fig. 3e	80.51	nd	nd	nd	0.92	nd	nd	18.57	nd	Ca crust (nanosize calcium carbonate)
Fig. 3f	85.68	nd	nd	nd	0.58	nd	nd	13.73	nd	Calcite crystals
Fig. 3g	84.28	nd	nd	2.70	0.81	3.78	nd	8.43	nd	Ettringite needles
Fig. 3h	75.72	4.53	1.96	17.39	0.39	nd	nd	nd	nd	*Portlandite
Fig. 3i	83.79	nd	nd	1.29	4.92	1.77	nd	8.07	nd	CASH (Calcium-Aluminium Silicate Hydrate)
Fig. 3j	76.83	nd	9.28	2.49	11.03	nd	nd	0.19	0.17	Mg-Si rich crust
Fig. 3k	76.20	nd	9.75	3.49	9.61	nd	0.25	0.09	0.62	Mg (minor-Fe) rich platy morphologies
Fig. 3l	76.44	nd	6.97	3.76	11.04	nd	0.23	1.12	0.45	Mg(Fe)-Si rich crust
Fig. 3m	61.92	nd	0.44	0.54	22.11	nd	nd	14.99	nd	Mixture of silicon and carbonate
Fig. 3n	75.71	0.08	1.49	0.76	1.79	nd	0.08	19.87	0.14	Calcite crusts
Fig. 3o	80.16	nd	0.46	0.72	1.96	nd	0.12	16.57	nd	Calcite crusts

Carbon has been removed from the analyses and data were normalized to 100%. *no carbon was found initially. nd: not detected.

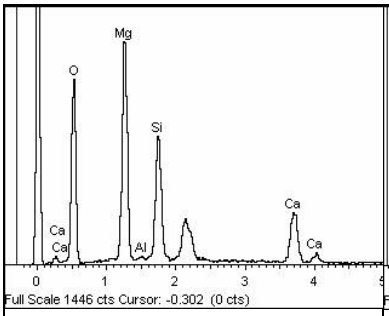

Fig. 3a

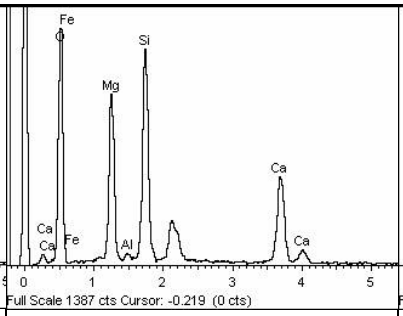

Fig 3b

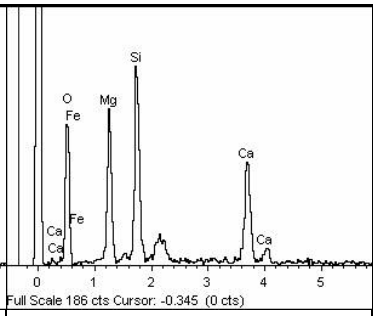

Fig 3c

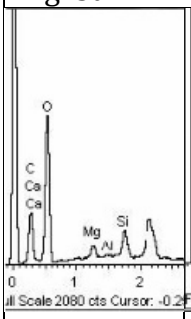

Fig. 3d

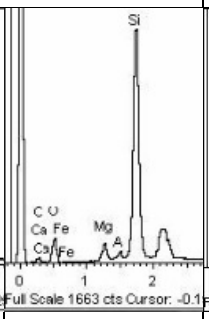

Fig. 3d'

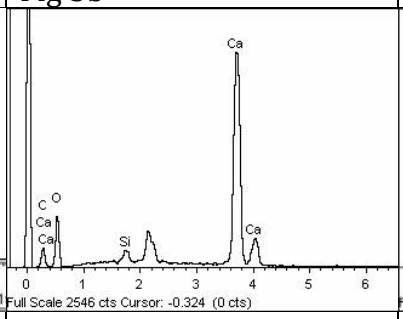

Fig. 3e

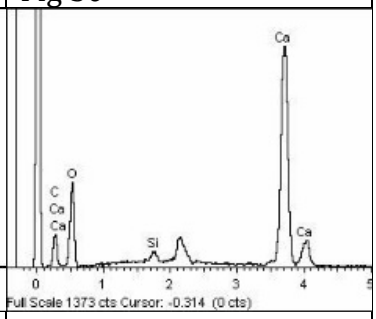

Fig. 3f

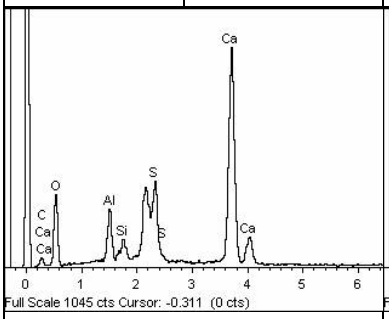

Fig. 3g

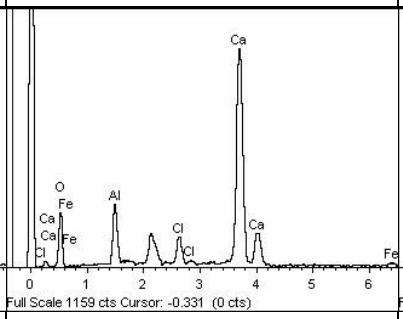

Fig. 3h

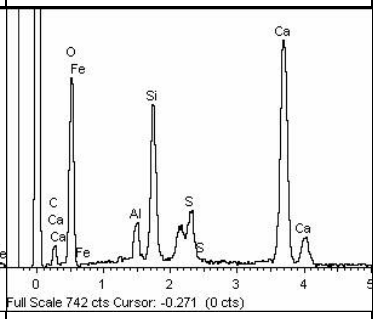

Fig.3i

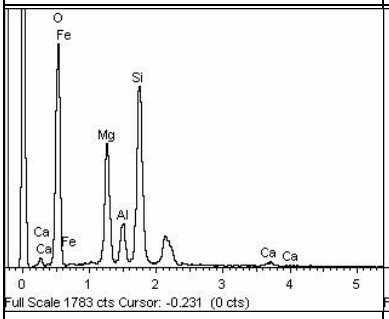

Fig. 3j

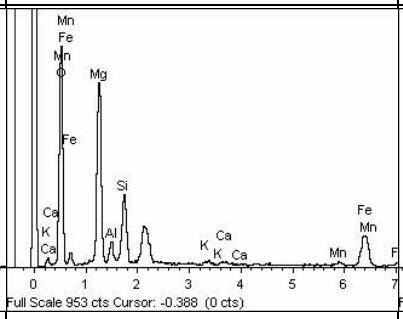

Fig. 3k

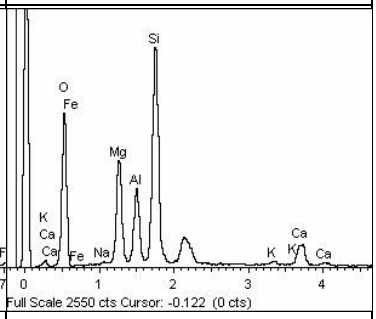

Fig.3l

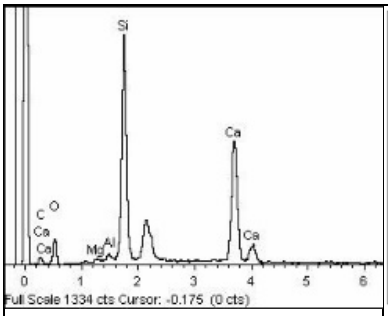

Fig. 3m

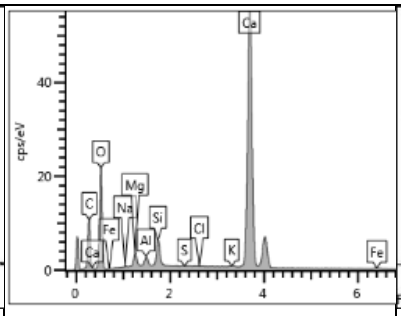

Fig. 3n

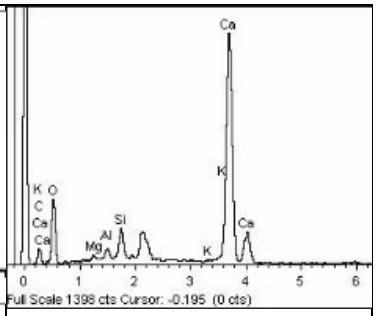

Fig. 3o

Table S3b. EDX spectra based on EDX analyses of crystal aggregates and undifferentiated masses.

Chemical projections of bentonite

Ternary scatterplot projections combining atomic proportions were related to mixtures of pure phases with the aim of capturing crystal-chemical trends among the different types of experiments (Cuevas et al., 2018). Two types of scatter plots, commonly used to differentiate the presence of di-octahedral and tri-octahedral clay minerals, were depicted (Velde, 1985; Bouchet et al., 2002) (Fig.S3). The first one (Fig. S3a) was built in a 2Si (upper pole) - $3R^{2+}$ (right pole) - 2(Al+Fe) (left pole) triangular diagram. The second (Fig. S3b) was built in $(M+R^{3+})_2$ (upper pole) - $3R^{2+}$(right pole) - $2R^{3+}$ (left pole) coordinates. In these diagrams, chemical analyses taken from in the surface of bentonite were projected. Theoretical compositions of reference minerals were superimposed to aid in the interpretation of ternary scatter plots (Table S4).

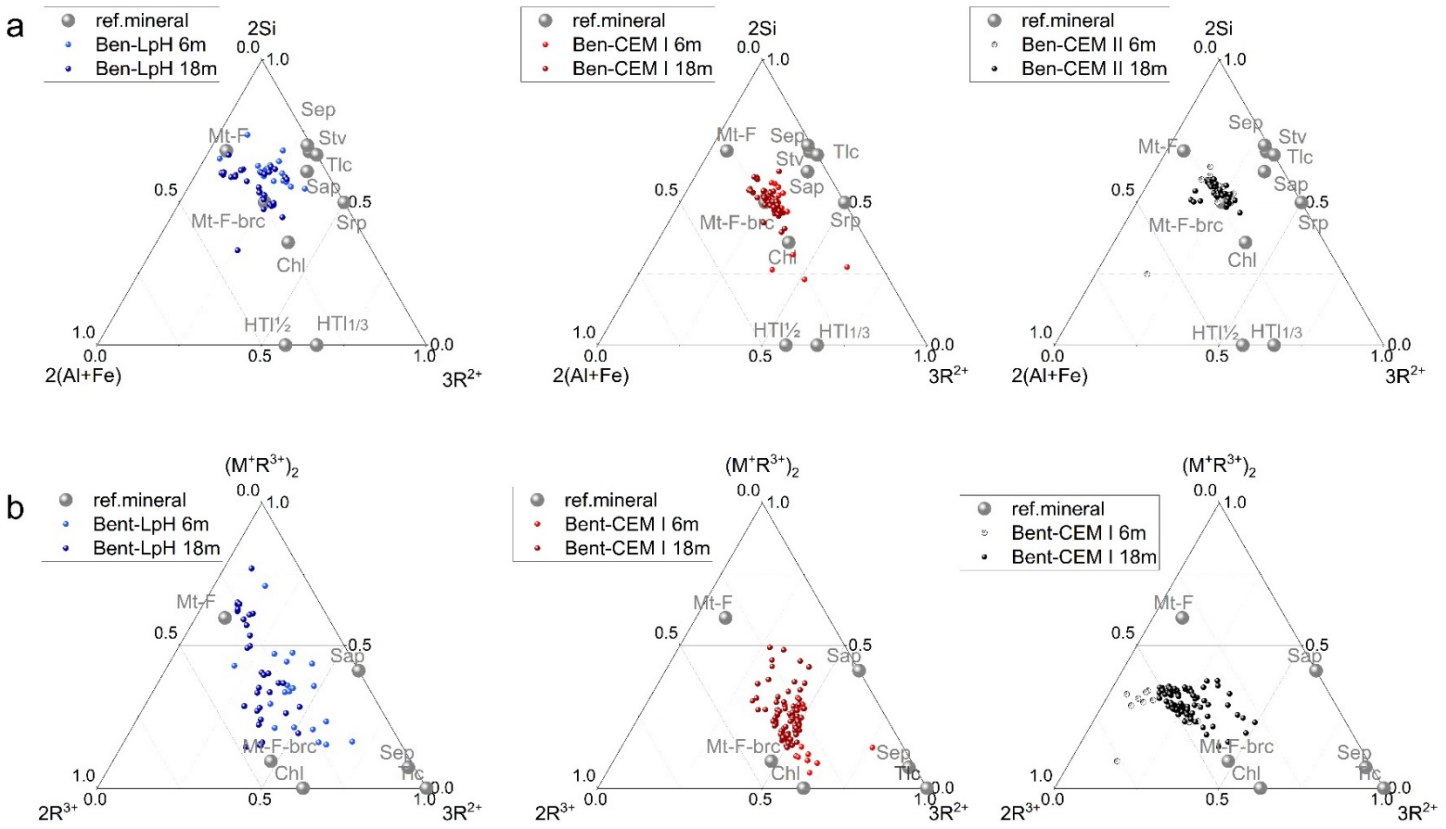

Fig. S3. Chemical projections of EDX surface analyses from bentonite. a) 2Si -- $3R^{2+}$ -- 2(Al+Fe): 2Si: Si/2; $3R^{2+}$: Mg/3; 2(Al+Fe): (Al+Fe)/2; b) $(M+R^{3+})2$ -- $3R^{2+}$ -- $2R^{3+}$: (M^{+}: charge of exchangeable cations: $Na^{+}+K^{+}+2\cdot Ca^{2+}$); $3R^{2+}$: Mg/3; $2R^{3+}$: (Al+Fe $-M^{+}$)/2. Mt-F: Montmorillonite FEBEX bentonite reference; Mt-F-bcr: Montmorillonite FEBEX bentonite intercalated with a brucitic layer; Sap: saponite; Srp: serpentine; Stv: stevensite; Tlc: talc; Sep: sepiolite; Chl: Chlorite; HTl ½: hydrotalcite ½ Al/Mg; HTl ⅓: hydrotalcite ⅓ Al/Mg. m: months.

Table S4. Idealized atomic composition of the single mineral phases used to plot the axis in Fig.S3.

Mineral Cation	Mt-F	Mt-F-bcr	Srp	Stv	Sap	Tlc	Sep	Chl	HTI ½	HTI ⅓
M^{+}	0.5	0.1	0	0.2	0.35	0	0.033	0	0	0
$Al+Fe^{(3+)}$	1.55	1.9	0	0.1	0.35	0	0.066	2	1	1
$Mg^{(2+)}$	0.45	3	3	2.7	3	3	2.466	5	3	2
$Si^{(4+)*}$	3.95	3.95	2	4	3.65	4	4	3	0	0

* basis of 4 Si in tetrahedral sheet; note: Mt-F: Montmorillonite FEBEX-bentonite reference; Mt-F-bcr: Montmorillonite FEBEX-bentonite intercalated with charged brucitic layer (0.35 mol Al^{3+} substitution); Srp: serpentine; Stv: stevensite; Tlc: talc; Sep: sepiolite; Chl: Chlorite; HTI ½: hydrotalcite ½ Al/Mg; HTI ⅓: hydrotalcite ⅓ Al/Mg (Table adapted from (Cuevas et al., 2018)).

Ternary plots from Fig. S3a showed how the chemical composition of bentonite evolves towards the $3R^{2+}$ pole at a nearly constant ~0.25-0.20 2(Al+Fe) pole (mostly Al), according to the conservation of the di-octahedral component of FEBEX-Mt. The CEM I and CEM II experimental spot coordinates were plotted in the line of a mixing trend of Mt and Mg-Al hydroxide components compatible with hydrotalcite 1/3 Al-Mg composition. In fact, the mixing line can be interpreted to be built considering the intercalation of a complete brucite layer in the Mt interlayer rather than by hydrotalcite mixing (Mt-F-brc in Fig. S3a and b). LpH follows this line at 6 months, although a group of analyses at 18 months deviate to tri-octahedral saponitic compositions according to Si and Al components. Using the $(M^{+}R^{3+})_2$ -$3R^{2+}$ - $2R^{3+}$ projection, the exchangeable cation contribution is considered together with the tri- or di-octahedral character calculated from the spot surface analyses (Fig. S3b). The Mt-brucite mixing line becomes extended and better developed in the case of the LpH and CEM I experiments, reaching chloritic and hydrotalcite-like coordinates in which no exchangeable cations are present. The saponitic composition of the Mg-Si phases becomes not obvious here for LpH. However, in the case of CEM I at 18 months, some of the analysed compositions are close to saponitic terms due to the exchangeable cation component (Fig. S3a). CEM II experiments showed more di-octahedral (Al) character in the analyses evolving to a mixture of tri- and di-octahedral compositions overtime at relative constant $(M^{+}R^{3+})_2$ exchangeable cation coordinates.

Cement mortar surface EDX analyses at the CB interface

For cement mortars, ternary diagrams designed to represent concrete mineralogy were plotted (Gaboreau et al., 2017; Lerouge et al., 2017)(Fig. S4). $(Al\text{-}Fe\text{-}Mg)_6$ in the right pole represents the brucitic component and separates aluminate (ferrite) compositions from pure calcium or calcium silicate phases. The $2Si\text{-}S_3$ component (upper pole) allowed separation of Ca silicates and Ca-Al sulphates (where S was added to Si for better visualization of the S phases). Ca was drawn in the left pole to represent pure calcite or portlandite composition (for HpH experiments). Reference minerals and depicted mineral phase areas were defined according to the structural formulas presented in Table S5. In addition, with the aim of differentiating the Mg phases from LpH, another ternary diagram was made. This scatter plot differs in the right pole, where Al_3FeMg was drawn instead $(Al\text{-}Fe\text{-}Mg)_6$ (Fig. S4b).

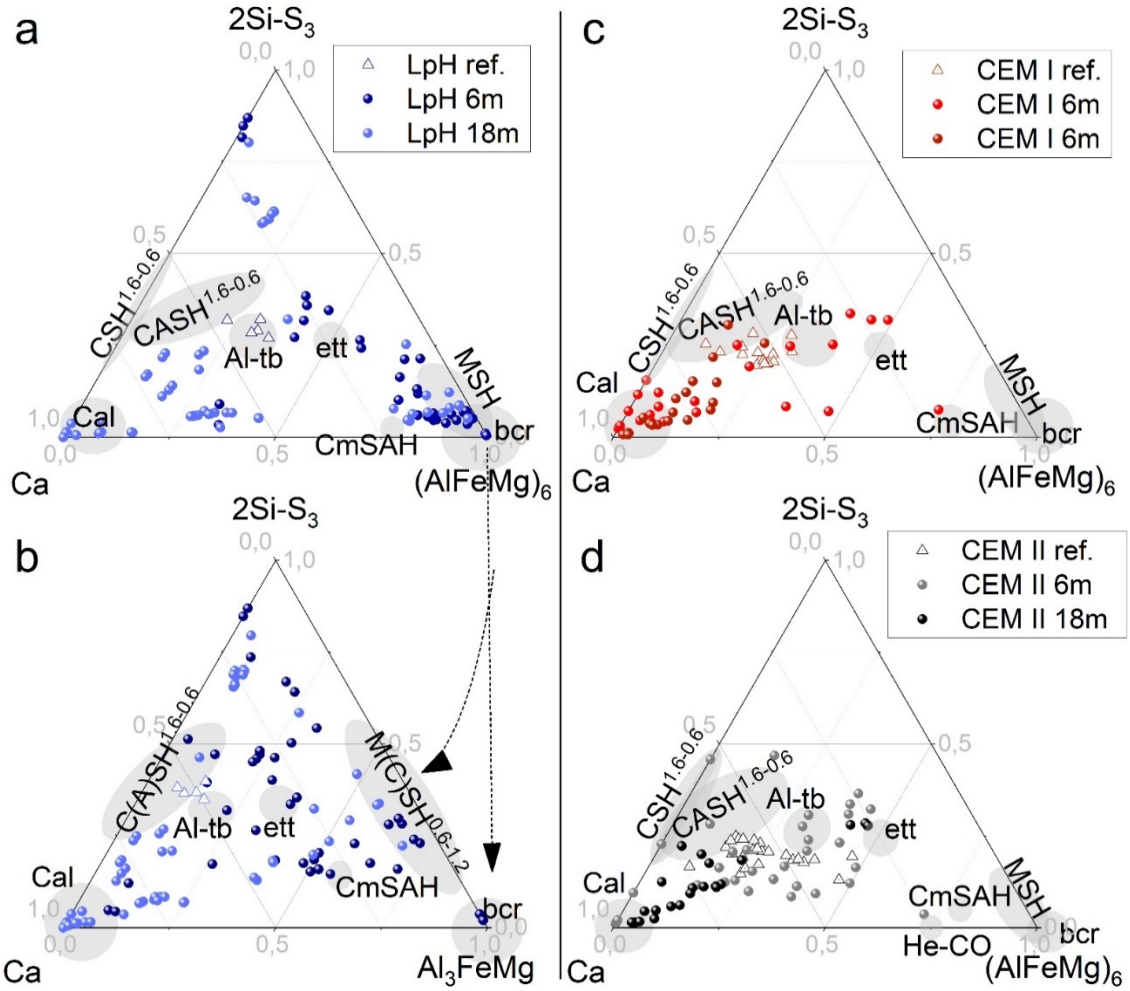

Fig. S4. Chemical projections of EDX surface analyses from cement mortars. $(AlFeMg)_6$: 6(Al+Fe+Mg), Al_3FeMg:3Al+Fe+Mg, 2Si-S_3: Si/2 +3·S. CSH 1.6-0.6: calcium silicate hydrates with 1.6 and 0.6 Ca/Si ratios, CASH 1.6-0.6: calcium aluminium silicate hydrates with 1.6 and 0.6 Ca/Si ratios, Cal: calcite, Al-tob: aluminium tobermorite, CmSAH: hydrated Ca-Al-Fe monosulphate, MSH: magnesium silicate hydrate, bcr: brucite, C(A)SH: calcium (aluminium) silicate hydrate, M(C)SH 0.6-1.2: magnesium (calcium) silicate hydrate. m: months.

Table S5. Reference mineral phases used to plot the areas.

Phase	Structural formulas
CSH 0.6	$Ca_{0.69}SiO_{2.415}(OH)_{0.55}$:$0.68H_2O$[a]
CSH 0.8	$(CaO)_{0.8}.SiO_2.(H_2O)1.94$[b]
CSH 1.0	$Ca_{1.06}SiO_{2.725}(OH)_{0.67}$:$0.89H_2O$[a]
CSH 1.2	$Ca_{1.23}SiO_{2.865}(OH)_{0.73}$:$1.06H_2O$ [a]
CSH 1.6	$Ca_{1.41}SiO_{2.96}(OH)_{0.90}$:$1.12H_2O$[a]
CASH 0.6	$Ca_{0.7}Al_{0.04}SiO_{2.485}(OH)_{0.55}$:$0.69H_2O$[a]
CASH 1.6	$Ca_{1.41}Al_{0.016}SiO_{2.984}(OH)_{0.9}$:$1.12H_2O$[a]
MSH 0.6	$Mg_{0.82}SiO_{2.385}(OH)_{0.87}$[a]
MSH 1.2	$Mg_{1.07}SiO_{2.075}(OH)_{1.99}$[a]
MSH	$(Ca_{0.5\pm0.2})$ $(Mg_{2.0\pm0.4}, Fe_{0.2\pm0.1}, Al_{0.5\pm03}, \square_{0.3\pm0.3})$ $(Al_{0.9\pm0.2}, Si_{3.1\pm0.2})$ O_{10} $(OH)_2$[c]
M(C)SH	$(MgO)_{0.78}(CaO)_{0.05}.SiO_2$[b]
Brucite	$Mg(OH)_2$
Al-tobermorite	$[Ca_4(Si_{5.5}Al_{0.5}O_{17}H_2)]Ca_{0.2}$:$Na_{0.1}$:$4H_2O$[d]
Calcite	$CaCO_3$
ettringite	$Ca_6[Al(OH)_6]_2(SO_4)_3$·:$26(H_2O)$
CmSAH	$3CaO·(Al,Fe)_2O_3·CaSO_4·nH_2O$
Hemi carbonate	$Ca_2Al(OH)_6·0.25(CO_3)·0.5(H_2O)$ $_{(aq)}$

[a]Data from (Roosz et al., 2018), [b]data from (Bernard et al., 2018), [c]data from (Lerouge et al., 2017), [d]data from (Jackson et al., 2013).

The spot analyses taken at the CB interface surfaces produced a very heterogeneous distribution of the projected data in all of the experiments. The reference data taken from undifferentiated surface zones of the hydrated cement mortars (not reacted in contact with the bentonite surface) revealed compositions characteristic of CSH mixed with Al-tobermorite (CASH) or ettringite. Taking these data as a reference, LpH surface analyses (Fig. S4a, b) show a very broad compositional distribution in which many data move to the brucitic pole, more represented at 18 months. Some spots deviate to the 2Si-Si_3 pole due to the presence of unreacted SF, and at 6 months, pure calcium spots are also observed. MSH, calcium (presumably calcite) and Al-sulphate phases are better separated when the Al_3FeMg projection is used in the right pole (Fig. S4b). The compositional heterogeneity and the presence of Mg-Al rich phases in the LpH cement mortar compared to CEM I and CEM II (Fig. S4c, d) may be related to the higher reactivity of LpH under bentonite influence.

In the HpH experiments, Mg phases (MSH or M(C)SH) were not found in cement mortar after CB interaction. Spot analysis traces convergent lines towards the calcium pole in which there are numerous concentrated 18 months data. At 6 months in CEM II, several plots were localized in the CASH (Al-tobermorite field) and ettringite area, in agreement with the higher Al and S contents observed in this cement mortar.

3.2. GI-XRD and θ/2θ scans; corresponding to results (section 3.2):

Comparison between θ/2θ scans and GI-XRD 0.5º θ

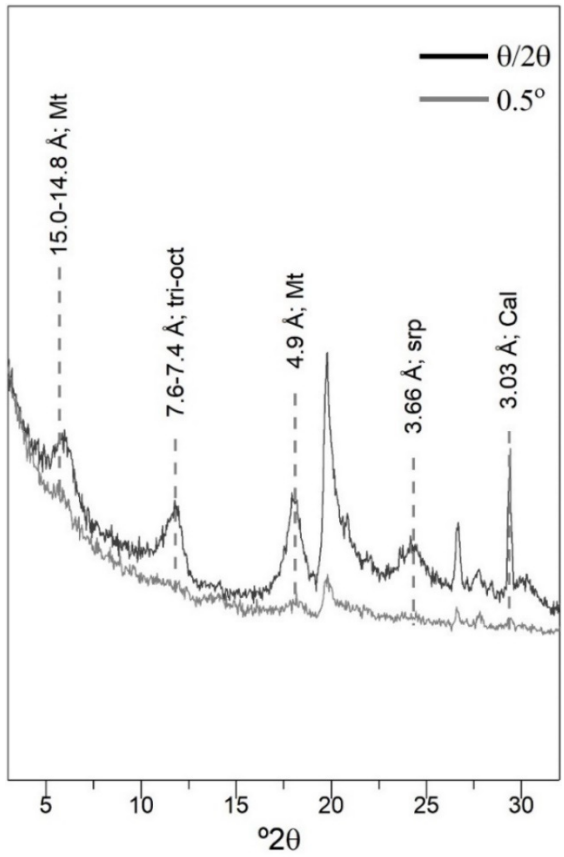

Fig. S5. Difference resolved θ/2θ scans and 0.5º θ fixed angle.

Cement mortar surface interfaces

With regard to cement mortars, the X-ray diffraction results showed differences depending on the type of experiment. On the LpH surface, characteristic brucite d-values at 4.77 and 2.36 Å were found at 6 and 18 months (Fig. S6a). Conversely, these diffraction reflections were not detected in the HpH cement mortars. Calcite 3.03 Å reflections were detected in all experiments (Fig. S6b). The intensity of this reflection increases with time, and comparing cement mortars, CEM I and CEM II presented the highest intensities for the 3.03 Å calcite reflection, which agrees with the EDX analysis line profiles of Fig. 2. Because no portlandite was detected in the X-ray surface analyses, the calcium enrichment characteristic of cement mortar at the HpH CB interface can be attributed to local precipitation of calcite.

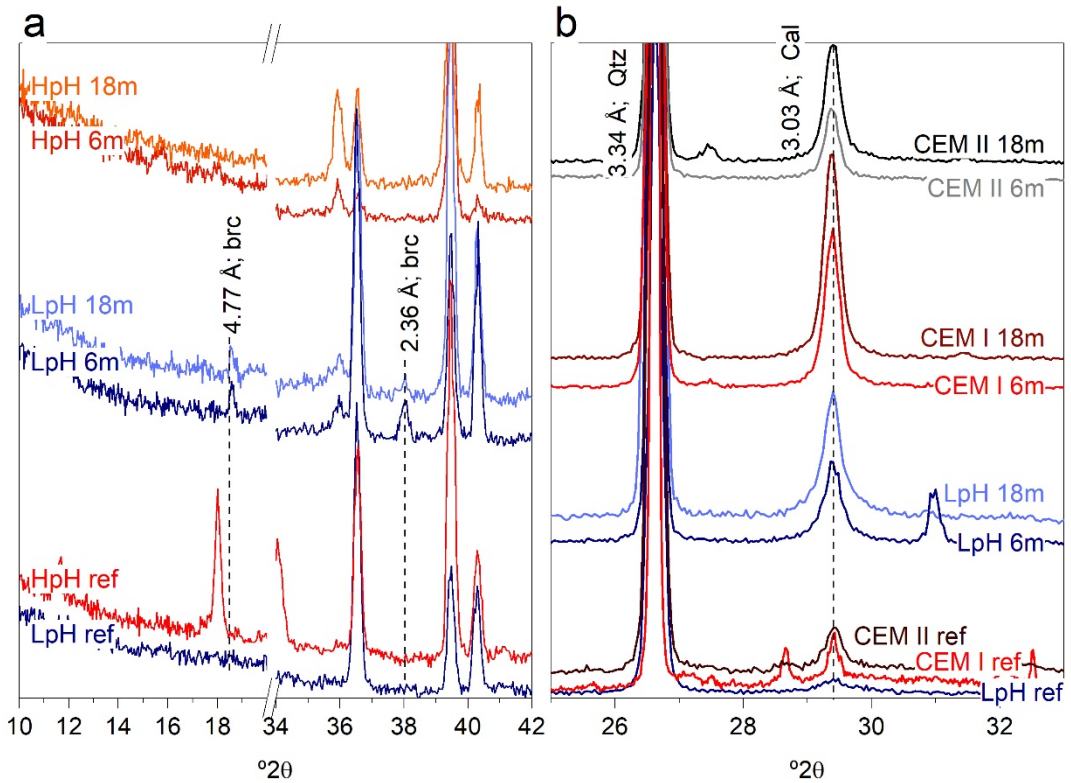

Fig. S6. θ/2θ scans carried out on the surface of cement mortars. a) Diffractograms of LpH and HpH cement mortars. HpH diffractograms represent the CEM I and CEM II experiments. b) Calcite reflection observed in the reference samples and cement mortars tested. m: months.

References

(This document includes the references no present in the source article).

Bernard, E., Dauzères, A., Lothenbach, B., 2018. Magnesium and calcium silicate hydrates, Part II: Mg-exchange at the interface "low-pH" cement and magnesium environment studied in a C-S-H and M-S-H model system. Applied Geochemistry 89, 210-218, https://doi.org/10.1016/j.apgeochem.2017.12.006.

Roosz, C., Vieillard, P., Blanc, P., Gaboreau, S., Gailhanou, H., Braithwaite, D., Montouillout, V., Denoyel, R., Henocq, P., Madé, B., 2018. Thermodynamic properties of C-S-H, C-A-S-H and M-S-H phases: Results from direct measurements and predictive modelling. Applied Geochemistry 92, 140-156, https://doi.org/10.1016/j.apgeochem.2018.03.004.

Techer, I., Bartier, D., Boulvais, P., Tinseau, E., Suchorski, K., Cabrera, J., Dauzères, A., 2012. Tracing interactions between natural argillites and hyper-alkaline fluids from engineered cement paste and concrete: Chemical and isotopic monitoring of a 15-years old deep-disposal analogue. Applied Geochemistry 27, 1384-1402, https://doi.org/10.1016/j.apgeochem.2011.08.013.

ANEXO-II. Artículos publicados

5.1. Low-pH cement mortar-bentonite perturbations in a small-scale pilot laboratory experiment

5.2. Bentonite/CEM-II cement mortar interface experiments: a proxy to in situ deep geological repository engineered barrier system surface reactivity

5.3. High-pH/Low-pH ordinary Portland cement mortars impacts on compacted bentonite surfaces: application to clay barriers performance

Clay Minerals, (2018) **53**, 237–254

Low-pH cement mortar-bentonite perturbations in a small-scale pilot laboratory experiment

D.E. GONZÁLEZ-SANTAMARÍA, M. ANGULO, A.I. RUIZ, R. FERNÁNDEZ, A. ORTEGA AND J. CUEVAS*

Departamento de Geología y Geoquímica, Facultad de Ciencias, Universidad Autónoma de Madrid, Cantoblanco s/n, 28049 Madrid, Spain

(*Received 14 October 2017; revised 9 March 2018; Guest Associate Editor: M.V. Villar*)

ABSTRACT: A novel method to perform small-scale laboratory experiments that reproduce concrete–bentonite and concrete–groundwater interactions has been developed. Such interfaces will prevail in engineered barrier systems used for isolation of nuclear waste. With the goal of optimizing the experimental method, this work has analysed the geochemical interaction of distilled water, low-pH cement mortar and FEBEX-bentonite for 75 days. Limited but evident reactivity between the materials was observed, mainly decalcification in cement mortar, carbonation at the interface with bentonite and Mg enrichment in bentonite. These results are consistent with the state-of-the-art literature and were used to validate this small-scale pilot laboratory experiment to establish the basis for further studies comparing the behaviour of different buffer and cement materials.

KEYWORDS: radioactive waste confinement, alkaline alteration, low-pH cements, bentonite, laboratory experiments.

The present and future management of high-level radioactive waste (HLRW) is a major environmental issue, especially considering its long radiotoxicity (10^4–10^6 years). Currently, the deep geological repository (DGR) is the most accepted management option for HLRW long-term isolation (NEA-OECD, 2003; U.S. DOE, 2014). Within the European Union, Finland, Sweden and France are expected to approve a final DGR location before 2020 (Gibney, 2015; Ewing *et al.*, 2016). The DGR concept is based on a multi-barrier system (engineered barrier system, EBS) to avoid/delay the release of radionuclides into the biosphere. A generic EBS constructed in a granitic host-rock formation consists of the following parts: (1) a metallic canister as a first barrier in contact with the radioactive waste; (2) a clay barrier surrounding the canister; and (3) concrete to seal and close the galleries.

The clay barrier acts as both a hydraulic seal and a physical-chemical buffer. Bentonite is a swelling clay material that has been selected by most of the waste-management organizations (IAEA-TECDOC-1718, 2013; NEA-OECD, 2003) as an optimal material for the backfilling and sealing of HLRW repositories due to its low permeability, low diffusivity, high retention of cations and swelling capacity (Meunier *et al.*, 1998; Kaufhold *et al.*, 2013; Gómez-Espina & Villar, 2016; Kaufhold & Dohrmann, 2018). Concrete and bentonite will be in close contact, and they will interact within each other. In addition, the EBS system will be in contact with flowing groundwater in the host rock, which will affect the long-term safety in case that degradation processes develop. In the long term, the interaction between water, concrete and clay will

This paper was originally presented during the session: 'ES-04 Clay barriers performance in the long-term isolation of waste' of the International Clay Conference 2017.
*E-mail: jaime.cuevas@uam.es
https://doi.org/10.1180/clm.2018.16

generate an indeterminately complex chemical system that might compromise the storage security (Savage, 2014). Furthermore, its evolution will vary depending on the type of cement and clay used as a barrier (Dauzères *et al.*, 2010; Jenni *et al.*, 2014). Thus, understanding the degradation pathways due to barriers and groundwater interactions and clarifying the critical parameters involved herein are of fundamental interest to advance the DGR design. Conventional Portland-type cementitious materials generate alkaline fluids (pH > 13) by the dissolution of alkali hydroxides and $Ca(OH)_2$ (portlandite) in the porewater of the cement matrix, which may attack smectite crystal lattice in neighbouring clay seals (Liu *et al.*, 2014). Therefore, the hyperalkaline front might modify the smectite mineralogy and its properties. Previous investigations have analysed the behaviour of different clays in contact with the hyperalkaline front. However, the concrete should not be simulated by means of a high-pH solution in equilibrium with $Ca(OH)_2$ (pH = 12) or alkali hydroxides (Bildstein & Claret 2015) alone, *i.e.* omitting the chemical and mineralogical evolution of the concrete itself. Previous works have outlined the relative absence of representative experiments in real clay/concrete interfaces (Gaboreau *et al.*, 2011, 2012; Bartier *et al.*, 2013; Mäder *et al.*, 2017) and the difficulty of taking into account the effects of real volumes and the composition of solutions migrating through connected porosities (Cuevas *et al.*, 2016). Moreover, few works have put low-pH cementitious materials in contact with clays (Jenni *et al.*, 2014; Dauzères *et al.*, 2016; Lerouge *et al.,* 2017). To avoid extreme alkalinity, experiments have been carried out with low-pH cement mortars (pH < 12). Several studies suggest that low-pH cement-based materials have insignificant effects on clay structures (Bäckblom, 2005; Berner *et al.*, 2013; Cuevas *et al.*, 2016), while simultaneously they have demonstrated a resistance to granitic groundwater exposure (García Calvo *et al.*, 2010). However, low-pH cements have shown a lower resistance than high-pH cements to the influence of carbonated waters (Dauzères *et al.*, 2014) as some of the cement paste hydration products, such as ettringite, are more unstable (Trotignon *et al*., 2007) and precipitate calcite and gypsum. Low-pH cement-based materials may display carbonation, but the high-pH cementitious materials may develop a larger protective calcium carbonate film that increases the retardation of the decalcification process, at least temporarily (Jenni *et al.,* 2014). In addition to these uncertainties, the complex structure and chemistry of the mineral phases formed during the alkaline perturbation at these interfaces were unclear until a few years ago (Bildstein & Claret, 2015), but recent experiments have examined and provided new characterizations of their structure and chemistry (Roosz *et al*., 2015; Nied *et al*., 2016; Lerouge *et al*., 2017). This might be the case for mineral phases such as magnesium silicate hydrates (M-S-H) or calcium aluminium silicate hydrates (C-A-S-H; Lothenbach *et al*., 2015). The composition of concrete includes a wide range of mineral phases such as calcium silicate hydrates (C-S-H) with different Ca/Si ratios and aluminate-, calcium- and sulfate-bearing phases such as ettringite and calcium monosulfate-aluminate hydrate (CmSAH; Van Damme & Pellenq, 2013). Experimental research on C-S-H in low-pH concretes is sparse, and their parameters of formation and stabilization are not yet known sufficiently to allow for a feasibility assessment.

In this context, small-scale laboratory experiments might be significant because they approach real conditions through a simplified system, facilitating the control of different parameters and allowing the assessment of the different possible conditions expected in a DGR. These experiments may provide reaction pathways on a short time scale, making them useful tools as sources of data for geochemical modelling. In addition, they can complement other types of experiments, such as batch experiments or large *in situ* underground laboratory experiments. Consequently, the aim of this study was the development and optimization of a new representative small-scale laboratory experiment able to reproduce the contact between concrete and bentonite that would occur in a DGR and to test procedures and methods for assessing and describing the geochemical perturbations under different conditions.

MATERIALS AND METHODS

Experimental setup and characterization techniques

The pilot experiment was performed using distilled water, simulating diluted granitic groundwater, low-pH cement mortar and FEBEX-bentonite as the reference Spanish bentonite for the DGR. The experiment was run for 75 days under isothermal conditions (25 ± 5°C), based on the range of temperatures expected at the concrete–bentonite interface according to the data provided by Villar *et al.* (2012) for a FEBEX *in situ* experiment after 13years for a sealing concrete plug in a granitic DGR. The low-pH cement mortar and the compacted FEBEX-bentonite clay were placed in a

4 mm-thick methacrylate sleeve confined by two stainless steel cylindrical caps (Fig. 1). The cell dimensions were 20 mm in internal diameter and 9 mm in height for each material (18 mm in total). The objective of the design of these cells included the minimization of undesirable effects during the dismantling of the cells for further solid characterization, such as the tedious separation of cement mortar and bentonite from the carcase and the creation of fractures or deformations in both materials, avoiding the interaction of the materials with the atmosphere. The design of a compact external stainless-steel case (together with connections and filters) able to resist the high-pressure conditions (1–5 MPa) caused by the hydration of bentonite (Villar & Lloret, 2004) was required. The setup of columns also involved two porous steel filters that allowed pressurized water infiltration. The constant hydraulic head of the distilled water was fixed to 1 MPa using an automatic piston pump (Gilson, 307 model) and carried through PEEK tubes. The cement mortar–bentonite interface generated (referred to hereafter as the C–B interface) and the cement mortar–distilled water interface (referred to hereafter as the C–W interface) were separated by a 0.45 μm polytetrafluoroethylene (PTFE) membrane to facilitate the separation of materials and access to both interfaces. The infiltrated water was collected in a syringe for the aqueous-phase survey. This effluent was subjected to the determination of the following: (1) alkalinity using a Metrohm 888™ potentiometric titrator; (2) soluble silica in water (as SiO_2) by spectrophotometric determination of molybdate-reactive silica in the effluent using a Milton Roy Spectronic® instrument at a wavelength of 825 nm; and (3) major chemical ions by ion chromatography coupled to a conductivity detector using a Metrohm 802 compact IC plus model.

The hydraulic conductivity (k) was calculated by Darcy's law according to equation 1:

$$Q = k/A * \Delta h/\Delta L \quad (1)$$

where Q = the quantity of water leached over time t (m^3/s); k = hydraulic conductivity (m/s); A = cross-sectional area (m^2); Δh = hydraulic head (m); and L = column length.

The solid-phase characterization was performed by X-ray diffraction (XRD), grazing incidence X-ray diffraction (GI-XRD) and by using a scanning electron microscope attached to an energy dispersive X-ray analyser (SEM-EDX). The mineral identification by XRD was performed on bulk, randomly oriented cement mortar and bentonite powders using a θ/2θ X'Pert PANalytical instrument with an X'Celerator detector. The XRD patterns were recorded over the angular range 3–70°2θ. This method allowed measurements equivalent to 0.016° angular steps for 100 s at each step. The voltage and intensity of the X-ray Cu tube were 45 kV and 40 mA, respectively. To perform

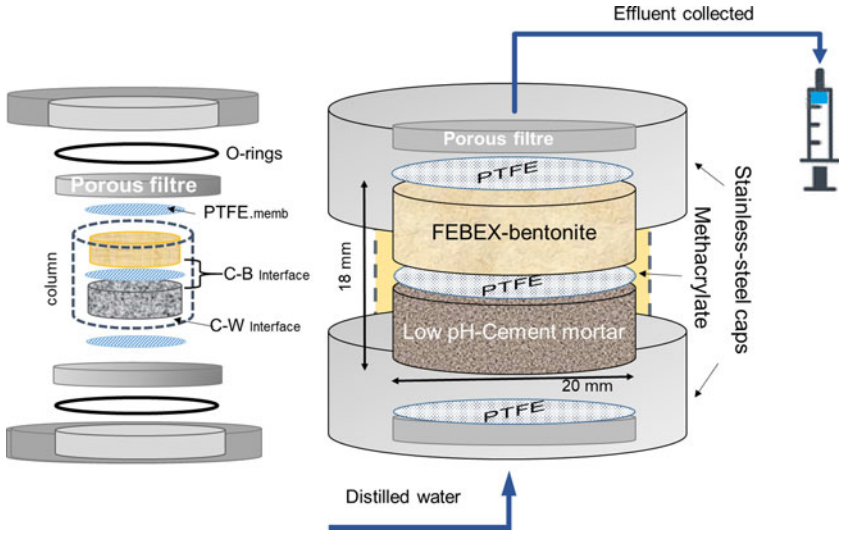

FIG. 1. Compacted column formed from cement mortar and compacted bentonite. Both materials are separated by a PTFE membrane and encased in an open, stainless-steel sleeve. A methacrylate piece seals the column. Two porous filters allow water transport at both column ends. C–B: cement mortar–bentonite interface; C–W: cement–water interface.

the GI-XRD analyses, angles of 1°, 5° and 8°2θ were used with 0.04°2θ of angular step and 2 s time step increases, respectively. The SEM-EDX equipment consisted of an Hitachi S-3000N SEM coupled with an INCAx-sight Oxford Instruments™ energy dispersive X-ray analyser. The EDX quantification was performed by means of internal standard semi-quantitative analyses.

Semi-quantitative EDX elemental composition analysis was performed for the following reasons: (1) to determine the elemental composition variations along a linear transect through the whole cement-mortar/bentonite composite probe, taken from the hydration mortar face to the porewater outflow at the end of the compacted bentonite; and (2) to perform localized point analyses to describe either the chemistry of the cement mortar matrix for the intergranular zones between the quartz grains or the discrete mineral-phase compositions where singular morphologies (crystals, polycrystalline aggregate-defined morphologies) were distinguished. To evaluate the quality of these results, EDX spectra of a heterogeneous 300 μm × 200 μm area, typical of the analysis performed on the linear transect in the cement mortar, were acquired using various integration times, from 10 s to 80 s, at 5 s intervals. The % deviation was calculated as 100 times the ratio of the standard deviation to the determined % chemical element value. For major elements in the concrete (Al, Si and Ca), instrumental % deviations, obtained by taking their average value in the 30–50 s interval, were <10%, related to their concentration being less for silicon (<1%) and greater for Al (9%) (Table 1). The % deviation from measured values, however, was <6% for the average measurement value. For elements that have contents within 1–5% (K, Fe), the % deviation from the average of the measured values was typically 10–15%. A period of 40 s was considered to be sufficient that the analysis quality would not be compromised and to avoid excessively time-consuming data acquisition. In terms of the point analyses, with a typical 5 μm × 5 μm spot, the analysis data for a needle-like ettringite polycrystalline aggregate are shown in Table 1. In general terms, the atomic ratios obtained, considering that some impurities are always present (Si phases and carbonates), are within 10–15% deviation using theoretical values for ettringite.

FEBEX-bentonite

The experiments were performed using FEBEX-bentonite from the Cortijo de Archidona deposit (Almería, Spain; Caballero *et al.*, 2005). The physical-chemical properties of the FEBEX-bentonite, as well as its most relevant thermo-hydro-mechanical and geochemical properties, have been studied extensively and published elsewhere (*e.g.* ENRESA, 2006). The FEBEX-bentonite was compacted with its hygroscopic water content (13%) at room conditions (23 ± 1°C) and at a nominal dry density of 1.60 g/cm^3. Finally, the bentonite was placed inside the methacrylate sleeve (Fig. 1).

Table 1. Relatiive error evaluation of SEM-EDX-determined chemical element concentrations.

Element	% element 40 s*	% ID 10 s–80 s**	Average ID % 30 s–50 s	Average MD % 30 s–50 s
Al	5.9	17–7.0	9.0	6.0
Si	69.2	6.5–2.3	0.8	3.2
Ca	18.0	9.0–3.2	1.9	4.5
Ettringite $Ca_6Al_2(SO_4)_3(OH)_{12}\cdot 26H_2O$ Example***			Ca/S theoretical = 2.0	Al/S theoretical = 0.7
Al	16.0	5.8	1.8	0.6
Si	6.6	10.5		
S	26.9	4.5		
Ca	48.8	2.9		
Fe, Mg	<0.2	50–75		

*The selected integration time to determine any SEM-EDX measurement was 40 s. The element % is referenced to the sum of the major analysed elements, excluding C and O (normally, the sum of Mg, Al, Si, K, S, Ca, and Fe).
**Deviation data are expressed as a percentage given by the ratio of the standard deviation to the value determined using either the instrumental standard deviation of the integrated signal counts (ID: instrumental deviation) or the average value of several measurements (MD: measurement deviation).
***Analyses for ettringite were described by Fernández *et al.* (2017).

Low-pH cement mortar

The low-pH cement binder was prepared with ordinary Portland cement (OPC) CEM I 42.5 R SR mixed with silica fume (SF) (OPC [60 wt.%] + SF [40 wt.%]). Both materials were provided by the Eduardo Torroja Institute for Construction Science from CSIC (Spanish National Research Council). Subsequently, a 0.42 ratio of distilled water/binder and a 1:3 ratio of binder/silica sand (grain size <1 mm) were added. The fresh, low-pH cement mortar obtained was pressed inside the methacrylate sleeve and covered by the PTFE membrane. After the bentonite was compacted to fill the whole sleeve, the cement mortar was stored in a hydration chamber and exposed to a water-saturated atmosphere for 90 days. The chemical composition of the low-pH cement mortar (Table 2) and the composition of major ions in the pore solution after 90 days of curing time (presumably at equilibrium) were provided by García Calvo (2012; Table 3). To obtain an initial reference sample, a slice of the initial low-pH cement mortar was cut, polished and characterized by SEM-EDX. The pH measured in the pore solution of the initial low-pH cement mortar (Table 3) was obtained following the leached *ex situ* method (García Calvo, 2012). The powder XRD patterns and GI-XRD showed the absence of portlandite [$Ca(OH)_2$] and the presence of C-S-H together with characteristic clinker phases that were not yet hydrated (Fig. 2). The SEM images showed homogeneously distributed grains of silica sand within the cement matrix (Fig. 3a). In addition, the reference low-pH cement mortar showed the presence of non-reacted silica fume grains which indicated incomplete dispersion. Nevertheless, the conversion of portlandite to C-S-H was complete. The EDX analyses were conducted considering only the cement matrix and taking a representative number of analyses, where silica grains were avoided intentionally. Under these conditions, a Ca/Si ratio of 0.9 ± 0.1 was obtained, representative of the cement matrix composition (based on 14 analyses; see the detail of the spot size selected in Fig. 3a; a supplementary Table S1 with EDX data has been provided and is available here (https://doi.org/10.1180/clm.2018.16)). This result can be applied to the C-S-H composition present in the reference low-pH cement mortar as C-S-H are the main and almost unique hydrated phases present in the binder (García Calvo *et al*., 2012). The Ca/Si ratios determined are in agreement with Stronach & Glasser (1997), who indicated that to obtain a low pH in the cement materials, the Ca/Si ratio should be <1.1. Additionally, the SiO_2 content in these ratios might be overestimated due to the presence of small micro-silica particles (silica fume) (García Calvo *et al*., 2010). In the point analysis, acicular morphologies typical of ettringite were observed locally (Fig. 3b). The EDX chemical analyses corroborate the identification of such mineral phases (Al/S = 0.8; theoretical Al/S = 0.67), although they cannot be detected and quantified in the XRD patterns.

TABLE 2. Chemical composition (wt.%) of ordinary Portland cement (OPC) and silica fume (SF) (García Calvo, 2012).

Element	OPC	SF
SiO_2	17.4	92.7
Al_2O_3	4.68	0.60
Fe_2O_3	5.08	5.38
total CaO	60.3	1.31
MgO	1.78	0.93
SO_2	3.17	–
Na_2O	0.18	0.15
K_2O	0.34	0.37
Free CaO	1.85	0.01

TABLE 3. Major ions, alkalinity, aqueous silica and pH in the effluent and chemical composition of a reference low-pH cement mortar (LpHC) pore solution (90 days old) provided by García Calvo (2012).

Ion/aqueous species	Effluent (mg/L)	LpHC(mg/L)
Ca^{2+}	93.2	612
Mg^{2}+	2.2	nd
Na^{+}	211.1	120
K^{+}	2.73	322
NO_3^-	3.9	nd
Cl^-	187.3	nd
F^-	2.2	nd
SO_4^{2-}	176.2	84.4
HCO_3^-	237.9	nd
$SiO_{2\ (aq)}$	12.8	nd
pH	8.3	11.1

nd: not determined

Dismantling, cutting and sampling

After 75 days of reaction, the cement mortar-bentonite column was dismantled and divided into

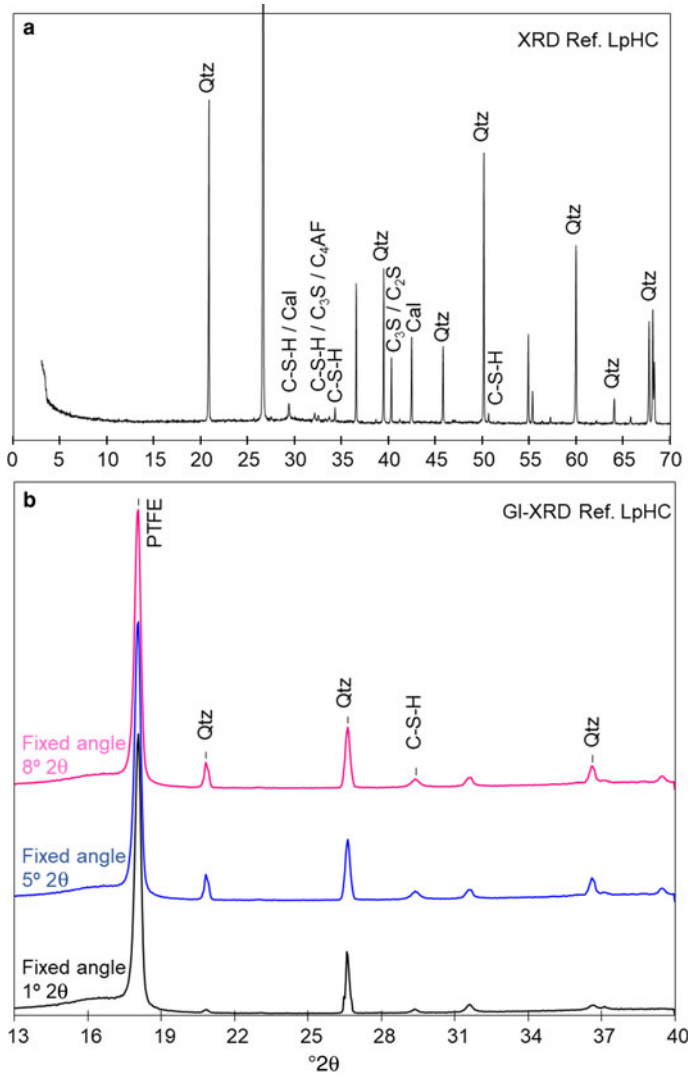

FIG. 2. (a) XRD traces of the reference low-pH cement mortar (ref. Low-pHC); (b) GI-XRD patterns with fixed angles of 8°, 5°, and 1°2θ of the initial-reference, low-pH cement mortar. Qtz: quartz. Cal: calcite. C_3S: tricalcium silicate. C_4AF: tetracalcium aluminoferrite. C-S-H: calcium silicate hydrates. C_2S: dicalcium silicate. PTFE: polytetrafluoroethylene. *d* spacings of reflections are given in Å.

subsamples using a Well®2000 cutting machine model with a diamond wire saw. Various subsamples were sliced from the initial column (Fig. 4). The number of subsamples and their sizes were determined by the quantity needed to carry out the post-mortem analyses.

A half-sample of the cement mortar-bentonite column was divided into two: one quarter was used to perform XRD and SEM-EDX analyses, and the other quarter was used to perform GI-XRD analyses. All analyses were performed to study the interaction between the cement and bentonite and the effects of the water flow. The subsample prepared for XRD and SEM-EDX analyses was sliced into six new subsamples, each 3 mm thick, parallel to the interface (Fig. 4). The segmentation permitted the study of perturbations as a function of distance from the interface (3, 6 and 9 mm) and then the assessment of the spatial progress of the geochemical reactions. Finally, prior to performing the analyses, these subsamples were dried in a vacuum chamber.

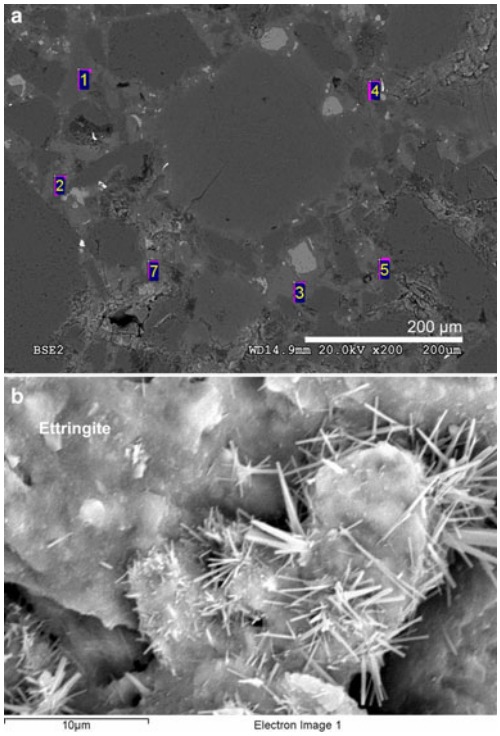

FIG. 3. (a) SEM-EDX spots analysed in the initial-reference, low-pH cement mortar to calculate the Ca/Si ratio in the cement matrix. (b) Acicular ettringite crystals in local regions of the initial-reference, low-pH cement mortar. The numbers correspond to EDX analysis points.

The other half-sample was used for optical inspection to analyse a longitudinal chemical profile of the elemental distribution along the column axis measured by SEM-EDX and was used to carry out spot EDX analyses on the cement matrix near the C–W interface and C–B interface. This profile sample was freeze-dried in liquid nitrogen, dried under vacuum in a P_2O_5-dehydrated atmosphere until 10^{-4} Pa and polished up to 2500 grit sheet sandpaper.

The chemical profile was obtained by SEM-EDX analyses in selected areas. Using the C–B interface as a reference, EDX analyses were conducted towards the bentonite end of the column and towards the interface with the infiltrating water solution (C–W interface). Ten analyses with rectangular dimensions of 10 µm in the direction perpendicular to the C–B interface and ~120 µm in the direction parallel to the C–B interface were performed. The next five analyses had dimensions of 100 µm × 300 µm in directions perpendicular and parallel to the C–B interface, respectively. Finally, eight analyses towards the bentonite column end and ten analyses towards the C–W interface of 1 µm × 3 mm were performed. The analysed areas are illustrated in Fig. 5.

RESULTS

Aqueous phase

The volume of aqueous solution effluent collected after 75 days was 2.03 mL. The concentrations of major ions, aqueous SiO_2, the alkalinity, and the pH are listed in Table 3. The calculated hydraulic conductivity (equation 1) was 1.6×10^{-13} m/s based on a single measurement.

General overview of the small-scale pilot laboratory experiment

The profile sample of the post-mortem low-pH cement mortar-bentonite column is shown in the backscattered electron image (Fig. 5). The freeze-drying process, in preparation for the SEM-EDX analyses, produced a decrease in the bentonite volume and a few macroscopic cracks in the bentonite part. However, the general aspect of the bentonite texture remained homogeneous. The low-pH cement mortar showed an increased presence of air voids (Fig. 5) compared to the reference cement mortar sample (Fig. 3a), suggesting a leaching process of the cement matrix towards bentonite.

The chemical composition profiles obtained by EDX analyses illustrate the elemental distribution along the complete column axis (Fig. 6a). The main chemical perturbations were observed at the C–B interface, although a visible decrease in Ca was also observed in the cement mortar near the C–W interface.

Low-pH cement mortar perturbations

The chemical profile showed a slight decrease in the percentage of Ca over the first 3 mm from the C–W interface (Fig. 6a). Conversely, the EDX profile showed an increase in Ca towards the C–B interface, and close to the C–B interface (in the range 0–100 µm); two peaks of Ca were observed with an associated opposite effect on the Si concentration (Fig. 6b-c). A slight increase in Al (2.5–4.0%) was observed in the cement mortar near the C–B interface (25 µm), and although the increase in concentration is low, it is significant within an established 20–25% relative error (Fig. 6c). In addition, spot SEM-EDX analyses performed on the polished cement mortar sample near the C–W interface showed

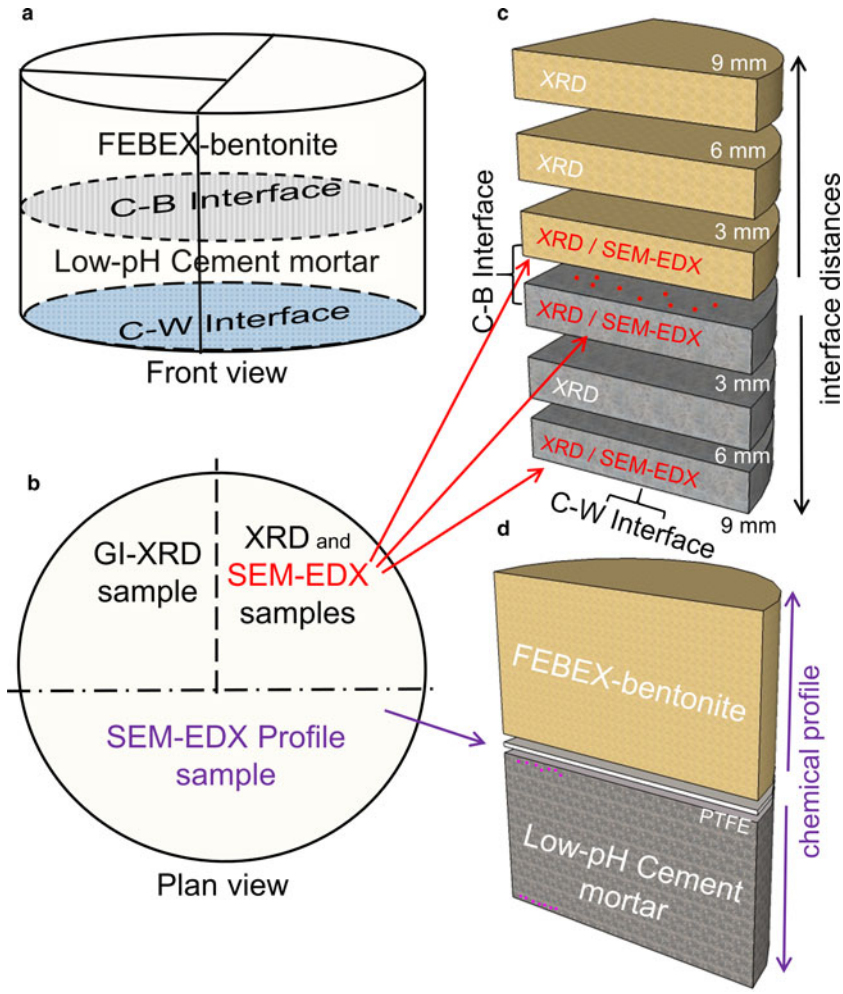

FIG. 4. Cutting and sampling scheme. (a) Front view where the cement mortar-bentonite (C–B) interface and the cement mortar–water (C–W) interface have been drawn. (b) Plan view of the cement mortar–bentonite column. (c) Subsample segmentation for XRD and punctual SEM-EDX analyses performed on the surfaces of the subsamples next to the C–B and C–W interfaces. (d) Sample for SEM-EDX profile analyses and punctual SEM-EDX analyses near the C–B and C–W interfaces.

Ca/Si ratios in the range 0.7 ± 0.1 (based on eight analyses performed on selected cement matrix regions; Fig. 7a), while the spot analyses obtained near the C–B interface showed Ca/Si ratios in the range 0.8 ± 0.1 (based on seven analyses also performed on selected cement matrix regions; Fig. 7b). Moreover, the morphologies of C-S-H (with a Ca/Si ratio = 0.6 obtained by EDX) and ettringite-like crystals (Al/S = 0.6) were observed on the surface of low-pH cement in contact with only the bentonite (Fig. 8a–b). The XRD analyses of the reference low-pH cement mortar sample and the post-mortem subsamples are shown in Fig. 9a–b. The XRD trace shows weak changes at 3.04–3.06 Å among the reference low-pH cement mortar and the low-pH cement mortar subsamples. Regarding the reference low-pH cement mortar, characteristic reflections of C-S-H phases (2.79 Å, 2.75 Å, 2.66 Å and 2.61 Å) were not observed clearly in the post-mortem subsamples. In addition, a reflection at 3.03 Å was observed in the subsample next to the C–B interface; this reflection is characteristic of calcite and sharper than the reflection at 3.04–3.06 Å. The GI-XRD patterns of the surface of the low-pH cement mortar (separated by a PTFE membrane from the bentonite)

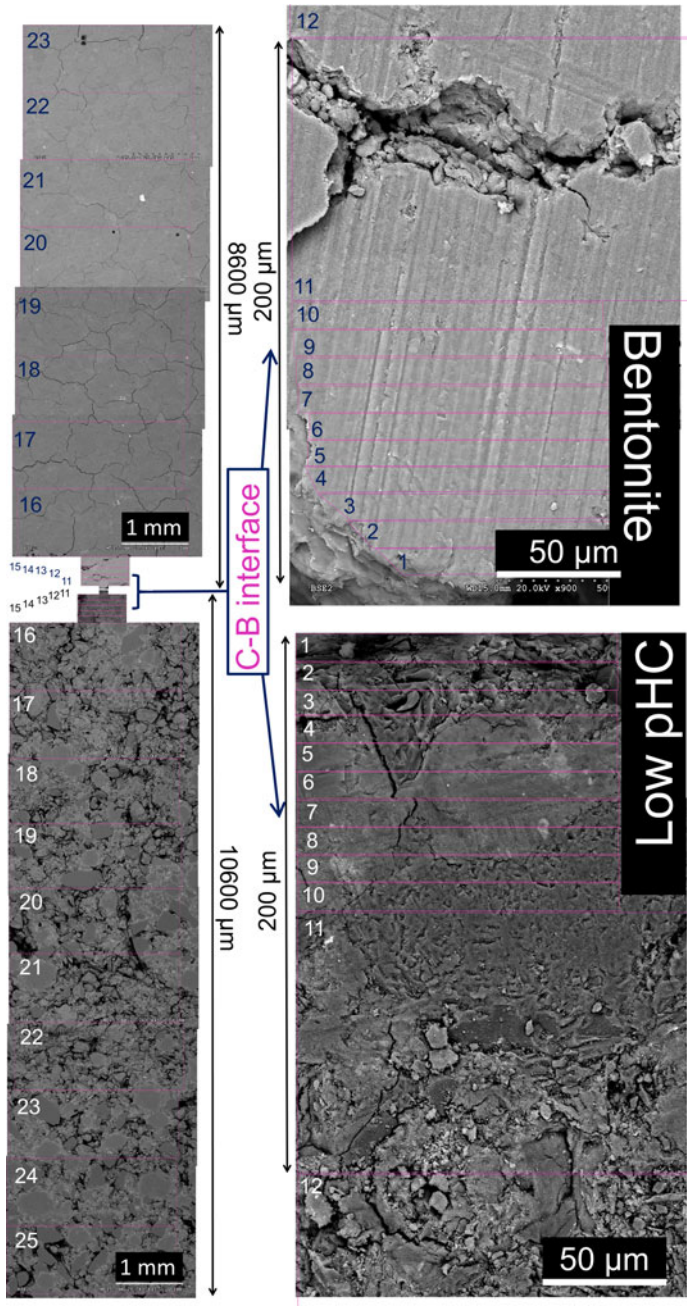

FIG. 5. Backscattered electron (BSE) images showing an overview of the methodology used to create the SEM-EDX profile of the elemental compositions in the cement mortar-bentonite column. Note the increasing magnification at the interface region.

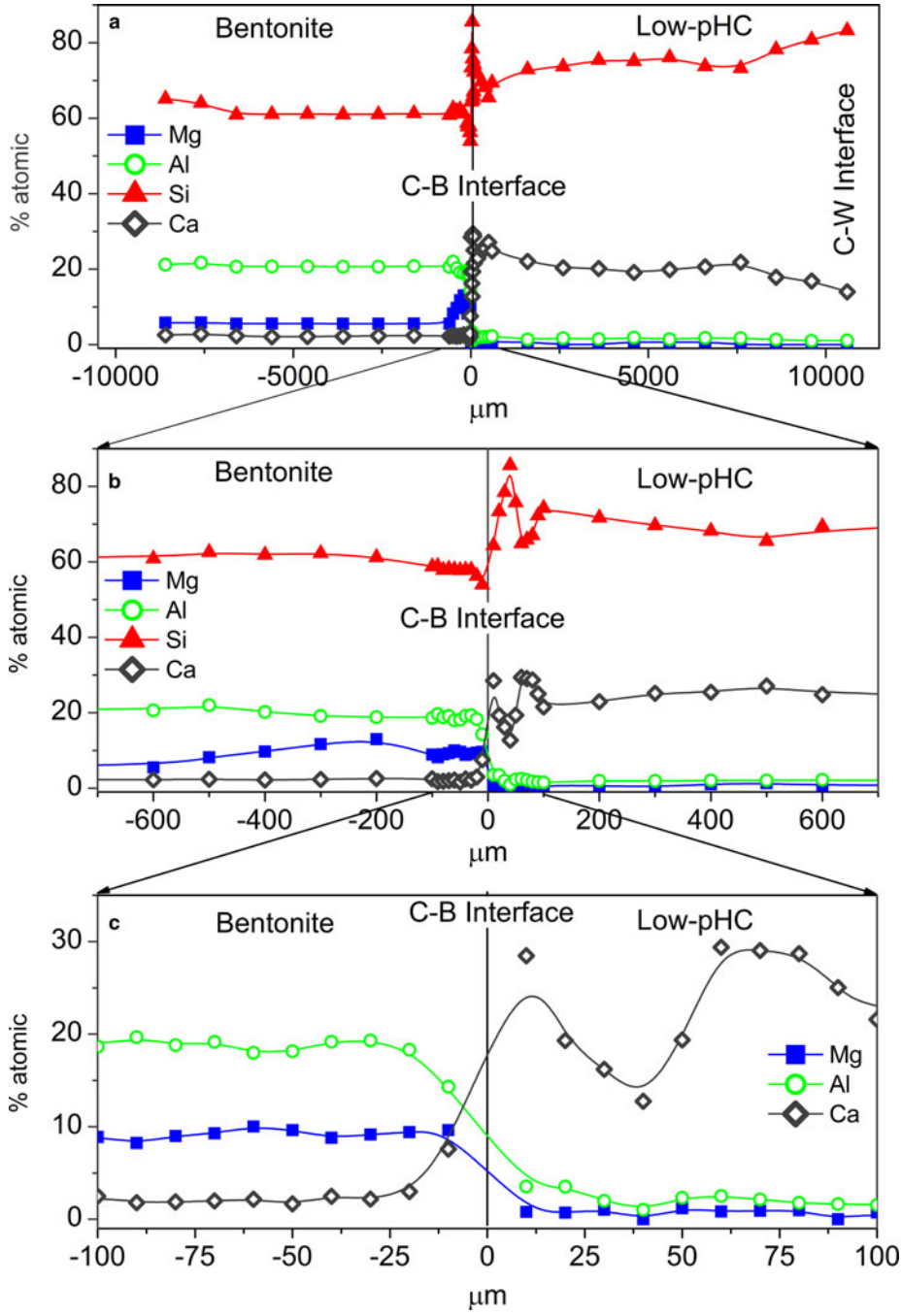

FIG. 6. EDX profile of the column at different scales: (a) 1000 μm, (b) 600 μm, and (c) 100 μm. Bentonite is shown on the left side and low-pH cement mortar (Low-pHC) on the right side of the figure.

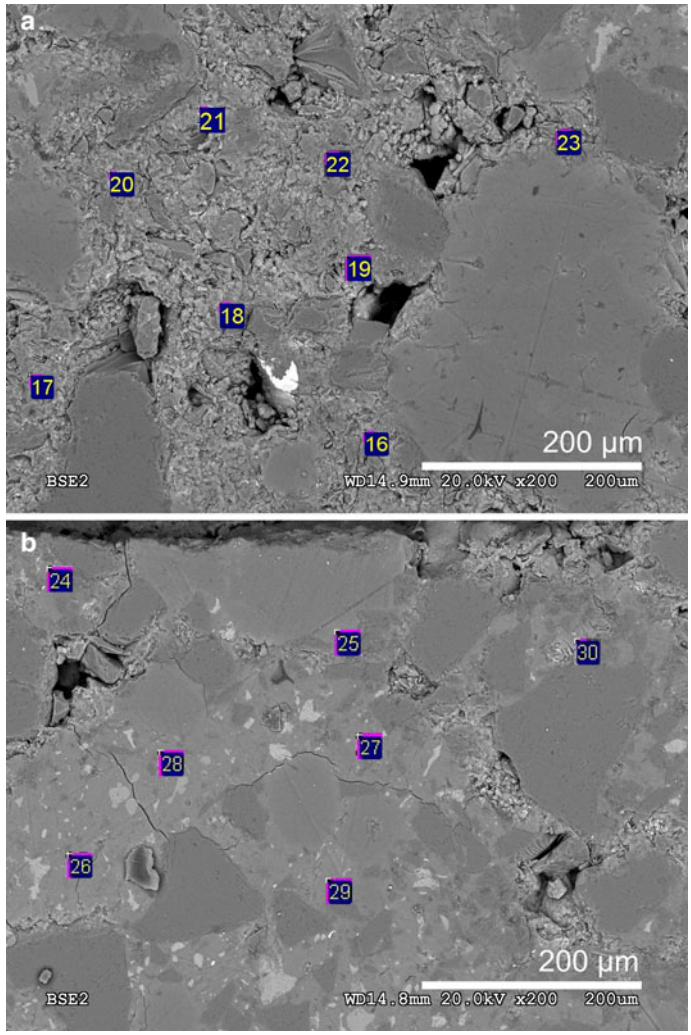

FIG. 7. (a) Locations of the SEM-EDX spots analysed in the cement matrix of the low-pH cement mortar near the C–W interface and (b) spots analysed in the cement matrix of the low-pH cement mortar near the C–B interface.

showed little difference from the patterns recorded on the reference material (Fig. 10a). A subtle peak broadening and a shift from 3.05 to 3.03 Å was also detected in the low fixed-angle (1°) pattern, representing a small thickness surficial cement mortar area accessible to the X-rays. The SEM-EDX images and spot analyses of the same subsample showed typical calcite morphologies composed of Ca and carbon (Fig. 11a).

FEBEX-bentonite perturbations

The chemical perturbations observed in the FEBEX-bentonite were ~500–600 µm thick from the C–B interface (Fig. 6b). The EDX compositional profile indicates a Ca increase at 20 µm from the C–B interface, in agreement with a depletion of Al in the same region (Fig. 6c). The EDX analyses showed a Mg/Si ratio of 0.5 ± 0.1 (based on eight analyses) at the surface of bentonite (Fig. 11b) which was in contact with the low-pH cement mortar only, and of 0.2 ± 0.05 where the Mg/Si ratio was obtained from the first 13 analyses performed from the C–B interface on the EDX profile, representative of a thickness of 400 µm from the C–B interface. The enrichment in Mg near the cement mortar interface contrasts with the Mg/Si ratio of 0.10 ± 0.05 obtained from nine analyses far from the

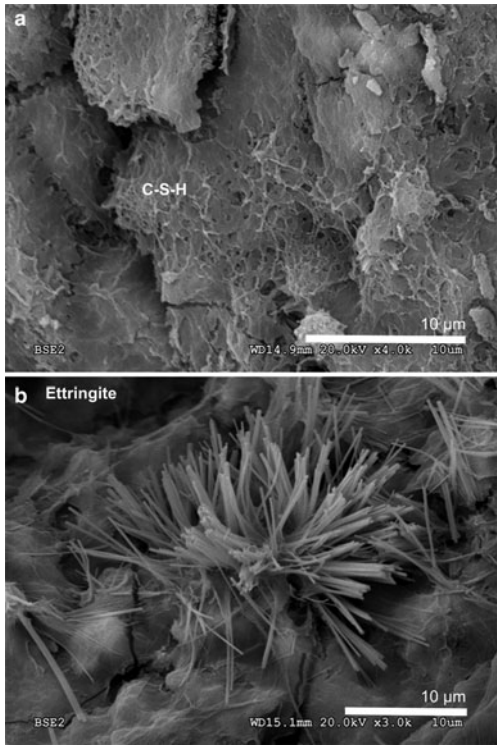

FIG. 8. Backscattered electron (BSE) images: (a) C-S-H present on the low-pH cement mortar side next to bentonite; and (b) ettringite present on the low-pH cement mortar side next to bentonite.

interface (in the range 600–8600 µm from the C–B interface) using the same approximation.

The mineralogical data obtained by XRD and GI-XRD (Figs 10b, 12) showed minimal changes in montmorillonite (Mnt) compared to those in the reference sample of FEBEX-bentonite. These changes are characterized by a weak decrease in the intensity of the Mnt basal reflection at 14.7 Å as the subsamples approach the C–B interface (Fig. 12). This effect was accompanied by an increase in the background towards higher angles using the Mnt basal reflection as the reference (from 7 to 17°2θ) in the subsample at 3 mm from the C–B interface.

DISCUSSION

The FEBEX-bentonite buffer capacity is manifested by to the pH 8.3 obtained from the water collected (Table 3), very close to the porewater pH measured in the original bentonite and consistent with the exchange complex and bentonite mineral equilibria (Fernández *et al*., 2004). Aqueous SiO_2 showed concentrations within the solubility equilibrium of quartz and cristobalite (Williams *et al.*, 1985), which are present in bentonite where the OH^- provided by cement mortar was consumed at the C–B interface (Gaucher & Blanc, 2006; Savage *et al*., 2007). In addition to the buffer capacity, bentonite also controls the hydraulic conductivity. The hydraulic conductivity of FEBEX-bentonite at room temperature (23°C) and at a dry density of 1.6 g/cm^3 has been reported previously to be on the order of 10^{-13} m/s (Villar, 2000, 2002; Villar & Lloret, 2004), in agreement with the value of hydraulic conductivity calculated in the present study (1.6×10^{-13} m/s). This might support the validity of the pilot experimental setup because the advective transport regime was very low and the diffusion was relevant (Muhammad, 2004; Bourg & Tournassat, 2015), as expected in a real repository scenario. Three main chemical modifications have been observed around the reactive interfaces in the experiment: (1) decalcification of C-S-H at the C–W and C–B interfaces; (2) carbonation at the C–B interface (on the low-pH cement mortar side); and (3) Mg-perturbation in bentonite next to the C–B interface.

Decalcification of C-S-H

The Ca leaching process has been identified mainly at the C–W interface. The deterioration of low-pH cement-based materials starts with Na and K release followed by decalcification of the C-S-H. Although low-pH cement leaching has not been studied extensively, aqueous silica is expected to remain saturated with respect to quartz. Then, Ca leaching in such a solution might cause the formation of secondary C-S-H with a lower Ca/Si ratio than the initial C-S-H phases. Compared with the thickness of decalcification at the C–W interface (~3 mm) observed in the present experiment, an alteration thickness of 700 µm was reported in a low-pH concrete composed of Portland cement with additions of silica fume after 14 months and exposure to granitic groundwater flow (García Calvo *et al*., 2010).

At the C–B interface, the decalcification of C-S-H may have occurred according to the lower Ca/Si ratio of the spot EDX analyses from the cement matrix (0.8 ± 0.1) and the C-S-H (Ca/Si = 0.6) observed at the surface of the cement mortar in contact with bentonite only. These low Ca/Si ratios are close to the results provided by García Calvo (2012), and they are also consistent with the leaching experiments of

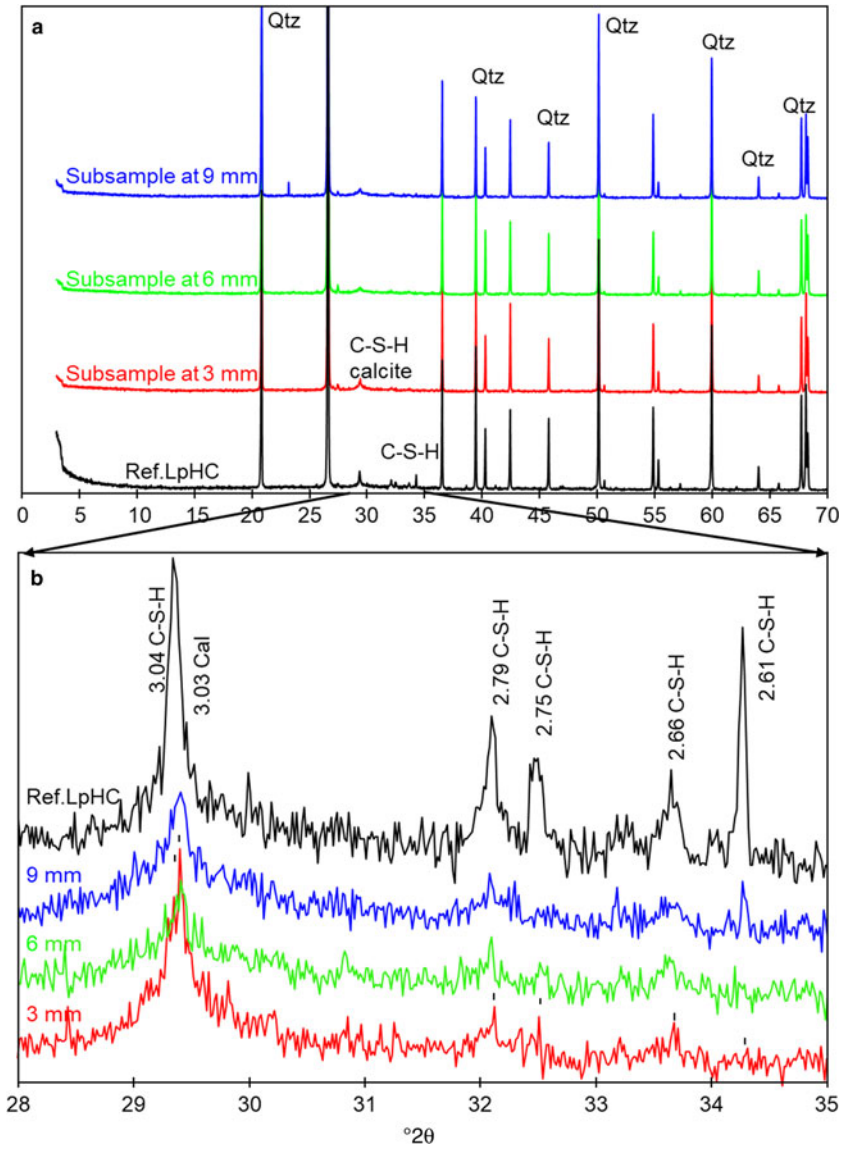

FIG. 9. (a) XRD of the reference low-pH cement mortar (Ref. LpHC) sample and reacted subsamples at 9, 6 and 3 mm from the C–B interface. (b) Magnification of the XRD trace in the range 28–35°2θ. Qtz: quartz, C-S-H: calcium silicate hydrates, and Cal: calcite. *d* spacings are given in Å.

Baston *et al*. (2012) with low-pH concrete under similar experimental conditions. Possible evidence for C-S-H alteration of the low-pH cement mortar was determined by means of the XRD patterns (Fig. 9a–b). Moreover, the migration of Al from bentonite next to the C–B interface might lead to the formation of metastable C-A-S-H (Pegado *et al.,* 2014); although C-A-S-H was not identified, this migration of Al to the low-pH cement mortar due to the exchange of soluble species (Fig. 6c), together with enough sulfate content, may favour the precipitation of ettringite, as suggested by the presence of needle morphologies in the EDX and SEM images from the point analyses. Low-pH concrete in contact with clayey rocks rich in sulfates was studied by the Cement–Opalinus Clay Interaction project (CI) experiment in Mont Terri, Switzerland

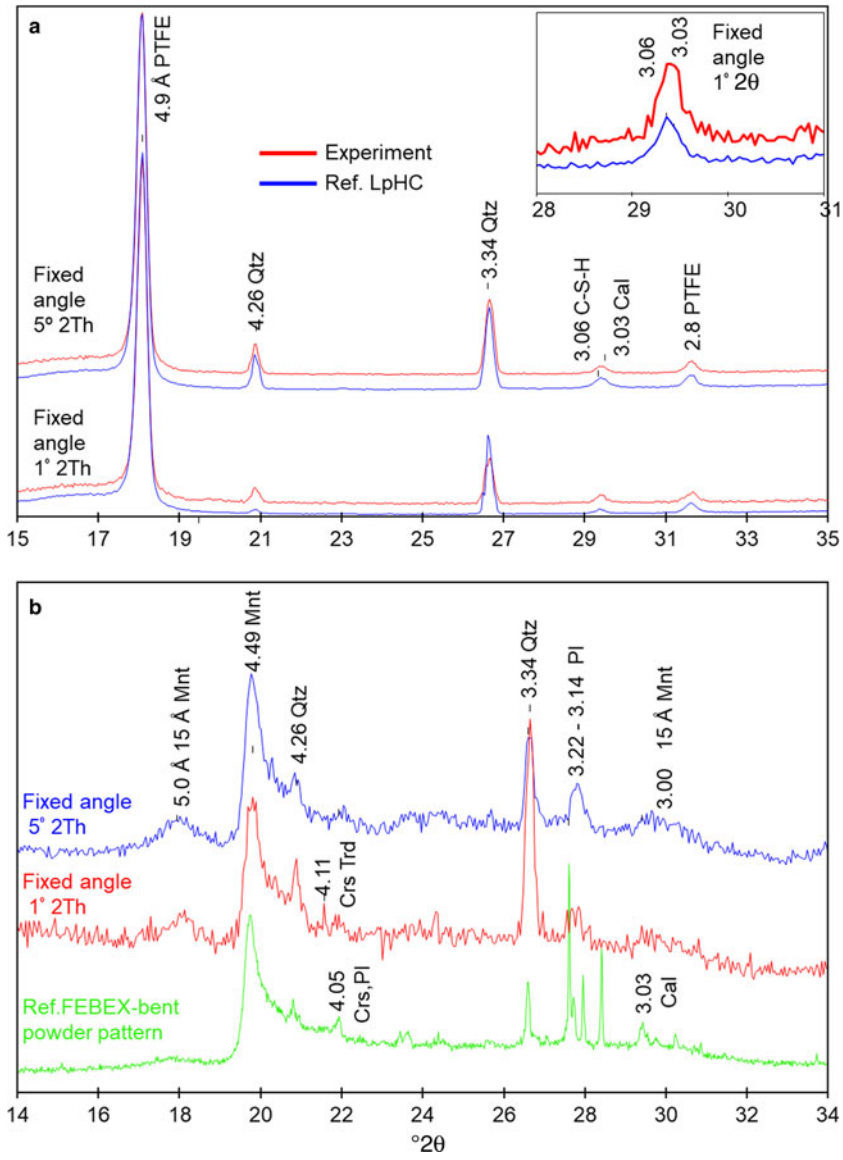

FIG. 10. (a) GI-XRD pattern recorded for the reference low-pH cement mortar (Ref. LpHC) and the surface of the sample exposed to bentonite after the experiment. (b) Conventional random powder XRD pattern recorded for the reference FEBEX-bentonite and GI-XRD for the surface of the sample exposed to low-pH cement mortar after the experiment. PTFE: polytetrafluoroethylene, Mnt: montmorillonite, Qtz: quartz, Crs: cristobalite; Crs-Trd: cristobalite-tridymite; Pl: plagioclase, and Cal: calcite. *d* spacings are given in Å.

(Dauzères *et al.*, 2016) where secondary ettringite precipitates at this interface, with this mineral being stable in the pH range of 11.0–12.5 (McCarthy *et al.*, 1991), as determined in the low-pH cement mortar in the present study.

Carbonation at the C–B interface

A carbonation process (calcite precipitation) was suggested by the SEM images (*e.g.* Fig. 11a) and the XRD and GI-XRD analyses (Figs 9a–b and 10a) at the C–B interface. The dissolved CO_2 species could be

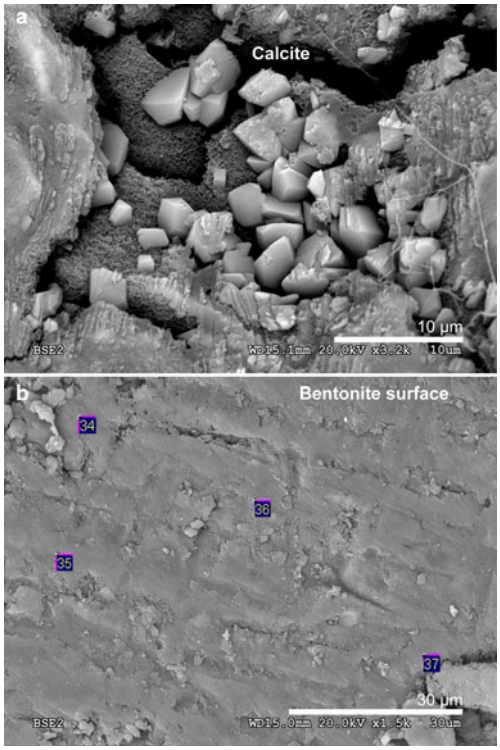

FIG. 11. (a) Backscattered electron (BSE) image of calcite present in the low-pH-cement mortar side near the interface with bentonite. (b) Backscattered electron image of the bentonite surface exposed to cement mortar. The numbers correspond to the EDX analysis points.

provided by the clayey pore solutions (Dauzères *et al*., 2014; Jenni *et al.,* 2014) mainly as HCO_3^-, which is unstable in alkaline environments compared to CO_3^{2-}. Then, these carbonates might react with the Ca ions available in the low-pH cement mortar pore solution to precipitate as $CaCO_3$ at the cement–mortar interface. This is observed experimentally by the increase in Ca observed at the C–B interface (0–100 µm on the cement mortar side), and is complemented by the images of the above-mentioned calcite. Calcite precipitation at the interface has been observed by other authors, conducting similar experiments over much longer periods of time, to lead to a decrease in porosity (Cuevas *et al.,* 2014).

Mg perturbation at the C–B interface

Mg is present as an exchangeable cation in FEBEX-bentonite so it can be displaced readily by Ca ions leached from the cement mortar porewater. In fact, the decrease in exchangeable Mg in the FEBEX-bentonite in contact with concrete has been probed in an *in situ* experiment at the Grimsel-test site (Switzerland) (Villar, 2018). The pH > 11.0 porewater of the low-pH cement mortar is sufficient to form new mineral Mg-phases, such as brucite (pH 10.5) or Mg-silicate hydrates (M-S-H; *e.g.* Nied *et al*., 2016). These Mg-rich phases were not detected by XRD in the present study because of the narrow thickness (<500 µm), in which a slight Mg enrichment was detected by EDX at the bentonite side of the C–B interface. Although not measured in the present study, a redistribution of the exchangeable cation population in bentonite is expected. Surface mobility may induce Mg to move from the exchange complex and precipitate in the alkaline medium. Mg perturbation at the bentonite–cement interface to a greater extent has been reported previously by other authors (*e.g.* Fernández *et al*., 2010). However, those previous studies were performed over longer experimental times and under more alkaline conditions imposed by OPC (ordinary Portland cement) concrete. The presence of larger amounts of Mg may expand the number of phases to be considered from brucite to brucite-intercalated Mnt and serpentine-like phases (Fernández *et al.,* 2009, 2013).

CONCLUSIONS

In the present study, a novel and reliable method to perform small-scale laboratory experiments concerning concrete–bentonite reactivity in a granitic DGR was tested. Only minor reactivity was observed. However, the following chemical perturbations were detected in spite of the short experimental time: (1) cement mortar decalcification at the cement mortar-bentonite and cement mortar–water interfaces; (2) slight carbonation in the low-pH cement mortar next to the interface with bentonite; and (3) Mg enrichment in bentonite at the interface with the cement mortar. These results are spatially limited but consistent with those observed previously over the long term, either at the laboratory scale or in large underground facilities. This experimental design is being applied to interactions of bentonite with high-pH cement mortar over longer times and using real groundwater compositions. Additional analytical techniques will be required for an improved interpretation of the results, which should provide valuable information and contribute to knowledge of the interaction between geochemical barriers under different scenarios planned for DGR.

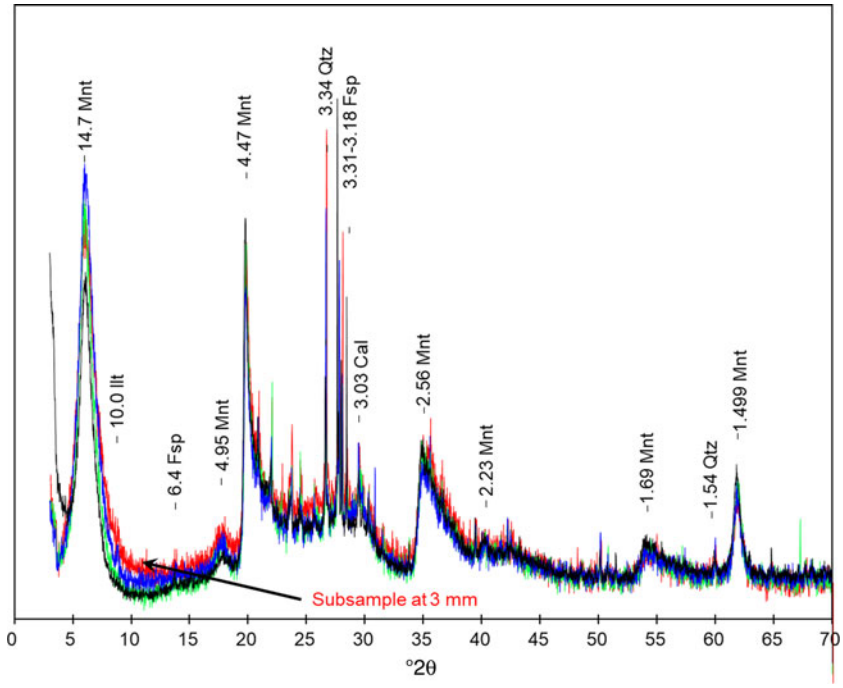

FIG. 12. FEBEX-bentonite XRD pattern. The reference FEBEX-bentonite is shown together with the overlapping subsamples at 9, 6 and 3 mm from the C–B interface. Mnt: montmorillonite, Ilt: illite, Qtz: quartz, Fsp: feldspar, Cal: calcite. *d* spacings are given in Å.

SUPPLEMENTARY MATERIAL

The supplementary material for this article can be found at https://doi.org/10.1180/clm.2018.16.

ACKNOWLEDGEMENTS

The research leading to these results has received funding from the European Union's Horizon 2020 Research and Training Programme of the EURATOM (H2020-NFRP-2014/2015) under grant agreement n° 662147 (CEBAMA). The authors area grateful for the expertise of Dr Enrique Rodríguez Cañas with the SEM-EDX equipment used in the Inter-Departmental Research Service (SIdI) of the Autonomous University of Madrid.

REFERENCES

Bäckblom G. (2005) R&D on low-pH cement for a geological repository in: *SKB and the ESDRED project: 2nd low-pH workshop proceedings*. ENRESA, Madrid, Spain.

Bartier D., Techer I., Dauzères A., Boulvais P., Blanc-Valleron M-M. & Cabrera J. (2013) In situ investigations and reactive transport modelling of cement paste/argillite interactions in a saturated context and outside an excavated disturbed zone. *Applied Geochemistry*, **31**, 94–108.

Baston G.M.N., Clacher A.P., Heath T.G., Hunter F.M.I., Smith V. & Swanton S.W. (2012) Calcium silicate hydrate (C-S-H) gel dissolution and pH buffering in a cementitious near field. *Mineralogical Magazine*, **76**, 3045–3053.

Berner U., Kulik D. & Kosakowski G. (2013) Geochemical impact of a low-pH cement liner on the near field of a repository for spent fuel and high-level radioactive waste. *Physics and Chemistry of the Earth*, **64**, 46–56.

Bildstein O. & Claret F. (2015) Stability of barriers under chemical perturbations. Pp. 155–188 in: *Natural and Engineered Clay Barriers* (C. Tournassat, C.I. Steefel, I.C. Bourg & F. Bergaya, editors). Elsevier Ltd, Amsterdam.

Bourg I.C. & Tournassat C. (2015) Self-diffusion of water and ions in clay barriers. Pp. 189–226 in: *Natural and Engineered Clay Barriers* (C. Tournassat, C.I. Steefel, I.C. Bourg & F. Bergaya, editors). Elsevier Ltd, Amsterdam.

Caballero E., de Cisneros C., Huertas F., Huertas F., Pozzuoli A. & Linares J. (2005) Bentonites from

Cabo de Gata, Almería, Spain: a mineralogical and geochemical overview. *Clay Minerals*, **40**, 463–480.

Cuevas J., Samper J., Turrero M.J. & Wieczorek K. (2014) Impact of the geochemical evolution of bentonite barriers on repository safety functions. Pp. 35–42 in: *PEBS Case 4. Proceedings International Conference on the Performance of Engineered Barrier: Physical and Chemical Properties, Behavior and Evolution* (BGR. A. Schäfers & S. Fahland, editors). Hannover, Germany.

Cuevas J., Ruiz A.I., Fernández R., Torres E., Escribano A., Regadío M. & Turrero M.J. (2016) Lime mortar-compacted bentonite–magnetite interfaces: An experimental study focused on the understanding of the EBS long-term performance for high-level nuclear waste isolation DGR concept. *Applied Clay Science*, **124–125**, 79–93.

Dauzères A., Le Bescop P., Sardini P. & Cau Dit Coumes C. (2010) Physico-chemical investigation of clayey/cement-based materials interaction in the context of geological waste disposal: Experimental approach and results. *Cement and Concrete Research*, **40**, 1327–1340.

Dauzères A., Le Bescop P., Cau-Dit-Coumes C., Brunet F., Bourbon X., Timonen J., Voutilainen M., Chomat L. & Sardini P. (2014) On the physico-chemical evolution of low-pH and CEM I cement pastes interacting with Callovo-Oxfordian pore water under its in situ CO_2 partial pressure. *Cement and Concrete Research*, **58**, 76–88.

Dauzères A., Achiedo G., Nied D., Bernard E., Alahrache S. & Lothenbach B. (2016) Magnesium perturbation in low-pH concretes placed in clayey environment – solid characterizations and modeling. *Cement and Concrete Research*, **79**, 137–150.

ENRESA (2006) Post-mortem bentonite analysis. Pp. 183 in: *FEBEX Project Final Report* (M.V. Villar, editor). Publicación técnica 1-5/2006, Madrid, Spain.

Ewing R., Whittleston R. & Yardley B. (2016) Geological disposal of nuclear waste: a primer. *Elements*, **12**, 233–237.

Fernández A.M., Baeyens B., Bradbury M. & Rivas P. (2004) Analysis of the porewater chemical composition of a Spanish compacted bentonite used in an engineered barrier. *Physics and Chemistry of the Earth*, **29**, 105–118.

Fernández R., Mäder U., Rastrero M., Vigil de la Villa Mencía R. & Cuevas J. (2009) Alteration of compacted bentonite by diffusion of highly alkaline solutions. *European Journal of Mineralogy*, **21**, 725–735.

Fernández R., Mäder U. & Cuevas J. (2010) Modeling experimental results of diffusion of alkaline solutions through a compacted bentonite barrier. *Cement and Concrete Research*, **40**, 1255–1264.

Fernández R., Vigil de la Villa R., Ruiz A.I., García R. & Cuevas J. (2013) Precipitation of chlorite-like structures during OPC porewater diffusion through compacted bentonite at 90°C. *Applied Clay Science*, **83–84**, 357–367.

Fernández R., Torres E., Ruiz A.I., Cuevas J., Alonso M. C., García Calvo J.L., Rodríguez E. & Turrero M.J. (2017) Interaction processes at the concrete-bentonite interface after 13 years of FEBEX-Plug operation. Part II: Bentonite contact. *Physics and Chemistry of the Earth*, Parts A/B/C, **99**, 49–63.

Gaboreau S., Prêt D., Tinseau E., Claret F., Pellegrini D & Stammose D. (2011) 15 years of in situ cement–argillite interaction from Tournemire Characterisation of the multi-scale spatial heterogeneities of pore space evolution. *Applied Geochemistry*, **26**, 2159–2171.

Gaboreau S., Lerouge C., Dewonck S., Linard Y., Bourbon X., Fialips C.I., Mazurier A., Prêt d., Borschneck D., Montouillout V., Gaucher E. C. & Claret F. (2012) In-situ interaction of cement paste and shotcrete with claystones in a deep disposal context. *American Journal of Science*, **312**, 314–356.

García Calvo J.L., Hidalgo A., Alonso C. & Fernández L. (2010) Development of low-PH cementitious materials for HLRW repositories. *Cement and Concrete Research*, **40**, 1290–1297.

García Calvo J.L. (2012) *Desarrollo De Materiales de Construcción con Cemento de Bajo pH, compatibles con la Barrera de Ingeniería de un Almacenamiento Geológico Profundo de Residuos Radiactivos de Alta Actividad*. PhD thesis, Instituto Eduardo Torroja de Ciencias de la Construcción, Spain.

Gaucher E. & Blanc P. (2006) Cement/clay interactions – A review: Experiments, natural analogues, and modelling. *Waste Management*, **26**, 776–788.

Gibney E. (2015) Why Finland now leads the world in nuclear waste storage. *Nature*. doi.org/10.1038/nature.2015.18903.

Gómez-Espina R. & Villar M.V. (2016) Time evolution of MX-80 bentonite geochemistry under thermo-hydraulic gradients. *Clay Minerals*, **51**, 145–160.

IAEA-TECDOC-1718 (2013) Characterization of swelling clays as components of the engineered barrier system for geological repositories. Results of an IAEA Coordinated Research Project, 2002–2007.

Jenni A., Mäder U., Lerouge C., Gaboreau S. & Schwyn B. (2014) In situ interaction between different concretes and Opalinus Clay. *Physics and Chemistry of the Earth*, **70–71**, 71–83.

Kaufhold S., Dohrmann R., Sandén T., Sellin P. & Svensson D. (2013) Mineralogical investigations of the first package of the alternative buffer material test – I. *Alteration of bentonites. Clay Minerals*, **48**, 199–213.

Kaufhold S. & Dohrmann R. (2016) Distinguishing between more and less suitable bentonites for storage

of high-level radioactive waste. *Clay Minerals*, **51**, 289–302.

Lerouge C., Gaboreau S., Grangeon S., Claret F., Warmont F., Jenni A., Cloet V. & Mäder U. (2017) In situ interactions between Opalinus Clay and Low Alkali Concrete. *Physics and Chemistry of the Earth*, **99**, 3–21.

Liu S., Jacques D., Govaerts J. & Wang L. (2014) Conceptual model analysis of interaction at a concrete-Boom Clay interface. *Physics and Chemistry of the Earth*, **70–71**, 150–159.

Lothenbach B., Nied D., L'Hôpital E., Achiedo G. & Dauzères A. (2015) Magnesium and calcium silicate hydrates. *Cement and Concrete Research*, **77**, 60–68.

Mäder U., Jenni A., Lerouge C., Gaboreau S., Miyoshi S., Kimura Y., Cloet V., Fukaya M., Claret F., Otake T., Shibata M. & Lothenbach B. (2017) 5-year chemico-physical evolution of concrete–claystone interfaces, Mont Terri rock laboratory (Switzerland). *Swiss Journal of Geosciences*, **110**, 307–327.

McCarthy G., Hassett D. & Bender J. (1991) Synthesis, crystal chemistry and stability of ettringite, a material with potential applications in hazardous waste immobilization. *MRS Proceedings*, **245**, 129. doi:10.1557/PROC-245-129.

Meunier A., Velde B. & Griffault L. (1998) The reactivity of bentonites: A review. An application to clay barrier stability for nuclear waste storage. *Clay Minerals*, **33**, 187–193

Muhammad N. (2004) *Hydraulic, Diffusion, and Retention Characteristics of Inorganic Chemicals in Bentonite*. PhD thesis, University of South Florida, EEUU, USA.

NEA-OECD (2003) *Engineered Barrier Systems and the Safety of Deep Geological Repositories*. State-of-the art Report. OECD Publications, Paris, 70 pp.

Nied D., Enemark-Rasmussen K., L'Hopital E., Skibsted J. & Lothenbach B. (2016) Properties of magnesium silicate hydrates (M-S-H). *Cement and Concrete Research*, **79**, 323–332.

Pegado L., Labbez C. & Churakov S. V. (2014) Supporting Information for: Mechanism of aluminium incorporation into C–S–H from ab initio calculations. *Journal of Materials Chemistry* A, **2**, 3477.

Roosz C., Grangeon S., Blanc P., Montouillout V., Lothenbach B., Henocq P., Giffaut E., Vieillard P. & Gaboreau S. (2015) Crystal structure of magnesium silicate hydrates (M-S-H): The relation with 2:1 Mg–Si phyllosilicates. *Cement and Concrete Research*, **73**, 228–237.

Savage D. (2014) An assessment of the impact of the long-term evolution of engineered structures on the safety-relevant functions of the bentonite buffer in a HLW repository. Pp. 88 in: *National Cooperative for the Disposal of Radioactive Waste. Technical Report 13-02* (Nagra Editor). Wettingen, Switzerland.

Savage D., Walker C., Arthur R., Rochelle C., Oda C. & Takase H. (2007) Alteration of bentonite by hyperalkaline fluids: a review of the role of secondary minerals. *Physics and Chemistry of the Earth*, **32**, 287–297.

Stronach S.A. & Glasser F.P. (1997) Modelling the impact of abundant geochemical components on phase stability and solubility of the CaO-SiO_2-H_2O system at 25 °C: Na+, K+, SO_3^{2-}, CT and CO_2^{3-}. *Advances in Cement Resesarch*, **9**, 167S–181S.

Trotignon L., Devallois V., Peycelon H., Tiffreau H. & Bourbon X. (2007) Predicting the long term durability of concrete engineered barriers in a geological repository for radioactive waste. *Physics and Chemistry of the Earth*, Parts A/B/C 32 (**1–7**): 259–274.

U.S. DOE (Department of Energy) (2014) Evaluation of options for permanent geologic disposal of spent nuclear fuel and high-level radioactive waste, Volume I. Used Fuel Disposition Campaign. Sandia National Laboratory, New Mexico, USA.

Van Damme H. & Pellenq R.J.M. (2013) Chapter 14.3–cement hydrates. Pp. 801–817 in: *Handbook of Clay Science* (F. Bergaya and G. Lagaly, editors). *Developments in Clay Science*, Elsevier Ltd, Amsterdam.

Villar M.V. (2000) *Caracterización termohidro-mecánica de una bentonita de Cabo de Gata*. PhD thesis, Universidad Complutense de Madrid, Spain.

Villar M.V. (2002) Thermo-hydro-mechanical characterisation of a bentonite from Cabo de Gata. Pp 285 in: *A Study Applied to the use of Bentonite as Sealing Material in high level Radioactive Waste Repositories*. Technical publication. ENRESA 01/2002, Madrid, Spain.

Villar M.V. & Lloret A. (2004) Influence of temperature on the hydro-mechanical behaviour of a compacted bentonite. *Applied Clay Science*, **26**, 337–350.

Villar M.V., Martín P.L., Bárcena I., García-Siñeriz J.L., Gómez-Espina R. & Lloret A. (2012) Long-term experimental evidence of saturation of compacted bentonite under repository conditions. *Engineering Geology*, **149–150**, 57–69.

Villar M.V., Fernández A.M., Romero E., Dueck A., Cuevas J., Plötze M., Kaufhold S., Dohrman R., Iglesias R.J., Sakaki T., Zheng L., Kawamoto K. & Kober F. (2018) FEBEX-DP Postmortem *Analysis Report*. Nagra Report NAB 16–017. 147 pp.

Williams L.A., Parks G.A. & Crerar D.A. (1985) Silica Diagenesis, I. Solubility Controls. *SEPM Journal of Sedimentary Research*, **55**, 0301–0311.

Applied Geochemistry 117 (2020) 104599

Contents lists available at ScienceDirect

Applied Geochemistry

journal homepage: http://www.elsevier.com/locate/apgeochem

Bentonite/CEM-II cement mortar INTERFACE EXPERIMENTS: A proxy to *in situ* deep geological repository engineered barrier system surface reactivity

Daniel E. González-Santamaría *, Raúl Fernández, Ana I. Ruiz, Almudena Ortega, Jaime Cuevas

Department of Geology and Geochemistry, Faculty of Sciences, Autonomous University of Madrid, Cantoblanco, 28049, Madrid, Spain

ARTICLE INFO

Handling editor: Michael Kersten

Keywords:
Deep geological repository
Alkaline alteration upscaling
Engineered barrier system
Cement-bentonite interface
Carbonation
Mg silicates hydrates

ABSTRACT

The present study focuses on the interaction between cement mortar (OPC-based CEM-II) and the FEBEX-bentonite; this interaction takes place at a small spatial scale (~1 cm/~1 cm; compacted cement mortar/compacted bentonite thickness) within a timeline of 6 and 18 months. This work was designed to determine the early interaction processes and compare them with large-scale FEBEX *in situ* underground research laboratory experiments. The study aimed at the primary reactions that occurred at the interface in a small spatial scale (nm-μm scale). The experimental device consisted of a composite column containing the cement mortar/bentonite materials. A granitic groundwater solution was injected through the cement mortar/bentonite system and collected out of the column in sequential syringes for analysis of the chemical composition evolution. For the study of the post-mortem samples, an innovative use of grazing incidence X-ray diffraction was performed to determine the phases produced at the interface. Scanning electron microscopy coupled to energy dispersive X-rays and local specific surface area measurements were also applied. The main results showed the initial development of a Mg perturbation in FEBEX-bentonite at the interface related to the formation of 7 Å precursors of Mg-clay 2:1 sheet silicates as the main neogenic phases expected in the long term. Additionally, a Ca-carbonation skin (calcite) occurred in cement mortar at the interface. The specifications of the reaction products observed at small scales of time and space (μm) are highly promising for the development of reaction concepts and support modelling in the future, which could offer a useful perspective for advancement in the upscaling of concrete/bentonite interface perturbation.

1. Introduction

In recent decades, concern related to high-level radioactive waste (HLRW) management has been growing. HLRW, mostly spent fuel, is presently safely hosted within the facilities of nuclear power plants but its storage at long term requires international consensus based on the safest technical and scientific practices due to its long-lived radiotoxicity (10^4–10^5 years). Currently, the deep geological repository (DGR) is considered as the best solution for long-term isolation of HLRW to avoid its release to the biosphere. The DGR is based on a multiple engineered barrier system (EBS), which is placed in a host rock formation (Ewing et al., 2016). Concrete and bentonite are two main components of the EBS when considering granitic bedrock for a DGR. Those materials are exposed to the groundwater from the granite, whose composition depends on the characteristics of each site. Cementitious materials produce alkaline pore fluids with a pH from 10 to 13.5 (Berner, 1992), in contrast with the almost neutral pH of bentonite. This disequilibrium results in geochemical reactions that progress at changing rates during the entire life span of the facility. It is crucial to assure the safety of EBS and to gain full knowledge of the key reaction pathways involved from the initial stages to understand its evolution in the long term. For this reason, efforts are being made to evaluate those disturbances and their evolution at different spatial scale (from small laboratory to real size *in-situ* experiments) and temporal scale (from a few months to over decades). Several approaches are underway, and pertinent knowledge is expected from the study of clay reactions in natural alkaline environments as natural reactivity analogues (Khoury et al., 1985; Savage, 2011). Long-term concrete/bentonite systems studies at repository scale are available throughout experiments performed in underground research laboratories (URLs). URLs are essential to supplying scientific and technical data from several years to decades of reaction to the real spatial scale of a repository.

The results of cement/clay interaction from large-scale facilities usually offer instant pictures of the resulting reactivity that characterizes

* Corresponding author.
E-mail address: daniel.g.santamaria@uam.es (D.E. González-Santamaría).

https://doi.org/10.1016/j.apgeochem.2020.104599
Received 9 August 2019; Received in revised form 24 February 2020; Accepted 7 April 2020
Available online 23 April 2020

interfaces after long periods of time (e.g. Fernández et al., 2018; Tinseau et al., 2006). However, the interpretation of results is not always straightforward because, due to the large dimensions, the reactivity is heterogeneous. Therefore, knowledge acquired on the reactivity by homogeneous laboratory scale experiments is useful to interpret and predict the reactivity at long-term (Cuevas et al., 2018a).

The state-of-the-art on the alkaline alteration of bentonite has been well described by Dauzères et al. (2010) and reviewed by Gaucher and Blanc (2006) and Savage et al. (2007).

Short-term laboratory-based experiments enable to study different materials in virtually equal controlled conditions in order to compare their behaviour, what is relevant to determine the most suited materials to be implemented, which is currently a discussion issue (González-Santamaría et al., 2018). For example, low-pH cement-base materials (pH < 12) were proposed to avoid the extreme alkalinity (Berner et al., 2013) and García-Calvo et al. (2010) demonstrated their resistance to granitic groundwater exposure after 2 years of interaction. In contrast, under the influence of carbonated water, low-pH cements exhibit lower resistance than that of high-pH cements (Dauzères et al., 2016), and hydration products such as ettringite are more unstable (Trotignon et al., 2007). The present short-term experiments might be able to supply complementary data on the early stage of geochemical interactions and evidence for reactions that are implemented in geochemical modelling (Churakov and Prasianakis, 2018). Additionally, this information can aid in the upscaling of processes that take place from months to decades.

This study focuses on the interactions of cement mortar with CEM II (hereafter referred to as cement mortar or CEM II-C) and FEBEX-bentonite. Our objective is to be able to compare materials interactions similar to those observed after 13 years from the dismantling of the FEBEX *in situ* experiment at the granitic Grimsel Test Site (GTS) URL in Switzerland (Fernández et al., 2017). The FEBEX *in situ* experiment simulated thermo-hydro-mechanical and chemical conditions of a DGR by substituting radioactive waste containers for two metallic heaters. The experiment lasted 18 years but one heater was switched off after 5 years and then extracted. The emptied part of the gallery was sealed with a sprayed concrete plug that remained in contact with the compacted bentonite barrier for the next 13 years until the final dismantling. The methodological approach of the present study is based on the previous procedures developed in a pilot project to study the geochemical reactions on a short-term scale (González-Santamaría et al., 2018).

The experiments performed in this work have been designed to detect early reactions at the interface in a small range extension (nm-µm scale) and have been practised in a composite column containing the cement mortar-bentonite (CB) materials. The innovative use of grazing incidence X-ray diffraction (GI-XRD) and θ-2θ scans on the solid post-mortem samples has been applied to determine the phases produced at the immediate interface of cement mortar and bentonite. The different X-ray diffraction (XRD) techniques applied have been combined with complementary scanning electron microscopy coupled to energy dispersive X-rays (SEM-EDX) and local specific surface area (SSA) measurements. In addition, the effluent displaced out of the column has been determined to study the evolution of the aqueous chemical composition.

2. Methods

2.1. Experimental setup

Cured cement mortar and FEBEX-bentonite (compacted at a dry density of 1.6 g/cm^3) were placed in a methacrylate cylindrical sleeve confined by two stainless steel caps, which constitute a transport cell, and separated by a 0.45 µm polytetrafluoroethylene (PTFE) membrane (Fig. 1). The cell dimensions were 20 mm in internal diameter and 9 mm in height for each material (18 mm in total). The objective of the design was ease of dismantling of the transport cells for further solid characterization, thus allowing the rapid separation of cement mortar and bentonite from the carcase. This design prevented deformation and drying of both materials and also avoided atmospheric interaction. The compact external stainless-steel case (together with connections and filters) was able to resist the high-pressure conditions caused by the hydration of bentonite (Villar and Lloret, 2004). In accordance with the *in situ* conditions at the GTS (Alonso et al., 2017; Fernández et al., 2017), granitic groundwater was injected at a constant 1 MPa hydraulic head through PEEK tubes using an automatic piston pump (Gilson, 307 model). The effluent volume was measured and collected at the bentonite end.

Two duplicated transport cells were run for 6 months, and the other two cells were run for 18 months, under virtually isothermal laboratory conditions (23 ± 2 °C). In fact, this condition is similar to the temperatures expected at the concrete bentonite interface, according to the data obtained from the FEBEX *in situ* experiment (Villar et al., 2012).

2.2. Sampling procedures (subsamples sectioning)

After the experiments were run, the cement mortar-bentonite columns were dismantled and divided into several samples using a cutting machine (Well®2000 model) with a diamond wire saw (Fig. 2) that allows to cut in dry conditions without heating the sample. The cut is

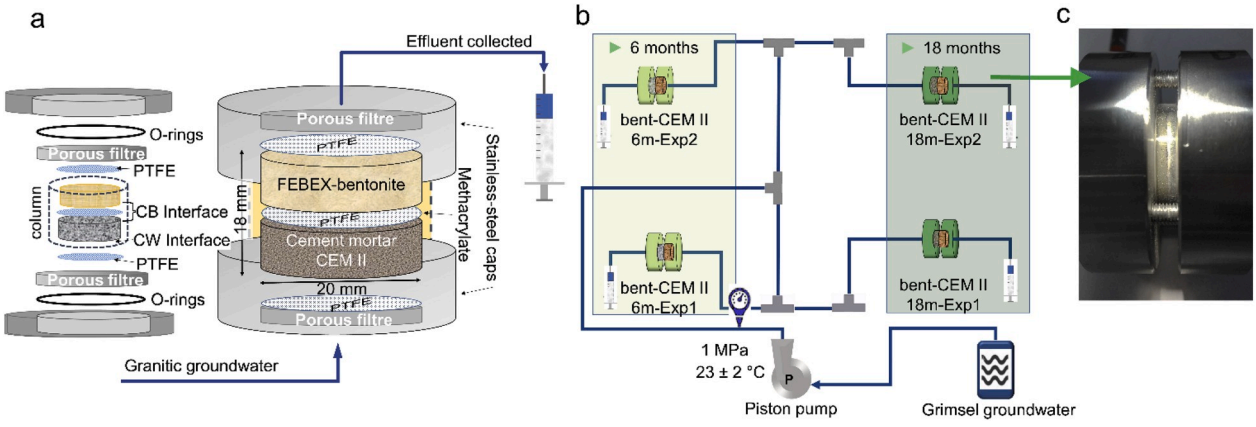

Fig. 1. Design of the transport cells. (a) Transport cells formed by cement mortar/compacted bentonite separated by a PTFE membrane and encased in an open stainless-steel sleeve. A methacrylate cylinder contains the column. Two porous filters allow water transport at both column ends. CB: cement mortar-bentonite interface; CW: cement-water interface. (b) It is represented the experimental scheme of the duplicated cells at two different periods: 6 and 18 months. ben: FEBEX-bentonite, CEM II. Cement mortar with CEM II as ordinary Portland cement (OPC). (c) Photograph of one of the transport cells.

slow and the sample is covered with parafilm to protect any interaction with the atmospheric air. The aim was to identify the presence of newly formed mineral phases at the CB-interface by studying the surfaces of the C1 and B1 slices, and the CW-interface was also studied in the external surface of the C3 slice (Fig. 2b) via SEM-EDX.

To assess the evolution of the materials in terms of distances, subsamples with 3 mm thickness sliced parallel to the interface were cut (Fig. 2b) for XRD and SSA analyses. After vacuum drying and grinding, cement mortar samples were stored in a hermetic chamber in the presence of NaOH lentils to prevent absorption of CO_2 by the cement-mortar, at a relative humidity (R. H.) <10%. The FEBEX-bentonite slices were also ground and equilibrated in 50% R. H. before XRD analysis to rehydrate the exchangeable cations and stabilize the smectite basal spacing.

GI-XRD and θ-2θ scans of the cement and bentonite interfaces (facing the PTFE membrane) were conducted on one of the cut quarters (Fig. 2c). The remaining flat surface of the half column perpendicular to the interface (Fig. 2e) was polished after freeze-drying treatment and was subsequently embedded in epoxy resin. Epoxy resin does not enter the materials and serves as a protective framework to confine the sample without destroying its integrity during the polishing operation, although the freeze-drying process can destabilize ettringite and other cement hydrates. After polishing, the sample was prepared for elemental chemical profiling via SEM-EDX. The linear transect selected to determine the elemental composition profile of the entire column was obtained using the CB-interface as the origin of distance coordinates. EDX measurements were collected towards the bentonite end of the column and towards the interface with the infiltrating groundwater solution (CW-interface) crossing the cement mortar. These analyses were performed in additional detail next to the CB-interface, with area dimensions of 10 μm height × 100 μm width in the direction perpendicular to the CB-interface. The following 5 analysis were executed with dimensions of 50 μm × 500 μm, followed by 7 and 16 analysis towards the bentonite column end and 10 analysis towards the CW-interface with dimensions of 100 μm × 1200 μm and 500 μm × 3000 μm, respectively. A similar methodology can be found in González-Santamaría et al. (2018) and Fernández et al. (2017). A schematic sketch of the number of analyses and increasing areas is shown in the latter paper.

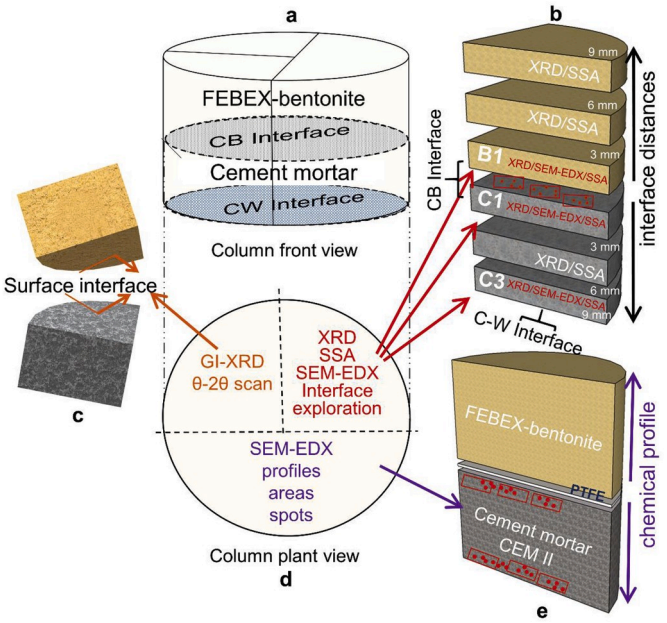

Fig. 2. Cutting and sampling scheme. (a) Front view with CB-interface and the CW-interface drawn (grey and blue ellipses). (b) Sample segmentation for XRD, SSA measurements and previous SEM-EDX exploration of the surface interfaces in slices B1, C1 and C3. (c) Sample quarter for GI-XRD and θ-2θ scans. (d) Plan view of the column. (e) Half column cut to show both the complete profile and also areas and punctual analysis next to the CB and CW-interfaces by SEM-EDX.

In the same half sample (Fig. 2e), the CEM II-C side was analysed as follows. Three rectangular areas of approximately 1 mm^2 were registered for major element quantification near the CB and CW-interfaces (Fig. 3a). Within these areas, punctual (also referred as spot) EDX analyses of the cement matrix were conducted at 200x magnification, and at least 7 spots were acquired in representative fields for the cement matrix (Fig. 3b).

2.3. Analytical techniques

XRD analysis of randomly oriented cement mortar and bentonite powders (samples shown in Fig. 2b) were conducted using a θ-2θ X'Pert PANalytical instrument with an X'Celerator detector. XRD patterns were recorded in an angular range of 3–70° 2θ. The detector allowed measurements equivalent to 0.016° angular steps for 100 s at each step. The voltage and intensity of the operated X-ray Cu tube were 45 kV and 40 mA, respectively. Complementarily, the GI-XRD analysis and θ-2θ scans were performed at both surfaces of the CB-interface (samples shown in Fig. 2c) to assess the perturbation that occurred in the first microns. The GI-XRD was configured with a fixed incidence angle of 0.5° 2θ. Both measurements were performed using 0.04° and 2 s of angular step and time step increases, respectively. Finally, the angular range recorded was 3-70° 2θ.

The SEM-EDX equipment was run on a Hitachi S–3000N scanning electron microscope coupled to an INCAx-sight Oxford Instruments™ energy-dispersive X-ray analyser. EDX semi-quantification of major elements was performed using internal standard semi-quantitative analysis. The statistical quality of elemental concentrations is detailed in (González-Santamaría et al., 2018). In summary, on the cement mortar side and for elements >20% (Al, Si, Ca), the instrumental % deviations obtained were less than 10% because their concentrations were lower for silicon (<1%), Ca (<5%) and higher for Al (9%). For elements with contents within 1–5% (Mg, Ca, K, Fe), the percentage of deviation from the average of the measured values was typically 10–15%. Punctual analysis acquired in EDX areas or spots acquired for characterizing cement matrix or phase composition were treated with IBM® SPSS® Statistic software. Test one-way ANOVA, multiple comparisons (Post Hoc Test) and test KrusKal-Wallis (p-value<0.05) were done to compare the different groups of experiments.

Specific surface area (SSA) was measured by means Gemini V porosimeter Micromeritics® equipment to relate the external surface and size of particles present in the materials. The technique is based on the method of adsorption of N_2(g) as analysed by the Brunauer, Emmett and Teller (BET) equation (Webb and Orr, 1997). Bentonite samples were heated at 90 °C for 24 h in a sample holder and then outgassed in a nitrogen current for 2 h in a degasification station before measurement, as in Cuevas et al. (2016). However, cement mortar samples were only heated for 2 h, instead of 24 h, to prevent dehydration of hydrated cement phases.

The aqueous effluent parameters picked up by the disc in the disposed syringe were analysed using a Metrohm 888™ automated potentiometric titration device for measurement of pH and alkalinity. Silica was determined by visible spectrophotometry using the molybdate blue complex method in a Milton Roy Spectronic® instrument at a wavelength of 825 nm. The major chemical ions were analysed with ion chromatography equipment coupled to a conductivity detector (IC-CD) using a Metrohm 802 compact IC plus model. Additionally, the hydraulic conductivity was also calculated for each transport cell by periodical weighing of the collection syringes to measure the flow rate and applying the Darcy's law.

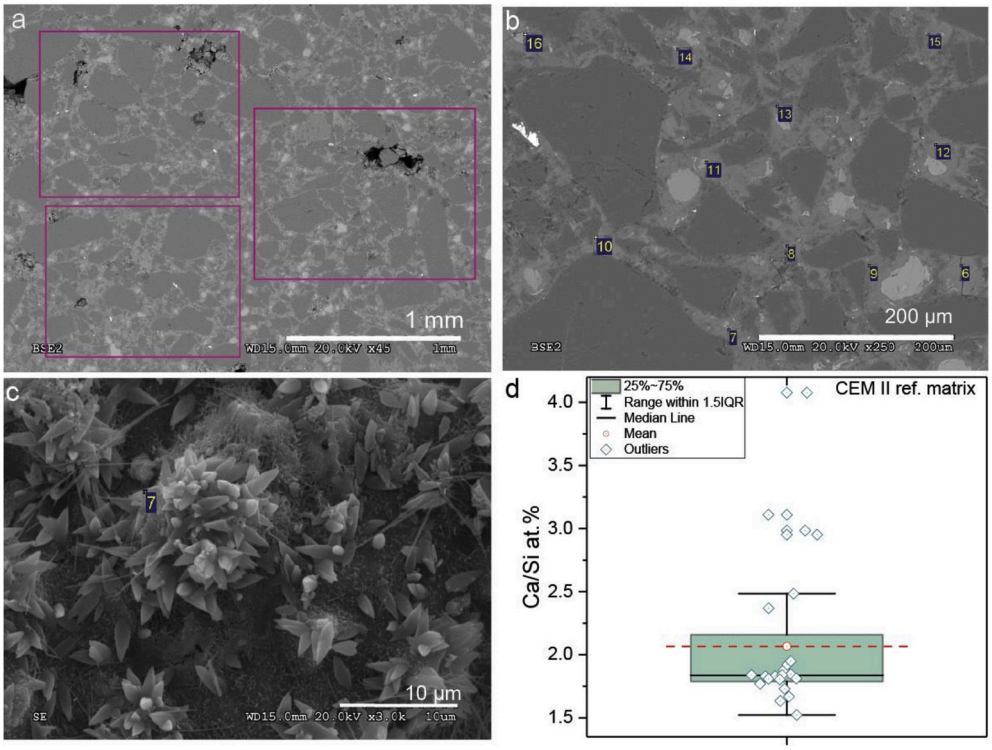

Fig. 3. SEM backscattering images from (a) area analyses conducted at 45x magnification, (b) matrix spot analysis locations conducted at 200x magnification and (c) micrograph in which calcium carbonate (bi-sphenoids) and ettringite needles are supported in the C–S–H cement matrix, and (d) statistical analysis of the Ca/Si atom ratio in the cement matrix.

3. Materials

3.1. Granitic groundwater

The main characteristics of the groundwater obtained from the GTS are its notably diluted composition of Na^+, Ca^{2+}, HCO_3^-, Cl^-, and SO_4^{2-} ions. GTS-groundwater has a value of 104 µS/cm for electrical conductivity, and the main ions concentrations (mg/L) are Cl^- (3.5), SO_4^{2-} (9.6), HCO_3^- (42.7), Na^+ (11.5), K^+ (<0.1), Ca^{2+} (12.0), and Mg^{2+} (<0.1), with a pH of 8.1 (Garralón et al., 2017).

3.2. FEBEX-bentonite

FEBEX-bentonite was obtained from the Cortijo de Archidona deposits (Caballero et al., 2005) and contains more than 90% montmorillonite (Mnt) and variable quantities of quartz (qtz; (2 ± 1), plagioclase (pl; 3 ± 1), K-feldspar (Kfp; (<1), calcite (Cal; < 1) and cristobalite (Crs; 2 ± 1). The FEBEX-bentonite contains approximately 1/3, 1/3 and 1/4 cmol (+charge)/kg of Mg^{2+}, Ca^{2+} and Na^+ exchangeable cations, respectively, for a cation exchange capacity (CEC) of 102 ± 2 cmol (+)/kg. The physical-chemical properties of the FEBEX bentonite and its most relevant thermo-hydro-mechanical and geochemical properties have been studied and are published elsewhere (e.g. Villar et al., 2006).

The bentonite, milled to a grain size <1 mm, was compacted with its hygroscopic water content (13 wt%) at room temperature conditions (23 ± 2 °C) and at a nominal dry density of 1.60 g/cm^3 inside the methacrylate sleeve, where the cement mortar was previously hardened.

3.3. Cement mortar

Cement mortar was prepared with CEM II/A-L 42.5 R SR cement formulated with powder limestone addition (10%). Subsequently, a 1/2.4 ratio of distilled water/cement and a 1/3 ratio of cement/silica sand (grain size <1 mm; 99% of quartz) were added. The materials used to prepare the CEM II-C were supplied by the Eduardo Torroja Institute for Construction Science (CSIC-IETcc) and were cast inside a methacrylate sleeve, uniaxially pressed at 1–2 kg/cm^2 and covered by pressing of a circular PTFE porous membrane. The cast CEM II-C was cured in a water-saturated chamber (100% R. H.) for 90 days. After the CEM II-C was cured, the compacted FEBEX-bentonite was emplaced.

The SSA of the cement mortar was 9.3 ± 0.1 m^2/g, and the pH value measured in the pore solution following the ex situ method of (García Calvo, 2012) was 12.2 ± 0.1.

To obtain an initial reference sample, the CEM II-C was prepared and characterized in manner similar to that of the other experimental samples.

The average elemental composition obtained by EDX analyses of the areas acquired at 45x magnification (approximately 1 mm^2) and the matrix punctual analyses acquired at 200x magnification are shown in Table 1. See that punctual analyses exclude mortar aggregates, mainly quartz grains, and consequently the Si content decreases in the cement matrix, increasing thereby the rest of elements.

The XRD powder patterns showed the presence of calcite, gypsum,

Table 1
Chemical composition of CEM II cement mortar (CEM II-C) and average composition of cement matrix. Major elements are recalculated to 100%.

	Areas at 45x mag;	Matrix at 200x mag
At.%	Mean ± Sx (3–5 areas)	Mean ± Sx (7 spots)
Mg	n.d.	n.d.
Al	2.36 ± 0.30	3.54 ± 2.85
Si	74.70 ± 1.29	30.62 ± 6.75
S	1.24 ± 0.39	2.26 ± 0.76
K	n.d.	n.d.
Ca	20.46 ± 1.01	60.39 ± 7.56
Fe	0.65 ± 0.09	0.85 ± 0.54

Sx: Standard deviation, At.%: atomic percentage, mag: magnification, n.d.: not detected.
Areas and matrix analyses are shown in Fig. 3a–b.

quartz, and phases commonly present in the hydrated cement, namely, portlandite, ettringite, ferrite and dicalcium/tricalcium silicate anhydrous phases (see section 4.3). Calcium silicate hydrates (C–S–H) are the major hydration products and binding phases in cements, but they were not detected by XRD because they do not diffract well (Techer et al., 2012). Instead, C–S–H were observed by SEM-EDX as nano-crystalline phases, mostly identified by their chemical composition because the SEM resolution do not reach the nm scale.

The presence of anhydrous phases determined by XRD is coherent with the analysis conducted at 200x magnifications for the characterization of cement mortar matrix. The median Ca/Si ratio based on 26 analyses ranged from ~ 1.7 to 2.0 (Fig. 3d). In general, this ratio indicates an excess of Ca, overestimated due to the size of the microanalysis area and the existence of limestone microparticles (Alonso et al., 2017). Several determinations exceed a Ca/Si ratio of 2.3 that clearly indicates that contribution. The SEM-EDX exploration confirmed a combination of phases determined by the presence of ettringite, portlandite, calcium carbonate (identified as calcite by XRD), and C–S–H (Fig. 3).

4. Results

4.1. SEM-EDX

4.1.1. SEM-EDX 45x (bulk cement mortar) and 200x (cement mortar matrix) analysis areas

Only the cement mortar side was analysed at 45x and 200x magnification because the bentonite composition is rather homogenous under area or spot analyses, and its variation is better described by EDX elemental profiles (see section 4.1.2). The area and spot measurements performed on the CEM II-C were acquired to assess the evolution of the entire cement mortar material and the matrix of the cement mortar, respectively. The data from the duplicated cells were grouped into 6 and 18 months, representing averaged values for each experiment.

The bulk cement mortar compositions acquired from area analyses at the CB or CW-interfaces after interaction are compared with the composition of the reference cement mortar in Table 2. The CB-interface shows a significant decrease in Ca and Si after 6 months. Conversely, Ca increases again up to the initial values after 18 months. In the CW-interface, Ca leaching after 6 months is not important and highly variable. Additionally, Mg is detected in the composition after 18 months at both the CB and CW-interfaces. Overall, no statistically significant differences were observed with respect to the area analyses.

At the CB-interface, the cement mortar matrix compositions showed an averaged significant decrease in the Ca/Si ratio from reference (0 months; ~ 1.8) to 6 months (1.5). After 6 months, this parameter remained stable until 18 months (Fig. 4a). Independently of the time of reaction, the Ca/Si displays a spread of values from 1.2 to 1.8, showing an uneven degree of hydration and decalcification of C–S–H. The spread of the Ca/Si ratio data is slightly larger after 18 months, with notably high values (>2), presumably due to calcite precipitation. In contrast, values < 1.0–0.6 are more typical of low Ca/Si tobermorite, C–S–H or C-A-S-H. The presence of C-A-S-H is detected in the CB-interface with Al/Si ratios that are clearly higher than in the reference cement mortar matrix (Fig. 4b).

At the CW-interface, the Ca/Si ratio does not decrease at the same rate as at the CB-interface. The slightly decreasing shift from 0 to 6 months and from 6 to 18 months is consistent with the presence of hydrated and lower Ca/Si C–S–H phases. Both interfaces show more dispersed data for the cement matrix than the reference.

The differences in distribution of Al/Si (Fig. 4b) were significant across categories of interfaces (CB-CW-interface) but not significant across the time scale (6 and 18 months experiments).

Table 2
EDX area analyses performed at different time-scales (0, 6 and 18 months) and interfaces (CB and CW). Averaged values include standard deviations.

Element (At.%)	Reference	CB-interface		CW-interface	
	0 months	6 months	18 months	6 months	18 months
Mg	n.d.	n.d.	0.28 ± 0.16	n.d.	0.24 ± 0.13
Al	2.36 ± 0.30	2.54 ± 0.85	2.48 ± 0.38	1.58 ± 0.43	2.39 ± 0.31
Si	74.70 ± 1.29	80.08 ± 2.87	74.10 ± 2.10	77.31 ± 4.48	72.88 ± 4.07
S	1.24 ± 0.39	0.76 ± 0.39	1.47 ± 0.39	0.86 ± 0.21	1.12 ± 0.37
K	n.d.	n.d.	n.d.	n.d.	n.d.
Ca	20.46 ± 1.01	15.54 ± 2.27	20.90 ± 1.44	19.09 ± 4.77	22.60 ± 3.44
Fe	0.65 ± 0.09	0.76 ± 0.26	0.76 ± 0.14	0.88 ± 0.16	0.73 ± 0.29

At.%: atomic percentage, n.d.: not detected.

4.1.2. SEM-EDX profiles of chemical composition in cement mortar and bentonite

The chemical evolution of Si, Ca, Al and Mg as a function of time (6 and 12 months) in cement mortar and bentonite is presented in Fig. 5a. In general, the Ca content shows a maximum on the cement mortar interface side, and Mg increases in the bentonite at the CB-interface. These anomalies are accompanied by the decreasing of Si and Al.

At the bentonite side, Mg concentration increased substantially in a length <1000 μm from the CB-interface (from approximately 5 to >20 at.% within the first 50 μm), but the increase of concentration from 6 to 18 months was short (Fig. 5a).

Ca increases its relative concentration near the CB interfase, in the cement mortar side. As for Mg, an increment of Ca concentration is observed from 6 to 18 month, but in this case, the increment is significant (20 at.% initially, 40% after 6 months and 60% after 18 months, as maximum averaged values). Therefore, the processes associated to the Ca enrichment does not seem to have reached a stationary state. Such a high increase is followed by a 1–2 mm Ca minimum, which is less pronounced after 18 months. This minimum agrees with the decalcification of C–S–H (lower Ca/Si ratios at the CB interface in Fig. 4a) and a presumably portlandite dissolution zone that causes calcite precipitation at the cement mortar side, as further confirmed by the GI-XRD study (section 4.3.1).

According to the possibility of C-A-S-H formation in the CB-interface, the Al profiles tend to increase with time in the first μm of the cement mortar side (<25 μm). Fig. 5b shows the profile evolution of S and Fe in a narrow −500 to 500 μm band. S is depleted after 6 months but is relatively concentrated in the cement mortar side of the interface after 18 months. However, a certain amount of transfer of Fe from bentonite to cement matrix is evident with rather irregular distribution.

4.1.3. SEM-EDX: surface interface crystal aggregate morphologies and composition

The nature of the Ca or Mg anomalies detected, mainly at the CB-interfaces and occasionally at the CW-interfaces (in the case of Ca), were first approached by exploration of singular crystal aggregates found in the fresh pristine surfaces separated at the end of the experiments. The composition of singular phases determined in the surface interfaces corresponding to B1, C1 and C3 slices and their distribution are indicated in Table 3. The characteristic morphologies of main phases and morphologies identified phases are illustrated by the SEM micrographs (Fig. 6).

Regarding to the bentonite interface, high Mg/Si platy (flat) and sheet (curled) like morphologies forming sometimes a Mg-rich crust were identified in B1 at any time (Fig. 6a and b). As for cement mortar side, the surface of the interface from C1 subsample was plenty of euhedral sphenoidal calcite microcrystals precipitation resulting in the formation of carbonated crusts (Fig. 6c, e, g). In addition, C–S–H, C-A-S-H, ettringite (6f, 6i and 6d, respectively) and hexagonal platy

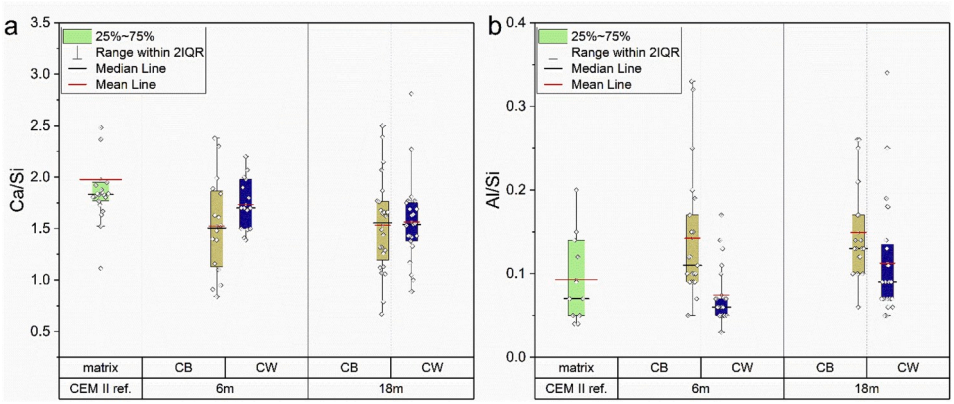

Fig. 4. Box plot of the Ca/Si ratios (a) and Al/Si ratios (b) analysed in the matrix of the cement mortar. Horizontal black lines inside the box charts represent the median value of the data. Colour boxes indicate the values contained within the 25–75% interquartile range (IQR), the range of the vertical bars extent to 2 IQR, median line is shown in black and mean line in red.

morphologies of Cl-Aluminium Ferrite monosulfate phases (AFm), presumably Friedel salt-monosulfate AFm phases (Fig. 6h), were observed. Mainly ettringite was found as the main mineral phase, either in C1 (from the CB-interface) or C3 (from the CW-interface), and was significantly less frequent in the 18 months experiments at the CW-interface, indicating dissolution in this extreme.

4.2. X-ray diffraction on bentonite

4.2.1. GI-XRD 0.5° and θ-2θ scans on bentonite

The GI-XRD analyses and θ-2θ scans under the GI-XRD configuration facilitated study of the mineralogy in the first 10 μm of the surface interface of bentonite exposed to the influence of the CEM II-C porewater (Fig. 7a). The difference between GI-XRD 0.5° and θ-2θ used in this description is that the first is more superficial and the second corresponds to the diffracting result of higher sample volume.

The diffractograms at the interface of the reacted surface bentonite samples are characterized by the presence of 7.6–7.4 Å broad reflections not visible in the reference bentonite. These reflections were developed in all the θ-2θ scans, but they are not developed in the GI-XRD analyses performed on samples that reacted for 6 months. At lower angles, a critical intensity decline of the 14–15 Å reflection was observed, more generalized after 6 than after 18 months. In addition, a small shift is detected from 15.0 Å in the bentonite reference towards 14.8–14.5 Å in both sets of experiments (6 and 18 months). This shift is correlated with a small decrease in the position of the second-order basal reflection at 4.9–4.8 Å *d*-spacings, that becomes significantly more intense compared with the reference sample. These effects are better visualized by the θ-2θ scans in all experiments.

Characteristic di-octahedral Mnt reflections at 1.49 Å were found in the reference bentonite, and a broad band centred in 1.54–1.53 Å is always present in the reacted bentonite samples, indicating a tri-octahedral component that can be linked to the Mg/Si increase near the interface with the cement mortar. Quartz is occasionally present, as evidenced by a sharp reflection at 1.55 Å.

With respect to the more superficial GI-XRD 0.5° analysis, a broad reflection at 1.54–1.53 Å, observed after 18 months, is not present after 6 months neither the reference bentonite, which could be an indication of the precipitation of a tri-octahedral phase at long term. The 14–15 Å reflection, characteristic of the basal spacing of smectite is not present, indicating that the neogenic clay mineral presents high stacking disorder at the surface.

It is important to note how the θ-2θ scans demonstrate the presence of the calcite 3.03 Å peak, which is not detectable in the reference sample, thus confirming that the carbonation is not homogeneously distributed at the first microns of the bentonite interfaces.

4.2.2. Random powder X-ray diffraction on bentonite

The XRD analyses on powder samples supply information on the time evolution and spatial alteration of bentonite as a function of distance from the CB interface (Fig. 7b). Subtle variations were found in the (001)-reflection region (5–8° 2θ position). Two shifts can be observed in that region related to the time evolution. First, the reference bentonite diffractogram shows reflections at~ 15.0 Å, and the diffractograms obtained after 6 months present these reflections at~ 14.5 Å, with a tail towards high angles compared with the 18 months experiments, where the basal reflection increases again to 15 Å and is more symmetrical. This differentiation in the basal space might be related to a change of the cations population in the interlayer. The initial Ca–Mg bentonite becomes slightly richer in monovalent cations (Na^+, K^+) as a result of local precipitation of Ca and Mg phases, however, the rate of transformation decreases with time and the population distribution is further homogenized as a result of the preferential leaching of monovalent cations out of the column (section 4.5).

In contrast to the small perturbations detected in Mnt by XRD on randomly oriented powder samples, the presence of the 3.03 Å reflection, characteristic of calcite, in one of the B1 slices run for 18 months (close to the cement mortar) is significant compared to all the other diffractograms. This observation is in agreement with the presumable calcite precipitation at both sides of the interface.

4.3. X-ray diffraction on cement mortar

4.3.1. GI-XRD 0.5° and θ-2θ scans on cement mortar

The main geochemical perturbations that can be remarked by XRD on the cement mortar are related to the evolution of ettringite, gypsum, portlandite and calcite mineral phases as they are well crystalline (Fig. 8a).

Distinctive reflections of gypsum and portlandite (7.6 Å and 4.9 Å, respectively) were identified in the reference CEM II-C but are absent after 6 and 18 months.

Characteristic reflections of ettringite (9.8 Å and 5.6 Å) were found after 6 and 18 months, but these reflections did not appear evident in the reference CEM II-C. Most of the ettringite found can be considered as secondary ettringite.

The reflections at 3.03 Å, 3.86 Å, 1.91 Å and 1.87 Å, characteristic of calcite, increase in intensity as time evolve. This is observed comparing the reference cement mortar with the altered cement mortars after 6 and 18 months, however, there is a substantial variation comparing the duplicated experiments. These variations indicate that the uneven distribution in calcite coatings might be better developed in macropores, as shown in Fig. 6g.

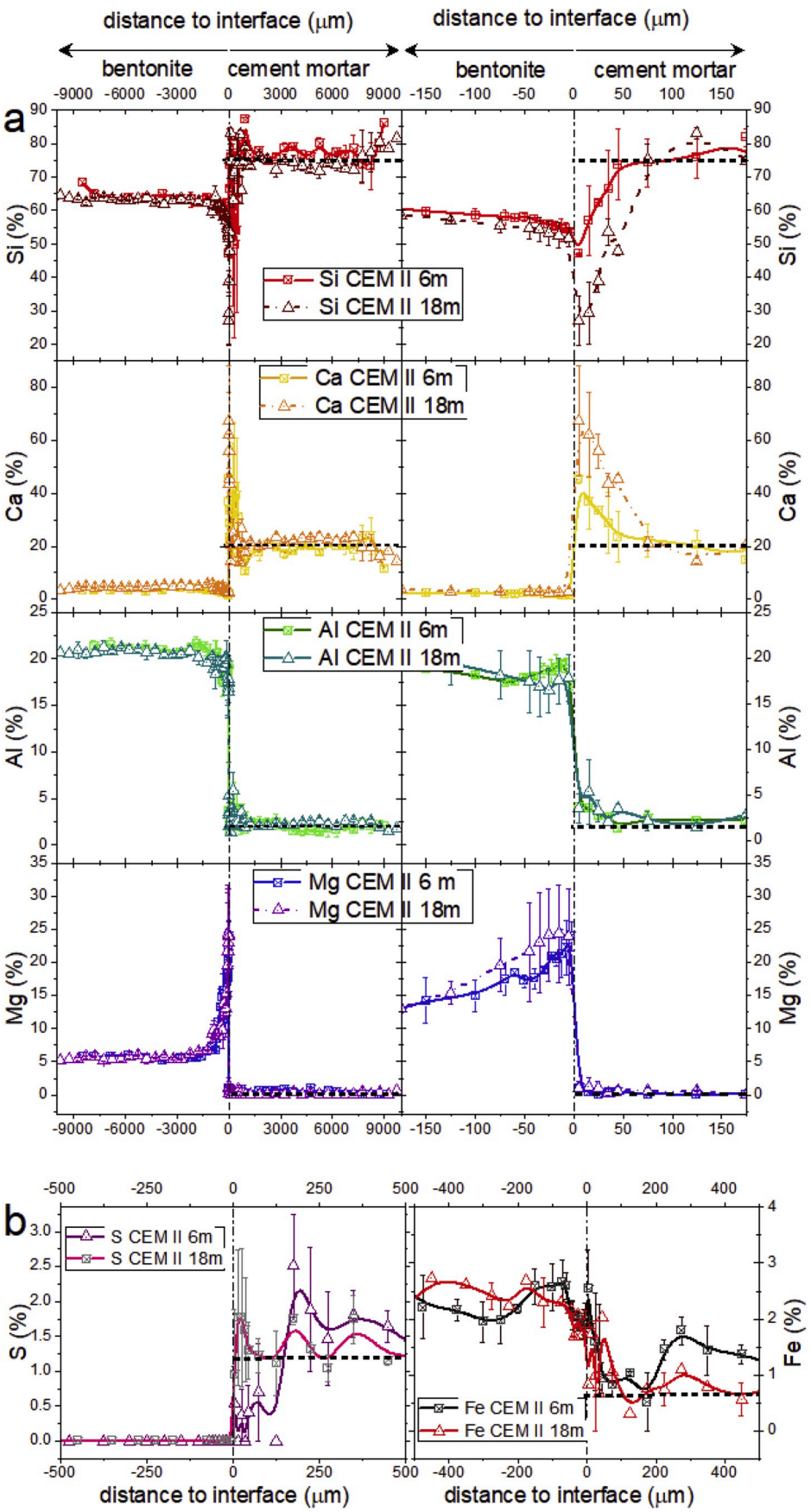

Fig. 5. Chemical profiles of composition in bentonite-CEM II cement mortar experiments after 6 and 18 months. All profiles were obtained based on the average values of the duplicated experiments and include error bars of standard deviation. Each profile is depicted at different ranges: from −9000 to 9000 μm (left column) and from −200 to 200 μm (right column) (a). The CB-interface (placed at 0 μm, black dashed line) was taken as a reference. Additionally, a reference horizontal dotted line of the unaltered cement mortar reference sample is plotted for each element. Separately, the S and Fe profiles nearest to CB-interface (0–500 μm) are plotted at the bottom of figure (b).

Table 3
Summary of the observed phases and morphologies localized in slices B1–C1 (CB-interface surfaces) and C3 (CW-interface surfaces).

Experiment	Surface interface	High Mg–Si crust/matrix	Mg–Si rich platelets	[a]C-A-S-H	Calcite	[b]Ettringite	[c]AFm	[d]C–S–H
	B1	X			X(−)			
18-Exp1	C1			X	X			
	C3					X		
	B1	X	X		X(−)			
18-Exp2	C1		X	X	X	X	X	
	C3			X				
	B1	X			X			
6-Exp1	C1				X(+)	X(+)	X(+)	X(+)
	C3							
	B1	X	X(−)			X		
6-Exp2	C1			X		X	X	
	C3					X(+)	X	

X, (+), (−) indicate "presence", "high presence", and "medium-low presence", respectively.
[a] C-A-S-H: Calcium aluminium silicate hydrate (Al/(Al + Si) = 0.2, and Ca/Si- 0.8).
[b] Ettringite (Al/S = 0.7, and Ca/S = 2).
[c] AFm: Calcium aluminium monosulphate (Al/S > 2; Ca/S > 4).
[d] C–S–H: Calcium silicate hydrate: Ca/Si = 0.6–2.3).

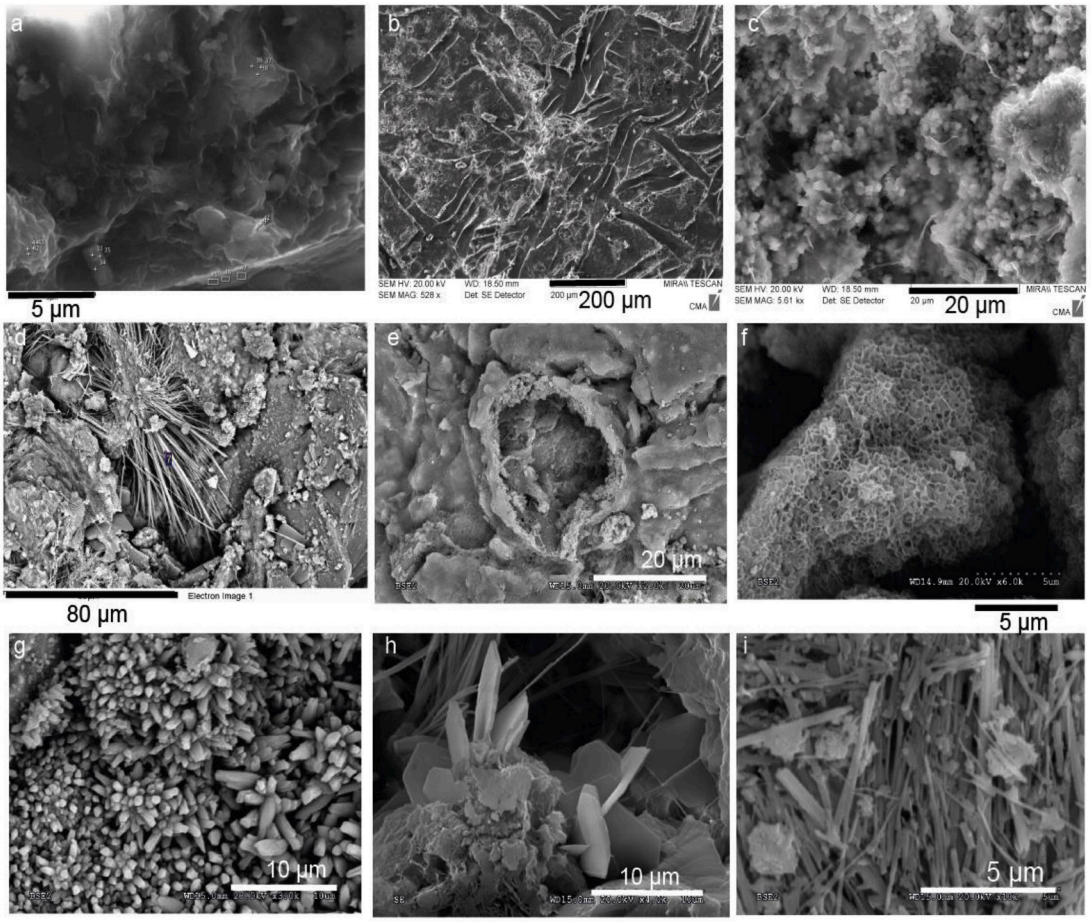

Fig. 6. SEM micrographs of the summary of phases and morphologies found in fresh pristine surface interfaces from B1–C1–C3 slices. (a) Mg–Si-rich platy morphologies. (b) Mg–Si-rich crust shaped by fibres of the PTFE membrane. (c) Calcite crystals growing among C–S–H. (d) Ettringite needles observed after 6 months in C1. (e) Calcite crust. (f) C–S–H. (g) Calcite sphenoidal crystal aggregates observed after 6 months. (h) Ca–Al-(S, Cl) crystals. (I) C-A-S-H needles. (Identification was made according to the chemical formula and the EDX).

4.3.2. Random powder X-ray diffraction on cement mortar

As observed for the bentonite slices, subtle differences were found in cement mortar by XRD on randomly oriented powder samples (Fig. 8b). A detailed study of the range between the 32 and 33 °2θ positions shows an intensity decrease in the characteristic reflections of anhydrous phases, such as calcium aluminoferrite (C_4AF) and di-calcium silicate (C_2S) after 18 months (2.74 Å and 2.78 Å, respectively). These rearrangements occur as a result of progressive hydration of the anhydrous phases and the formation of secondary C–S–H characterized by a disordered structure and broad and weak diffraction maxima (Grangeon et al., 2013), which complicate their identification.

Minor differences were also found in the spatial progress by the study

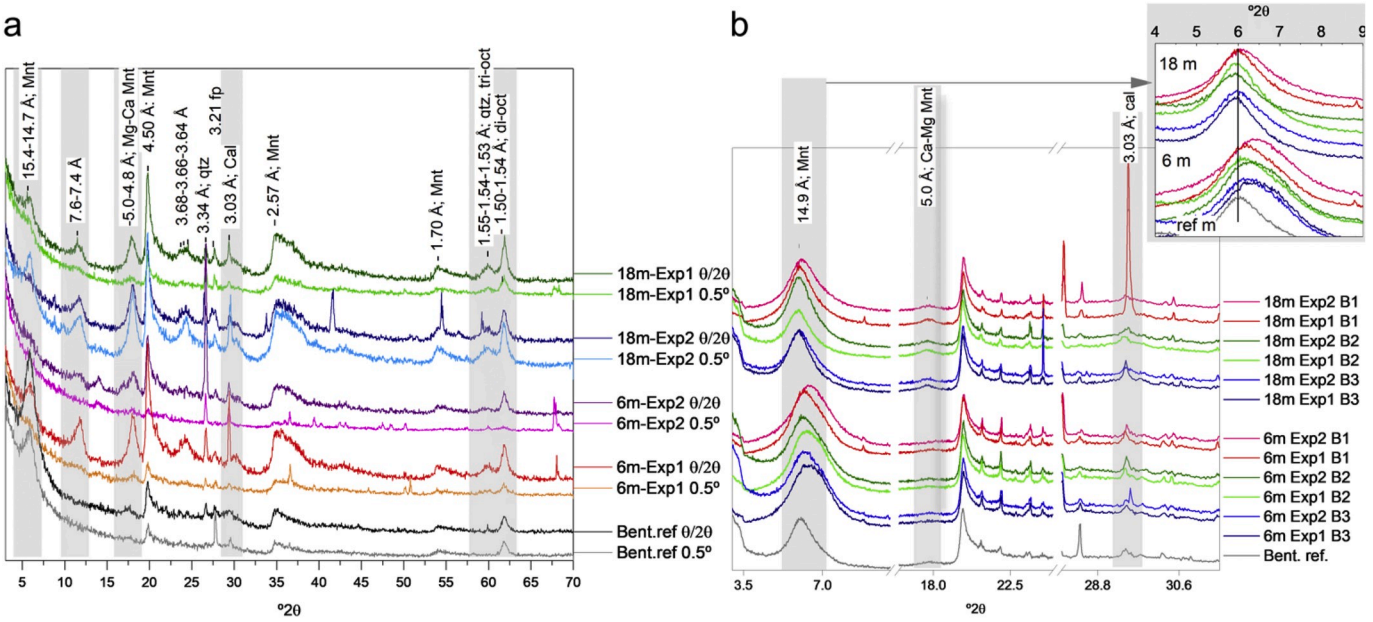

Fig. 7. (a). GI-XRD analyses and θ-2θ scans over flat fresh solid subsamples from the surface of bentonite. Numbers indicate d-values in Å; Mg–Ca Mnt: Mg–Ca montmorillonite, qtz: quartz, fp: feldspars, Cal: calcite, di: di-octahedral sheet, tri: tri-octahedral sheet. (b) XRD on randomly oriented powder bentonite samples at different distances from the interface (0–3 mm at B1; 3–6 mm at B2; 6–9 mm at B3) and different time scales (6 and 18 months). Upper right corner: close-up image of the (001) basal reflection region (4–9° 2θ). Bent. ref: diffractograms of the unaltered reference bentonite.

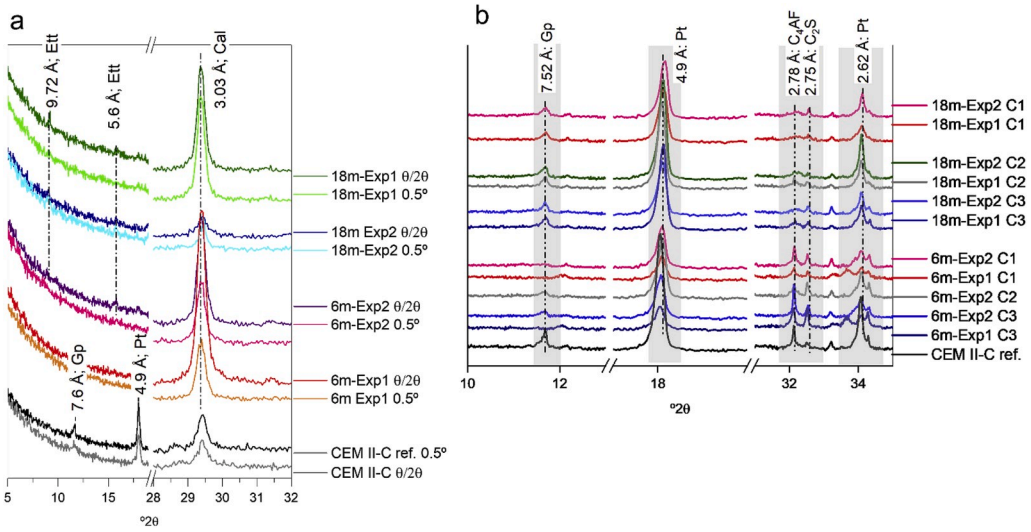

Fig. 8. (a) Close-up view of the θ-2θ scans and GI-XRD analyses performed on the flat surface interface of CEM II-C. (b) Close-up view of the XRD patterns of cement mortar on randomly oriented powder samples at different distances from the interface (0–3 mm at C1; 3–6 mm at C2; 6–9 mm at C3) and at different time scales (6 and 18 months). Numbers indicate d-values in Å. Ett: ettringite, Cal: calcite, Gp: gypsum, Pt: portlandite, C_4AF: calcium aluminoferrite, C_2S: di-calcium silicate.

of samples C1, C2 and C3. The 6 and 18 months experiments showed a small decrease in the 7.56 Å reflection, characteristic of gypsum, and the reflections at 4.9 and 2.62 Å, characteristic of portlandite, suggesting their dissolution (Fig. 8b). However, the increase of calcite reflections, previously shown by the θ-2θ scans in the first μm of the surface interfaces, were not found across C1, C2 and C3 and, therefore, the carbonation process could occur only in a close spatial range at the immediate proximity to the interface with bentonite.

4.4. Specific surface area

The SSA analyses performed throughout the bentonite and cement mortar slices to assess their spatial and temporal evolution are shown in Fig. 9. At the bentonite side, three main observations can be outlined: (i) the lower SSA values compared with the reference bentonite, (ii) the decrease in SSA from 6 to 18 months, and (iii) the decreasing tend of SSA away from the interface. At the CEM II-C side, C3 slices (facing the water interface) presents a slightly higher SSA than the reference sample. In addition, as time evolves from 6 to 18 months, the C2 and C1 slices increase in SSA.

4.5. Effluent parameters

The hydraulic conductivity (H. C.) was calculated by the outflow data considering that the initial time corresponds to the beginning of the infiltration. The H. C. remains stable in the range 10^{-12}-10^{-13} m/s

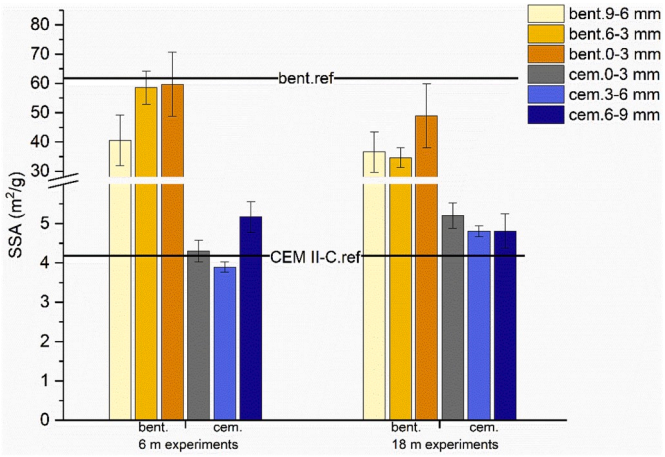

Fig. 9. SSA of bentonite and CEM II-C as a function of distance from the C–B interface. Note that the CB-interface is located between the orange and grey bars, and the CW-interface is located at the end of the dark blue bars.

(Fig. 10a) for the whole experimental time (up to 18 months). In the averaged experiments performed for 6 months the H. C. is higher than in the experiments performed for 18 months, but this should only be attributed to random differences derived from the preparation of the initial materials that are not completely homogeneous. The accumulated volume of effluent collected in one of the experiments run for 6 months was similar to those collected in the experiments run for 18 months, indicating the presence of preferential pathways for fluid circulation in that specific experiment. As the data are presented as averaged values for experiments performed for 6 and for 18 months, the error bars for the 6 months experiments in Fig. 10a are large.

Bentonite is compacted at its characteristic water content (approximately 14 wt%) in its dried state at the laboratory ambient conditions (30–50% R. H.). Therefore, the initial conditions are unsaturated. Aqueous SO_4^{2-}, Cl^-, Na^+ and K^+ are leached initially in higher concentrations than all other ions and correspond with the displaced bentonite porewater (Fig. 10b), known to be concentrated in these ions (Cuevas et al., 2002). SO_4^{2-} is almost exhausted after 7–8 pore volumes (one pore volume is calculated as the total porosity of bentonite, ~1.3 cm^3), whereas Cl^- decreases drastically its concentration at the beginning and gets mostly exhausted after 13–14 pore volumes. Na^+ is the dominant cation and achieves a low constant value after 6–10 pore volumes, presumably regulated by the cation exchange equilibrium ruled by Mnt, since Na^+ is the less selective cation in the cation exchange equilibrium concerning the FEBEX bentonite (Fernández et al., 2004). The alkalinity, represented mainly by HCO_3^- (with certain contribution of CO_3^{2-}, not accounted in the charge balance), becomes the main anion with time (after 6 pore volumes). The Ca^{2+} concentration critically decreases to 21–23 mg/L, and aqueous Mg^{2+} becomes negligible in solution due to fixation related to the Mg increase in the solid phase determined at the bentonite interface with cement mortar (section 4.1.2).

The pH and aqueous silica remained almost constant regardless of time (Table 4). These values are near the characteristics of FEBEX-bentonite porewater: 10–30 mg/L SiO_2 (cristobalite dissolution, Williams et al., 1985), pH = 9–7, depending on leaching or squeezing method used, respectively (Fernández et al., 2004). In spite of these authors, who used edge site protonation constants to explain the FEBEX bentonite pH buffering, Cuevas et al. (2006) calculated that the characteristic pH is obtained by taking into account the coupled reaction of cation exchange and calcite dissolution present in bentonite: $CaCO_3 + H^+ + 2\ NaX \rightleftharpoons HCO_3^- + CaX_2 + 2\ Na^+$.

5. Discussion

5.1. Mg perturbation

The results of small-scale laboratory experiments reveal the development of Mg perturbation in the cement mortar/FEBEX-bentonite interface at a notably shorter time compared with the FEBEX *in situ* experiment performed at large scale. Indeed, limited development of this perturbation is observed in the laboratory experiments from 6 to 18 months. Large accumulation of Mg was identified in the FEBEX *in situ* experiment after 13 years of concrete-bentonite interaction in highly similar conditions but at much larger spatial scale (Fernández et al., 2017). 10 m^3 of concrete in contact with 40 m^3 of FEBEX-bentonite were placed in the *in situ* experiment, while 0.57 cm^3 of cement mortar and 0.57 cm^3 of FEBEX-bentonite were placed in the laboratory experiment. The Mg perturbation reached an extension of 2–3 mm from the CB-interface in the FEBEX *in situ* experiment, whereas a length <1 mm was observed in this work. The magnitude of the Mg perturbation in the FEBEX *in situ* experiments, that reached up to 20–45 wt% in bentonite at the interface (Fernández et al., 2017) cannot be directly compared with the results obtained in the present study (~25 at.%) because of the different units of measurement. However, a simple estimation reveals

Table 4
pH and aqueous silica results after 6 and 18 months.

Experiment	pH	$SiO_{2(aq)}$ (mg/L).
6m-Exp	8.2 ± 0.1	12.8 ± 0.1
18m-Exp	8.3 ± 0.1	17.3 ± 0.2

6m-Exp: experiments conducted for 6 months, 18m-Exp: experiments conducted for 18 months.

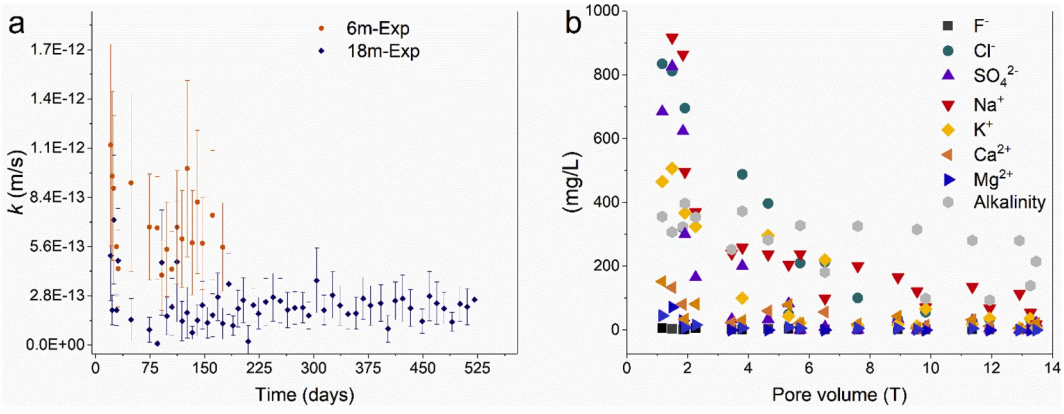

Fig. 10. (a) Averaged hydraulic conductivity calculated as a function of time for experiments performed for 6 (orange) and 18 months (blue). (b) Concentrations of major ions collected at the end of the bentonite side; data for experiments conducted for 6 and 18 months are represented in the same plot.

similar degree of Mg enrichment in the accumulation zone near the interface.

The Mg increase has not only been observed in cement or concrete/bentonite interfaces. Stiff clay rocks under the influence of high-pH concrete pore water (pH > 12) showed a characteristic Mg perturbation (e.g. Mäder et al., 2017; Moyce et al., 2014). In concrete/clay systems, this perturbation is also evidenced at the concrete side and it is remarkable when low-pH cementitious materials have been tested (Dauzères et al., 2016).

Mg-silicates can precipitate as a result of the alkaline influence supplied by the cement. The nature of the Mg-silicates formed in large scale experiments, such as the FEBEX *in situ* experiment, is complex considering the variety of compositions that have been identified as a result of the bentonite alkaline alteration. In a similar way as Al may be accommodated in C–S–H phases to form C-A-S-H, exchangeable Mg can also be incorporated in silicates to form saponite-like smectites, as predicted by Roosz et al. (2015) or used to form a variety of Mg-silicates, including M-S-H phases (e.g. R. Fernández et al., 2018).

The variety of Mg-silicates identified in literature as a result of cement/clay interaction are compatible with the presence of trioctahedral phyllosilicates 1:1 or 2:1 sheet silicate (Shimbashi et al., 2018). The complex chemical compositions of the zone with anomalous high Mg concentrations have been found to be compatible with a mixture of brucite and Mnt, as the Al content maintained constant, and the di-octahedral character of the Mnt remained, as observed by the XRD-diffraction patterns (Cuevas et al., 2018b; Fernández et al., 2017). In fact, Lerouge et al. (2017) identified grain compositions related to Mg perturbation that were highly rich in Mg and compatible with these types of mixtures. In the present experiments, structural characterization of the bentonite interface surface reveals a broad peak at 7.5 Å, that can be related to mixture such as an intercalated $Mg(OH)_2$-Mnt complex. This mixture was considered as one of the main reaction components of the early stage hyperalkaline alteration of Mg-Mnt in presence of KOH 0.5 M solutions (Fernández et al., 2013). The generalized presence of this type of phase in these early surface experiments can point to these types of phases as a precursor of more common mineral phases formed in Mg-rich natural alkaline environments as saponite or stevensitic minerals (Eberl et al., 1982). These Mg neogenic phases reveal structural properties similar to those of 2:1 and 1:1 sheet silicates and generally form a poorly crystalline but precise structure that is still under investigation (Walling and Provis, 2016). As in this work, M-S-H has been described as a homogeneous gel-like structure with a sheet-like morphology and Mg/Si ratios greater than 0.8 (Bernard et al., 2017, 2019; Lothenbach et al., 2015), but their formation has been primarily reported in the concrete side. The presence of any Mg-silicate hydrated phase in bentonite is highly difficult to ascertain because of mixing with other complex clay mineral phases with significant Al quantities.

5.2. Ca perturbation

At the cement mortar side, the formation of a calcite skin (≤ 50 μm from the CB-interface) was identified after 6 months and more pronounced after 18 months. This Ca increase, associated with the precipitation of soluble inorganic carbon species, occurs coupled to the decalcification of the C–S–H, identified by SEM-EDX analyses on the cement and by the profiles of chemical composition. HCO_3^-, that becomes the dominant aqueous anion species after 6 months, may act as a source of carbonates precipitation at high pH, which indeed, is supported by the dissolution of portlandite.

The formation of calcite at the concrete-bentonite interface was also reported in the FEBEX *in situ* experiment as a result of interaction of HCO_3^- from the clay porewater and Ca^{2+} from concrete (Fernández et al., 2017), resulting in calcite precipitation that forms a protective crust of low porosity, that increases its resistance against groundwater and porewater penetration (Jenni et al., 2014). Therefore, the localized development of Ca increase, in the order of μm in cement mortar observed in the present study, evolves to the mm scale (≤ 1 mm) after 13 years of ageing in the FEBEX *in situ* experiment.

At the bentonite side, the Ca increase observed by the SEM-EDX profiles of chemical composition was not as significant as in the cement mortar side, although higher amounts of calcite than those naturally present in the reference bentonite were detected by XRD. The Ca increase can be estimated as 1–5 at.% in the bentonite side, which is far from the Ca increase of 29–80 at.% detected at the cement mortar interface. It has been observed a certain amount of calcite dissolution affecting several cm to the concrete interface in certain locations in the FEBEX *in situ* experiments. Precipitation of calcite at the interface was also found in both, the bentonite and concrete sides, an effect that was clearly separated in the Mg-silicate precipitation. (Turrero and Cloet, 2017).

5.3. Al–S phase dynamics

Ettringite was almost always present in the studied cement mortar interface. SEM-EDX and XRD data suggest its formation as a secondary phase within the interface. Ettringite was not detected by XRD in the reference cement mortar sample or was less often observed, presenting different morphologies. The presence of ettringite is favoured by the limestone additions, since cement materials with higher quantities of carbonate additions tend to avoid the conversion of ettringite to AFm (Lothenbach et al., 2008). The origin of secondary ettringite comes from the incorporation of (i) Al supplied by Mnt dissolution (Gaucher and Blanc, 2006), (ii) S released by dissolution of gypsum and supplied by the porewater from bentonite, and (iii) Ca delivered by decalcification of C–S–H and portlandite present in the cement mortar (Cuevas et al., 2016). At long-term, ettringite is not stable at the interface. In the FEBEX *in situ* experiment, ettringite was detected within the concrete matrix but further from the interface and as secondary phase-filling pores (Alonso et al., 2017).

AFm phases seem to have been occasionally stabilized by incorporating Cl^- diffusing as a soluble species in bentonite porewater. Friedel salt is a more stable Cl-AFm phase and has also been described in the FEBEX *in situ* experiment further from the interfase (Alonso et al., 2017). Cl^- monitoring is important because it is a potential corrosion agent of reinforced concrete (Chen and Mahadevan, 2008), but in this context, its role is of little relevance because Cl^- has a high diffusion rate, and Cl^- fixation by the cement AFm phases was not significant, as demonstrated by the Cl^- performance in the present experiment, that was easily leachable.

Al can also follow other reaction pathways, rather than forming Al–S ettringite phases. Ettringite coexists with carbonates, and C-A-S-H forms as a result of the Al supplied by bentonite pore fluids, as suggested by the SEM-EDX profiles of chemical composition (Section 4.1.2). The ability to accommodate cations from the pore fluid is inversely related to the Ca content of C–S–H, and after the observed decalcification process, C–S–H with lower Ca/Si ratios could easily uptake Al to form C-A-S-H phases (Fernández et al., 2016).

5.4. Specific surface area

The SSA represents the external surface area exposed to the porous space, considering the edge sites (Fernández et al., 2013) and excluding the surface area of the internal basal planes. This parameter depends on sample pretreatment, exchangeable cations and microporosity (Kaufhold et al., 2010).

At the bentonite side, the SSA reduction in the samples compared with the reference bentonite could be related with the existence of certain clogging processes, presumably due to calcite or other nanoscale cements. This process promotes the aggregation of clay particles, thus hindering N_2(g) access to occluded pores, and consequently, the SSA decreases. With respect to the spatial evolution studied from the interface to the bentonite end, the increasing trend of the SSA nearest the CB-

interface can be attributed to the decrease in the average size of the smectite particles affected by neogenic Mg-clay mineral nanocrystal aggregates. This newly formed phase can occupy larger pores, thus increasing the weight of the microporosity in the original pore distribution. We consider this interpretation to be more reliable than the increment of the microporosity due to a decrease in the major exchangeable cations of Ca^{2+} and Mg^{2+} (Metz et al., 2005) or the dissolution of Mnt and the consequent reduction of the 2:1 layers (Lowell and Shields, 2013). In our case, only a weak reflection displacement towards lower d-spacings in the basal reflection (001) was observed.

At the cement mortar side, the higher SSA found after 6 and 18 months at the CB and CW-interfaces compared with the intermediate sample (3–6 mm) and the reference cement mortar is attributed to the decalcification and formation of low Ca/Si C–S–H of lower crystal size and greater disorder, thus increasing the SSA (Phung et al., 2016).

5.5. Evaluation of leachate

If the general SSA decrease observed in bentonite were attributed to precipitation of nanoscale cements and formation of Mg-Clays near the interface, as evidenced after 6 months, it could be related to the lower hydraulic conductivity values (Alonso et al., 2017) stabilized after < 6 months. (section 4.5). However, this observation does not agree with the increase in SSA from 6 to 18 months in the cement mortar side. This difference in behaviour can be explained because the leachate was collected at the end of the bentonite side, which control the fluid flow due to its low effective porosity and hydraulic conductivity. In the same way, the pH and silica results were similar to those characteristics of the reference FEBEX-bentonite. Therefore, the buffer characteristic of bentonite is demonstrated.

The high concentrations of sulphate and chloride found in the first pore volumes and the subsequent absolute decline mostly occur as a result of their depletion from the porewater of bentonite. Na^{+} is naturally present as 1/3 of the exchangeable cation complex in FEBEX-bentonite, but a subset of the Na^{+} and K^{+} might originate from the alkalis of the cement mortar, increasing their concentration at an early leaching stage. Later, the monovalent ions, together with Ca^{2+} and Mg^{2+}, suffer a decrease related to their regulation as exchangeable cations (mainly Ca^{2+}, Na^{+}) and the precipitation of calcite and Mg-silicates (Mg^{2+}). The decrease in these exchangeable cations has also been described nearest the interface (Mäder et al., 2017) related to the precipitation of Mg-silicates.

6. Conclusions

This study assesses the geochemical reactions occurring at the early stage (0.5–1.5 years) of the interaction between cement mortar-CEM II and FEBEX-bentonite with the aim to facilitate a better comprehension of the large-spatial and long-term results observed after 13 years of concrete-bentonite interaction from the dismantling of the FEBEX *in situ* experiment. The expected reaction paths, which are more progressed in long-term experiments, are consistent with the initial evolution of the results summarized in this study:

Decalcification of C–S–H in an environment in which portlandite dissolution occurs and anhydrous phases are progressive hydrated.

Development of a Ca-carbonation skin (calcite) in the cement mortar side and dispersed precipitation of calcite in localized zones of bentonite.

Initial development of a Mg-perturbation at the bentonite side, related to the formation of precursors of Mg-clay 2:1 sheet silicates as the main neogenic phases expected at the long-term.

Formation of secondary ettringite at the cement mortar interface.

The geochemical reactions observed at small spatial scale (μm) and short-term (up to 18 months) are promising for development of reaction concepts and support modelling in the future, thus offering a useful prospective to advance upscaling of the concrete-bentonite interface perturbations at long-term.

Declaration of competing interests

The authors declare that they have no known competing financial interests or personal relationships that could have appeared to influence the work reported in this paper.

Acknowledgements

This work was supported by funding from the European Union's Horizon 2020 Research and Training programme from EUROATOM [H2020-NFRP 2014, 2015] under grant agreement nº662147; CEBAMA. The authors thank Juan D. Rodriguez-Blanco Professor in Nano-mineralogy from Trinity College Dublin for assistance with analytical support.

Appendix A. Supplementary data

Supplementary data to this article can be found online at https://doi.org/10.1016/j.apgeochem.2020.104599.

References

Villar, M., Fernández, A., Rivas, P., Lloret, A., Daucausse, D., Montarges-Pelletier, E., Devineau, K., Villieras, F., Hynková, E., Cechova, Z., 2006. FEBEX Project: Final Report: Post-mortem Bentonite Analysis. ENRESA (Madrid. Spain).

Alonso, M.C., García Calvo, J.L., Cuevas, J., Turrero, M.J., Fernández, R., Torres, E., Ruiz, A.I., 2017. Interaction processes at the concrete-bentonite interface after 13 years of FEBEX-Plug operation. Part I: concrete alteration. Phys. Chem. Earth, Parts A/B/C 99, 38. https://doi.org/10.1016/j.pce.2017.03.008.

Bernard, E., Lothenbach, B., Rentsch, D., Pochard, I., Dauzères, A., 2017. Formation of magnesium silicate hydrates (M-S-H). Physics and Chemistry of the Earth. Parts A/B/C 99, 142. https://doi.org/10.1016/j.pce.2017.02.005.

Bernard, E., Lothenbach, B., Chlique, C., Wyrzykowski, M., Dauzères, A., Pochard, I., Cau-Dit-Coumes, C., 2019. Characterization of magnesium silicate hydrate (M-S-H). Cement Concr. Res. 116, 309. https://doi.org/10.1016/j.cemconres.2018.09.007.

Berner, U., 1992. Evolution of pore water chemistry during degradation of cement in a radioactive waste repository environment. Waste Manag. 12, 201. https://doi.org/10.1016/0956-053X(92)90049-O.

Berner, U., Kulik, D.A., Kosakowski, G., 2013. Geochemical impact of a low-pH cement liner on the near field of a repository for spent fuel and high-level radioactive waste. Phys. Chem. Earth, Parts A/B/C 64, 46. https://doi.org/10.1016/j.pce.2013.03.007.

Caballero, E., Jiménez de Cisneros, C., Huertas, F.J., Huertas, F., Pozzuoli, A., Linares, J., 2005. Bentonites from Cabo de Gata, Almería, Spain: a mineralogical and geochemical overview. Clay Miner. 40, 463. https://doi.org/10.1180/0009855054040184.

Chen, D., Mahadevan, S., 2008. Chloride-induced reinforcement corrosion and concrete cracking simulation. Cement Concr. Compos. 30, 227. https://doi.org/10.1016/j.cemconcomp.2006.10.007.

Churakov, S.V., Prasianakis, N.I, 2018. Review of the current status and challenges for a holistic process-based description of mass transport and mineral reactivity in porous media. Am. J. Sci. 318, 921. https://doi:10.2475/09.2018.03.

Cuevas, J., Villar, M.V., Martín, M., Cobeña, J.C., Leguey, S., 2002. Thermo-hydraulic gradients on bentonite: distribution of soluble salts, microstructure and modification of the hydraulic and mechanical behaviour. Appl. Clay Sci. 22, 25–38. https://doi.org/10.1016/S0169-1317(02)00109-6.

Cuevas, J., Vigil de la Villa, R., Ramírez, S., Sánchez, L., Fernández, R., Leguey, S., 2006. The alkaline reaction of FEBEX bentonite: a contribution to the study of the performance of bentonite/concrete engineered barrier systems. J. Iber. Geol. 32, 151–174.

Cuevas, J., Ruiz, A.I., Fernández, R., Torres, E., Escribano, A., Regadío, M., Turrero, M.J., 2016. Lime mortar-compacted bentonite–magnetite interfaces: an experimental study focused on the understanding of the EBS long-term performance for high-level nuclear waste isolation DGR concept. Appl. Clay Sci. 124–125, 79. https://doi.org/10.1016/j.clay.2016.01.043.

Cuevas, J., Ruiz, A.I., Fernández, R., 2018a. Investigating the potential barrier function of nanostructured materials formed in engineered barrier systems (EBS) designed for nuclear waste isolation. Chem. Rec. 18 (7–8), 1065–1075. https://doi.org/10.1002/tcr.201700094.

Cuevas, J., Ruiz, A., Fernández, R., González-Santamaría, D., Angulo, M., Ortega, A., Torres, E., Turrero, M., 2018b. Authigenic clay minerals from interface reactions of concrete-clay engineered barriers: a new perspective on Mg-clays formation in alkaline environments. Minerals 8, 362. https://doi:10.3390/min8090362.

Dauzères, A., Le Bescop, P., Sardini, P., Cau Dit Coumes, C., 2010. Physico-chemical investigation of clayey/cement-based materials interaction in the context of

geological waste disposal: experimental approach and results. Cement Concr. Res. 40 (8), 1327–1340. 10.1016/j.cemconres.2010.03.015.
Dauzères, A., Achiedo, G., Nied, D., Bernard, E., Alahrache, S., Lothenbach, B., 2016. Magnesium perturbation in low-pH concretes placed in clayey environment—solid characterizations and modeling. Cement Concr. Res. 79, 137. https://doi.org/10.1016/j.cemconres.2015.09.002.
Eberl, D.D., Jones, B.F., Khoury, H.N., 1982. Mixed-layer kerolite/sstevensite from the amargosa desert, Nevada. Clay and Clays Minerals. https://doi.org/10.1346/CCMN.1982.0300501.
Ewing, R.C., Whittleston, R.A., Yardley, B.W.J.E., 2016. Geological disposal of nuclear waste: a primer. Elements 12, 233. https://doi.org/10.2113/gselements.12.4.233.
Fernández, A.M., Baeyens, B., Bradbury, M., Rivas, P., 2004. Analysis of the porewater chemical composition of a Spanish compacted bentonite used in an engineered barrier. Phys. Chem. Earth 29, 105–118. https://doi.org/10.1016/j.pce.2003.12.001.
Fernández, R., Vigil de la Villa, R., Ruiz, A.I., García, R., Cuevas, J., 2013. Precipitation of chlorite-like structures during OPC porewater diffusion through compacted bentonite at 90°C. Appl. Clay Sci. 83–84, 357. https://doi.org/10.1016/j.clay.2013.07.021.
Fernández, R., Ruiz, A.I., Cuevas, J., 2016. Formation of CASH phases from the interaction between concrete or cement and bentonite. Clay Miner. 51, 223. https://doi.org/10.1180/claymin.2016.051.2.09.
Fernández, R., Torres, E., Ruiz, A.I., Cuevas, J., Alonso, M.C., García Calvo, J.L., Rodríguez, E., Turrero, M.J., 2017. Interaction processes at the concrete-bentonite interface after 13 years of FEBEX-Plug operation. Part II: bentonite contact. Phys. Chem. Earth, Parts A/B/C 99, 49. https://doi.org/10.1016/j.pce.2017.01.009.
Fernández, A.M., Kaufhold, S., Sánchez-Ledesma, D.M., Rey, J.J., Melón, A., Robredo, L. M., Fernández, S., Labajo, M.A., Clavero, M.A., 2018. Evolution of the THC conditions in the FEBEX in situ test after 18 years of experiment: smectite crystallochemical modifications after interactions of the bentonite with a C-steel heater at 100 °C. Appl. Geochem. 98, 152–171. https://doi.org/10.1016/j.apgeochem.2018.09.008.
Fernández, R., González-Santamaría, D., Angulo, M., Torres, E., Ruiz, A.I., Turrero, M.J., Cuevas, J., 2018. Geochemical conditions for the formation of Mg silicates phases in bentonite and implications for radioactive waste disposal. Appl. Geochem. 93, 1. https://doi.org/10.1016/j.apgeochem.2018.03.012.
García Calvo, J.L., 2012. Desarrollo de materiales de construcción con cemento de bajo pH, compatibles con la barrera de ingeniería de un almacenamiento geológico profundo de residuos radiactivos de alta actividad. Universidad Autónoma de Madrid, Madrid, Spain. http://hdl.handle.net/10486/12309.
García Calvo, J.L., Hidalgo, A., Alonso, C., Fernández Luco, L., 2010. Development of low-pH cementitious materials for HLRW repositories: resistance against ground waters aggression. Cement Concr. Res. 40, 1290. https://doi.org/10.1016/j.cemconres.2009.11.008.
Garralón, A., Gómez, P., Turrero, M.J., Torres, E., Buil, B., Sánchez, L., Peña, J., 2017. Hydrogeochemical characterisation of the groundwater in the FEBEX gallery. NAGRA Tech. Rep. NAB 16–14, 125.
Gaucher, E.C., Blanc, P., 2006. Cement/clay interactions–a review: experiments, natural analogues, and modeling. Waste Manag. 26, 776. https://doi.org/10.1016/j.wasman.2006.01.027.
González-Santamaría, D., Angulo, M., Ruiz, A., Fernández, R., Ortega, A., Cuevas, J., 2018. Low-pH cement mortar-bentonite perturbations in a small-scale pilot laboratory experiment. Clay Miner. 53, 237. https://doi.org/10.1180/clm.2018.16.
Grangeon, S., Claret, F., Linard, Y., Chiaberge, C., 2013. X-ray diffraction: a powerful tool to probe and understand the structure of nanocrystalline calcium silicate hydrates. Acta Crystallogr. B Struct Sci. Cryst. Eng. Mater. 69, 465. https://doi.org/10.1107/S2052519213021155.
Jenni, A., Mäder, U., Lerouge, C., Gaboreau, S., Schwyn, B., 2014. In situ interaction between different concretes and Opalinus Clay. Phys. Chem. Earth 70–71, 71. https://doi.org/10.1016/j.pce.2013.11.004. Parts A/B/C.
Kaufhold, S., Dohrmann, R., Klinkenberg, M., Siegesmund, S., Ufer, K.J., 2010. N2-BET specific surface area of bentonites. J. Colloid Interface Sci. 349, 275. https://doi.org/10.1016/j.jcis.2010.05.018.
Khoury, H.N., Salameh, E., Abdul-Jaber, Q., 1985. Characteristics of an unusual highly alkaline water from the Maqarin area, northern Jordan. J. Hydrol. 81, 79. https://doi.org/10.1016/0022-1694(85)90168-4.
Lerouge, C., Gaboreau, S., Grangeon, S., Claret, F., Warmont, F., Jenni, A., Cloet, V., Mäder, U., 2017. In situ interactions between opalinus clay and low alkali concrete. Phys. Chem. Earth, Parts A/B/C 99, 3. https://doi.org/10.1016/j.pce.2017.01.005.
Lothenbach, B., Le Saout, G., Gallucci, E., Scrivener, K., 2008. Influence of limestone on the hydration of Portland cements. Cement Concr. Res. 38, 848. https://doi.org/10.1016/j.cemconres.2008.01.002.
Lothenbach, B., Nied, D., L'Hôpital, E., Achiedo, G., Dauzères, A., 2015. Magnesium and calcium silicate hydrates. Cement Concr. Res. 77, 60. https://doi.org/10.1016/j.cemconres.2015.06.007.
Lowell, S., Shields, J.E., 2013. Powder Surface Area and Porosity. Springer Science & Business Media.
Mäder, U., Jenni, A., Lerouge, C., Gaboreau, S., Miyoshi, S., Kimura, Y., Cloet, V., Fukaya, M., Claret, F., Otake, T., Shibata, M., Lothenbach, B., 2017. 5-year chemico-physical evolution of concrete–claystone interfaces, Mont Terri rock laboratory (Switzerland). Swiss J. Geosci. 110, 307. https://10.1007/s00015-016-0240-5.
Metz, V., Raanan, H., Pieper, H., Bosbach, D., Ganor, J., 2005. Towards the establishment of a reliable proxy for the reactive surface area of smectite. Geochem. Cosmochim. Acta 69, 2581. https://doi.org/10.1016/j.gca.2004.11.009.
Moyce, E.B.A., Rochelle, C., Morris, K., Milodowski, A.E., Chen, X., Thornton, S., Small, J.S., Shaw, S., 2014. Rock alteration in alkaline cement waters over 15 years and its relevance to the geological disposal of nuclear waste. Appl. Geochem. 50, 91. https://doi.org/10.1016/j.apgeochem.2014.08.003.
Phung, Q.T., Maes, N., Jacques, D., De Schutter, G., Ye, G., 2016. Investigation of the changes in microstructure and transport properties of leached cement pastes accounting for mix composition. Cement Concr. Res. 79, 217. https://doi.org/10.1016/j.cemconres.2015.09.017.
Roosz, C., Grangeon, S., Blanc, P., Montouillout, V., Lothenbach, B., Henocq, P., Giffaut, E., Vieillard, P., Gaboreau, S., 2015. Crystal structure of magnesium silicate hydrates (M-S-H): the relation with 2:1 Mg–Si phyllosilicates. Cement Concr. Res. 73, 228. https://doi.org/10.1016/j.cemconres.2015.03.014.
Savage, D., 2011. A review of analogues of alkaline alteration with regard to long-term barrier performance. Mineral. Mag. 75 (4), 2401–2418. https://doi.org/10.1180/minmag.2011.075.4.2401.
Savage, D., Walker, C., Arthur, R., Rochelle, C., Oda, C., Takase, H., 2007. Alteration of bentonite by hyperalkaline fluids: a review of the role of secondary minerals. Phys. Chem. Earth, Parts A/B/C 32 (1–7), 287–297. https://doi.org/10.1016/j.pce.2005.08.048.
Shimbashi, M., Sato, T., Yamakawa, M., Fujii, N., Otake, T., 2018. formation of Fe- and Mg-rich smectite under hyperalkaline conditions at narra in palawan, the Philippines. Minerals 8, 155. https://doi:10.3390/min8040155.
Techer, I., Bartier, D., Boulvais, P., Tinseau, E., Suchorski, K., Cabrera, J., Dauzères, A., 2012. Tracing interactions between natural argillites and hyper-alkaline fluids from engineered cement paste and concrete: chemical and isotopic monitoring of a 15-years old deep-disposal analogue. Appl. Geochem. 27, 1384. https://doi.org/10.1016/j.apgeochem.2011.08.013.
Tinseau, E., Bartier, D., Hassouta, L., Devol-Brown, I., Stammose, D., 2006. Mineralogical characterization of the Tournemire argillite after in situ interaction with concretes. Waste Manag. 26 (7), 789–800. https://doi.org/10.1016/j.wasman.2006.01.024.
Trotignon, L., Devallois, V., Peycelon, H., Tiffreau, C., Bourbon, X., 2007. Predicting the long term durability of concrete engineered barriers in a geological repository for radioactive waste. Phys. Chem. Earth, Parts A/B/C 32, 259. https://10.1016/j.pce.2006.02.049.
Turrero, M.J., Cloet, V., 2017. FEBEX-DP Concrete ageing, concrete/bentonite and concrete/rock interaction analysis. Nagra Arbeitsbericht NAB 16–18, 282, 5430 Wettingen Switzerland. http://www.grimsel.com/gts-phase-vi/febex-dp/febex-dp-literature-publications.
Villar, M.V., Lloret, A., 2004. Influence of temperature on the hydro-mechanical behaviour of a compacted bentonite. Appl. Clay Sci. 26, 337. https://doi.org/10.1016/j.clay.2003.12.026.
Villar, M.V., Martín, P.L., Bárcena, I., García-Siñeriz, J.L., Gómez-Espina, R., Lloret, A., 2012. Long-term experimental evidences of saturation of compacted bentonite under repository conditions. Eng. Geol. 149–150, 57. https://doi.org/10.1016/j.enggeo.2012.08.004.
Walling, S.A., Provis, J.L., 2016. Magnesia-based cements: a journey of 150 Years, and cements for the future? Chem. Rev. 116, 4170. https://doi.org/10.1021/acs.chemrev.5b00463.
Webb, P.A., Orr, C., 1997. Analytical Methods in Fine Particle Technology. Micromeritics Instrument Corp.
Williams, L.A., Parks, G.A., Crerar, D.A., 1985. Silica diagenesis, I. Solubility controls. SEPM J. Sediment. Res. 55, 301–311. https://doi.org/10.1306/212F86AC-2B24-11D7-8648000102C1865D.

Applied Clay Science 193 (2020) 105672

Contents lists available at ScienceDirect

Applied Clay Science

journal homepage: www.elsevier.com/locate/clay

Research Paper

High-pH/low pH ordinary Portland cement mortars impacts on compacted bentonite surfaces: Application to clay barriers performance

Daniel E. González-Santamaría, Raúl Fernández, Ana.I. Ruiz, Almudena Ortega, Jaime Cuevas*

Department of Geology and Geochemistry, Faculty of Sciences, Autonomous University of Madrid, Cantoblanco, 28049 Madrid, Spain

ARTICLE INFO

Keywords:
Engineered barrier system
Cement mortar
Bentonite
Geochemical perturbation
High pH
Low pH

ABSTRACT

The design of engineered barrier systems for high-level radioactive waste isolation requires the use of cement-based materials. Small-scale surface reactivity interface experiments were designed to perform a reference laboratory study. It simulated granitic groundwater infiltration through cement mortar/bentonite (CB) binary columns. The tests ran duplicated over 6 and 18 months and included low-pH, CEM I and CEM II ordinary Portland cement mortars in contact with bentonite. After the experiments, the materials were analysed using scanning electron microscopy attached to energy dispersive energy X-ray analysis (EDX), surface mineralogy using grazing incidence X-ray diffraction configurations, specific surface area and effluent chemistry. EDX chemical profiles measured from CB interface contact reproduced, in 100 μm to 1 mm thickness, a characteristic geochemical Mg perturbation in the bentonite and calcite precipitation in cement materials. These processes are known to be developed in 10–15-years within < 5 mm of the interface. The comparison of these long, large scale experiments with the small scale experiments showed that the chemical perturbation thickness development rate will decrease over time. The limestone addition (CEM II) leaves less room for calcite precipitation, and ettringite became stabilized, which limited the extent of dissolution-precipitation processes. Then, the CEM II mortar had better resistance to perturbation.

1. Introduction

In the context of high-level radioactive waste isolation, the engineered barrier system (EBS) is a cornerstone among the different concepts of deep geological repositories (DGR) (e.g., Tournassat et al. 2015). An EBS restrains the radionuclides mobility for as long as required and keeps it isolated from groundwater.

Clays are planned to be implemented either in the role of a repository host rock (Nagra, 2002; ANDRA, 2005) or as part of the repository in the EBS as backfill and/or buffer and sealing material (Keusen et al. 1989). Clays present properties such as very low permeability, slow diffusive transport mechanisms, high retention capacity for radionuclides, chemical buffer effects, and self-sealing and swelling capacities (Galán et al. 1986; Meunier et al. 1998; Gómez-Espina and Villar 2016; Kaufhold and Dohrmann 2016; Norris 2017). Concrete is used as structural support for galleries and for plugging seals for galleries. In spite of these adequate functional properties, chemical gradients produced when concrete and clays are held in contact, induce their mutual perturbation, causing reaction diffusive fluxes that lead to the formation of new solid phases and the alteration of material properties in the near field (Savage 2014).

To date, a small spatial progression of the perturbations in concrete/clay rock or concrete/bentonite interfaces has been observed, within a centimetre scale in the laboratory or in situ experiments run for a decade (i.e., Fernández et al. 2017; Lerouge et al. 2017; Mäder et al. 2017; Duro et al. 2020, and references therein); whereas numerical models, either built with early state-of-the-art knowledge or more detailed recent approaches (ECOCLAY-II, 2005, Idiart et al. 2020 and references therein), predicted several decimetres impact in the long term. However, the nature of the neogenic phases formed at the interface (e.g., calcium aluminium silicate hydrates (CASH) and magnesium silicate hydrates (MSH)), as well as their role in the alteration of porosity/permeability and swelling pressure, remain unclear (Lothenbach et al. 2015; Walling and Provis 2016).

Geochemical processes observed within the concrete (OPC-based)/clay interface, based on laboratory and in situ experiments can be related to decalcification of concrete; dissolution of montmorillonite (Mt); precipitation of calcium silicate hydrates (CSH), calcite and secondary chloride or sulphate Ca−Al phases (ettringite and calcium aluminate monosulfate); cation exchange in Mt.; and MSH formation. All these reactions seem to produce a porosity increase in concrete and pore clogging at the clay interface (Read et al. 2001; Baur et al. 2004;

* Corresponding author.
E-mail address: jaime.cuevas@uam.es (J. Cuevas).

https://doi.org/10.1016/j.clay.2020.105672
Received 11 January 2020; Received in revised form 8 May 2020; Accepted 11 May 2020

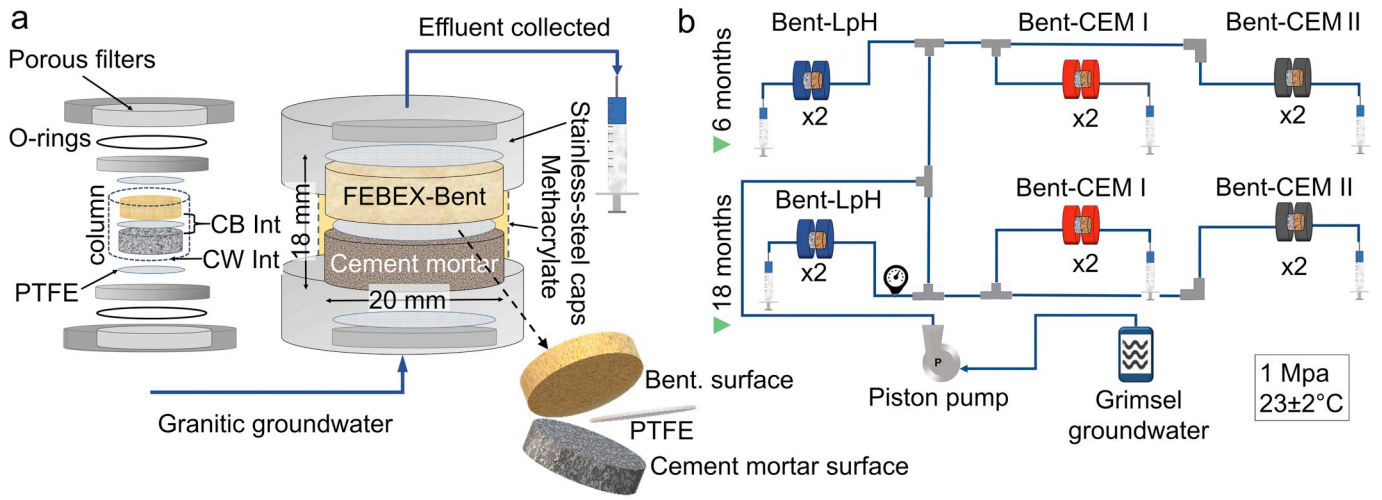

Fig. 1. Scheme of the experiments. (a) Transport cell and (b) representation of the experimental setup. The cell dimensions were 20 mm in internal diameter and 9 mm in height for each material (18 mm in total). PTFE: polytetrafluoroethylene membrane, CB int: cement mortar/bentonite interface, CW int: cement mortar/water interface. Bent: bentonite.

Fernández et al. 2006; Florea and Brouwers 2012; Dauzères et al. 2014a; Jenni et al. 2014; Cuevas et al. 2016; Fernández et al. 2016; Fernández et al. 2017; Turrero and Cloet 2017). The extent and location of these perturbations are conditioned by the composition of the cementitious material (Lerouge et al. 2017). In this context, some authors suggested the better performance of high-pH cement materials (pH > 13), e.g., CEM I OPC, by the development of a protective calcium carbonate film, which would reduce the decalcification process (Jenni et al. 2014; Mäder et al. 2017). Conversely, others reported the advantage of using low-pH cements (pH < 11) to reduce the influence of alkaline dissolution of clays and, at the same time, improving the resistance of concrete to granitic groundwater exposure (García Calvo et al. 2010; García Calvo 2012). However, less resistance to concrete matrix dissolution of low pH cement products was described for these materials under the influence of clay pore waters (Trotignon et al. 2007; Dauzères et al. 2014b).

Underground research laboratories (URL) are long-term in situ facilities in which demonstration tests are carried out in support of the development of DGR (Blechschmidt and Vomvoris 2010; Wang 2014). These demonstration tests help to determine the future evolution of the materials interfaces in the repository system considering, in this case, groundwater, cementitious materials and clays interactions. Geochemical perturbations have been observed in URL experiments testing reference cement-based materials, mainly ordinary Portland Cement (OPC) based cement: CEM I, CEM II (limestone addition to improve its durability, Hawkins et al. 1996; Vuk et al. 2001) and CEM I mixed with silica fume (SF) as a low-pH material. URL emplacements have different types of clay rocks such as Opalinus (OPA) in Switzerland or Callovo-Oxfordian argillite in France as host rocks and bentonite as backfill (Ewing et al. 2016). Table S1, in the supplementary file, summarizes the timescale and spatial extent of geochemical perturbations produced in these URL tests.

The comparison of in situ and laboratory experiments is valuable to obtain a multiscale approach of the material performances. The nature of the reaction products depend on the experimental conditions (Dauzères et al. 2010; Fernández et al. 2016) and reveal a high degree of heterogeneity in their spatial length distribution. Thus, in situ experiments are more realistic and may need many sampling locations at the interface to be representative (Gaboreau et al. 2011; Gaboreau et al. 2012; Bartier et al. 2013; Mäder et al. 2017); unfortunately, this is not usually done because of cost reasons. In this context, small-scale, homogeneous, reproducible and controlled experiments concerning real EBS interfaces are needed as alternative to have an experimental reference in order to disclose what happened in situ. The present work compares the behaviour of different types of cement materials, CEM I and CEM II as high-pH cement and CEM I + SF as a low-pH, in a simulated EBS under virtually equal conditions. The geochemical reactions observed at a small scale of time and space (μm) in the present work are envisaged to be used in the development of reaction concepts to model the experiments in the future, thus offering a useful prospective to advance the upscaling of concrete-bentonite interface chemical perturbation.

2. Materials and methods

2.1. Materials

2.1.1. Granitic groundwater

The groundwater used as injecting water in the experiments was obtained from the Grimsel Test Site (GTS) research facility excavated in granite. The GTS groundwater is characterized by a dilute (104 μS/cm), pH = 8.1 composition of Na^+, Ca^{2+}, HCO_3^-, Cl^-, and SO_4^{2-} ions (Garralón et al. 2017; Torres et al. 2019).

2.1.2. FEBEX bentonite

FEBEX bentonite was obtained from the Cortijo de Archidona deposits (Caballero et al., 2005). It contains > 90% montmorillonite, with accessory quartz (qtz; (2 ± 1), plagioclase (pl; 3 ± 1), K-feldspar (Kfs; (< 1), calcite (Cal; < 1) and cristobalite (Crs; 2 ± 1). The FEBEX bentonite contains close to 1/3, 1/3 and 1/4 cmol (+)/kg of Mg^{2+}, Ca^{2+} and Na^+ exchangeable cations, respectively, for a cation exchange capacity (CEC) of 102 ± 2 cmol(+)/kg (ENRESA 2006).

The bentonite was compacted (dry density of 1.60 g/cm^3) with its hygroscopic water content (13 wt%) at room temperature (23 ± 2 °C) and inside a methacrylate cylinder sleeve, where the mortar was previously hardened and cured (100% R. H. for 90 days), Fig. 1.

2.1.3. Cement mortars

Three types of mortars were used: one low-pH (LpH) mortar and two high-pH (HpH). The LpH cement mortar was made with 60 wt% CEM I 42.5 R SR mixed with 40 wt% SF, similar to the ESRED EU project formulation (Jenni et al. 2014; Dauzères et al. 2016). The HpH mortars were based on CEM I 42.5 R SR (CEM I) and CEM II/A-L 42.5 R formulated with 10 wt% limestone (CEM-II). The materials were supplied by the Eduardo Torroja Institute for Construction Science (CSIC-IETcc) (CEM I, SF and quartz sand) and Cementos Portland Valderivas

group Company (CEM II). Each material was mixed using a 0.42 distilled water/binder ratio and 1 + 3 binder/quartz sand. The pH indicative of the pore solution of the initially cured mortars (references) was measured according to the leached or aqueous extract ex situ method (García Calvo 2012), obtaining a pH of 11.0 ± 0.1 for LpH, 11.5 ± 0.1 for CEM I and 12.2 ± 0.1 for CEM II.

2.2. Methods

A detailed explanation for a pilot experiment is available in González-Santamaría et al. (2018) and a short description of the setup of the experiments is provided here. The column arrangement (Fig. 1) allowed separate study of the cement mortar or bentonite surfaces at the interface as they were separated by a PTFE membrane (< 0.45 μm pore size, 10 μm thickness), limiting the mineral complexity of the cement mortar/bentonite mixtures (Huertas and Santiago 1997; Alonso et al. 2017; Fernández et al. 2017). Each experiment was duplicated (r) and run for two periods (p) of time: 6 and 18 months (m). Thus, 12 experiments were studied under virtually equal conditions: 2r × 2p × 3 cell types: LpH, CEM I and CEM II.

Scanning electron microscopy combined with energy dispersive X-ray detection (SEM-EDX), powder X-ray diffraction methods (XRD), and specific surface area analyses (SSA) were performed to study the mineralogical and physical perturbations of the solid samples. For this task, at the end of the tests, the column was divided into several subsamples according to the different analyses carried out. Regarding the collected aqueous solution effluents, the volume flow rates were measured for hydraulic conductivity calculation. Water was injected through the mortar at a constant hydraulic pressure of 0.1 MPa. The collected effluent, at the bentonite end, filled syringes, which were periodically weighed to calculate flow rates, and eventually used for aqueous chemical analysis.

2.2.1. SEM-EDX analyses

The average bulk chemical composition of mortars was assessed by areas (1 mm^2) and spot analyses by means of SEM-EDX. For spot analyses, quartz grains were avoided. These measurements were performed in a 2 mm thickness polished section taken from the CB interface. Bentonite analysis was made by areas.

The variation of the elemental composition of both mortar and bentonite materials in relation to the distance from the CB interface was studied by tracing a line perpendicular to the CB, where detailed EDX area analysis was acquired. Previously the samples were polished after a freeze-drying and embedded in epoxy resin. SEM-EDX analysis was conducted on a Hitachi S-3000 N scanning electron microscope coupled to an INCAx-sight Oxford Instruments™ energy-dispersive X-ray analyser. For EDX semi-quantification of major elements, the statistical quality of the measurements is better than 10% determination error for the elements analysed (González-Santamaría et al. 2018).

Finally, the morphology and composition of crystals or crystal aggregates at the surfaces facing to each other were also explored and analysed.

2.2.2. XRD and grazing incidence X-ray diffraction (GI-XRD) analysis

GI-XRD configuration was used at a fixed incidence angle of 0.5° θ, and also to obtain θ/2θ scans. The exploration of the mortar and bentonite fresh surfaces provided information from the first ~100 μm thickness from the PTFE membrane. This configuration allowed to study the interface mineralogy by maximizing the sampling area using a fixed low diffraction angle. XRD experiments were recorded in a 3–70° 2θ angular range using 0.04° angular step (2 s time). The equipment used was an X'Pert PRO PANalytical θ/θ diffractometer with parallel beam optics, secondary monochromator and Xenon detector. XRD powder patterns of mortar and bentonite were obtained from slices cut at different distances (0–3, 3–6, 6–9 mm) from the CB interface. The equipment used was a θ-2θ X'Pert PANalytical instrument with an X'Celerator detector. XRD patterns were recorded for 0.016° angular steps (100 s time) in an angular range of 3–70° 2θ. The voltage and intensity of the operated X-ray Cu tube were 45 kV and 40 mA.

2.2.3. SSA analyses

SSA analyses determined by the BET equation method (N_2 gas adsorption, Webb and Orr 1997) were performed in the slices. A 0.2 g subsample was ground in an agate mortar and oven dried to 90 °C prior to SSA analyses using Micromeritcs® GEMINI V equipment. The degassing phase (18 h 90 °C in N_2 gas atmosphere), was carried following standard UNE-EN 1015–11.

2.2.4. Aqueous solution analyses

The characterization of the effluents consisted in pH and alkalinity measurement (Metrohm 888™ titration device); silica analysis (825 nm visible spectrophotometry using the molybdate blue complex method in a Milton Roy Spectronic® 1200 instrument); and major ions (Cl^-, SO_4^{2-}, Na^+, K^+, Ca^{2+} and Mg^{2+}) determination by ion chromatography (Metrohm 802™ compact IC plus).

3. Results

3.1. SEM-EDX analyses

The average chemical compositions of the areas of the mortars are accessible in the supplementary file (Table S2). Whit regards to spot chemical compositions, the Ca/Si ratio was 0.88 ± 0.13 for LpH, whereas the Ca/Si ratio of CEM I and CEM II presented mean ratios of 1.76 ± 0.13 and 1.72 ± 0.33, respectively (Fig. S1). These values are characteristic of a mixture of calcium silicate (CS) anhydrous and CSH hydrated phases in low pH and high pH concrete matrices (Grangeon et al. 2013; Grangeon et al. 2016). The ratios tended to decrease slightly over time although with a high dispersion owing to the redistribution of Ca in a 100 μm scale.

The measured elemental chemical profiles presented significant perturbations at the 0–200 μm scale from the interface towards both sides, cement mortar and bentonite, focusing mainly on Ca, Mg, Al and S variations (Fig. 2). Si was the element with the highest concentration due to quartz sand grains, and its change counteracted the relative variations of the others, so its variation is not interpreted as net precipitation or dissolution of silica. In general, there was less elemental variability beyond 200 μm, affecting both sides in the three tested materials, with high homogeneity on the bentonite side.

At the mortar side, Ca at.% presented a significant increase next to the interfaces (< 100 μm thickness). These increases contrast with the general decrease in Ca observed in the averaged data corresponding to the spots matrix analyses within a 2 mm thickness (Table S2). In the LpH cement mortar, Ca at.% grew from 14 to ~20 at.% and reached two maxima at 6 months, approximately 20 and 80 μm from the interface. For CEM I and CEM II, the Ca increase was higher than that in LpH and reached maxima of ~50 and ~ 60 at.%, respectively. Low Ca at.% levels in CEM I are due to differences and heterogeneities in duplicated experiments (wide error bars), and also to the absence in limestone addition in the cement paste. The Ca/Si ratios in these Ca-rich zones were > > 2, higher than cement matrix CSH, which suggests the presence of calcite. CEM I and CEM II Ca at.% profiles also suggested the presence of small decalcification zones between 60 and 170 μm. Ca at.% increased from 6 to 18 m for all experiments. FEBEX bentonite is not affected by this Ca perturbation in any of the materials tested.

Mg at.% was increased in the FEBEX bentonite surface facing the PTFE membrane. This pattern is the opposite to that described for Ca at.% in the mortar material behind the CB interfaces. Minor Mg at.% increments were developed near the CB interface in the LpH mortar side (< 50 μm), where relative Mg at.% increases in bentonite reached an extension of approximately 600 μm. The bentonite interface Mg at.% values were higher in the experiments performed with CEM I

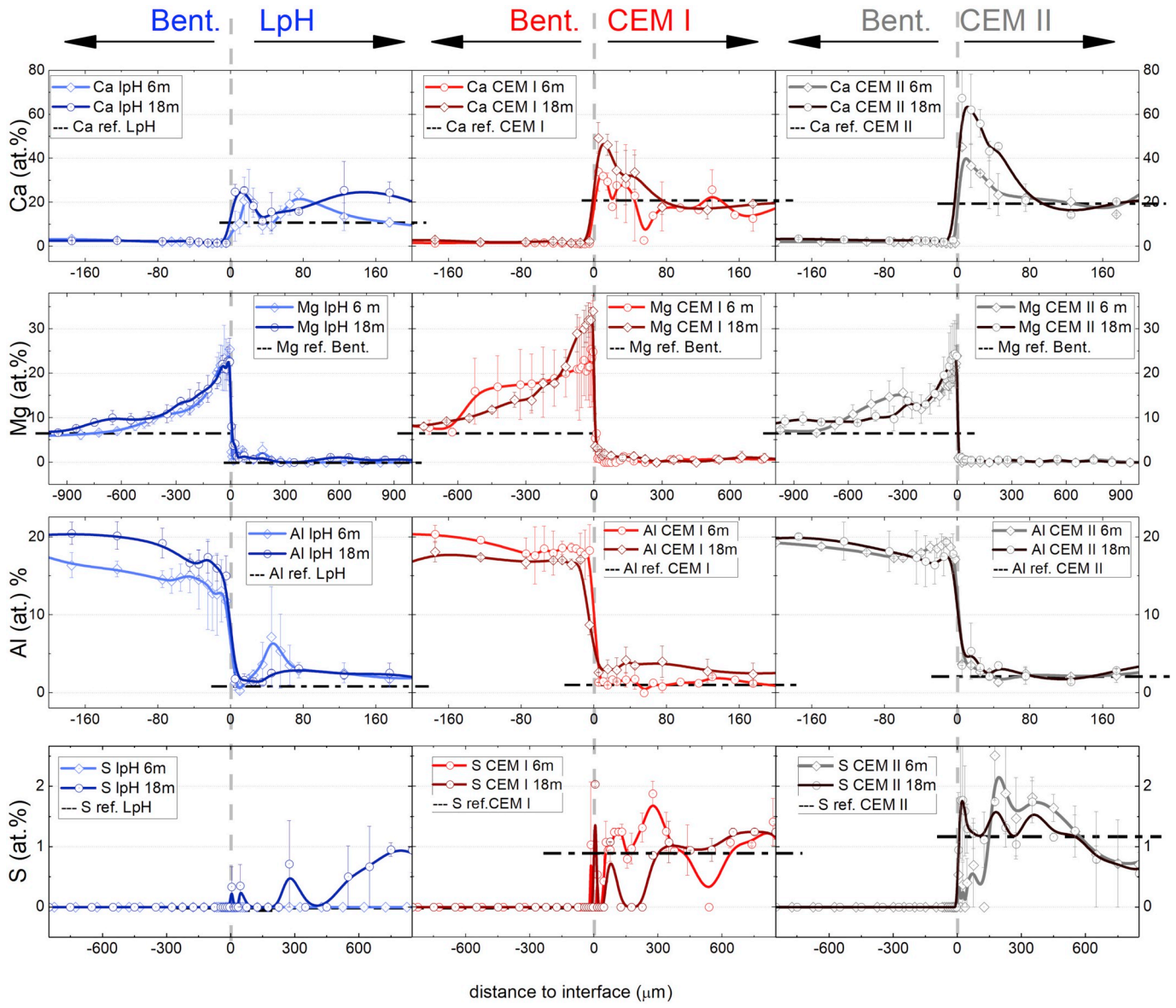

Fig. 2. Ca, Al and S (at.%). chemical profiles of the three types of mortar/bentonite interfaces. All profiles were obtained based on the average values of the duplicated experiments (error bars marked). The interface is represented at 0 μm as a vertical grey dashed line. Reference (ref.) at.% of Ca, Al and S of each type of cement mortar, and basal at.% Mg of FEBEX bentonite have been plotted (horizontal dashed lines). The whole experimental scale profiles at the whole experimental scale can be found in the supplementary file (Fig. S2). m: months.

(~25–35 Mg at.%) than in LpH and CEM II (~ < 25 Mg at.%). Both HpH experiments presented a Mg at.% step at 600–400 μm from the interface, which is smoothed from 6 to 18 months, whereas the Mg at.% is maximum at the CB wall (> 40% in CEM I). Mg at.% reaches the reference line at ≈ 1500 μm.

For Al behaviour, its at.% was above reference lines in CEM I (at 18 months) and CEM II mortars within a few μm (~100 μm) near the CB wall. These increases grew from 6 to 18 months. Different behaviour was observed in LpH; a broad Al peak was detected at ~60 μm for 6 months profiles. The presence of Al sulphates can presumably be inferred as Al at.% and S at.% are in some regions together above the reference lines. However they are not correlated, presumably due to the error in the determination of the low S content (~ < 2 at.%).

At the FEBEX bentonite side, in all experiments, Al at.% showed a smooth continuous decrease up to the CB interface from ~150 μm, being more noticeable in general at 18 months and in the CEM I tests. Both in LpH and in CEM I, a general increase of Al at.% in cement mortar is produced in a ~ 100 μm region with respect to the CB interface. In CEM II was less pronounced, although also detected.

As regards crystal aggregates and undifferentiated mineral masses, they were presumably produced due to pore fluids interactions. They were found on the fresh surfaces of the facing planes and identified by their singular chemical compositions or morphologies. The distribution of these phases according to the type of experiment and time scale is summarized in Table 1.

Concerning cement mortar surfaces, brucite ($Mg(OH)_2$) was identified only at LpH mortar surfaces after 6 months (Fig. 3a, b), filling voids with crystal aggregates of trigonal prism morphologies (Fernández et al. 2006). Later, at 18 months, similar voids were filled with mixtures, alternatively rich in Mg–Si mixed with Ca signals, these ones coming from precipitates of calcium carbonates scalenohedral calcite crystals and undifferentiated coatings of Ca phases (Fig. 3c). Calcite crystals and coatings were found in the three types of experiments but were mostly found in CEM II experiments (Fig. 3d, e, f), which agrees with the Ca wt % from EDX profiles as shown in Fig. 2. Euhedral calcite crystals with sizes of 5–10 μm were also found in CEM II voids at the surface of

Table 1
Distribution of phases in the surface of the facing planes.

Time	Surface	Brucite	Mg-Si crust	Mg-Si platelets	Cal	CSH	CH	C-A-S-H	ett(+)/CmSAH(-)
18 months	Bentonite		LpH / CEM I / CEM II	L CEM I / CEM II	CEM I$^{(-)}$ / CEM II$^{(-)}$				
	CEM mortar	LpH	LpH		LpH / CEM I$^{(+)}$/ CEM II$^{(+)}$	LpH / CEM I / CEM II			CEM I / CEM II
6 months	Bentonite		LpH /CEM I / CEM II	LCEM I / CEM II	CEMI$^{(-)}$ / CEM II$^{(-)}$			CEM I$^{(?)}$	
	CEM mortar	LpH			LpH / CEM I / CEM II	CEM I	CEM I	LpH / CEM I / CEM II	LpH / CEM I / CEM II$^{(+)}$

CH: portlandite, Cal: calcite, CSH: calcium silicate hydrates, CASH, calcium aluminium silicate hydrates, ett: ettringite, CmSAH: calcium monosulphate aluminate hydrate, LpH: low-pH cement mortar, CEM I: high-pH cement mortar, CEM II: high-pH cement mortar with limestone addition, (+) High frequency; (−) Low frequency; (?) possible, Mg-Si: Mg-silicates.

mortars (Fig. 3f).

Hydrated cement products were found mixed in aggregates or needle-tabular morphologies. Examples of CSH (Fig. 3d, on the right side), ettringite (Fig. 3g), and CASH (Fig. 3i) in HpH and LpH were identified. Portlandite was just found at 6 months in CEM I (Fig. 3h). Regarding CEM II, the presence of Al−S phases, as ettringite, is related to the relative high content of Al in the cement mortar (Table S2).

On the bentonite side, Mg-(minor Fe)-Si phases were found in the three types of interfaces. These phases were characterized by crusts morphologies, which exhibit moulded shapes of the PTFE membrane (Fig. 3j, l). In some depressions, edge-to-face aggregates of platy crystals are visible on the nm to μm scales (Fig. 3k.). Crusts and platelets showed the highest Mg contents (Mg/Si ratios ranged from 0.6 to > 2). Punctually, small and localized Ca enrichment areas with an extension < 10 μm in diameter were found in bentonite surfaces exposed to HpH mortars (Fig. 3m, n, o).

With regard to the EDX analysis conducted in the fresh surfaces arising from the open CB interface, the results exceeded several times the Mg/Si ratios of reference FEBEX bentonite (Table 2). The analyses taken from these surfaces in Mg-Si-Al rich compositional zones, exhibit high standard deviations for silicate structural cations, including areas with high Mg/Si ratios (> 1.5). Conversely, unaltered reference FEBEX bentonite presented a very homogenous chemical composition at the same scale of observation, and Mg/Si ratios remained constant at reference levels (Mg/Si 0.14 ± 0.02). Irrespective of time, the average Mg/Si ratios recorded were as follows: LpH, Mg/Si 0.53 ± 0.26, CEM I: 0.88 ± 0.18 and CEM II: 0.66 ± 0.15. CEM II exhibits intermediate values not as high as those of CEM I.

The crystal-chemical nature of bentonite surface zones at the interface was approached by the use of chemical coordinates ternary plots (Velde 1985, see the supplementary file, Fig. S3). The presence of di-octahedral and tri-octahedral clay minerals compositions can be determined using the chemical analyses taken from surface zones of bentonite in the CB interface. Most of the CEM I and CEM II experimental spot coordinates were located in a linear combination built considering the intercalation of a complete brucite layer in the Mt. interlayer (Mt-F-brc in Fig. S3). However, a small group of analyses tended to saponitic compositions over time in CEM I and LpH. This was less obvious for LpH if the ecxhangeable cation component is taken into account (M + R3-2R3-3R2 diagrams in Fig. S3), in which 18 months data visibly depart from saponite (Fig. S3b). In the case of CEM I at 18 m, the analysed compositions tended to saponitic terms in the representations of Fig.S3.

Concerning cement matrices and diagrams designed for hydrated cement phases (Gaboreau et al. 2017; Lerouge et al. 2017; Fig. S4 in supplementary file) a large number of spots tended to calcite (Ca pole) due to cement mortar interface surface enrichments. In the case of LpH, the dispersion of dots in the diagrams was specially complex due to the Mg,Al,Ca,Si mixing phases in the mortar. In contrast, regarding CEM II interface mortars compositions that fit Al-tobermorite (CASH) with structure similar to Al-tobermorite), were frequent, where the incorporation of Al is favoured in the low Ca/Si CSH. Al-tobermorite has been described in specific environments, such as relict lime clasts in volcanics (Jackson et al. 2013), and in the context of cement-based materials and bentonite interactions (Fernández et al. 2016).

3.2. X-ray diffraction analyses

Results based on the surface θ/2θ scans are presented in Fig. 4. Powder patterns of parallel slices exhibited no differences with untreated materials, and GI- XRD on surfaces showed, with less quality, the same information as surface θ/2θ scans (comparison is shown in the supplementary file, Fig. S5). The XRD patterns registered at the bentonite surface interfaces showed the characteristic d001-value of Mt. at 14.8 Å, followed by a decrease in intensity as a function of time. Position changes are also presented in comparison with the reference

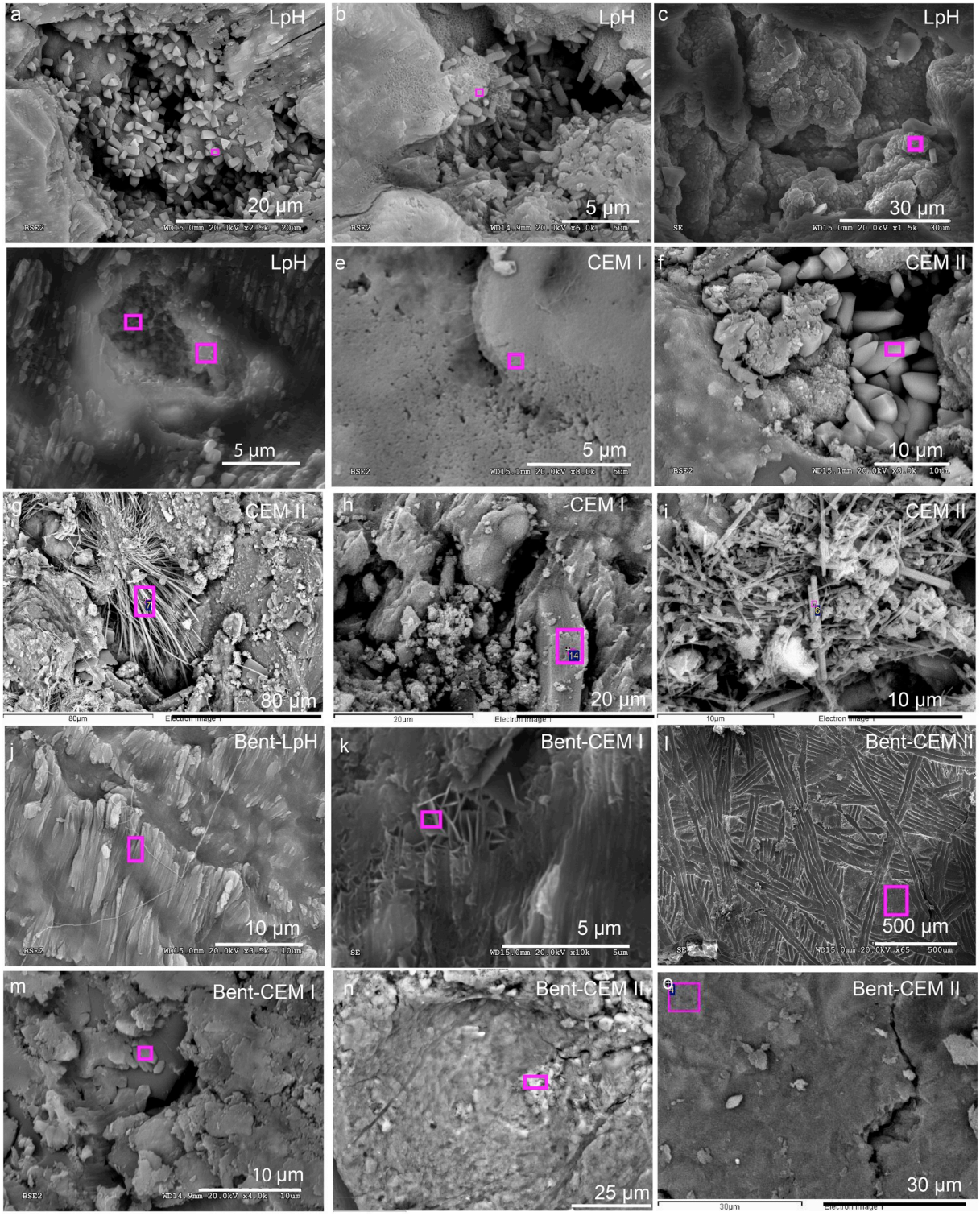

Fig. 3. SEM-EDX micrographs in the surface of the facing planes. a) Brucite prismatic trigonal crystal aggregates in LpH cement mortar at 6 m. b) Brucite crystals and honeycomb coatings of Mg, Ca−Si phases in LpH cement mortar at 6 m. c) Mg−Si spheroidal aggregates from LpH at 18 m experiments. d)Crystal aggregates of calcite mixed with Ca−Si coatings growing in between (18 m sample in LpH cement mortar). e) Ca crust (nanosized calcium carbonate) from a CEM I cement mortar in 6 m experiments. f) Scalenohedral calcite crystals from the CEM II experiment run over 6 m. g) Ettringite needles from the CEM II 6 m sample. h) Portlandite from the CEM I 6 m sample. i) CASH from CEM II 6 m. j) Mg−Si rich crust from Bent-LpH in 6 m. k) Mg (minor Fe) rich platy morphologies from bentonite in contact with CEM I in 6 m samples. l) Mg(Fe)-Si rich crust characteristic of Bent-CEM II experiments where the marks of the separation PTFE membrane are visible. m) Mixture of silicon and carbonate from the bentonite surface at the CEM I. n and o) Calcite crusts from Bent-CEM II at 18 and 6 m, respectively. Purple rectangles show the area covered by the analysis (the EDX analyses and EDX spectra of crystal aggregates are listed in Table S3a and b). m: months. (For interpretation of the references to colour in this figure legend, the reader is referred to the web version of this article.)

Table 2
Mean and standard deviation of Mg/Si ratios from the surface of the facing planes.

Experiment	Bent-LpH	N° analyses	Bent-CEM I	N° analyses	Bent-CEM II	N° analyses	Ref. Bent.	N°analyses
Bent. 6 months	0.50 ± 0.22	23	0.85 ± 0.16	8	0.68 ± 0.15	19	0.14 ± 0.02	
Bent. 18 months	0.55 ± 0.28	33	0.88 ± 0.19	86	0.64 ± 0.16	37		21
Total mean	0.53 ± 0.26	56	0.88 ± 0.18	94	0.66 ± 0.15	56		

Bent: bentonite, Ref: reference.

bentonite (Fig. 4a). The d001-value disappeared after 18 months in the CEM I and CEM II experiments, and at the same time, a broad 7.6–7.4 Å and 3.66 Å reflections developed at 6 and 18 m. These reflections were only evidenced in bentonite exposed to CEM I after 18 m, whereas in bentonite exposed to CEM II it was well developed already after 6 months. In contrast, bentonite exposed to LpH and reference FEBEX-bentonite did not show any 7.6–7.4 Å d-value. Both 7.5 and 3.66 Å reflections are typical of Mg-tri-octahedral layered minerals such as serpentine or chlorite (Brindley and Brown 1980; Shimbashi et al. 2018) With regard to the 06 *l* reflection the CEM I experiments developed broad diffraction peaks at 1.53 Å not present in reference bentonite at 1.49–1.50 Å (Fig. 4b). However, the predominant presence of the 1.50 Å reflection indicated the persistence of di-octahedral smectites (Mt). Finally, it is worth noting that there was no evidence for the 3.03 Å calcite reflection in the LpH experiments, whereas CEM I after 18 months, and CEM II after 6 and 18 months contains clear calcite reflections.

With regards to cement mortars, the X-ray diffraction results showed minor differences regarding reference hydrated mortars (Fig. S6). On the LpH surface, characteristic brucite d-values at 4.77 and 2.36 Å were found after 6 and 18 months (Fig. S6a). Conversely, these reflections were not detected in the HpH surfaces, whereas calcite 3.03 Å d-values were detected in all experiments (Fig.S6b).

3.3. Specific surface area

SSA changes indicate the existence of new phase precipitation processes with small crystal sizes and high external SSA, which led to an increase in global SSA; alternatively, it is possible that the formation of cement made N_2 gas inaccessible to part of the external surface pores with an associated SSA decrease (Lai and Krevor 2014). Due to the short spatial extension of the perturbations observed in experiments, limited to < 1 mm at the CB interface, only the SSA of the first 3 mm slices sampled in both sides of the CB interface is presented (Fig. 5). Overall, the SSA of all samples next to the CB interface showed a decreasing tendency from 6 to 18 m, in both cement mortar and bentonite samples. After 6 and 18 months, bentonite in contact with CEM I presented the lowest values, compared to LpH and CEM II.

Compared to bentonite, the cement mortars SSA showed more significant changes. At 6 m, LpH and CEM I presented higher SSA than their references. Later, the LpH and CEM I SSA decreased over time, whereas CEM II remained close to the reference CEM II SSA, increasing from 4.2 m^2/g to 5.2 m^2/g after 18 months.

3.4. Aqueous solution

Effluent flow measurements show how the hydraulic conductivity is consistent with the reference FEBEX bentonite, in the order of 10^{-13} m/s (Villar and Lloret 2004). Concrete and mortars made with similar

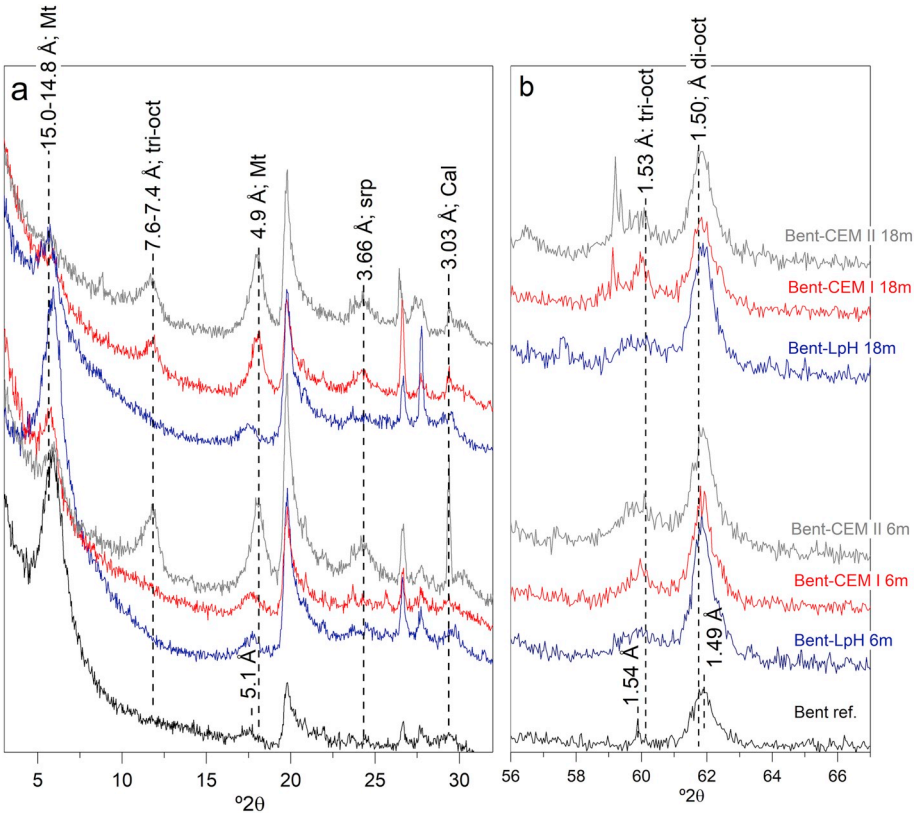

Fig. 4. θ/2θ scans performed on bentonite surface interfaces. a) Region of the diffractograms from the 3 to 31°2θ position. b) Region from 56 to 67°2θ position. Numbers indicate d-values in Å. Mt.: montmorillonite, tri-oct: tri-octahedral clay mineral, srp: serpentine mineral group, di-oct: di-octahedral clay mineral.

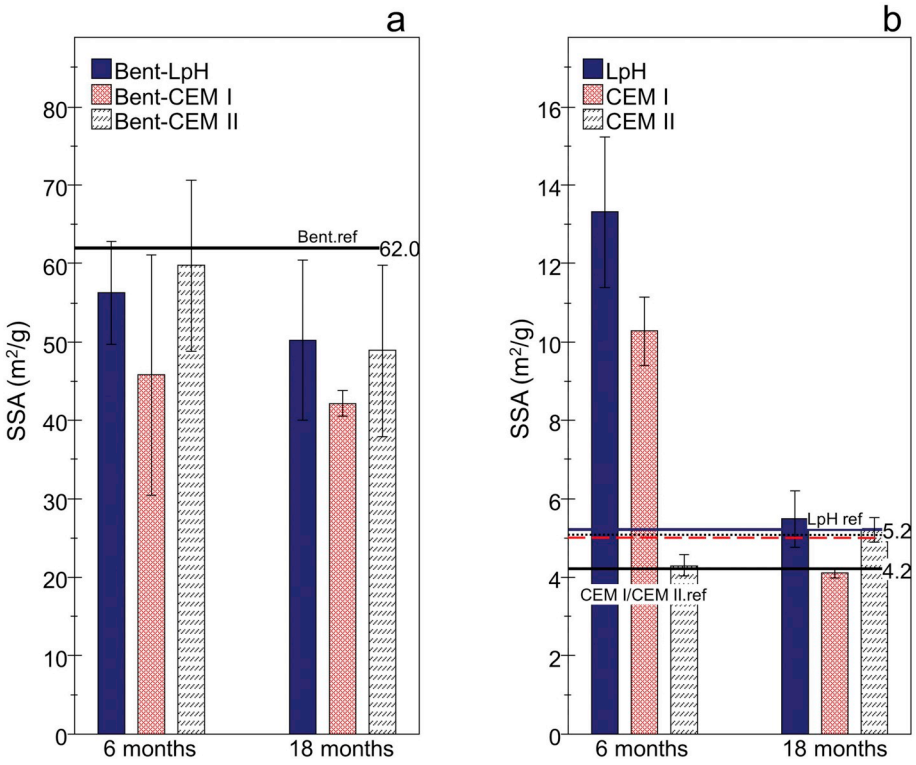

Fig. 5. Specific surface area (SSA; m^2/g) of the experiments performed at 6 and 18 months. a) SSA results of the first 3 mm of bentonite from the CB interface. b) Results of the first 3 mm obtained for cement mortars. SSA: specific surface area.

Table 3
Mean values of the pH, aqueous silica and hydraulic conductivity registered during the 18 months.

Experiment	pH	$SiO_{2(aq)}$ (mg/L)-	Hydraulic conductivity (m/s)
Bent-LpH	8.2 ± 0.3	13.0 ± 2.3	2.1×10^{-13} ± 1.3×10^{-13}-
Bent-CEM I	7.9 ± 0.3	12.7 ± 0.9	1.7×10^{-13} ± 1.1×10^{-13}
Bent-CEM II	8.3 ± 0.1	15.1 ± 3.2	3.2×10^{-13} ± 1.9×10^{-13}

materials, displayed high variability in hydraulic conductivity (i.e., 10^{-11} m/s for FEBEX CEM II concrete plug or 10^{-13} -10^{-14} m/s for CEM I concrete or CEM III mortar with limestone addition; Schneider et al., 2012; Turrero and Cloet 2017;). It depends on porosity, initial water content, water/cement ratio, etc. Hydraulic conductivity slightly decrease over time, especially in CEM I experiments (Table 3).

The evolution of the major chemical ions is presented as a function of the dimensionless number of pore volumes (V_p; V_p = 1.3 cm^3; Fig. 6). Fewer data were obtained for experiments conducted with HpH cement mortars, owing to the low hydraulic conductivity of these experiments. The ions solution concentration decrease exponentially with time due to the relatively higher measured initial concentrations than in the long term collected fluids, due to initial soluble salts leaching. Highly soluble salts, chlorides, sulphates and bicarbonates with alkaline counter-ions (i.e. Na^+ and K^+), were readily leached, followed by an asymptotic decrease. Most of the ions were at very low concentrations at the end of the experiments, but not in the case of $HC\Theta_3^-$, which ranged from 400 to 100 mg/L. The experiments with CEM II and LpH maintained higher $HC\Theta_3^-$ concentrations because of the presence of calcite or the relatively lower pH at the CB interface, respectively. CEM I showed a sharp decrease in Mg and Ca to close to zero, in agreement with the more intense precipitation of hydrated Mg silicates and calcite. Conversely, CEM II leached more Ca because of the influence of the limestone addition. The values of the pH (7.9–8.3) and silica (13.0–15.1 mg/L) were homogenous and their content remained stable and constant regardless of the type of cement mortar and time.

4. Discussion

The study of the early reaction steps within the experimental simulated concrete/bentonite interfaces revealed perturbations influenced by the use of different types of cement mortars. The redistribution of Ca and Mg at both sides of the interface are indicators of the geochemical reactions involved. The Ca redistribution was mainly due to the decalcification of high Ca/Si CSH (1.7–1.4) to form (1) tobermorite (CSH Ca/Si ~0.8), (2) Al-tobermorite (C(A)SH) if dissolved Al is available; (3) calcite if there exists a source for dissolved carbonate ions, and (4) Ca−Al sulphates, mainly ettringite, incorporating chloride and carbonate ions if there exists a source for sulphate or other anions. These processes were identified with different intensities related to the formation of by-products located on the mortar side of the interface. The precipitation of Mg-containing phases is characteristic of bentonite perturbation, except in LpH mortar in which they were present at both sides of the interface. Due to the mobility of this element (i.e., cation exchange from smectites interlayers to be incorporated to porewater solution), they were concentrated as (1) brucite, driven by precipitation at pH > 10.5,as observed by Pokrovsky and Schott 2004) and (2) hydrated Mg silicate in the form of 2:1 or 1:1 tri-octahedral clay minerals if reactive silica was available and activated by the alkaline conditions at pH > 9 imposed by cement hydrated phase equilibrium. Examples of the combination of the aforementioned processes in concrete/clay interfaces were described for instance by Dauzères et al. (2010), Dauzères et al. (2014a), Jenni et al. (2014), Dauzères et al. (2016), Fernández et al. (2017) and Mader et al. (2017).

The Ca geochemical perturbation within the CB interface was related to the precipitation of calcite in the mortar pores at the interface wall. HpH cement mortars developed a Ca maximum corresponding to calcite, increasing with time, as detected by surface θ/2θ scans. On the other hand, EDX profiles revealed a decrease in Ca compared to reference values, with high heterogeneity, produced beyond 80 μm from

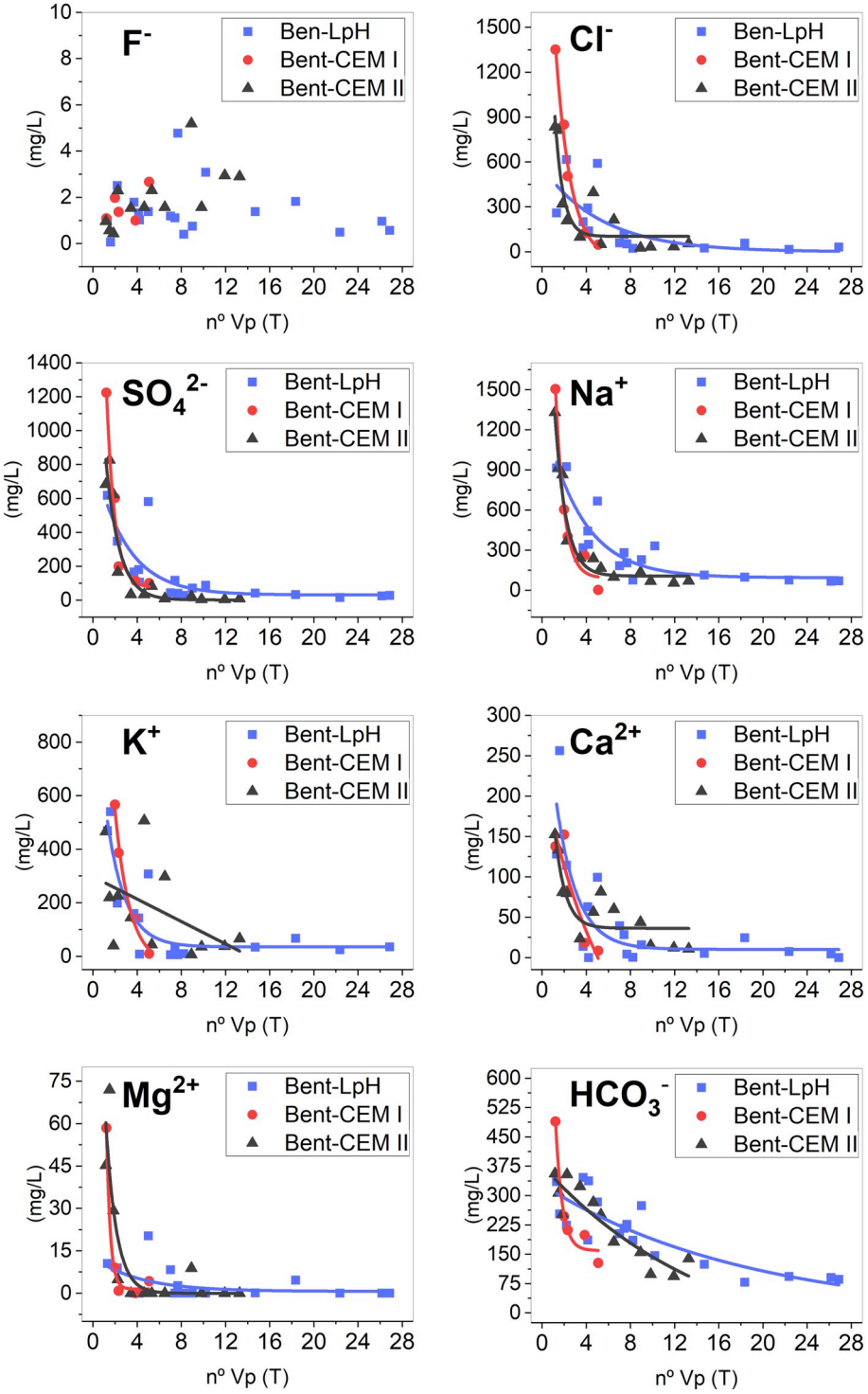

Fig. 6. Major chemical ions of the leachate collected at the end of the bentonite side.

the CB interface. Portlandite and high Ca/Si CSH dissolution was the calcium source for calcite precipitation, which is produced in the mixing zone where carbonated bentonite porewaters (pH 8–9) react with pH > 11 mortar porewaters (Dauzères et al. 2014a; Alonso et al. 2017). Significant calcite precipitation did not occur in the LpH experiments as far as portlandite was not present in the reference LpH hydrated mortar, and CSH already had a relatively low Ca/Si (0.8).

Concerning Al and S redistribution, an increase located at the interface was generally observed in all mortars. In the case of CEM II, the limestone addition favoured the formation of ettringite at the expense of CmSAH as stated by Lothenbach et al. 2008. The Al diffusion from bentonite to mortars was due to the partial dissolution of *Al*-di-octahedral Mt. increasing after 18 months. These alterations have been reported at similar studied interfaces in larger scale experiments: clay/LpH, clay/CEM I and clay/CEM II (Jenni et al. 2014; Dauzères et al. 2016; Alonso et al. 2017; Mäder et al. 2017), where Al dissolved from bentonite precipitated as CASH and secondary ettringite.

Mg perturbations characterized the bentonite material at the CB interface. HpH CEM I, imposing the high pH gradient initially without calcite buffering, produced the highest perturbations compared to HpH

CEM II and LpH. The development of a calcite crust may limit transport by diffusion, favouring the high intensity of Mg phase accumulation on this clay side as observed by Lalan et al. 2016. Exchangeable Mg in Mt. was transferred to the pore solution, replaced by Ca and precipitated as hydroxide or hydrated silicates as discussed by Gaucher and Blanc (2006) and observed experimentally by Fernández et al. (2013) and Mäder et al. (2017).

LpH cement mortar induced the precipitation of brucite, which were not identified in the other cement mortar interfaces (CEM I and CEM II). Initially (6 months), there was not sufficient silica in solution to produce hydrated Mg-silicates, further identified at 18 months by SEM-EDX with honeycomb morphologies similar to those described in Cuevas et al. 2018, for the in situ 13-year-old concrete-bentonite FEBEX experiment. HpH experiments XRD θ/2θ scans in the bentonite interface (Fig. 4) reveal structures related to the presence of Mg minerals with 7.5 Å spacing (chlorite-like) not identified in the LpH bentonite interface. As far as the characteristic basal spacing of divalent exchanged Mt. (~14.8 Å) disappeared with time, the hypothesis of brucite intercalation, introducing disorder in the layer stacking in the interlayer structure of Mt. is coherent with the observed linear chemical compositional mixture of brucite and Mt. (Fig. S3). This fact was shown in previous studies (Fernández et al. 2013; Cuevas et al. 2018). However, clay mineral tri-octahedral sheet characteristic XRD reflections (06 l reflection at 1.53 Å) were also identified in HpH cement mortar experiments, in agreement with time-dependent compositions trending to saponitic chemical coordinates. The nature and proximity of these MSH to clay minerals structures and compositions was already discussed by many authors (Lothenbach et al. 2015; Roosz et al. 2015; Walling and Provis 2016; Lerouge et al. 2017). The Mg/Si ratios in CB bentonite surfaces (Table 2) matched with those characteristics of 2:1 clay minerals such as talc, saponite (Mg/Si: 0.75) sepiolite (Mg/Si: 0.67) and 1:1 serpentine group minerals (Mg/Si: 1.5), i.e., chrysotile. In any case, regardless of the cement type, the bentonite Mg-concentrated zone reaches 10% relative Mg at.% at 600 µm, smoothly reaching a homogeneous content in bentonite at 6.5% after 1500 µm. Relatively further distances (~4–5 mm) were observed after 13 years ageing of CEM II and FEBEX bentonite in the in situ FEBEX experiment (Fernández et al. 2017), where Mg at.% maximum was higher than those observed in Opalinus clay and closer to the Mg content showed in this study for CEM I (Fig. 2). FEBEX bentonite has far more exchangeable Mg than Opalinus clay, and if a high pH is maintained, the potential Mg precipitation under the exchanged Mg displacement process will be more important.

The chemical profiles developed in these small scale experiments reproduced those found in large- (in situ) to medium-scale (laboratory) long-term interfaces studied previously. Taking into account that the time scale ratio is approximately 10:1 between the two groups of scenarios (long-term: short-term) and that the thickness affected for chemical perturbation in larger experiments was 2–5 mm; it can be estimated that the comparable progression of the Mg or Ca chemical fronts represents in the worst (more rapid) case a 2:1 rate factor. Thus, considering the mineralogical and chemical heterogeneity of real-like interfaces in long-term experiments, this slow time advance is a good sign for EBS safety.

Apart from the mineralogical and chemical evidence for the geochemical perturbation, SSA changes could indicate the existence of new phase precipitation processes with small crystal sizes and high external SSA (Schoonheydt, 1995, Kaufhold et al. 2010) or the formation of cement clogging micropores (Lai and Krevor 2014). This may be the case, as far as bentonite experienced a decrease in SSA from 6 to 18 months in contact with CEM I, with more intense Mg-phase and calcite precipitation. In fact, these phenomena have been supported by reactive transport modelling that predicts a clogging process at concrete-clay interfaces (De Windt et al. 2008; Marty et al. 2009; Kosakowski and Berner, 2013).

The resistance of CEM II against the change in SSA was remarkable. The limestone addition left less room for calcite precipitation, and Al−Ca sulphates became stabilized, which limited the extent of dissolution-precipitation processes as was predicted by (Matschei et al. 2007). This agrees with the low sulphate concentration in the CEM II effluents collected at the compacted bentonite end compared with those in the other experiments. In any case, irrespective of the type of cement mortar, pH and dissolved silica were in the range of those characteristic of FEBEX bentonite being regulated by clay mineralogy and accessory constituents in accordance with the buffer capacity of FEBEX bentonite (Fernández et al. 2000; Lloret and Villar 2007). The presence of cristobalite and the pH buffer built by the presence of accessory calcite dissolution and the cation exchange equilibrium made these variables stable in the effluent collected at the bentonite end of the transport column.

5. Conclusions

Chemical reactivity at the cement-bentonite interface was assessed using three types of mortars and FEBEX compacted bentonite, infiltrating water from a granite source. The processes at the interface were analysed in terms of the spatial extension of the redistribution of Ca and Mg at both sides of the interface, as perturbation indicators. The high-pH mortars CEM I and CEM II developed a calcite rim (< 100 µm) at the mortar/compacted bentonite interface. There, near-neutral bentonite porewater, containing carbonate aqueous species, reacted within the generated pH gradient to precipitate the Ca ions leached from the mortars as $CaCO_3$. The Mg perturbation affected < 1500 µm thickness on the bentonite side and was less developed on the Low-pH and CEM II interfaces. However, Low-pH was the only mortar affected by the precipitation of Mg hydroxides and silicates within a 100 µm interface region.

Geochemical reactions observed at small scales of time and space (µm) in the present work are thought to have value to support modelling concepts of the behaviour of different materials that can configure the engineered barrier system. The presence of calcite in CEM II attenuated the reactivity in this High-pH cement mortar compared to CEM I, and exhibited less reactivity than Low-pH. Then, the combination of CEM II with bentonite seems to have advantages compared to the other two simulated mortars in Engineered Barrier System).

The geochemical reactions observed at small spatial scale (µm) and short-term (up to 18 months) are promising for the development of reaction concepts and support modelling in the future, thus offering a useful prospective to advance upscaling of the concrete-bentonite interface perturbations at long-term.

Declaration of Competing Interest

The authors declare that they have no known competing financial interests or personal relationships that could have appeared to influence the work reported in this paper.

Acknowledgements

It is important to us to pay credit to prof. Emilio Galán Huertos, for the motivation we had from him to work in the environmental application of clays during his fruitful life. We want also to acknowledge the comments of two anonymous referees and María Victoria Villar (editor) allowing us to improve the paper.

The experimental work was supported by funding from the European Union's Horizon 2020 Research and Training programme from EURATOM [H2020-NFRP 2014, 2015] under grant agreement n°662147; CEBAMA.

Appendix A. Supplementary data

Supplementary data to this article can be found online at https://

doi.org/10.1016/j.clay.2020.105672.

References

Nagra, 2002. Project Opalinus Clay—safety report. Demonstration of disposal feasibility for spent fuel, vitrified high-level waste and long-lived intermediate-level waste. In: Nagra Technical Report, 02–05, Nagra, Wettingen, Switzerland.

ECOCLAY-II, 2005. Effects of Cement on Clay Barrier Performance—Phase II, Final Report (Contract FIKW-CT-2000-00028). European Commission, Nuclear Science and Technology.

ANDRA, 2005. Dossier 2005 argile, synthesis: Evaluation of the feasibility of a geological repository in an argillaceous formation. In: Meuse/Haute-Marne site. ANDRA, Agence nationale pour la gestion des de'chets adioactifs, Paris, France.

Alonso, M.C., García Calvo, J.L., Cuevas, J., Turrero, M.J., Fernández, R., Torres, E., Ruiz, A.I., 2017. Interaction processes at the concrete-bentonite interface after 13 years of FEBEX-Plug operation. Part I: Concrete alteration. Physics Chem. Earth A/B/C 99, 38–48. https://doi.org/10.1016/j.pce.2017.03.008.

Bartier, D., Techer, I., Dauzères, A., Boulvais, P., Blanc-Valleron, M.-M., Cabrera, J., 2013. In situ investigations and reactive transport modelling of cement paste/argillite interactions in a saturated context and outside an excavated disturbed zone. Appl. Geochem. 31, 94–108. https://doi.org/10.1016/j.apgeochem.2012.12.009.

Baur, I., Keller, P., Mavrocordatos, D., Wehrli, B., Johnson, C.A., 2004. Dissolution-precipitation behaviour of ettringite, monosulfate, and calcium silicate hydrate. 34. pp. 341–348. https://doi.org/10.1016/j.cemconres.2003.08.016.

Blechschmidt, I., Vomvoris, S., 2010. 4 - Underground research facilities and rock laboratories for the development of geological disposal concepts and repository systems. In: Ahn, J., Apted, M.J. (Eds.), Geological Repository Systems for Safe Disposal of Spent Nuclear Fuels and Radioactive Waste. Woodhead Publishing, pp. 82–118.

Brindley, G.W., Brown, G., 1980. Crystal Structures of Clay Minerals and their X-Ray Identification. Mineralogical Society of Great Britain and Ireland.

Caballero, E., Jiménez de Cisneros, C., Huertas, F.J., Huertas, F., Pozzuoli, A., Linares, J., 2005. Bentonites from Cabo de Gata, Almería, Spain: a mineralogical and geochemical overview. Clay Miner. 40, 463–480. https://doi.org/10.1180/0009855054040184.

Cuevas, J., Ruiz, A.I., Fernández, R., Torres, E., Escribano, A., Regadío, M., Turrero, M.J., 2016. Lime mortar-compacted bentonite–magnetite interfaces: an experimental study focused on the understanding of the EBS long-term performance for high-level nuclear waste isolation DGR concept. 124-125, 79-93. https://doi.org/10.1016/j.clay.2016.01.043.

Cuevas, J., Ruiz, A., Fernández, R., González-Santamaría, D., Angulo, M., Ortega, A., Torres, E., Turrero, M., 2018. Authigenic clay minerals from interface reactions of concrete-clay engineered barriers: a new perspective on Mg-clays formation in alkaline environments. Minerals 8, 362. https://doi.org/10.3390/min8090362.

Dauzères, A., Le Bescop, P., Sardini, P., Cau Dit Coumes, C., 2010. Physico-chemical investigation of clayey/cement-based materials interaction in the context of geological waste disposal: Experimental approach and results. Cem. Concr. Res. 40, 1327–1340. https://doi.org/10.1016/j.cemconres.2010.03.015.

Dauzères, A., Le Bescop, P., Cau-Dit-Coumes, C., Brunet, F., Bourbon, X., Timonen, J., Voutilainen, M., Chomat, L., Sardini, P., 2014a. On the physico-chemical evolution of low-pH and CEM I cement pastes interacting with Callovo-Oxfordian pore water under its in situ CO2 partial pressure. Cem. Concr. Res. 58, 76–88. https://doi.org/10.1016/j.cemconres.2014.01.010.

Dauzères, A., Le Bescop, P., Cau-Dit-Coumes, C., Brunet, F., Bourbon, X., Timonen, J., Voutilainen, M., Chomat, L., Sardini, P., 2014b. On the physico-chemical evolution of low-pH and CEM I cement pastes interacting with Callovo-Oxfordian pore water under its in situ CO2 partial pressure. 58. pp. 76–88. https://doi.org/10.1016/j.cemconres.2014.01.010.

Dauzères, A., Achiedo, G., Nied, D., Bernard, E., Alahrache, S., Lothenbach, B., 2016. Magnesium perturbation in low-pH concretes placed in clayey environment—solid characterizations and modeling. Cem. Concr. Res. 79, 137–150. https://doi.org/10.1016/j.cemconres.2015.09.002.

De Windt, L., Marsal, F., Tinseau, E., Pellegrini, D., 2008. Reactive transport modeling of geochemical interactions at a concrete/argillite interface, Tournemire site (France). Physics Chem. Earth A/B/C 33, S295–S305. https://doi.org/10.1016/j.pce.2008.10.035.

Duro, L., Altmaier, M., Holt, E., Mader, U., Claret, F., Grambow, B., Idiart, A., Valls, A., Montoya, V., 2020. Contribution of the results of the CEBAMA project to decrease uncertainties in the Safety Case and Performance Assessment of radioactive waste repositories. Appl. Geochem. 112, 104479. https://doi.org/10.1016/j.apgeochem.2019.

ENRESA, 2006. FEBEX Project Final Report. Post-mortem bentonite analysis, Enresa publicación técnica 05–1/2006. Madrid. Spain. pp. 183.

Ewing, R.C., Whittleston, R.A., Yardley, B.W.J.E., 2016. Geological disposal of nuclear waste: a primer. Elements 12, 233–237. https://doi.org/10.2113/gselements.12.4.233.

Fernández, A.M., Cuevas, J., Rivas, P., 2000. Pore water chemistry of the febex bentonite. MRS Proc. 663, 573. https://doi.org/10.1557/PROC-663-573.

Fernández, R., Cuevas, J., Sánchez, L., De La Villa, R.V., Leguey, S., 2006. Reactivity of the cement–bentonite interface with alkaline solutions using transport cells. Appl. Geochem. 21, 977–992. https://doi.org/10.1016/j.apgeochem.2006.02.016.

Fernández, R., Vigil de la Villa, R., Ruiz, A.I., García, R., Cuevas, J., 2013. Precipitation of chlorite-like structures during OPC porewater diffusion through compacted bentonite at 90°C. Appl. Clay Sci. 83-84, 357–367. https://doi.org/10.1016/j.clay.2013.07.021.

Fernández, R., Ruiz, A.I., Cuevas, J., 2016. Formation of C-A-S-H phases from the interaction between concrete or cement and bentonite. 51. pp. 223–235. https://doi.org/10.1180/claymin.2016.051.2.09.

Fernández, R., Torres, E., Ruiz, A.I., Cuevas, J., Alonso, M.C., García Calvo, J.L., Rodríguez, E., Turrero, M.J., 2017. Interaction processes at the concrete-bentonite interface after 13 years of FEBEX-Plug operation. Part II: Bentonite contact. Physics Chem. Earth A/B/C 99, 49–63. https://doi.org/10.1016/j.pce.2017.01.009.

Florea, M.V.A., Brouwers, H.J.H., 2012. Chloride binding related to hydration products. Cem. Concr. Res. 42, 282–290. https://doi.org/10.1016/j.cemconres.2011.09.016.

Gaboreau, S., Prêt, D., Tinseau, E., Claret, F., Pellegrini, D., Stammose, D., 2011. 15 years of in situ cement–argillite interaction from Tournemire URL: Characterisation of the multi-scale spatial heterogeneities of pore space evolution. Appl. Geochem. 26, 2159–2171. https://doi.org/10.1016/j.apgeochem.2011.07.013.

Gaboreau, S., Lerouge, C., Dewonck, S., Linard, Y., Bourbon, X., Fialips, C., Mazurier, A., Prêt, D., Borschneck, D., Montouillout, V., 2012. In-situ interaction of cement paste and shotcrete with claystones in a deep disposal context. Am. J. Sci. 312, 314–356. https://doi.org/10.2475/03.2012.03.

Gaboreau, S., Prêt, D., Montouillout, V., Henocq, P., Robinet, J.-C., Tournassat, C., 2017. Quantitative mineralogical mapping of hydrated low pH concrete. Cem. Concr. Compos. 83, 360–373. https://doi.org/10.1016/j.cemconcomp.2017.08.003.

Galán, E., Alvarez, A., Esteban, M.A., 1986. Characterization and technical properties of a Mg-rich bentonite. Appl. Clay Sci. 1, 295–309. https://doi.org/10.1016/0169-1317(86)90006-2.

García Calvo, J.L., 2012. Desarrollo de materiales de construcción con cemento de bajo pH, compatibles con la barrera de ingeniería de un almacenamiento geológico profundo de residuos radiactivos de alta actividad. Universidad Autónoma de Madrid, Madrid, Spain.

García Calvo, J.L., Hidalgo, A., Alonso, C., Fernández Luco, L., 2010. Development of low-pH cementitious materials for HLRW repositories. 40. pp. 1290–1297. https://doi.org/10.1016/j.cemconres.2009.11.008.

Garralón, A., Gómez, P., Peña, J., Buil, B., Turrero, M., Torres, E., Sánchez, L., 2017. Hydrogeochemical Characterization of the Groundwater in the FEBEX Gallery. In: Nagra Arbeitsbericht, N. (Ed.), Nagra Arbeitsbericht, NAB.

Gaucher, E.C., Blanc, P., 2006. Cement/clay interactions–a review: experiments, natural analogues, and modeling. Waste Manag. 26, 776–788. https://doi.org/10.1016/j.wasman.2006.01.027.

Gómez-Espina, R., Villar, M.V., 2016. Time evolution of MX-80 bentonite geochemistry under thermo-hydraulic gradients. Clay Miner. 51, 145–160. https://doi.org/10.1180/claymin.2016.051.2.03.

González-Santamaría, D., Angulo, M., Ruiz, A., Fernández, R., Ortega, A., Cuevas, J., 2018. Low-pH cement mortar-bentonite perturbations in a small-scale pilot laboratory experiment. Clay Miner. 53, 237–254. https://doi.org/10.1180/clm.2018.16.

Grangeon, S., Claret, F., Linard, Y., Chiaberge, C., 2013. X-ray diffraction: a powerful tool to probe and understand the structure of nanocrystalline calcium silicate hydrates. Acta Crystallogr. Sect. B: Struct. Sci. Cryst. Eng. Mater. 69, 465–473. https://doi.org/10.1107/S2052519213021155.

Grangeon, S., Claret, F., Roosz, C., Sato, T., Gaboreau, S., Linard, Y., 2016. Structure of nanocrystalline calcium silicate hydrates: insights from X-ray diffraction, synchrotron X-ray absorption and nuclear magnetic resonance. J. Appl. Crystallogr. 49, 771–783. https://doi.org/10.1107/S1600576716003885.

Hawkins, P., Tennis, P.D., Detwiler, R.J., 1996. The Use of Limestone in Portland Cement: A State-of-the-Art Review. Portland Cement Association.

Huertas, F., Santiago, J.L., 1997. The FEBEX project. General overview. In: MRS Proceedings. 506. pp. 343. https://doi.org/10.1557/PROC-506-343.

Idiart, A., Laviña, M., Kosakowski, A., Cochepin, B., Meeussen, J.C.L., Javier Samper, J., Mon, A., Montoya, V., Munier, I., Poonoosamy, J., Montenegro, L., Deissmann, G., Rohmen, S., Damiani, L.H., Coene, E., Naves, A., 2020. Reactive transport modelling of a low-pH concrete / clay interface. Appl. Geochem. 115, 104562. https://doi.org/10.1016/j.apgeochem.2020.

Jackson, M.D., Chae, S.R., Mulcahy, S.R., Meral, C., Taylor, R., Li, P., Emwas, A.-H., Moon, J., Yoon, S., Vola, G., Wenk, H.-R., Monteiro, P.J.M., 2013. Unlocking the secrets of Al-tobermorite in Roman seawater concrete†. Am. Mineral. 98, 1669–1687. https://doi.org/10.2138/am.2013.4484.

Jenni, A., Mäder, U., Lerouge, C., Gaboreau, S., Schwyn, B., 2014. In situ interaction between different concretes and Opalinus Clay. Physics Chem. Earth A/B/C 70-71, 71–83. https://doi.org/10.1016/j.pce.2013.11.004.

Kaufhold, S., Dohrmann, R., 2016. Distinguishing between more and less suitable bentonites for storage of high-level radioactive waste. Clay Miner. 51, 289–302. https://doi.org/10.1180/claymin.2016.051.2.14.

Kaufhold, S., Dohrmann, R., Klinkenberg, M., Siegesmund, S., Ufer, K., 2010. N_2-BET specific surface area of bentonites. J. Colloid Interface Sci. 349, 275–282. https://doi.org/10.1016/j.jcis.2010.05.018.

Keusen, H.R., Ganguin, J., Schuler, P., Buletti, M., 1989. Grimsel Test Site: Geology, Switzerland. pp. 167.

Kosakowski, G., Berner, U., 2013. The evolution of clay rock/cement interfaces in a cementitious repository for low- and intermediate level radioactive waste. Physics Chem. Earth A/B/C 64, 65–86. https://doi.org/10.1016/j.pce.2013.01.003.

Lai, P., Krevor, S., 2014. Pore scale heterogeneity in the mineral distribution and surface area of Berea sandstone. Energy Procedia 63, 3582–3588. https://doi.org/10.1016/j.chemgeo.2015.07.010.

Lalan, P., Dauzères, A., De Windt, L., Bartier, D., Sammaljärvi, J., Barnichon, J.-D., Techer, I., Detilleux, V., 2016. Impact of a 70°C temperature on an ordinary Portland cement paste/claystone interface: an in situ experiment. Cem. Concr. Res. 83, 164–178. https://doi.org/10.1016/j.cemconres.2016.02.001.

Lerouge, C., Gaboreau, S., Grangeon, S., Claret, F., Warmont, F., Jenni, A., Cloet, V., Mäder, U., 2017. In situ interactions between Opalinus Clay and Low Alkali Concrete. Physics Chem. Earth A/B/C 99, 3–21. https://doi.org/10.1016/j.pce.2017.01.005.

Lloret, A., Villar, M.V., 2007. Advances on the knowledge of the thermo-hydro-mechanical behaviour of heavily compacted "FEBEX" bentonite. Physics Chem. Earth A/B/C 32, 701–715. https://doi.org/10.1016/j.pce.2006.03.002.

Lothenbach, B., Le Saout, G., Gallucci, E., Scrivener, K., 2008. Influence of limestone on the hydration of Portland cements. Cem. Concr. Res. 38, 848–860. https://doi.org/10.1016/j.cemconres.2008.01.002.

Lothenbach, B., Nied, D., L'Hôpital, E., Achiedo, G., Dauzères, A., 2015. Magnesium and calcium silicate hydrates. Cem. Concr. Res. 77, 60–68. https://doi.org/10.1016/j.cemconres.2015.06.007.

Mäder, U., Jenni, A., Lerouge, C., Gaboreau, S., Miyoshi, S., Kimura, Y., Cloet, V., Fukaya, M., Claret, F., Otake, T., Shibata, M., Lothenbach, B., 2017. 5-year chemico-physical evolution of concrete–claystone interfaces, Mont Terri rock laboratory (Switzerland). Swiss J. Geosci. 110, 307–327. https://doi.org/10.1007/s00015-016-0240-5.

Marty, N.C.M., Tournassat, C., Burnol, A., Giffaut, E., Gaucher, E.C., 2009. Influence of reaction kinetics and mesh refinement on the numerical modelling of concrete/clay interactions. J. Hydrol. 364, 58–72. https://doi.org/10.1016/j.jhydrol.2008.10.013.

Matschei, T., Lothenbach, B., Glasser, F.P., 2007. The role of calcium carbonate in cement hydration. Cem. Concr. Res. 37, 551–558. https://doi.org/10.1016/j.cemconres.2006.10.013.

Meunier, A., Velde, B., Griffault, L., 1998. The reactivity of bentonites: a review. An application to clay barrier stability for nuclear waste storage. Clay Miner. 33, 187–196. https://doi.org/10.1180/000985598545462.

Norris, S., 2017. Radioactive waste confinement: clays in natural and engineered barriers – introduction. Geol. Soc. Lond., Spec. Publ. 443, 1–8. https://doi.org/10.1144/SP443.26.

Pokrovsky, O.S., Schott, J., 2004. Experimental study of brucite dissolution and precipitation in aqueous solutions: surface speciation and chemical affinity control. Geochim. Cosmochim. Acta 68, 31–45. https://doi.org/10.1016/S0016-7037(03)00238-2.

Read, D., Glasser, F.P., Ayora, C., Guardiola, M., Sneyers, A., 2001. Mineralogical and microstructural changes accompanying the interaction of Boom Clay with ordinary Portland cement. Adv. Cem. Res. 13, 175–183. https://doi.org/10.1680/adcr.2001.13.4.175.

Roosz, C., Grangeon, S., Blanc, P., Montouillout, V., Lothenbach, B., Henocq, P., Giffaut, E., Vieillard, P., Gaboreau, S., 2015. Crystal structure of magnesium silicate hydrates (M-S-H): the relation with 2:1 Mg–Si phyllosilicates. Cem. Concr. Res. 73, 228–237. https://doi.org/10.1016/j.cemconres.2015.03.014.

Savage, D., 2014. An Assessment of the Impact of the Long Term Evolution of Engineered Structures on the Safety-Relevant Functions of the Bentonite Buffer in a HLW Repository. National Cooperative for the Disposal of Radioactive Waste.

Schneider, S., Mallants, D., Diederik, J., 2012. Determining hydraulic properties of concrete and mortar by inverse modelling. Mater. Res. Soc. Symp. Proc. 1475https://doi.org/10.1557/opl.2012.601. © 2012 Materials Research Society.

Schoonheydt, R., 1995. Clay mineral surfaces. In: Vaughan, D.J., Pattrick, R.A.D. (Eds.), Mineral Surfaces. Chapman & Hall The Mineralogical Society.

Shimbashi, M., Sato, T., Yamakawa, M., Fujii, N., Otake, T., 2018. Formation of Fe- and Mg-rich smectite under hyperalkaline conditions at Narra in Palawan, the Philippines. Minerals 8, 155. https://doi.org/10.3390/min8040155.

Torres, E., Turrero, M.J., Garralón, A., Cuevas, J., Fernández, R., Ortega, A., Ruíz, A.I., 2019. Stable isotopes applied to the study of the concrete/bentonite interaction in the FEBEX in situ test. Appl. Geochem. 100, 432–443. https://doi.org/10.1016/j.apgeochem.2018.12.017.

Tournassat, C., Steefel, C.I., Bourg, I.C., Bergaya, F., 2015. Natural and engineered clay barriers. In: Steefel, C.I., Bourg, I.C., Bergaya, F. (Eds.), Tournassat, C. Elsevier, Developments in Clay Science, pp. 1–4.

Trotignon, L., Devallois, V., Peycelon, H., Tiffreau, C., Bourbon, X., 2007. Predicting the long term durability of concrete engineered barriers in a geological repository for radioactive waste. Physics Chem. Earth A/B/C 32, 259–274. https://doi.org/10.1016/j.pce.2006.02.049.

Turrero, M.J., Cloet, V., 2017. FEBEX-DP Concrete ageing, concrete/bentonite and concrete/rock interaction analysis. In: Nagra (Ed.), NAB 16-18, 5430 Wettingen Switzerland, pp. 282.

Velde, B., 1985. Clay Minerals. Elsevier Science Pub. Co., Inc., New York, NY, United States.

Villar, M.V., Lloret, A., 2004. Influence of temperature on the hydro-mechanical behaviour of a compacted bentonite. Appl. Clay Sci. 26, 337–350. https://doi.org/10.1016/j.clay.2003.12.026.

Vuk, T., Tinta, V., Gabrovšek, R., Kaučič, V., 2001. The effects of limestone addition, clinker type and fineness on properties of Portland cement. Cem. Concr. Res. 31, 135–139. https://doi.org/10.1016/S0008-8846(00)00427-0.

Walling, S.A., Provis, J.L., 2016. Magnesia-based Cements: a Journey of 150 years, and Cements for the Future? Chem. Rev. 116, 4170–4204. https://doi.org/10.1021/acs.chemrev.5b00463.

Wang, J., 2014. On area-specific underground research laboratory for geological disposal of high-level radioactive waste in China. 6. pp. 99–104. https://doi.org/10.1016/j.jrmge.2014.01.002.

Webb, P.A., Orr, C., 1997. Analytical Methods in Fine Particle Technology. Micromeritics Instrument Corp.

Universidad Autónoma de Madrid

UNIVERSIDAD AUTÓNOMA DE MADRID
Facultad de Ciencias
Departamento de Geología y Geoquímica

Tesis Doctoral
Daniel González Santamaría
Madrid, 2020